Springer Proceedings in Earth and Environmental Sciences

Debabrata Mazumder *Editor*

Sustainable Advanced Technologies for Industrial Pollution Control

Proceedings of ATIPC 2022

Springer

Springer Proceedings in Earth and Environmental Sciences

The series Springer Proceedings in Earth and Environmental Sciences publishes proceedings from scholarly meetings and workshops on all topics related to Environmental and Earth Sciences and related sciences. This series constitutes a comprehensive up-to-date source of reference on a field or subfield of relevance in Earth and Environmental Sciences. In addition to an overall evaluation of the interest, scientific quality, and timeliness of each proposal at the hands of the publisher, individual contributions are all refereed to the high quality standards of leading journals in the field. Thus, this series provides the research community with well-edited, authoritative reports on developments in the most exciting areas of environmental sciences, earth sciences and related fields.

Debabrata Mazumder
Editor

Sustainable Advanced Technologies for Industrial Pollution Control

Proceedings of ATIPC 2022

Springer

Editor
Debabrata Mazumder
Department of Civil Engineering
Indian Institute of Engineering Science
and Technology, Shibpur
Howrah, India

ISSN 2524-342X ISSN 2524-3438 (electronic)
Springer Proceedings in Earth and Environmental Sciences
ISBN 978-3-031-37595-8 ISBN 978-3-031-37596-5 (eBook)
https://doi.org/10.1007/978-3-031-37596-5

This Springer imprint is published by the registered company Springer Nature Switzerland AG
The registered company address is: Gewerbestrasse 11, 6330 Cham, Switzerland

Dedicated to
All Scientist, Engineers and Technologists
Who devoted their life for the cause
of Sustainable Environment

Preface

Abatement of industrial pollution nowadays becomes a crucial issue for the survival of civilization. It not only induces environmental degradation but also imparts detrimental effects on human health as well as climate. With a view to combat this challenge, a number of innovative technologies have been developed, but few of them are found to be sustainable and globally acceptable. Under this background, all the advanced technologies for industrial pollution control should be economically viable as well as easily maintainable. To disseminate state-of-the-art knowledge on this issue among the relevant stakeholders, the Third Version of International Conference on Advanced Technologies for Industrial Pollution Control (ATIPC-2022) was organized by the Department of Civil Engineering, Indian Institute of Engineering Science and Technology, Shibpur (I.I.E.S.T., Shibpur), West Bengal, India, during December 21–23, 2022, in hybrid mode. The Springer Nature AG, Switzerland, a premier internationally acclaimed publishing organization, has agreed to bring in light one proceedings book of the above international conference. It is our great pleasure that "Sustainable Advanced Technologies of Industrial Pollution Control – Proceedings of ATIPC-2022" has been published with some selected and peer-reviewed full-length papers, presented in the above conference.

There are 7 thematic sections containing a total of 29 chapters on various aspects of advanced technologies for industrial pollution control. The thematic sections are spread over the titles – Water quality monitoring and treatment in industrial area; Industrial effluent treatment, reuse and conservation; Monitoring of industrial emission and control; Industrial solid waste management; Handling and disposal of hazardous waste; Case studies on industrial pollution control; and Innovative technologies in industrial waste management. Utmost care has been taken to include the chapters in their appropriate section as far as possible.

In spite of our best possible effort, some inadvertent errors might have occurred, for which we solicit comments from the readers.

We sincerely believe that the "Sustainable Advanced Technologies of Industrial Pollution Control – Proceedings of ATIPC-2022" would be gladly received by the scientific and engineering community and will definitely inspire us to bring more such proceedings book in future.

Howrah, India
31 March 2023

Debabrata Mazumder

Acknowledgement

At the outset, we express our deep sense of gratitude to Prof. Parthasarathi Chakrabarti, Honorable Director, IIEST, Shibpur, for his continuous encouragement in organizing ATIPC-2022. We are thankful to Prof. Ambarish Ghosh, Chairman, ATIPC-2022 and the Head, Department of Civil Engineering, IIEST, Shibpur, for his continuous support at every moment. Indeed, we would like to acknowledge our sincere thanks to all the faculty and staff members of the Civil Engineering Department for their instrumental role in materializing ATIPC-2022. In this context, we take opportunity to deeply acknowledge the sincere contribution of Dr. Chanchal Majumder and Dr. Asok Adak, two Co-Chairman of the above international conference. We would also like to extend our sincere thanks to Dr. Dipankana Bhattacharjee and Dr. Kaniska Biswas, two Co-ordinators of ATIPC-2022 for rendering their valuable service throughout the conference. We extend our heartiest thanks and sincere appreciation to Dr. Biswabandhu Chatterjee, a former Research Scholar of the Department of Civil Engineering, IIEST, Shibpur, for his dedicated assistance in processing of the manuscripts during pre-review stage.

We would like to extend our sincere thanks and indebtedness to the Members of the Editorial Board of Springer Nature AG for their consideration of the proposal for publication of the Proceedings Book of ATIPC-2022. In this context, we deeply acknowledge the kind motivation and co-operation of Dr. Zachary Romano and all his editorial team members, who have worked with great patients to bring out this Proceedings Book into light. We are also extremely thankful to Mr. Clement Wilson and his production team members for their relentless effort to make the present book with a perfect outlook.

We extend our sincere thanks and gratitude to all the Reviewers, who have contributed their best expertise in evaluating the technical papers. We cordially acknowledge, with heartiest admiration, the scholastic contribution of the authors, who promptly responded with their final articles.

At the last, but not the least, we sincerely acknowledge the contribution of all the stakeholders of the ATIPC-2022, whose names might have been omitted above inadvertently. It would have not been possible to publish the present proceedings book without their concerted effort and kind co-operation.

Prof. Debabrata Mazumder
Howrah, India
31 March 2023

Contents

Part IV Industrial Solid Waste Management

Part V Handling and Disposal of Hazardous Waste

Part VI Case Studies on Industrial Pollution Control

Part VII Innovative Technologies in Industrial Waste Management

Author Biography

Debabrata Mazumder did his Bachelor's and Master's degree in Civil Engineering from Jadavpur University in 1993 and 1996, respectively. He received his Ph.D. degree in Civil Engineering (Environmental Engineering Specialization) from Bengal Engineering and Science University, Shibpur (presently Indian Institute of Engineering Science and Technology, Shibpur) in 2004. He has a total 30 years of industrial, teaching and research experience. He published more than 150 technical papers and 7 book chapters in various national and international journals and conference proceedings. He has co-authored one reference book and edited one proceedings book in Springer Nature. He is the Member of American Water Works Association (AWWA) and the Member of International Water Association (IWA). He is also the Life Fellow of Institution of Engineers (India) (IE, India) and the Life Fellow of the Institution of Public Health Engineers (India) (IPHE, India). Apart from these, he is the Life Member of Indian Water Works Association (IWWA). He has supervised 6 Ph.D. (Engg.) and 25 M.Tech. thesis in the field of Environmental Engineering. He has also supervised more than 40 B.Tech. projects in the same field. He has adjudicated several Ph.D. thesis from a number of institutions of India and abroad.

He is as a Consultant in National Mission for Clean Ganga (NMCG) and National River Conservation Directorate (NRCD) under Ministry of Environment, Forests and Climate Change, Government of India. Apart from that he has been serving as a Principal

Consultant in several government and private organizations. He has been granted one Indian Patent titled "Shaft-type Hybrid Bioreactor," and other four filed Indian Patents are in final examination stage. He is presently serving as Professor of Civil Engineering Department, Indian Institute of Engineering Science and Technology, Shibpur. He was also the Dean (Students' Welfare) in the same institute for 3 years since 2019. He has been regularly organizing National Conference on "Sustainable Advanced Technologies for Environmental Management" (SATEM) as well as International Conference on "Advanced Technologies for Industrial Pollution Control" (ATIPC) from 2017 and 2018, respectively, in the Department of Civil Engineering, IIEST, Shibpur.

Part I
Water Quality Monitoring and Treatment in Industrial Area

Water Decontamination Through Thiamethoxam Removal Using DL-Menthol/Octanoic Acid Deep Eutectic Solvent: Molecular Dynamics Insights

Nabendu Paul and Tamal Banerjee

Abstract Deep eutectic solvents (DESs) have demonstrated the potential as an effective extractive medium in removing micropollutants from wastewater. Pesticide (thiamethoxam) extraction performance was investigated from aqueous feed using DL-menthol/octanoic acid (1:1) DES via molecular dynamics (MD) simulation. Structural properties such as radial distribution function (RDF) and spatial distribution function (SDF), interaction energy, and hydrogen bond analysis confirmed the relatively comparable interactions of thiamethoxam with DL-menthol, octanoic acid, and water. By measuring the mean square displacement (MSD), the dynamics of the pesticide and DES components in both phases (DES and aqueous) were studied. HOMO-LUMO analysis confirmed the stable hydrophobic DES formation. A closer three-dimensional density distribution of water around thiamethoxam was witnessed by the structural property analysis such as SDF. Extraction efficiency (45%), selectivity of the DES (60.25), and distribution ratio (0.81) related to thiamethoxam extraction were obtained by the MD simulation of the DES-water-thiamethoxam ternary system, and the results were in coherence with the experimental findings, and thus the viability of MD simulation in pharmaceutical extraction can be substantiated.

Keywords DES · Micropollutant · Pesticide · MD simulation · RDF · SDF · MSD · HOMO-LUMO · Extraction efficiency · Selectivity · Distribution ratio

1 Introduction

Water pollution is one of the most concerning environmental degradation processes across the globe [1]. Among various water pollutants, micropollutants such as pesticides, insecticides, pharmaceuticals, food additives and preservatives, and cosmetics are quite challenging to remove due to the scarcity of the nonspecific

N. Paul · T. Banerjee (✉)
Chemical Engineering Department, Indian Institute of Technology, Guwahati, Assam, India
e-mail: paul176107106@iitg.ac.in; tamalb@iitg.ac.in

D. Mazumder (ed.), *Sustainable Advanced Technologies for Industrial Pollution Control*, Springer Proceedings in Earth and Environmental Sciences,
https://doi.org/10.1007/978-3-031-37596-5_1

wastewater treatment processes [2–5]. Pesticides used in the agricultural lands can very easily leach to the groundwater as well as to the local drinking water facilities [6–7]. Traditional treatment processes (adsorption, chlorination, reverse osmosis, membrane distillation, and electrodialysis) have some drawbacks such as being nonspecific, expensive, and non-regenerative; high energy consumption; weak selectivity; and saturation of filter media [8, 9]. Thus, a task-specific pesticide decontamination technique should be devised for an efficient and economic water treatment process with less energy consumption [10, 11]. Liquid-liquid extraction (LLE) and microextraction (LLME) are quite effective and sustainable processes with enhanced biocompatibility and cost-effectiveness. Apart from the traditionally used solvents, ionic liquids (ILs) and deep eutectic solvents (DESs) have been quite effective in water cleaning [12, 13]. Hydrophobic DESs (HDESs) are exceptionally efficient in eradicating various micropollutants from water streams to prevent the evolution of the drug-resistant microorganisms. Various attractive qualities of DESs such as a low volatility, biodegradability (a large number of DESs), ease of preparation, non-toxicity (mostly), being economical, and reusability have highlighted them as the suitable candidate for extraction processes [13]. Finding an effective hydrophobic DES is a challenging task, and to associate that with a specific application requires a great deal of research and innovation. DL-menthol/fatty acid-based HDESs were effectively applied in extracting pesticides from water [14]. While the experimental studies get affected by various hindering factors, molecular simulation can be effective in understanding the systems and the inherent mechanism of the processes at a deep molecular as well as atomistic level [15–17]. Combining the experiments with molecular dynamics (MD), simulation can lead to futuristic approaches. The current work involves the study of pesticide (thiamethoxam) extraction from water by utilizing DL-menthol/octanoic acid (1:1) DES using MD simulation as a tool. The study was carried out at 298.15 K and 1 atm. The thiamethoxam molecules were initially placed in a separate phase along with water molecules and a separate phase containing DL-menthol, and octanoic acid was prepared for MD simulation. After that the trajectory was obtained at the end of simulation. We have studied the interaction energy, structural distribution function (RDF & SDF), hydrogen bond analysis, mean square displacement (MSD), and the HOMO-LUMO orbital analysis along with extraction properties to enhance the understanding of the system at atomistic level. The simulation results were validated by experimental data from literature substantiating the validity of the results. Figure 1 presents the optimized structures of the various components present in the system along with their required atomic notations.

2 Simulation Methodology

The simulation box was obtained in PACKMOL for the NAMD simulation with 100 molecules for each of DL-menthol and octanoic acid, 837 water molecules, and 5 molecules of thiamethoxam pesticide within the simulation box

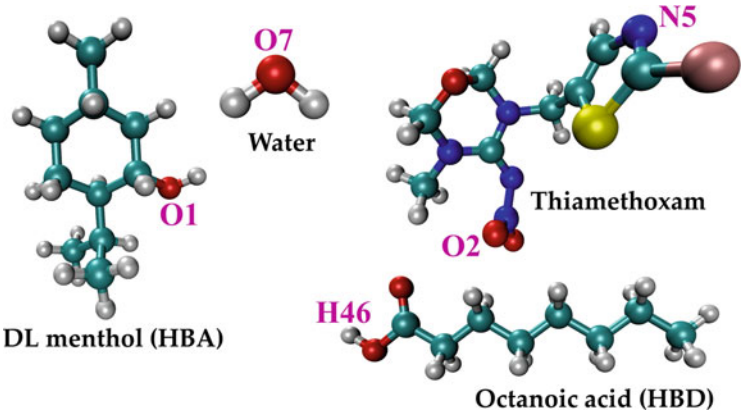

Fig. 1 Optimized structures of the components

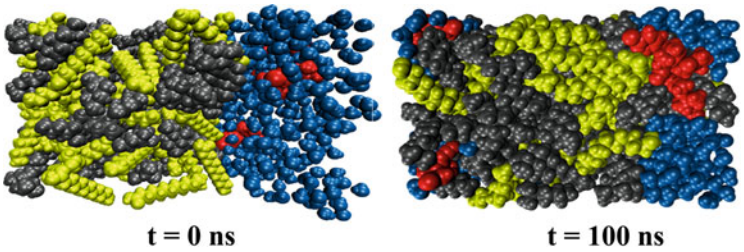

Fig. 2 Snapshots of thiamethoxam distribution in the system at 0 and 100 ns, respectively. [Color representation: DL-menthol (gray); octanoic acid (yellow); water (blue); and thiamethoxam (red)]

[18, 19]. GaussView 05 builder and Gaussian 09 for geometry optimization at the B3LYP/6-311G + (d,p) level of theory was carried out [20, 21]. AMBER Force field parameters were used [22]. MD simulation was carried out in NAMD 2.10 [19] for 6 ns minimization, 0.5 ns heating at 298.15 K, and 10 ns equilibration (NPT ensemble), followed by 100 ns production (NVT ensemble) at 25 °C and 1 atm pressure. The dimension of the system box was 29.02 Å × 17.41 Å × 17.41 Å. Periodic boundary condition (PBC) [23] was utilized. VMD 1.9.3 [24] and TRAVIS [25] packages were used for post-processing and visualizing the results.

3 Results and Discussion

Figure 2 presents the distribution of thiamethoxam molecules at the start (0 ns) and the end (100 ns) of the simulation. The two distinct phases (DES and water phase) were intact after the simulation. It clearly confirms the hydrophobic nature of the DL-menthol/octanoic acid DES. The presence of some of the thiamethoxam

Table 1 MD simulated extraction at 25 °C

System name	Extraction efficiency (% EE)	Distribution ratio	Selectivity (S)
DES + thiamethoxam + water	45	0.81	60.25

molecules can be observed in the DES phase after 100 ns production simulation suggesting the transport of the pesticide molecules towards the DES phase.

The extraction performance of the DES was assessed, and the MD simulated results were evaluated to compare with the experiments [14] as presented in Table 1. The extraction efficiency (%EE), distribution ratio, and selectivity (S) were calculated as per the following equations:

$$\%\mathrm{EE} = (C_0 - C)/C_0,$$

where C_0 and C are the concentrations of thiamethoxam in water phase before and after extraction, respectively.

$$S = \left(\beta_{\text{Thiamethoxam}} / \beta_{\text{Water}}\right),$$

where $\beta = \left(x^E_{\text{Thiamethoxam}} / x^R_{\text{Thiamethoxam}}\right)$, as $x^E_{\text{Thiamethoxam}}$ and $x^R_{\text{Thiamethoxam}}$ are the mole fractions of thiamethoxam in the DES-rich phase as well as the water-rich phase, respectively.

$$\text{Distribution ratio} = \left(\text{Concentration of thiamethoxam}_{\text{DES phase}} / \text{Concentration of thiamethoxam}_{\text{Water phase}}\right)$$

45% extraction efficiency was obtained by MD simulation, whereas the distribution ratio and selectivity of 0.81 and 60.25 were obtained, respectively. The values are in excellent agreements with the experiments [14]. The probable reason behind the lower % EE with the DES is the higher solubility of thiamethoxam in water as compared to the DES, and the same is reflected in the lower distribution ratio (0.81). A higher S value suggests a higher ability of the DES to extract thiamethoxam from aqueous environment. The value suggests that the DL-menthol/octanoic acid DES can be useful in extracting thiamethoxam. Other structural and dynamic properties can be informative in understanding the fundamentals of the extraction of thiamethoxam.

The non-bonded interaction energy obtained by MD simulation is presented in Fig. 3. It is very evident that DES integrity is well maintained with a higher interaction energy (−11.72 kcal/mol) even in the presence of water due to its hydrophobic nature.

Thiamethoxam displayed a higher interaction energy with menthol (−3.18 kcal/mol) and octanoic acid (−4.95 kcal/mol) as compared to water (−1.39 kcal/mol),

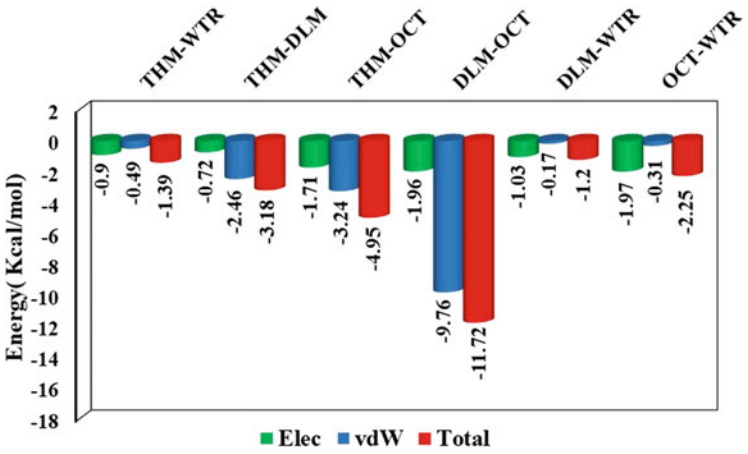

Fig. 3 Non-bonded interaction energy (THM thiamethoxam, DLM DL-menthol, OCT octanoic acid, and WTR water)

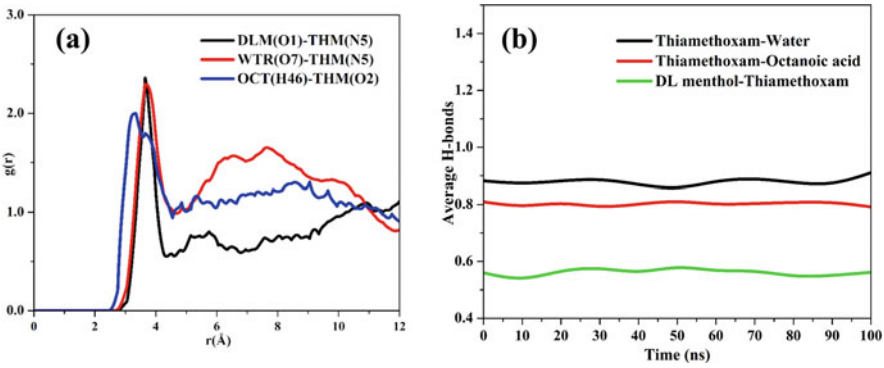

Fig. 4 (**a**) Radial distribution function (RDF); (**b**) average number of hydrogen bonds

suggesting favorable DES-thiamethoxam interaction. Another notable observation is that the electrostatic interaction (−0.9 kcal/mol) dominates over the van der Waals counterpart (−0.49 kcal/mol) for water-thiamethoxam contacts, whereas the opposite phenomena was witnessed for menthol-thiamethoxam and octanoic acid-thiamethoxam contacts. The presence of polar groups induced the electrostatic interactions with thiamethoxam. The DES-thiamethoxam and DES-water interactions are in comparable limits suggesting that thiamethoxam has favorable interactions with both water as well as DES.

The structural properties and the hydrogen bonding analysis can be explored to find the answers behind the lower extraction efficiency of thiamethoxam with DES as presented in Fig. 4. The RDF plot highlights the probabilistic distribution to find a molecule at a certain distance from another molecule in comparison with the ideal gas distribution. In Fig. 4a, it is clearly witnessed that water molecule and

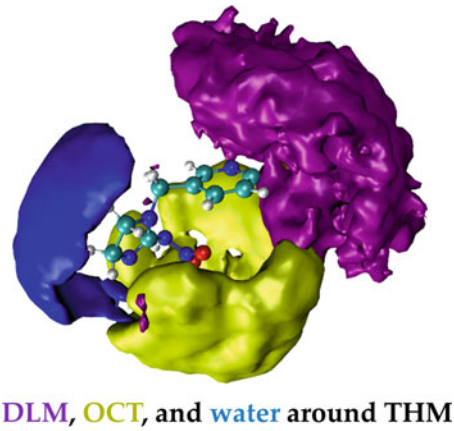

Fig. 5 Spatial distribution function (SDF); DLM (magenta), OCT (yellow), and water (blue) around THM

DL-menthol have a very similar distribution of molecules at 3.9 Å at the first solvation shell around a central thiamethoxam molecule. Octanoic acid showed slightly less g(r) value at a solvation shell around 3.1 Å. We can observe a second solvation shell of water-thiamethoxam at around 6–8 Å, suggesting a longer correlation between water and pesticide, thus affecting the extraction efficiency. Similarly, the average number of hydrogen bonding is higher for thiamethoxam-water as compared to thiamethoxam-DES. The higher hydrogen bonding of water and thiamethoxam is not only due to the multiple hydrogen bonding sites present in thiamethoxam and its affinity towards the polar water molecules that are present in higher number as compared to the DES molecules. Quantitatively, the hydrogen bonding follows the order: thiamethoxam-water (0.9) > thiamethoxam-octanoic acid (0.8) > thiamethoxam-DL menthol (0.57).

Spatial distribution function (SDF) is shown in Fig. 5 which is the three-dimensional density distribution of DES molecules and water around a reference thiamethoxam entity. These SDFs highlight the average distribution of density of the system components around a reference molecule (thiamethoxam). Thiamethoxam molecule was densely enclosed by water (blue contour lobe), octanoic acid (yellow color), and DL-menthol molecules (magenta color) (Fig. 5). The water molecules interacted with the polar side of the thiamethoxam molecule inducing a relatively stronger water-thiamethoxam interaction. The hydrophobic nature of the DES compels the components to interact with the opposite part of thiamethoxam, thus limiting the DES-pesticide contacts and affecting the extraction efficiency.

The transport properties were explored by the mean square displacement (MSD) plot through VMD using the diffusivity equation of Einstein. The equation defines the three-dimensional diffusivity of a compound where the bracketed part expresses the MSD of the species. Here, $r_i(0)$ represents the positions of i^{th} atom at times 0, and $r_i(t)$ represents the positions at time t, respectively.

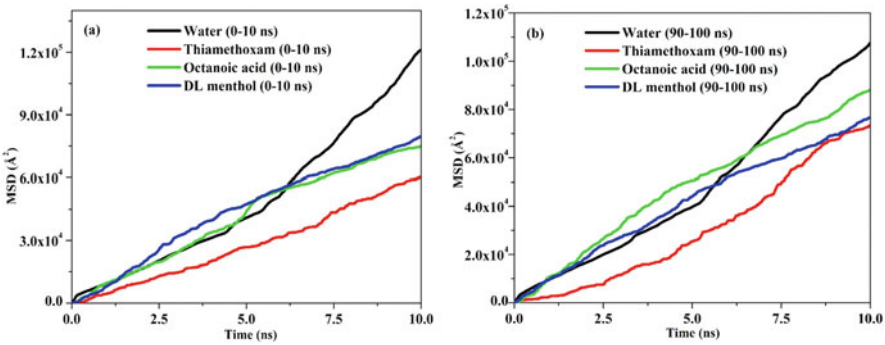

Fig. 6 MSD plot for DES-thiamethoxam-water system at (**a**) 0–10 and (**b**) 90–100 ns, respectively

$$D = \frac{1}{6} \lim_{t \to \infty} \frac{d}{dt} \left\langle \sum_{i=1}^{N} |r_i(t) - r_i(0)|^2 \right\rangle$$

The MSD plots were obtained for the start (0–10 ns) and the end (90–100 ns) of the simulation for a comparative transport property analysis as presented in Fig. 6a, b, respectively. The linear trend of the MSD curves was witnessed. The water curve was not affected throughout the simulation indicating a separate diffusive character possibly due to the presence of a separate DES phase that restricted its movement. Thus, the phase separation can be confirmed. When we compare the octanoic acid and DL-menthol curves at the start and at the end of the simulation, it can also clearly be stated that both the curves were almost of similar nature, suggesting the nonmiscible character of the DES. The DES-water noninteractive nature is the outcome of this MSD study. In case of the thiamethoxam MSD curves, the slope of the curve for 90–100 ns slightly increased after the halfway time mark, suggesting an increase in the diffusivity. It means that the thiamethoxam moiety moves through the two phases (DES and aqueous) based on the relative affinity of the pesticide towards that phase. Adding to that, the parallel nature of the water and thiamethoxam curve showed a comparable diffusive nature of both the species. Hence, DES having slightly less interaction with thiamethoxam as compared to water was unable to extract the pesticide aggressively from water.

We have obtained the stability of the DES and thiamethoxam via frontier molecular orbital (FMO) analysis as presented in Fig. 7. HOMO is the "highest occupied molecular orbital," and LUMO is the "lowest unoccupied molecular orbital." A larger HOMO-LUMO gap (ΔE) indicates a higher chemical stability and a lesser reactivity or polarizability. From Fig. 7, we can conclude that the DES based on DL-menthol and octanoic acid was having a higher ΔE (172.60 kcal/mol) value which indicates a relatively stable DES formation. This higher stability of the DES helps in maintaining its integrity around a water environment, thus behaving as a hydrophobic solvent. The ΔE value of thiamethoxam is less than that of the DES, indicating a slightly lower chemical stability of the former. This lower stability of the pesticide is indicative of a lower resistance to charge transfer.

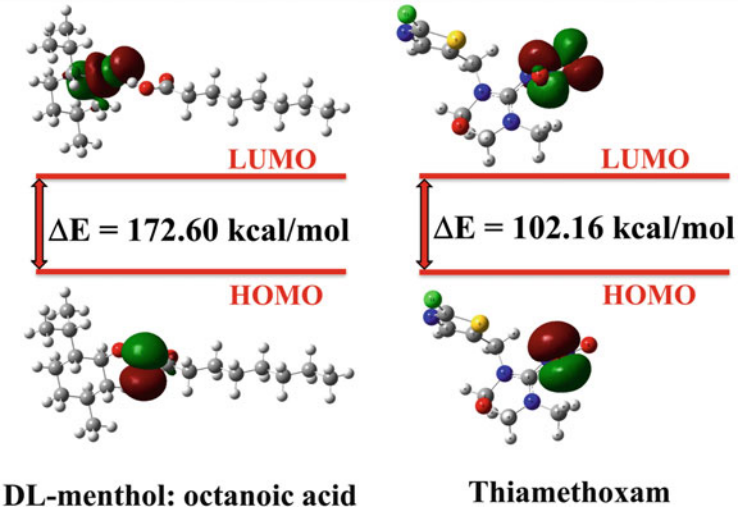

Fig. 7 HOMO-LUMO orbitals and the energy gap for DL-menthol/octanoic acid DES and thiamethoxam moiety

4 Conclusion

We have carried out NAMD simulation of thiamethoxam extraction from water with menthol/fatty acid DES. The interaction energy and RDF analysis highlight the stronger interaction of the pesticide molecule with DES components and the favorable structural arrangement of water molecules around thiamethoxam, suggesting a relatively higher water-pesticide interaction. A second solvation shell of water-thiamethoxam at around 6–8 Å in the RDF study suggests a higher correlation among the molecules of water and pesticide at a longer distance. Similar findings were obtained from hydrogen bonding analysis where the order was found to be as thiamethoxam-water (0.9) > thiamethoxam-octanoic acid (0.8) > thiamethoxam-DL menthol (0.57). The relatively stronger hydrogen bonding between water and thiamethoxam was supported by the SDF plots where a closer three-dimensional density distribution of water around thiamethoxam was witnessed. The MSD plots suggest similar transport property among the thiamethoxam and the water molecules leading to a lower extraction efficiency (45%) by the DES. A stable DES formation was established by the higher HOMO-LUMO gap of the DES, and the computational findings are in line with the experiments.

Acknowledgments The present research work is financially supported through the SPARC Programme (SPARC/2018-19/P848/SL) dated 15/03/2019.

References

1. N. Abdel-Raouf, A.A. Al-Homaidan, I.B.M. Ibraheem, Microalgae and wastewater treatment. Saudi J. Biol. Sci **19**, 257–275 (2012)
2. K. Fent, A.A. Weston, D. Caminada, Ecotoxicology of human pharmaceuticals. Aquat. Toxicol. **76**, 122–159 (2006)
3. Y. Luo, W. Guo, H.H. Ngo, L.D. Nghiem, F.I. Hai, J. Zhang, S. Liang, X.C. Wang, A review on the occurrence of micropollutants in the aquatic environment and their fate and removal during wastewater treatment. Sci. Total Environ. **473–474**, 619–641 (2014)
4. H. Sontheimer, H.J. Brauch, W. Kühn, Impact of different types of organic micropollutants present on sources of drinking water on the quality of drinking water. Sci. Total Environ. **47**, 27–44 (1985)
5. M.T. Amin, A.A. Alazba, U. Manzoor, A review of removal of pollutants from water/wastewater using different types of nanomaterials. Adv. Mater. Sci. Eng. **2014**, 24 (2014)
6. V.K. Gupta, B. Gupta, A. Rastogi, S. Agarwal, A. Nayak, Pesticides removal from waste water by activated carbon prepared from waste rubber tire. Water Res. **45**, 4047–4055 (2011)
7. M.P. Ormad, N. Miguel, A. Claver, J.M. Matesanz, J.L. Ovelleiro, Pesticides removal in the process of drinking water production. Chemosphere **71**, 97–106 (2008)
8. M.D. Dlugolecka, Alf-Goran, E. Plaza, Low concentrations of high priority' pharmaceutical and Personal Care Products (PPCPs); occurrence and removal at wastewater treatment plants. Vatten **62**, 139–148 (2006)
9. C. Rodriguez, P. Van Buynder, R. Lugg, P. Blair, B. Devine, A. Cook, P. Weinstein, Indirect potable reuse: A sustainable water supply alternative. Int. J. Environ. Res. Public Health **6**, 1174–1203 (2009)
10. M.O.F. Carballa, J.M. Lema, Removal of pharmaceuticals and personal care products (PPCPs) from municipal wastewaters by physico-chemical processes. Electron. J. Environ. Agric. Food Chem **2**, 309–313 (2003)
11. J.C. Lopez-Montilla, S. Pandey, D.O. Shah, O.D. Crisalle, Removal of non-ionic organic pollutants from water via liquideliquid extraction. Water Res. **39**, 1907–1913 (2005)
12. A. Paiva, R. Craveiro, I. Aroso, M. Martins, R.L. Reis, A.R.C. Duarte, Natural deep eutectic solvents - solvents for the 21st century. ACS Sustain. Chem. Eng. **2**, 1063–1071 (2014)
13. M. Francisco, A. van den Bruinhorst, M.C. Kroon, Low-Transition-Temperature Mixtures (LTTMs): A new generation of designer solvents. Angew. Chem. Int. Ed. **52**, 3074–3085 (2013)
14. C. Florindo, L.C. Branco, I.M. Marrucho, Development of hydrophobic deep eutectic solvents for extraction of pesticides from aqueous environments. Fluid Phase Equilib. **448**, 135–142 (2017)
15. D.M. Eike, E.J. Maginn, Atomistic simulation of solid-liquid coexistence for molecular systems: Application to triazole and benzene. J. Chem. Phys. **124**, 164503 (2006)
16. N. Paul, P.K. Naik, B.D. Ribeiro, P.S. Gooh Pattader, I.M. Marrucho, T. Banerjee, Molecular dynamics insights and water stability of hydrophobic deep eutectic solvents aided extraction of Nitenpyram from an aqueous environment. J. Phys. Chem. B **124**, 7405–7420 (2020)
17. N. Paul, T. Banerjee, Study on the extraction of Acetamiprid and Imidacloprid from an aqueous environment using menthol-based hydrophobic eutectic solvents: Quantum chemical and molecular dynamics insights. ACS Sustain. Chem. Eng. **10**, 4227–4246 (2022)
18. L. Martínez, R. Andrade, E.G. Birgin, J.M. Martínez, PACKMOL: A package for building initial configurations for molecular dynamics simulations. J. Comput. Chem. **30**(13), 2157–2164 (2009)
19. J.C. Phillips, R. Braun, W. Wang, J. Gumbart, E. Tajkhorshid, E. Villa, C. Chipot, R.D. Skeel, L. Kale, K. Schulten, Scalable molecular dynamics with NAMD. J. Comput. Chem. **26**(16), 1781–1802 (2005)

20. M. Frisch, G. Trucks, H. Schlegel, G. Scuseria, M. Robb, J. Cheeseman, G. Scalmani, V. Barone, B. Mennucci, G. Petersson, et al., *Gaussian 09 Program* (Gaussian, Inc., Wallingford, CT, 2009)
21. W. Kohn, A.D. Becke, R.G. Parr, Density functional theory of electronic structure. J. Phys. Chem. **100**(31), 12974–12980 (1996)
22. J. Wang, R.M. Wolf, J.W. Caldwell, P.A. Kollman, D.A. Case, Development and testing of a General Amber force field. J. Comput. Chem. **25**, 1157–1174 (2004)
23. M.P. Allen, D.J. Tildesley, *Computer Simulation of Liquids* (Oxford University Press, New York, 1989)
24. W. Humphrey, A. Dalke, K. Schulten, VMD: Visual molecular dynamics. J. Mol. Graph. **14**(1), 33–38 (1996)
25. M. Brehm, B. Kirchner, TRAVIS-a free analyzer and visualizer for Monte Carlo and molecular dynamics trajectories. J. Chem. Inf. Model. **51**(8), 2007–2023 (2011)

Methyl Red Dye Abatement from Aqueous Solution Using Calcium Ferrite and Manganese Ferrite Magnetic Nanocomposite: Kinetics and Isotherm Study

Subhajit Das, Sajal Rudra Paul, and Animesh Debnath

Abstract This study investigated the adsorptive efficacy of novel calcium ferrite ($CaFe_2O_4$) and manganese ferrite ($MnFe_2O_4$) magnetic nanocomposite (CF-MF-MNC) for the abatement of toxic methyl red (MR) dye from aqua medium. CF-MF-MNC was prepared by utilizing co-precipitation process, and the fabricated nanocomposite was characterized using various methods including XRD, SEM, VSM, FTIR, and BET analysis. The effects of different parameters like solution pH (2.0–10), nanocomposite dose (0.25–1.5 g/L), adsorption time (2–60 min), and initial concentration of pollutant (20–140 mg/L) were examined thoroughly. CF-MF-MNC exhibited 93.02% dye abatement from aqueous medium at solution pH 4.0, with 100 mg/L of initial MR concentration and 1.0 g/L of sorbent dose. The kinetics and isotherm study demonstrated that the MR dye sorption onto the surface of CF-MF-MNC obeys pseudo-second-order (PSO) kinetics and Langmuir isotherm, correspondingly. The adsorption-desorption experiment reveals that the synthesized CF-MF-MNC can be used successfully for the abatement of MR dye up to five regeneration cycles.

Keywords Adsorption · Co-precipitation method · Calcium ferrite · Isotherm study · Kinetic study · Manganese ferrite · MR dye · Nanocomposite · Regeneration study · Wastewater remediation

Symbols and Abbreviations

$CaFe_2O_4$	Calcium ferrite
$MnFe_2O_4$	Manganese ferrite
CF-MF-MNC	Calcium ferrite-manganese ferrite magnetic nanocomposite

S. Das (✉) · S. R. Paul · A. Debnath
Civil Engineering Department, National Institute of Technology Agartala, Jirania, West Tripura, India

D. Mazumder (ed.), *Sustainable Advanced Technologies for Industrial Pollution Control*, Springer Proceedings in Earth and Environmental Sciences,
https://doi.org/10.1007/978-3-031-37596-5_2

MR	Methyl red
XRD	X-ray diffraction
SEM	Scanning electron microscope
VSM	Vibrating-sample magnetometer
FTIR	Fourier transform infrared spectroscopy
BET	Brunauer-Emmett-Teller
PFO	Pseudo-first-order
PSO	Pseudo-second-order
$MgFe_2O_4$	Magnesium ferrite
HCl	Hydrochloric acid
NaOH	Sodium hydroxide
$FeCl_3.6H_2O$	Ferric chloride hexahydrate
$CaCl_2.2H_2O$	Calcium chloride dihydrate
$MnCl_2.4H_2O$	Manganese (II) chloride tetrahydrate
UV-VIS	Ultraviolet-visible
rpm	Revolutions per minute
H^+	Hydrogen ions
pH	Potential of hydrogen
OH^-	Hydroxide ions
MΩ-cm	Megaohms-cm

1 Introduction

One of the utmost pervasive environmental issues affecting people around the world is water contamination. Industrialization and urbanization were considered to be the fundamental for the fiscal development. Industrial sewage contains several poisonous and harmful pollutants [1]. Due to the rapid development of modern industries, dyes are considered as significant water pollutant [2], and their direct discharge into waterbodies causes various pollutions into the environment because most of the dyes are noxious and hazardous for animals and human health [3]. Dye-loaded effluents are mostly introduced into the environment by many industries, namely, paper, pharmaceutical, food, textile, paint, leather, and plastic industries [4]. The decontamination of dyes from industrial sewage is a challenging matter. Numerous methods such as coagulation-precipitation [5], membrane filtration, adsorption, photo-catalysis, membrane filtration [6], and biological methods [7] have been employed to decontaminate dyes from effluent. However, in current scenario adsorption technique is considered to be one of the superior practices because of its economic effectiveness, easy design, efficiency, and capability to treat different types of dyes [2]. Nowadays magnetic nanomaterials are considered to be affordable and efficient adsorbents for the abatement of dyes and various pollutants, because of their good saturation of magnetization, high surface area, and outstanding chemical stability and because it can be easily separated magnetically from the treated solution

[8]. In recent years, several reports were published for the sequestration of dyes and other pollutants from waste effluents by several magnetic nanoadsorbents ($MnFe_2O_4$, $CaFe_2O_4$, $MgFe_2O_4$, etc.) [9–11]. Katubi et al. examined the application of $MnFe_2O_4$ for the sequestration of lead ion and neutral red dye from aqueous solution as a promising material for water treatment [9]. Adarsha et al. investigated the application of $CaFe_2O_4$ for the abatement of Evans blue dye from aqua matrix, and they found it to be very effective [10]. It has also been observed that composite materials with two or more nanoparticles exhibit superior adsorptive performance as compared to single nanomaterials for wastewater remediation on the account of synergistic effects of parent materials available in the composite itself [12]. Al–Ti–Mn trimetal oxide used for the exclusion of arsenic from water and wastewater and stated that, the mixed phase has higher adsorption capacity as compared to single phases. Compared to various metallic ferrites, $CaFe_2O_4$ nanomaterials have a lesser saturation of magnetization and better biocompatibility which prevent particle accumulation and speed up the dispersal process in the aqua matrix [13], whereas $MnFe_2O_4$ nanomaterials gain specific attention due to its moderate biocompatibility and magnetocrystalline anisotropy [14]. Methyl red (MR) is an azo dye, one of the lethal and hazardous contaminants in water. Its direct discharge into the environment affects both water and human health [15]. It causes hypersensitivity of the skin and eyes and irritation of the digestive area when ingested [16]. Several studies were performed using magnetic materials like $MnFe_2O_4$, $CaFe_2O_4$, $MgFe_2O_4$, etc. to remove toxic dyes from water. But the application of mixed-phase magnetic nanocomposites for the abatement of dye, especially for MR dye removal, is scanty in literature. Thus, in this research, MR dye abatement was explored by utilizing the magnetic mixed phase of $CaFe_2O_4$ and $MnFe_2O_4$ composite as adsorbent.

In this study, CF-MF-MNC was fabricated, and its feasible application for the abatement of MR dye from aqua matrix was investigated. The effects of various experimental conditions were thoroughly examined, in order to examine the nature of adsorption of MR dye on CF-MF-MNC, and also the adsorption kinetics and isotherm, in order to discover the mechanism of sorption. The primary goal of the current endeavour was to find a solution to the issue of wastewater pollution from the dye sector.

2 Materials and Methods

2.1 Chemicals and Reagents

Methyl red (MR) dye ($C_{15}H_{15}N_3O_2$) powder (molecular weight 269.3 g/mol), HCl, NaOH pellets (>97%), $FeCl_3.6H_2O$, $CaCl_2.2H_2O$, and $MnCl_2.4H_2O$ were supplied by Merck (India). Ultrapure distilled water (Millipore, 18 MΩ.cm) was used for stock solution (500 mg/L) preparation of MR dye by mixing 500 mg of MR dye powder in 1000 mL of distilled water. Wastewater of different concentrations such

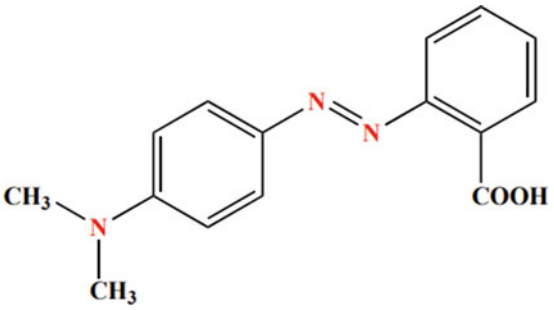

Fig. 1 MR dye molecular structure

as 10, 20, 40, 60, 80, 100, 120, and 140 mg/L were equipped from this stock by serial dilution with distilled water. The molecular structure of MR dye is shown in Fig. 1.

2.2 Preparation of CF-MF-MNC

An easy co-precipitation procedure was performed to construct CF-MF-MNC using $CaCl_2$, $MnCl_2$, and $FeCl_3$ as calcium, manganese, and iron sources, respectively, with molar ratio of Ca:Mn:Fe = 1:1:2. Firstly, a homogeneous NaOH (1.0 M) solution was prepared by liquifying NaOH pellets in distilled water. Subsequently three more standardized solutions (0.1 M $CaCl_2$, 0.2 M $MnCl_2$, and 0.2 M $FeCl_3$) were prepared by dissolving 27.75 g of $CaCl_2{\cdot}2H_2O$, 31.25 g of $MnCl_2.4H_2O$, and 81.25 g of $FeCl_3.6H_2O$ in three different Erlenmeyer flasks with distilled water. Afterwards, these prepared solutions were mixed slowly to NaOH solution and stirred @80 rpm for 20 min to form the uniform solution without any floc formation. Afterwards, the flocculate was separated from the solution using simple filtration and oven dried at 90 °C. This dried sample was continually washed with distilled water until the solution pH stabilized. Lastly, the cleaned samples were oxidized in furnace for 6.0 hours at 450 °C, taken out to cool, and ground accurately to attain the powder form of CF-MF-MNC.

2.3 Adsorption Experiment on Batch Mode

The experiment was performed with CF-MF-MNC as the adsorbent to estimate the impact of solution pH, nanocomposite dose, and MR dye initial concentration in batch adsorption technique. In this experiment, certain concentration of MR dye solution (100 mL) and predetermined amount of CF-MF-MNC were transferred in an Erlenmeyer flask (250 mL), and the sorbent assimilated dye was agitated (@80 rpm) at 25 ± 3 °C for 60 min sorption time. After that CF-MF-MNC adsorbent was separated magnetically from the dye-containing solution which was being treated. After the separation of sorbent, supernatant solution of residual MR dye

was analysed by UV-Vis spectrophotometer (Hach DR 5000) at 520 nm. The removal efficacy of MR dye ($R\%$) and the maximum sorption capacity (Q_e) were examined by Eqs. (1) and (2) correspondingly at different time intervals.

$$R(\%) = (C_o - C_e)/C_0 \times 100 \tag{1}$$

$$Q_e(\text{mg/g}) = (C_o - C_e) \times \ (V/m) \tag{2}$$

where

C_0 is the dye concentration at the initial condition (mg/L) and
C_e the dye concentration at the equilibrium condition (mg/L).
'V' and 'm' indicate volume (L) of dye solution and amount of the adsorbent (CF-MF-MNC) (g), correspondingly.

3 Results and Discussion

3.1 Characterization of CF-MF-MNC

The fabricated nanocomposite was characterized using numerous practices, namely, XRD, FEG-SEM, VSM, FTIR, and BET analysis. It is evident from the XRD pattern (Fig. 2a) that at diffraction angles (2θ) ranging from 25° to 65°, six diffraction peaks were seen. The peaks at 32.9, 43.07, and 45.38 are the result of diffraction from $CaFe_2O_4$ nanoparticles in the (320), (400), and (231) miller planes [17]. Remaining three peaks seen at 2θ value of 30.20, 35.50, and 56.50 are the result of $MnFe_2O_4$ nanoparticles which represent (220), (311), and (511) Miller planes, respectively [18]. Henceforth, XRD pattern depicts the successful formation of CF-MF-MNC magnetic nanocomposite. To check the stability of the adsorbent after the MR dye adsorption, XRD pattern of MR dye-loaded CF-MF-MNC was also recorded (Fig. 2a). It was revealed that there is no significant alteration in the XRD pattern even after the adsorption of MR dye, indicating good stability of CF-MF-MNC. FEG-SEM image analysis was used to do the morphological study of the adsorbent (Fig. 2b). FEG-SEM image clearly shows spherical grains with diameter ranging from 20 to 50 nm. The super-paramagnetic nature of CF-MF-MNC was assured by the VSM study (Fig. 2c), indicating a higher saturation of magnetization (Ms) of 37.05 emu/g and a coercivity (H_c) of 226.9 O_e at 25 ± 3 °C in the magnetic field (±15 KO_e). The simple separation of CF-MF-MNC from the treated dye-containing solution is made possible by the outstanding magnetic property seen in the VSM investigation. FTIR spectroscopy examination was carried out to investigate the existence of active surface bonding on the nanocomposite surface. FTIR spectrum (Fig. 2d) of CF-MF-MNC reveals numerous significant peaks that are related to different surface bonds of the adsorbent. The O-H stretch and twist vibrations due to the existence of moisture on the composite surface caused the peaks to appear around 3443 and 1632 cm^{-1}. Ca-Fe metallic vibrations caused the peak to appear at

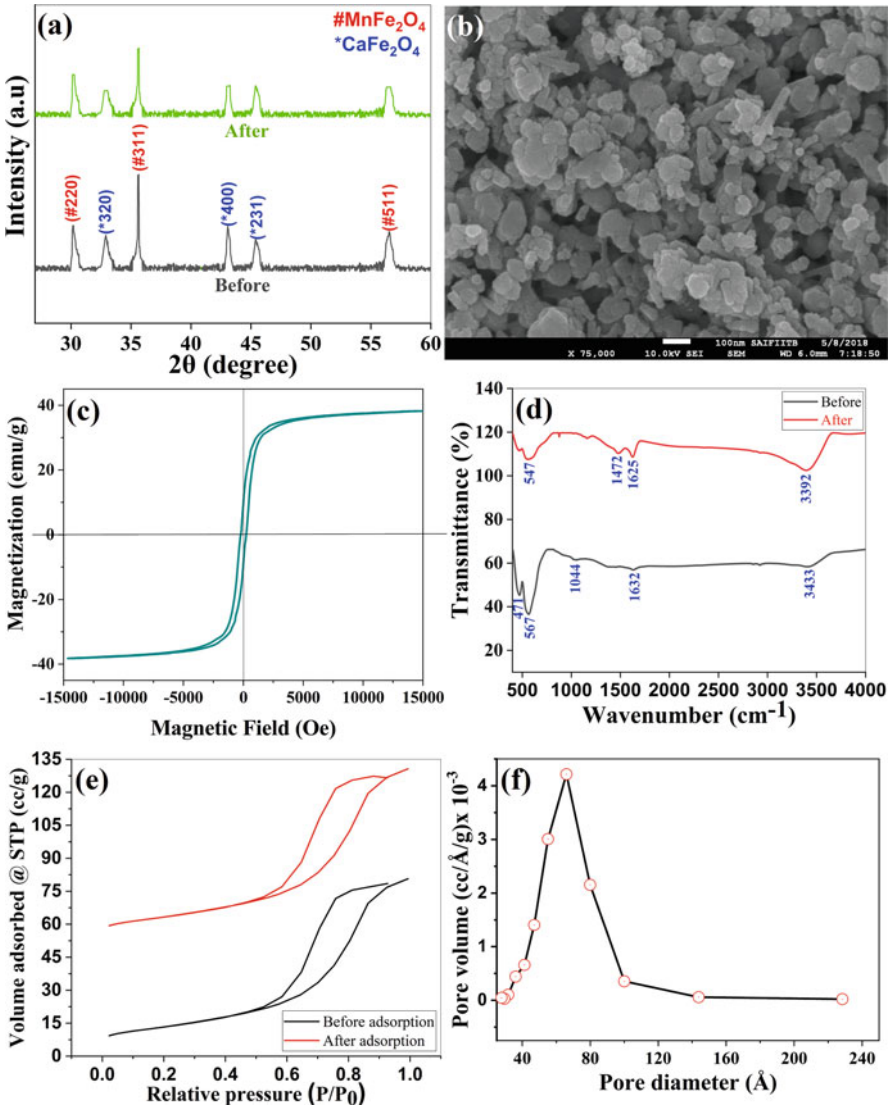

Fig. 2 (**a**) XRD patterns of CF-MF-MNC (before and after adsorption); (**b**) FEG-SEM image; (**c**) VSM study at room temperature; (**d**) FTIR spectra of CF-MF-MNC (before and after adsorption); (**e**) isotherm plot of N_2 adsorption-desorption (before and after adsorption); and (**f**) pore size dispersal plot of CF-MF-MNC

1044 cm^{-1}. Owing to the presence of metallic oxygen vibrational interactions between Ca-O and Mn-O in $CaFe_2O_4$ and $MnFe_2O_4$ nanomaterials, correspondingly, two additional significant peaks were seen at 567 and 471 cm^{-1}. The functional groups of post-sorption of MR dye were affected by wavelength shifts, and band desertions, as depicted from the FTIR spectrum (Fig. 2d) of MR dye-loaded CF-MF-

MNC [19]. Utilizing a surface area analyser device, the N_2 adsorption-desorption isotherm (Fig. 2e) was analysed to investigate the surface area of CF-MF-MNC. The material was outgassed for five hours at 200 °C temperature before analysis. The pore dispersal of CF-MF-MNC is shown in Fig. 2f. BET analysis revealed that the CF-MF-MNC exhibits a good surface area of 47.67 m^2/g with a total pore volume of 0.121 cc/g and a mean pore diameter of 7.2 nm. The surface area of the CF-MF-MNC was also analysed after the MR dye adsorption (Fig. 2e), indicating a marginal reduction in the surface area (40.51 m^2/g).

3.2 Effect of Solution pH

The solution pH influences the sorbent surface charge, degree of ionization of organic contaminants, and functional group separation on effective places of the sorbent along with dye formation. The sorption experiments of MR dye on CF-MF-MNC were examined at solution pH from 2.0 to 10. The result shows that removal efficacy of MR dye was almost the same (95.67–93.02%) in the pH from 2.0 to 4.0; thereafter, with the upsurge of pH (5.0–10.0), a decreasing trend (60.13–14.83%) was observed in the removal efficacy (Fig. 3a). At extremely acidic pH, the active functional group of nanocomposite (CF-MF-MNC) surface is simply protonated which causes electrostatic attraction between protonated CF-MF-MNC surface and anionic MR dye. Meanwhile, MR dye adsorption decreases with further increase of pH because at a high pH, OH^- ions replace the H^+ ions from the adsorbent surface, which reduces the electrostatic attractive force between CF-MF-MNC and MR dye [20]. Based on the results, the optimum MR dye abatement was seen at solution pH 4.0 with a maximum removal of 93.02% within 60 minutes of stirring.

3.3 Effect of Sorption Time and MR Initial Concentration

The impacts of the initial concentration of MR dye (20–140 mg/L) and sorption time (up to 60 min) were also examined, with constant CF-MF-MNC dose (1.0 g/L) and MR dye solution pH (4.0). The results clearly show that (Fig. 3b) the maximum dye abatement was attained (initial concentration: 20–120 mg/L) within the initial 10–30 minutes of contact between the dye and the adsorbent; afterwards, the process reached the equilibrium position. At the same time CF-MF-MNC nanocomposite has shown a higher removal efficacy at a lower concentration of MR dye as compared to a higher one. At MR concentration of 20 mg/L, the abatement was 96.89%, whereas at a higher concentration (140 mg/L), the removal dropped to 75.36%. The drop in removal efficacy with the increment of MR concentration was due to the nonavailability of requisite adsorbent active surface at a given dose of CF-MF-MNC [21].

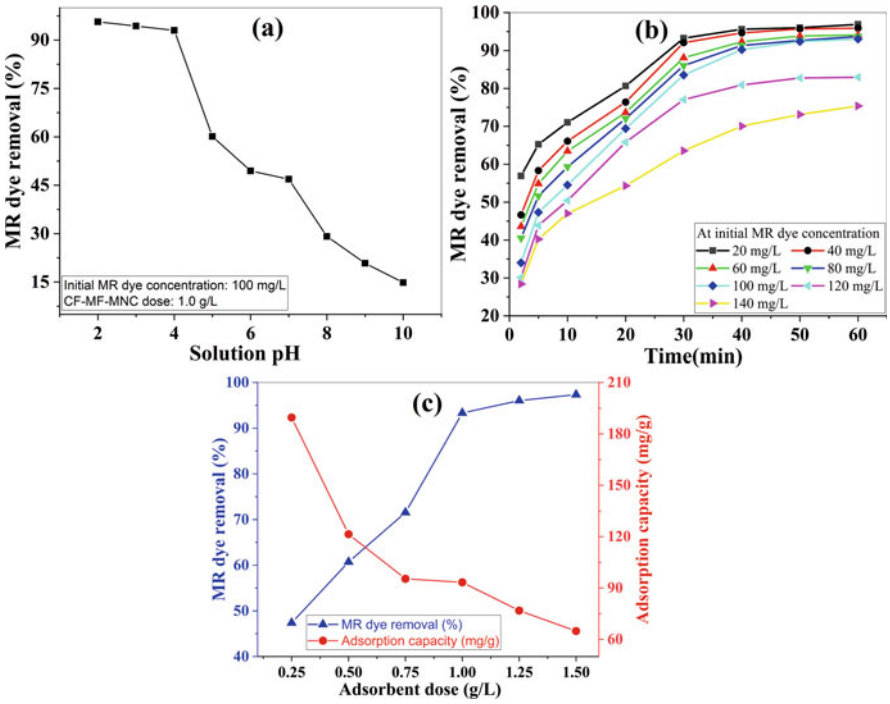

Fig. 3 Influence of (**a**) solution pH of MR, (**b**) initial concentration of MR dye (mg/L) and sorption time (min), and (**c**) nanocomposite dose (g/L) on MR dye abatement efficacy of CF-MF-MNC

3.4 Effect of Sorbent Dose

The impact of nanocomposite dose (0.25–1.5 g/L) on MR dye abatement was examined at solution pH 4.0, 100 mg/L of initial concentration of MR dye, and sorption time 60 min. The results clearly show that the increment of CF-MF-MNC dose (0.25–1.0 g/L) increases the MR dye abatement efficacy from 47.38% to 93.32%; this may be due to the higher-energy active places present on CF-MF-MNC surface, and after that no substantial enhancement was perceived in the elimination of MR dye. Further increase in adsorbent dose might have caused accumulation of particles in the solution and thus yielded to reduction in surface area, which ultimately results in the reduction of adsorption efficacy. It is also observed from Fig. 3c that adsorption capacity of CF-MF-MNC decreases (189.52–64.89 mg/g) with the increment of CF-MF-MNC dose (0.25–1.50 g/L). The decreases of sorption capability at a higher CF-MF-MNC dose may be due to the limited amount of MR dye molecule extant in the solution [22].

3.5 Adsorption Kinetic Study

The kinetics analysis leads to the exploration of the mechanism of sorption on the basis of investigational results. These analyses are important to design any adsorption arrangements. In this study, pseudo-first-order (PFO), pseudo-second-order (PSO), and Elovich models were utilized to reveal the sorption kinetics. This analysis was carried out with constant CF-MF-MNC dose (1.0 g/L), with solution pH of 4.0, and with varying initial concentrations (20–140 mg/L) of MR dye. The linear equations and various parameters related to each considered model are shown in Table 1. Correlation coefficient signifies that MR dye sorption onto CF-MF-MNC best represents PSO (Fig. 4a) kinetic model as compared to the other two kinetic models, because the values of R^2 for PSO model are higher than the other models. From the above results, it is distinct that MR dye sorption onto the surface of CF-MF-MNC is mostly because of the chemical sorption that occurs due to the distribution and exchange of electrons of anionic groups of MR and the positive charge of CF-MF-MNC surface [23].

3.6 Adsorption Isotherm Study

Isotherm models have a broader application to comprehend and design the mechanism of interface between adsorbate and adsorbent at the state of equilibrium. The sorption equilibrium of MR on CF-MF-MNC was considered by Langmuir and Freundlich isotherm models. These models were being used with constant dose (1.0 g/L) of CF-MF-MNC, solution pH of 4.0, and sorption time up to 60 min with varying initial MR concentrations (20–140 mg/L). The experimental values of these two isotherm models are assimilated in Table 2. It is clearly revealed in Table 2 that the Langmuir model well fitted with a higher R^2 value (0.999) as compared to the Freundlich isotherm model (R^2: 0.777) and well described the MR dye uptake progression on CF-MF-MNC surface (Fig. 4b). The Langmuir analysis depicts monolayer dispersal of MR dye molecules on homogeneous CF-MF-MNC surface [4]. The sorption capability evaluated from Langmuir modelling is observed to be 109.89 mg/g. The performance of the prepared adsorbent (CF-MF-MNC) for MR dye removal was compared with other research in relation to contact time (min) and sorption capability (mg/g) which is shown in Table 3. It has been shown that CF-MF-MNC has a sorption amount of 109.89 mg/g for MR dye that is either higher or comparable to that of other adsorbents used for MR abatement.

Table 1 PFO, PSO, and Elovich kinetic rate constants for the sorption of MR dye onto CF-MF-MNC

Kinetic model	Parameters	Initial MR conc. (mg/L)						
		20	40	60	80	100	120	140
PFO $\ln(Q_e - Q_t) = \ln Q_e - (K_f/2.303)t$	Q_e (mg/g)	12.83	22.24	52.72	70.67	81.26	79.29	62.63
	R^2	0.959	0.973	0.976	0.977	0.977	0.981	0.987
PSO $t/Q_t = 1/K_s Q_e^2 + (1/Q_e)\ t$	Q_e (mg/g)	20.70	41.67	62.89	84.75	104.17	120.48	114.94
	R^2	0.997	0.998	0.998	0.997	0.998	0.998	0.997
Elovich $Q_t = (1/\beta)\ \ln\alpha\beta + (1/\beta)\ \ln t$	α	95.53	66.22	66.14	64.85	54.26	68.41	81.97
	β	0.389	0.171	0.108	0.076	0.057	0.052	0.056
	R^2	0.956	0.966	0.977	0.979	0.982	0.993	0.995
Experimental value	Q_e (mg/g)	19.80	39.72	59.49	79.312	97.05	113.56	111.22

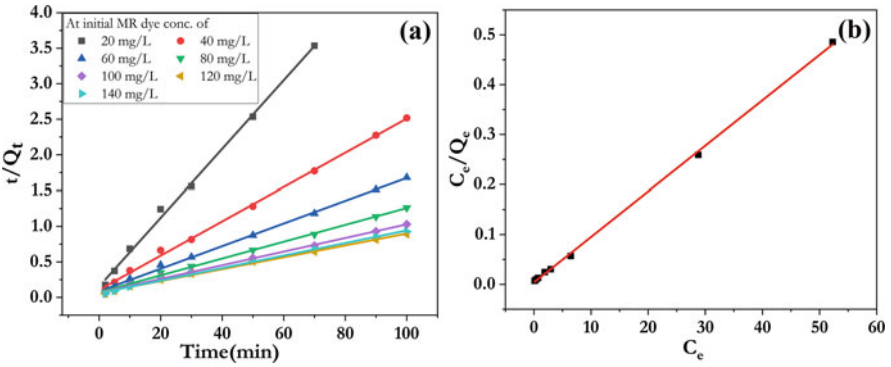

Fig. 4 Plot of (**a**) PSO kinetic model and (**b**) Langmuir isotherm model for MR dye sorption on $CaFe_2O_4$-$MnFe_2O_4$-MNC

Table 2 Isotherm modelling results of MR dye sorption on CF-MF-MNC

Isotherm model	Parameters		
Langmuir: $C_e/Q_e = 1/bQ_m + C_e/Q_m$	Q_m (mg/g)	b (L/mg)	R^2
	109.89	2.33	0.999
Freundlich: $\ln Q_e = \ln K_f + (1/n) \ln C_e$	n	k_f (mg/g)	R^2
	3.77	53.09	0.777

Table 3 Comparison of CF-MF-MNC for sorption of MR dye in relation to sorption time (min) and sorption capacity (mg/g) with other published adsorbents

Adsorbent	Equilibrium contact time (min)	Uptake capacity (mg/g)	Reference
Fe_3O_4@SiO_2@NH_2 nanocomposite	–	125	[24]
α-MnO_2 nanoparticles (NPs)	–	74.02	[25]
UiO-66 metal-organic frameworks (MOFs)	120	384	[26]
NaAlg-g-CHIT/nZVI	60	72	[27]
Na_2CO_3-treated jute fibre	180	32.11	[28]
CF-MF-MNC	100	109.89	Present study

3.7 Regeneration Study

The regeneration tests were carried out up to five successive cycles in order to evaluate the reutilization and recycling of CF-MF-MNC for MR dye sorption. For this investigation, MR dye of 100 mg/L and 1.0 g/L dose of CF-MF-MNC were used, and the combination was agitated for 60 min at MR solution pH 4.0 to promote adsorption, and a 93.02% dye removal was observed. CF-MF-MNC loaded with MR dye was combined with 50 mL of NaOH solution (1.0 M), and the combination was agitated for 60 min for desorption of MR dye from CF-MF-MNC surface. Following

the desorption of dye, the CF-MF-MNC was repeatedly rinsed with deionized water before being separated by an external magnetic field. The cleaned CF-MF-MNC was then dried and again utilized for the sorption of MR dye. The same procedure was followed up to five cycles, and it was observed that there was no significant drop in the MR dye elimination efficiency, and 83.62% of MR dye removal was detected in the fifth cycle. Only a 10% drop in dye removal efficiency was observed when CF-MF-MNC was used after five regeneration cycles, which makes the prepared composite a reusable material.

4 Conclusion

CF-MF-MNC adsorbent was successfully synthesized by chemical precipitation method and was used for the abatement of MR dye from aqua solution. CF-MF-MNC was quite efficient for MR dye subtraction, and ~93% MR dye amputation was obtained. The adsorption process was mainly administrated by chemisorption progression, and the loading pattern of the MR on CF-MF-MNC was monolayer in nature. The synthesized CF-MF-MNC has shown an optimum dye uptake capability of ~110 mg/g, which is either superior or equivalent to other stated adsorbents for MR dye. On account of high reusability, good uptake capability, and easy fabrication process, the produced magnetic nanocomposite (CF-MF-MNC) can be considered as an effective sorbent for the sequestration of MR dye-loaded wastewater. This research can be extended in continuous mode also with fixed and variable column depth in order to develop the scale-up design of a pilot plant for the treatment of dye-laden wastewater.

References

1. T.K. Mahto, A.R. Chowdhuri, S.K. Sahu, Polyaniline-functionalized magnetic nanoparticles for the removal of toxic dye from wastewater. J. Appl. Polym. Sci. **131**, 40840 (2014)
2. M.R. Patil, V.S. Shrivastava, Adsorption removal of carcinogenic acid violet19 dye from aqueous solution by polyaniline-Fe2O3 magnetic nano-composite. J.Mater. Environ. Sci. **6**(1), 11–21 (2014)
3. R.D. Ambashta, M. Sillanpaa, Water purification using magnetic assistance: A review. J. Hazard. Mater. **180**, 38–49 (2010)
4. C. Wang, C. Feng, Y. Gao, X. Ma, Q. Wu, Z. Wang, Preparation of a graphene-based magnetic nanocomposite for the removal of an organic dye from aqueous solution. Chem. Eng. J. **173**, 92–97 (2011)
5. A. Debnath, R. Thapa, K.K. Chattopadhyay, B. Saha, Spectroscopic studies on interaction of Congo Red with ferric chloride in aqueous medium for wastewater treatment. Sep. Sci. Technol. **50**, 1684–1688 (2015)
6. E. Sahinkaya, A. Sahin, A. Yurtsever, M. Kitis, Concentrate minimization and water recovery enhancement using pellet precipitator in a reverse osmosis process treating textile wastewater. J. Environ. Manag. **222**, 420–427 (2018)

7. H. Singh, G. Chauhan, A.K. Jain, S.K. Sharma, Adsorptive potential of agricultural wastes for removal of dyes from aqueous solutions. J. Environ. Chem. Eng. **5**, 122–135 (2017)
8. L.A. Kafshgari, M. Ghorbani, A. Azizi, Synthesis and characterization of manganese ferrite nanostructure by coPrecipitation, Sol- Gel, and hydrothermal methods. Part. Sci. Technol. **37**, 904–910 (2018)
9. K.M.M. Katubi, N.S. Alsaiari, F.M. Alzahrani, S.M. Siddeeg, M.A. Tahoon, Synthesis of manganese ferrite/graphene oxide magnetic nanocomposite for pollutants removal from water. MDPI **9**, 589 (2021)
10. J.R. Adarsha, T.N. Ravishankar, C.R. Manjunatha, T. Ramakrishnappa, Green synthesis of nanostructured calcium ferrite particles and its application to photocatalytic degradation of Evans blue dye. Materialstoday: Proc **49**, 777–788 (2021)
11. M. Adel, M.A. Ahmed, A.A. Mohamed, Effective removal of indigo carmine dye from wastewaters by adsorption onto mesoporous magnesium ferrite nanoparticles. Environ. Nanotechnol. Monitor. Manag **16**, 100550 (2021)
12. D.N. Thanh, Z. Bastl, K. Černá, P. Ulbrich, J. Lederer, Amorphous nanosized Al–Ti– Mn trimetal hydrous oxides: Synthesis, characterization and enhanced performance in arsenic removal. RSC Adv **6,** 100732–100742 (2016)
13. S. An, X. Liu, L. Yang, L. Zhang, Enhancement removal of crystal violet dye using magnetic calcium ferrite nanoparticle: Study in single- and binary-solute systems. Chem. Eng. Res. Des. **94**, 726–735 (2015)
14. A. Asfaram, M. Ghaedi, K. Dashtian, G.R. Ghezelbash, Preparation and characterization of $Mn_{0.4}Zn_{0.6}Fe_2O_4$ nanoparticles supported on dead cells of Yarrowia lipolytica as a novel and efficient adsorbent/biosorbent composite for the removal of Azo food dyes: Central composite design optimization study. ACS Sustain. Chem. Eng **6**, 4549–4563 (2018)
15. M.A. Ahmad, N. Ahmad, O.S. Bello, Modified durian seed as adsorbent for the removal of methyl red dye from aqueous solutions. Appl Water Sci **5**, 407–423 (2014)
16. A. Bafana, S.S. Devi, T. Chakrabarti, Azo dyes: Past, present and the future. Environ. Rev. **19**, 350 (2011)
17. N.H. Sulaiman, M.J. Ghazali, B.Y. Majlis, J. Yunas, M. Razali, Superparamagnetic calcium ferrite nanoparticles synthesized using a simple sol-gel method for targeted drug delivery. Biomed. Mater. Eng. **26**, 103–S110 (2015)
18. R.H. Vignesh, K.V. Sankar, S. Amaresh, Y.S. Lee, R.K. Selvan, Synthesis and characterization of $MnFe_2O_4$ nanoparticles for impedometric ammonia gas sensor. Sensors Actuators B Chem. **220**, 50–58 (2015)
19. R. Lafi, L. Abdellaoui, I. Montasser, W. Mabrouk, A. Hafiane, The effect of head group of surfactant on the adsorption of methyl red onto modified coffee residues. J. Mol. Struct. **1249**, 131527 (2022)
20. M. Arshadi, F.S. Vahid, J.W.L. Salvacion, M. Soleymanzadeh, A practical organometallic decorated nano-size SiO_2–Al_2O_3 mixed-oxides for methyl orange removal from aqueous solution. Appl. Surf. Sci. **280**, 726–736 (2013)
21. S. Dadfarnia, A.M.H. Shabani, S.E. Moradi, S. Emami, Methyl red removal from water by iron-based metal–organic frameworks loaded onto iron oxide nanoparticle adsorbent. Appl. Surf. Sci. **330**, 85–93 (2015)
22. T.A. Saleh, A.M. Musa, S.A. Ali, Synthesis of hydrophobic cross-linked polyzwitterionic acid for simultaneous sorption of Eriochrome black T and chromium ions from binary hazardous waters. J. Colloid Interface Sci. **468**, 324–333 (2016)
23. V. Vadivelan, K.V. Kumar, Equilibrium, kinetics, mechanism, and process design for the sorption of methylene blue onto rice husk. J. Colloid. Interface Sci **286**, 90–100 (2015)
24. F. Ghorbani, S. Kamari, Core–shell magnetic nanocomposite of Fe_3O_4@SiO_2@NH_2 as an efficient and highly recyclable adsorbent of methyl red dye from aqueous environments. Environmental Technology & Innovation **14**, 100333 (2019)
25. V. Srivastava, A.K. Choubey, Study of adsorption of anionic dyes over biofabricated crystalline α-MnO2 nanoparticles. Environ. Sci. Pollut. Res. **28**, 15504–15518 (2021)

26. F. Ahmadijokani, R. Mohammadkhani, S. Ahmadipouya, A. Shokrgozar, M. Rezakazemi, H. Molavi, T.M. Aminabhavi, M. Arjmand, Superior chemical stability of UiO-66 metal-organic frameworks (MOFs) for selective dye adsorption. Chem. Eng. J. **399**, 125346 (2020)
27. J.K. Adusei, E.S. Agorku, R.B. Voegborlo, F.K. Ampong, B.Y. Danu, F.A. Amarh, Removal of Methyl red in aqueous systems using synthesized NaAlg-g-CHIT/nZVI adsorbent. Sci. African **17**, e01273 (2022)
28. A.K. Dey, A. Dey, R. Goswami, Adsorption characteristics of methyl red dye by Na_2CO_3-treated jute fibre using multi-criteria decision making approach. Appl Water Sci **12**, 179 (2022)

Adsorption of Fluoride onto PANI-Cl Jute Fibre: Designing a Higher-Flow-Rate and Higher-Initial-Concentration Column Reactor from a Batch Reactor

Sarungbam Pipileima, Potsangbam Albino Kumar, and Anuj Kumar Purwar

Abstract In this study, polymer adsorbent polyaniline was doped with chloride on the jute fibre (PANI-Cl jute) and was used for defluoridation. FTIR, XRD, SEM and EDX study was conducted to confirm the mechanism of F^- removal by the adsorbent in the continuous column mode studies. The main emphasis was given to the design of a continuous column reactor for defluoridation from a batch experiment process through the application of the theoretical breakthrough curve method. Further, applying the bed depth service time (BDST) model, the column data were treated and designed for the higher concentration of F^- from 5 mg/L to 10 mg/L and flow rate from 1.2 mL/min to 1.5 mL/min. This finding confirms that up to 30% of breakthroughs can use BDST effectively. Desorption was studied using NaOH, and the PANI-Cl jute fibre could be employed for another six cycles of adsorption; thus, the uptake capacity of the adsorbent was also able to increase.

Keywords Doping · Breakthrough curve · Bed depth service time · Langmuir isotherm · Desorption

Abbreviation

BDST	Bed depth service time
F^-	Fluoride ion
FTIR	Fourier transform infrared
NaOH	Sodium hydroxide

S. Pipileima · P. A. Kumar (✉)
Civil Engineering Department, National Institute of Technology Manipur, Langol, Imphal, India

A. K. Purwar
School of Engineering and Technology, IGNOU, Delhi, India
e-mail: akpurwar@ignou.ac.in

D. Mazumder (ed.), *Sustainable Advanced Technologies for Industrial Pollution Control*, Springer Proceedings in Earth and Environmental Sciences,
https://doi.org/10.1007/978-3-031-37596-5_3

N-H	Nitrogen and hydrogen bonding
PANI-Cl	Polyaniline-doped chloride
pH	Potential of hydrogen ion
PVC	Polyvinyl chloride
SEM	Scanning electron microscope
XRD	X-ray diffraction

1 Introduction

Fluoride in water is the most efficient way to prevent tooth decay and dental carries; however, concentrations over 1.5 mg/L can have serious effects on skeletal tissue as well as bone structure and can cause other diseases like moulting of the teeth, brain damage, cancer, Alzheimer's syndrome and thyroid disorder [1]. Many techniques have been used for the removal of excess fluorides such as ion exchange, precipitation, electrolysis, reverse osmosis and nanofiltration [2]. However, adsorption is found to be broadly used, gainful and flexible in process with several activated carbon-based adsorbent and polymer functionalized groups used extensively [3]. The synthesis of functionalized polymer with different functional groups (e.g. amines, carboxylate, phenolic, chloride, hydroxyl, etc.) is a developing method in the ground of water treatment. They are easy to handle, acceptable for the users, regenerable and quick to process and provide good water [3]. The amine-based polymer was used for the removal of fluoride solution for its cationic behaviour in an acidic medium due to protonation in amine groups. This amine-based polymer, polyaniline is environmentally stable and even and has reversible acid/base doping/de-doping chemistry [4, 5]. As several researchers studied laboratory-based batch and continuous column mode operation separately, there are hardly any studies on the design of continuous column processes from the laboratory-scale batch process and the design of larger-scale column reactor with respect to initial fluoride concentration and flow rate. Therefore, in this study, amine-rich polymer polyaniline is synthesized and doped with chloride onto the surface of jute fibre for replacement of Cl^- by F^-, as F^- has more affinity for binding with polyaniline than Cl^- and can be employed for fluoride uptake in the batch process followed by the design of a column reactor from the batch data and its validation. Besides synthesis of chloride doped polyaniline adsorbent, this study also focuses on the design of a column reactor with a higher flow rate and a higher initial fluoride concentration.

2 Materials and Methods

2.1 Materials and Methodology

The adsorbent PANI-Cl jute was arranged as per our earlier studies [6]. The column experiment was conducted at different bed depths (1.5–3 m) using PVC pipe with a diameter of 4 cm and fed with adsorbent (165–330 g); the sample of different flow rates (1.2 mL/min and 1.5 mL/min) was fed from the top of the reactor; and the initial concentration is 5–10 mg/L. The discharge rate was maintained by a peristaltic pump (model: Miclins PP-60). The concentration of F^- was estimated using an ion selectivity electrode.

2.2 Bed Depth Service Time

The Bohart-Adams equation was further simplified in linear form as [7] (Eq. 1)

$$t_S = \frac{NZ}{C_o u} - \frac{1}{k_{ads} C_o} \mathrm{Ln}\left(\frac{C_o}{C_b} - 1\right) \tag{1}$$

where t_s is the breakthrough time (h); N the bed volume (mg/L); Z the adsorbent depth of the column (cm); u the ratio of the flow rate Q (cm^3/h) to the plan area A (cm^2); C_o and C_b the influent and the F^- concentration at breakthrough (mg/L), respectively; and k_{ads} the constant for uptake (L/mg.h). A graph of service time (t_s) and bed depth (Z) will create a linear equation with the slope of ($N/C_o.u$) and

$$\text{intercept} = (-)\frac{1}{k_{ads} C_o} \mathrm{Ln}\left(\frac{C_o}{C_b} - 1\right) \tag{2}$$

A critical bed depth (Z_o) which represents the minimum depth of the column that would be able to prevent the F^- concentration from exceeding C_b theoretically can be obtained when a breakthrough is instantaneous and is evaluated by substituting $t_S = 0$ in Eq. 1 as shown below:

$$Z_0 = \frac{u}{k_{ads}\, N} \left(\frac{C_o}{C_b} - 1\right) \tag{3}$$

The data composed from one discharge experiment can forecast the structure with different discharges. When an experiment directed at flow rate Q_1 gives

$$t_s = a_1 Z + b_1 \tag{4}$$

the predicted equation for the new discharge/flow rate Q_2 is given by

$$t_s = a_2 Z + b_1 \tag{5}$$

$$a_2 = a_1 \left(\frac{Q_1}{Q_2} \right) \tag{6}$$

where a_1 is the slope at Q_1 condition and correspondingly a_2 for Q_2, respectively. However, the intercept b_1 remained unchanged as it is independent of the Q_1 and Q_2 in the linearized BDST Eq. (1). It can also be used to plan the systems for evaluating different influent F^- concentrations employing the data of a known laboratory experiment of any F^- concentration. When a test is conducted at initial concentration C_1, the new equation obtained is

$$t = p_1 X \tag{7}$$

The predicted equation for the new flow rate Q_2 is given by

$$t = p_2 X + s_2 \tag{8}$$

The new slope and intercept values can be evaluated as

$$p_2 = (p_1 C_1)/C_2 \tag{9}$$

$$s_2 = s_1 \frac{C_1}{C_2} \left(\frac{\mathrm{Ln}[(C_2/C_F) - 1]}{\mathrm{Ln}\,[(C_1/C_b) - 1]} \right) \tag{10}$$

where p_1 and p_2 are slopes at C_1 and C_2 conditions, respectively; s_1 and s_2 are the intercepts, correspondingly; and C_F and C_b are the effluent concentrations at C_2 and C_1, respectively.

2.3 Theoretical Breakthrough Curve

Further for the analysis of continuous column data from batch mode experimental data, the theoretical breakthrough curve was designed with the following steps:

(i) Firstly, an operating line which crosses the equilibrium curve (C_e versus q_e of batch data) at C_o and passes through the origin is attained. The adsorption data of batch and column modes are identical at the initiation and exhaustion of the reaction.

(ii) Furthermore, the alteration between the operating line and the equilibrium, which is the driving force of adsorption and denoted by ($C - C_e$), is evaluated by integrating the rate of transfer (Eq. 11):

$$QdC = K^{o}A(C - C_{e})\mathrm{dh} \tag{11}$$

where Q is the flow rate, K^{o} the overall mass transfer number, A the external surface area, dh the differential depth of column, C_e the equilibrium concentration of F^- in the solution corresponding to an adsorbed F^- concentration q_e and C the concentration of the adsorbate at a given time t [8].

(iii) Integrating Eq. 11 and evaluating the depth of the adsorption zone (h_z) at inundation, and the height of adsorption (h) less than h_z, we obtain the following equation:

$$h_z = \frac{Q}{K^{o}\alpha}\int_{C_B}^{C_E}\frac{dc}{(C - C_e)} \tag{12}$$

$$h = \frac{Q}{k_o\alpha}\int_{C_B}^{C}\frac{dc}{(C - C_e)} \tag{13}$$

where C_B and C_E are the concentrations of F^- in effluent at (i) breakthrough condition and at (ii) exhaustion condition respectively.

(iv) Dividing Eq. (12) by Eq. (13) results in

$$\frac{h}{h_z} = \frac{\int_{C_B}^{C} dC/(C - C_e)}{\int_{C_B}^{C_E} dC/(C - C_e)} = \frac{V_t - V_B}{V_E - V_B} \tag{14}$$

where suffixes B and E represent breakthrough and exhaust points respectively for throughput volume V. The value of the above integration is given by the area under the curve of C versus $(C - C_e)^{-1}$. However, the plot should be concluded for C at a value less than C_o, say exhaust point of $C = 0.95$ as $(C - C_e)^{-1}$ approaches infinity at C equals C_o.

(v) Finally the plot of $(V_t - V_B)/(V_E - V_B)$ versus (C/C_o) denotes the theoretical breakthrough.

3 Results and Discussion

3.1 Characterization

The Fourier transmission infrared (FTIR) analysis of PANI-Cl jute was carried out on adsorbent before and after fluoride adsorption, and the respective spectra are shown in Fig. 1. The bands at 3700–3500 cm^{-1} are associated with water molecule

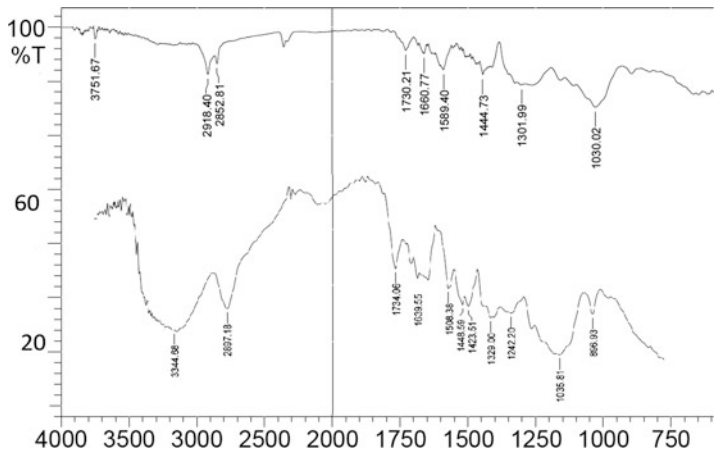

Fig. 1 FTIR for PANI-Cl jute fibre before and after adsorption

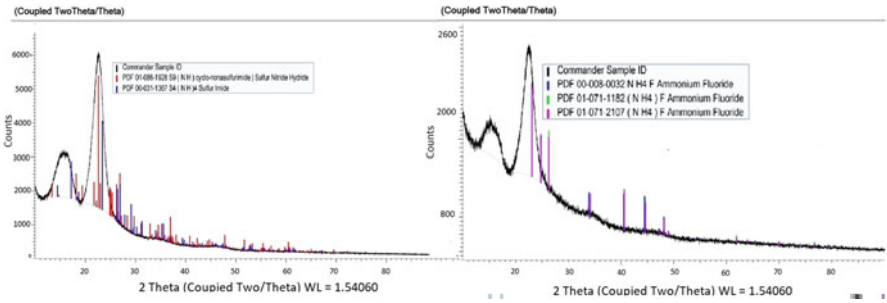

Fig. 2 XRD patterns of PANI-Cl jute fibre before and after adsorption

present in PANI-Cl jute fibre. The peak around 3300 cm^{-1} corresponds to the characteristic N-H stretching and the peak at 1589 cm^{-1} for N-H bending. The sharp peak at 1035 cm^{-1} assigned the stretching of the fluoro-compound which shows the adsorption of F^- onto the PANI-Cl jute fibre [9].

The XRD patterns of PANI-Cl jute fibre before contacting with the F^- solution and after the adsorption are shown in Fig. 2. It was observed that in the diffraction ray of PANI-Cl jute before adsorption, there is no presence of fluoride ions on it. However, after adsorption, the pattern where $2\theta = 230$, 260 and 270 shows the presence of fluoride ions onto the PANI-Cl jute fibre. The similar XRD peak pattern at $2\theta = 160$ and 230 between 'before adsorption' and 'after adsorption' also indicates that the structural integrity of PANI-Cl jute is retained after adsorption [10]. The SEM pictures of PANI-Cl jute before and after F^- adsorption are shown in Fig. 3a, b. The SEM of PANI-Cl jute before adsorption is smooth and even where the surface evenness disappears after F^- adsorption.

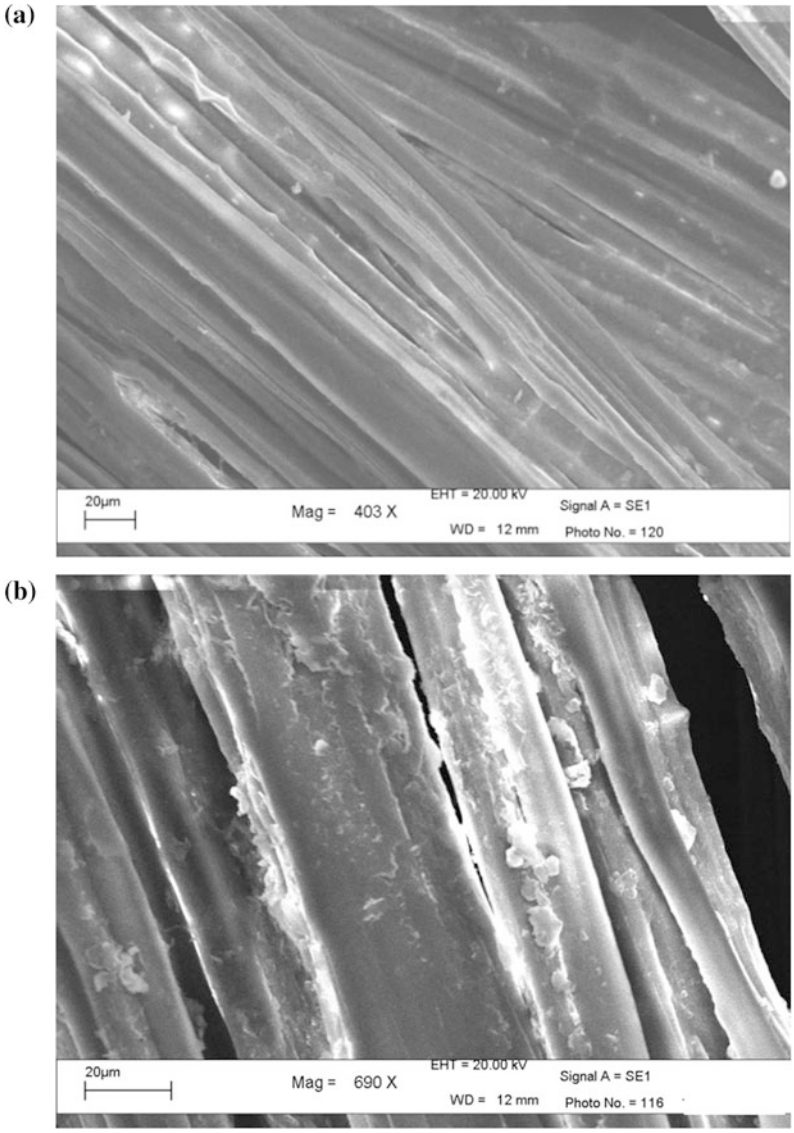

Fig. 3 (**a**) SEM images of PANI-Cl jute before adsorption. (**b**) SEM images of PANI-Cl jute after F^- adsorption

These characterizations confirm that F^- is adsorbed onto the PANI-Cl jute fibre which reveals the binding of F^- at acidic pH by (i) electrostatic attraction between protonated amines (NH^{3+}) at the terminal end of the polymer with anionic F^- and by (ii) ion exchange of F^- with doped chloride throughout the chain length of PANI-Cl jute.

3.2 Theoretical Breakthrough Curve

To obtain a theoretical breakthrough curve which derives from a batch adsorption process, we initially run batch adsorption at pH 1, initial F^- concentration of 20 mg/L and varied doses of 2, 4, 6, 8 and 10 g/L. To fix the batch data into an adsorption isotherm, the data were treated with a linearized Langmuir isotherm (Eq. 14) [11–13], and a plot was drawn between $1/C_e$ and $1/q_e$ as shown in Fig. 4. Other studies also reveal that the F^- adsorption is

$$\frac{C_e}{q_e} = \frac{1}{Q_{max}b} + \frac{C_e}{Q_{max}} \tag{15}$$

The correlation coefficient of $R^2 = 0.985$ suggests the fixing of F^- adsorption on PANI-Cl jute. The Langmuir coefficients were evaluated as Q_{max} (1.15 mg/g) and 'b' (0.5304), and using the Langmuir coefficient, an equilibrium line was prepared following the concept of Michael's [14]. Operating lines for both concentrations were then prepared and yielded q_e of 0.84 mg/g and 0.97 mg/g, respectively. A graph between C and $(C - C_e)^{-1}$ was then prepared, and the area below the curve which is the integration of Eqs. 11, 12, and 13 was evaluated as 4.85 and 3.19 square units for initial F^- concentrations of 5 and 10 mg/L. Finally, the theoretical breakthrough curve for 5 and 10 mg/L was obtained by plotting a graph between $(V_t - V_B)/(V_E - V_B)$ and C/C_o. As can be seen in Fig. 5, the theoretical and experimental breakthroughs follow the same trend for both F^- initial concentrations.

3.3 Bed Depth Service Time

To predict or design the new fixed bed with different flow rates and different initial F^- concentrations, two new columns were run (Column I: Q @ 1.5 mL/min and C_o same as 5 mg/L. Column II: Q same @ 1.2 mL/min and initial F^- concentration of 10 mg/L) at various reactor depths of 1.5, 2 and 3 m. The experimental and predicted

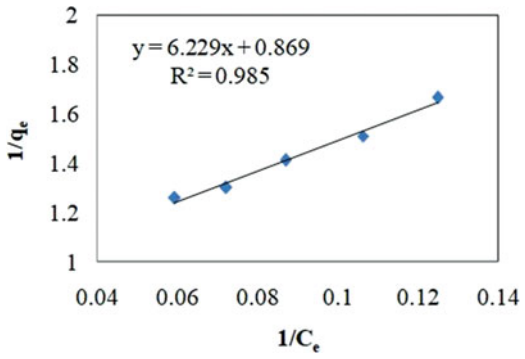

Fig. 4 The plot of batch adsorption data into linear Langmuir isotherm

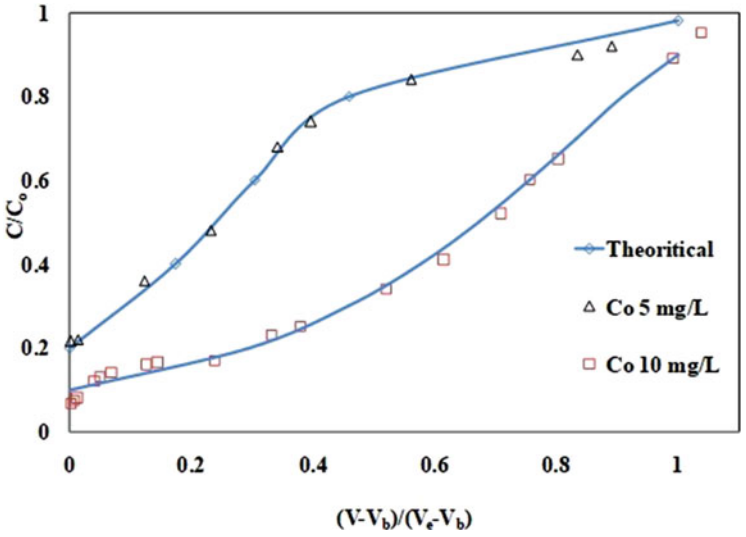

Fig. 5 Theoretical and experimental breakthrough for F^- adsorption on PANI-Cl jute at 1.5 m bed depth

Table 1 Comparison of breakthrough (experimental vs predicted) using the BDST model

Ex	Parameter	Breakthrough (%)	Breakthrough time (mins)		RSD
			Exp	Predicted	
I	$Q = 1.5$ mL/min $C_o = 5$ mg/L	1	5.5	6.7	0.86
		30	15	13.6	0.97
		60	28	29.3	0.96
		90	56	112.7	40.09
II	$Q = 1.2$ mL/min $C_o = 10$ mg/L	1	4	3.6	0.22
		30	7.1	7.06	0.66
		60	25	17.1	5.55
		90	70	34.2	25.25

breakthrough time for a bed depth of 1 .5 m is shown in Table 1 along with their relative standard deviation (RSD). The RSD (%) value of less than 1 is observed for Column I (different flow rate) till a breakthrough of 60%. At 90% breakthrough, the RSD (%) is above 40%. Similarly, for Column II (different initial F^- concentration), the RSD (%) is below 1 till only a breakthrough of 30% for all different bed depths. With the increase in breakthrough (%), the RSD range also increases. This finding confirms that at least till 30% breakthrough (%) (i.e. the permissible limit of 1.5 mg/L), the BDST model can predict and design different flow rates and different F^- initial concentrations effectively. Similarly, observation was also made at bed depths of 2 and 3 m with RSD ranging from 0.51 to 0.96 for a higher flow rate and from 0.13 to 0.86, respectively, for a higher F^- concentration. Other researchers adopted

Table 2 Reuse of PANI-Cl jute

Adsorption-desorption cycle	Desorption (%)	q_e (mg/g)
1st	93	3.4
2nd	93	3.4
3rd	93	3.4
4th	92	3.3
5th	92	3.2
6th	90	3.2
7th	86	3.1
8th	83	1.6
9th	65	1.28

breakthrough percentages of 0.05, 0.1, 0.3, 0.5, 0.6, 0.8 and 0.9 for the study of adsorption at different breakthroughs [15, 16].

3.4 Desorption

As the adsorption is predominantly chemical adsorption, it was carried out effectively using NaOH and was able to employ the adsorbent for another six cycles as shown in Table 2 and thereby enhance the F^- adsorption capacity by sevenfold, i.e. 22.80 mg F^-/g.

4 Conclusion

The study on the adsorption of F^- by PANI-Cl jute reveals a maximum defluoridation uptake of 1.15 mg/g following Langmuir isotherm. The FTIR, XRD and SEM give the confirmation of the adsorption of F^- onto the PANI-Cl jute fibre by electrostatic binding between protonated end and F^- and by ion exchange between Cl^- in adsorbent and F^-. The predicted breakthrough curve for initial F^- concentrations of 5 and 10 mg/L from the batch adsorption study was able to correlate with the breakthrough of experimental column data with an RSD of 0.2–0.96%. Finally, the BDST model predicted a column reactor with a higher flow rate up to a breakthrough effluent of 60% and a higher initial F^- concentration of 30%, suggesting an effective adsorption of F^- by PANI-Cl jute in continuous column mode. The desorption experiment with NaOH could recover F^- up to 80–90% and can be reemployed for another six cycles effectively.

References

1. A. Goswami, M.K. Purkait, Removal of fluoride from drinking water using nano magnetite aggregated schwertmannite. J. Water Proc. Eng **1**, 91–100 (2014)
2. R.C. Menakshi, Maheshwari, Fluoride in drinking water and its removal. J. Hazard. Mater. **37**, 456–463 (2006)
3. M. Zendehdel, S.B. Yeganesh, H. Khanmohamadi, G. Cruciani, Removal of Fluoride from aqueous solution by adsorption on NaP:HAp nanocomposite using response surface methodology. Proc. Safe Environ. Protect **109**, 172–191 (2017)
4. M. Karthikeyan, K.K. Satheeshkumar, K.P. Elango, Conducting polymer/alumina composites as viable adsorbents for the removal of fluoride ions from aqueous solution. J. Fluor. Chem. **130**, 894–901 (2009)
5. M. Karthikeyan, K.K. Satheesh Kumar, K.P. Elango, Studies on the defluoridation of water using conducting polymer/montmorillonite composites. Environ. Technol. **33**(7), 733–739 (2012)
6. S. Pipileima, P.A. Kumar, Kinetics study of fluoride uptake by functionalized polymer polyaniline synthesized on jute fibre. J. Basic Appl. Eng. Res **3**(12), 1136–1137 (2016)
7. R. Hutchins, New method simplifies the design of activated-carbon systems. Chem. Eng. **80**, 133–138 (1973)
8. W.J. Weber, *Physico-Chemical Process for Water Quality Control* (Wiley Interscience, New York, 1972), pp. 261–305
9. M. Karthikeyan, K.K. Satheeshkumar, K.P. Elango, Defluoridization of water via doping of polyanilines. J. Hazard. Mater. **163**, 1026–1032 (2009)
10. P.A. Kumar, S. Chakraboty, Fixed bed column study for hexavalent chromium removal and recovery by short chain polyaniline synthesized on jute fibre. J. Hazard. Mater **162**, 1086–1098 (2009)
11. M. Karthikeyan, K.K. Satheeshkumar, K.P. Elango, Batch sorption studies on the removal of fluoride ions from water using eco-friendly conducting polymer/bio-polymer composite. Desalination **267**, 49–56 (2011)
12. K.Y. Lin Andrew, Y.T. Liu, S.Y. Chen, Adsorption of fluoride to UiO-66-NH2 in water: Stability, kinetic, isotherm and thermodynamic studies. J. Colloidal Interface Sci **461**, 79–87 (2016)
13. I. Langmuir, The adsorption of gases on plane surfaces of glass, mica and platinum. J. American Chem. Soc **40**, 1361–1403 (1918)
14. A.S. Michaels, Simplified method of interpreting kinetic data in fluid bed ion exchange. Ind. Eng. Chem. **44**, 1922 (1952)
15. P.R. Rout, P. Bhunia, D.R. Roshan, Evaluation of kinetic and statistical models for predicting breakthrough curves of phosphate removal using dolochar-packed columns. J. Water Proc. Eng **17**, 168–180 (2017)
16. S. Roy, P. Das, S. Sengupta, S. Manna, Calcium impregnated activated charcoal: Optimization and efficiency for the treatment of fluoride-containing solution in batch and fixed bed reactor. Proc. Safe Environ. Protect **109**, 18–29 (2017)

Biosynthesis of Nano Zero Valent Iron (nZVI) Using *Shorea robusta* Leaf Extract and Its Application in UV-Assisted Photocatalytic Degradation of Methyl Orange

Aditya Kumar Jha and Sukalyan Chakraborty

Abstract Synthetic dyes are highly toxic and recalcitrant in nature. Dyes can form secondary pollutants in water bodies which are also harmful. Conventional treatments have various shortcomings in their removal. This study investigated the photocatalytic degradation of methyl orange (MO) dye using nanozerovalent iron particles (nZVI) assisted by UV light. nZVI was biosynthesized using $FeSO_4.7H_2O$ and leaf extract of *Shorea robusta* (Sal) as a reducing agent. Characterization of nZVI was done using SEM, FTIR, DLS and ZP, AFM, XRD, and TEM. Degradation of methyl orange was performed by nZVI particles under UV illumination. Degradation was optimized by varying the concentration of dyes, dose of nZVI, pH of dyes, and time and studied using a UV spectrophotometer (peak at 465 nm). Characterization of nZVI indicated its successful synthesis. The optimum degradation efficiency was 78% for MO. Germination test and FTIR of dyes before and after degradation also showed degradation of MO.

Keywords Degradation kinetics · Green synthesis · Methyl orange · Nanoparticles · Photocatalysis · UV illumination · Dye degradation · nZVI · Seed germination test · Mechanism of degradation

Abbreviations

MO	Methyl orange
nZVI	nano Zero Valent Iron particles
Sal	*Shorea robusta*

A. K. Jha · S. Chakraborty (✉)
Department of Civil and Environmental Engineering, Birla Institute of Technology, Mesra, Ranchi, India
e-mail: sukalyanchakraborty@bitmesra.ac.in

D. Mazumder (ed.), *Sustainable Advanced Technologies for Industrial Pollution Control*, Springer Proceedings in Earth and Environmental Sciences,
https://doi.org/10.1007/978-3-031-37596-5_4

1 Introduction

Toxic dyes are a significant source of environmental pollution worldwide. Dyes have a major role in human and environmental health risks. Nowadays, the disposal of dyes and pigments in wastewater discharged from factories has received significant attention. Approximately $7 * 10^5$ tons of dyes is generated annually; most of them are azo dyes [1]. Synthetic dyes are extensively used in the cosmetic, paper, plastic, printing, textile, and leather industries. Synthetic dyes are released in wastewater, most of which are generally carcinogenic and toxic even at low concentrations. The deep color, complex aromatic structures, and low biodegradability of dyes have impacts such as aesthetic pollution, toxicity, and disturbance. This can also damage aquatic biota or humans through mutagenic and carcinogenic effects. However, several methods for treating dyes in wastewater, such as adsorption, ion exchange, membrane separation, photocatalytic degradation, and biological treatments, have been studied [2–5]. However, they have various shortcomings like ineffective degradation, generation of toxic sludge, being economically unfeasible, high energy consumption, and production of secondary toxic products. The application of nanoparticles for the degradation of dyes has been reported by several scientists as practical and feasible, though chemically synthetic nanoparticles themselves pose contamination problems in water bodies.

MO [Sodium 4-[(4-(dimethylamino) phenyl) diazenyl] benzene-1-sulfonate] is a textile dye soluble in water. It is an anionic dye. It is an azo dye having a complex structure with N=N group. MO has extensive applications in the textile industry. MO is highly toxic and carcinogenic. It also imparts deep color to water [6, 7].

nZVI has unique characteristics such as a high reactivity, degree of functionalization, and surface area-to-volume ratio, super-magnetism, antimicrobial properties, and photocatalysis, making it an effective photocatalyst against organic pollutants. nZVI has been used in the treatment of heavy metal pollutants, COD removal, textile dye degradation, soil remediation, and surface and sub-surface water remediation. It also has antimicrobial properties and is highly reactive. The reactivity of nZVI can be improved by integrating it with other techniques [8].

The best method for the synthesis of nZVI is the bottom-up approach, where nanoparticles are synthesized from simple precursor molecules. The variation in the concentration of precursor and reaction parameters such as temperature and pH can regulate the size and shape of the nanoparticle produced by this method. However, this production method may require using harsh chemicals like hydrazine hydrate and sodium borohydride, which are highly reactive and toxic [9, 10].

Green synthesis of nanoparticles minimizes the application of chemicals, extreme temperatures, or pressure in the process, thus making the synthesis economical. Plants contain reducing agents, antioxidants, and functional groups such as polyphenols and flavonoids. They also serve as stabilizing and capping agents for nanoparticles [11]. Biosynthesis of nanoparticles proves to be cost-effective and environmentally friendly compared to chemical and physical methods. nZVI has been synthesized from microorganisms, leaves and plant extracts, and macroalgae [11, 12].

To identify the publications based on the removal of MO by nZVI, a search was conducted on Web of Science Core Collection using the keyword "methyl orange" nZVI in all fields. Fifty-eight results were obtained, including five review articles, which were excluded. Articles were manually shorted, resulting in 29 related research articles, of which 10 were based on decolorization, 10 on adsorption, and 9 on degradation. The study of articles suggested that these degradations were carried out with nZVI composites like TiO_2 and Pd or supporting materials such as bentonite, activated carbon, calcium sulfate whiskers, polyaniline, and attapulgite, or activated using persulfate, or assisted by ultrasound and electro-catalysis. The only study which reported the application of bare nZVI showed a degradation efficiency of about 43% for MO [13]. Thus, in this study, we investigated the degradation of MO using nZVI in UV light.

2 Materials and Methods

The biosynthesis of nZVI was performed by reducing ferrous sulfate heptahydrate with Sal (*Shorea robusta*) leaf extract with slight modifications to Jha and Chakraborty, (2020) [14]. Briefly, in 100 ml of 0.01 M $FeSO_4.7H_2O$, 100 ml of the leaf extract, containing 10 g of matured Sal leaves, was added dropwise (1 drop per 2 seconds) and placed in an orbital shaker at 100 rpm at room temperature for 30 minutes. The solid particles were obtained using vacuum filter from the aqueous solution and were washed with absolute ethanol to eliminate the water and prevent their rapid oxidation.

In the process, Sal leaf extract was prepared by crushing 10 g of leaves with water to a fine aqueous paste using a mortar and pestle. Water was added to reach the final concentration of 10 ml of water per gram of leaf. After filtering the solution (pore size: 45 microns), the extract was then stored at 4 °C for further use [9].

The synthesized material was characterized for morphology and particle size using transmission electron microscopy (CM 200, 20–200 KV) and atomic force microscopy (Solver Pro-4). Energy-dispersive X-ray (JEOL: JSM-6390 LV) was employed to study the elemental composition of the synthesized particles. The presence of functional groups in leaf extract and the synthesized particles were studied using Fourier transform infrared spectroscopy (Shimadzu: IRPrestige-21). The synthesis of nZVI was verified using X-ray diffraction (Rigaku: SmartLab 9 kW, Japan) and UV-visible spectrophotometer (Shimadzu: UV-1800).

The photocatalytic degradation was performed in a 30 cm * 30 cm * 45 cm UV box using an 11 W UV light (Philips). To study the photocatalytic degradation of MO, the initial concentration of MO was optimized from 50 to 400 ppm with a constant gap of 50 ppm. Once the concentration of MO was optimized, this concentration pH was varied to 2, 4, 6, 8, and 10. At optimum MO concentration and solution pH, the dose of nZVI was optimized in the range of 0.5–2.5 g/L with a gap of 0.5 g/L, and the time of reaction was varied from 10 to 60 minutes. The treated samples were centrifuged at 10000 rpm for 10 minutes. The supernatant was

collected and scanned in a UV-visible spectrophotometer (200–800 nm). The peak of MO was studied at 465 nm [15]. The degradation efficiency was obtained using Eq. 1. The results were used to plot reaction kinetics as well. Pseudo-first-order rate of reaction was calculated based on Eq. 2, and the pseudo-second-order rate of reaction was calculated using Eq. 3 [16]. Seed germination tests were performed to determine the residual toxicity of MO after degradation.

$$\text{Degradation efficiency} = \left(\frac{C_o - C_t}{C_o}\right) * 100\% \tag{1}$$

$$\ln\left(\frac{C_t}{C_o}\right) = K_1 t \tag{2}$$

$$\frac{1}{C_t} = \frac{1}{C_o} + K_2 t \tag{3}$$

C_o is the initial concentration of MO; C_t, the concentration of MO after time t; K_1, the rate constant for pseudo-first-order reaction; and K_2, the rate constant for pseudo-second-order reaction.

3 Results and Discussion

The introduction of Sal leaf extract into the $FeSO_4.7H_2O$ solution led to an instant change in color from light green to black, indicating the synthesis of nZVI. The UV-visible spectrophotometric peaks of nZVI were observed at 215 and 264 nm, further confirming this outcome. Similar spectra of nZVI were reported by Pattanayak and Nayak (2013) [9]. Morphological characterization like TEM and AFM (Fig. 1a) indicated poly-dispersed particles with spherical shapes in the nano-size range. Analysis of TEM image by ImageJ software indicated the size in the range of 20–72 nm, while processing of AFM image in NOVA software indicated the size range to be 50–70 nm. SAED image of nZVI (Fig. 1b) showed rings with bright spots, indicating its crystalline nature. XRD indicated successful synthesis of nZVI with a 2θ peak around 44° (Fig. 1c). This result matches with that obtained by Qu et al. (2020) [17]. FTIR showed the presence of carboxyl, phenol, or water O-H stretching of polyphenols, C-O stretching of alcohol, C=O stretching of ketones and alkyl groups, hydroxyl group of alcohol, and C-H bond of alkyl group (Fig. 1d). The presence of alcohols and polyphenols in Sal leaf probably reduced the $FeSO_4.7H_2O$ to nZVI and worked as the capping agent for nZVI, reducing its rapid oxidation [18].

Photocatalytic degradation of MO was performed under UV illumination (11 W) in a 100 ml conical flak with a 50 ml sample under magnetic stirring at 200 rpm. The initial MO concentration, solution pH, nZVI dose, and time were optimized for maximum degradation efficiency (Fig. 2). Details of the photocatalytic degradation study of MO using nZVI are shown in Table 1. Degradation efficiency increased

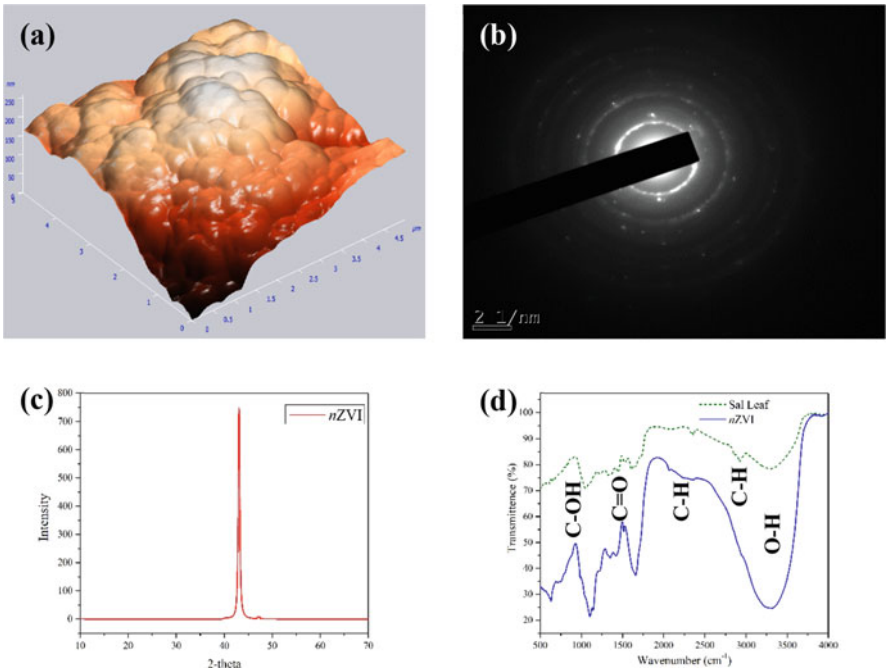

Fig. 1 (**a**) AFM of *n*ZVI shows spherical particles, (**b**) SAED image shows ringlike structure, (**c**) XRD shows a peak at 44°, and (**d**) FTIR of Sal leaf extract and synthesized nZVI

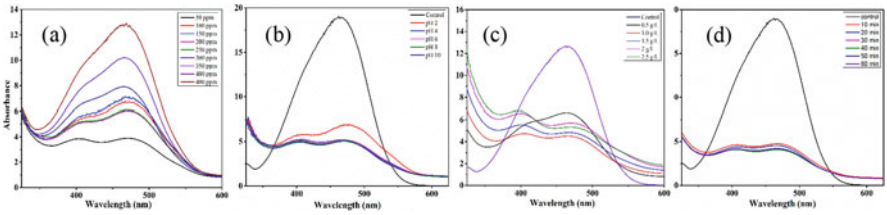

Fig. 2 Optimization of (**a**) initial concentration of MO, (**b**) pH of the aqueous solution, (**c**) dose of nZVI, and (**d**) reaction time

Table 1 Degradation study of nZVI

Parameters	Range	Optimum range	Efficiency (%)
Initial concentration	50–400 ppm	250 ppm	67
pH	2–10	6	72
Dose	0.5–2.5 g/L	1 g/L	76
Time	10–60 minutes	40 minutes	78

Fig. 3 Germination and growth study of *Cicer arietinum* seeds at various degraded MO concentrations

with an increase in MO concentration up to 250 ppm and then decreased with a further increase in concentration (Fig. 2a). The reason behind the increase in efficiency is that a large number of MO molecules increase the chances of interaction with the photocatalyst. The decrease in efficiency with further increase in MO concentration could be attributed to the limited number of photocatalyst molecules and the decrease in light penetration due to intense color at higher dye concentrations [14]. The effect of pH in the range of 4–10 had a very low impact on the degradation of MO, indicating that nZVI could be suitable for the degradation of MO at a wide range of pH. As the dose of the photocatalyst increases, the chances of the interaction of photocatalyst and MO molecules increase, thus increasing the photocatalytic efficiency. But nZVI imparts a black color to the solution, which reduces the light penetration, thus reducing the generation of active species [19]. Removal efficiency of 76 was recorded at 1 g/L dose of nZVI (Fig. 2c). The removal efficiency of MO by nZVI increased with time up to 40 minutes, after which no further increase was observed. At 250 ppm MO concentration, pH 6, and 1 g/L dose of nZVI under UV illumination, 78% removal was observed in 40 minutes. The mechanistic insight of the process can be described in the following manner: The nZVI particles serve as electron donors, while dye molecules act as electron acceptors. In an aqueous solution, $\mathbf{Fe^{o}}$ reduces to Fe^{2+}, which further reacts with water's oxygen to create a highly reactive superoxide ion ($\mathbf{O_2^{\circ -}}$). $\mathbf{Fe^{2+}}$, $\mathbf{O_2^{\circ -}}$, and $\mathbf{H^{+}}$ also react to produce peroxide ($\mathbf{H_2O_2}$), a potent oxidizing agent. $\mathbf{Fe^{2+}}$**r**eacts with $\mathbf{H_2O_2}$ to produce hydroxide radicle (**OH•**) and hydroxide ion ($\mathbf{OH^{-}}$). **OH•**, $\mathbf{OH^{-}}$, and $\mathbf{O_2^{\circ -}}$ are responsible for the degradation of MO.

Seeds of Bengal gram (*Cicer arietinum*) were exposed to the degraded MO solutions, and control was set up with distilled water (Fig. 3). No substantial difference in the germination and growth of seeds was recorded, implying the degraded MO solutions had no inhibitory impact on the germination and growth of seeds.

4 Conclusion

This study demonstrates the successful biosynthesis of nZVI particles through the reduction of $FeSO_4.7H_2O$ by mature Sal leaf extract and its successful utilization in the photocatalytic degradation of MO in UV light. Various characterization techniques confirmed the synthesis of stable nanoparticles. The presence of alcohols and polyphenols in the leaf extract of Sal leaf was responsible for its reducing and capping capabilities. This suggests that Sal leaf extract can also be used in synthesizing other nanoparticles. Sal leaf extract can act as an economical and environmentally friendly reducing agent. This nZVI degraded MO with an efficiency of 78%. The optimum conditions were 250 ppm concentration of MO and 4 g/L dose of nZVI at pH 6 in 40 minutes. The rapid and efficient degradation of MO by nZVI makes it a promising material for the degradation of MO and other azo dyes. nZVI produces hydroxyl radicals, hydroxide, and superoxide radical anions in water, which are responsible for successfully degrading MO. The presence of these active functional groups in nZVI suggests its future potential application in the photocatalytic degradation of other dyes and organic waste.

Acknowledgments The present research work is supported by funding from BIT, Mesra. Recipient: Aditya Kumar Jha. Funding agency: Birla Institute of Technology, Mesra, Ranchi, India. Award no: GO/Estb/Ph.D/2018-19/2184. Registration no: 170406. The authors are thankful to the Indian Institute of Technology, Bombay and Central Instrumentation Facility of Birla Institute of Technology, Mesra, for facilitating the characterization part of the study.

References

1. K.V.G. Ravikumar et al., Biogenic nano zero valent iron (Bio-nZVI) anaerobic granules for textile dye removal. J. Environ. Chem. Eng. **6**(2), 1683–1689 (2018). https://doi.org/10.1016/j.jece.2018.02.023
2. M. Malakootian, N. Radhakrishna, M.P. Mazandarany, H. Hossaini, Bacterial-aerosol emission from wastewater treatment plant. Desalin. Water Treat. **51**, 4478–4488 (2013)
3. G.K. Parshetti, A.A. Telke, D. Kalyani, S.P. Govindwar, Decolorization and detoxification of sulfonated azo dye methyl orange by Kocuria rosea MTCC 1532. J. Hazard. Mater. **176**(1–3), 503–509 (2010)
4. T. Robinson, G. McMullan, R. Marchant, P. Nigam, Remediation of dyes in textile effluent: A critical review on current treatment technologies with a proposed alternative. Bioresour. Technol. **77**(3), 247–255 (2001). https://doi.org/10.1016/S0960-8524(00)00080-8
5. A.K. Jha, S. Chakraborty, Environmental application of graphene and its forms for wastewater treatment: A sustainable solution toward improved public health. Appl. Biochem. Biotechnol. (2023). https://doi.org/10.1007/s12010-023-04381-5
6. Y. Liang, H. Li, A comparison of trimeric surfactant intercalated montmorillonite with its gemini modified one: Characterization and application in methyl orange removal. J. Mol. Liq. **227**, 139–146 (2017). https://doi.org/10.1016/j.molliq.2016.11.104
7. L. Zhai, Z. Bai, Y. Zhu, B. Wang, W. Luo, Fabrication of chitosan microspheres for efficient adsorption of methyl orange. Chin. J. Chem. Eng. **26**(3), 657–666 (2018). https://doi.org/10.1016/j.cjche.2017.08.015

8. M. Anjum, R. Miandad, M. Waqas, F. Gehany, M.A. Barakat, Remediation of wastewater using various nano-materials. Arab. J. Chem. **12**(8), 4897–4919 (2016). https://doi.org/10.1016/j.arabjc.2016.10.004
9. M. Pattanayak, P.L. Nayak, Green synthesis and characterization of zero valent iron nanoparticles from the leaf extract of Azadirachta indica (Neem). World J. Nano Sci. Technol. **2**(1), 06–09 (2013). https://doi.org/10.5829/idosi.wjnst.2013.2.1.21132
10. S. Saif, A. Tahir, Y. Chen, Green synthesis of iron nanoparticles and their environmental applications and implications. Nanomaterials **6**(11), 209 (2016). https://doi.org/10.3390/nano6110209
11. G. Kozma, A. Rónavári, Z. Kónya, Á. Kukovecz, Environmentally benign synthesis methods of zero-valent iron nanoparticles. ACS Sustain. Chem. Eng. **4**(1), 291–297 (2016). https://doi.org/10.1021/acssuschemeng.5b01185
12. C.D. Raman, S. Kanmani, Textile dye degradation using nano zero valent iron: A review. J. Environ. Manag. **177**, 341–355 (2016). https://doi.org/10.1016/j.jenvman.2016.04.034
13. K.V.G. Ravikumar, S. Dubey, M. Pulimi, N. Chandrasekaran, A. Mukherjee, Scale-up synthesis of zero-valent iron nanoparticles and their applications for synergistic degradation of pollutants with sodium borohydride. J. Mol. Liq. **224**, 589–598 (2016). https://doi.org/10.1016/j.molliq.2016.10.040
14. A.K. Jha, S. Chakraborty, Photocatalytic degradation of Congo Red under UV irradiation by zero valent iron nano particles (nZVI) synthesized using Shorea robusta (Sal) leaf extract. Water Sci. Technol. **82**(11), 2491–2502 (2020). https://doi.org/10.2166/wst.2020.517
15. E. Bazrafshan, A. Zarei, H. Nadi, M.A. Zazouli, Adsorptive removal of Methyl Orange and Reactive Red 198 dyes by Moringa peregrina ash. Indian J. Chem. Technol **21**(2), 105–113 (2014)
16. A.K. Jha, S. Chakraborty, Photocatalytic degradation of tetracycline and ciprofloxacin antibiotic residues in aqueous phase by biosynthesized nZVI using Sal (Shorea robusta) leaf extract. J. Water Supply Res Technol. (2023). https://doi.org/10.2166/aqua.2023.113
17. G. Qu et al., Simultaneous removal of chromium(VI) and tetracycline hydrochloride from simulated wastewater by nanoscale zero-valent iron/copper–activated persulfate. Environ. Sci. Pollut. Res. **27**(32), 40826–40836 (2020). https://doi.org/10.1007/s11356-020-10120-8
18. Y. Rashtbari, S. Hazrati, A. Azari, S. Afshin, M. Fazlzadeh, M. Vosoughi, A novel, eco-friendly and green synthesis of PPAC-ZnO and PPAC-nZVI nanocomposite using pomegranate peel: Cephalexin adsorption experiments, mechanisms, isotherms and kinetics. Adv. Powder Technol. **31**(4), 1612–1623 (2020). https://doi.org/10.1016/j.apt.2020.02.001
19. G. Bandekar, N.S. Rajurkar, I.S. Mulla, U.P. Mulik, D.P. Amalnerkar, P.V. Adhyapak, Synthesis, characterization and photocatalytic activity of PVP stabilized ZnO and modified ZnO nanostructures. Appl. Nanosci. **4**(2), 199–208 (2014). https://doi.org/10.1007/s13204-012-0189-2

Method Development for the Detection of 2-Methylpyridine by High-Performance Liquid Chromatography

Rajat Chatterjee and Chanchal Majumder

Abstract A method for detection and quantification of 2-methylpyridine (2Mp) from aqueous solution was developed in this study by utilizing high-performance liquid chromatography (HPLC). The analysis was performed using a reversed-phase C18 column. The effects of chromatographic factors such as initial 2Mp concentration, C_0 (mg/L), acetonitrile (ACN) percent in water as carrier and flow rate, Q (mL/min), on peak asymmetry were determined by means of mathematical modelling using three-factor Doehlert design of experiments. A polynomial model equation containing constant, linear, squared and two-factor interaction terms was developed for predicting peak asymmetry. The optimum values for the factors were found to be 2Mp concentration of 12.28 mg/L, ACN percent of 59% and flow rate of 0.74 mL/min. At these factor values, the model projected an optimum peak asymmetry of 1.048, which was verified through experimentation. The results of the study were further represented by means of response surface method (RSM). The most important factor affecting peak asymmetry was ACN percent. A good correlation between the experimental data and model-predicted data was obtained with a correlation coefficient (R^2) value of 0.982. Also, the model was designed with a low prediction error of 2.2%. Additionally, the method developed in this study was reliable and reproducible. It was successfully applied in the detection of 2Mp in textile industry effluent.

Keywords HPLC · Emerging contaminant · Mathematical modelling · Optimization · Phenol · Response surface method · 2-Methylpyridine · Liquid chromatography · Design of experiment · Hazardous · Model development · Data analysis · Industrial effluent · Wastewater treatment

R. Chatterjee (✉) · C. Majumder
Civil Engineering Department, Indian Institute of Engineering Science and Technology, Shibpur, Howrah, West Bengal, India
e-mail: rchatterjee.rs2018@civil.iiests.ac.in; chanchal@civil.iiests.ac.in

D. Mazumder (ed.), *Sustainable Advanced Technologies for Industrial Pollution Control*, Springer Proceedings in Earth and Environmental Sciences,
https://doi.org/10.1007/978-3-031-37596-5_5

Abbreviations

2Mp	2-Methylpyridine
ACN	Acetonitrile
DD	Doehlert design
EU	European Union
HPLC	High-performance liquid chromatography
RSM	Response surface method
USEPA	US Environmental Protection Agency

1 Introduction

The chemical 2-methylpyridine (2Mp) is used as a solvent and a precursor reagent in many industries such as tar, petroleum, harbour, fishery and textile [1]. It is refractory in nature; therefore, its detection in the effluent is of the highest importance, so that it may be treated before being discharged into the environment [2, 3]. Industries such as coal and petroleum discharge 2Mp in a concentration range of 2.5–20 mg/L [1, 3]. The US Environmental Protection Agency (USEPA) and EU guidelines have set a discharge standard limit of 1 mg/L for 2Mp [4, 5]. Repeated contact with 2Mp-polluted waters can result in the bioaccumulation (bioaccumulation factor = 11.2) of neurotoxin in the liver and kidney. In humans, this eventually leads to endocrine disruption and multi-organ failure [6, 7]. A few researchers have attempted to detect 2Mp by using HPLC [8]. However, the effects of chromatographic conditions such as 2Mp concentration, C_0 (mg/L), solvent ratio and flow rate, Q (mL/min), on peak characteristics were not optimized by mathematical modelling. Further, 2Mp was detected in a composite mixture along with amprolium hydrochloride ($C_{14}H_{19}N_4Cl{\cdot}HCl$) at a common wavelength of 254 nm using a mobile phase of acetonitrile/methanol/sodium heptanesulfonate (5:35:60) [8]. Thus, no method was found in literature for the sole detection of 2Mp at its maximum wavelength of 262 nm using a simplified mobile phase [1]. Thus, the objective of this study was set as:

(i) To develop a method for the detection and quantification of 2Mp in the concentration range of 2.5–25 mg/L by using HPLC.
(ii) To suggest a mathematical model by using Doehlert design (DD) to obtain the optimal operating conditions for best peak characteristics.

2 Materials and Methods

2.1 Reagents Used

HPLC-grade chemicals were utilized in this study, namely, 2-methylpyridine (Loba Chemie, India), HPLC-grade water (Fisher Scientific, India), acetonitrile (Loba Chemie, India) and methanol (Loba Chemie, India).

2.2 Solution Preparation

The stock solution of 2Mp (100 mg/L) was prepared and diluted further as needed using DI water in order to attain the solution of the required concentration. Acetonitrile, methanol and HPLC-grade water were utilized in the required ratios without any specific sample preparation [9].

2.3 HPLC Analysis

The analytical studies were carried out using uHPLC (Dionex UltiMate 3000, Thermo Scientific) fitted with a pump, autosampler and a reversed-phase C18 Hypersil GOLD column (4.6 × 250 mm, 5 µm). Software utilized for data assessment was Thermo Scientific Dionex Chromeleon Chromatography Data System (CDS) version 7.2.7. A mobile phase composed of ACN and HPLC water was chosen for the analysis. Mixtures of methanol, ACN and HPLC water did not give good results when used as mobile phase. The wavelength set for 2Mp detection was 262 nm.

2.4 Doehlert Design

Even spreading of data points at a high resolution level is attained by the use of Doehlert design of experiments [10]. Doehlert design of experiment was chosen to carry out the experimental scheme as it is the most efficient technique which requires a minimum number of experimentations compared to other designs of experiments [11]. In this study, peak asymmetry in 2Mp detection by HPLC was optimized by utilizing Doehlert design matrix formulation. Model development was carried out by the use of a three-factor DD. The important factors which determine the accuracy of 2Mp detection using HPLC are initial 2Mp concentration, ACN percent (i.e. ratio of ACN and HPLC water) and flow rate. These factors were represented as X_1, X_2 and X_3 in coded form respectively. It was observed during test runs that increasing the

Table 1 Ranges for the factors studied

	Factor		
Level	2Mp concentration, C_0 (mg/L)	ACN percent	Flow rate, Q (mL/min)
Lower level	5	40	0.5
Higher level	25	70	1

Table 2 The preliminary three-factor Doehlert design simplex in coded form

Design point	2Mp concentration X_1	ACN percent X_2	Flow rate X_3
1	0	0	0
2	1	0	0
3	0.5	0.866	0
4	0.5	0.289	0.816

concentration of 2Mp resulted in an increase in base width of the peak, thereby resulting in an increase in peak asymmetry. Thus, initial 2Mp concentration was chosen as an independent factor in Doehlert design of experiments. The selected range of factor levels is shown in Table 1. The DD simplex for a three-factor design is shown in Table 2.

If n is the number of experimental runs and f is the number of factors (3 in this case), then $n = f^2 + f + 1$. Thus, the number of experimental runs turns out to be 13. Real experimental presets (P) and coded values (C) for each factor are related by the equation below:

$$C = \frac{P - (H + L)/2}{(H - L)/2\gamma} \tag{1}$$

where L and H are the lower-range limit and the higher-range limit respectively and γ signifies the range. Using the experimental scheme prepared according to Doehlert design, the samples of 2Mp were analysed using HPLC. Every experimental run was performed in duplicate, and the averaged values were utilized in model development. Blank samples analysed to perceive interferences due to impurities showed negative results. Upon conclusion of experimentation, a model based on constant term, single factor, square terms and two-factor interaction effects of the factor values (X_i) was suggested for assessing peak asymmetry. The suggested model equation can be given in the following form:

$$Y = a_0 + \sum_{i=1}^{3} b_i X_i + \sum_{i=1}^{3} c_i X_i^2 + \sum_{i \neq j = 1}^{3} d_{ij} X_i X_j + \varepsilon_{ij} \tag{2}$$

where a_0, b_i, c_i and d_{ij} are the coefficients of regression, ε_{ij} is the prediction error and Y is output of the model, signifying peak asymmetry.

3 Results and Discussion

3.1 Doehlert Design

The entire experimental design, accompanied by experimental peak asymmetry, predicted peak asymmetry and prediction error, is displayed in Table 3. MATLAB (version 9.0) software was used for regression analysis and model development.

The resulting model equation for the prediction of HPLC peak asymmetry (Y) can be written in polynomial form as follows:

$$Y = 1.06 - 0.0025^{*}X_1 - 0.1184^{*}X_2 + 0.0082^{*}X_3 + 0.005^{*}X_1^2 + 0.2917^{*}X_2^2 + 0.0608^{*}X_3^2 + 0.0231^{*}X_1{}^{*}X_2 - 0.0082^{*}X_1{}^{*}X_3 - 0.0263^{*}X_2{}^{*}X_3 \quad (3)$$

where X_i are the coded form of factor values. Regression analysis was performed with up to two-factor interactions. Using three-factor interactions in the model based on regression, a poor fit was obtained since the coefficients of the factor effects were negligible. The correlation between experimental and model predicted values was found to be high (coefficient of determination, $R^2 = 0.982$), indicating that 98.2%

Table 3 Three-factor DD matrix, showing outcomes (predicted and experimental) and the associated error

Run no.	Coded values			Experimental peak asymmetry	Predicted peak asymmetry	Error (%)
	X_1	X_2	X_3			
1	0	0	0	1.06	1.06	0.00
2	1	0	0	1.07	1.06	0.71
3	0.5	0.866	0	1.17	1.19	−1.37
4	−0.5	0.866	0	1.16	1.17	−0.74
5	−1	0	0	1.06	1.07	−0.70
6	−0.5	−0.866	0	1.41	1.39	1.17
7	0.5	−0.866	0	1.38	1.37	0.64
8	0.5	0.289	0.816	1.1	1.09	0.81
9	−0.5	0.289	0.816	1.11	1.09	1.49
10	0	−0.577	0.816	1.26	1.29	−1.95
11	0.5	−0.289	−0.816	1.13	1.15	−1.41
12	−0.5	−0.289	−0.816	1.14	1.15	−0.76
13	0	0.577	−0.816	1.16	1.14	2.20

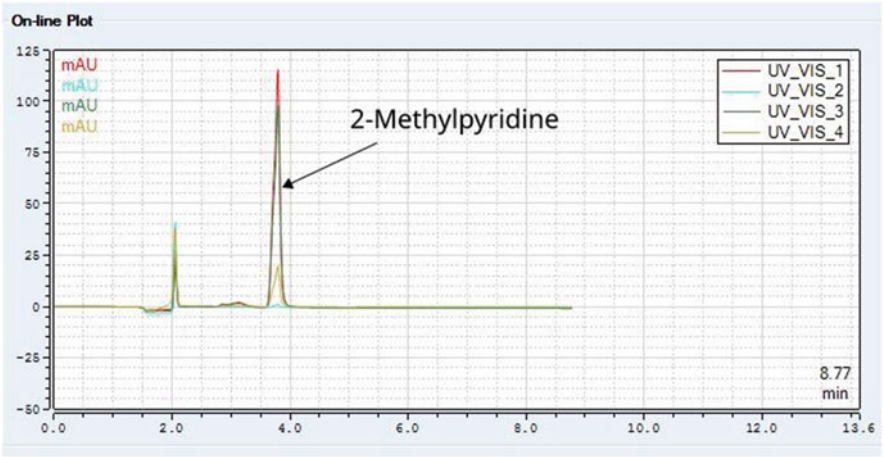

Fig. 1 HPLC chromatogram peak for the detection of 2-methylpyridine in synthetic sample

variability of experimental results was handled well by the model. A maximum error of +2.20% was observed in data prediction, as seen in Table 3. To attain the optimum peak asymmetry, Lagrange's criterion was applied as shown below [1]. A positive value of the determinant function was obtained, indicating the occurrence of a minimum in the determination of peak asymmetry.

$$A = \begin{pmatrix} \frac{\partial^2 Y}{\partial (X_1)^2} & \frac{\partial^2 Y}{\partial (X_1)(X_2)} & \frac{\partial^2 Y}{\partial (X_1)(X_3)} \\ \frac{\partial^2 Y}{\partial (X_2)(X_1)} & \frac{\partial^2 Y}{\partial (X_2)^2} & \frac{\partial^2 Y}{\partial (X_2)(X_3)} \\ \frac{\partial^2 Y}{\partial (X_3)(X_1)} & \frac{\partial^2 Y}{\partial (X_3)(X_2)} & \frac{\partial^2 Y}{\partial (X_3)^2} \end{pmatrix} \tag{4}$$

The model equation was differentiated with regard to each individual factor to obtain the gradient vectors. Optimum factor settings were attained by solving these gradient vectors simultaneously. The optimal coded values were $X_1 = -0.272$, $X_2 = 0.212$ and $X_3 = -0.040$, which in natural values are converted to be 2Mp concentration of 12.28 mg/L, ACN percent of 59% water and flow rate of 0.74 mL/min. An optimum peak asymmetry of 1.048 was predicted by the model. This was further validated experimentally. The chromatogram obtained for 2Mp detection is given in Fig. 1.

3.2 Linearity

A standard calibration graph was developed at the optimal solvent ratio for quantification of 2Mp concentrations in the range of 0–50 mg/L and shown in Fig. 2. The line was found to be linear, having a correlation coefficient (R^2) value of 0.99.

3.3 Factor Effects

In the model equation, the output was affected by the negative/positive sign of the regression coefficient of each factor, which contributed by taking away or adding to the total output respectively. The effect of a unit change in variable value on total predicted yield is captured by regression coefficients. Absolute magnitudes of regression coefficients were used to plot the Pareto chart in Fig. 3. Quadratic effect of ACN percent ($X_2{}^2$), followed by linear effect of ACN percent (X_2) and quadratic effect of flow rate ($X_3{}^2$) had the most impact on peak asymmetry, i.e. nearly 50%, 22% and 12%, respectively. The plot gives around 98% of the 2Mp removal prediction which was accounted for by the factor effects shown in the plot.

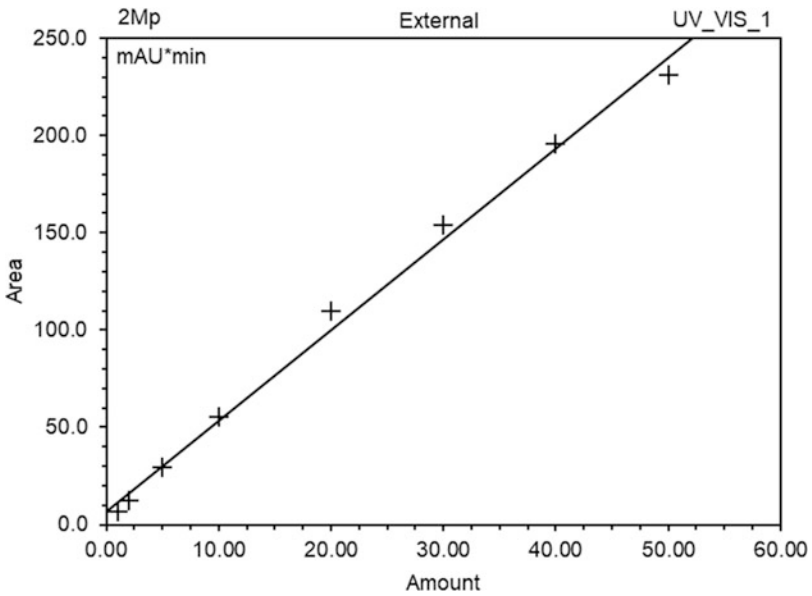

Fig. 2 Standard calibration curve for the quantification of 2-methylpyridine by HPLC

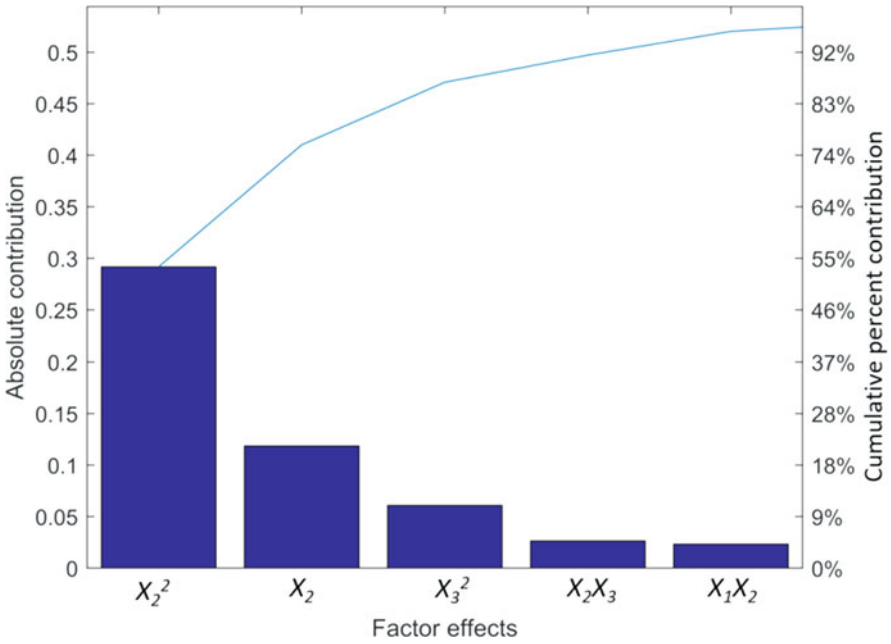

Fig. 3 Pareto plot representing the effects of factors on peak asymmetry for 2-methylpyridine detection

3.4 Adequacy of the Model

An assumption made during model formulation was that the regression coefficients are normally distributed. In order to validate this, the predicted peak asymmetry was plotted against respective errors in Fig. 4. Error is the difference of experimental and predicted values. The errors were distributed in a trendless-cum-haphazard manner, implying that the model-predicted data followed a normal distribution. Upon charting the experimental peak asymmetry with respect to the predicted peak asymmetry (Fig. 5), a correlation coefficient (R^2) of 0.982 was seen, which implied an accurate method design.

The normal probability plot of the factor effects provides more evidence of the model's suitability. It is presented in Fig. 6 with cumulative probability on the vertical axis and factor effects on the horizontal axis. A plot in the shape of a straight line emerges from plotting the graph with a focus on the central values rather than the extremes. A few factor effects are observed to fall outside of the straight line in the illustration. According to the sparsity of effects principle, some important factors and some low-order factor interactions have a major impact on any system. The straight line represents the distribution of the factor effects with a mean of zero and a certain variance, which have the least influence on the output [12]. Higher-order interactions would lie along this straight line, and thus their impacts are inconsequential. The most important factors causing disruptive effects on the model-predicted peak asymmetry were X_2^2, X_2 and X_3^2.

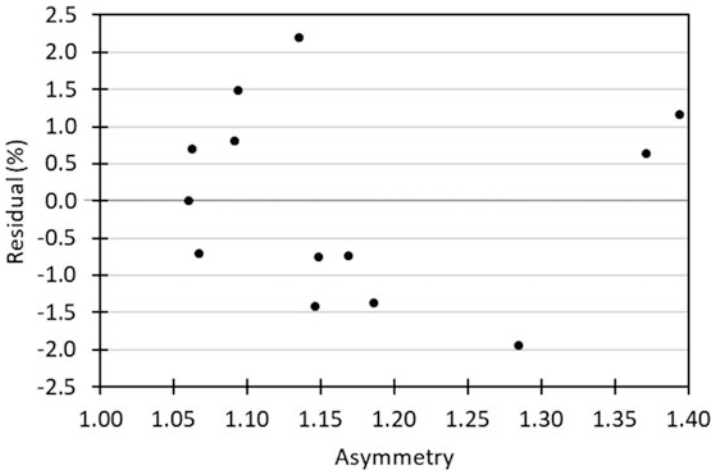

Fig. 4 Predicted peak asymmetry versus error

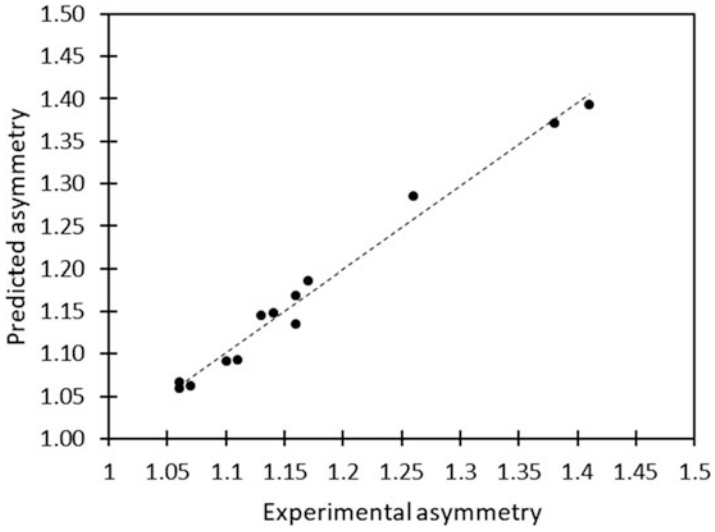

Fig. 5 The correlation between model-predicted peak asymmetry and experimental data

3.5 Response Surface Analysis

Visualization of the model output on a 3D plane is difficult when more than two factors are studied at the same time. Thus, by restricting the model equation to two factors, three equations ($^3C_2$) were generated, consisting of linear, quadratic and interaction terms. The remaining factors were maintained at a constant coded value of zero, corresponding to mid-level experimental values for each factor. Using this

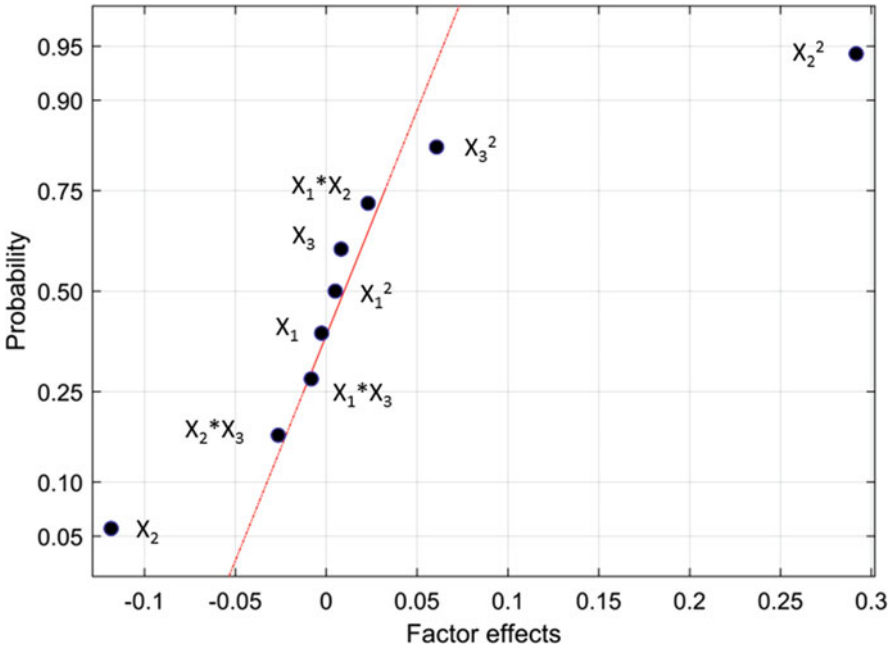

Fig. 6 Normal probability plot of factors affecting peak asymmetry in 2-methylpyridine detection

rule, the equations that were developed for the visualization of predicted peak asymmetry are given below:

$$Y_{12} = 1.06 - 0.0025^{*}X_1 - 0.1184^{*}X_2 + 0.005^{*}X_1^2 + 0.2917^{*}X_2^2 + 0.0231^{*}X_1{}^{*}X_2$$
$$Y_{13} = 1.06 - 0.0025^{*}X_1 + 0.0082^{*}X_3 + 0.005^{*}X_1^2 + 0.0608^{*}X_3^2 - 0.0082^{*}X_1{}^{*}X_3$$
$$Y_{23} = 1.06 - 0.1184^{*}X_2 + 0.0082^{*}X_3 + 0.2917^{*}X_2^2 + 0.0608^{*}X_3^2 - 0.0263^{*}X_2{}^{*}X_3 \quad (5)$$

Contour diagrams and response surfaces shown in Fig. 7 were generated in order to evaluate the effect of these factor interactions on peak asymmetry. It is discernable from Fig. 7a that as the concentration of 2Mp (X_1) increases, the peak asymmetry remains nearly constant. Also, as the ACN ratio (X_2) increases, there is initially a decrease and then an increase in peak asymmetry. This is possibly because 2Mp is an electron-deficient compound [1]. At high ACN ratio, ACN acts as an electron pair donor for 2Mp. This results in the detachment of 2Mp from the column media and finally its elution from the column [3]. Next in Fig. 7b, it is seen that as the flow rate (X_3) increases, the peak asymmetry increases slightly. Also, as the 2Mp concentration (X_1) increases, the peak asymmetry remains nearly constant. Thereafter, in Fig. 7c it is seen that as the flow rate (X_3) increases, the peak asymmetry increases

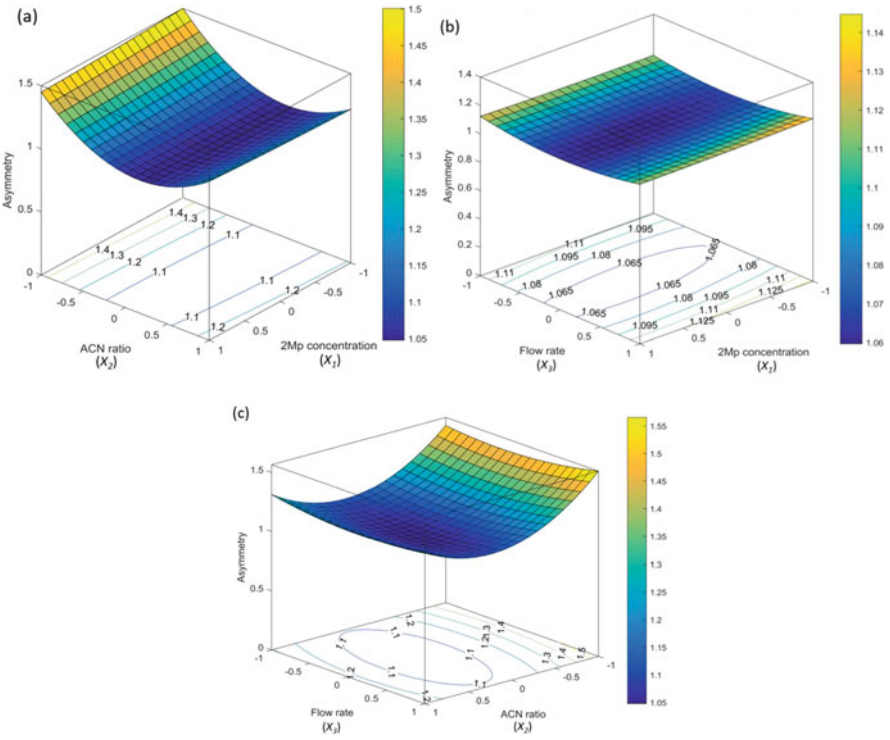

Fig. 7 Response surfaces and contours representing the interaction between the factors affecting peak asymmetry in 2-methylpyridine detection, considered two at a time: (**a**) 2Mp concentration vs. ACN ratio; (**b**) 2Mp concentration vs. flow rate; (**c**) ACN ratio vs. flow rate

slightly. But as the ACN ratio (X_2) increases, the peak asymmetry first decreases and then increases. From all the three plots in Fig. 7, it can thus be seen that ACN percent is the most important factor affecting peak asymmetry.

3.6 Model Validation and Repeatability

Validating a mathematical model with data from literature is the next crucial step. However, no other research using the same experimental conditions and setup as used in this study could be located. To ensure that the results of this study could be repeated and reproduced, a set of five runs was performed by setting each factor to its experimental mid-level value. While the average experimental peak asymmetry from these five runs was 1.07, the model-predicted peak asymmetry was found to be 1.06. The maximum absolute error percentage was 0.94%. Additionally, a set of five runs was performed at the optimal values of factors. In this case, the average experimental peak asymmetry was 1.06, and the model-predicted peak asymmetry was found to be

1.048. Thus, it can be agreed within reason that the model is proficient in the prediction of peak asymmetry. This is however subject to the chosen range of values for the factors affecting the detection and quantification of 2Mp by HPLC.

3.7 Detection and Quantitation Limits

The quantification limit (QL) and the detection limit (DL) were determined according to the procedure described elsewhere [13]. A chosen standard solution with 2Mp concentration of 2 mg/L was injected five consecutive times. If s is the standard deviation of the standard solution chosen, and S is the calibration curve slope, then, DL and QL are given by Eqs. (6) and (7), respectively:

$$\mathrm{DL} = 3.3 \times s/S \tag{6}$$

$$\mathrm{QL} = 10 \times s/S \tag{7}$$

Using Eqs. (6) and (7), DL was determined to be 0.14 mg/L, and QL was determined to be 0.42 mg/L. This implies that the method developed in the above study has adequate sensitivity for determination of 2Mp concentration.

3.8 Application for Industrial Effluent

Application of this study is in the detection of 2Mp found in textile dyeing industry effluent. The wastewater from this industry contains 2Mp since it is utilized as a solvent in the cotton-dyeing process. The effluent was diluted five times before use in order to protect the health of the column and reduce noise. Three identical runs were performed using an ACN percent of 59% and averaged. The average 2Mp concentration present in the original raw textile dyeing effluent was found to be 10.1 mg/L (Fig. 8).

4 Conclusion

A mathematical model was successfully developed using Doehlert design of experiments for the minimization of peak asymmetry in the detection and quantification of 2-methylpyridine by HPLC. The chromatographic conditions necessary for the detection of 2Mp by HPLC were successfully optimized. The acetonitrile-to-water ratio was found to be the most important factor affecting the peak asymmetry. The results of the study were presented using the response surface method (RSM). There was a good correlation between the experimental and model-predicted data. The

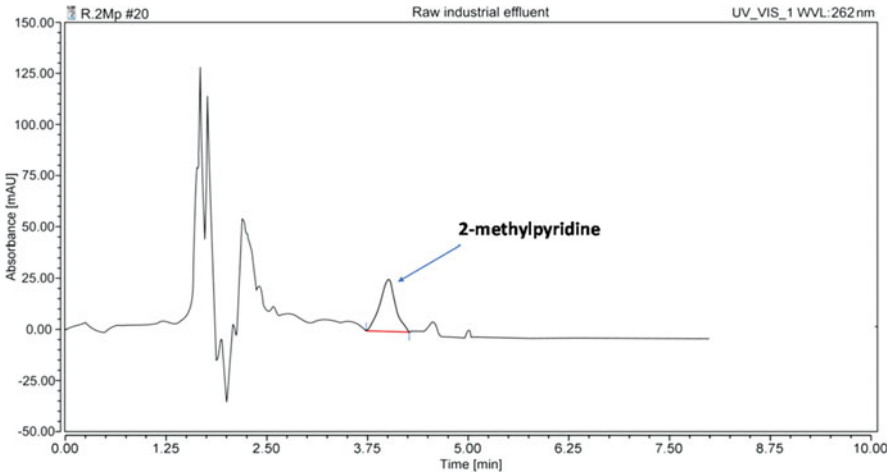

Fig. 8 Detection of 2-methylpyridine in raw textile dyeing industry effluent

model was designed with a low prediction error. The developed method was successfully applied in the detection of 2Mp found in textile dyeing industry effluent.

Acknowledgement The authors are grateful to the Ministry of Human Resource Development, Government of India, for supporting the parent institute in research.

References

1. R. Chatterjee, C. Majumder, Uptake of azaarenic 2-Methylpyridine by pre-cooled carboxyl functionalized graphene nanocomposite: Detection, sorption and optimization. J. Water Process Eng. **39**, 101686 (2021). https://doi.org/10.1016/j.jwpe.2020.101686
2. F. Ullmann, W. Gerhartz, Y.S. Yamamoto, F.T. Campbell, R. Pfefferkorn, J.F. Rounsaville, *Ullmann's Encyclopedia of Industrial Chemistry*, 5th edn. (VCH Publishers, Deerfield Beach, 1993). https://agris.fao.org/agris-search/search.do?recordID=US201300377147. Accessed 22 Nov 2020
3. R. Chatterjee, C. Majumder, Low-temperature synthesis of functionalized activated carbon from blackboard (Alstonia scholaris) with improved selectivity for 2-methylpyridine removal: Batch and column analyses. Environ. Sci. Pollut. Res. **29**, 28031–28049 (2022). https://doi.org/10.1007/s11356-021-18377-3
4. Y. Bai, Q. Sun, C. Zhao, D. Wen, X. Tang, Bioaugmentation treatment for coking wastewater containing pyridine and quinoline in a sequencing batch reactor. Appl. Microbiol. Biotechnol. **87**, 1943–1951 (2010). https://doi.org/10.1007/s00253-010-2670-8
5. R. Chatterjee, C. Majumder, Application of modified graphene oxide-chitosan composite for the removal of 2-methylpyridine using fixed bed adsorption and subsequent regeneration of the adsorbent by UV photolysis. J. Water Process Eng. **53**, 103654 (2023). https://doi.org/10.1016/j.jwpe.2023.103654

6. S. Kumar, D. Surana, J. Gupta, S. Sharma, P. Ghosh, A review on advances in removal of endocrine disrupting compounds from aquatic matrices: Future perspectives on utilization of agri-waste based adsorbents. Sci. Total Environ. **826**, 154129 (2022). https://doi.org/10.1016/j.scitotenv.2022.154129
7. R.A. Pandey, S. Sandhya, Microbial degradation of heterocyclic bases in a completely mixed activated sludge process. J. Environ. Sci. Health. Part A: Environ. Sci. Eng. Toxicol. **32**, 1325–1338 (1997). https://doi.org/10.1080/10934529709376612
8. F. Ban, Z. Song, H. Liu, Z. Jia, F. Guo, Determination of amprolium hydrochloride and 2-picoline impurity by HPLC. Chin. J. Vet. Drug **7** (2005). https://en.cnki.com.cn/Article_en/CJFDTotal-ZSYY200507009.htm. Accessed 9 Dec 2022
9. A.M. Faria, C.H. Collins, I.C.S.F. Jardim, State-of-the-art in immobilized polymer stationary phases for high-performance liquid chromatography. J. Braz. Chem. Soc. **20**, 1385–1398 (2009). https://doi.org/10.1590/S0103-50532009000800002
10. D.H. Doehlert, Uniform shell designs. Appl. Stat. **19**, 231 (1970). https://doi.org/10.2307/2346327
11. M.D. Morris, A class of three-level experimental designs for response surface modeling. Technometrics **42**, 111–121 (2000). https://doi.org/10.1080/00401706.2000.10485990
12. C. Daniel, Use of half-normal plots in interpreting factorial two-level experiments. Technometrics **1**, 311–341 (1959). https://doi.org/10.1080/00401706.1959.10489866
13. P.K. Sahu, N.R. Ramisetti, T. Cecchi, S. Swain, C.S. Patro, J. Panda, An overview of experimental designs in HPLC method development and validation. J. Pharm. Biomed. Anal. **147**, 590–611 (2018). https://doi.org/10.1016/j.jpba.2017.05.006

Part II
Industrial Effluent Treatment, Reuse and Conservation

Importance of Cost Functions for Biological Treatment of Wastewater

Bhaskar Sengupta and Somnath Mukherjee

Abstract The availability of many technological alternatives for the biological treatment of wastewater, ranging from conventional treatment options to advanced technologies, introduces the requirement for scrutiny to select the most appropriate technology for the treatment of wastewater for any specific project. Use of cost function may be an approach to compare the costs of alternatives for the biological treatment of wastewater. It enables better engineering decisions and suitable selection of the appropriate treatment scheme based on parametric criteria, requirement of space, construction cost and annual cost of operation as well as maintenance. The literatures available in the context of selection of appropriate technology for biological treatment of wastewater on the basis of engineering economics and other issues are limited, and in most of the studies, the cost functions for wastewater treatment plants have been derived from region-specific historic cost data collected. The objective of this paper is to highlight the importance of initiatives to develop the cost functions and present a methodology for its development by the application of modelled algorithms for process design as well as cost estimation and the use of different statistical regression techniques. This research initiative is believed to be useful in the planning of new facilities by the stakeholders of assets.

Keywords Biological treatment · CAPEX · Cost function · Cost estimation · Methodology · OPEX · Regression · Space saving · Wastewater · WWTP

Abbreviations

ASP	Activated sludge process
BOD_5	Five-day biochemical oxygen demand
BOD_u	Ultimate biochemical oxygen demand

B. Sengupta (✉) · S. Mukherjee
Environmental Engineering Division, Department of Civil Engineering, Jadavpur University, Kolkata, India
e-mail: somnath.mukherjee@jadavpuruniversity.in

D. Mazumder (ed.), *Sustainable Advanced Technologies for Industrial Pollution Control*, Springer Proceedings in Earth and Environmental Sciences,
https://doi.org/10.1007/978-3-031-37596-5_6

CAPEX	Total bare construction cost
CMAS	Complete-mix activated sludge
COD	Chemical oxygen demand
EA	Extended aeration
FAB	Fluidized aerobic bioreactor
MAPE	Mean absolute percentage error
MBBR	Moving bed biofilm reactor
MLD	Million litres per day
MLSS	Mixed liquor suspended solids
MLVSS	Mixed liquor volatile suspended solids
NH_4-N	Ammonia nitrogen
NO_3-N	Nitrate nitrogen
ON	Organic nitrogen
OP	Oxidation pond
OPEX	Levelized cost based on energy requirement, operation and maintenance
SBR	Sequential batch reactor
TKN	Total Kjeldahl nitrogen
TP	Total phosphorous
TSS	Total suspended solids
UASB	Upflow anaerobic sludge blanket
VSS	Volatile suspended solids
WSP	Waste stabilization pond
WWTP	Wastewater treatment plant

1 Introduction

Industrial and urban activities of developing countries like India result in significant wastewater generation. A number of incentives and policy structures are promulgated by the local governments as well as other agencies to encourage different stakeholders to treat and reuse wastewater. A biological treatment system is an important component of a wastewater treatment plant (WWTP), which requires proper selection of site-specific, appropriate and cost-efficient treatment technology for the economy and for sustainability. In connection with this, stakeholders often need a rapid cost estimation of biological treatment systems for various capacities and technologies with due consideration of operation as well as maintenance issues and requirement of space. In the last five decades, it has been noted from literature review that several researches have been undertaken in respect of the development of cost functions for rapid estimation of construction and operation costs of biological treatment systems in WWTPs [1–31]. The initiatives were targeted for techno-economic evaluations of several treatment technologies. Several methods have been used to develop cost functions. Gratziou et al. [9] compared the total costs for several small-scale sewage treatment systems by calculating the costs of

construction and operation based on functions for cost elements available in literature. Hernandez-Sancho et al. [11] published a set of cost functions for different technologies based on the collected data from 341 WWTPs in Spain. Koul and John (2015) presented a life cycle cost analysis for upflow anaerobic sludge blanket reactor, sequential batch reactor (SBR) and moving bed biofilm reactor (MBBR) based on the available information from different existing WWTPs [13]. Papadopoulos et al. (2007) collected data for land requirement and costs of construction, operation and maintenance of existing wastewater treatment facilities. They developed 12 equations applying ordinary least squares and fuzzy linear regression techniques [19]. It has been noted that in most of the studies, the cost functions for land, construction, operation and maintenance of biological treatment systems in WWTPs have been derived from region-specific historic cost data collected [6, 22, 25–27]. In few cases evaluations of few preselected technologies have been made by using software like CapdetWorks for a specific input flow rate [2, 12]. However, the literatures published in the context of cost functions developed based on engineering economics and other issues applicable in India are limited in number.

The intent of rapid cost analysis in the early phase of a project requires the availability of applicable cost functions, if accurate and reliable estimation is being pursued. However, there are no tools in India or literatures or other kinds of database to select such technology based on flow and other requisite parameters which may assist government-level engineers and practicing engineers to adopt a technology without any biasness. Such paucity brought in the motivation to examine various biological treatment technologies with detailed cost estimate and to explore suitable cost functions for the selection of the most suitable technology for a specific project requirement. The required quality of treated effluent must be achieved by the selection of proper technology, and at the same time, a minimal land footprint needs to be considered. It is required to evaluate civil cost, electromechanical cost, land cost and operation and maintenance cost for the development of cost functions.

The objective of this paper is to highlight the importance of initiatives to develop the cost functions and present a methodology for its development by the application of developed modelled algorithms for process design as well as cost estimation and the use of different statistical regression techniques. This research initiative is believed to be useful in the planning of new facilities by the stakeholders of assets.

2 Materials and Methods

Different technologies available for biological treatment of wastewater are furnished below as Ref. [32] (Table 1).

The requirement of plan area for use of various biological treatment technologies ranges between 0.2 and 1.0 hectare per MLD based on the technology adopted except that for WSP [32].

Table 1 Technologies for biological treatment of wastewater

Sl. no.	Technology
1.	Activated sludge process (ASP)
2.	Extended aeration (EA)
3.	Sequential batch reactor (SBR)
4.	Moving bed biofilm reactor (MBBR)
5.	Fluidized aerobic bioreactor (FAB)
6.	Upflow anaerobic sludge blanket (UASB)
7.	Waste stabilization pond (WSP)
8.	Oxidation pond (OP)
9.	Others

With the gap as noticed from literature review and objective to establish a rational base, a novel research initiative is required to develop a tool for basic engineering design and forecasting cost by means of cost functions on the basis of realistic cost estimation in detail. The purpose and objective of this study is to present a methodology to develop cost functions based on detail engineering design and cost estimations with due consideration of Indian rates but not based on historic cost data.

Conventionally wastewater is treated in sequential stages such as primary, secondary and treatment of biological sludge for safe disposal into the environment. Methods of treatment of wastewater in grit chambers and that of biological sludge are more or less the same in most of the cases as alternatives for such treatment are restricted. Therefore, the cost of such treatment for a specific input rate of wastewater and biological load will remain more or less the same for a technology under concern. However, the cost of biological treatment will depend upon the kind of the bioreactor technology selected for treatment. Thus, comparison among the costs of bioreactors along with pre-treatment and post-treatment facilities as necessary will enable to select the most suitable technology for a specific case.

A novel and unique method is proposed as follows and may be adopted to develop a tool in respect of rapid estimation for life cycle cost of biological treatment for each kind of the above technologies.

The salient features adopted for the design as well as estimation and the methodology to derive cost functions are delineated below.

2.1 Capacity Groups

A single cost function for all the capacity range is not considered as appropriate. The costs of biological treatment systems generally decrease with increase in capacity due to economy of scale. Therefore, biological treatment systems may be categorized capacity-wise in three groups, viz. small (0.5–5.0 MLD), medium (5.0–50.0 MLD) and large (50.0–150.0 MLD).

2.2 Design Inlet Quality of Wastewater

The characteristics of raw wastewater depend on the rate of water supply and pollution load per capita. The concentrations of impurities in raw wastewater as envisaged for design purpose are furnished below. This is based on water supply at 135 lit/cap/day [33] (Table 2).

2.3 Design Treated Quality of Wastewater

The design treated water quality as adopted for the development of cost functions are presented in Table 3:

The above are in line with the stipulations documented by the Ministry of Environment and Forests (MoEF) of the Government of India (GOI).

2.4 Design Parameters

The typical design parameters as follows may be adopted for biological treatment in WWTPs [34] (Table 4):

Table 2 Design inlet quality of wastewater

Parameters	Value	Unit
Biological oxygen demand (BOD_5)	250.00	g/m^3
Chemical oxygen demand (COD)	425.00	g/m^3
Volatile suspended solids (VSS)	262.50	g/m^3
Total suspended solids (TSS)	375.00	g/m^3
Ammonia nitrogen (NH_4-N)	32.50	g/m^3
Organic nitrogen (ON)	17.50	g/m^3
Nitrate nitrogen (NO_3-N)	5.00	g/m^3
Total Kjeldahl nitrogen (TKN)	50.00	g/m^3
Total phosphorous (TP)	7.10	g/m^3

Table 3 Design treated water quality of wastewater

Parameters	Value	Unit
Biological oxygen demand (BOD_5) design limit	10.00	g/m^3
Total suspended solids (TSS)	10.00	g/m^3

Table 4 Design parameters for biological treatment in WWTPs

Parameters	Value	Unit
Peak factor	2.25	
Lean factor	0.45	
Thickener overflow return as fraction of plant flow	0.15	
BOD in thickener overflow return	500.00	g/m^3
Centrate from sludge dewatering as fraction of plant flow	0.0060	
BOD in centrate from sludge dewatering return	380.00	g/m^3
BOD_u/VSS	1.42	g BOD/g VSS
BOD_5/BOD_u	0.67	
Kinetic parameters for BOD removal		
Reference temperature for kinetic parameters	20.00	°C
Half velocity constant	20.00	g bs COD/m^3
Maximum specific bacterial growth rate	6.00	(g VSS/g VSS)/d
Endogenous decay coefficient	0.06	(g VSS/g VSS)/d
True yield coefficient	0.3125	g VSS/g b COD
	0.5000	g VSS/g BOD
Fraction of biomass that remains as cell debris	0.15	
θ values		
Temperature activity coefficient for K_s	1.00	
Temperature activity coefficient for μ_m	1.07	
Temperature activity coefficient for k_d	1.04	
Design temperature of reactor basin	12.00	°C
Design MLSS	*Variable (technology specific)*	g/m^3
Ratio of VSS to TSS	0.70	
Design MLVSS	*Variable (technology specific)*	g/m^3
Percentage clean water oxygen transfer efficiency (for fine bubble ceramic diffusers)	35.00	%
Elevation at site	9.00	m
Atmospheric pressure at elevation of site	95.60	kPa
Effective liquid depth in reactor basin	4.07	m
Point of air release for ceramic diffusers from the bottom of reactor basin	0.50	m
Standard temperature	20.00	°C
Concentration of dissolved oxygen at standard temperature & pressure of 101,325 N/m^2	9.08	g/m^3
Aeration α factor for BOD removal	0.50	
Salinity and surface tension correction factor for both conditions, i.e. BOD removal	0.95	
Diffuser fouling factor	0.90	
Percentage (by weight) of oxygen in air	23.20	%

(continued)

Table 4 (continued)

Parameters	Value	Unit
Density of air	1.20	kg/m^3
Oxygen transfer efficiency	8.00	%
Factor of safety	2.00	
Oxygen consumption	1.42	mg/mg of cell

2.5 Components of WWTPs

The major components as required for a specific biological treatment technology in WWTP need to be identified. For example, in case of conventional complete-mix activated sludge (CMAS) process or moving bed biofilm reactor (MBBR) – a modern and space saving technology – the equipment will be as follows:

(a) Primary clarifiers
(b) Primary clarifier sludge sump
(c) Primary clarifier sludge transfer pumps and pump-house
(d) Reaction basins and accessories
(e) Reactor basin waste transfer pumps and pump-house
(f) Secondary clarifiers
(g) Secondary clarifier sludge sump
(h) Secondary clarifier sludge transfer pumps and pump house
(i) Blowers and blower building

2.6 Design, Detailing and Cost Estimation

Design and estimations have been envisaged to be carried out by means of a model developed in Microsoft Excel (2010 version).

The model will facilitate the development of cost functions as follows:

Process design and sizing of the major components for the technology-specific biological treatment system based on the design criteria as addressed earlier [34].

Determination of schedule of quantities for the designed components by use of algorithms suggested for basins with diffused aeration, pumping and blowers as addressed in CAPDET – USEPA [35].

Estimation of cost for each of the major components for biological treatment system based on schedule of rates (latest publication) of Public Works Department (PWD), Government of India [36], for scheduled components of civil works (for cost of earthwork, R.C. wall in-place, R.C. slab in-place and handrails in-place) and market rates (rate data collected from vendors) for non-scheduled mechanical as well

as electrical equipment with applicable accessories including contingencies at 10% to account for the minor cost items such as piping system, control equipment, painting, site cleaning and preparation etc.

Determination of total bare construction cost (CAPEX); levelized cost based on energy requirement, operation and maintenance (OPEX) for 25 years of life of WWTP; and cost of land for installation of the complete system (based on space requirements with due consideration of adequate access for operation and maintenance of major equipment).

The inputs to the model will be design capacity of biological treatment system in MLD, concentrations of BOD_5, TSS of raw wastewater and the permissible effluent BOD_5 and TSS. The output from the model will be the overall cost of major components for biological treatment in the WWTP inclusive of CAPEX and OPEX with 2021 considered as base year.

3 Results and Discussion

Data sets comprised of different groups in terms of capacities [at the interval of 0.5 MLD for small group, 5 MLD for medium group and 10 MLD for large group] and respective integrated costs inclusive of capital cost, operation as well as maintenance cost and cost of land are envisaged to be determined as addressed above by means of model algorithms for detail design and estimation developed in Microsoft Excel.

Regression analysis of data generated from the model is envisaged to be applied in Microsoft Excel based on trend lines with five different equations (viz. exponential, linear, logarithmic, polynomial and power) to determine the relationship between capacity and respective overall cost for the treatment envisaged. The equation that will correspond to the maximum coefficient of determination shall be selected as cost function for each case.

The cost function derived for each of the three capacity groups will be validated based on comparison between predicted value by use of the cost function and the respective estimated cost. The accuracy of predicted cost shall be analysed based on mean absolute percentage error – a widely used measure of accuracy. MAPE is defined as average of absolute percentage errors. It is calculated as follows:

$$\text{MAPE} = \sum \{(|A - F|/A) * 100\}/N \tag{1}$$

where A is the estimated cost, F the forecasted cost by use of cost function as determined and N the number of elements in the data set.

The significance of MAPE value is furnished below which interprets the accuracy of prediction (Table 5).

For reference, a summary of results derived for medium range of MBBRs are presented hereinafter in Appendix I. Regression analysis has been carried out on generated data sets based on different equations as addressed above for

Table 5 Interpretation of MAPE

MAPE	Interpretation
<10	Accurate forecasting result
10–20	Good forecasting result
20–50	Reasonable forecasting result
>50	Inaccurate forecasting result

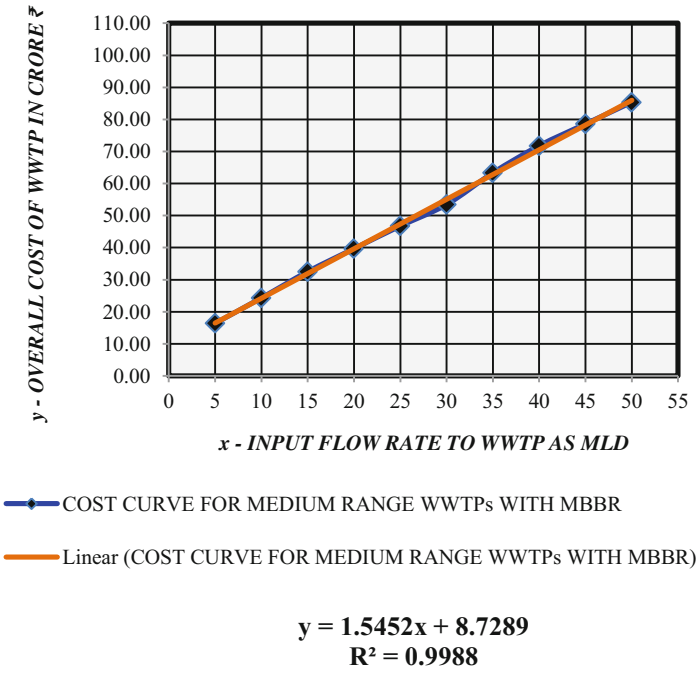

Fig. 1 Cost curve

determination of the relationship between capacity and respective overall cost for the treatment envisaged. For medium-capacity range, the cost curve with the capacities of WWTPs [as MLD] along X-axis and integrated costs of biological treatment in WWTPs [as ₹ (crore)] along Y-axis is shown in Fig. 1 based on the results obtained by the application of the developed design and estimation algorithms as well as optimization. The curve out of the above five alternative equations, which corresponds to coefficient of determination (R^2) closest to unity, has been displayed, and the respective cost function is embedded therein.

The cost function determined for medium-capacity range of WWTPs with MBBR is furnished in Table 6.

It has been noted that cost function for medium group is best expressed by linear equation. The respective determination coefficient in respect of cost function for capacity-wise medium group is 0.9988. The mean absolute percentage error with

Table 6 Cost functions for medium range of WWTPs with MBBR

Description	Equation	Value of R^2	Value of MAPE
Cost function for medium range (5MLD-50 MLD) of WWTPs with MBBR (5 MLD–50 MLD)	$C_{MR} = 1.5452 * Q_{MR} + 8.7289$	0.9988	1.12

Where:
C_{MR} – cost [₹ (in crore)] of a WWTP within medium range
Q_{MR} – input flow rate [in MLD] for a WWTP within medium range

reference to the cost functions for medium range is 1.12%. The mean absolute percentage error is found to be below 10%.

4 Conclusion

It may be concluded that accurate forecast cost may be inferred by integrated cost functions developed for small, medium and large groups of WWTPs with any type of technology as presented for medium-range capacity of MBBR. The cost functions are not derived from historic cost database. Rather, cost functions have been developed based on detailed engineering design and cost estimations with due consideration of rates applicable in India. The approach as adopted and addressed may be followed to develop cost functions applicable for any location in any country across the world either based on use of design and estimation algorithms developed and region-specific schedule of rates for precise forecast or adjustment of projected costs (by cost functions developed) by location-specific currency conversion factor for tentative forecast.

The exercise for the development of cost functions for rapid life cycle cost estimation in connection with construction and operation of a WWTP with different technologies will create a platform for quick comparison among the technologies with due consideration of costs for construction, operation and maintenance as well as requirement of space. It is anticipated that accurate cost forecasts can be made by cost functions for small, medium and large capacities for the selection and use of the most appropriate technology for a specific flow rate at a specific site. As obvious such forecasted cost of biological treatment system for WWTP as to be projected by developed cost function will not represent the overall cost of the entire project. The actual estimated cost of a project is always site specific and should be worked out based on all components to be included for the project.

Acknowledgement The research for the development of cost functions with reference to space-saving modern technologies available for biological treatment is under progress and is at an advanced stage. I would like to thank all the members of the Environmental Engineering Division, Department of Civil Engineering, Jadavpur University, Kolkata 700032, India, for their support and assistance.

Appendix I: Medium-range WWTPs with MBBR

Design summary for moving bed biofilm reactor basins											
BOD removal											
		Capacity in mld	Capacity in mld	Capacity in mld	Capacity in mld	Capacity in mld	Capacity in mld	Capacity in mld	Capacity in mld	Capacity in mld	Capacity in mld
		5	10	15	20	25	30	35	40	45	50
Design parameter	Unit	Value	Value	Value	Value	Value	Value	Value	Value	Value	Value
Average wastewater flow rate	m^3/d	5000.00	10000.00	15000.00	20000.00	25000.00	30000.00	35000.00	40000.00	45000.00	50000.00
Influent flow rate to reactor basins	m^3/d	5723.75	11447.50	17171.25	22895.00	28618.75	34342.50	40066.25	45790.00	51513.75	57237.50
Average BOD load	kg/d	1198.90	2397.80	3596.70	4795.60	5994.50	7193.40	8392.30	9591.20	10790.10	11989.00
Average TKN load	kg/d	275.25	550.50	825.75	1101.00	1376.25	1651.50	1926.75	2202.00	2477.25	2752.50
Two stages for BOD removal											
Number of tanks for stage 1 (for preliminary BOD removal)	Number	2	3	4	4	4	4	6	6	6	6
Volume of each tank for stage 1 (for preliminary BOD removal)	m^3	99.91	133.21	149.86	199.82	249.77	299.73	233.12	266.42	299.73	333.03
Concentration of BOD in effluent from stage 1	g/m^3	47.13	47.13	47.13	47.13	47.13	47.13	47.13	47.13	47.13	47.13
Number of tanks for stage 2 (for final BOD removal)	Number	2	3	4	4	4	4	6	6	6	6
Volume of each tank for stage 2 (for final BOD removal)	m^3	97.74	130.32	146.60	195.47	244.34	293.21	228.05	260.63	293.21	325.79
Concentration of BOD in effluent from stage 2	g/m^3	2.98	2.98	2.98	2.98	2.98	2.98	2.98	2.98	2.98	2.98

(continued)

Design summary for moving bed biofilm reactor basins											
BOD removal											
		Capacity in mld	Capacity in mld	Capacity in mld	Capacity in mld	Capacity in mld	Capacity in mld	Capacity in mld	Capacity in mld	Capacity in mld	Capacity in mld
		5	10	15	20	25	30	35	40	45	50
Design parameter	Unit	Value	Value	Value	Value	Value	Value	Value	Value	Value	Value
Design features											
MLSS (X_{MLSS})	g TSS/m^3	5000.00	5000.00	5000.00	5000.00	5000.00	5000.00	5000.00	5000.00	5000.00	5000.00
MLVSS (X_{MLVSS})	g VSS/m^3	2832.63	2832.63	2832.63	2832.63	2832.63	2832.63	2832.63	2832.63	2832.63	2832.63
F/M	(g BOD/d)/g VSS	1.27	1.27	1.27	1.27	1.27	1.27	1.27	1.27	1.27	1.27
Volumetric BOD loading	(kg BOD/d)/m^3	3.61	3.61	3.61	3.61	3.61	3.61	3.61	3.61	3.61	3.61
Total sludge (TSS) purged per day	kg TSS/d	1145.43	2290.86	3436.29	4581.72	5727.15	6872.58	8018.01	9163.44	10308.87	11454.30
Observed yield based on VSS	g bVSS/g bCOD	0.34	0.34	0.34	0.34	0.34	0.34	0.34	0.34	0.34	0.34
	g bVSS/g BOD	0.55	0.55	0.55	0.55	0.55	0.55	0.55	0.55	0.55	0.55
Observed yield based on TSS	g TSS/g bCOD	0.61	0.61	0.61	0.61	0.61	0.61	0.61	0.61	0.61	0.61
	g TSS/g BOD	0.97	0.97	0.97	0.97	0.97	0.97	0.97	0.97	0.97	0.97
Overall oxygen demand	kg oxygen/h	45.65	91.31	136.96	182.62	228.27	273.93	319.58	365.24	410.89	456.55
Air flow rate at average wastewater flow rate	m^3/min	38.92	77.83	116.75	155.66	194.58	233.50	272.41	311.33	350.24	389.16
RAS recycle ratio	Number	0.69	0.69	0.69	0.69	0.69	0.69	0.69	0.69	0.69	0.69

(continued)

Design summary for moving bed biofilm reactor basins											
BOD removal											
		Capacity in mld	Capacity in mld	Capacity in mld	Capacity in mld	Capacity in mld	Capacity in mld	Capacity in mld	Capacity in mld	Capacity in mld	Capacity in mld
		5	10	15	20	25	30	35	40	45	50
Design parameter	Unit	Value	Value	Value	Value	Value	Value	Value	Value	Value	Value
Quality of effluent											
Concentration of BOD of effluent	g/m^3	9.99	9.99	9.99	9.99	9.99	9.99	9.99	9.99	9.99	9.99
Concentration of TSS of effluent	g/m^3	10.00	10.00	10.00	10.00	10.00	10.00	10.00	10.00	10.00	10.00
Concentration of NH_4-N of effluent	g/m^3	34.19	34.19	34.19	34.19	34.19	34.19	34.19	34.19	34.19	34.19
Concentration of NO_3-N of effluent	g/m^3	5.00	5.00	5.00	5.00	5.00	5.00	5.00	5.00	5.00	5.00

Equipment summary for moving bed biological reactor-based system											
BOD removal											
		Capacity in mld	Capacity in mld	Capacity in mld	Capacity in mld	Capacity in mld	Capacity in mld	Capacity in mld	Capacity in mld	Capacity in mld	Capacity in mld
		5	10	15	20	25	30	35	40	45	50
Description	Unit	Value	Value	Value	Value	Value	Value	Value	Value	Value	Value
Primary clarifiers											
Number of primary clarifiers	Number	2	2	2	2	2	2	2	4	4	4
Diameter of each primary clarifier	m	10.00	13.50	16.60	19.10	21.40	23.40	25.30	19.10	20.30	21.40

(continued)

Equipment summary for moving bed biological reactor-based system											
BOD removal											
		Capacity in mld	Capacity in mld	Capacity in mld	Capacity in mld	Capacity in mld	Capacity in mld	Capacity in mld	Capacity in mld	Capacity in mld	Capacity in mld
		5	10	15	20	25	30	35	40	45	50
Description	Unit	Value	Value	Value	Value	Value	Value	Value	Value	Value	Value
Side water depth of each primary clarifier	m	4.00	4.00	4.00	4.00	4.00	4.00	4.00	4.00	4.00	4.00
Primary clarifier sludge sump											
Number of sludge sumps	Number	1	1	1	1	1	1	1	1	1	1
Length of each sludge sump	m	6.10	6.10	6.10	6.10	6.10	6.10	6.10	6.10	6.10	6.10
Width of each sludge sump	m	6.10	6.10	6.10	6.10	6.10	6.10	6.10	6.10	6.10	6.10
Depth of each sludge sump	m	3.10	3.10	3.10	3.10	3.10	3.10	3.10	3.10	3.10	3.10
Primary clarifier sludge transfer pumps & pump-house											
Number of pump-houses	Number	1	1	1	1	1	1	1	1	1	1
Total number of pumps provided in each pump-house	Number	2	2	2	2	2	2	2	2	2	2
Design capacity for each pump	m^3/h	10.00	10.00	10.00	10.00	20.00	20.00	20.00	20.00	30.00	30.00
Head to be developed by each pump	mlc	20.00	20.00	20.00	20.00	20.00	20.00	20.00	20.00	20.00	20.00
Stage 1 of double-stage BOD removal reaction basins & accessories											
Number of reactor basins	Number	2	3	4	4	4	4	6	6	6	6

(continued)

Equipment summary for moving bed biological reactor-based system											
BOD removal											
		Capacity in mld	Capacity in mld	Capacity in mld	Capacity in mld	Capacity in mld	Capacity in mld	Capacity in mld	Capacity in mld	Capacity in mld	Capacity in mld
		5	10	15	20	25	30	35	40	45	50
Description	Unit	Value	Value	Value	Value	Value	Value	Value	Value	Value	Value
Length of each reactor basin	m	5.50	6.30	6.70	7.70	8.60	9.40	8.30	8.90	9.40	10.00
Width of each reactor basin	m	4.60	5.30	5.60	6.50	7.20	7.90	7.00	7.50	7.90	8.40
Depth of each reactor basin	m	4.57	4.57	4.57	4.57	4.57	4.57	4.57	4.57	4.57	4.57
Stage 2 of double-stage BOD removal reaction basins & accessories											
Number of reactor basins	Number	2	3	4	4	4	4	6	6	6	6
Length of each reactor basin	m	5.30	6.10	6.50	7.40	8.40	9.20	8.10	8.60	9.20	9.60
Width of each reactor basin	m	4.60	5.30	5.60	6.50	7.20	7.90	7.00	7.50	7.90	8.40
Depth of each reactor basin	m	4.57	4.57	4.57	4.57	4.57	4.57	4.57	4.57	4.57	4.57
Secondary clarifiers											
Number of secondary clarifiers	Number	2	2	2	2	2	2	4	4	4	4
Diameter of each secondary clarifier	m	20.90	28.10	34.50	39.80	44.50	48.70	37.20	39.80	42.20	44.50
Side water depth of each secondary clarifier	m	4.50	4.50	4.50	4.50	4.50	4.50	4.50	4.50	4.50	4.50

(continued)

Equipment summary for moving bed biological reactor-based system											
BOD removal											
		Capacity in mld	Capacity in mld	Capacity in mld	Capacity in mld	Capacity in mld	Capacity in mld	Capacity in mld	Capacity in mld	Capacity in mld	Capacity in mld
		5	10	15	20	25	30	35	40	45	50
Description	Unit	Value	Value	Value	Value	Value	Value	Value	Value	Value	Value
Secondary clarifier sludge sump											
Number of sludge sumps	Number	1	1	1	1	1	1	1	2	2	2
Length of each sludge sump	m	10.99	21.98	32.97	43.97	54.96	65.95	76.94	43.97	49.46	54.96
Width of each sludge sump	m	6.10	6.10	6.10	6.10	6.10	6.10	6.10	6.10	6.10	6.10
Depth of each sludge sump	m	3.10	3.10	3.10	3.10	3.10	3.10	3.10	3.10	3.10	3.10
Secondary clarifier sludge transfer pumps & pump-house											
Number of pump-houses	Number	1	1	1	1	1	1	1	1	1	1
Total number of pumps provided in each pump-house	Number	2	2	2	2	2	2	2	2	2	2
Design capacity for each pump	m^3/h	170.00	340.00	510.00	680.00	840.00	1010.00	1180.00	1350.00	1510.00	1680.00
Head to be developed by each pump	mlc	20.00	20.00	20.00	20.00	20.00	20.00	20.00	20.00	20.00	20.00

Estimated cost summary for moving bed biological reactor-based system											
BOD removal											
		Capacity in mld	Capacity in mld	Capacity in mld	Capacity in mld	Capacity in mld	Capacity in mld	Capacity in mld	Capacity in mld	Capacity in mld	Capacity in mld
		5	10	15	20	25	30	35	40	45	50
Description	Unit	Value	Value	Value	Value	Value	Value	Value	Value	Value	Value
Primary clarifiers											
Total bare construction cost (CAPEX)	Crore ₹	1.05	1.40	1.71	1.97	2.22	2.44	2.65	3.95	4.20	4.44
Levelized cost based on energy requirement, operation and maintenance for 25 years of life of primary clarifiers (OPEX)	Crore ₹	0.31	0.38	0.47	0.54	0.61	0.67	0.73	0.89	0.95	1.01
Overall cost inclusive of CAPEX & OPEX	Crore ₹	1.36	1.77	2.18	2.51	2.83	3.11	3.38	4.84	5.16	5.45
Primary clarifier sludge sump											
Total bare construction cost (CAPEX)	Crore ₹	0.05	0.05	0.05	0.05	0.05	0.05	0.05	0.05	0.05	0.05
Levelized cost based on energy requirement, operation and maintenance for 25 years of life of primary clarifier sludge sump (OPEX)	Crore ₹	0.14	0.14	0.14	0.14	0.14	0.14	0.14	0.14	0.14	0.14
Overall cost inclusive of CAPEX & OPEX	Crore ₹	0.19	0.19	0.19	0.19	0.19	0.19	0.19	0.19	0.19	0.19

(continued)

Estimated cost summary for moving bed biological reactor-based system											
BOD removal											
		Capacity in mld	Capacity in mld	Capacity in mld	Capacity in mld	Capacity in mld	Capacity in mld	Capacity in mld	Capacity in mld	Capacity in mld	Capacity in mld
		5	10	15	20	25	30	35	40	45	50
Description	Unit	Value	Value	Value	Value	Value	Value	Value	Value	Value	Value
Primary clarifier sludge transfer pumps & pump-house											
Total bare construction cost (CAPEX)	Crore ₹	0.67	0.67	0.67	0.67	0.70	0.70	0.70	0.70	0.73	0.73
Levelized cost based on energy requirement, operation and maintenance for 25 years of life of primary clarifier sludge transfer pumps & pump-house (OPEX)	Crore ₹	0.21	0.21	0.21	0.21	0.25	0.25	0.25	0.25	0.28	0.28
Overall cost inclusive of CAPEX & OPEX	Crore ₹	0.87	0.87	0.87	0.87	0.95	0.95	0.95	0.95	1.01	1.01
Stage 1 of double-stage BOD removal reaction basins & accessories											
Total bare construction cost (CAPEX)	Crore ₹	0.51	0.95	1.50	1.90	2.31	2.71	3.24	3.60	3.95	4.30
Levelized cost based on energy requirement, operation and maintenance for 25 years of life of stage 1 of double-stage BOD removal reaction basins & accessories (OPEX)	Crore ₹	2.58	4.81	7.05	9.23	11.41	13.56	15.74	17.87	20.00	22.12

(continued)

Estimated cost summary for moving bed biological reactor-based system											
BOD removal											
		Capacity in mld	Capacity in mld	Capacity in mld	Capacity in mld	Capacity in mld	Capacity in mld	Capacity in mld	Capacity in mld	Capacity in mld	Capacity in mld
		5	10	15	20	25	30	35	40	45	50
Description	Unit	Value	Value	Value	Value	Value	Value	Value	Value	Value	Value
Overall cost inclusive of CAPEX & OPEX	Crore ₹	3.09	5.75	8.56	11.13	13.72	16.27	18.98	21.48	23.95	26.42
Stage 2 of double-stage BOD removal reaction basins & accessories											
Total bare construction cost (CAPEX)	Crore ₹	0.32	0.54	0.86	1.02	1.19	1.35	1.64	1.79	1.96	2.11
Levelized cost based on energy requirement, operation and maintenance for 25 years of life of stage 2 of double-stage BOD removal reaction basins & accessories (OPEX)	Crore ₹	0.10	0.14	0.20	0.22	0.25	0.27	0.31	0.33	0.35	0.37
Overall cost inclusive of CAPEX & OPEX	Crore ₹	0.42	0.68	1.06	1.25	1.44	1.62	1.95	2.12	2.30	2.48
Blowers and blower-building											
Total bare construction cost (CAPEX)	Crore ₹	2.13	3.03	3.75	4.38	4.94	5.35	5.82	6.27	6.69	7.09
Secondary clarifiers											
Total bare construction cost (CAPEX)	Crore ₹	2.21	3.04	3.85	4.56	5.25	5.89	8.41	9.13	9.82	10.49

(continued)

Estimated cost summary for moving bed biological reactor-based system											
BOD removal											
		Capacity in mld	Capacity in mld	Capacity in mld	Capacity in mld	Capacity in mld	Capacity in mld	Capacity in mld	Capacity in mld	Capacity in mld	Capacity in mld
		5	10	15	20	25	30	35	40	45	50
Description	Unit	Value	Value	Value	Value	Value	Value	Value	Value	Value	Value
Levelized cost based on energy requirement, operation and maintenance for 25 years of life of secondary clarifiers (OPEX)	Crore ₹	0.60	0.83	1.04	1.24	1.42	1.59	1.94	2.10	2.26	2.41
Overall cost inclusive of CAPEX & OPEX	Crore ₹	2.81	3.87	4.89	5.81	6.67	7.48	10.35	11.23	12.07	12.90
Secondary clarifier sludge sump											
Total bare construction cost (CAPEX)	Crore ₹	0.08	0.13	0.18	0.24	0.29	0.34	0.40	0.42	0.47	0.52
Levelized cost based on energy requirement, operation and maintenance for 25 years of life of secondary clarifier sludge sump (OPEX)	Crore ₹	0.14	0.16	0.19	0.21	0.24	0.27	0.30	0.32	0.35	0.37
Overall cost inclusive of CAPEX & OPEX	Crore ₹	0.22	0.29	0.37	0.45	0.53	0.61	0.70	0.74	0.82	0.89
Secondary clarifier sludge transfer pumps & pump-house											
Total bare construction cost (CAPEX)	Crore ₹	0.92	1.06	1.16	1.25	1.33	1.41	1.50	1.65	1.80	1.96

(continued)

Estimated cost summary for moving bed biological reactor-based system											
BOD removal											
		Capacity in mld	Capacity in mld	Capacity in mld	Capacity in mld	Capacity in mld	Capacity in mld	Capacity in mld	Capacity in mld	Capacity in mld	Capacity in mld
		5	10	15	20	25	30	35	40	45	50
Description	Unit	Value	Value	Value	Value	Value	Value	Value	Value	Value	Value
Levelized cost based on energy requirement, operation and maintenance for 25 years of life of secondary clarifier sludge transfer pumps & pump-house (OPEX)	Crore ₹	0.69	1.14	1.58	2.02	2.43	2.87	3.31	3.75	4.17	4.61
Overall cost inclusive of CAPEX & OPEX	Crore ₹	1.61	2.20	2.75	3.28	3.76	4.27	4.80	5.40	5.97	6.57
Estimated consolidated costs											
Total bare construction cost (CAPEX)	Crore ₹	7.94	10.87	13.74	16.05	18.28	20.26	24.42	27.58	29.66	31.70
Levelized cost based on energy requirement, operation and maintenance for 25 years of life of WWTP	Crore ₹	4.76	7.80	10.89	13.82	16.74	19.61	22.70	25.65	28.49	31.30
Overall cost inclusive of CAPEX & OPEX	Crore ₹	12.70	18.67	24.63	29.87	35.02	39.87	47.12	53.23	58.15	63.00
Cost of land											
Cost of land	Crore ₹	3.70	5.65	7.90	9.82	11.72	13.57	16.23	18.57	20.45	22.36

(continued)

Estimated cost summary for moving bed biological reactor-based system											
BOD removal											
		Capacity in mld	Capacity in mld	Capacity in mld	Capacity in mld	Capacity in mld	Capacity in mld	Capacity in mld	Capacity in mld	Capacity in mld	Capacity in mld
		5	10	15	20	25	30	35	40	45	50
Description	Unit	Value	Value	Value	Value	Value	Value	Value	Value	Value	Value
Overall cost											
Overall cost	Crore ₹	16.39	24.32	32.52	39.69	46.74	53.44	63.35	71.80	78.60	85.36
Overall cost	Million $	2.05	3.04	4.07	4.96	5.84	6.68	7.92	8.97	9.83	10.67

Regression analysis and determination of MAPE											
BOD removal											
		Capacity in mld	Capacity in mld	Capacity in mld	Capacity in mld	Capacity in mld	Capacity in mld	Capacity in mld	Capacity in mld	Capacity in mld	Capacity in mld
		5	10	15	20	25	30	35	40	45	50
Design parameter	Unit	Value	Value	Value	Value	Value	Value	Value	Value	Value	Value
Predicted value (as per exponential cost function)		20.94	24.90	29.60	35.19	41.84	49.74	59.13	70.30	83.58	99.37
Value of R^2		0.9488									
Absolute percentage error		27.77	2.38	8.98	11.32	10.49	6.93	6.66	2.08	6.33	16.40
Mean absolute percentage error (MAPE)		9.94									
Predicted value (as per linear cost function)		16.45	24.18	31.91	39.63	47.36	55.08	62.81	70.54	78.26	85.99
Value of R^2		0.9988									
Absolute percentage error		0.39	0.57	1.89	0.13	1.32	3.07	0.86	1.75	0.43	0.73

(continued)

Regression analysis and determination of MAPE											
BOD removal											
		Capacity in mld	Capacity in mld	Capacity in mld	Capacity in mld	Capacity in mld	Capacity in mld	Capacity in mld	Capacity in mld	Capacity in mld	Capacity in mld
		5	10	15	20	25	30	35	40	45	50
Design parameter	Unit	Value	Value	Value	Value	Value	Value	Value	Value	Value	Value
Mean absolute percentage error (MAPE)		1.12									
Predicted value (as per logarithmic cost function)		5.39	26.42	38.73	47.46	54.23	59.76	64.44	68.49	72.06	75.26
Value of R^2		0.9032									
Absolute percentage error		67.14	8.64	19.08	19.58	16.01	11.82	1.71	4.61	8.32	11.83
Mean absolute percentage error (MAPE)		16.87									
Predicted value (as per polynomial cost function)		16.55	24.21	31.88	39.57	47.27	54.99	62.72	70.47	78.23	86.01
Value of R^2		0.9988									
Absolute percentage error		0.99	0.45	1.97	0.29	1.13	2.89	1.00	1.85	0.48	0.75
Mean absolute percentage error (MAPE)		1.18									
Predicted value (as per power cost function)		15.13	25.11	33.77	41.68	49.06	56.05	62.74	69.17	75.39	81.42
Value of R^2		0.9918									
Absolute percentage error		7.69	3.25	3.85	5.01	4.95	4.88	0.97	3.66	4.09	4.62
Mean absolute percentage error (MAPE)		4.30									

References

1. G. Acampa, M.G. Giustra, C.M. Parisi, Water treatment emergency: cost evaluation tools' MDPI – 07 May. Sustainability **11**, 2609, 1–18 (2019)
2. A.U.A. Arif, M.T. Sorour, S.A. Aly, Cost analysis of activated sludge and membrane bioreactor WWTPs using CapdetWorks simulation program: case study of Tikrit WWTP (middle Iraq). Alex. Eng. J. Hosted by ELSEVIER – Alexandria University, 1–9 (2020)
3. P. Balmer, B. Mattson, Wastewater treatment plant operation costs. Wat. Sci. Technol. **30**(4), 7–15 (1994)
4. E. Doherty, Development of new benchmarking systems for wastewater treatment facilities. A thesis submitted to the College of Engineering and Informatics, National University of Ireland, Galway, in partial fulfilment of the requirements for the Degree of Doctor of Philosophy (2017)
5. L.R. Dysert, An introduction to parametric estimating. AACE Int. Trans. **EST.03**, 1–7 (2008)
6. E. Friedier, E. Pisanty, Effects of design flow and treatment level on construction and operation costs of municipal wastewater treatment plants and their implications on policy making. Water Res. **40**(2), 3751–3758 (2006)
7. S. Gautam, S. Ahmed, A. Dhingra, Z. Fatima, Cost-effective treatment technology for small size sewage treatment plants in India. J. Sci. Ind. Res. **76**(April 2017), 249–254 (2017)
8. S. Gillot, B. De Clercq, D. Defour, F. Simoens, K. Gernaey, P.A. Vanrolleghem, *Optimization of Wastewater Treatment Plant Design and Operation Using Simulation and Cost Analysis* (Biomath Department, University of Gent/Biotim, Gent/Wilrijk, 1999), pp. 1–9
9. M.K. Gratziou, M. Tsalkatidou, N.E. Kotsovinos, Economic evaluation of small capacity sewage processing units. Glob. Nest J. **8**(1), 52–60 (2006)
10. R.C. Gumerman, R.L. Culp, S.P. Hanesan, *Estimating Cost for Water Treatment as a Function of Size and Treatment Efficiency* (USEPA (EPA-600/2-78-182), 1978)
11. S.F. Hernandez, M.M. Senante, R.S. Garrido, Cost modeling in wastewater treatment processes. Desalination **268**, 1–5 (2011)
12. S. Jafarinejad, Cost estimation and economical evaluation of three configurations of activated sludge process for a wastewater treatment plant (WWTP) using simulation. Appl. Water Sci. Springer, 1–9 (2016). https://doi.org/10.1007/s13201-016-0446-8
13. A. Koul, S. John, A life cycle cost approach for evaluation of sewage treatment plants. Int. J. Innov. Res. Adv. Eng. (IJIRAE) **2**(7), 105–109 (2015) ISSN: 2349-2163
14. R. Martins, A. Fortunato, F. Fernando Coelho, Cost structure of the Portuguese water industry: a cubic cost function application. Estudos do GEMF, 1–33 (2006)
15. G. McNamara, Economic and environmental cost assessment of wastewater treatment systems: a life cycle perspective. A thesis submitted in fulfilment of the requirements for the Degree of Doctor of Philosophy (PhD), School of Mechanical and Manufacturing Engineering, Dublin City University, 2018
16. J.P.R. Miranda, C.A.G. Ubaque, J.C.P. Londoño, Analysis of the investment costs in municipal wastewater treatment plants in Cundinamarca. Universidad Nacional de Colombia, Medellín. Dyna **82**(192), 230–238 (2015)
17. R. Nogueira, I. Ferreira, P. Janknecht, J.J. Rodriguez, P. Oliveria, A.G. Brito, Energy-saving wastewater treatment systems: formulation of cost functions. Water Sci. Technol. **56**(3), 85–92 (2007)
18. M. Panaitescu, F.V. Panaitescu, I.A. Anton, Theoretical and experimental researches on the operating costs of a wastewater treatment plant. IOP Conf. Ser. Mater. Sci. Eng. **95**, 012131, 1–7 (2015)
19. B. Papadopoulos, P. Konstantinos, Tsagarakis, A. Yannopoulos, Cost and land functions for wastewater treatment projects: typical simple linear regression versus fuzzy linear regression. ASCE. J. Environ. Eng. **133**, 581 (2007)
20. O.J. Prado, D. Gaabriel, J. Lafuente, Economical assessment of the design, construction and operation of open-bed bio filters for waste gas treatment. J. Environ. Manag. **90**(8), 2515–2523 (2009)

21. S.R. Qasim, S.W. Lim, E.M. Motley, K.G. Heung, Estimating costs for treatment plant construction. J. Am. Water Work. Assoc. **84**, 56–62 (1992)
22. N. Sato, T. Okubo, T. Onodera, L.K. Agrawal, A. Ohashi, H. Harada, Economic evaluation of sewage treatment processes in India. J. Environ. Manag. **84**, 447–460 (2007)
23. A.W. Sekandari, Cost comparison analysis of wastewater treatment plants. Int. J. Sci. Technol. Eng. **6**(1), 65–72 (2019)
24. M.M. Senante, F.H. Sancho, R.S. Garrido, Economic feasibility study for new technological alternatives in wastewater treatment processes: a review. Water Sci. Technol. **65**(5), 896–906 (2012)
25. W. Singhirunnusorn, M.K. Stenstrom, A critical analysis of economic factors for diverse wastewater treatment processes: case studies in Thailand. Sustain. Environ. Res. **20**(4), 263–268 (2010)
26. K.P. Tsagarakis, D.D. Mara, A.N. Angelakis, Application of cost criteria for selection of municipal wastewater treatment systems. Water Air Soil Pollut. **142**(January), 187–211 (2003)
27. USEPA, *An Analysis of Construction Cost Experiences for Wastewater Treatment Plants* (EPA 430-9-76-002, 1976)
28. USEPA, *Detailed Costing Document for the Centralized Waste Treatment Industry* (EPA 821-R-98-016, 1998)
29. P.A. Vanrolleghem, U. Jeppsson, J. Carstensen, B. Carlsson, G. Olsson, Integration of wastewater treatment plant design and operation – a systematic approach using cost functions. Wat. Sci. Technol. **34**, 159–171 (1996)
30. C.G. Wen, C.S. Lee, Development of cost functions for wastewater treatment system with fuzzy regression. Fuzzy Sets Syst. **106**, 143–153 (1999)
31. R.J.Z. Yengejeh, K. Davideh, A. Baqeri, Cost/benefit evaluation of wastewater treatment plant types (SBR, MLE, Oxidation Ditch), case study: Khouzestan, Iran. Bull. Environ. Pharmacol. Life Sci. **4**(1), 55–60 (2014)
32. Central Pollution Control Board – Government of India, National Inventory of Sewage Treatment Plant (2021)
33. Central Public Health and Environmental Engineering Organization in collaboration with JICA, Manual on Sewerage and Sewage Treatment Systems (2013)
34. Metcalf & Eddy, Inc, *Wastewater Engineering – Treatment and Reuse*, 4th edn
35. USEPA, *Process Design and Cost Estimating Algorithms for the Computer Assisted Procedure for Design and Evaluation of Wastewater Treatment Systems (CAPDET)* (USEPA, 1982)
36. Public Works Department (PWD), Government of India, Schedule of Rates (2021)

Removal of Heavy Metals by Laterite Soil

Saikat Shome, Bijoli Mondal, and Souvik Das

Abstract The current research investigates the utilization of laterite soil to adsorb the combined metals of Zn and Cu in batch mode. Laboratory experiments were conducted to analyze the adsorption isotherms at a fixed pH of 8, with an initial concentration of 10 mg/L, different adsorption doses ranging from 1 to 30 g/L, and an equilibrium contact time of 120 min. The isotherms were plotted, and the findings indicate that the Freundlich isotherm model is the most suitable fit. For Zn@20 g/L soil dose, the R^2 value is 0.9906, and the RMSE is 0.054. Similarly, for Cu@20 g/L soil dose, the R^2 value is 0.9912, and the RMSE is 0.053.The soil's ability to adsorb Cu and Zn is demonstrated by its high adsorption capacity values (qZn = 1845 mg/kg, qCu = 1796.8 mg/Kg), indicating that it has excellent attenuative potential. To prove the heavy metal adsorption onto the soil sample and ascertain its mechanism, the natural soil sample and its heavy metal-loaded forms were characterized using scanning electron microscopy (SEM) and Fourier transform infrared spectroscopy (FTIR).

Keywords Adsorption · Heavy metals · Isotherm studies · Laterite soil

Abbreviations

AAS	Atomic adsorption spectrophotometer
BOD	Biochemical oxygen demand
EDX	Energy-dispersive X-ray spectroscopy
EU	European Union
FTIR	Fourier transform infrared
RMSE	Root mean square error
SEM	Scanning electron microscope
SEM-EDX	Scanning electron microscopic energy-dispersive X-ray

S. Shome (✉) · B. Mondal · S. Das
Haldia Institute of Technology, Haldia, West Bengal, India

D. Mazumder (ed.), *Sustainable Advanced Technologies for Industrial Pollution Control*, Springer Proceedings in Earth and Environmental Sciences,
https://doi.org/10.1007/978-3-031-37596-5_7

US EPA United States Environmental Protection Agency
WHO World Health Organization

1 Introduction

Pollution due to anthropogenic activities, particularly due to untreated or ill-treated effluents when released to the lithosphere, creates nuisance to the soil and water. Pollution due to heavy metals is a major concern for the environment as they are toxic and non-biodegradable and have a high potential to pollute surface as well as underground water, making it unfit for plants and humans. The effluent containing Cu and Zn is normally discharged from mining, tanneries, metal plating, fertilizer industries [1, 2], galvanized industry, dyeing industries, paper industries [3], zinc processing units, etc. The main focus of this study is on Zn and Cu due to their high mobility and toxicity. Copper is more toxic for plants than animals and less impacted by other heavy metals [4].The mobility of Zn is significantly high in aqueous media, and it tends to be closely associated with the oxide and carbon-bound fractions [5]. Due to their toxicity, carcinogenic nature, persistence, and propensity to bioaccumulate [6], severe restrictions (such as those set forth by the WHO, US EPA, or EU) regarding the quality of wastewaters released have been developed. For instance, the WHO recommends that Cu and Zn concentrations in mining and electroplating wastewater be less than 2.0 and 5.0 mg/L, respectively, while the US EPA has established a limit of 1.3 and 1.7 mg/L, respectively. The presence of these substances in industrial wastewater makes it more harmful for the receiving habitats, which upsets the equilibrium of the aquatic fauna and flora and has a severe effect on human health [7]. To ensure the protection of surface water quality, it is necessary to remove or reduce heavy metals before they are released into aquatic habitats. Various methods can be used to treat wastewater, including solvent extraction [8, 9], ion exchange resins [10], complexation [11], membrane approaches [12], precipitation [13], and adsorption [14–16]. Among these methods, adsorption is commonly used due to its effectiveness and ease of use in removing heavy metals from liquid effluents. Adsorbents can be of mineral or organic origin, such as natural zeolite [17], calcium silicate powders [16], activated carbon, and bio-sorbents [14, 15, 18]. In this study, the adsorption process was chosen due to its low cost and simplicity. The study aims to remove heavy metals using a low-cost adsorbent, laterite soil, which is readily available in Durgapur.

2 Materials and Methods

2.1 Chemicals

The chemicals used were zinc sulfate ($ZnSO_4$) and copper sulfate ($CuSO_4$) for the preparation of stock solution. To prepare the stock solution of heavy metal ions, 1 g $ZnSO_4$ and $CuSO_4$ was dissolved in a 1 L volumetric flask filled with distilled water, resulting in a concentration of 1000 mg/L, which was then diluted to required concentration for working solution. For maintaining pH level, NaOH and HCl were used. All chemicals used were of analytical grade and were procured from Merck in India.

2.2 Instruments

A high-precision electrical balance (Sartorius GMBH) was used for weighing. Digital pH meter (DHP-500, SICO, India) was used for pH measurements. BOD shaker (Instrumentation, India) was used for all batch experiments. Atomic absorption spectrometer (PerkinElmer, PinAAcle 900 T) was used to measure the absorbance of zinc and copper solution.

2.3 Preparation and Characterization of the Adsorbent

The laterite soil sample was collected from a gravel quarry surroundings of Durgapur, West Bengal, and separated from different lumps of kankar. Then it was grounded and sieved. Finally it was kept in the oven for 24 hours at a temperature of 100 ± 2 °C. After drying properly it was kept in a desiccator before use. The BIS codes were followed to conduct tests on the physicochemical characteristics of the soil specimen. The physicochemical properties of the soil sample are listed in Table 1. Both natural and heavy metal-loaded soil samples were characterized as a confirmatory test using soil digestion, scanning electron microscopic energy-dispersive X-Ray (SEM-EDX), and instrumental analysis of Fourier transform infrared (FTIR). Soil digestion was done with the reference of US EPA (3050B) to determine the amount of naturally available heavy metals in the soil sample using flame atomic adsorption spectrophotometer (PerkinElmer). SEM images of soil sample with or without heavy metal loaded were taken using scanning electron microscope (ZEISS, SIGMA HD, and Germany) to determine the structural characteristics of the adsorbent. Scanning electron microscope (SEM) was employed to analyze the high-resolution surface morphology of the soil both before and after the adsorption of Zn^{+2} and Cu^{+2} ions. Fourier transform infrared (FTIR) spectroscopy (IRPrestige-21, SHIMADZU, Japan) was used to examine the functional

Table 1 Physicochemical properties of lateritic soil

Physical properties	Value
Bulk density (g/cc)	1.25
Specific gravity	2.69
Natural moisture content (%)	12.61
Hydraulic conductivity (cm/s)	3.71×10^{-8}
pH	6.51
Total porosity (%)	53.53
Organic carbon (%)	0.55
Liquid limit (%)	26
Sand (%)	49
Silt (%)	39
Plastic limit (%)	13.12
Clay (%)	12
Max dry density (g/cc)	1.93
Plasticity index (%)	12.88
Zero point charge	7.2

groups of both the original adsorbent and the adsorbent that had absorbed heavy metals. The spectra data over 400–4000 cm^{-1} were studied.

2.4 Experimental Studies

To investigate the metal mobilization from soil, batch experiments were conducted at constant room temperature (32 ± 2 °C) and shaking speed of 150 rpm. The effects of various process parameters (effect of adsorbent dose, contact time, pH) were studied. The initial concentration of each heavy metal was selected (10 mg/L) for the entire batch test and pH adjusted from 4 to 12 by 1 N HCl and 1 N NaOH. The adsorbent dose was varied from 1 to 30 g/L for the batch study. The experiment was conducted in a BOD shaker at constant room temperature at 150 rpm. Following every test, the filtered substance was examined through AAS. The stock solution was also confirmed by AAS. The maximum adsorption of the soil was determined by Eq. (1).

$$\text{Removal } (\%) = \frac{(C_0 - C_e) \times 100}{C_0} \tag{1}$$

C_0 is the initial concentration of the heavy metal solution (mg/L), and C_e is the equilibrium concentration of the heavy metals in solution (mg/L). Isotherm studies were carried out to find out the adsorption capacity of soil sample.

3 Results and Discussion

3.1 Characterization Result of the Adsorbent

3.1.1 SEM Result

The SEM-EDX technique was employed to analyze the structural characteristics of the raw soil and soil after adsorption. The microstructure of soil formation and the state of individual particles were accurately determined by SEM-EDX. The SEM images in Fig. 1 depict the uneven and porous surface of the untreated adsorbent, while Fig. 2 displays a clear distinction in the surface features of the soil after adsorption. The SEM images in Fig. 2 were captured using a magnification of 26.79 KX and a scale bar of 5 µm and show the soil samples containing Zn^{+2} and Cu^{+2}. The addition of Zn and Cu led to particle agglomeration and smoothening effect. In contrast, the SEM images of the raw soil mineral in Fig. 1 reveal several small discrete particles scattered across a rough surface. Figure 2 shows that the particle size slightly increased and became smoother after adsorption, which could be attributed to the introduction of Zn and Cu.

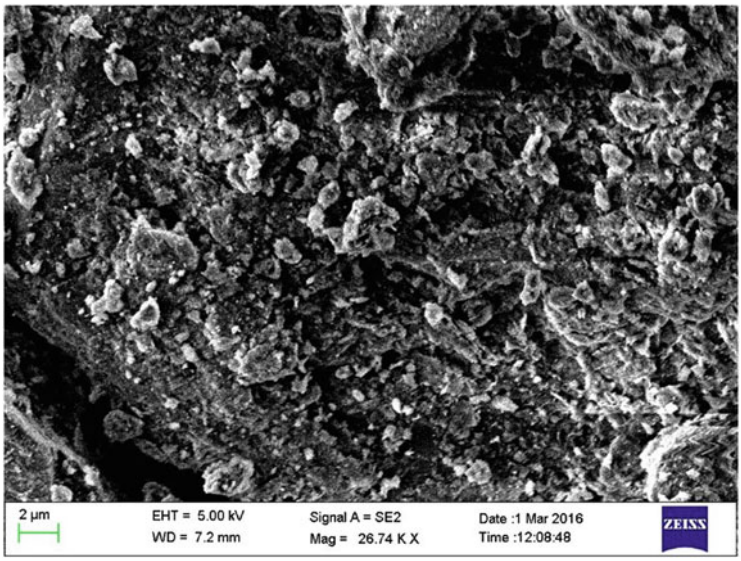

Fig. 1 SEM micrographs of raw soil sample at a magnification of 26.74 KX and a scale bar of 5 µm done by ZEISS

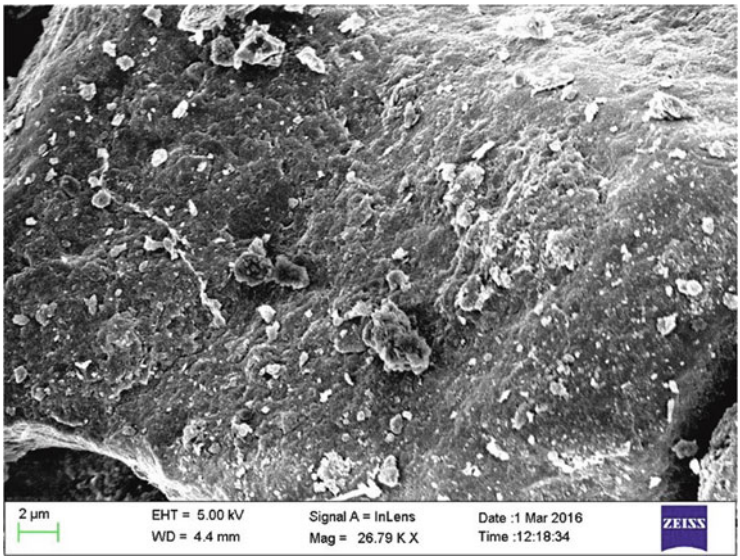

Fig. 2 SEM micrographs of heavy metal-loaded soil sample at a magnification of 26.79 KX and a scale bar of 5 µm done by ZEISS

3.1.2 FTIR Result

To investigate the functional groups present in both the untreated soil and the soil treated with heavy metals, Fourier transform infrared (FTIR) analysis was conducted over a range of wavelengths from 400 to 4000 cm^{-1}. The results showed that certain peaks had shifted in wave number after the adsorption process, suggesting that these functional groups were involved in binding heavy metals to the soil. The surface functional groups of the untreated and treated soils are depicted in Figs. 3 and 4, respectively. The Y-axis represents % transmittance, while the X-axis represents wave number (cm^{-1}).

In the virgin soil, peaks at wave numbers of 485.1, 789.1, 930.5, 1026.5, 1620.2, 2943.4, and 3610.5 cm^{-1} representing C-I (stretch), C-Cl (stretch), =C-H (bending), C-F (stretch), C=C (stretch), C-H (stretch), and O-H (stretch, free), respectively, are found. After being loaded with heavy metals, one of the bonds disappears and appears, and the initial wave numbers are shifts from their original position. The wave number of C-I (stretch) shifts from 485.1 to 479.6 cm^{-1} as evident from Fig. 3 to Fig. 4. Based on Fig. 4, a strong peak at 1886.5 cm^{-1} and 670.5 cm^{-1} shows the presence of C-O (stretch, carbonyl) and C-Cl (stretch, alkyl halide), respectively, indicating the mentioned group appears new into the adsorbed soil and in the same time 2943.4 cm^{-1} indicating C-H (stretch) disappears, and the other peaks are found to shift from IR spectra of soil loaded with Zn^{+2} and Cu^{+2}. Soil is an organic material, and it is likely to contain chloride in the natural form. In the heavy metal-loaded sample, the peaks which were in the virgin soil shifted from its original

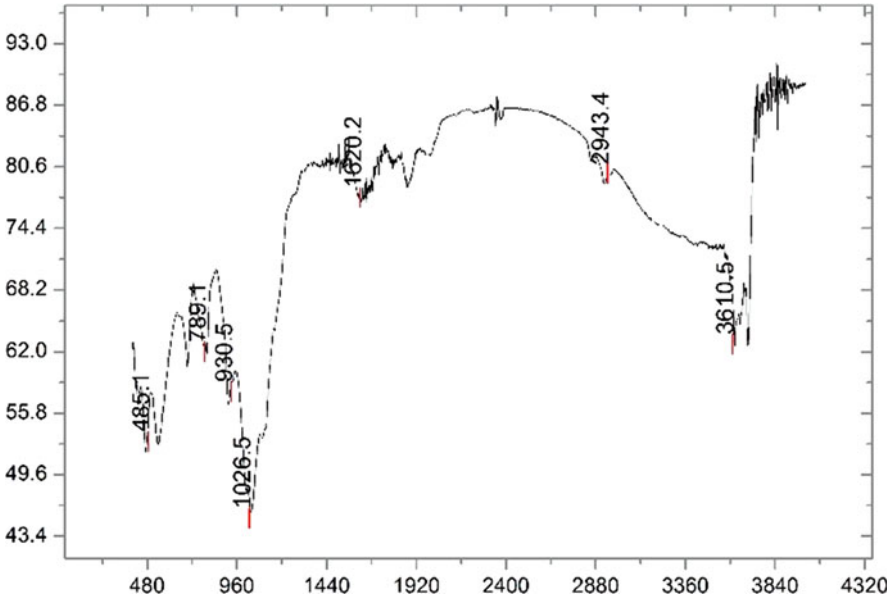

Fig. 3 FTIR peaks of raw soil sample

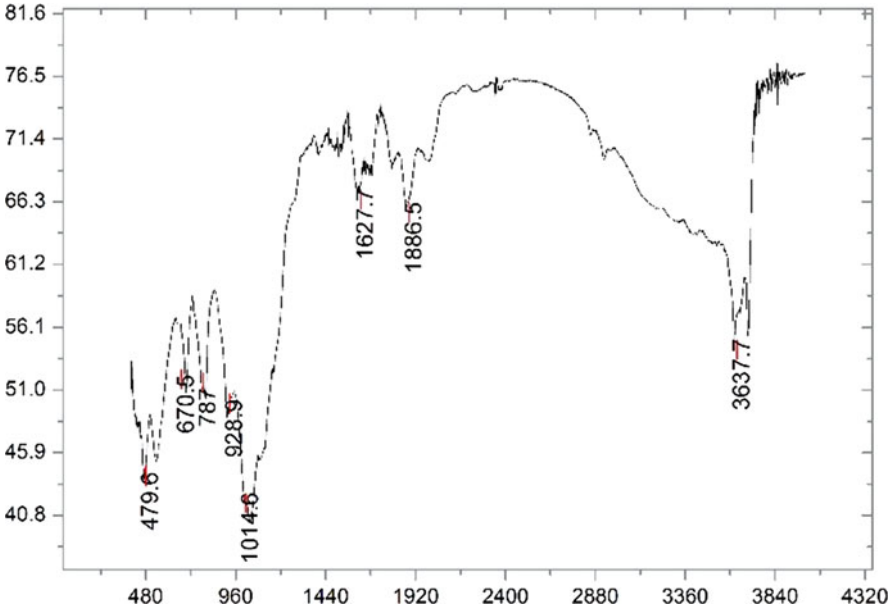

Fig. 4 FTIR peaks of heavy metal-loaded soil sample

position and changed to 479.6, 670.5, 787, 928.9, 1014.6, 1627.7, 1886.5, and 3637.7 cm^{-1} indicating C-I (stretch), =C-H (bending), C-Cl (stretch), C-H (stretch), C-F (stretch), C=C (stretch), C=O (stretch), and O-H (stretch, free). It seems that these functional groups have a significant impact on the adsorption of heavy metals, particularly zinc and copper. The spectra undergo an evident alteration in both shape and position as a result of the adsorption of Zn and Cu, causing a shift in the peaks of the original sample. All these changes of peak positions with the appearance of C=O (stretch) and C-Cl (stretch) bonds and disappearance of C-H (stretch) bonds are surely a conclusive evidence of adsorption into the soil due to heavy metals.

3.1.3 EDX Result

In contrast, the EDX assessments were carried out in a high-vacuum environment, utilizing a 15 Kev accelerating voltage. This method revealed the X-ray spectrum characteristic of several elements including carbon (C), oxygen (O), magnesium (Mg), aluminum (Al), potassium (K), silicon (Si), calcium (Ca), phosphorous (P), sulfur (S), and iron (Fe). An analysis was conducted on the proportion of all the components. The elemental analysis and mapping are illustrated in Figs. 5 and 6, respectively, for raw as well as adsorbed soil sample.

Based on Table 2, C, O, Si, and Al have a high content, and for the same sample Fe, Ti, K, and Mg are having a lesser percentage. The major components as determined by EDX are C, O, Si, and Al, with percentage compositions of 6.55%, 58.13%, 18.51%, and 9.82%, respectively. There was also the presence of heavy metals in the virgin soil but in a lesser extent.

The EDX study of heavy metal-loaded soil with Zn and Cu is also tabulated in Table 3, which shows that soil with heavy metals also contains a higher percentage of oxygen, carbon, silicon, and aluminum and has a reasonable percentage of

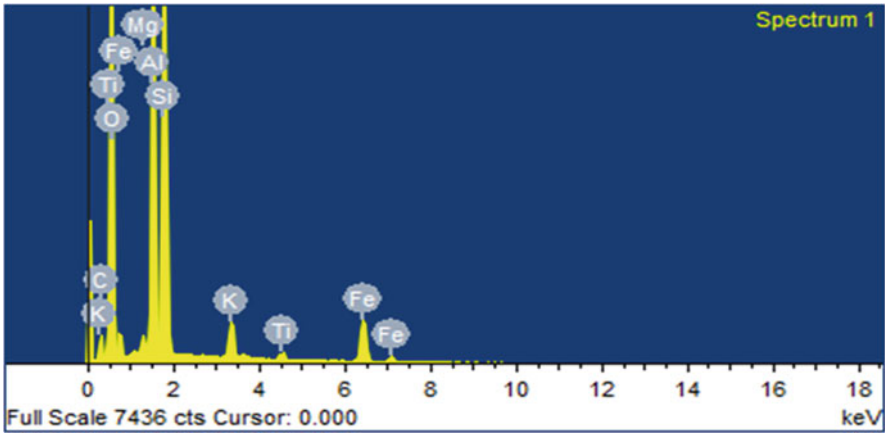

Fig. 5 EDX spectra of raw soil sample

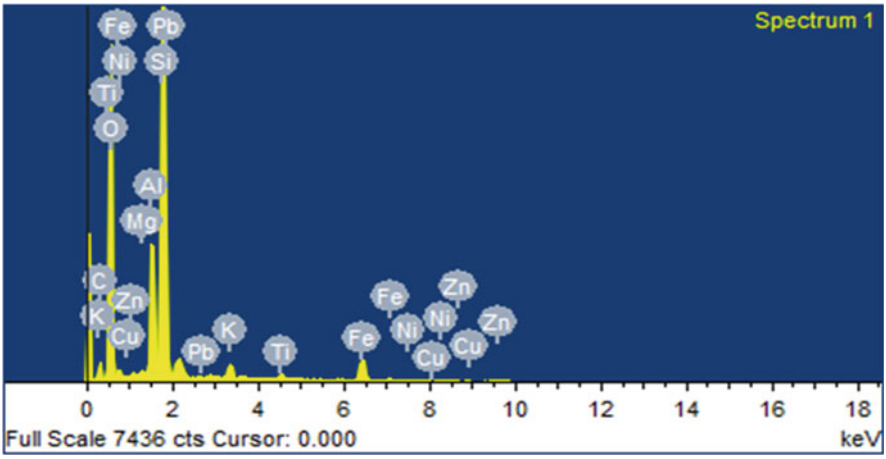

Fig. 6 EDX spectra of heavy metal-loaded soil sample

Table 2 EDX elemental analysis of natural soil sample

Element	Weight %	Atomic %
C	6.55	10.20
O	58.13	67.93
Mg	0.43	0.33
Al	9.82	6.81
Si	18.51	12.32
K	1.40	0.67
Ti	0.42	0.16
Fe	4.74	1.59
Totals	100.00	

Table 3 EDX elemental analysis of heavy metal loaded soil sample

Element	Weight %	Atomic %
C	9.87	15.38
O	51.90	60.72
Mg	0.25	0.19
Al	5.40	3.75
Si	26.80	17.86
K	0.87	0.42
Ti	0.54	0.21
Fe	4.37	1.47
Cu	0.10	0.03
Zn	0.22	0.06
Totals	100.00	

adsorbed heavy metals. The Zn and Cu peaks could be seen in the spectra of the Zn- and Cu-loaded soil and the unloaded soil from Fig. 5. It implies that the process of adsorption has effectively attached heavy metals onto the surface of soil particles.

3.2 *Effect of Contact Time*

To identify the removal efficiency of the adsorbent accurately, it is important to consider sufficient contact time. Consideration of optimum time for the best removal efficiency is done by a time-dependent batch test. It has been observed that the removal efficiency increases gradually up to 120 min and then it becomes constant for both Zn and Cu (initial concentration of Cu & Zn = 10 mg/L, dose = 20 g/L) as shown in Fig. 7. The reason behind this is that at the beginning, there were no adsorbate molecules occupying the adsorbent sites, resulting in a rise in the concentration gradient between the adsorbate present in the solution and the adsorbent surface. Hence, during a contact time of 2 hours, the adsorbent is effective to remove the most.

3.3 *Effect of Soil Dose*

In Fig. 8, the quantity of heavy metal removal from the synthetic solution is displayed as a function of adsorption dosage. The adsorbent dose varies from 1, 2, 3, 5, 7.5, 10, 12, 15, 20, 25 to 30 g/L for initial concentrations of 10 mg/L. The heavy metal removal efficiencies of lateritic soil have been seen to increase with an increase in adsorption dose from 1 to 20 g/L, and then it decreases in 25 g/L as shown in Fig. 8, for both Zn and Cu. The increase in percentage removal with the increase in adsorbent dose is attributed to the increase in adsorbent sites available for the same amount of heavy metal cations.

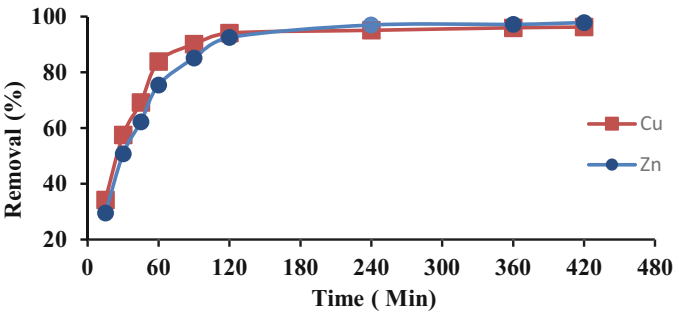

Fig. 7 Kinetic study (initial concentration 10 mg/L, dose 20 g/L)

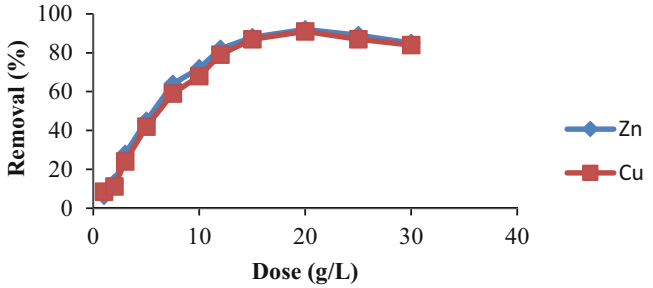

Fig. 8 Variation in the amount of adsorbate and the removal efficiency of Zn and Cu (initial concentration 10 mg/L and contact time 120 min)

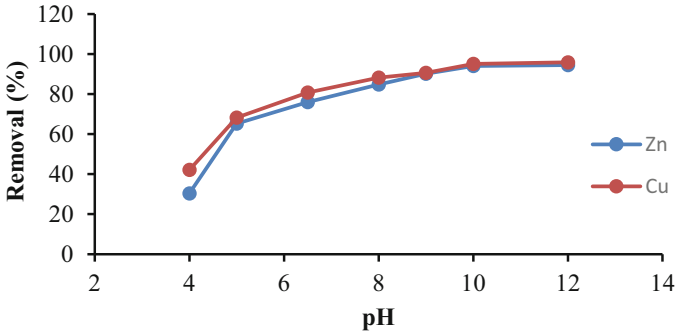

Fig. 9 Effect of the pH on Cu and Zn onto laterite soil (initial concentration 10 mg/L, dose 20 g/L, and contact time 120 min)

3.4 Effect of pH

Figure 9 shows the variation in removal of heavy metals, and it is found that the removal efficiency can increase up to 90% with the pH varying from 4 to 12, and then it becomes constant for both the heavy metals (Zn and Cu). As the pH_{zpc} of soil was found to be 7.2 and it is well known that below pH_{zpc} ($pH < pH_{zpc}$) the adsorbents are positively charged, the repulsive force between the metal cations and adsorbent surface becomes dominant resulting in reduced adsorption of the metal cations. On the other hand, at a higher pH ($pH > pH_{zpc}$), the surface charges become negative, and they can effectively adsorb both Zn and Cu cations [19].

3.5 Isotherm Studies

The investigation of adsorption isotherm is beneficial in evaluating the capability of soil to adsorb heavy metals from wastewater. Through batch adsorption

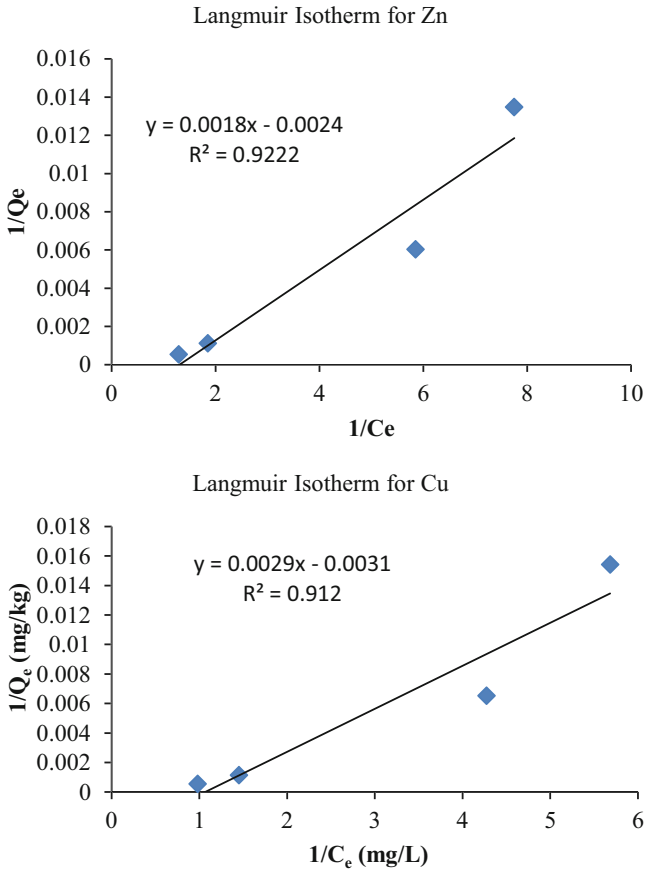

Fig. 10 $1/Q_e$ vs $1/C_e$ graph Langmuir isotherm curve for Zn and Cu

experiments, the manner in which the adsorbate attaches to the adsorbent was determined. A graph displaying the correlation between the quantity of heavy metal adsorbed per unit mass of soil and the equilibrium concentration of heavy metals was created. Typically, the Langmuir (Fig. 10) and Freundlich isotherm (Fig. 11) models are employed to describe the adsorption isotherm. Table 4 provides a summary of the R^2 and RMSE values, as well as the coefficients of the models.

Table 4 shows that the test results were reasonably suited by the Freundlich and Langmuir isotherm models, which had greater coefficients of determination and smaller error values. Moreover, multiple binding and heterogeneity for heavy metal adsorption in soil media are indicated by the Freundlich isotherm model which was close fitting to the experimental batch adsorption results [5]. For the Freundlich isotherm studies, it shows higher R^2 and lower RMSE values, and also the values of K_f and "n" signify the favorable adsorption capacity of the soil. In the present investigation, "n" values of 0.59 and 0.55 for Zn and Cu both clearly indicate a

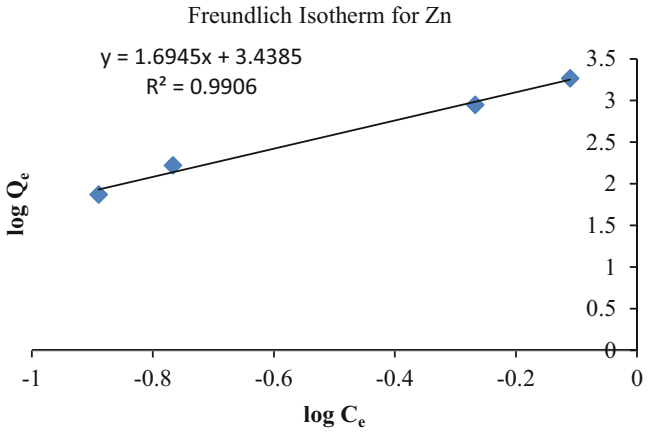

Fig. 11 log Q_e vs log C_e graph Freundlich isotherm curve for Zn and Cu

Table 4 Summarization of adsorption isotherm parameters of heavy metal adsorption on laterite soil

Adsorption isotherm model	Expression	Constants	
		Zn	Cu
Langmuir model	$Q_e = K_f C_e^n$	$Q_{max} = 416.67$ mg/kg $b = 1.33$ L/mg $R^2 = 0.9222$ RMSE = 0.000962	$Q_{max} = 322.58$ mg/kg $b = 0.666$ L/mg $R^2 = 0.912$ RMSE = 0.00177
Freundlich model	$Q_e = \frac{Q_{max}\ bC_e}{1+bC_e}$	$K_f = 31.14$ L/kg $n = 0.59$ $R^2 = 0.9906$ RMSE = 0.054023	$K_f = 25.57$ L/kg $n = 0.55$ $R^2 = 0.9912$ RMSE = 0.053872

favorable adsorption process for heavy metals in soil. Due to higher R^2 values and better RMSE values than Langmuir isotherm, we have taken Freundlich isotherm as satisfactory.

4 Conclusion

The study aimed to investigate the capacity of lateritic soil to eliminate two types of heavy metals (Zn^{+2} and Cu^{+2}) from an aqueous solution. According to the batch adsorption study, the most effective removal of heavy metals occurred when the pH was set to 8, the soil dose was 20 g/L, and the contact time was 120 min. When the aforementioned optimal conditions are met, the lateritic soil exhibits the ability to eliminate over 90% of both Zn and Cu. It was observed that the laterite soil had a higher tendency to absorb Cu^{+2} compared to Zn^{+2}. The results of the adsorption isotherm studies indicated that there was a good match between the Langmuir and

Freundlich isotherm models. The test results revealed that Freundlich model is best fit with $R^2 = 0.9906$ and RMSE = 0.054 for Zn and $R^2 = 0.9912$ and RMSE = 0.053 for Cu.

References

1. A. Alcolea, M. Vázquez, A. Caparrós, I. Ibarra, C. García, R. Linares, R. Rodríguez, Heavy metal removal of intermittent acid mine drainage with an open limestone channel. Miner. Eng. **26**, 86–98 (2012)
2. H. Davies, P. Weber, P. Lindsay, D. Craw, J. Pope, Characterisation of acid mine drainage in a high rainfall mountain environment, New Zealand. Sci. Total Environ. **409**, 2971–2980 (2011)
3. T.G. Chuah, A. Jumasiah, I. Azni, S. Katayon, S.Y. Thomas Choong, Rice husk as a potentially low-cost biosorbent for heavy metal and dye removal: an overview. Desalt **175**, 305–316 (2005)
4. C.W. Daniel, C.L.O. Tsangandirenem, Competitive Cu and Cd sorption and transport in soils: a combined batch kinetics, column, and sequential extraction study. Environ. Sci. Technol. **40**, 6655–6661 (2006)
5. W.S. Wan Ngah, M.A.K.M. Hanafiah, Removal of heavy metal ions from wastewater by chemically modified plant wastes as adsorbents: a review. Bioresour. Technol. **99**, 3935–3948 (2008)
6. M. Syrynskyy, Solid–liquid–solid extraction of heavy metals (Cr, Cu, Cd, Ni and Pb) in aqueous systems of zeolite–sewage sludge. J. Hazard. Mater. **161**, 1377–1383 (2009)
7. R. Leyma, S. Platzer, F. Jirsa, W. Kandioller, R. Krachler, B.K. Keppler, Novel thiosalicylate-based ionic liquids for heavy metal extraction. J. Hazard. Mater. **314**, 164 (2016)
8. D. Kołodyńska, J. Krukowska-Bąk, J. Kazmierczak-Razna, R. Pietrzak, Uptake of heavy metal ions from aqueous solutions by sorbents obtained from the spent ion exchange resins. Microporous Mesoporous Mater. **78**, 102–114 (2017)
9. C. Zhang, X. Liu, X. Lu, M. He, Complexation of heavy metal cations on clay edges at elevated temperatures. Chem. Geol. Microporous Mesoporous Mater. **49**, 852–860 (2017)
10. K. Sunil, G. Karunakaran, S. Yadav, M. Padaki, V. Zadorozhnyy, R.K. Pai, Al-Ti_2O_6 a mixed metal oxide based composite membrane: a unique membrane for removal of heavy metals. Chem. Geol. **47**, 410–418 (2018)
11. P. Yuan-Zhen, H. Yong-Ming, Y. Dong-Xing, L. Yan, G. Zhen-Bin, Rapid analysis of heavy metals in coastal seawater using preconcentration with precipitation/co-precipitation on membrane and detection with X-Ray fluorescence. Chin. J. Anal. Chem. **40**, 877–882 (2012)
12. Y. Huanga, X. Zenga, L. Guoa, J. Lanc, L. Zhanga, D. Cao, Heavy metal ion removal of wastewater by zeolite-imidazolate framework. Sep. Purif. Technol. **194**, 462–469 (2018)
13. A.E. Burakov, E.V. Galunin, I.V. Burakova, A.E. Kucherova, S. Agarwal, A.G. Tkachev, V.K. Gupta, Adsorption of heavy metals on conventional and nanostructured materials for wastewater treatment purposes: a review. Ecotoxicol. Environ. Saf. **148**, 702–712 (2018)
14. H. Es-sahbany, M. Berradi, M. Belfaquir, H. Nassali, M.S. Elyoubi, Removal of heavy metals (nickel) contained in wastewater-models by the adsorption technique on natural clay. ICMES **10**, 421–431 (2018)
15. J. Ma, G. Qin, Y. Zhang, J. Sun, S. Wang, L. Jiang, Heavy metal removal from aqueous solutions by calcium silicate powder from waste coal fly-ash. J. Clean. Prod. **14**, 547–555 (2018)
16. L. Mao, H. Guo, W. Zhang, Addition of waste glass for improving the immobilization of heavy metals during the use of electroplating sludge in the production of clay bricks. Constr. Build. Mater. **163**, 875–879 (2018)

17. K. Hanna, L. Lassabatere, B. Bechetn, Zinc and lead transfer in a contaminated roadside soil: Experimental study and modeling. J. Hazard. Mater. **161**, 1499–1505 (2009)
18. A.Z. Al-Hamdan, K.R. Reddy, Surface speciation modeling of heavy metals in Kaolin: implications for electro kinetic soil remediation processes. Adsorption **11**, 529–546 (2005)
19. I. Vázquez, J.R. Iglesias, E. Marañón, L. Castrillón, M. Alvaeez, Removal of residual phenols from coke wastewater by adsorption. J. Hazard. Mater. **147**, 395–400 (2007)

Removal of Methylene Blue from Wastewater by Red Sandy Soil-Based Alkali-Activated Binder

Souvik Das, Bijoli Mondal, Sahil Pritam Swain, Dibyendu Adak, and Saikat Shome

Abstract Methylthioninium chloride, commonly called methylene blue, is a cationic dye. Methylene blue (MB) is a heterocyclic aromatic compound that is used as a synthetic dye for textile industries. In the present study, adsorption of methylene blue (MB) was studied using red sandy soil-based alkali-activated binder as an adsorbent. The batch experiments were carried out with various parameters like effect of initial concentration, particle size, contact time, adsorbent doses, temperature, and agitation speed. The results revealed that the significant removal efficiency was achieved around 80% when initial concentration of MB and dose of adsorbent were 50 mg/L and 3 g/L, respectively, at pH 9. In the study, thermodynamics parameters were calculated. The experimental results were analyzed using various reaction kinetic models, including first-order, second-order, pseudo-first-order, and pseudo-second-order models. To identify the optimum adsorption capacity, an adsorption isotherm investigation was done, and different isotherm models were explored. The findings of the study suggest that alkali-activated binder made from red sandy soil could potentially serve as an effective and affordable adsorbent for MB removal from aqueous solution.

Keywords Absorbance · Adsorption · Alkali activator · Isotherm study · Kinetic models · Low-cost adsorbent material · Methylene blue · Process parameters · Red sandy soil · Spectrophotometric technique · Thermodynamics parameters

S. Das (✉) · B. Mondal · S. Shome
Haldia Institute of Technology, Haldia, West Bengal, India

S. P. Swain · D. Adak
National Institute of Technology Meghalaya, Shillong, India
e-mail: dadak@nitm.ac.in

D. Mazumder (ed.), *Sustainable Advanced Technologies for Industrial Pollution Control*, Springer Proceedings in Earth and Environmental Sciences,
https://doi.org/10.1007/978-3-031-37596-5_8

Abbreviations

MB Methylene blue
rpm Revolutions per minute

1 Introduction

Methylene blue is most popularly used in various industries like leather, paper, cotton dyeing, plastic, textile, and automotive industries. These are very much dangerous to human health and the environment [1]. After use the wastewater is directly discharged into the surface water. The presence of dye pigments in the water body stops light from passing through the water and affects the photosynthesis process of aquatic plants. It is also harmful to human health, as it can impact the reproductive and central nervous systems and can cause kidney malfunction, asthma, nausea, tumors, cysts, allergies, urticaria, and cancer [2]. The most significant environmental concern at the moment is reducing hazardous organic wastes, such as dye (methylene blue). Industrial effluents must be thoroughly treated before entering the aquatic environment. According to recent research, there are numerous methods available for removing refractory organics from wastewater and water, including coagulation-flocculation [3], biological method [4], precipitation, ion transfer [5], adsorption [6], and membrane filtration [7]. Since most of the dyes are fundamentally nonbiodegradable, traditional dye removal treatments have relied on both biological and chemical approaches, but these are not particularly effective to treat dye effluent [8]. All of these methods have some demerits like labor-intensive processes, high operating costs, partial removal, and significant energy and reagent usage. Careful disposal is necessary when hazardous sludge or other waste products are produced. Adsorption process has proven to be a reliable and affordable replacement for conventional contaminated water treatment facilities due to its straightforward technique and long-term economic viability [9]. The commonly utilized absorbents in the adsorption process are silica gel, activated carbon, alumina, and zeolites. But they are quite expensive. It can be replaced by less expensive materials such as perlite, clay, geopolymer, fly ash, etc. that can absorb organic and inorganic pollutants [10]. In the current study, MB was removed from the industrial effluent using a cost-effective adsorbent made of red sandy soil-based alkali-activated binder.

2 Materials and Methodology

2.1 Reagents

Methylene blue ($C_{16}H1_8CIN_3S$), with a molecular weight of 319.852 g/mol, was purchased from Sigma-Aldrich. Sodium hydroxide pellets and liquid sodium silicate were obtained from Merck, while all other compounds used were of high purity.

2.2 Adsorbent Preparation

Red sandy soil was collected from the local area of Shillong, Meghalaya. The ingredients such as cement/slag, sand, and red sandy soil were dry mixed for 2 min. Then it was blended with alkali sources (NaOH/KOH) and silicate solutions (Na_2SiO_3/K_2SiO_3) and well mixed for another 5 min rigorously to ensure uniform mixing before placing it into 70.6 mm cube mold. The specimens were demolded after 24 h. Then the specimens were cured for 7 days in the laboratory at ambient temperature. Then the specimens were crushed into powdered form and sieved in different sizes (150 μ, 300 μ, and 600 μ).

2.3 Instrumentation

Weighing was done using a high-precision electronic balance (Shimadzu AUX220). A spectrophotometer (Thermo Scientific Visible SPECTRONIC™ 200) was used to measure absorbance, and the measurement of pH was done by a digital pH meter (Systronics 335).

2.4 Analytical Method

MB concentrations between 0 and 12 mg/L were determined using a spectrophotometric technique at a wavelength of 663 nm. A calibration curve between dye concentration and absorbance was prepared (absorbance 0.1657, concentration (mg/L) + 0.0098 (with an R^2 value of 0.9996)) to determine the unknown concentration of MB.

2.5 Experimental Studies

MB spiked distilled water sample was used in batch experiments at 27 ± 2 °C. A mechanical shaker was employed to agitate the samples at 150 revolutions per minute. A 50 ml MB sample was used in each experiment to investigate the effects of various process parameters on MB removal when adsorbent dose and initial concentration of MB were 3 g/L and 50 mg/L, respectively. The effects of adsorbent size (150–600 μ), adsorbent quantity (1–12 g/L), contact time (0–300 min), temperature (17–37 °C), and agitation speed (90–200 rpm) were studied. The removal of MB (%) was equated by the following equation:

$$R = \frac{C_0 - C_t}{C_0} \times 100 \tag{1}$$

where, C_0 is the starting concentration of methylene blue and C_t is the concentration of MB at any time t.

2.6 Study of Kinetics Models

To enhance the comprehension of solvent adsorption mechanism on adsorbents, four distinct kinetic models were studied. These models encompassed the first-order model [11], which is dependent on the solution concentration; the pseudo-first-order model [12], which is reliant on the capacity of solid; the second-order model [11, 12], which is linked to solution concentration; and the pseudo-second-order model [13], which is correlated to solid-phase sorption. The analysis and comparison of these four models were conducted to determine which sorption mechanism fitted the best.

The equations of four models are given below:

$$\text{First-order kinetic model}: \ln C_t = \ln C_0 - k_1 t \tag{2}$$

$$\text{Pseudo-first-order kinetic model}: \frac{dq_t}{dt} = k_{S1}(q_e - q_t) \tag{3}$$

$$\text{Second-order kinetic model}: \frac{1}{C_t} - \frac{1}{C_0} = k_2 t \tag{4}$$

$$\text{Pseudo-second-order kinetic model}: \frac{1}{q_t} = \frac{1}{k_{S2} q_e^2} + \frac{1}{q_e} t \tag{5}$$

Where:

C_t = At time t, concentration of MB
C_0 = MB initial concentration

q_t = At time t, quantity of MB adsorbed/weight of red sandy soil-based alkali-activated binder
q_e = At equilibrium, quantity of MB adsorbed/weight of red sandy soil-based alkali-activated binder
k_1 = Rate constant of the first-order reaction model
k_{S1} = Rate constant of the pseudo-first-order reaction model
k_2 = Rate constant of the second-order reaction
k_{S2} = Rate constant of the pseudo-second-order reaction

3 Results and Discussions

3.1 Impact of Particle Size

Particle size can affect the removal process in a batch study, with smaller particles leading to a higher removal efficiency. To investigate this impact, three different particle size ranges (150 μ, 300 μ, and 600 μ) were studied when adsorbent dose and initial concentration of MB were 3 g/L and 50 mg/L at pH 9. From Fig. 1 it is noticed that MB removal varied between 30% and 80%. The smallest particle size (150 μ) resulted in the highest removal, likely due to its greater surface area and adsorption sites. Thus, the 150 μ size was chosen for the entire experiment.

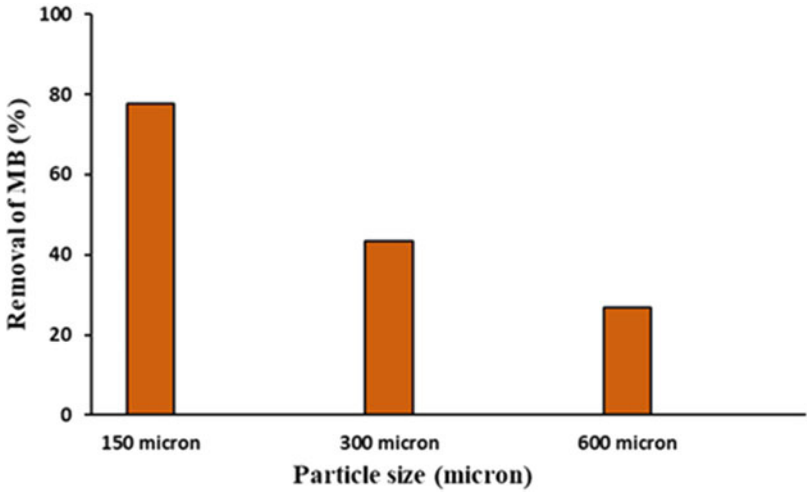

Fig. 1 Particle size effect on adsorption of MB onto red sandy soil-based alkali-activated binder (initial concentration of MB 50 mg/L, dose 3 g/L, time of contact 120 min, and pH 9)

3.2 Impact of Adsorbent Dosage

The availability of sites to adsorb the pollutants in the adsorption process is influenced by the quantity of adsorbent used. In this study, the adsorbent dosage was varied within the range of 1–15 g/L, while the adsorbate concentration remained constant at 50 mg/L.

The experiment was conducted at a constant temperature of 27 + 2 °C, shaking rate of 120 rpm, and contact period of 2 h at pH 9. The removal efficiencies of MB increased as the adsorbent dosage increased, as shown in Fig. 2. The ideal adsorbent dosage was determined to be 3 g/L.

3.3 Kinetic Study

The determination of contact time between solid and solute and the determination of reaction coefficients are crucial aspects of kinetic studies in batch experiments. To conduct kinetic studies, a maximum adsorbent dose of 3 g/L was employed for MB-spiked distilled water samples. The agitating time ranged between 0 and 4 h, and the removal of MB over time was recorded and plotted in Fig. 3. The results indicated a rapid initial rate of adsorption, with an equilibrium time of 2 h observed. The adsorption procedure exhibited a quick pace during the initial phases and gradually decreased over time until it reached a state of equilibrium. This behavior can be explained by the availability of vacant adsorption sites on the surface of the alkali-activated binder during the initial stages, resulting in a greater uptake of MB molecules. However, with time, the accessibility of these sites decreased, causing a decline in the adsorption rate.

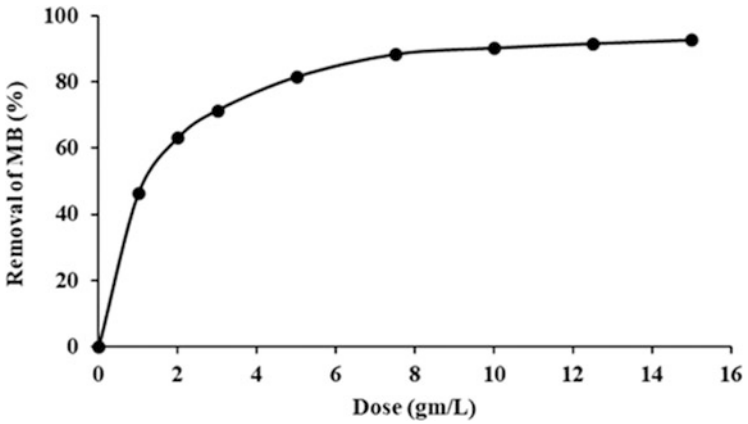

Fig. 2 Influence of adsorbent dosage on MB removal onto red sandy soil-based alkali-activated binder (initial concentration of MB 50 mg/L, time of contact 120 min, pH 9)

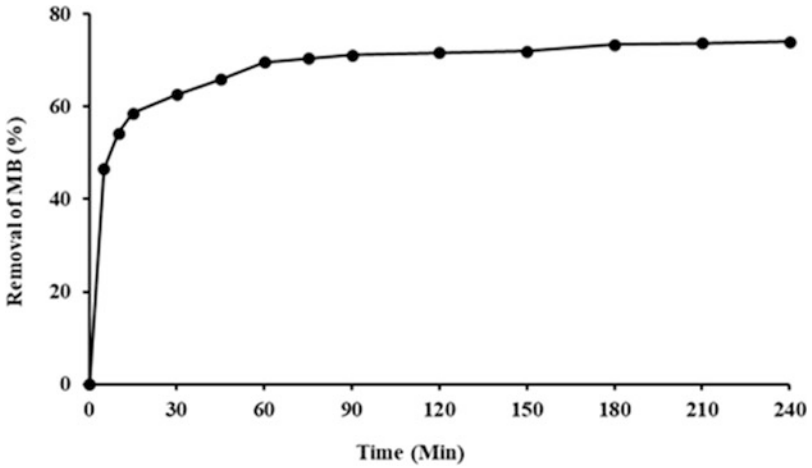

Fig. 3 Effect of contact time on adsorption of MB onto red sandy soil-based alkali-activated binder (initial concentration of MB 50 mg/L, dose 3 g/L, and pH 9)

Table 1 Equations and r^2 data of the graph of kinetics models for MB removal by alkali-activated binder

Model	Equation of linear fit line	r^2
First-order kinetic model	$\ln C_t = 3.3249 - 0.0075t$	0.6146
Pseudo-first-order kinetic model	$\ln(q_1 - q_t) = 1.642 - 0.019t$	0.9583
Pseudo-first-order kinetic model	$\frac{1}{C_t} - 0.2044 = 0.001t$	0.5675
Pseudo-second-order kinetic model	$\frac{t}{q_t} = 0.2178 + 0.0535t$	0.9996

In Sect. 2.6, four reaction models were used to analyze the reaction kinetics data for the adsorption of MB by red soil-based alkali-activated binder. Table 1 shows the equations of four kinetic models and the corresponding values of determining coefficients (r^2) of the regression model fitting lines for four reaction models. The values of the r^2 of the best fit graph indicated that the pseudo-seond-order kinetics model was the most suitable among the other models. This model assumes that the process is due to chemical adsorption or chemisorption [14].

3.4 Effect of Agitation Speed

The speed at which the mixture was agitated did not impact the removal of MB by red soil-based alkali-activated binder. The removal process was investigated within a range of 90–210 rpm agitation speed, using an initial MB concentration of 50 mg/L, a pH of 9, and an adsorbent dose of 3 g/L. Results showed that varying the agitation speed within this range had no influence on the removal technique.

3.5 Study of Isotherm

The isotherm describes the equilibrium state of the adsorption process. Freundlich isotherm model and Langmuir isotherm model were studied in our current research. The isotherm study was conducted at a temperature of 27 ± 2 °C and an initial MB concentration of 50 mg/L. The amount of red sandy soil-based alkali-activated binder utilized was varied between 1 and 15 g/L, and the agitation period lasted for 2 h. Experimental results were used to compare the Langmuir and Freundlich isotherm models, both of which displayed linear patterns. However, the Langmuir isotherm was found to be more accurate than the Freundlich isotherm based on their respective r^2 values. The constants were computed and presented in Table 2. The capacity of adsorption on red sandy soil-based alkali-activated binder for MB removal was determined to be 29.94 mg/g.

3.6 Adsorption Thermodynamics Studies

The experimental data were obtained at the temperatures of 290, 300, and 310 K. The data were used to calculate the thermodynamic specification of the adsorption of MB onto red sandy soil-based alkali-activated binder. By calculating thermodynamics parameters, it becomes possible to evaluate the characteristics and feasibility of the adsorption process. The equations utilized to determine the entropy change (ΔS°), enthalpy change (ΔH°), and standard free energy change (ΔG°) associated with the adsorption processes are as follows:

$$k_d = \frac{q_e}{C_e} \tag{6}$$

$$\Delta G^\circ = -RT \ln k_d \tag{7}$$

$$\ln k_d = \frac{\Delta S^\circ}{R} - \frac{\Delta H^\circ}{RT} \tag{8}$$

Table 2 Langmuir and Freundlich isotherm models for MB removal by alkali-activated binder

Isotherm	Parameters	Values
Langmuir isotherm model	Equation	$\frac{1}{q_e} = 0.731\left(\frac{1}{C_e}\right) + 0.135$
	Maximum adsorption capacity, q_{max} (mg/g)	29.94
	Constant related to energy of sorption system, b	1.28
	r^2	0.997
Freundlich isotherm mode	Equation	$\ln q_e = .3595 \ln C_e + .546$
	Freundlich constant related to adsorption capacity, k_f [(mg/g) (L/mg)$^{1/n}$]	13.14
	Adsorption intensity, $1/n$	1.1223
	r^2	0.984

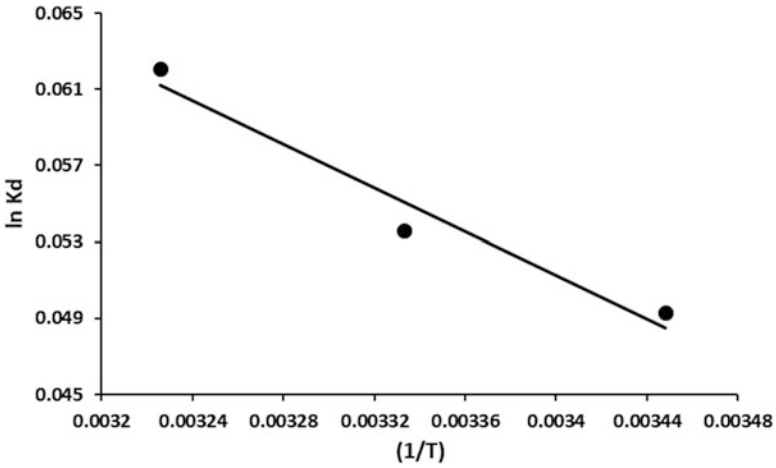

Fig. 4 Thermodynamics study for MB removal onto red sandy soil-based alkali-activated binder (initial concentration of MB 50 mg/L, dose 3 g/L, pH 9)

Table 3 Thermodynamics parameter data for MB removal by red sandy soil-based alkali-activated binder

	Thermodynamics parameters			
Temperature (K)	k_d	ΔG°	ΔH°	ΔS°
290	1.05	−118.809	−475.428	2.041918
300	1.055	−133.541		
310	1.064	−159.903		

Where:

k_d = Distribution coefficient
q_e = Concentration of MB that has been adsorbed onto red sandy soil-based alkali-activated binder at equilibrium (in mg/L)
C_e = Equilibrium concentration of MB in liquid phase (in mg/L)
R = Universal gas constant (8.314 J/mol K)
T = Absolute temperature (in K)

ΔH° and ΔS° were determined by analyzing the slope and intercept of the van't Hoff plot (ln k_d vs. 1/T) (Fig. 4), and the corresponding data are presented in Table 3.

The study showed that as the temperature increased, the adsorption capacity of MB onto the alkali-activated binder made from red sandy soil decreased. This indicates that the adsorption process is exothermic. This implies that the process of adsorption is exothermic. This could be caused by the weaker bonds that form when adsorbate molecules are subjected to high temperatures at the active regions of

adsorbents [14]. The negative quantity of ΔG° implies that the process of adsorption is rather impulsive and favored at low temperatures. Additionally, the negative (−) value of ΔH° confirms the exothermic character of the adsorption process, while the positive value of ΔS° indicates a rise in variations at the solid-solution connection. The magnitude of ΔH° provides insight into the forces that govern the process. Physical forces, such as van der Waals, hydrophobic interaction, hydrogen bonding, coordination exchange, dipole bond forces, and electrostatic interaction, typically range from 2 to 80 kJ/mol, whereas chemical forces are greater than 60 kJ/mol [15, 16]. The calculated value of ΔH° in this study was 475.34 kJ/mol, indicating that chemical forces play a role in the adsorption of MB onto the red sandy soil-based alkali-activated binder.

4 Conclusion

Red sandy soil-based alkali-activated binder was found to be extremely effective (more than 80%) adsorbent for the removal of MB. A particle size of 150 micron allowed for the greatest amount of removal. The MB adsorption demonstrates that the adsorption process was initially vigorous and then gradually slowed until equilibrium was reached (120 min). According to our research, the removal of MB increased along with the dose of the red sandy soil-based alkali-activated binder up to 5 g/L with a removal rate of more than 80%, but further addition had no significant influence on the removal of MB. The pseudo-second-order kinetics governs the rate of the reaction. Adsorption of MB follows the Langmuir isotherm model with a q_{max} value of 29.94 mg/g. According to the thermodynamics parameter values, the MB adsorption by the red sandy soil-based alkali-activated binder was exothermic and spontaneous in nature.

References

1. N.H. Othman, N.H. Alias, M.Z. Shahruddin, N.F. Abu Bakar, N.R. Nik Him, W.J. Lau, Adsorption kinetics of methylene blue dyes onto magnetic graphene oxide. J. Environ. Chem. Eng **6**, 2803–2811 (2018)
2. Y. Yu, Y.-Y. Zhuang, Z.-H. Wang, M.-Q. Qiu, Adsorption of water-soluble dyes onto modified resin. Chemosphere **54**, 425–430 (2004)
3. C. Tocchi, E. Federici, L. Fidati, E. Manzi, V. Vincigurerra, M. Petruccioli, Water Res. **46**, 3334–3344 (2012)
4. Y. Zhang, C. Causserand, P. Aimar, J.P. Cravedi, Water Res. **40**, 3793–3799 (2006)
5. Y. Al-Ani, Y. Li, J. Taiwan Ins, Chem. Eng. **43**, 942–947 (2012)
6. S. Stopic, B. Friedrich, A. Widigdo, Metalurgia **13**, 27–34 (2007)
7. S.G. Muntean, M.A. Nistor, E. Muntean, A. Todea, R. Ianos, C. Pacurariu, Removal of colored organic pollutants from wastewaters by magnetite/carbon nanocomposites: single and binary systems. J. Chem. **2018**, 1–16 (2018). https://doi.org/10.1155/2018/6249821

8. A. Gürses, S. Karaca, Ç. Doğar, R. Bayrak, M. Açıkyıldız, M. Yalçın, Determination of adsorptive properties of clay/water system: methylene blue sorption. J. Colloids Interf. Sci. **269**, 310–314 (2004)
9. S. Chowdhury, R. Mishra, P. Saha, P. Kushwaha, Adsorption thermodynamics, kinetics and isosteric heat of adsorption of malachite green onto chemically modified rice husk. Desalination **265**, 159–168 (2011)
10. M. El Alouani, S. Alehyen, M. El Achouri, M. Taibi, Adsorption of cationic dye onto fly ash-based geopolymer: batch and fixed bed column studies. MATEC Web Conf. **149**, 02088 (2018). https://doi.org/10.1051/matecconf/201814902088
11. Y.S. Ho, G. Mckay, Pseudo second order model for sorption process. Process Biochem. **34**, 451 (1999)
12. L.D. Benefield, C.W. Randall, *Biological Process Designs for Wastewater Treatment* (Prentice-Hall Inc., 1980), p. 1
13. S. Lagergren, B.K. Svenska Ventenskapsakad, Handl. 24 (1898), as cited by Wasay et al., Water Res. **30**, 1143 (1996)
14. Y.S. Ho, G. Mckay, Process Biochem. **34**, 451 (1999)
15. O. Hamdaoui, Batch study of liquid-phase adsorption of methylene blue using cedar sawdust and crushed brick. J. Hazard. Mater. **135**(1–3), 264–273 (2006)
16. F.M. Machado, C.P. Bergmann, E.C. Lima, B. Royer, F.E. de Souza, I.M. Jauris, T. Calvete, S.B. Fagan, Adsorption of Reactive Blue 4 dye from water solutions by carbon nanotubes: experiment and theory. Phys. Chem. Chem. Phys. **14**(31), 11139–11153 (2012)

Assessment and Treatment of Iron from Industrial Wastewater Using *Parkia Speciosa* Pod as Activated Carbon

Reenarani Wairokpam and Potsangbam Albino Kumar

Abstract In this study, surface water contaminated with Fe(II) in the periphery of industries in Imphal, Manipur, is identified, and activated carbon synthesized from *Parkia speciosa* (ACPP) pod was used as an adsorbent for its removal. The adsorbent characterization was done with a scanning electron microscope, energy-dispersive X-ray, and Brunauer-Emmett-Teller. The presence of Fe(II) peak in the EDAX spectrum after the adsorption confirms its adsorption. A maximum adsorption was obtained at pH 5.5–6 and precipitated thereafter. Batch mode adsorption studies were conducted, and adsorption kinetics was studied with Lagergren's pseudo-first-order and Lagergren's second-order, Elovich, and diffusion models. A varied adsorbent dose test was analyzed for isotherms using Langmuir and Freundlich isotherms on the adsorbent ACPP. The kinetics and isotherm studies showed that the Fe(II) adsorption was better described by Lagergren's second-order and Langmuir isotherm, respectively. The maximum adsorption capacity obtained from Langmuir isotherm is 157.23 mg/g. The thermodynamic study showed that the Fe(II) adsorption is exothermic and spontaneous with increased randomness.

Keywords Adsorption · Desorption · Lagergren's first-order · Lagergren's second-order · Elovich model · Diffusion model · Langmuir isotherm · Freundlich isotherm · Thermodynamic · Exothermic

Abbreviations

ACPP	Activated carbon synthesized from *Parkia speciosa*
BET	Brunauer-Emmett-Teller
DO	Dissolved oxygen
EC	Electrical conductivity
EDAX	Energy-dispersive X-ray

R. Wairokpam · P. A. Kumar (✉)
Civil Engineering Department, National Institute of Technology, Manipur, Lamphelpat, India

D. Mazumder (ed.), *Sustainable Advanced Technologies for Industrial Pollution Control*, Springer Proceedings in Earth and Environmental Sciences,
https://doi.org/10.1007/978-3-031-37596-5_9

SEM Scanning electron microscope
TDS Total dissolved solid

1 Introduction

Heavy metals such as ferrous [Fe(II)] from industrial effluents are a significant concern as they pose a great risk. The generation of Fe(II) from industries, such as iron and steel, electroplating-gold manufacturing, etc., without any treatment is rising in an alarming state and poses a great risk to both the surface and subsurface water. According to the BIS, the permissible limit for Fe(II) content in wastewater is 3 mg/L [1]. Several removal techniques have inherent limitations, such as the generation of toxic sludge from precipitation, fouling in membrane technique, the ineffectiveness of filtration, etc. [2–4]. The adsorption method is one of the most commonly applied Fe(II) treatment techniques [5–8]. However, the search for nontoxic and low-cost adsorbents leads to synthesizing several biomass-derived activated carbons [9, 10]. With an emphasis on easily available local biomaterials, this study aims to synthesize activated carbon from petai (*Parkia speciosa*) pods, which are abundant and low-cost in Manipur, India. The study will emphasize the effective adsorption of Fe(II) by activated carbon derived from *Parkia speciosa* pod from the contaminated surface water which is located on the periphery of industries in Imphal City, Manipur.

2 Materials and Methods

2.1 Sample Collection

The wastewater samples were collected from April to September 2022 from the effluent of the iron and steel and electroplating-gold manufacturing industries of Imphal City, Manipur, and assessed for Fe(II) concentration by phenanthroline technique using UV spectrophotometer (Thermo Scientific Evolution 201, USA) at 510 nm [11]. The in situ parameters, pH, EC, DO, and TDS, were estimated according to standard procedure using testing probes.

2.2 Synthesis and Characterization of Adsorbent

For the synthesis of the adsorbents, activated carbon derived from petai (*Parkia speciosa*) pods (ACPP), the petai pods were procured from local markets and then rinsed with distilled water and dried at 120 °C for 24 hours. The completely dried

petai pods were then crushed and sieved using a 300 μ sieve. Phosphoric acid was used as an activating agent, and carbonization was conducted at 400 °C. Then, ACPP was again sieved using a 125 μ sieve to obtain its effective size of 125 μ and stored in desiccators for further use in the batch adsorption experiments. The adsorbent surface area, pore volume, and pore size distribution were acquired using the BET technique. The surface morphology of the adsorbents (both before and after) was identified by SEM (Sigma 300), and the elemental analysis and composition evaluation of the sample were determined by EDAX (Zeiss Gemini).

2.3 Adsorbent Experiment

The adsorption experiment was performed in a batch process using Phipps and Bird Model PB-600, USA, jar test apparatus. The amount of Fe(II) ion adsorbed by adsorbent is calculated from Eq. (1):

$$q_t = \frac{C_0 - C_t}{m} V \tag{1}$$

where q_t (mg/g) is the quantity of Fe(II) ions adsorbed at time t, C_0 is the initial concentration, C_t is the concentrations of Fe(II) ions (mg/L) at time t, $V(L)$ is the volume of Fe(II) ion sample, and m (in gram) is the mass of the adsorbent.

2.4 Adsorption Kinetics

The adsorption kinetic data were simulated to find the rate of the adsorption process, with the linear models of pseudo-first-order, pseudo-second-order, intraparticle diffusion, and Elovich kinetic models, and the models are expressed as follows respectively [12–14]:

$$\log(q_e - q_t) = \log q_e - \frac{k_1 t}{2.303} \tag{2}$$

$$\frac{t}{q_t} = \frac{1}{k_2 q_e^2} + \frac{t}{q_e} \tag{3}$$

$$q_t = k_d t^{0.5} \tag{4}$$

$$q_t = \frac{1}{\beta} \ln(1 + \alpha\beta t) \tag{5}$$

where q_e and q_t (both in mg per g) are adsorption capacity at equilibrium and time t, respectively. k_1 (min^{-1}) and k_2 (g per mg min) are rate constants of pseudo-first-order and pseudo-second-order adsorption, respectively. k_d [mg per (g $min^{1/2}$)] is the

rate constant of intraparticle diffusion, whereas α [mg per (g min)] and β (g per mg) are the Elovich rate constants.

2.5 Adsorption Isotherm

Adsorption isotherm defined the equilibrium relationships amid adsorbent and adsorbate [15]. The most commonly used isotherms are Langmuir and Freundlich isotherms.

The linearized form of the Langmuir isotherm is given by [12, 13]

$$\frac{C_e}{q_e} = \frac{1}{q_m b} + \frac{C_e}{q_m} \tag{6}$$

The linear expression of the Freundlich isotherm is as follows [12, 13]:

$$\log q_e = \log K_f + \frac{1}{n} \log C_e \tag{7}$$

where C_e is the equilibrium concentration of adsorbate in wastewater sample after adsorption (mg/L), q_e is the amount of metal adsorbed per unit mass of adsorbent (g), q_m is the monolayer adsorption capacity (mg/L), and b is the Langmuir constant. K_f and n are Freundlich constants.

A Chi-square test was evaluated to find the better-fit isotherm using the equation [16]

$$\chi 2 = \Sigma \frac{(q_e - q_{em})^2}{q_{em}} \tag{8}$$

where q_e and q_{em} (mg/g) are equilibrium iron adsorbed calculated from the experiment and predicted isotherm models, respectively.

2.6 Thermodynamic Study

To determine the effect of temperature on the adsorption of Fe(II), the adsorption study was done at different temperatures i.e., 298 K, 308 K, and 318 K. The thermodynamics parameters were evaluated as [17, 18]:

$$\Delta G^\circ = -RT \ln K_L \tag{9}$$

$$\ln K_L = \frac{\Delta S^\circ}{R} - \frac{\Delta H^\circ}{RT} \tag{10}$$

$$K_L = \frac{q_e}{C_e} \tag{11}$$

where R (8.314 JK^{-1} mol^{-1}) is the universal gas constant, $T(K)$ is the absolute temperature, K_L is the thermodynamic constant, q_e (mg/g) is the amount of Fe (II) adsorbed at equilibrium, and C_e (mg/L) is the concentration of Fe(II) at equilibrium time.

3 Results and Discussion

3.1 Site Assessment

The assessment of industrial effluents from the wastewater of Imphal City near the small-scale gold industries at Waheng Leikai (24.803937, 93.933712) and iron and steel industries at Sagolband (24.805791, 93.914470) were in the range of 4.5–7 mg/L against the permissible limit of 3 mg/L in the wastewater. However, during the monsoon season of June to August, the concentration of Fe(II) was below 0.5 mg/L and not significant, because of the stormwater diluting Fe(II). The characteristics of the wastewater are shown in Table 1.

3.2 Surface Characterization of the Adsorbent

The surface area, pore diameter, and pore volume of activated carbon are some of the important parameters as higher values will result in a higher adsorption capacity. For ACPP, carbonization of the adsorbent was conducted at 400 °C, and the surface area, pore diameter, and pore volume were achieved as 218 m^2/g, 3.112 nm, and 0.086cm^3/g, respectively. The surface area of ACPP was observed to be higher than a few reported activated carbons: bamboo, 6.79 m^2/g [19]; rice straw, 4.39 m^2/g [20]; cauliflower leaves, 12.3 m^2/g [21]; *Alternanthera philoxeroides*, 19.79 m^2/g [22]; and pig manure, 11.37 m^2/g [19]. During the study of its surface with SEM images, the ACPP adsorbent before the adsorption had a very rough surface with granular structure and cavities as illustrated in Fig. 1; however, the surface has become relatively smoother throughout the whole surface and also the cavities due to

Table 1 Parameters of wastewater site

Parameters	Values	Permissible limit (CPCB, 2012)
pH	7.8	6–8.5
Turbidity (NTU)	30	5
Conductivity (mS/cm)	10.5	–
TSS (mg/L)	165	100
BOD (mg/L)	88	30
COD (mg/L)	340	250
Iron (mg/L)	5.5	3

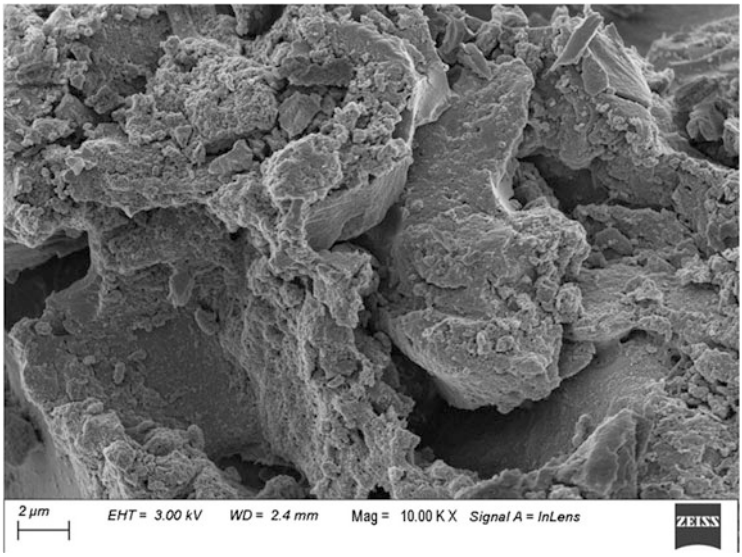

Fig. 1 SEM image of the adsorbent ACPP before adsorption

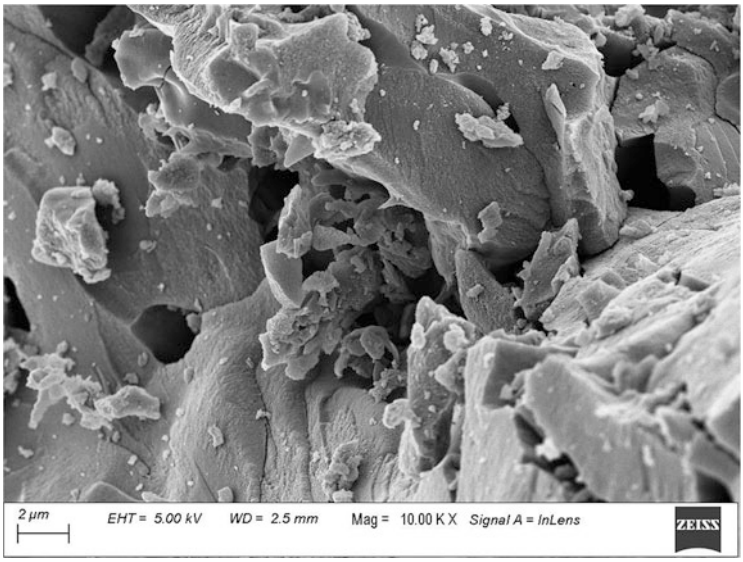

Fig. 2 SEM image of the adsorbent ACPP after adsorption

the deposition of ions (Fig. 2). The EDAX of ACPP before and after the Fe (II) adsorption was also conducted. Before the adsorption, Fe was absent (Fig. 3) but emerge after the adsorption in Fig. 4, confirming the adsorption of Fe(II) on ACPP.

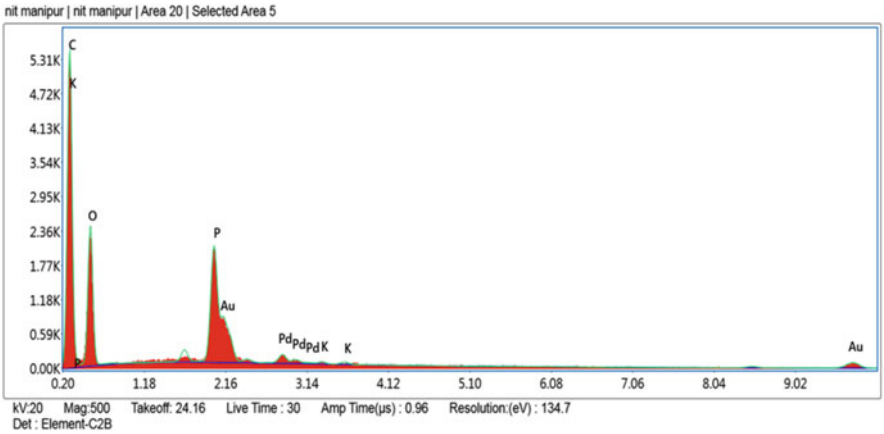

Fig. 3 EDAX image of the adsorbent ACPP before adsorption

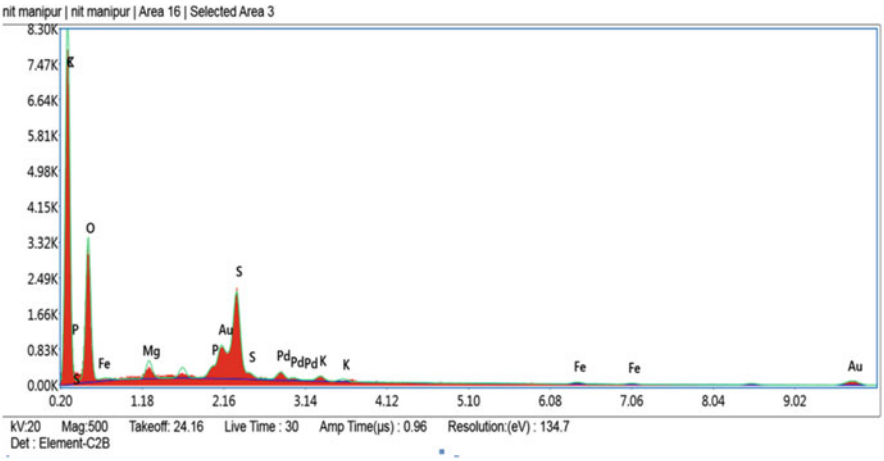

Fig. 4 EDAX image of the adsorbent ACPP after adsorption

3.3 Effect of pH

The effect of ACPP with different activating agents like HCl, HNO_3, H_2SO_4, and H_3PO_4 was studied at various pH (Fig. 5) with an adsorbent dose of 2 g/L. The adsorption efficiencies of Fe(II) with HCl, H_2SO_4, and HNO_3 are 80%, 76.56%, and 80.78%, respectively, at pH 6, and the highest adsorption was observed with H_3PO_4 yielding 93.78%. Hence, H_3PO_4 is chosen as an activating agent for ACPP for all the remaining studies. It can also be seen in Fig. 5 that, at acidic pH 2, the adsorption of

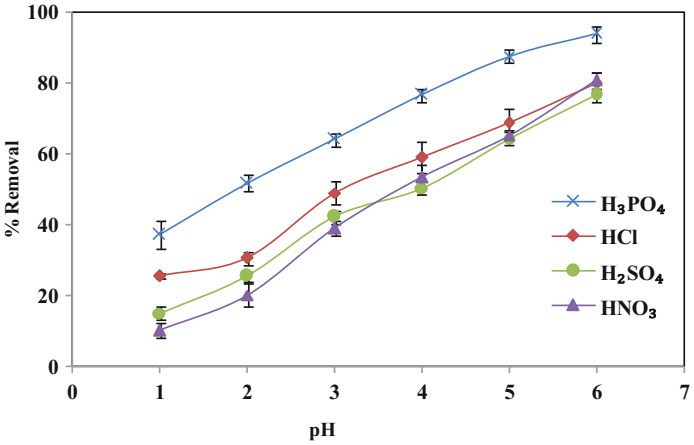

Fig. 5 Effect of pH on different activating agents

Fe(II) at acidic pH occurred with 39% for ACPP activated with H_3PO_4. A lower adsorption is due to the repulsion of cationic Fe(II) by the protons on the surface of ACPP. With the increase in pH to 6, the protonation decreases resulting in lesser repulsion of Fe(II), and hence adsorption increases to 76.50–93.78% for all the ACPP activated with different acids. Further increase in solution pH above pH 6 yields precipitation, and adsorption is thus not conducted for pH above 6.

3.4 Effect of Time and Adsorption Kinetics

The effect of contact time between Fe(II) and ACPP was studied to find the equilibrium time required for adsorption. The experiment was performed at pH 5 and a dose of 3 g/L with contact time variation ranging from 0 to 180 minutes. The removal percentage of Fe(II) ion was observed to increase with an increase in contact time as indicated in Fig. 6a. The maximum removal efficiency of 94.61% for Fe (II) ion removal reaching the equilibrium at 120 min was observed for adsorbent ACPP. The adsorption data of time variation was treated with the Lagergren's pseudo-kinetic-order equation, Elovich model, and diffusion model. Adsorption kinetics reveals Lagergren's pseudo-second-order model with correlation coefficients, i.e., R^2 of 0.99, against that of Lagergren's pseudo-first-order model with 0.98 as shown in Fig. 6b, c, respectively. Also, the Chi-square (χ^2) test of Lagergren's pseudo-second-order is 0.03 against 0.1 for pseudo-first-order. This finding suggests the predominant chemical adsorption behavior of Fe(II) on ACPP. A similar observation for Fe(II) adsorption on egg shell was also reported [23, 24]. In Table 2, the correlation coefficient of the Elovich model and diffusion

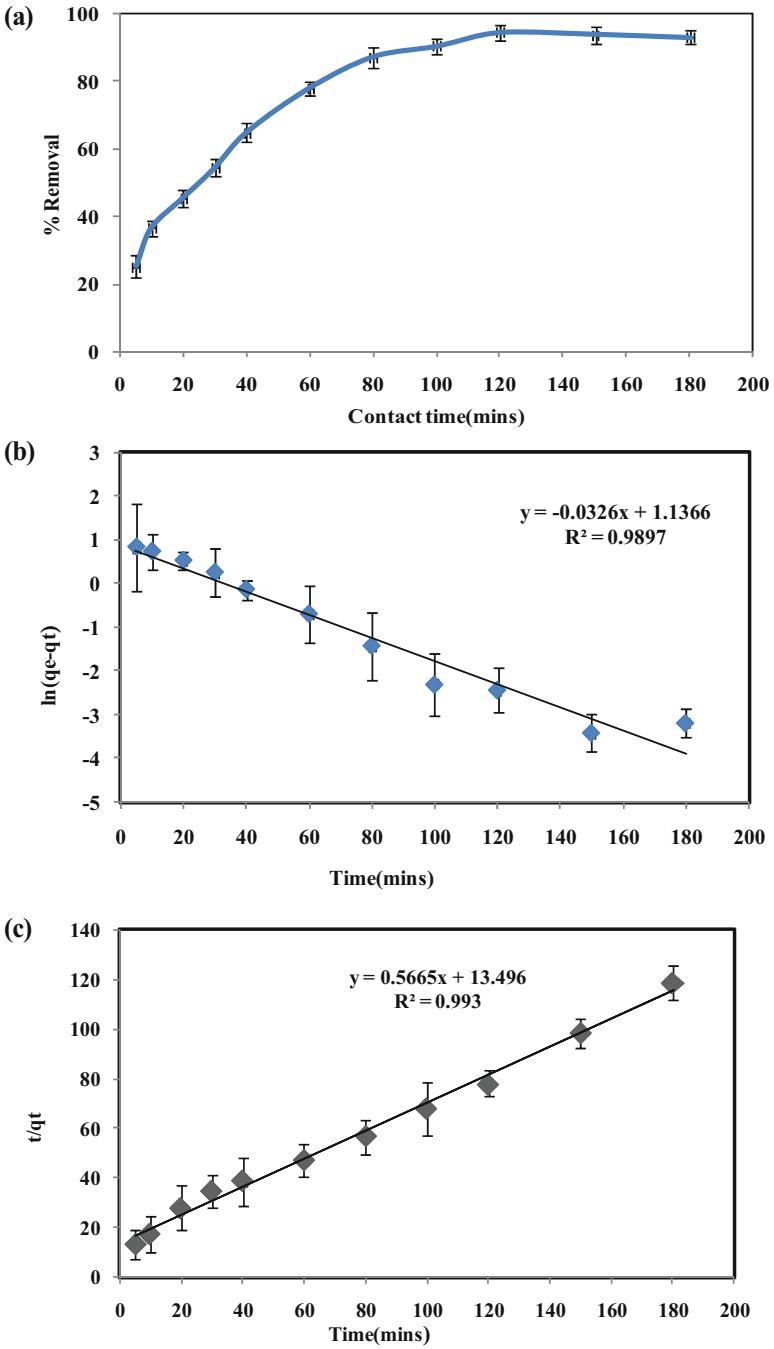

Fig. 6 (**a**) Effect of contact time on Fe(II) adsorption. (**b**) Pseudo-first-order for Fe(II) adsorption. (**c**) Pseudo-second-order for Fe(II) adsorption

Table 2 Coefficients of kinetic models for Fe (II) removal

Kinetic models	Parameters	R^2	χ^2
Pseudo-first-order	K_1 (min^{-1}) = 0.124	0.98	0.1
	q_e (cal) = 4.78 mg/g		
Pseudo-second-order	K_2 (g/mgmin) = 0.043	0.99	0.03
	q_e (cal) = 4.56 mg/g		
Elovich	$\alpha = 7.4$	0.91	0.8
	$\beta = 11.3$		
Diffusion	$k_d = 5.4$	0.90	1.1

model is projected and observed at 0.91 and 0.90, confirming insignificant physical adsorption.

3.5 Adsorbent Dose and Adsorption Isotherms

In order to find the optimum adsorbent dose, the adsorbent dosage was done from 0.2 to 3.5 g as shown in Fig. 7a. Also from Fig. 7a, it is found that the optimum dosage was achieved at 3 g/L with a removal percentage of 95.43%. On the analysis of adsorption isotherm from this data, the adsorption of Fe(II) by ACPP was explained by Langmuir's isotherm (Fig. 7b) with respective correlation coefficients (R^2) of 0.99 and 0.81 for Freundlich's isotherm (not shown in the figure). This finding suggests that the surface nature of ACPP is partly homogenous, with a maximum adsorption capacity of 157.23 mg/g through monolayer adsorption on the ACPP surface [7, 8, 23]. The adsorption coefficient is shown in Table 3.

3.6 Effects of Temperature

The effect of temperatures on Fe(II) adsorption was carried out at various temperatures at 25 °C, 30 °C, and 40 °C. The plot of $1/T$ Vs Ln K_L (K_L is adsorption constant) is shown in Fig. 8. The coefficients were evaluated, and Gibb's energy values ($\Delta G°$) are in the range from −2.118 to −3.741 $KJmol^{-1}$, and the negative values indicate the thermodynamic feasibility and spontaneity of the adsorption process. The values of enthalpy ($\Delta H°$) and entropy ($\Delta S°$) are −28.245 $KJmol^{-1}$ and −83.362 $KJmol^{-1}$, respectively. The negative enthalpy value suggests that the adsorption of Fe(II) by ACPP adsorbent is an exothermic reaction. Similar studies of exothermic reaction in adsorption were also observed [16–18, 25].

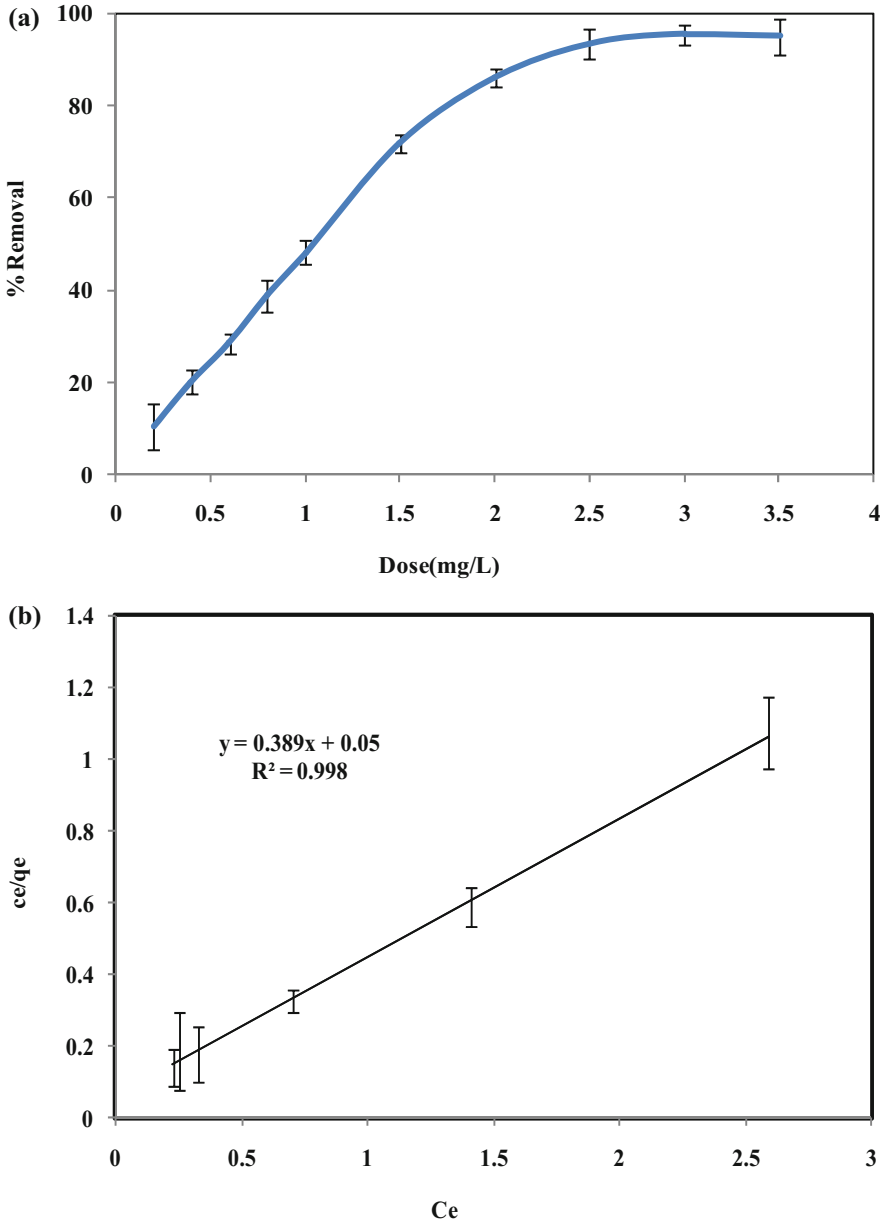

Fig. 7 (**a**) Effect of dose for Fe(II) adsorption. (**b**) Langmuir isotherm for Fe(II) adsorption

Table 3 Isotherm coefficients for Fe(II) removal

Langmuir isotherm	R^2	χ^2	q_m(mg/g)	b
	0.99	0.05	157.23	1.78
Freundlich isotherm	R^2	χ^2	K_f	$1/n$
	0.81	2.1	2.68	0.25

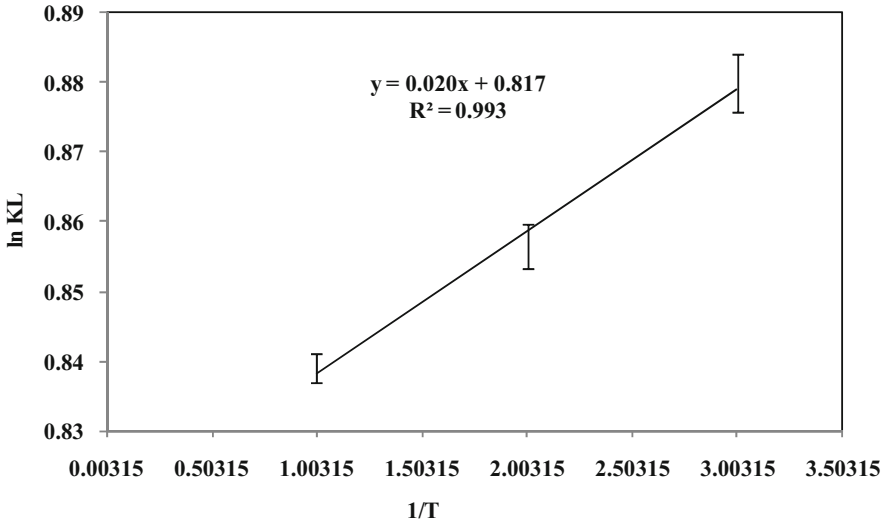

Fig. 8 Thermodynamic plot (ln K_LVs $1/T$) for Fe(II) adsorption

4 Conclusion

The wastewater effluents of small-scale gold industries at Waheng Leikai (24.803937, 93.933712) and iron and steel industries at Sagolband (24.805791, 93.914470) in Imphal, Manipur, was found to be 5.5 mg/L which reveals an alarming Fe(II) contamination. Application of *Parkia speciosa* (petai) pods as activated carbon for the adsorption of Fe(II) showed effective reduction at pH 5.5–6. The isotherm study showed that the Fe(II) adsorption was better described by Langmuir isotherm with the adsorption capacity of 157.23 mg/g describing monolayer and predominantly chemical adsorption. The desorption and reuse of the adsorbent increased the Fe(II) uptake by threefold and confirmed that ACPP is an effective adsorbent. From the study, it can be concluded that *Parkia speciosa* (petai) pods as activated carbon for the adsorption of Fe(II) from industrial wastewater are a good adsorbent and highly recommendable for the treatment of industrial wastewater.

References

1. L.S. Suman, A comparative study of Fe (II) ion adsorption onto chemically activated banana peel and sawdust bio-adsorbent. Int. J. Appl. Sci. Biotechnol. **6**(2), 137–141 (2018)
2. M. Forouzesh, E. Fatehifar, R. Khoshbouy, M. Daryani, Experimental investigation of iron removal from wet phosphoric acid through chemical precipitation process. Chem. Eng. Res. Des. **189**, 308–318 (2023)
3. K. Norherdawati, M.A. Wahab, A.S.R. Sheikh, Performance of membrane filtration in the removal of iron and manganese from Malaysia's groundwater. Membr. Water Treat. **7**(4), 277–296 (2016)
4. D. Barloková, J. Ilavsky, Removal of iron and manganese from water using filtration by natural materials. Pol. J. Environ. Stud. **19**(6), 1117–1122 (2010)
5. N. Anusha, Adsorption of iron from aqueous solution using almond shell as adsorbent. Int. J. Sci. Res. **3**(10), 1–3 (2014)
6. K. Urbian, E. Aime, Y. Jacques, Adsorption of iron and zinc on commercial activated carbon. J. Environ. Chem. Ecotoxicol. **5**(6), 168–171 (2013)
7. M. Gabriela-Nicoleta, A. Ecaterina, B. Laura, Adsorption of heavy metals ions onto surface-functionalised polymer beads. I. Modelling of equilibrium isotherms by using non-linear and linear regression analysis. Water Air Soil Pollut. **227**, 260 (2016)
8. O. Taynara, G. Roger, S. Marcio, Statistical analysis of linear and non-linear regression for the estimation of adsorption isotherm parameters. Adsorpt. Sci. Technol. **31**(5), 433–458 (2013)
9. F.T. Ademiluyi, E.O. David-West, Effect of chemical activation on the adsorption of heavy metals using activated carbons from waste materials. ISRN Chem. Eng. **2012**, 1–5 (2012)
10. R. Mohamad, Z. Alias, R.M. Ghazi, Removal of methyl red using chemical impregnated activated carbon prepared from Parkia speciosa pod (petai) as potential adsorbent. J. Trop. Resour. Substain. Sci. **5**, 62–65 (2017)
11. APHA AWWA, *WEF Standard Method for the Examination of Water & Wastewater*, 21st edn. (American Public Health Association, 2005)
12. L. Lim, N. Priyantha, Parkia speciosa (Petai) pod as a potential low-cost adsorbent for the removal of toxic crystal violet dye. Scientia Bruneiana Spec. Issue **2016**, 99–106 (2018)
13. T.H. Rao, R. Mohammad, N.F. Shoparwe, Adsorption of methyl blue from aqueous solutions using Parkia speciosa pod-based magnetic biochar. Int. Conf. Sci. Technol. **596**, 1–6 (2020)
14. N.A.A. Qasem, R.H. Mohammad, D.U. Lawal, Removal of heavy metal ions from wastewater: a comprehensive and critical review. Clean Water. **36**, 1–15 (2021)
15. Renu, M. Agarwal, K. Singh, Heavy metals removal from wastewater using various adsorbents: a review. Water Reuse **4**, 387–419 (2017)
16. M.N. Rashed, M.E. Soltan, M.M. Ahamed, A.N.A. Abdou, Heavy metals removal from wastewater by adsorption on modified physically activated sewage sludge. Arch. Org. Inorg. Chem. Sci. **1**, 1–7 (2018)
17. S. Mustapha, D.T. Shuaib, U.M. Mohammed, M.B. Nasirudeen, Adsorption isotherm, kinetic and thermodynamic studies for the removal of Pb(II), Cd(II), Zn(II) and Cu(II) ions from aqueous solutions using Albizia lebbeck pods. Appl. Water Sci. **9**(141), 1–11 (2019)
18. N.M. Malima, S.J. Owonubi, E.H. Lugwisha, A.S. Mwakaboko, Thermodynamic, isothermal and kinetic studies of heavy metals adsorption by chemically modifed Tanzanian Malangali kaolin clay. Int. J. Environ. Sci. Technol. **18**, 3153–3168 (2021)
19. R.-Z. Wang, D.-L. Huang, Y.-G. Liu, C. Zhang, C. Lai, G.-M. Zhang, M. Cheng, X.-M. Ghong, J. Wan, H. Luo, Investigating the adsorption behavior and the relative distribution of Cd2+ sorption mechanisms on biochars by different feedstock. Bioresour. Technol. **261**, 265–271 (2018)
20. Y. Deng, S. Huang, X. Wang, Z. Meng, Adsorption behaviour and mechanisms of cadmium and nickel on rice straw biochars in single-and binary-metal systems. Chemosphere **218**, 308–318 (2019)

21. Z. Ahmad, Z. Ahmad, B. Gao, A. Mosa, H. Yu, X. Yin, A. Bashir, H. Ghoveisi, S. Wang, Removal of Cu (II), Cd (II) and Pb (II) ions from aqueous solutions by biochars derived from potassium-rich biomass. J. Clean. Prod. **180**, 437–449 (2018)
22. Y. Yang, Z. Wei, X. Zhang, X. Chen, D. Yue, Q. Yin, L. Xiao, L. Yang, Biochar from Alternanthera philoxeroides could remove Pb (II) efficiently. Bioresour. Technol. **171**, 227–232 (2014)
23. N. Yeddou, A. Bensmaili, Equilibrium and kinetic modelling of iron adsorption by eggshells in a batch system: effect of temperature. Desalination **206**, 127–134 (2007)
24. J. Konga, X. Jinb, Y. Liua, D. Weia, S. Jianga, S. Gaoa, Z. Fenga, P. Xinga, X. Luoc, Study on the kinetics of iron removal from silicon diamond-wire saw cutting waste: comparison between heterogeneous and homogeneous reaction methods. Sep. Purif. Technol. **221**, 261–268 (2019)
25. M.D. Víctor-Ortega, J.M. Ochando-Pulido, A. Martínez-Ferez Chemical, Thermodynamic and kinetic studies on iron removal by means of anovel strong-acid cation exchange resin for olive mill effluentreclamation. Ecol. Eng. **86**, 53–59 (2016)

Activated Carbon Developed from Phumdi Biomass and Deccan Hemp for the Adsorption of Methylene Blue

Lairenlakpam Helena and Potsangbam Albino Kumar

Abstract This study focuses on the assessment of toxic methylene blue dye from the small-scale textile industries in Imphal, Manipur, which is directly drained to the sewers, and methylene blue is removed by the adsorption process. The adsorbents employed are activated carbon derived firstly from phumdi, which is a solid waste of biomass, in Loktak Lake, Manipur, and secondly from Deccan hemp. Parameters for the study include pH and adsorption time, and morphological studies of the adsorbent were analyzed using SEM images and EDX. The optimum pH for both adsorbents is observed in the range of pH 6–8. Adsorbent doses of 2–2.5 g/L for activated carbon from phumdi and 2–3 g/L for Deccan hemp were able to remove methylene blue completely from all different effluents whose concentration ranges from 5.3 to 7.8 mg/L. The adsorption kinetics is well described by the pseudo-second-order model, while the Langmuir model complies with the adsorption isotherm at equilibrium**.** The maximum adsorption capacity for methylene blue uptake is observed as 126 and 85 mg/g for ACP and ACDH, respectively.

Keywords Loktak Lake · Industrial effluent · Adsorbent · Batch adsorption · Specific surface area · Pore diameters · Electrostatic attraction · Lagergren's pseudo-first-order · Second-order · Langmuir isotherm

Abbreviations

ACDH	Activated carbon Deccan hemp
ACP	Activated carbon phumdi
MB	Methylene blue
SEM	Scanning electron microscope

L. Helena · P. A. Kumar (✉)
Civil Engineering Department, National Institute of Technology, Manipur, Lamphelpat, Langol, India

D. Mazumder (ed.), *Sustainable Advanced Technologies for Industrial Pollution Control*, Springer Proceedings in Earth and Environmental Sciences,
https://doi.org/10.1007/978-3-031-37596-5_10

1 Introduction

The wastewater effluent from the textile industry, due to the presence of dyes make it difficult to decompose naturally and dyes (as low as 1.0 ppm) could bring substantial effects. Methylene blue (MB), which has a synthetic origin and complex aromatic molecular structure, is generally difficult to biodegrade and photodegrade and may cause gastrointestinal irritation if swallowed, cyanosis if inhaled, and irritation of the skin. Textile industries are being developed on small scales in Manipur for the last few decades without proper treatment facilities for the effluents, and the removal of toxic dyes, especially the methylene blue is thus very essential. Chemical precipitation, nanofiltration, advanced oxidation, ion exchange, reverse osmosis, membrane separation, electrocoagulation, and electrodialysis are the advanced wastewater treatments that are mostly used [1, 2]. However, especially in poorer nations, these technologies are extremely expensive and unsustainable methods of wastewater treatment. These techniques also needed significant levels of energy, chemicals, operational and capital inputs, and cutting-edge technology [2]. Because of these differences in wastewater treatment techniques, researchers are motivated to find new and more effective ways to remove color from textile industry wastewater. The adsorption method is proven to be one of the most effective methods for methylene blue removal in terms of low cost and effectiveness as compared to other methods like precipitation, membrane techniques, etc. [3, 4]. Several easily available agro-industrial waste biomasses have been explored as a source of activated carbon [5]. The phumdis of Loktak Lake which is a tangled clump of biomass, vegetation, and organic matter cover around 50% of the lake and can be an excellent feedstock for the preparation of activated carbon due to its organic nature and the presence of several functional groups which can bind toxic heavy metals and dyes. The objective of this study is the assessment of methylene blue from the effluents of small-scale industries using activated carbon derived from the biomass phumdi and Deccan hemp and their comparison.

2 Materials and Methods

2.1 Collection of Raw Materials

Phumdis are floating islands found solely in Loktak Lake in Manipur. These landmasses are composed of plants, soil, and organic material that has hardened into a solid form and is in various phases of decomposition. The other raw material used is Deccan hemp or kenaf of the Malvaceae family. The leaves are the only part of the plant that is consumed in the Manipuri cuisine. So, the stems lie as waste most of the time. Phumdi collected from Loktak Lake was washed properly and dried in sunlight for 10 days, and it was dried in an oven at 100 °C for 2 hours. In the case of Deccan hemp, it was collected from the local market. To remove the dirt and

impurities, the uneatable leftover stems were washed thoroughly with distilled water. Then, it was cut into pieces and dried in the oven at 150 °C for 15 hours. Both phumdi and Deccan hemp, after being dried, are crushed using a grinder and sieved to a particle size of 5–10 mm and stored in different sealed containers for experimentation.

2.2 Synthesis of Activated Carbon

For the synthesis of activated carbon, the processed raw materials, Deccan hemp and the phumdi biomass, were soaked in a phosphoric acid solution and impregnated at a ratio of 1:1 for 24 hours. It was dried in an oven at 180 °C for 30 minutes [6, 7]. After activation, both samples were allowed to cool and subsequently washed with distilled water several times. It was grounded and sieved at the last step of the preparation. The resulting (i) activated carbon phumdi (ACP) and (ii) activated carbon Deccan hemp (ACDH) products were kept in a desiccator for further use.

2.3 Methodology

The wastewater effluents were collected from the three nearby sites of small-scale textile industries at Wangkhei, and their coordinates are 93.555, 24.797; 93.959, 24.793; and 93.957, 24.802. The effluents were analyzed after the filtration of all the other solid impurities using a spectrophotometer (Thermo Scientific Evolution 201, USA) at a wavelength of 665 nm [8]. The activated carbon adsorbent's pore size distribution and the specific area's measurement were carried out using Brunauer-Emmett-Teller (BET) technique. Morphological study of the surface area before and after the adsorption of methylene blue was investigated using scanning electron microscopy (SEM) (Sigma 300) operated at 20.00 KV, magnification 500X.

2.4 Batch Adsorption Studies

The batch adsorption study was carried out in 500 ml of the industrial effluent samples with varying doses of both ACP and ACDH (4–10 g), varying pH (3–10), and contact time (0–180 minutes) for the determination of the adsorption optimum conditions. The adsorption test was conducted by adding a fixed amount of activated carbon (ACP and ACDH) to the jar test apparatus (Phipps and Bird Model PB-600). Either 0.10 M HCl or NaOH was used for pH adjustment [9].

3 Results and Discussion

3.1 Site Assessment

The assessment of the industrial effluent sites was conducted at three various stations and observed a concentration of 5.3–7.8 mg/L MB. The total solid concentration in the sample was 20–50 mg/L, and after digestion of the solid samples, the MB concentration increased to 9–10.2 mg/L, indicating the adsorption of MB on solids of the sewers too.

3.2 Surface Characterization of the Adsorbent

The activated carbons ACP and ACDH were analyzed for specific surface area and pore volumes and obtained a specific surface area as 4.754 m^2/g and 4.381 m^2/g respectively. The respective total pore volumes are 0.017 cm^3/g and 0.013 cm^3/g, and that of average pore diameters are 7.085 nm and 3.054 nm, respectively.

The surface morphology of the adsorbent before and after the MB adsorbent are shown in Fig. 1a, b respectively for the adsorbent ACP. Ridges and pores of size 5–10 μm are visible in Fig. 1a and are completely covered by MB, resulting in a lesser heterogeneous surface as compared to the raw ACP. Similar observations were made for ACDH in Fig. 2a with more pores in the ranges 1–5 μm before the adsorption. After MB adsorption, the surface of ACDH is almost homogenous (Fig. 2b).

3.3 Effect of pH

The pH of the effluent was in the range of 9.8–10.2; however, to achieve the maximum MB adsorption, the sample pH was altered and studied in the range of

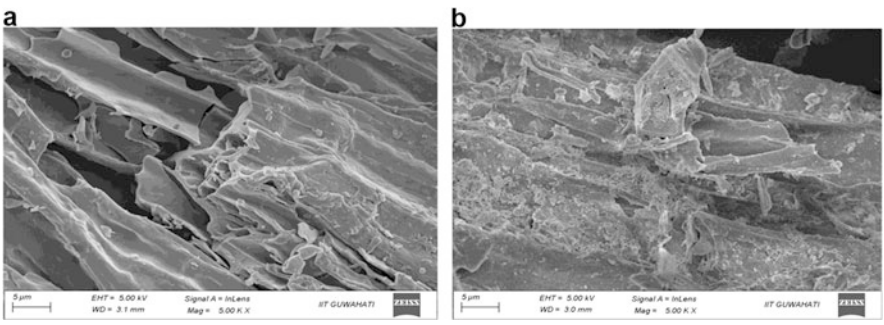

Fig. 1 (**a**, **b**) SEM images of ACP before and after adsorption of MB

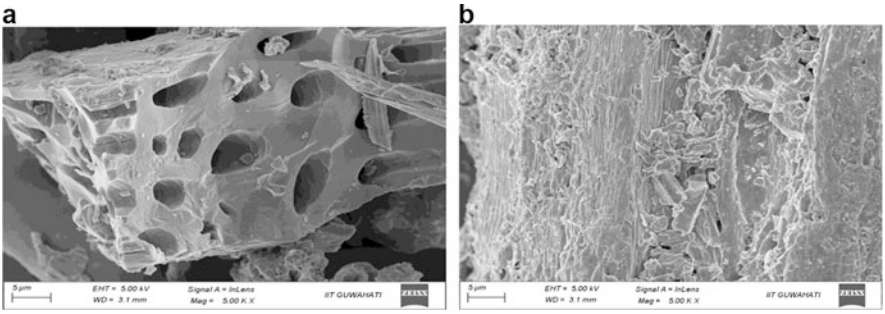

Fig. 2 (**a**, **b**) SEM images of ACDH before and after adsorption of MB

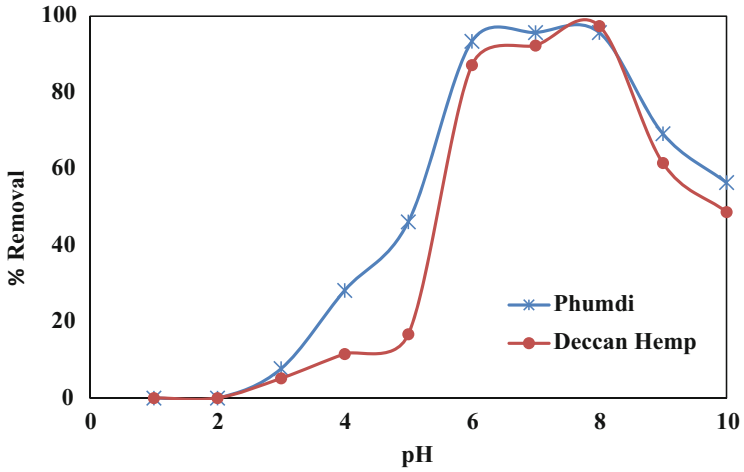

Fig. 3 Effect of pH for MB adsorption by ACP and ACDH

pH 1–10. The results are shown in Fig. 3. The maximum adsorption range of both adsorbents, ACP and ACDH, was observed to be 6–8 with MB adsorption of 90–94%. The mechanisms of MB adsorption onto ACP and ACDH are almost similar probably due to the electrostatic attraction of cationic MB onto the deprotonated surface of ACP and ACDH at this basic pH range [10]. Similar findings were also observed. Hereafter, all the remaining experiments were conducted at an optimum pH of 7.

3.4 Effect of Time and Adsorption Kinetics

The effect of contact time between MB and the activated carbon adsorbents were studied, and an adsorption equilibrium was observed within 120 minutes, suggesting rapid adsorption due to the high surface area and also chemisorption.

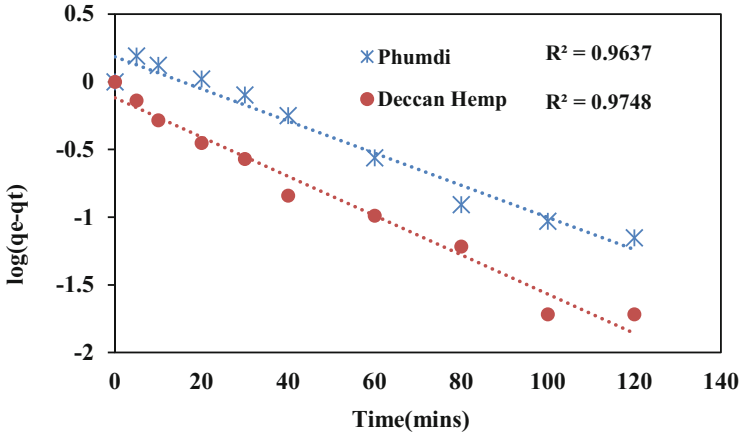

Fig. 4 Pseudo-first-order kinetic plot for MB adsorption by ACP and ACDH

The kinetic rate of the adsorption process was treated using Lagergren's pseudo-first-order model and pseudo-second-order model Eqs. (1) and (2). The principle of the pseudo-first-order kinetic model is that the reaction rate is proportional to the number of ions remaining in the solution [11, 12]. The linear equation is shown below:

$$\mathrm{Ln}\,(q_\mathrm{e} - q_t) = \ln q_\mathrm{e} - K_1 t \tag{1}$$

The pseudo-second-order kinetic model assumes that if the reaction rate is proportional to the concentrations of the two reactants, then the adsorption is regulated by chemical adsorption steps [11, 12]. The equation is shown below:

$$\frac{t}{Q_t} = \frac{1}{K_{2Q_\mathrm{e}}2} + \frac{1}{Q_\mathrm{e}} \tag{2}$$

where q_e is the amount of dye adsorbed at equilibrium (mg. g^{-1}), q_t is the equilibrium concentration at various periods t (in mg. L^{-1}), and k_1 and k_2 are the adsorption rate constants (min^{-1}) of the first-order equation and second-order equation, respectively.

The plots of the pseudo-first and second-order are illustrated in Figs. 4 and 5, respectively. For both ACP and ACDH, the correlation coefficients (R^2) were lesser in the case of pseudo-first-order for both the adsorbents, i.e., 0.9637 and 0.9748, as compared to that of pseudo-second-order with 0.9931 and 0.9935, respectively. The chi-square test was also conducted to precisely check the error between the experimental q_t and predicted q_t. From Table 1, it is obvious that with $\chi 2$ of 0.42–0.5 for pseudo-first-order equation, pseudo-second-order fixed better for adsorption kinetics with $\chi 2$ of 0.0.1–0.2. The fixing of kinetics data onto a pseudo-second-order equation further confirms the chemically predominant adsorption behavior of MB [13].

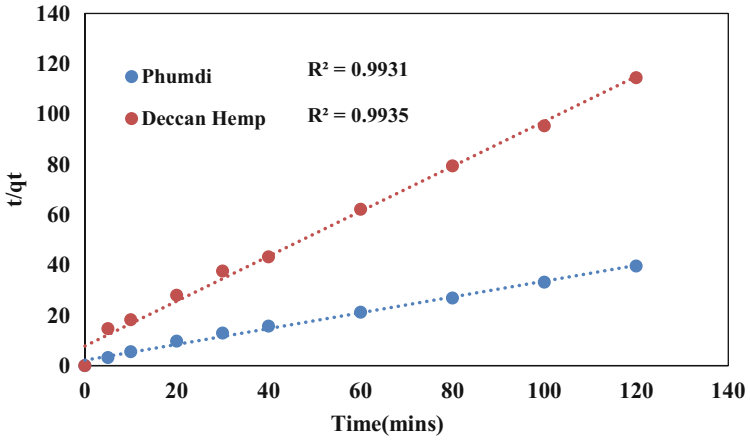

Fig. 5 Pseudo-second-order kinetic plot for MB adsorption by ACP and ACDH

Table 1 Coefficients of kinetic models for methylene blue removal

SN	Kinetic models	Adsorbent	K (min^{-1})	R^2	$\chi 2$
1	Pseudo-first-order	ACP	0.0016	0.9612	0.42
		ACDH	0.0013	0.9748	0.5
2	Pseudo-second-order	ACP	3.7	0.9935	0.01
		ACDH	1.3	0.9931	0.2

3.5 Adsorbent Dose and Adsorption Isotherms

An adsorbent dose variation study was carried out with varying adsorbent (ACP and ACDH) doses 0.5–4 g/L and the results are shown in Fig. 6. As usual, the increase in adsorbent dose increases the uptake of MB for both the adsorbents, and the optimum adsorption was achieved by 2.5 g/L ACP and 3.0 g/L ACDH with respective removal of 95% and 84%, respectively. As ACP has a higher surface area, pore volume, and pore diameter (4.754 m^2/g, 0.017 cm^3/g, and 7.085 nm, respectively) than ACDH (4.381 m^2/g, 0.013 cm^3/g, and 3.054 nm, respectively), the uptake of higher MB by ACP is obvious.

Adsorption isotherm, or the relationship between the number of adsorbates on the adsorbents and the equilibrium concentrations of the adsorbates at constant temperatures, was examined using the data from adsorbent dosage experiments [13]. The most commonly applied linear models, Langmuir isotherm and Freundlich isotherm, were applied as shown in Eqs. (3) and (4). Langmuir isotherm is successfully used in monolayer molecular adsorption processes [13, 14].

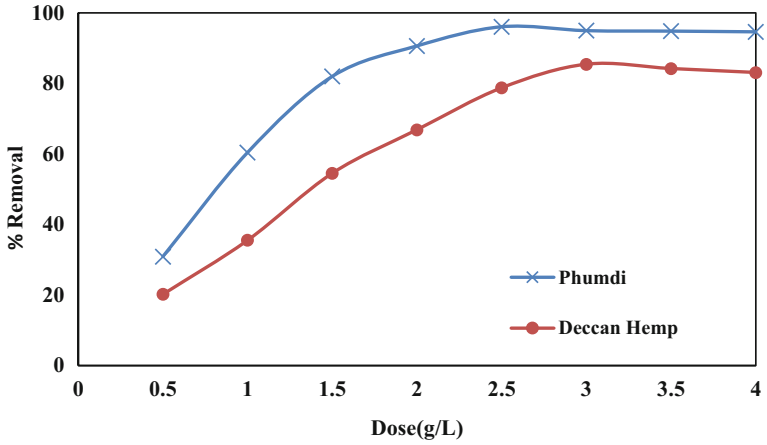

Fig. 6 Effect of dose for MB adsorption by ACP and ACDH

$$\frac{C_e}{q_e} = \left(\frac{1}{a}\right)\left(\frac{1}{K_L}\right) + \left(\frac{1}{a}\right)C_e \tag{3}$$

where K_L is the Langmuir equilibrium constant related to the heat of adsorption, C_e is the equilibrium concentration (mgL^{-1}), q_e is the amount adsorbed per unit mass of sorbent (mg. g^{-1}), and b is the monolayer capacity. As a result, the straight line on a plot of C_e/q_e vs. C_e should have an intercept of ($1/a\ K_L$) and a slope of $1/a$. Freundlich isotherm model is commonly used for multilayer adsorption over a heterogeneous surface [13, 14].

$$\ln q_e = (\ln K_f)\left(\frac{1}{n}\ln C_e\right) \tag{4}$$

where K_f is the adsorption capacity (mg . g^{-1}) and $1/n$ is the sorption intensity. If the value of $n = 1$, then the partition between the two phases is independent of the concentration; the value below 1 indicates a normal adsorption process, whereas the value above 1 indicates cooperative adsorption. Thus, a plot of ln q_e vs. ln C_e should be a straight line with a slope of $1/n$ and an intercept of ln K_f [14]. After a linear equation plot of Langmuir and Freundlich isotherms, the coefficients are evaluated and are given in Table 2. Chi-square test was done to evaluate the better fit isotherm using Eq. (5).

$$\chi^2 = \sum \frac{(q_e - q_{em})^2}{q_{em}} \tag{5}$$

where q_e and q_{em} (mg/g) are MB adsorbed at equilibrium evaluated from the experiment and the predicted isotherm models. From Table 2, the correlation

Table 2 Isotherm coefficients for mb removal

Langmuir isotherm	R^2		$\chi 2$		a (mg/g)		b	
	ACP 0.992	ACDH 0.984	ACP 0.02	ACDH 0.1	ACP 126	ACDH 85	ACP 0.198	ACDH 0.161
Freundlich isotherm	R^2		$\chi 2$		K_f		$1/n$	
	ACP 0.835	ACDH 0.813	ACP 1.2	ACDH 1.5	ACP 11	ACDH 8	ACP 0.1011	ACDH 0.1103

coefficients for both ACP and ACDH adsorbents are obtained as 0.992 and 0.984, respectively, and are much higher than that of corresponding Freundlich with 0.835 and 0.813, respectively. The better fit isotherm with Langmuir is further confirmed with lesser $\chi 2$ of 0.02 and 0.1 for ACP and ACDH, respectively, against that of 1.2 and 1.5. The maximum monolayer coverage/capacity for MB uptake is observed as 126 and 85 mg/g for ACP and ACDH, respectively. In comparison with other reported literatures for the adsorption of MB with activated carbon, a maximum adsorption capacity of 48.2 mg/g was found in the case of corn cob activated carbon [5]; barley bran-derived activated carbon has a maximum MB adsorption capacity of 63.2 mg/g, and enset midrib leaf-derived activated carbon has 35.5 mg/g [6]. A higher MB adsorption capacity of 113.63 mg/g by activated carbon developed from baobab fruit shell was also reported [14]. With ACP and ACDH exhibiting maximum adsorption capacities of 126 mg/g and 85 mg/g, respectively, the performance of both the activated carbons is comparatively high as compared to the reported literatures.

4 Conclusion

The effluent of small-scale textile dye industries in Manipur is observed to contain the toxic dye methylene blue above the permissible limit of 0.05 mg/L. Activated carbons prepared from Loktak Lake biomass phumdi (ACP) and Deccan hemp (ACDH) with phosphoric acid activation were able to treat the contaminated effluent effectively with an adsorbent dose of 2–2.5 mg/L through rapid adsorption within 120 minutes. The maximum adsorption was observed in the pH range of 6–8 for both adsorbents. The adsorption properties are well described by the pseudo-second-order model, while the Langmuir model complies with the adsorption results at equilibrium and maximum methylene blue uptake of 126 mg/g and 85 mg/g, respectively, by ACP and ACDH. These studies showed that this solid waste-activated carbon-based adsorbent is effective for treating industrial dye effluents.

References

1. M. Maryudi, S. Amelia, S. Salamah, Removal activated carbon using adsorption method. Reaktor **19**(4), 168–171 (2019)
2. S. Arivoli, M. Hema, S. Parthasarathy, N. Manju, Adsorption dynamics of methylene blue by acid activated carbon. J. Chem. Pharm. Res. **2**(5), 626–641 (2010)
3. R.M. Shrestha, Effect of preparation parameters on methylene blue number of activated carbons prepared from a locally available material. J. Inst. Eng. **12**(1), 169–174 (2016)
4. S.A. Borghei, M.H. Zare, M. Ahmadi, M.H. Sadeghi, A. Marjani, Synthesis of multi-application activated carbon from oak seeds by KOH activation for methylene blue adsorption and electrochemical supercapacitor electrode. Arab. J. Chem. **14**(2), 1–16 (2021)
5. A. Medhat, H.H. El-Maghrabi, A. Abdelghanya, N.M.A. Menema, P. Raynaudd, Y.M. Moustafae, M.A. Elsayed, A.A. Nada, Efficiently activated carbons from corn cob for methylene blue adsorption. Appl. Surf. Sci. Adv. **3**, 1–8 (2021)
6. D. Mekuria, A. Diro, F. Melak, T.G. Asere, Adsorptive removal of methylene blue using biowaste materials: Barley Bran and Enset midrib leaf. J. Chem. **2022**, 1–13 (2022)
7. R. Rahimian, S. Zarinabadi, A review of studies on the removal of methylene blue dye from industrial wastewater using activated carbon adsorbents made industrial from almond bark. Prog. Chem. Biochem. Res. **3**(3), 251–268 (2020)
8. J.-J. Gao, Y.-B. Qin, T. Zhou, D.-D. Cao, Adsorption of methylene blue onto activated carbon produced from tea (Camellia sinensis L.) Seed shells: kinetics, equilibrium, and thermodynamics studies. J. Zhejiang Univ. Sci. B **14**(7), 650–658 (2013)
9. J. Fito, S. Abrham, K. Angassa, Adsorption of methylene blue from textile industrial wastewater onto activated carbon of Parthenium hysterophorus. Int. J. Environ. Res. **14**(5), 501–511 (2020)
10. A.H. Jawad, R.A. Rashid, M.A.M. Ishak, K. Ismail, Adsorptive removal of methylene blue by chemically treated cellulosic waste banana (Musa sapientum) peels. J. Taibah Univ. Sci. **12**(6), 809–819 (2018)
11. T.C. Andrade Siqueira, I. Zanette da Silva, A.J. Rubio, et al., Sugarcane bagasse as an efficient biosorbent for methylene blue removal: kinetics, isotherms and thermodynamics. Int. J. Environ. Res. Public Health **17**(2), 526 (2020)
12. R. Chikri, N. Elhadiri, M. Benchanaa, Y. El, Efficiency of sawdust as low-cost adsorbent for dyes removal. J. Chem. **2020**, 17 (2020)
13. R. Nedjai, M.F.R. Alkhatib, M.Z. Alam, N.A. Kabbashi, Adsorption of methylene blue onto activated carbon developed from baobab fruit shell by chemical activation: kinetic equilibrium studies. IIUM Eng. J. **22**(2), 31–49 (2021)
14. G. Vijayalakshmi, B. Ramkumar, S.C. Mohan, Isotherm and Kinetic studies of methylene blue adsorption using activated carbon prepared from teak wood waste biomass. J. Appl. Sci. **19**(9), 827–836 (2019)

An Experimental Study of Metanil Yellow Dye Remediation Using Fe-Mn Bimetal Oxide Composites

Arunita Pal, Sajal Rudra Paul, and Animesh Debnath

Abstract Herein, magnetic mesoporous iron-manganese bimetal oxide (IMBO) composite adsorbent was synthesized for effective sorption of metanil yellow (MY) dye from dye-laden wastewater. The as-synthesized IMBO is characterized using various characterization techniques like XRD, BET, FESEM, VSM, and FTIR spectroscopy. The BET analysis shows that the pore volume and surface area of IMBO is 0.484 cm^3/g and 178.27 m^2/g, respectively. Also, the FTIR analysis confirmed the diversity of functional groups over the IMBO composite. These physical and chemical properties of IMBO make it a good adsorbent for MY sorption from contaminated water. The MY dye removal efficacy of 99.57% was obtained at an operational condition of solution pH of 3.0, for 50 mg/L of initial dye concentration at 1.0 g/L of IMBO dose, for an equilibrium time of ~100 min. The adsorption reaction follows pseudo-second-order (PSO) kinetics, and a maximum dye uptake capacity of 114.94 mg/g is obtained from the Langmuir isotherm model.

Keywords Magnetic materials · Metal oxide composites · Metanil yellow · Adsorbent · Adsorbent dose · Equilibrium time · Uptake capacity · Sorption · Kinetic study · Langmuir isotherm

Abbreviations

BET	Brunauer-Emmett-Teller
emu/g	Electromagnetic unit
Fe_2O_3	Ferric oxide
$FeCl_3$	Iron(III) chloride
FESEM	Field emission scanning electron microscopy
FTIR	Fourier transform infrared
IMBO	Iron manganese bimetal oxide

A. Pal (✉) · S. R. Paul · A. Debnath
Civil Engineering Department, National Institute of Technology, Agartala, Jirania, India

D. Mazumder (ed.), *Sustainable Advanced Technologies for Industrial Pollution Control*, Springer Proceedings in Earth and Environmental Sciences,
https://doi.org/10.1007/978-3-031-37596-5_11

KOe	Unit of coercivity
M	Molar mass
Mn_3O_4	Manganese oxide
$MnCl_2$	Manganese(II) chloride
MY	Metanil yellow
NaOH	Sodium hydroxide
nm	Nanometer
PFO	Pseudo-first-order
PSO	Pseudo-second-order
rpm	Revolutions per minute
UV	Ultraviolet
VIS	Visible
VSM	Vibrating Sample Magnetometer
XRD	X-ray diffraction

1 Introduction

Synthetic dye released from industries is one of the major concerns for environmentalists because it is challenging to remove dyes once they contaminate water [1]. Synthetic dyes such as azo dyes are used by several industries, predominantly textile industries [2]. Synthetic dye is quite stable in nature and soluble in water and is responsible in forming aromatic amines [3]. Metanil yellow (MY) ($C_{18}H_{14}N_3NaNO_3S$) is an azo dye, which has been proven to have carcinogenic effects, chromosomal aberrations, and genetic disorders [4]. Oral consumption of MY dye by animals has been detected to generate testicular lesions and affect the spermatogenesis rate [5]. The phytotoxicity study reported by Anjaneya et al. [6] demonstrated significant inhibitory effects on the growth of pea seeds, for a concentration of 0.4 g/L of MY dye. Thus, it has become imperative to eliminate these dyes from wastewater before their disposal.

Among several treatment technologies, the adsorption process is relatively easier to adopt because of its simple design, low cost, enhanced efficiency, and easy operation for dye as well as heavy metal remediation [7]. The adsorbent in use should have a high efficacy and good recycling ability [8]. Metal oxides with magnetic properties are a better choice owing to their easy segregation from wastewater [9]. Iron oxide (Fe_2O_3) is used as an adsorbent for navy blue and safranin dye remediation with 49.3% and 66.0% removal of dyes, respectively, by Hammad et al. [10]. The magnetic properties of iron oxide have been explored by Parashar et al. [11] to remove pharmaceuticals. The effectivity of the use of iron oxide-based nanocomposites in removing heavy metals like Cu, Cr, and Pb ions has been reviewed by Dave and Chopda [12]. Nanoparticles of green Mn_3O_4 are seen effective in removing malachite green dye, which has followed a pseudo-first-order reaction with a maximum uptake capacity of 162 mg/g [13]. Moreover,

Ullah et al. [14] used Mn_3O_4 to eliminate methylene blue dye and could remove 80% of the dye. There are a few reports for the adsorptive removal of MY dye from water using adsorption technology also. Bhowmik et al. [15] used the adsorbent ($CaFe_2O_4$/ZrO_2) for the effective removal of MY dye from water with a removal efficiency of 86.08%. In one more study, Guo et al. [16] have described the successful solicitation of amino-functionalized graphene for the eradication of MY dye with an uptake capacity of 71.62 mg/g. Ibrahim and Ibrahim [17] used Cu_2O nanoparticles for the sequestration of MY dye from water with a removal efficiency of 70.7%. Although the metal oxide-based nanomaterial was explored widely for dye-loaded wastewater sequestration, mixed-phase metal oxide nanocomposite like a composite of Fe_2O_3-Mn_3O_4 has been less explored so far.

Thus, MY dye removal by batch mode adsorption process was studied using a mixed phase of iron-manganese bimetal oxide (IMBO) as adsorbent material. The key objectives of this research are (i) to investigate the influence of the key reaction parameters (solution pH, IMBO dose, interaction time, and dye concentrations) on the removal efficacy of MY dye, (ii) to explore the mechanism of the adsorption process by conducting the kinetic and isotherm modelling, and (iii) to study the stability and reusability of IMBO.

2 Materials and Methods

2.1 Chemical Reagents and Materials Used

The chemicals used in this study such as $FeCl_3.6H_2O$, $MnCl_2.4H_2O$, NaOH pellets, and MY ($C_{18}H_{14}N_3NaNO_3S$) dye powder were procured from MERCK & CO. (India). Extra pure deionized water was used in all adsorption experiments.

2.2 Methods

In the batch mode adsorption process, the IMBO adsorbent was added with variable initial concentrations (50–120 mg/L) of MY dye solution (200 mL), and the mixture of MY dye and IMBO was stirred @ 300 rpm for varying contact times. The UV-Vis-NIR spectrophotometer (HACH, DR 5000) was used to evaluate the residual concentration of MY dye, at a wavelength of 434 nm. To calculate the MY dye removal efficiency and adsorption capacity, the following equations were used [18]:

$$\text{MY dye sequestration efficiency } (\%) = \frac{C_0 - C_t}{C_0} \times 100 \quad (1)$$

$$\text{MY dye adsorption capacity } (\text{mg/g}) = \frac{(C_0 - C_t)}{m} \times V \tag{2}$$

where C_0 and C_t are the initial concentrations (mg/L) of MY at time t, the sample volume is denoted by V (L), and the mass of IBMO is indicated by m (g).

2.3 Synthesis of IMBO

To synthesize the IMBO nanoparticles, a modified facile co-precipitation method has been adopted. Firstly, two separate solutions of $FeCl_3.6H_2O$ (0.48 M) and $MnCl_2.4H_2O$ (0.1 M) were prepared and mixed together to prepare a homogenous solution. Thereafter, a NaOH solution of 0.875 M was added dropwise to the mixture of $FeCl_3$ and $MnCl_2$ solutions to reach a pH of ~8.0 and gently stirred for a few minutes. A dark brownish precipitate was formed immediately upon the addition of NaOH solution, and this precipitate was separated by filtering. This is followed by calcination at 400 °C for 4 h which results in the formation of homogenous IMBO.

3 Results and Discussion

3.1 Characterization of Synthesized IMBO

3.1.1 XRD

The structural characteristics of the prepared IMBO were performed by studying the diffraction pattern formed in an XRD (Bruker, D8 Advance). Figure 1a exhibits that due to the crystalline structure of the nanocomposite, diffraction peaks (2θ) are obtained at 31.6°, 33.14°, 35.7°, and 54.2° in the diffractometer. The diffraction peak at 31.6° is due to the Bragg reflection from the (200) plane of Mn_3O_4 crystal, whereas the intensity peaks at 33.14°, 35.7°, and 54.2° correspond to the reflections from (104), (110), and (116) planes of Fe_2O_3 crystal, respectively, which confirms the effective fabrication of Fe_2O_3/Mn_3O_4 [9].

3.1.2 FESEM

The geometrical features of IMBO were investigated using FESEM, Hitachi, S-4800. The FESEM image Fig. 1b depicts the pervious structure of the nanocomposite with a typical grain size (in diameters) of 60–90 nm.

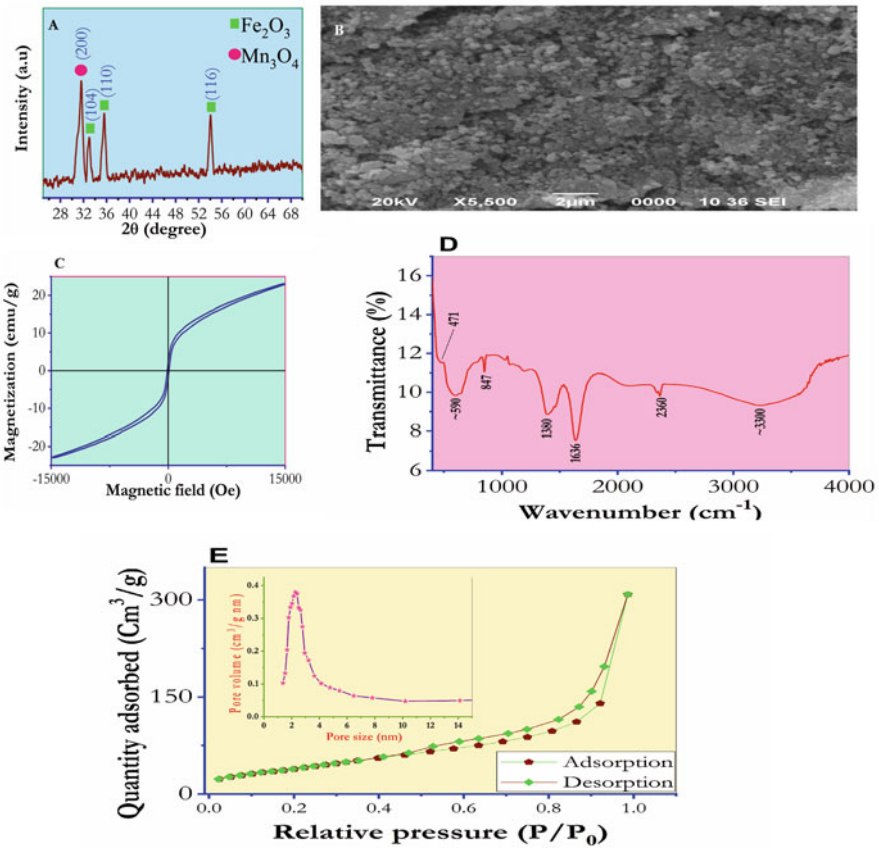

Fig. 1 (**a**) XRD pattern, (**b**) FESEM images, (**c**) VSM, (**d**) FTIR spectrum, and (**e**) BET analysis of IMBO

3.1.3 VSM

The VSM magnetization curve describes the hysteresis loop of the sample IMBO, which shows a high saturation magnetization (23.1 emu/g) at room temperature, for a range of magnetic field −15–15 kOe in Fig. 1c. The observed coercivity and retentivity are 113.3 Oe and 0.28 emu/g, correspondingly. The measured squareness value was found to be 0.08. This indicates that IMBO has a super-paramagnetic behavior which is essentially helpful in segregating IMBO from the aqueous solvents using external magnetic field [19].

3.1.4 FTIR

The plots obtained after conducting FTIR analysis (Fig. 1d) on IMBO show a wide peak at ~3300 cm^{-1} and a peak at ~1636 cm^{-1}. These are due to the presence of interstitial water molecules undergoing stretching and bending, i.e., vibrations in the O–H bond. The oscillatory modes of the metal-oxygen bonds (Mn-O and Fe-O) in the compounds Mn_3O_4 and Fe_2O_3 can be attributed to two additional peaks at ~471 cm^{-1} and ~590 cm^{-1}, correspondingly. The sole peak at the O–H bond is linked to Mn atoms [19].

3.1.5 BET Surface Area

The multipoint BET method is employed to evaluate the external area and the pore features of the IMBO which is illustrated in Fig. 1e. The microporosity was determined to be in the range of 2–50 nm (average diameter ~2.87 nm), distributed over a surface area of ~178.27 m^2/g, having a pore volume of ~0.471 cm^3/g.

3.2 Impact of Various Experimental Variables on MY Adsorption

3.2.1 Influence of Solution pH

To evaluate the adsorption behavior of MY dye with different solution pH, a widespread pH range of 2.0–10.0 was selected. The experiments were conducted with an initial MY concentration of 100 mg/L and an IMBO dose of 1.0 g/L, and the reaction was continued for 100 min. The results of pH variation on the MY sorption are shown in Fig. 2a, which depicts that at solution pH 3.0, IMBO exhibits the maximum removal (95.86%) of MY dye. However, because of the decline in protonation and consequent decrease in adsorption, the removal efficiency substantially declines as pH increases [20]. The minimum removal was recorded as ~15.89% at solution pH 10.0. This study demonstrates that the extent of MY dye adsorption was substantially influenced by solution pH. MY dye contains a sulfonated group ($–SO_3Na$), which dissociates in aqueous media and exists in anionic form. An electrostatic attractive force develops between the anionic MY dye and the positively charged IMBO surface, as shown in Fig. 3. The optimum solution pH of 3.0 was chosen for attaining the maximum abatement percentage of MY dye.

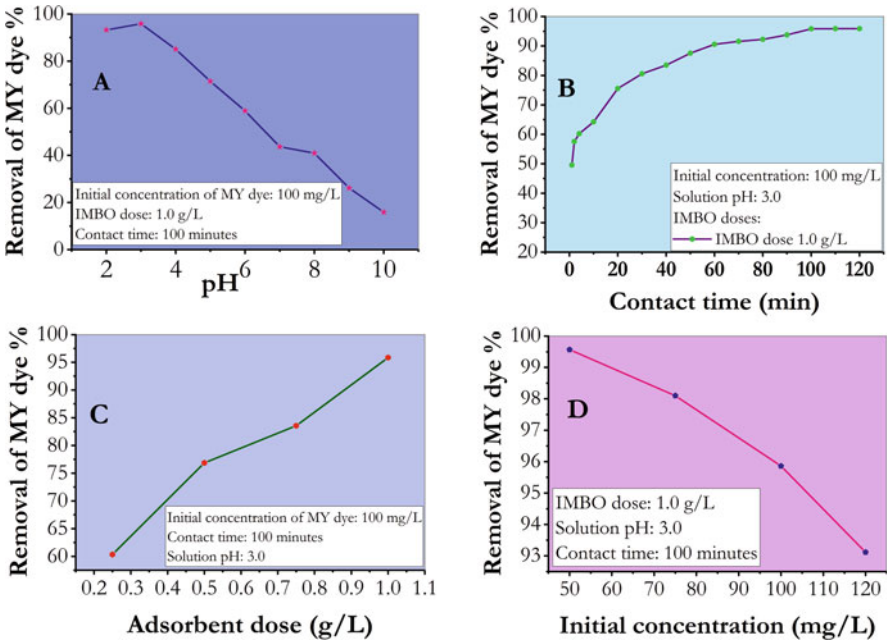

Fig. 2 Effects of (**a**) solution pH, (**b**) adsorption time, (**c**) adsorbent dose, and (**d**) initial concentration on MY dye abatement

3.2.2 Impact of Adsorption Time

To investigate the influence of sorption time, studies were carried at a fixed pH of 3.0, an original concentration of MY dye (100 mg/L), and a contact duration range of 1–120 min. According to Fig. 2b, the maximum uptake of MY dye by IMBO is higher during the first 10–70 min, and equilibrium was achieved at around 100 min (*R*: 95.86%). The accessibility of a substantial surface area, high pore features, and the active functional groups contribute to a higher adsorption rate during this small time period. Afterwards, no significant uptake of MY dye was perceived owing to the nonavailability of IMBO active sites [21].

3.2.3 Impact of IMBO Dose

The deviation of the efficacy of MY dye with diverse dose of IMBO at a fixed MY concentration of 100 mg/L was studied and portrayed in Fig. 2c. The solution pH in all cases was maintained at 3.0, and the reaction adsorption process was continued for 100 min. Figure 2c shows that the abatement percentage increases from 60.35% to 95.86% with an upsurge in IMBO dose from 0.25 g/L to 1.0 g/L, and further upsurge in dose did not make any substantial alterations to MY dye removal.

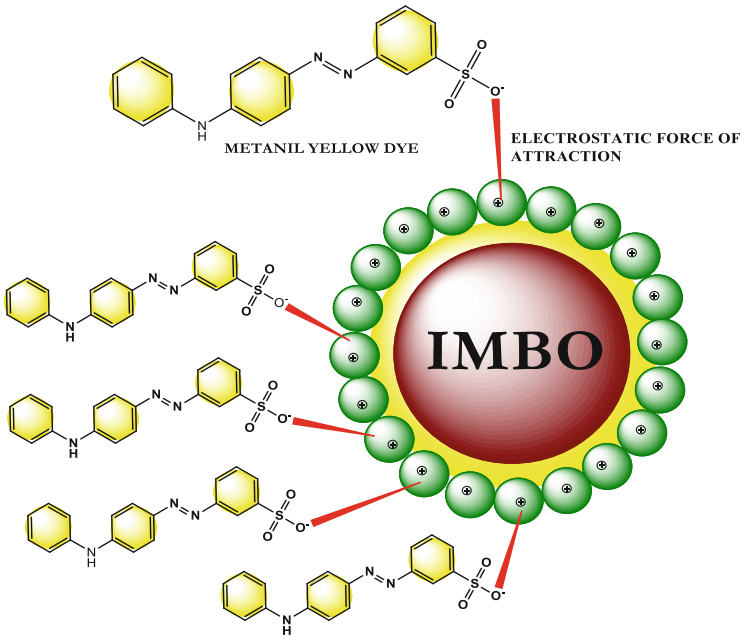

Fig. 3 Adsorption mechanism of MY dye onto IMBO surface

Therefore, the optimized dose of IMBO was considered to be 1.0 g/L for the rest of the study.

3.2.4 Impact of MY Concentration

The influence of MY dye concentration was investigated at a fixed solution pH (3.0), IMBO dose (1.0 g/L), and adsorption time (100 min), and the result is illustrated in Fig. 2d. The extent of MY dye adsorption onto the IMBO surface was found to be declined as the initial concentration of MY dye augmented. The amputation efficacy of MY dye was found to be a maximum of 99.57% at MY concentration of 50 mg/L. Permeation of all active places of IMBO with an upsurge in the concentration of MY dye leads to a decrement in the removal efficacy [2].

3.3 Kinetic Study

In this kinetic investigation, two widely used kinetic models, pseudo-first-order (PFO) and pseudo-second-order (PSO), were used to understand the process in depth. The linear forms of PFO and PSO are exhibited in Eqs. (3) and (4), correspondingly.

Table 1 Kinetic constants of MY dye adsorption onto IMBO (IMBO dose: 1.0 g/L)

Models	Parameters	MY dye concentration (mg/L)			
		50	75	100	120
PFO	Q_e (mg/g)	18.882	31.721	49.789	66.08
	R^2	0.977	0.968	0.967	0.960
PSO	Q_e (mg/g)	50.761	75.187	99.009	116.27
	R^2	0.995	0.999	0.998	0.996

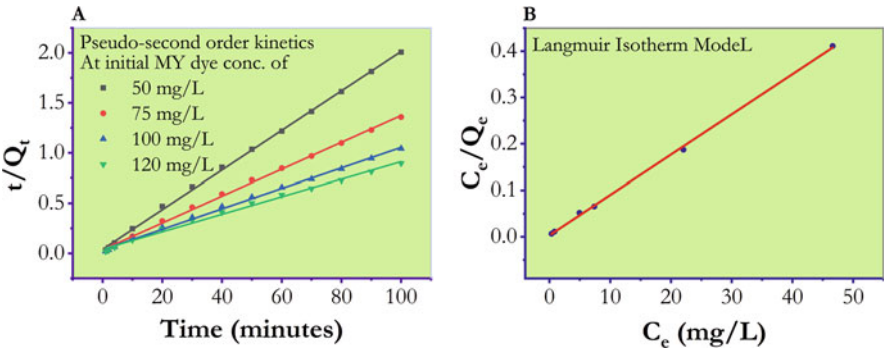

Fig. 4 Plots of (**a**) PSO kinetic model and (**b**) Langmuir isotherm model

$$\ln(Q_e - Q_t) = \ln Q_e - \frac{k_f}{2.303} t \tag{3}$$

$$\frac{t}{Q_t} = \frac{1}{K_s Q_e^2} + \frac{1}{Q_e} t \tag{4}$$

In Eqs. (3) and (4), Q_t, Q_e, k_f, and K_s represent the adsorptive capacity (mg/g) at time t, equilibrium uptake capacity (mg/g), rate constant of PFO (min^{-1}), and rate constant of PSO (mg min^{-1}). The adsorptive capacity at equilibrium Q_e and the regression value R^2 are all listed accordingly in Table 1. It is perceived that the Q_e values obtained from the PFO model immensely deviate from the calculated theoretical values of Q_e for the same reaction. Hence, PFO kinetic modeling cannot be the best model to fit the situation. However, the values of parameter R^2 for the PSO model are ~0.99, and the adsorption capacity of the theoretical values is also very close to the obtained values [18], which can be seen from Fig. 4a also.

3.4 Equilibrium Isotherm Study

The equilibrium isotherm analysis was carved by different isotherm models, i.e., Langmuir, Freundlich, and Temkin, wherein the linear equations and different variables are presented in Table 2. Concerning the correlation coefficient obtained, the experimental results of MY adsorption over IMBO are best suited to the linear

Table 2 Adsorption isotherms in linear form and their parameter values

Isotherms	Equations	Parameters	Values
Langmuir	$\frac{C_e}{Q_e} = \frac{1}{Q_m b} + \frac{C_e}{Q_m}$	Q_m (mg/g)	114.94
		b (L/mg)	0.0087
		R^2	0.999
Freundlich	$\ln Q_e = \ln K_F + \frac{1}{n} \ln C_e$	n	8.620
		K_F (L/mg)	69.540
		R^2	0.857
Temkin	$Q_e = \beta_1 \ln K_T + \beta_1 \ln C_e$	β_1	13.55
		K_T (L/mg)	215.93
		R^2	0.892

Table 3 Evaluation between the uptake capacities of several adsorbents with IMBO for MY dye

Name of adsorbent	Maximum adsorption capacity (mg/g)	References
Amino-functionalized graphenes (NH_2)	71.62	[18]
Rice husk silica with bovine serum albumin	82.35	[2]
The pitaya peel (*Hylocereus undatus*)	144.07	[22]
IMBO	114.94	This paper

version of the Langmuir isotherm model ($R^2 \sim 0.999$) which shows that mainly monolayer adsorption was followed. However, the R^2 values obtained for Freundlich and Temkin models were found to be 0.857 and 0.892, respectively. The parameters Q_m (theoretical maximum adsorption capacity) and b (the Langmuir isotherm constant) were estimated from the plot C_e/Q_e v/s C_e as shown in Fig. 4b, where Q_e and C_e are the quantity of dye loaded at reaction equilibrium (mg/g) and the concentration of MY dye (mg/L) at reaction equilibrium in the solution, respectively. The n (capacity and adsorption intensity) and k_F (which indicates the bonding energy) are the two Freundlich isotherm constants measured from the plot $\ln Q_e$ v/s $\ln C_e$. Likewise, the slope k_T (equilibrium binding constant) and intercept β_1 (heat of adsorption) are measured from the Temkin isotherm plotted as Q_e v/s $\ln C_e$ [18].

A comparison of the maximum adsorption capacity (Q_m) for MY dye adsorption using different reported adsorbents with IMBO is reported in Table 3, which shows that the synthesized IMBO has an adsorption capability that is either superior or equivalent to other reported adsorbents.

3.5 *Regeneration Study*

To assess the reuse and recycling ability of IMBO for MY dye adsorption, the regeneration tests were run up to five times in a row. In regeneration experiment, 50 mg/L of MY dye solution and 1.0 g/L of IMBO were employed, and the mixture was stirred for 100 min at a solution pH 3.0 to complete the adsorption reaction. For

the purpose of desorbing the MY dye from the surface of the IMBO, 100 mL of 1.0 M NaOH solution was added together with the MY dye-loaded IMBO and agitated for 30 min. The separated IMBO was repeatedly cleaned with deionized water after dye desorption and was then dried and put to work once more for MY dye adsorption. The same process was carried out for five cycles. The aforementioned finding demonstrates that, when IMBO was employed after five regeneration cycles, there was less than 10% loss in removal efficiency, making the created composite reusable.

4 Conclusion

In this work, the IMBO adsorbent was fabricated by chemical process, and its potential was investigated for effective elimination of MY dye with 99.5% removal efficiency at solution pH of 3.0. This adsorption reaction was governed by the robust electrostatic interaction amid the anionic MY dye and the positively ionized IMBO surface. The process was found to follow the Langmuir isotherm, which reveals a monolayer adsorption process. The adsorption kinetics was observed to obey a PSO-type reaction, which means the reaction is mainly administered by chemical adsorption. The IMBO nanocomposite was having a high uptake capacity of 114.94 mg/g for MY dye. Therefore, in view of simple fabrication process of IMBO, a high surface area, appreciable adsorption capacity, and a high reusability, the IMBO can be a capable adsorbent for the abatement of MY dye.

References

1. H.S. Rai, M.S. Bhattacharyya, J. Singh, T.K. Bansal, P. Vats, U.C. Banerjee, Removal of dyes from the effluent of textile and dyestuff manufacturing industry: a review of emerging techniques with reference to biological treatment. Crit. Rev. Environ. Sci. Technol. **35**(3), 219–238 (2005)
2. R. Zein, Z.B. Tomi, S. Fauzia, Z. Zilfa, Modification of rice husk silica with bovine serum albumin (BSA) for improvement in adsorption of metanil yellow dye. J. Iran. Chem. Soc. **17**(10), 2599–2612 (2020)
3. D. Garg, C.B. Majumder, S. Kumar, B. Sarkar, Removal of Direct Blue-86 dye from aqueous solution using alginate encapsulated activated carbon (PnsAC-alginate) prepared from waste peanut shell. J. Environ. Chem. Eng. **7**(5), 103365 (2019)
4. S. Gupta, M. Sundarrajan, K.V.K. Rao, Tumor promotion by metanil yellow and malachite green during rat hepatocarcinogenesis is associated with dysregulated expression of cell cycle regulatory proteins. Teratog. Carcinog. Mutagen. **23**(S1), 301–312 (2003)
5. D. Garg et al., Application of waste peanut shells to form activated carbon and its utilization for the removal of Acid Yellow 36 from wastewater. Groundw. Sustain. Dev. **8**, 512–519 (2019)
6. O. Anjaneya et al., Decolorization of sulfonated azo dye Metanil Yellow by newly isolated bacterial strains: Bacillus sp. strain AK1 and Lysinibacillus sp. strain AK2. J. Hazard. Mater. **190**(1–3), 351–358 (2011)

7. H. Guo, F. Lin, J. Chen, F. Li, W. Weng, Metal–organic framework MIL-125 (Ti) for efficient adsorptive removal of Rhodamine B from aqueous solution. Appl. Organomet. Chem. **29**(1), 12–19 (2015)
8. J. Abdi, M. Vossoughi, N.M. Mahmoodi, I. Alemzadeh, Synthesis of metal-organic framework hybrid nanocomposites based on GO and CNT with high adsorption capacity for dye removal. Chem. Eng. J. **326**, 1145–1158 (2017)
9. A. Debnath, M. Majumder, M. Pal, N.S. Das, K.K. Chattopadhyay, B. Saha, Enhanced adsorption of hexavalent chromium onto magnetic calcium ferrite nanoparticles: kinetic, isotherm, and neural network modeling. J. Dispers. Sci. Technol. **37**(12), 1806–1818 (2016)
10. E.N. Hammad, S.S. Salem, A.A. Mohamed, W. El-Dougdoug, Environmental impacts of ecofriendly iron oxide nanoparticles on dyes removal and antibacterial activity. Appl. Biochem. Biotechnol., 1–15 (2022)
11. A. Parashar, S. Sikarwar, R. Jain, Removal of pharmaceuticals from wastewater using magnetic iron oxide nanoparticles (IOPs). Int. J. Environ. Anal. Chem. **102**(1), 117–133 (2022)
12. P.N. Dave, L.V. Chopda, Application of iron oxide nanomaterials for the removal of heavy metals. J. Nanotechnol. **2014**, 1 (2014)
13. T. Van Tran, D.T.C. Nguyen, P.S. Kumar, A.T.M. Din, A.S. Qazaq, D.V.N. Vo, Green synthesis of Mn3O4 nanoparticles using Costus woodsonii flowers extract for effective removal of malachite green dye. Environ. Res. **214**, 113925 (2022)
14. A.K.M. Atique Ullah, A.K.M. Fazle Kibria, M. Akter, M.N.I. Khan, A.R.M. Tareq, S.H. Firoz, Oxidative degradation of methylene blue using Mn3O4 nanoparticles. Water Conserv. Sci. Eng. **1**(4), 249–256 (2017)
15. M. Bhowmik, A. Debnath, B. Saha, Scale-up design and treatment cost analysis for abatement of hexavalent chromium and metanil yellow dye from aqueous solution using mixed phase CaFe2O4 and ZrO2 nanocomposite. Int. J. Environ. Res. **16**(5), 80 (2022)
16. X. Guo et al., Removal of Metanil Yellow from water environment by amino functionalized graphenes (NH2-G)–influence of surface chemistry of NH2-G. Appl. Surf. Sci. **284**, 862–869 (2013)
17. M.A. Ibrahim, M.B. Ibrahim, Adsorption of Alkali Blue, metanil yellow and Neutral Red dyes using copper (II) oxide particles: kinetic and thermodynamic studies. ChemSearch J. **9**(2), 13–23 (2018)
18. X. Guo, Q. Wei, B. Du, Y. Zhang, X. Xin, L. Yan, H. Yu, Removal of Metanil Yellow from water environment by amino functionalized graphenes (NH2-G)–influence of surface chemistry of NH2-G. Appl. Surf. Sci. **284**, 862–869 (2013)
19. M. Bhowmik, K. Deb, A. Debnath, B. Saha, Mixed phase Fe2O3/Mn3O4 magnetic nanocomposite for enhanced adsorption of methyl orange dye: neural network modeling and response surface methodology optimization. Appl. Organomet. Chem. **32**(3), e4186 (2018)
20. K. Ahmadi, M. Ghaedi, A. Ansari, Comparison of nickel doped zinc sulfide and/or palladium nanoparticle loaded on activated carbon as efficient adsorbents for kinetic and equilibrium study of removal of Congo red dye. Spectrochim. Acta A Mol. Biomol. Spectrosc. **136**, 1441–1449 (2015)
21. A. Mittal, V.K. Gupta, A. Malviya, J. Mittal, Process development for the batch and bulk removal and recovery of a hazardous, water-soluble azo dye (Metanil Yellow) by adsorption over waste materials (Bottom Ash and De-Oiled Soya). J. Hazard. Mater. **151**(2–3), 821–832 (2008)
22. J. Georgin, K. da Boit Martinello, D.S. Franco, M.S. Netto, D.G. Piccilli, M. Yilmaz, et al., Residual peel of pitaya fruit (Hylocereus undatus) as a precursor to obtaining an efficient carbon-based adsorbent for the removal of metanil yellow dye from water. J. Environ. Chem. Eng. **10**(1), 107006 (2022)

Optimization of Electrocoagulation Process Parameters Using Magnesium Electrodes for Treating Pharmaceutical Wastewater Containing Salicylic Acid

Azhan Ahmad, Monali Priyadarshini, and Makarand M. Ghangrekar

Abstract The adaptation of unscientific waste management and improper discharge of effluent from pharmaceutical industry has led to the frequent occurrence of emerging contaminants in the environment. One such contaminant is salicylic acid, which is an anti-inflammatory drug and is highly toxic towards the aquatic environment. In order to treat salicylic acid wastewater, batch-scale electrocoagulation (EC) process was performed using magnesium electrodes, and about 87.8 ± 3.4% removal of salicylic acid (50 mg/L) was achieved employing optimum current density (CD) of 4.8 mA/cm^2, 1.5 g/L NaCl, initial pH of 7.0, and electrolysis time of 120 min. About 5.7% more removal of salicylic acid was obtained at an alkaline pH of 9.0 compared to neutral pH. Moreover, an energy consumption of 1.86 kWh/m^3 was also observed during the wastewater treatment. The reduction in salicylic acid concentration followed the first-order kinetics having a rate constant of 0.008 (min^{-1}) and $R^2 = 0.977$. Additionally, magnesium hydroxide flocs were formed during the EC treatment of salicylic acid with magnesium electrodes.

Keywords Electrocoagulation · Electrochemical treatment · Emerging contaminants · Hospital effluent · Magnesium · Personal care products · Pharmaceutical wastewater · Salicylic acid · Wastewater treatment

A. Ahmad
Department of Civil Engineering, Indian Institute of Technology Kharagpur, Kharagpur, India

M. Priyadarshini
School of Environmental Science and Engineering, Indian Institute of Technology Kharagpur, Kharagpur, India

M. M. Ghangrekar (✉)
Department of Civil Engineering, Indian Institute of Technology Kharagpur, Kharagpur, India

School of Environmental Science and Engineering, Indian Institute of Technology Kharagpur, Kharagpur, India
e-mail: ghangrekar@civil.iitkgp.ac.in

D. Mazumder (ed.), *Sustainable Advanced Technologies for Industrial Pollution Control*, Springer Proceedings in Earth and Environmental Sciences,
https://doi.org/10.1007/978-3-031-37596-5_12

Abbreviations

A	Ampere
BES	Bioelectrochemical systems
CD	Current density
EC	Electrocoagulation
EEC	Electrical energy consumption
EPA	Environmental Protection Agency
FTIR	Fourier transform infrared spectroscopy
T_{EC}	Electrolysis time
V	Voltage
v	Volume
XRD	X-ray diffraction

1 Introduction

The pharmaceutical industry is considered one of the major threats to freshwater sources due to the release of effluent-containing pharmaceutical pollutants into the environment. One such pharmaceutical is salicylic acid, which is an anti-inflammatory drug often prescribed for treating skin disorders [1]. A high concentration of salicylic acid can potentially affect aquatic organisms and human health. Moreover, it is challenging to remove salicylic acid through conventional wastewater treatment technologies due to its high toxicity and persistent nature [2]. Generally, pharmaceuticals are not regulated and do not have any discharge limit by the Environmental Protection Agency (EPA), thereby possessing a high risk towards the aquatic environment, and are termed as compounds of emerging concern [3].

Treatment technologies like bioelectrochemical systems (BES), ultrafiltration, electrochemical oxidation, constructed wetlands, adsorption, membrane processes, coagulation, ozonation, and electro-Fenton are comprehensively used in order to eliminate salicylic acid from contaminated water [4–6]. Though these techniques are effective in terms of removal efficiency, there are a few limitations associated with them. For instance, BES required prolonged treatment time for the remediation of pharmaceuticals owing to sluggish start-up time. Similarly, ozonation is highly costly, and toxic intermediates might be formed during this process. Also, the external addition of chemicals and high sludge generation are significant limitations of the coagulation process [7]. In this regard, EC has gained tremendous attention from researchers due to its simple operation, shorter operational time, and lower production of metal sludge than conventional coagulation. For instance, Bajpai and co-authors applied EC with an aluminium anode for the remediation of cefazolin

from pharmaceutical wastewater and obtained nearly 86.7% removal by imposing an optimum CD of 16 mA/cm^2 during 40 min of electrolysis time [8]. Similarly, Yoosefian et al. noticed 87.3% reduction of ciprofloxacin (85 mg/L) by applying EC with iron electrodes at a CD of 15.65 mA/cm^2 during 17.5 min of electrolysis time [9]. In an exploration, Merzouk et al. (2011) revealed 95% removal of disperse red dye from wastewater at an operating cost of 0.34–0.52 USD/kg of dye with aluminium electrodes [10]. However, in the case of chemical coagulation only, 87% removal of dye was obtained [10]. Similarly, more than 99% of heavy metals like lead and zinc was successfully treated with iron-based EC process [11].

Previously aluminium and iron electrodes are generally used in EC to treat pharmaceutical wastewater. However, the application of novel electrode materials like magnesium for the treatment of wastewater is limited [12]. The advantage of magnesium is that apart from emerging contaminant removal, nutrient recovery in the form of struvite can be achieved during real wastewater treatment [13]. Moreover, magnesium (2.15×10^7) has a high electrical conductivity than conventional iron electrodes (1.04×10^7), which is advantageous for electrolysis [14]. Also, for EC with iron electrode the treated effluent might result in yellow colour due to the presence of Fe^{+2} and Fe^{+3} ions, which is aesthetically unpleasant and requires posttreatment [15]. Considering all these gaps, it is essential to explore magnesium as novel electrode material in the EC process to treat pharmaceutical wastewater. To our knowledge, this is the first demonstration with magnesium electrode pair for treating pharmaceutical wastewater containing salicylic acid.

In this regard, current work aims to determine the impact of EC parameters, such as initial pollutant concentration, operating period, electrode distance, applied current, and electrolyte concentration, on the efficiency of EC chamber for treating wastewater containing salicylic acid. Moreover, the kinetics of removal, sludge analysis, and electrical energy consumption with magnesium electrodes have also been elucidated in the present demonstration.

2 Experimentation

2.1 Materials and Analysis

Sodium chloride (58.44 g/mol), salicylic acid (138.121 g/mol), sodium hydroxide (39.99 g/mol), and hydrochloric acid (36.45 g/mol) were purchased from Sigma-Aldrich, India. Salicylic acid was analysed at λ_{max} of 297 nm via a spectrophotometer (T80 PG Instruments Ltd.) [16]. An electronic water quality meter (Thermo Scientific, USA) was utilized to determine the pH of contaminated water.

2.2 Fourier Transform Infrared Spectroscopy (FTIR) and X-Ray Diffraction (XRD) of Sludge

The FTIR and XRD of sludge formed during magnesium EC were explored to investigate the compositional characteristics of the sludge. The FTIR (Thermo Fisher Scientific Instruments, USA) of sludge was assessed between 400 and 4000 cm^{-1} wavenumbers. In contrast, the XRD (Bruker D2 Phaser, USA) was carried out via altering 2θ ($20 > 2\theta < 80°$) at a scan rate of $2°\ min^{-1}$.

2.3 Electrocoagulation Setup

The EC chamber was a 1 L glass beaker filled with synthetic salicylic acid solution, wherein magnesium electrodes with submerged measurements of 10.5 cm × 3.5 cm × 0.1 cm were assembled at an electrode gap of 2 cm (Fig. 1). A regulated direct current (DC) of range between 0.2 and 0.35 A was provided to the electrodes by connecting a DC supply (1502 D-VAR Tech). Moreover, NaCl electrolyte (1.5 g/L) was externally mixed into the wastewater to obtain the required conductivity for EC operation. The samples were collected at fixed operating period during every EC run. Before each experiment, the passive layer was removed from

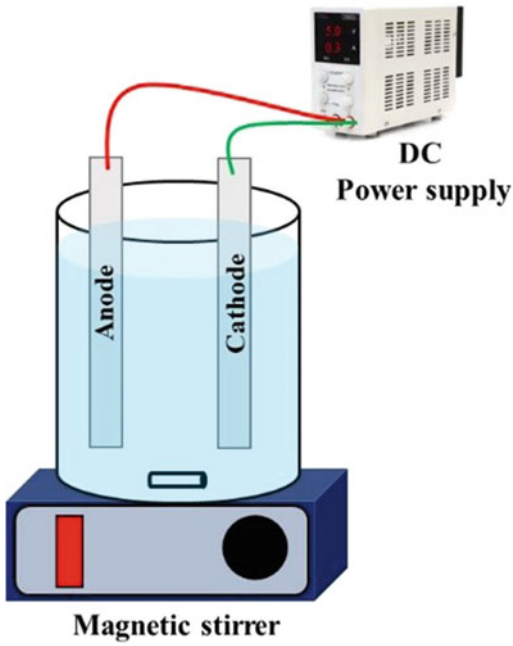

Fig. 1 Basic setup of electrocoagulation process

the electrodes using diluted HCl and water. Every investigation was carried out at room temperature. Before measuring salicylic acid concentration, the samples were passed through a 0.45 μm Whatman filter paper to remove impurity.

3 Results and Discussions

3.1 Impact of Current Density (CD)

In EC technique, CD is one of the vital factors regulating performance efficacy. The CD was varied between 3.2 and 5.6 mA/cm^2 for an electrolysis time of 140 min in the presence of 1.5 g/L of NaCl. The results revealed that at a CD of 3.2 mA/cm^2, 4.0 mA/cm^2, 4.8 mA/cm^2, and 5.6 mA/cm^2, about 48.5 ± 3.2%, 70.3 ± 3.4%, 88.5 ± 3.1%, and 80.8 ± 2.5% reduction of salicylic acid (50 mg/L) were obtained (Fig. 2), thus indicating an increment in abatement efficiency with elevated CD. Besides, when CD was raised from 4.8 to 5.6 mA/cm^2, the performance decreased from 88.5% to 80.8% due to the evolution of side reactions at a higher CD applied [17]. Similarly, up to 120 min of electrolysis time, about 87.8% separation of salicylic acid molecules was attained at CD of 4.8 mA/cm^2, which increases only about 1% as the electrolysis time was further increased to 140 min from 120 min. Hence, 4.8 mA/cm^2 and 120 min were considered as an optimal CD and electrolysis time for salicylic acid removal from wastewater, respectively.

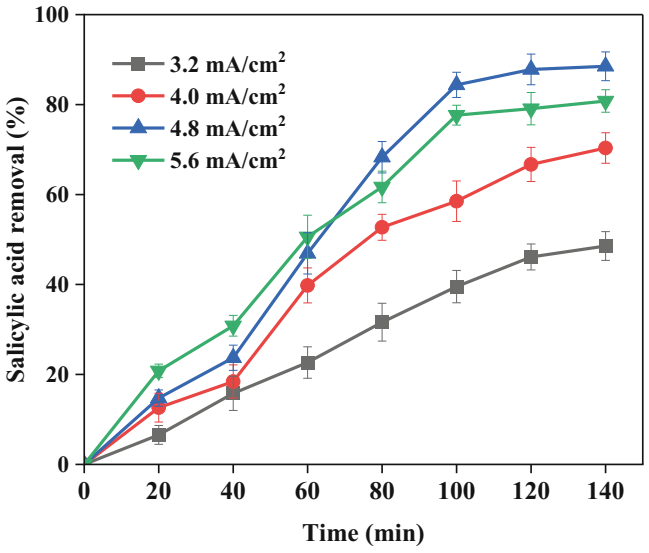

Fig. 2 Impact of CD on the abatement of salicylic acid (pH = 7.0; NaCl = 1.5 g/L; and salicylic acid dose = 50 mg/L)

3.2 *Impact of Initial pH*

The pH is a crucial factor during EC operation that can influence the solubility and precipitation of the metal hydroxide complexes [18], thereby affecting the EC performance. The pH of the wastewater was altered between 4 and 9, with 1.5 g/L of NaCl and applied CD of 4.8 mA/cm^2 during 120 min of electrolysis period. The results revealed that at a pH of 3.0, 7.0, and 9.0, about 52.5 ± 4.3%, 87.8 ± 3.8%, and 93.5 ± 2.5% abatement of salicylic were obtained, respectively (Fig. 3). The enhanced removal at alkaline pH conditions might be due to the lower solubility of Mg^{+2} ions around the pH of 9.0; as a result, most of the Mg^{+2} coagulants might be converted into $Mg(OH)_2$ and precipitates [12], thus improving the removal efficacy of the process. However, the solubility of Mg^{+2} is higher at an acidic pH of 4.0; thus, limited flocs are formed at this pH, resulting in a lower reduction of salicylic acid.

Besides, the final pH values of 6.6 ± 0.1, 8.4 ± 0.1, and 10.7 ± 0.1 were also obtained, corresponding to starting pH of 4.0, 7.0, and 9.0, respectively (Fig. 3). The increment in pH can be attributed to the generation of OH^- ions in the system due to hydrolysis of water [15]. Nonetheless, considering the real wastewater condition and avoiding the utilization of external chemicals, all the investigations were carried out in a neutral wastewater condition.

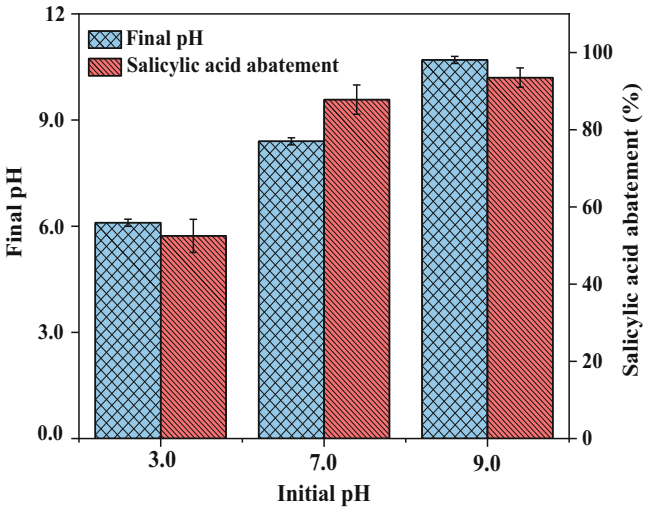

Fig. 3 Impact of solution pH on salicylic acid removal (NaCl = 1.5 g/L; CD = 4.8 mA/cm^2; and initial salicylic acid dose = 50 mg/L)

3.3 Impact of Electrolyte Concentration

The wastewater conductivity is highly affected by the electrolyte dose, which eventually impacts the electric consumption during the EC operation. To investigate the impact of electrolyte concentration, the NaCl dose was varied between 0.5 and 2.0 g/L with 2.0 cm of electrode gap and CD of 4.8 mA/cm^2 during 120 min operating time. The result revealed an improvement in the removal efficacy of salicylic acid with an elevated dose of electrolyte. For example, when the electrolyte dosage was raised from 0.5 to 1.5 g/L, the salicylic reduction efficiency also increased from 69 ± 3.8 to 87.8 ± 3.4% (Fig. 4). However, when NaCl was further elevated to 2 g/L from 1.5 g/L, a decrease in removal was observed (65 ± 3.9%). The decrement in performance with higher electrolyte doses might be due to the formation of species, such as $MgCl_2$, which do not participate in flocs formation [19]. Hence, a decrease in removal was obtained at a higher electrolyte dose than the optimum.

3.4 Impact of Pollutant Dose

To investigate the impact of an initial dose of contaminant on the performance efficacy, the initial concentration of salicylic acid was varied between 50 and 100 mg/L with an electrolyte dose of 1.5 g/L and at imposed CD of 4.8 mA/cm^2

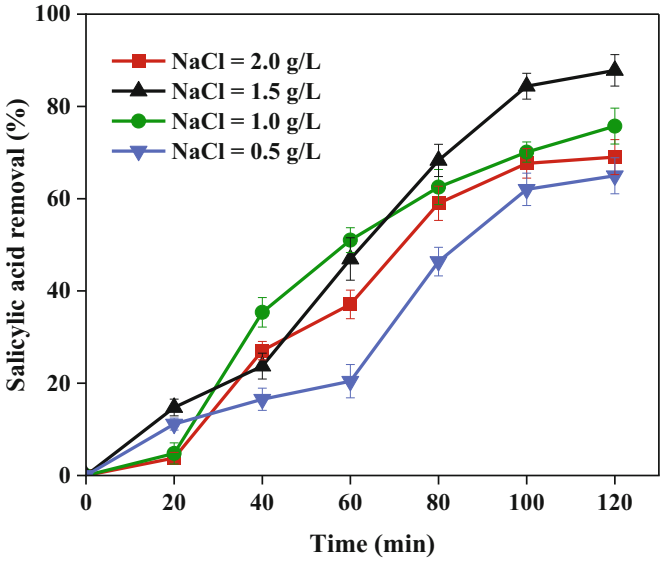

Fig. 4 Impact of electrolyte dose on salicylic acid abatement (pH = 7.0; initial salicylic acid dose = 50 mg/L; and CD = 4.8 mA/cm^2)

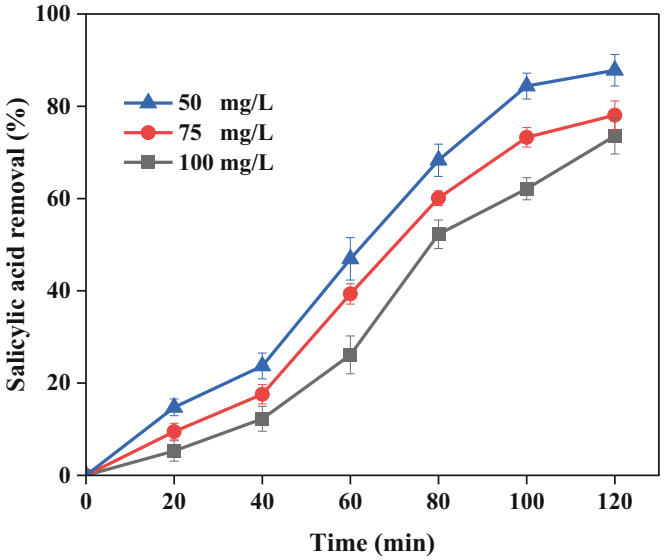

Fig. 5 Impact of pollutant dose on salicylic acid removal (pH = 7.0; CD = 4.8 mA/cm^2; and NaCl = 1.5 g/L)

for an operating period of 120 min. Figure 5 demonstrated that with varying salicylic acid dose from 50 to 100 mg/L, percentage reduction of salicylic acid concentration from wastewater decreases from 87.8 ± 3.4 to 73.6 ± 3.9%. The decrease in abatement of salicylic acid at elevated concentrations can be ascribed to the limited availability of coagulants for the neutralization and flocs formation of a higher number of salicylic acid molecules. Hence, lower contaminants get attached to the surface of flocs and settle down at the base of the reactor, resulting in a lower removal efficiency. Thus, 50 mg/L was considered as an optimum concentration of salicylic acid in the present investigation.

3.5 Removal Kinetics

The kinetics of removal with magnesium EC was explored at the optimum operating conditions for the first- and second-order models (Eqs. 1 and 2) [20].

$$C_t = C_o e^{-k_1 t} \tag{1}$$

$$1/C_t = 1/C_o + k_2 t \tag{2}$$

where k_1 (min^{-1}) and k_2 (mg/L × min^{-1}) are the first- and second-order rate constants, respectively. Also, t, C_t, and C_o are the time of reaction (min), the concentration at a time 't' (mg/L), and initial concentration of the pollutant

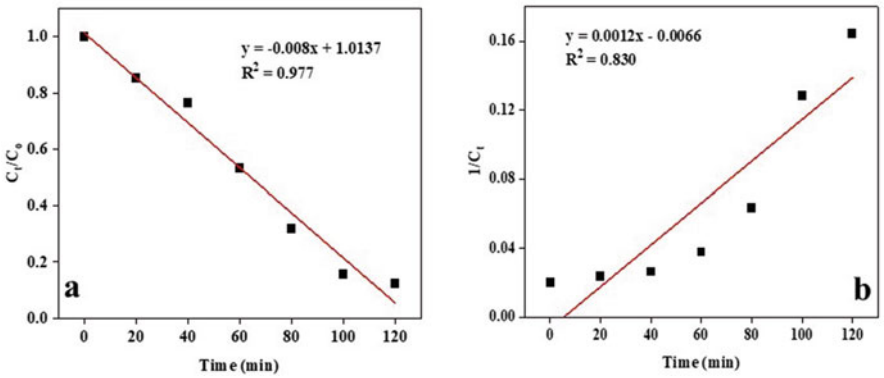

Fig. 6 (**a**) First- and (**b**) second-order kinetic for salicylic acid abatement with magnesium electrodes (salicylic acid = 50 mg/L; pH = 7.0; and CD = 4.8 mA/cm^2)

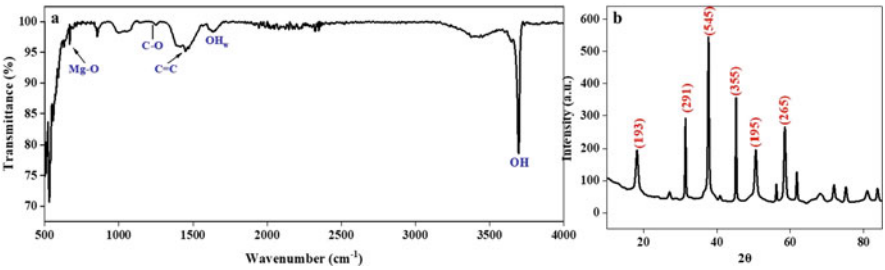

Fig. 7 (**a**) FTIR and (**b**) XRD of the magnesium sludge produced in the EC through magnesium electrodes

(mg/L), respectively. After operating the EC at an ideal CD of 4.8 mA/cm^2 and initial salicylic acid concentration of 50 mg/L for 120 min of operating time, the result revealed that the abatement of salicylic acid follows the first-order kinetic having a rate constant (k_1) = 0.008 (min^{-1}) and R^2 = 0.977 (Fig. 6a). However, in the second-order model, the rate constant (k_2) and R^2 were 0.0012 (mg/L × min^{-1}) and 0.830, respectively (Fig. 6b).

3.6 FTIR and XRD Analysis of Sludge

To assess the formation of magnesium flocs in the sludge, FTIR and XRD of the dried sludge were executed. The FTIR (Fig. 7a) peak around 3700 cm^{-1} revealed the vibration of OH stretching in $Mg(OH)_2$ structures [21]. Besides, the vibrations at 1632 cm^{-1} indicated the deformation (OH_w) vibrations of adsorbing OH molecules in the sludge. Further, IR of around 1450 cm^{-1} signified the existence of C=C in the sludge, and the IR at 1233 cm^{-1} revealed the occurrence of C−O in sludge. Lastly,

the peaks at 670 cm^{-1} might be due to the presence of Mg−O species in the sludge [22].

In addition, XRD was also carried out to further assess the sludge characteristics. The XRD spectra (Fig. 7b) revealed the sharp crystalline peak at 2θ around 18° that might be ascribed to the generation of $Mg(OH)_2$, also known as brucite. Similar observations were also noticed during the remediation of pollutants from the cooling tower blowdown industrial water with magnesium electrodes [23]. Hence, the FTIR and XRD exhibited the production of $Mg(OH)_2$ species during the EC process, thereby indicating the attachment of salicylic acid on the surface of magnesium flocs as the dominant removal mechanism.

3.7 Energy Consumption

The electrical energy required for the reduction of salicylic acid using magnesium electrodes was evaluated at the optimum operating condition (Eq. 3) [7].

$$\mathrm{EEC}\left(\frac{\mathrm{kWh}}{\mathrm{m}^3}\right) = \frac{UIt}{v} \tag{3}$$

where I, v, U, and t represent the applied current (A), average voltage (U), volume (v) of wastewater (m^3), and electrolysis time (h). Hence, at the optimal treatment conditions of NaCl dose of 1.5 g/L, a CD of 4.8 mA/cm^2, distance between the electrodes of 2.0 cm, the initial salicylic dose of 50 mg/L, and operating time of 120 min, about 1.86 kWh/m^3 of EEC was obtained during the EC treatment of pharmaceutical wastewater containing salicylic acid. Similarly, the economic evaluation of other electrodes used in EC for the remediation of pharmaceuticals is provided in Table 1.

4 Conclusion

The recent work elucidated the use of magnesium electrodes in the EC procedure to treat wastewater containing salicylic acid. About 87.8 ± 3.4% reduction of 50 mg/L of salicylic acid was achieved at an ideal pH of 7.0 and CD of 4.8 mA/cm^2 for an operating time of 120 min. Performance efficiency of EC process was significantly affected by the kind of electrolyte used, CD, pH of the wastewater, and initial pollutant concentration. The kinetics of removal followed the first-order kinetic model. Moreover, about 1.86 kWh/m^3 of electrical energy consumption was also obtained during the EC of salicylic acid wastewater. Nonetheless, considering the capability of magnesium to produce struvite, future explorations can be studied for treating real wastewater containing salicylic acid along with the recovery of nitrogen

Table 1 Comparison of cost of operation of EC to remove pharmaceutical from wastewater

Pharmaceutical	Wastewater type	Operating conditions	Observations	References
Ciprofloxacin	Hospital	Aluminium electrodes, CD: 12.5 mA/cm^2; T_{EC}: 20 min; C_o: 32.5 mg/L	88.57% removal; $C_{electrode}$: 0.067 kg/m^3; C_{energy}: 0.613 kWh/m^3	[24]
Amoxicillin	Synthetic	Aluminium electrodes; voltage: 60 V; pH 7; KCl: 3 g/L; T_{EC}:75 min	98.80% removal; C_{Energy}: 30–180 kWh/m^3	[25]
Cefazolin	Pharmaceutical	Iron-aluminium electrodes; T_{EC}: 33 min; CD: 16 mA/cm^2; C_o: 25.7 mg/L	86.74% removal; C_{Energy}: 0.739 kW h/kg COD; $C_{Electrode}$: 1.51 kg/kg COD; Operating cost: 0.89 US$/kg COD or 64.8 INR/kg COD	[8]
Acetaminophen	River	Aluminium electrodes; Voltage: 9 V; T_{EC}: 60 min; Electrode gap: 2 cm	95% removal; Operating cost: US$ 0.22/m^3 or INR 17.39/m^3	[26]
Salicylic acid	Synthetic and municipal	Punched aluminium electrodes; T_{EC}: 50 min; CD: 2.5 mA/cm^2; C_o: 50 mg/L; cationic surfactant: 20 mg/L	92.1% removal; C_{energy}: 0.328 kWh/m^3 Operating cost: US$ 0.19/m^3	[19]
Salicylic acid	Synthetic	Magnesium electrodes; electrode gap: 2 cm; T_{EC}: 120 min; CD: 4.8 mA/cm^2; C_o: 50 mg/L	87.8 ± 3.4% removal; C_{energy}: 1.86 kWh/m^3 was obtained	Present investigation

Note: *CD* Current density, T_{EC} Electrolysis time

and phosphorus. This might help in the handling of sludge produced in the EC procedure, as the recovered products can be used as nutrients to replace commercial fertilizers.

Acknowledgement The current investigation is supported by a research grant from the Department of Science and Technology, Government of India (File No.: DST/TMD (EWO)/OWUIS-2018/RS-10).

References

1. A. Szabelak, A. Bownik, Behavioral and physiological responses of Daphnia magna to salicylic acid. Chemosphere **270**, 128660 (2021). https://doi.org/10.1016/j.chemosphere.2020.128660
2. M. Silva, J. Baltrus, C. Williams, A. Knopf, L. Zhang, J. Baltrusaitis, Mesoporous Fe-doped MgO nanoparticles as a heterogeneous photo-Fenton-like catalyst for degradation of salicylic acid in wastewater. J. Environ. Chem. Eng. **9**(4), 105589 (2021). https://doi.org/10.1016/j.jece.2021.105589
3. I. Chakraborty, S.M. Sathe, C.N. Khuman, M.M. Ghangrekar, Bioelectrochemically powered remediation of xenobiotic compounds and heavy metal toxicity using microbial fuel cell and microbial electrolysis cell. Mater. Sci. Energy Technol. **3**, 104–115 (2020). https://doi.org/10.1016/j.mset.2019.09.011
4. N. Rajic, A. Dakovic, Microporous and mesoporous materials the adsorption of salicylic acid, acetylsalicylic acid and atenolol from aqueous solutions onto natural zeolites and clays: clinoptilolite, bentonite and kaolin. Microporous Mesoporous Mater. **166**, 185–194 (2013). https://doi.org/10.1016/j.micromeso.2012.04.049
5. E. Brillas, A review on the photoelectro-Fenton process as efficient electrochemical advanced oxidation for wastewater remediation. Treatment with UV light, sunlight, and coupling with conventional and other photo-assisted advanced technologies. Chemosphere **250**, 126198 (2020). https://doi.org/10.1016/j.chemosphere.2020.126198
6. M. Taheran, S.K. Brar, M. Verma, R.Y. Surampalli, T.C. Zhang, J.R. Valero, Membrane processes for removal of pharmaceutically active compounds (PhACs) from water and wastewaters. Sci. Total Environ. **547**, 60–77 (2016). https://doi.org/10.1016/j.scitotenv.2015.12.139
7. A. Ahmad, M. Priyadarshini, S. Das, M.M. Ghangrekar, Electrocoagulation as an efficacious technology for the treatment of wastewater containing active pharmaceutical compounds: a review. Sep. Sci. Technol. **57**, 1234–1256 (2021). https://doi.org/10.1080/01496395.2021.1972011
8. M. Bajpai, S.S. Katoch, A. Kadier, P.C. Ma, Treatment of pharmaceutical wastewater containing cefazolin by electrocoagulation (EC): optimization of various parameters using response surface methodology (RSM), kinetics and isotherms study. Chem. Eng. Res. Des. **176**, 254–266 (2021). https://doi.org/10.1016/j.cherd.2021.10.012
9. M. Yoosefian, S. Ahmadzadeh, M. Aghasi, M. Dolatabadi, Optimization of electrocoagulation process for efficient removal of ciprofloxacin antibiotic using iron electrode; kinetic and isotherm studies of adsorption. J. Mol. Liq. **225**, 544–553 (2017). https://doi.org/10.1016/j.molliq.2016.11.093
10. B. Merzouk, B. Gourich, K. Madani, C. Vial, A. Sekki, Removal of a disperse red dye from synthetic wastewater by chemical coagulation and continuous electrocoagulation. A comparative study. Desalination **272**(1–3), 246–253 (2011). https://doi.org/10.1016/j.desal.2011.01.029
11. J. Nepo et al., Electrocoagulation process in water treatment: a review of electrocoagulation modeling approaches. Desalination **404**, 1–21 (2017). https://doi.org/10.1016/j.desal.2016.10.011
12. T.R. Devlin, M.S. Kowalski, E. Pagaduan, X. Zhang, V. Wei, J.A. Oleszkiewicz, Electrocoagulation of wastewater using aluminum, iron, and magnesium electrodes. J. Hazard. Mater. **368**(September 2017), 862–868 (2019). https://doi.org/10.1016/j.jhazmat.2018.10.017
13. D.J. Kruk, M. Elektorowicz, J.A. Oleszkiewicz, Struvite precipitation and phosphorus removal using magnesium sacrificial anode. Chemosphere **101**, 28–33 (2014). https://doi.org/10.1016/j.chemosphere.2013.12.036
14. T. Bell, Electrical conductivity of metals, p. 2340117 (2021)
15. S.Y. Lee, G.A. Gagnon, Review of the factors relevant to the design and operation of an electrocoagulation system for wastewater treatment. Environ. Rev. **22**(4), 421–429 (2014). https://doi.org/10.1139/er-2014-0009

16. İ.Y. Köktaş, Ö. Gökkuş, Removal of salicylic acid by electrochemical processes using stainless steel and platinum anodes. Chemosphere **293**(December 2021), 133566 (2022). https://doi.org/10.1016/j.chemosphere.2022.133566
17. P.V. Nidheesh, A. Kumar, D. Syam Babu, J. Scaria, M. Suresh Kumar, Treatment of mixed industrial wastewater by electrocoagulation and indirect electrochemical oxidation. Chemosphere **251**, 126437 (2020). https://doi.org/10.1016/j.chemosphere.2020.126437
18. A. Ahmad, S. Das, M.M. Ghangrekar, Removal of xenobiotics from wastewater by electrocoagulation: a mini-review. J. Indian Chem. Soc. **97**(4), 493–500 (2020)
19. A. Ahmad, M. Priyadarshini, I. Das, M.M. Ghangrekar, R.Y. Surampalli, Surfactant aided electrocoagulation/flotation using punched electrodes for the remediation of salicylic acid from wastewater. J. Environ. Chem. Eng. **11**(1), 109049 (2023). https://doi.org/10.1016/j.jece.2022.109049
20. E. Nariyan, A. Aghababaei, M. Sillanpää, Removal of pharmaceutical from water with an electrocoagulation process; effect of various parameters and studies of isotherm and kinetic. Sep. Purif. Technol. **188**, 266–281 (2017). https://doi.org/10.1016/j.seppur.2017.07.031
21. S. Vasudevan, J. Lakshmi, M. Packiyam, Electrocoagulation studies on removal of cadmium using magnesium electrode. J. Appl. Electrochem. **40**(11), 2023–2032 (2010). https://doi.org/10.1007/s10800-010-0182-y
22. A. Zaffar, N. Krishnamoorthy, N. Nagaraj, S. Jayaraman, B. Paramasivan, Optimization and kinetic modeling of phosphate recovery as struvite by electrocoagulation from source-separated urine. Environ. Sci. Pollut. Res. **29**(45) (2022). https://doi.org/10.1007/s11356-022-23446-2
23. H.I. Abdel-Shafy, M.A. Shoeib, M.A. El-Khateeb, A.O. Youssef, O.M. Hafez, Electrochemical treatment of industrial cooling tower blowdown water using magnesium-rod electrode. Water Resour. Ind. **23**, 100121 (2020). https://doi.org/10.1016/j.wri.2019.100121
24. S. Ahmadzadeh, A. Asadipour, M. Pournamdari, B. Behnam, H.R. Rahimi, M. Dolatabadi, Removal of ciprofloxacin from hospital wastewater using electrocoagulation technique by aluminum electrode: optimization and modelling through response surface methodology. Process Saf. Environ. Prot. **109**, 538–547 (2017). https://doi.org/10.1016/j.psep.2017.04.026
25. D. Balarak, K. Chandrika, M. Attaolahi, Assessment of effective operational parameters on removal of amoxicillin from synthetic wastewater using electrocoagulation process. J. Pharm. Res. Int. **29**(1), 1–8 (2019). https://doi.org/10.9734/jpri/2019/v29i130227
26. S. Kumari, R.N. Kumar, River water treatment using electrocoagulation for removal of acetaminophen and natural organic matter. Chemosphere **273**, 128571 (2021). https://doi.org/10.1016/j.chemosphere.2020.128571

Optimization of Process Parameters for Biodegradation of Cresol by Mixed Bacterial Culture Using Response Surface Methodology

Sonali Hazra Das, Srabanti Basu, Bhaswati Chakraborty, Sudipta Dey Bandyopadhyay, Aritra Paul, Ananya Bhattacharjee, Srijit Seth, Subhranil Hazra, Promit Banerjee, and Megha Pal

Abstract Bioremediation is important in reducing the load of toxic by-products in industrial effluents which has dramatically got increased due to industrialization and urbanization. In this study, we have used mixed bacterial culture (MBC) to convert the model pollutant cresol into a less toxic form. A kinetic study for bacterial growth and substrate removal showed that maximum MBC growth rate and cresol degradation rate took place in 800 ppm of initial cresol concentration at pH 7 and in an aerated condition. The maximum specific growth rate (μ_{max}) and maximum specific degradation rate (q_{max}) in the above condition were found as 0.119 h^{-1} and 0.011 h^{-1}, respectively. The optimized condition of process parameters for maximum percentage removal efficiency (%RE) of 83% in 24 h as obtained by response surface methodology was under 1095 mg/L of initial cresol concentration at pH 7 and in the presence of both shaking and aeration. The quadratic model was found to be the best-fit model. The R^2 value of 0.9272 showed that the model is well fit. The C.V.% of 14.78 showed the precision of the data. The model is significant with a *p*-value of less than 0.0001 and an *F* value of 41.41. Two bacterial strains showing maximum cresol degradation have been identified as *Stenotrophomonas* sp. (Gram-negative) and *Bacillus cereus* (Gram-positive). Both of them showed positive responses in catalase, citrate, and triple sugar iron test.

Keywords Bioremediation · Cresol biodegradation · Maximum specific degradation rate · Kinetic study · Maximum specific growth rate · MBC · Optimization · Percentage removal efficiency (%RE) · Response surface methodology · East Calcutta Wetlands

S. H. Das (✉) · S. Basu · B. Chakraborty · S. D. Bandyopadhyay · A. Paul · A. Bhattacharjee
S. Seth · S. Hazra · P. Banerjee · M. Pal
Department of Biotechnology, Heritage Institute of Technology, Kolkata, India
e-mail: sonalihazra.das@heritageit.edu; srabanti.basu@heritageit.edu; bhaswati.chakraborty@heritageit.edu; sudipta.dey@heritageit.edu

D. Mazumder (ed.), *Sustainable Advanced Technologies for Industrial Pollution Control*, Springer Proceedings in Earth and Environmental Sciences,
https://doi.org/10.1007/978-3-031-37596-5_13

Abbreviations

%RE	Percentage removal efficiency
C.V.	Coefficient of variance
CCD	Central composite design
ECW	East Calcutta Wetlands
MBC	Mixed bacterial culture
O.D.	Optical density
Ppm	Parts per million
q_{max}	Maximum specific degradation rate
rRNA	Ribosomal ribonucleic acid
RSM	Response surface methodology
μ_{max}	Maximum specific growth rate

1 Introduction

The surge of industries and rapid urbanization has resulted in accumulation of toxic pollutants in industrial effluents [1]. Several of those compounds are recalcitrant and persistent pollutant causing serious health effects. The most common strategies employed for the removal of phenolics from industrial discharge include ozonation, adsorption, photolytic degradation, ion exchange, and membrane-based separation. But these processes are not only expensive employing hazardous reagents but also cause generation of secondary byproducts. On the other hand, bioremediation of wastewater, i.e., the use of microbes to degrade the pollutants, is gaining popularity over chemical treatment methods due to a lot of factors. It is a simpler, cost-effective process leading to complete mineralization of the pollutants to carbon dioxide and water [2, 3].

In our study, we have isolated the mixed bacterial cultures (MBC) from the soil of East Calcutta Wetlands (ECW), which is a natural sewage treatment plant for the city. Its microbial richness attracted us to explore the various bacterial consortium needed to remediate the pollutants from the industrial effluent. Individual microorganisms can degrade only a limited number of organic pollutants, whereas a consortium of mixed bacterial populations with overall broad enzymatic spectrum can enhance the rate and range of biodegradation of the pollutants. In a mixed culture, mutualism and symbiotic association among different species ensure better degradation ability of the consortium as a whole. It is easy to maintain and subculture mixed microbial culture indefinitely by maintaining the environmental conditions such as temperature, pH, and nature of substrate [4, 5]. We have chosen cresol as the model pollutant. Cresols are organic methyl phenols and are widely occurring natural and anthropogenic products [6]. The industries such as petrochemical, textile, dye, pharmaceutical, pulp and paper industries, and petroleum refineries

release cresol in the effluent. Chronic exposure to even low concentrations of cresol results in vomiting, diarrhea, loss of appetite, headache, fainting, dizziness, and skin rashes [7–9].

This study aims in optimizing the process parameters for cresol removal from the wastewater by MBC using response surface methodology (RSM). The usual methods of kinetic studies consist of varying only one parameter at a time while maintaining others constant. It becomes a prolonged process since it requires many experimental runs. RSM is a structured method where the output can be affected by changing various experimental domains concurrently. It can spot the components that can bring the change in the response. It is also used to examine a considerable number of variables in a limited number of experimental runs, reducing the time and cost. RSM helps in determining the interactive effect of the process parameters. It is also one of those mechanisms that can figure out the optimal operating conditions of a system [10, 11].

2 Materials and Methods

2.1 Kinetic Study of Bacterial Growth and Cresol Removal by the Mixed Bacterial Culture in Various Substrate Concentration and in Different Modes of Agitation: Agitation with External Aeration, Agitation Without External Aeration, and No Agitation

The soil of East Calcutta Wetlands (ECW) was chosen to isolate the mixed bacteria which were acclimatized to 1500 ppm of cresol as their sole carbon source. The MBC attuned to cresol were then used for batch kinetic study for bacterial growth and cresol removal in the presence of various substrate concentrations (100, 300, 500, 800, and 1000 ppm) and in different modes of agitation: agitation with external aeration, agitation without external aeration, and no agitation.

- *Agitation with external aeration*: The bacterial cultures were made to grow in external aerated condition at room temperature till the cells reached their stationary phase or concentration of residual cresol dropped below the detection level.
- *Agitation without external aeration*: The cultures were let to grow in the absence of external aeration and with an agitation speed of 60 rpm at room temperature.
- *No agitation*: In this case, the MBC flasks were allowed to stand undisturbed without any agitation or aeration.

At regular interval, samples were collected, and bacterial concentration and residual cresol concentration was checked. The cell growth was measured by spectrophotometer (Labman visible spectrophotometer LMSP V320) by checking the optical density (OD) at 600 nm. The cell concentration was calculated with the help of a standard curve (absorbance at 600 nm vs. cell concentration (mg/L)). The

cresol in the supernatant was checked by antipyrine assay, whose (OD) was checked at 490 nm. The cresol concentration was calculated from the absorbance at 490 nm with the help of a standard graph (absorbance at 490 nm vs. cresol concentration). The bacterial growth curve and cresol degradation curve in various substrate concentrations were plotted. The kinetic parameters such as maximum specific growth rate (μ_{max}), maximum specific degradation rate (q_{max}), and percentage removal efficiency (RE%) were calculated for each concentration and compared in the presence of different modes of agitation.

The maximum specific growth rate (μ_{max}) was calculated from the slope of another graph ($\ln(X/X_0)$ vs. t) (Fig. 2) using Eq. (1).

$$\ln(X/X_0) = \mu_{max} t \tag{1}$$

where X is the bacterial cell concentration at time t in the log phase of bacterial growth and X_0 is the bacterial cell concentration at time t_0.

- Cresol removal efficiency by mixed bacterial culture was calculated using Eq. (2).

$$\%\text{RE} = [(C_i - C_f)/C_i] \times 100 \tag{2}$$

  where %RE is the percentage removal efficiency; C_i is the initial concentration of cresol at time $t = 0$; and C_f is the final concentration at time $t = t$.
- The maximum specific degradation rate (q_{max}) of Cresol by MBC was calculated using Eq. (3).

$$1/q = 1/q_{max} + \text{Ks}/(q_{max}.S) \tag{3}$$

2.2 *Optimization of Operating Conditions by Response Surface Methodology (RSM)*

Response surface methodology was analyzed by Design Expert software (Version 13.0.5). Central composite design (CCD) was used to analyze the interaction between the operating conditions and output responses [11, 12]. Different process parameters such as concentration of cresol (100–800 mg/L), pH (3–11), aeration, and agitations together with their ranges in the system were fed into the software. The concentration of cresol and pH was considered to be the numeric factors as they can be varied within a defined range. Agitations and aerations were categorical factors as they were either present or absent in the runs. The tool then designed a set of 52 experimental runs with various combinations of the parameters. These tests were then performed in the laboratory followed by calculating the percentage

removal efficiency (%RE). The results obtained were fed into the software which provided us with the optimum response. It also provided us with 3D graphs that showed the interactions of the different process parameters [13–15].

2.3 Isolation of Pure Bacterial Colonies

The cultures grown in optimized condition were chosen for the isolation of pure bacterial strains because the MBC in this condition showed maximum removal efficiency (%).

2.4 Characterization of Pure Strains

- *Gram Staining and Biochemical Characterization*
  Gram staining and biochemical profile such as catalase, citrate, and triple sugar iron test of these two isolates were performed.
- *Identification by 16s rRNA*
  The isolated bacterial strains showing maximum removal efficiency were outsourced for identification by the 16s rRNA method.

3 Results and Discussion

3.1 Kinetic Study of Growth of Mixed Bacterial Culture (MBC) in Presence of Different Concentrations of Cresol and Under Various Modes of Agitations

The bacterial cell concentration with time has been plotted as shown in Fig. 1a–c, in the presence of different cresol concentrations (100, 300, 500, 800, and 1000 ppm) and under three different modes of agitations (agitation with external aeration, agitation without external aeration, no agitated condition).

By plotting the graph, it has been observed that the growth rate was enhanced with the increase of the initial substrate concentration from 100 to 500 ppm. In spite of having a slight lag phase, the growth of bacteria was found to be maximum in the presence of 500 ppm of cresol in agitation without external aeration and no agitation condition. The growth of bacteria was observed to be maximum at 800 ppm of cresol in agitation with external aerated condition. This may be due to the induction of degrading enzymes which have resulted in more efficient utilization of cresol as the sole carbon source leading to increased bacterial growth [16]. Moreover, aeration may have some positive role in metabolism which has led to an increase in bacterial

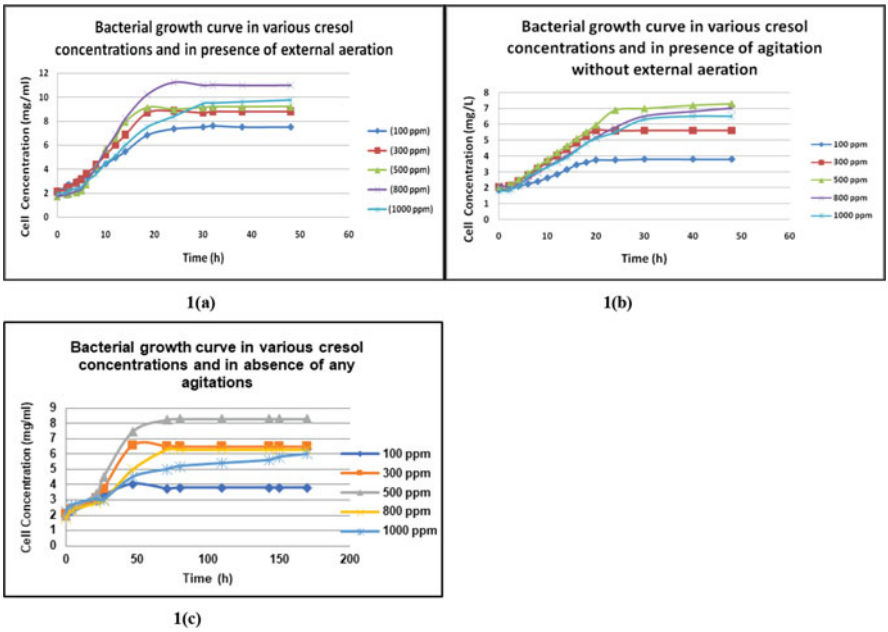

Fig. 1 Bacterial growth curve in different concentrations of cresol and in the presence of (**a**) agitations with external aeration, (**b**) agitations without external aeration and shaking only, and (**c**) no agitations

growth. In the presence of higher initial concentrations of cresol, after a prolonged lag phase, the growth rate was decreased markedly. This was probably due to the substrate inhibition caused by the toxic nature of high cresol concentrations which was intolerable by most of the bacterial strains in the consortium.

3.2 Comparative Study of Maximum Specific Growth Rate (μ_{max}) of MBC in Different Concentrations of Cresol

The maximum specific growth rate (μ_{max}) of mixed bacterial culture is obtained from the graph ($\ln(X/X_0)$ vs. t) (Fig. 2a–c) using Eq. (1).

$$\ln(X/X_0) = \mu_{max} t \tag{1}$$

where X is the bacterial cell concentration at time t in the log phase of bacterial growth and X_0 is the bacterial cell concentration at time t_0.

The μ_{max} of MBC in the presence of different concentrations of cresol was compared in Fig. 2a–c. The culture having 500 ppm of Cresol showed the highest maximum specific growth rate (μ_{max}) of 0.0491 h^{-1} and 0.0296 h^{-1} in the presence

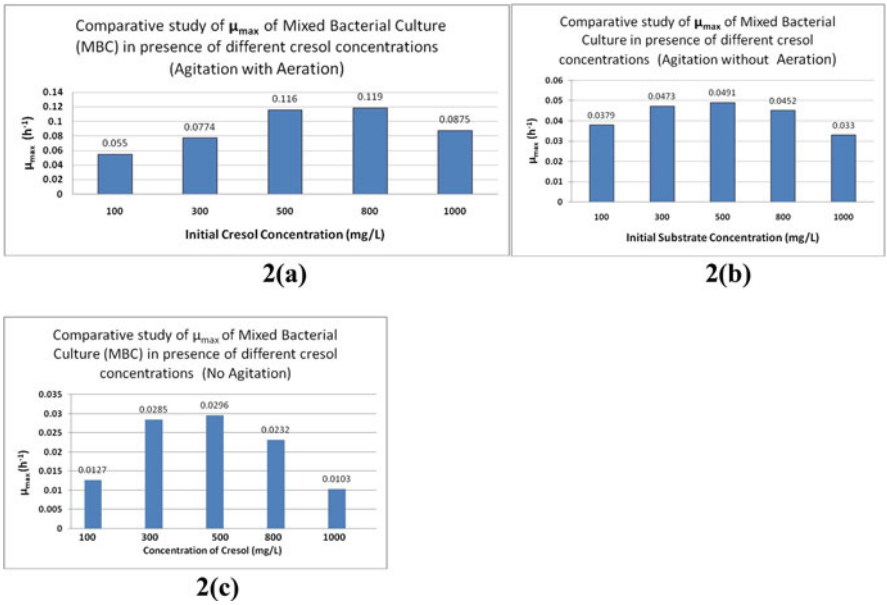

Fig. 2 Comparative study of μ_{max} of mixed bacterial culture in different cresol concentrations and (**a**) in the presence of external aeration (no shaking), (**b**) agitations (shaking) without any external aeration, and (**c**) no agitations

of agitations with no aeration and no agitation condition, respectively. It was also noted that the (μ_{max}) increased gradually from 100 to 500 ppm of cresol and then showed a decreasing trend till the concentration of cresol reached 1000 ppm in the culture media, thus indicating substrate inhibition beyond 500 ppm of initial cresol concentration in the growth media. On the other hand, (μ_{max}) of 0.12 h^{-1} was found to be maximum at 800 ppm of cresol concentrations in agitations with external aerated condition.

3.3 Degradation Kinetics of Cresol by MBC in Different Cresol Concentrations and in Presence of Varying Modes of Agitations

The mixed bacterial culture (MBC) metabolized cresol completely from the growth media which was using it as the sole carbon source. A graph (residual cresol concentration vs. time) has been plotted as depicted in Fig. 3a–c, showing cresol degradation in the presence of different substrate concentrations and various modes of agitations.

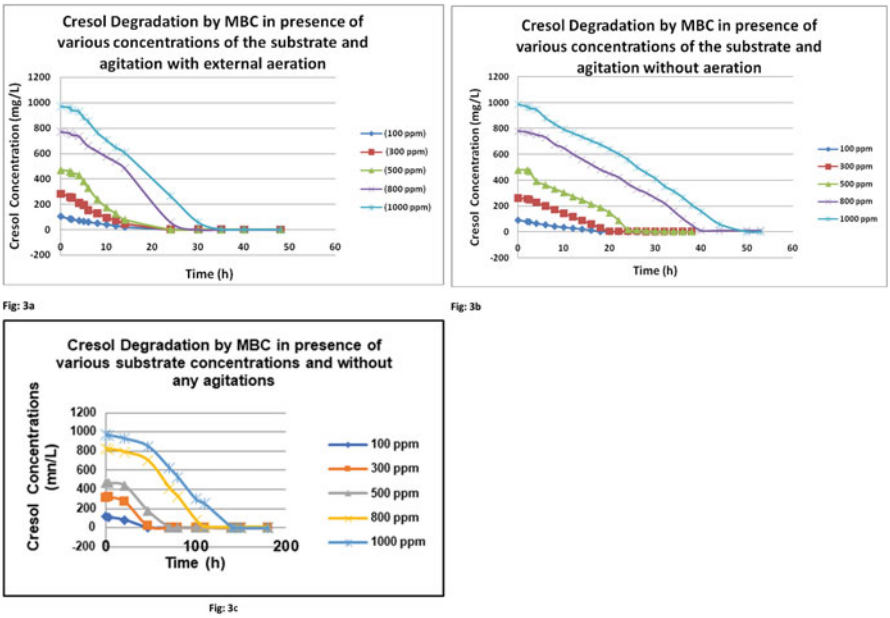

Fig. 3 Cresol degradation by mixed bacterial culture (MBC) in the presence of different substrate concentrations and (**a**) in the presence of external aeration (no shaking), (**b**) agitations (shaking) without any external aeration, and (**c**) no agitations

From the comparative study of cresol degradation by the MBC shown in Fig. 3a–c, it was obtained that the time required for completely degrading cresol got enhanced with the increase of substrate concentration. The maximum specific degradation rate (q_{max}) in the presence of external aeration got increased with the increase of the initial substrate concentration to 800 ppm, after which it got decreased with the increase in cresol concentration in the growth medium (Figure). This was probably due to the expression of Cresol degrading enzymes induced by stress in response to the substrate concentration.

3.4 Comparative Study of Maximum Specific Degradation Rate (q_{max}) of MBC in Different Concentrations of Cresol

The maximum specific degradation rate (q_{max}) of the mixed bacterial culture in the presence of different concentrations of cresol and in various modes of agitations was calculated from Eq. (3) as stated above. The q_{max} as obtained in different conditions was compared in Fig. 4a–c.

The reduction of q_{max} in the presence of high substrate concentration (1000 ppm) was most likely due to the inhibitory effect of cresol on the metabolic enzymes. The

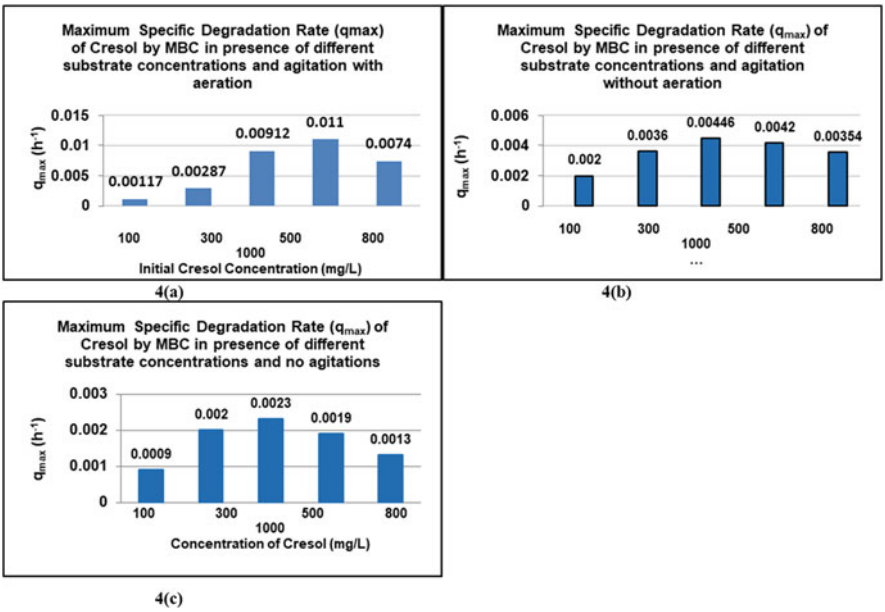

Fig. 4 Comparative study of q_{max} of cresol by mixed bacterial culture in different substrate concentrations and (**a**) in the presence of external aeration (no shaking), (**b**) agitations (shaking) without any external aeration, and (**c**) no agitations

maximum specific degradation rate (q_{max}) was found to be maximum at 500 ppm of initial cresol concentration in both agitations without external aerated and no aerated condition. The q_{max} at 800 ppm of cresol concentration was calculated to be 0.011 h^{-1}, 0.0042 h^{-1}, and 0.0019 h^{-1} in agitation with external aeration, agitation without external aeration, and no agitated condition, respectively. This also supports the theory that aeration not only accelerates degradation but also aids in mineralizing higher concentrations of cresol.

3.5 Study of Optimization of Operating Conditions by Response Surface Methodology (RSM)

The response surface methodology suggested 52 experimental runs with various combinations of process parameters as depicted in Fig. 5. These tests were performed in the laboratory followed by calculating the removal efficiency (%RE) in 24 h. The calculated (%RE) was fed into the software which then designed 3D graphs showing a change in response with a simultaneous change in cresol concentration and pH in different modes of agitations (Fig. 6a–c). In all the modes of agitations, the (%RE) was found to be maximum at pH 7 and decreases gradually with the increase of cresol concentration. Acidity and alkalinity of the medium

11	1100	4	0	1	0
12	800	7	1	1	98.85
13	1100	4	0	0	0
14	1200	7	1	0	43
15	800	3	1	1	41
16	400	7	0	1	95
17	500	10	0	0	14
18	800	7	0	1	41
19	800	7	0	0	58
20	500	10	0	1	53
21	1200	7	1	1	73
22	800	7	1	1	99
23	800	7	0	1	32
24	1100	10	0	1	44
25	800	11	1	1	96
26	1200	7	0	1	30
27	800	7	1	0	98
28	800	7	0	0	59
29	800	11	0	1	53
30	800	7	1	0	42
31	1100	10	0	0	21
32	1100	4	1	1	28
33	500	10	1	1	96
34	1100	4	1	0	61
35	1100	10	1	0	99
36	500	10	1	0	98
37	800	7	0	1	57
38	400	7	1	1	98.3
39	800	11	1	0	99
40	800	7	0	0	58
41	300	4	1	0	38
42	400	7	0	0	86
43	800	3	1	0	67
44	800	7	0	0	61
45	800	11	0	0	59
46	800	7	1	1	99
47	1100	10	1	1	97
48	500	4	1	1	33
49	800	7	1	0	99
50	800	7	1	1	99
51	800	3	0	0	12
52	800	7	1	1	99

Fig. 5 Tabular representation of the various combinations of process parameters depicted by Design Expert software (Version 13)

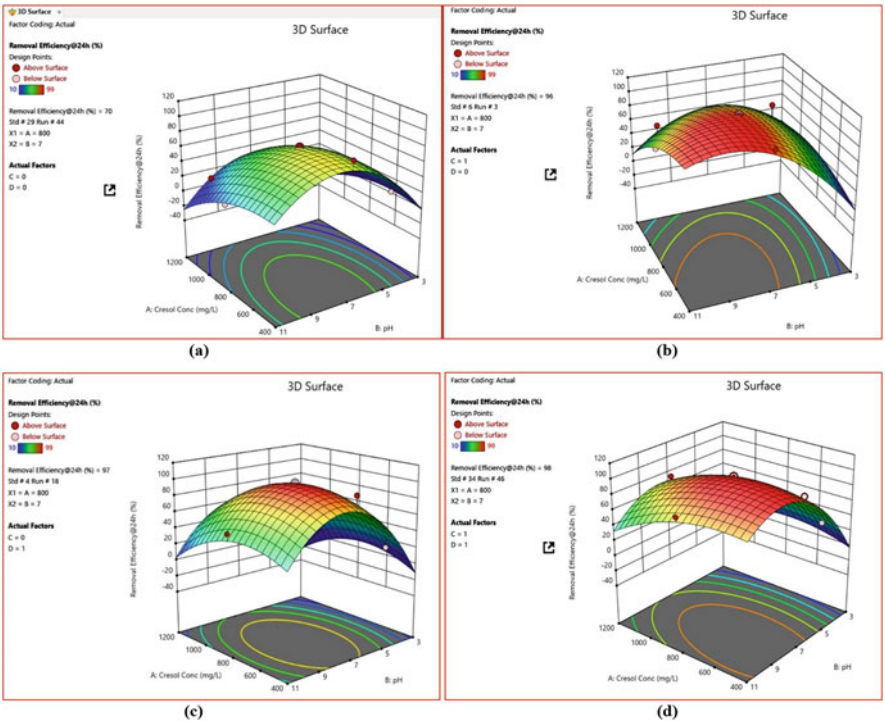

Fig. 6 3D graph representing a change in removal efficiency (%) with a simultaneous change in cresol concentration and pH in different modes of agitations: (**a**) without any agitations or aeration, (**b**) with agitations (shaking) and no aeration, (**c**) with external aeration but no agitations (shaking), and (**d**) both in the presence of external aeration and agitations (shaking)

reduce the growth of the bacteria resulting in substrate degradation. Percentage removal efficiency (%) was observed to be maximum in both aerated and agitated condition and was least in unaerated and unagitated condition. This showed that most of the strains in the consortium are aerobic in nature and aeration can enhance the mineralization of cresol.

The fit statistics depicted in Fig. 7a showed a reasonably high R^2 value. The difference between the adjusted R^2 and predicted R^2 is also less than 0.2. The CV (%) was appreciably low. Adequate precision value was found to be greater than 4. The quadratic model was suggested by the software to be the best-fit model (Fig. 7b). Moreover p-value is less than 0.0001 (Fig. 7c). The above statistical results showed that the model is significant. The software has also designed an actual equation (Fig. 8) and optimized condition for maximum removal efficiency shown in Fig. 9.

Fit Statistics:

Standard Deviation	9.56	R^2	0.9272
Mean	64.72	Adjusted R^2	0.9048
Coefficient of Variance(%)	14.78	Predicted R^2	0.8372
		Adeq Precision	19.8894

7(a)

Lack of Fit Test:

Source	Sum of Squares	df	Mean Square	F-value	p-value	
Linear	32563.12	31	1050.42	1750.71	<0.0001	
2FI	29390.86	25	1175.63	1959.39	<0.0001	
Quadratic	**3557.00**	**23**	**154.65**	**257.75**	**<0.0001**	**Suggested**
Cubic	1713.86	13	131.84	219.73	<0.0001	
Pure Error	9.60	16	0.6000			

7(b)

ANOVA for quadratic Model:

Source	Sum of Squares	df	Mean Square	F-value	p-value	
Model	45444.14	12	3787.01	41.41	<0.0001	significant

7(c)

Fig. 7 Fit statistics (**a**), lack of fit tests (**b**), and ANOVA for quadratic model (**c**) recommended by Design Expert software

3.6 Isolation of Pure Bacterial Colonies

The culture grown in 1095 mg/L of cresol concentration at pH 7 and under aerated and agitated condition was selected for bacterial colony isolation. Those single colonies were chosen based on the difference in size, shape, color, and transparency of the colonies. A total of 20 pure single colonies were selected. All the colonies were whitish in color, opaque in consistency, and fairly circular in shape with varying sizes.

Out of the 20 pure strains isolated from the MBC, the characterization of two strains (A and B) was done based on maximum removal efficiency.

Fig. 8 Actual equations as depicted by the software

Removal Efficiency @ 24 h	=
Agitation	**0**
Aeration	**0**
-205.152	
+0.208	*Cresol Conc.
+58.076	*pH
-0.00785	*Cresol conc. *pH
-0.000126	*Cresol conc.^{2}
-3.528	*pH^2
Agitation	**0**
Aeration	**1**
-213.040	
+0.226	*Cresol Conc.
+59.995	*pH
-0.008	*Cresol conc. *pH
-0.000126	*Cresol conc.^{2}
-3.528	*pH^2
Agitation	**1**
Aeration	**0**
-203.7	
+0.213	*Cresol Conc.
+61.333	*pH
-0.007847	*Cresol conc. *pH
-0.000126	*Cresol conc.^{2}
-3.528	*pH^2
Agitation	**1**
Aeration	**1**
-230.58	
+0.231	*Cresol Conc.
+63.25	*pH
-0.0078	*Cresol conc. *pH
-0.000126	*Cresol conc.^{2}
-3.528	*pH^2

Cresol Conc. (mg/L)	pH	Agitation	Aeration	Removal Efficiency in 24 h (%)
1094.632	7.746	1	1	82.981

Fig. 9 Optimized condition for maximum removal efficiency (RE%) designed by the software

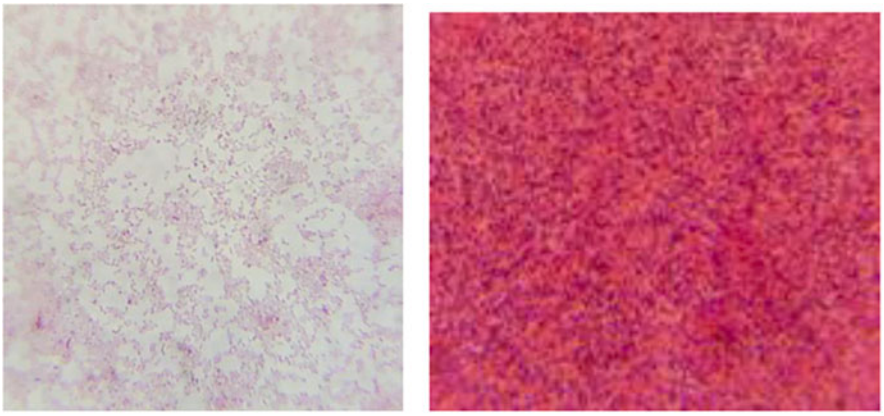

Fig. 10 Gram staining showed that sample A was Gram-positive cocci and sample B was Gram-negative cocci

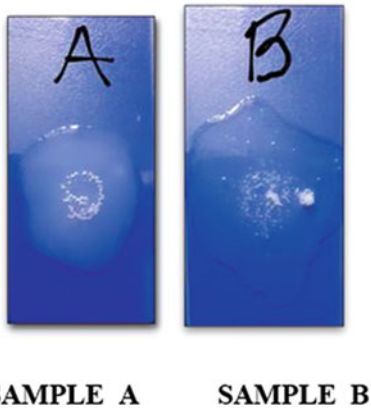

Fig. 11 Both the samples scoring for a positive test for catalase

3.7 Characterization of Pure Strains

- *Gram Staining*

Gram staining of the two isolates showed that sample A was Gram-positive cocci whereas sample B was Gram-negative cocci (Fig. 10).

- *The biochemical tests with the results are shown below*:
  - *Catalase Test*: Both the test cultures reacted with hydrogen peroxide to form effervescence as in Fig. 11 showing a positive test for catalase.
  - *Citrate Test*: Both the pure cultures could utilize citrate as their sole carbon source. When they metabolized citrate, the ammonium salts were broken down to ammonia, which lead to an increase in alkalinity. The shift in pH turned the bromothymol blue indicator in the medium from green to blue as depicted in Fig. 12.

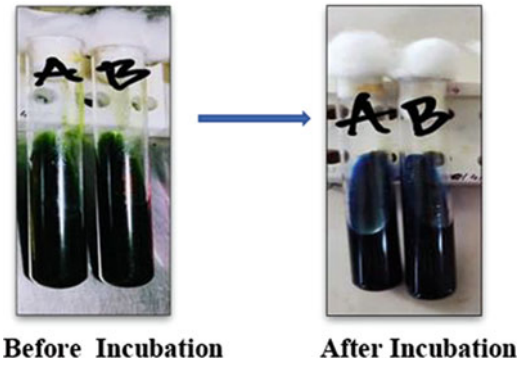

Fig. 12 Both the samples scoring for a positive test for citrate as their sole carbon source

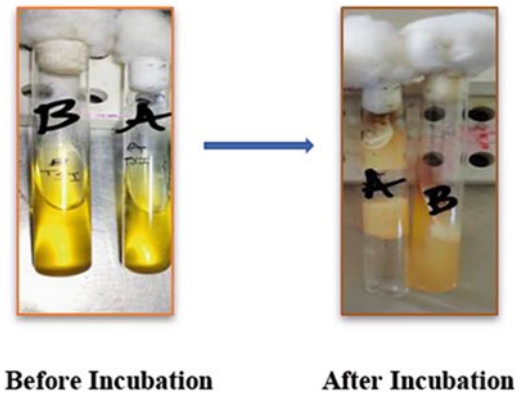

Fig. 13 Samples A and B showing different results in the triple sugar iron test

- *Triple Sugar Iron Test*: In the tube containing sample B (Fig. 13), the bottom part was observed to be turbid yellow and the slope red. We can infer that the strain in sample B has rapidly metabolized glucose only giving an acid slope and an acid bottom. The strain was not able to use lactose and sucrose as their carbon source within the said period. Sample A agar turned out to be turbid yellow indicating that the strain could metabolize the triple sugar simultaneously and produce CO_2 and O_2 gas seen by the detachment of the agar slant (Fig. 13).

- *Identification by 16s rRNA*:

The pure bacterial strains were identified as *Stenotrophomonas* sp. (sample A) and *Bacillus cereus* (sample B) as shown in Fig. 14.

Fig. 14 Phylogenetic tree of *Stenotrophomonas* sp. (sample A) and *Bacillus cereus* (sample B)

4 Conclusion

Our work emphasized the viability of using the isolated bacterial consortium to bioremediate cresol in industrial effluents. The optimized condition as obtained by response surface methodology for maximum percentage removal efficiency (%RE) of 83% was found to be 1095 mg/L of initial cresol concentration at pH 7 and in the presence of both shaking and aeration in 24 h. The biochemical characterization together with 16s rRNA gene sequencing helped to identify the bacterial strains present in mixed bacterial culture as *Stenotrophomonas* sp. and *Bacillus cereus*.

References

1. G. Durai, M. Rajasimman, Biological treatment of tannery wastewater – a review. J. Environ. Sci. Technol. **4**(1), 1–17 (2011)
2. V. Pazhamalai, R. Ravi, Biodegradation of phenol using mixed cultures. Int. J. Bioprocess Technol. **1**(1), 1–6 (2012)
3. K.K. Wong, B. Quilty, A. Hamzah, S. Surif, Phenol biodegradation and metal removal by a mixed bacterial consortium. Biorem. J. **9**(2), 104–112 (2015)
4. V.S. Cerqueira, E.B. Hollenbach, F. Maboni, M.H. Vainstein, F.A.O. Camargo, M.C.R. Peralba, F.M. Bento, Biodegradation potential of oily sludge by pure and mixed bacterial cultures. Bioresour. Technol. **102**, 11003–11010 (2011)
5. S. Dey, S. Mukherjee, Performance and kinetic evaluation of phenol biodegradation by mixed microbial culture in a batch reactor. International Journal of Water Resources and Environmental Engineering **2**(3), 40–49 (2010)
6. L.M. Tormoehlen, K.J. Tekulve, K.A. Nañagas, Hydrocarbon toxicity: a review. Clin. Toxicol. (Phila). **52**(5), 479–489 (2014)
7. Z. Kyselova, Toxicological aspects of the use of phenolic compounds in disease prevention. Interdiscip. Toxicol. **4**(4), 173–183 (2011)
8. B. Chakraborty, Kinetic study of degradation of p-nitro phenol by a mixed bacterial culture and its constituent pure strains. Mater. Today Proc. **3**(10), 3505–3524 (2016)
9. S. Bera, A. Sarma Roy, K. Mohanty, Biodegradation of phenol by a native mixed bacterial culture isolated from crude oil contaminated site. Int. Biodeterior. Biodegradation **121**, 107–113 (2017)
10. S. Hazra Das, J. Saha, A. Saha, A.K. Rao, B. Chakraborty, S. Dey, Adsorption study of chromium (VI) by dried biomass of tea leaves. J. Indian Chem. Soc. **96**, 447–454 (2019)
11. K.Y. Leong, S. See, J.W. Lim, M.J.K. Bashir, C.A. Ng, L. Tham, Effect of process variables interaction on simultaneous adsorption of phenol and 4-chlorophenol: statistical modeling and

optimization using RSM. Appl. Water Sci. **7**, 2009–2020 (2017). https://doi.org/10.1007/s13201-016-0381-8
12. M.J.K. Bashir, H.A. Aziz, M.S. Yusoff, M.N. Adlan, Application of response surface methodology (RSM) for optimization of ammoniacal nitrogen removal from semi-aerobic landfill leachate using ion exchange resin. Desalination **254**(1–3), 154–161 (2010)
13. A. Shehzad, M.J.K. Bashir, S. Sethupathi, J.W. Lim, An insight into the remediation of highly contaminated landfill leachate using sea mango based activated bio-char: optimization, isothermal and kinetic studies. Desalination **57**(47), 22244–22257 (2016)
14. S.C. Chua, F.K. Chong, M.A. Malek, M.R. Ul Mustafa, N. Ismail, W. Sujarwo, Optimized use of ferric chloride and sesbania seed gum (SSG) as sustainable coagulant aid for turbidity reduction in drinking water treatment. Sustainability **12**(6), 2273 (2020)
15. B. Bhunia, A. Dey, Statistical approach for optimization of physiochemical requirements on alkaline protease production from Bacillus licheniformis NCIM 2042. Enzyme Res. **2012**, 905804 (2012). https://doi.org/10.1155/2012/905804
16. B. Chakraborty, L. Ray, S. Basu, Study of phenol biodegradation by an indigenous mixed consortium of bacteria. Indian J. Chem. Technol. **22**, 227–233 (2015)

Biological Degradation of Cresol Containing Waste Water Using Mixed Microbial Culture in Presence of Heavy Metals

Sudipta Dey Bandyopadhyay, Sonali Hazra Das, Anuvab Dey, Ahiri Mukherjee, Anwesha Roy, Debasmita Sarma Chaudhuri, Madhurima Koley, and Souhardya Bandyopadhyay

Abstract A major percent of hazardous waste sites in India are co-contaminated with organic and metal pollutants. Data from both aerobic and anaerobic systems demonstrate that biodegradation of the organic component can be reduced by metal toxicity. In this chapter, a mixed microbial consortium was isolated from soil collected from East Calcutta Wetlands, Kolkata. The culture was acclimatized to cresol, a member of phenol family, and the mixed consortium was capable to degrade up to 750 mg/L of cresol in only 26 h under aerobic condition. The consortium is very unique as it contains bacteria which are tolerant to different heavy metals like Cr(VI), Pb(II), and Cd(II) to a very high concentration level irrespective of cresol concentration, studied here. It is observed that the culture is tolerant to 60 mg/L of Cr(VI), 320 mg/L of Pb(II), and 80 mg/L of Cd(II). Half minimal inhibitory concentration (IC50) value for the tested metals have inhibitory effect on cresol biodegradation ability of the culture as per the following series Pb (II) < Cd(II) < Cr(VI).

Keywords Biodegradation · Pollution · Cresol · Heavy metal · Kinetics · Inhibition · Chromium · Lead · Cadmium · Mixed microbial culture · Minimal inhibitory concentration

Abbreviations

IC50 Half minimal inhibitory concentration

S. D. Bandyopadhyay (✉) · S. H. Das · A. Dey · A. Mukherjee · A. Roy · D. S. Chaudhuri
M. Koley · S. Bandyopadhyay
Department of Biotechnology, Heritage Institute of Technology, Kolkata, India
e-mail: sudipta.dey@heritageit.edu; sonalihazra.das@heritageit.edu

D. Mazumder (ed.), *Sustainable Advanced Technologies for Industrial Pollution Control*, Springer Proceedings in Earth and Environmental Sciences,
https://doi.org/10.1007/978-3-031-37596-5_14

1 Introduction

Along with the increasing need of industrial chemicals, many pollutants are discharged into the environment from the industries such as refinery, pharmaceutical manufacturing industry, or chemical industry, resulting in impoverished living circumstances and increasing environmental pollution [1–5]. Phenolic compounds such as phenol, cresol, resorcinol, and nitrophenol are a group of priority pollutants. Cresol is a member of phenol family present in wastewater emanated from petrochemicals, steel plants, phenol resin, paper and pulp, coal gasification units, etc. Exposures to cresols at very low levels are not detrimental. When cresols are inhaled, ingested, or applied to the skin at very high levels, they can be very harmful. Effects observed in people include irritation and burning of skin, eyes, throat, abdominal pain, vomiting, heart damage, liver, and kidney damage. Such exposure may even lead to coma and death. Co-contamination of phenolics and heavy metal is also found in nature. The removal of phenolic compounds such as cresol, phenol, and resorcinol from wastewater is widely practiced by physicochemical methods such as adsorption, electrochemical methods, and advanced oxidation method, although economical cost studies have shown physicochemical studies are costly and many times produce secondary effluent even more toxic. Therefore biodegradation of cresol is found to be cost-effective and environment friendly method. In this study, the impact of heavy metals on biodegradation of cresol containing wastewater using a mixed microbial culture was examined. Evaluation of cresol biodegradation rate and specific growth rate of the mixed consortium employed for cresol biodegradation in the presence and absence of heavy metals was done [6–10]. Isolation and biochemical characterization of most potent heavy-metal-tolerant and cresol-degrading bacteria from the mixed consortium was also reported. Though individual studies have been done on biodegradation of cresol and bioremediation of heavy metals, reports on kinetics study on cresol biodegradation in the presence of heavy metals as co-contaminant are rare. This is probably the first study to report a novel organism which can tolerate a variety of heavy metals of very high concentration while degrading cresol. Such a culture which can tolerate Pb(II) up to 320 mg/L and simultaneously biodegrade cresol of 750 mg/L was not reported earlier.

2 Materials and Methods

Soil samples were collected from East Calcutta Wetland (ECW), which is a dumping ground of all type of waste generated in Kolkata, West Bengal. First, the consortium of bacteria was grown in nutrient media in laboratory at 37 °C. Then this mixed bacterial culture of the soil was acclimatized to cresol in mineral salt media (MS media). Initially MS media was supplemented with glucose along with cresol as carbon source. Then cresol concentration in the MS media was gradually increased in every batch, whereas glucose concentration was gradually decreased

simultaneously. After a few batches of acclimatization run, it was found that the culture was able to grow in MS media with no glucose but only cresol as sole carbon and energy source. In this way, the mixed bacterial culture was acclimatized to 1000 mg/L of cresol as sole carbon source. After acclimatization, biodegradation of cresol in MS media was tested by varying its concentration in the range of 250–750 mg/L in with and without various concentration of heavy metals, for example, Cr(VI) (5–60 ppm), Cd(II) (5–80 ppm), and Pb(II) (5–320 ppm). For each of fixed concentration of cresol and heavy metal, samples were withdrawn at regular time interval and tested for bacterial growth and residual concentration of cresol. Concentration of cresol was tested by 4-aminoantipyrine test followed by absorbance taken at 490 nm [2] and growth of mixed culture was observed at 600 nm in spectrophotometer. The effect of various concentrations of cresol and metal on the rate of cresol degradation and specific growth rate were reported. IC50 value of the metals was also calculated. Two most potent cresol-degrading and heavy-metal-tolerant bacteria were isolated and tested for its morphology, biochemical tests such as catalase, citrate, TSI, and carbohydrate utilization tests. The isolates were further identified based on 16srRNA method.

3 Results and Discussion

3.1 Effect of Cr(VI) on Biodegradation of Cresol

Degradation of cresol by acclimatized mixed culture in the presence and absence of metals was examined. Cresol biodegradation in the presence of Cr(VI) took more time than in the absence of Cr(VI), for higher concentration of initial cresol. For example, degradation of 250 mg/L of cresol takes only 22 h to reach to undetectable range, whereas the same concentration of cresol is degraded to undetectable range in 26 h in the presence of 5, 10, and 15 ppm of Cr(VI). But when initial concentration of cresol was 750 mg/L, then 32 h were taken by the culture to degrade it completely, whereas complete degradation was not possible when 750 mg/L of cresol was present in the media in the presence of 5 and 10 ppm of Cr(VI) (Figs. 1 and 2). It suggests that there is inhibition caused by Cr(VI) even at low concentration on the degradation of cresol that is pronounced when initial cresol concentration is high. It was also observed that increasing Cr(VI) concentration at 30 and 60-ppm degradation of cresol was possible to happen only near 20–30%, irrespective of initial cresol concentration. Inhibition caused by Cr(VI) starts at its 30-ppm concentration. The growth of the culture also shows very limited growth at Cr(VI) concentration beyond 30 ppm when compared with its growth with no metal (Fig. 3). The culture takes almost the same time to degrade 250 and 500 mg/L of cresol, as these concentration seems non-inhibitory to the culture. But 750 mg/L of cresol seems high enough for it so that time needed to degrade it is slightly more (32 h).

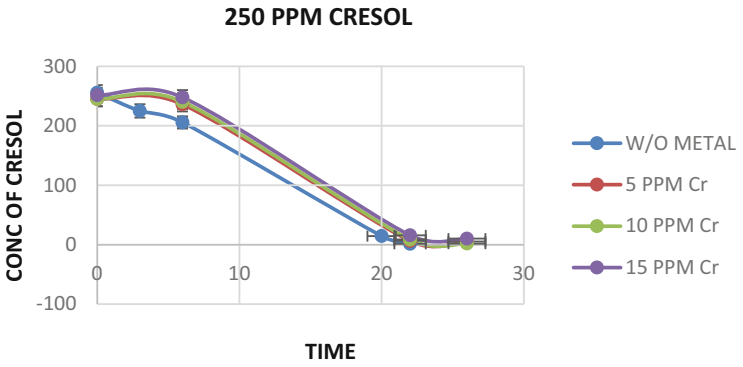

Fig. 1 Biodegradation 250 ppm of cresol with low concentration of Cr

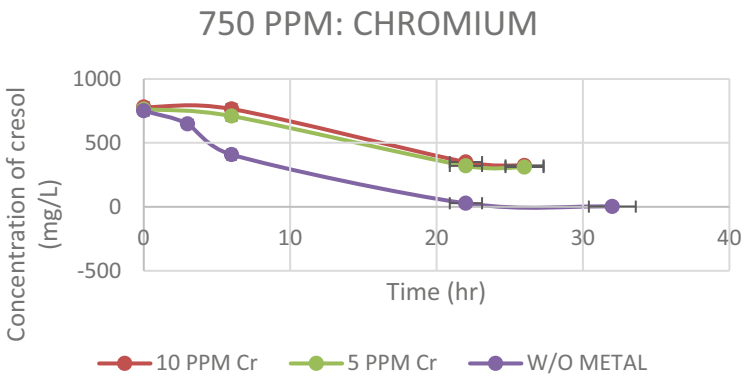

Fig. 2 Biodegradation 750 ppm of cresol with low concentration of Cr

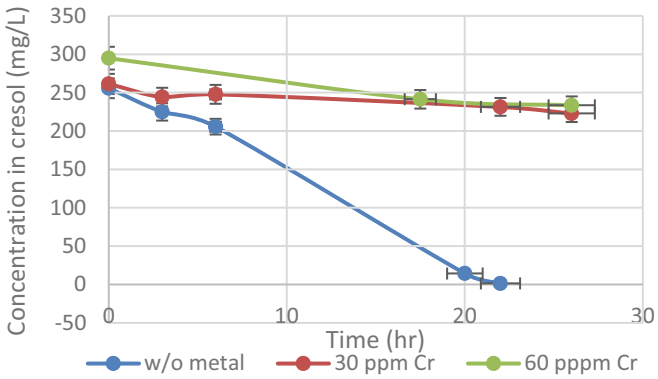

Fig. 3 Biodegradation 250 ppm of cresol with high concentration of Cr

3.2 *Effect of Pb(II) on Biodegradation of Cresol*

The effect of Pb(II) on cresol biodegradation was also examined. It is observed that the more than 99% degradation of cresol both in the presence and absence of Pb (II) took around 25 h, 28 h, and 32 h when initial concentration of cresol was 250 mg/L, 500 mg/L, and 75 mg/L, respectively. Concentration of Pb(II) was varied from 5 to 320 ppm. It showed low concentration of Pb(II) did not show any inhibition to cresol degradation or bacterial growth. Pb(II), even at its high concentration such as 160 and 320 ppm showed insignificant inhibitory effect on growth of the culture and biodegradation of cresol (Figs. 4 and 5). The reason for this high level

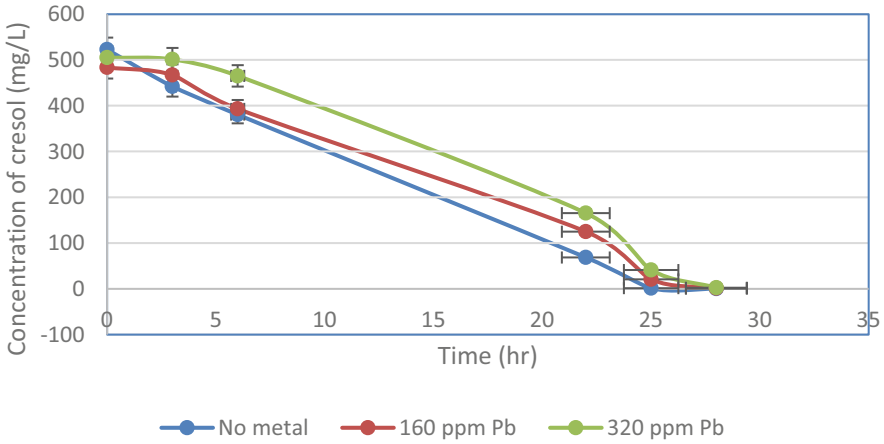

Fig. 4 Biodegradation 500 ppm of cresol with high concentration of Pb

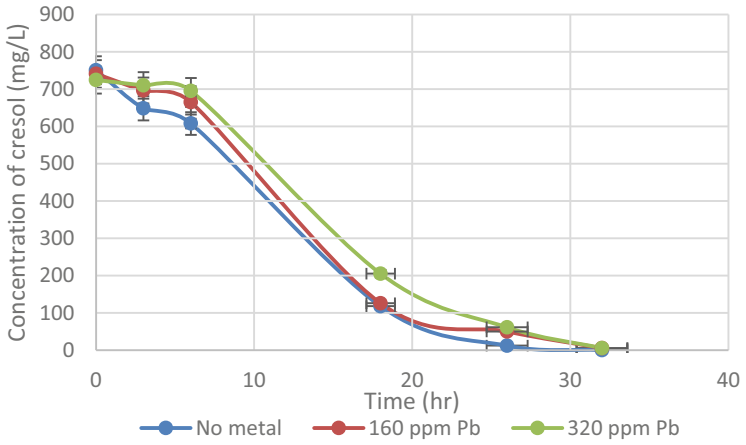

Fig. 5 Biodegradation 750 ppm of cresol with high concentration of Pb

of tolerance of Pb(II) is yet to be examined. But this culture is novel in the fact that it is capable of tolerating so high concentration of Pb(II) though it is not acclimatized to Pb(II) prior to the experiment.

3.3 *Effect of Cd(II) on Biodegradation of Cresol*

While testing the effect of Cd(II), it was observed that complete degradation of 750-mg/L cresol took approximately 32 h in the presence of 5 and 20 ppm of Cd(II). The growth is also high in the presence of Cd(II) of 5 ppm, suggesting no inhibition on bacterial growth by 5 ppm of Cd(II), whereas 20 ppm of Cd(II) lowered down the growth showing inhibition. Moreover, the degradation of cresol was very less in the presence of 40 ppm and almost no degradation in the presence of 80 ppm of Cd(II), irrespective of initial cresol concentration. This shows that Cd(II) has a high inhibitory effect on degradation of cresol and growth of culture (Figs. 6 and 7).

3.4 *Variation of Specific Growth Rate of the Culture with a Variety of Cresol and Metal Combinations*

Specific growth rate of the culture is given by Eq. (1) and its value was calculated by Eq. (2) as follows:

$$\mu = \frac{1}{X}\left(\frac{dX}{dt}\right) \tag{1}$$

$$\mu = \frac{\ln(X_2/X_1)}{(t_2 - t_1)} \tag{2}$$

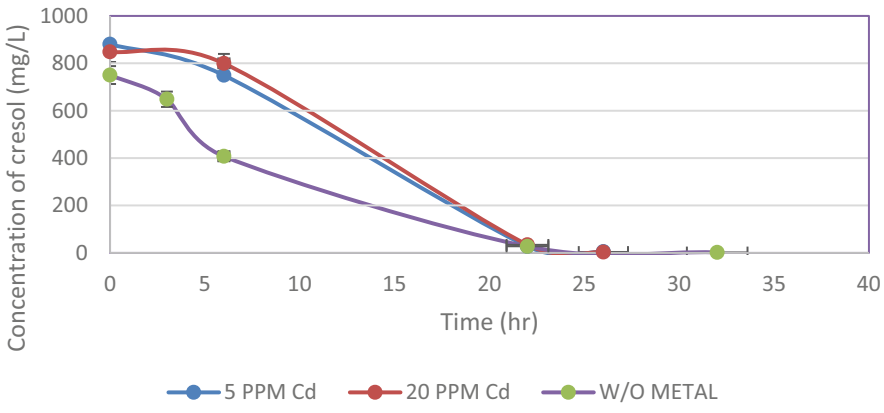

Fig. 6 Biodegradation 750 ppm of cresol with low concentration of Cd

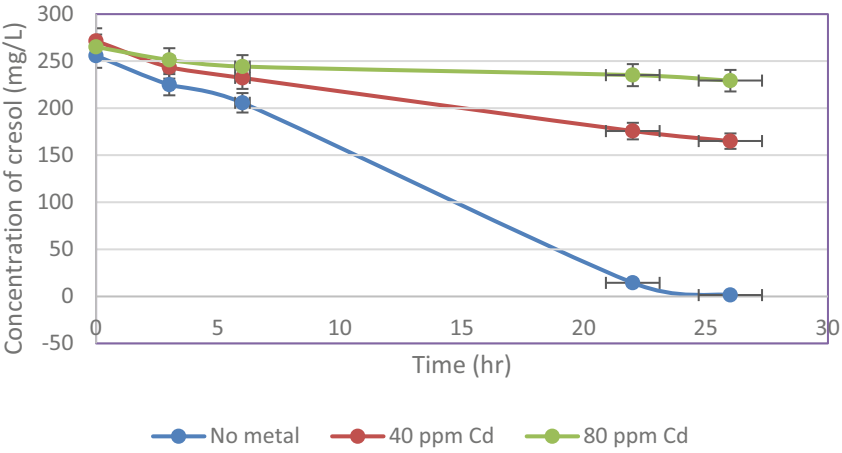

Fig. 7 Biodegradation 250 ppm of cresol with high concentration of Cd

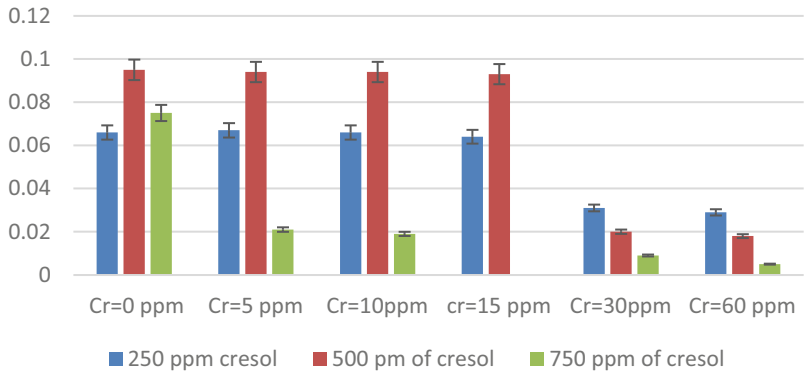

Fig. 8 Specific growth rate of the culture (h^{-1}) with cresol in the presence of Cr(VI)

where μ is the specific growth rate of the mixed microbial culture (h^{-1}); t_1 and t_2 are initial and final time (h), respectively; and X_1 and X_2 are biomass concentration (measured as OD at 600 nm) at t_1 and t_2 time, respectively. The specific growth rate of the culture was found to be varied with variation of initial cresol and heavy metal loas (Figs. 8, 9, and 10). From the figures it is evident that specific growth rate remains high and almost constant when initial cresol concentration is 250–500 mg/L and Cr(VI) concentration is below 15 ppm, but decreases a lot when Cr (VI) concentration is increased to 30 and 60 ppm. When initial cresol concentration is itself high as 750 mg/L, then the growth of culture is low enough and keeps on decreasing with the increase of Cr(VI) concentration (Fig. 8). Surprisingly, the culture did not showed any inhibition to its growth in the presence of Pb(II) in the range of 5–320 ppm, irrespective of initial cresol concentration. Though some reports are available showing the ability of some pure bacterial strain to degrade

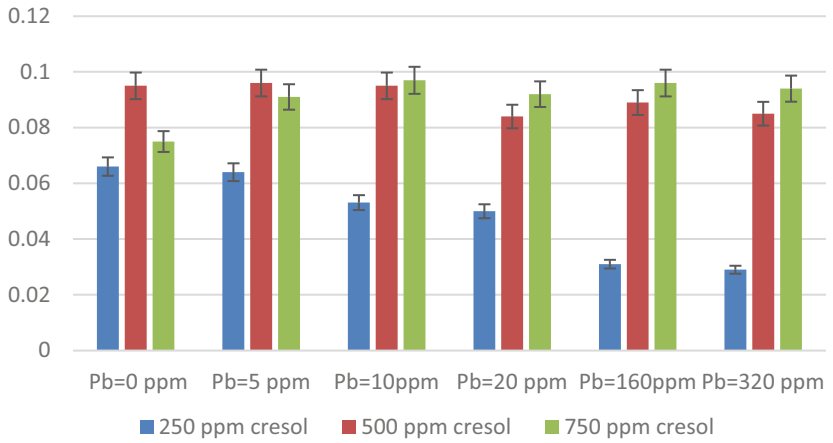

Fig. 9 Specific growth rate of the culture (h^{-1}) with cresol in the presence of Pb(II)

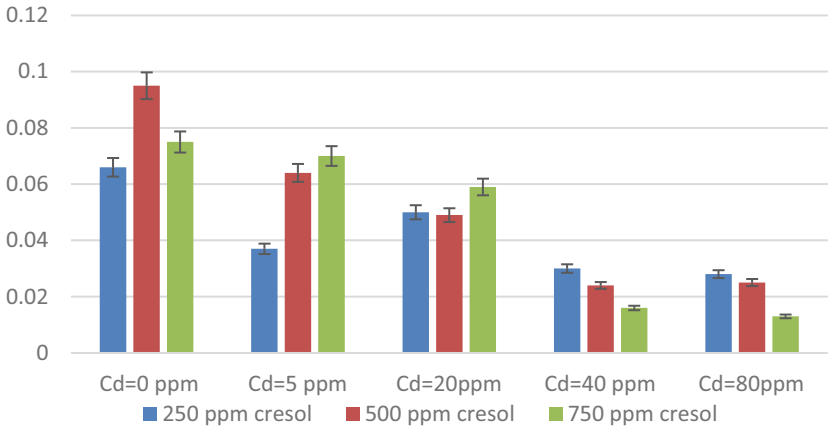

Fig. 10 Specific growth rate of the culture (h^{-1}) with cresol in the presence of Cd(II)

phenol while removing Pb(II) at high concentration from a contaminated site, probably, this is the first report that shows the ability of a mixed microbial consortium to withstand so high concentration of Pb(II) while degrading cresol up to 750 mg/L (Fig. 9). A slightly different observation was found in the case of the effect of Cd(II) on the growth of the culture. It was maximum when the culture was fed with no Cd(II), but only cresol (250–750 mg/L), whereas Cd(II) at any concentration inhibited the growth. Also, the inhibition increased with the increase of Cd (II) concentration. The inhibition on growth was predominant when Cd (II) concentration was beyond 40 ppm.

3.5 Determination of IC50 Value of Heavy Metals

IC50 value of any heavy metal tested here was considered as the concentration of metal which caused not more than 50% removal of cresol. This value was found for cresol concentration 250–750 mg/L. Some representative figures are shown in Figs. 11, 12, and 13.

From Table 1, it is found that, based on the range of degradation of cresol concentration studied here, Cr(VI) has average IC50 value of 21 and Cd(II) has IC50 value of 32, while Pb(II) showed no inhibition up to its concentration of 320 ppm. This proves that this mixed microbial culture is unique enough and has the ability to tolerate very high concentration of heavy metal while degrading cresol in wastewater.

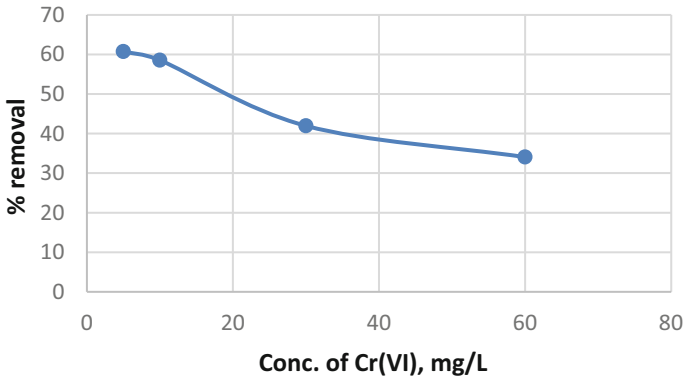

Fig. 11 Percentage removal of cresol (250 mg/L) in the presence of Cr(VI)

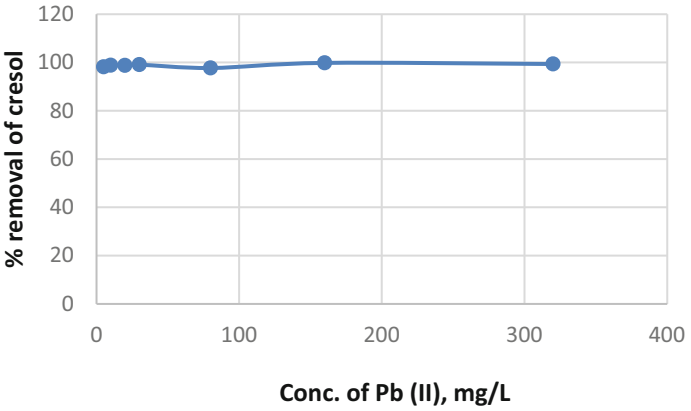

Fig. 12 Percentage removal of cresol (500 mg/L) in the presence of Pb(II)

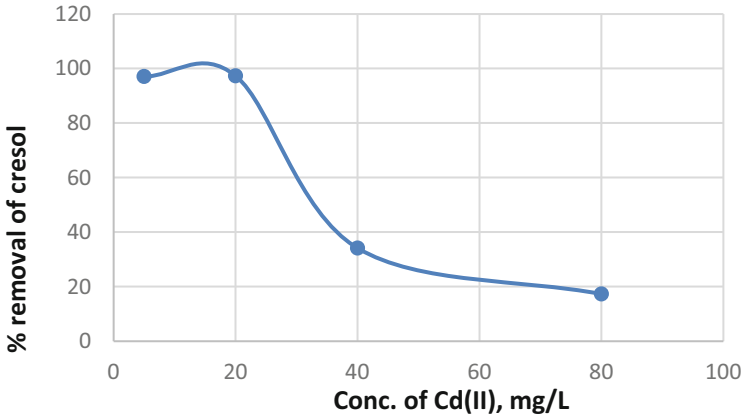

Fig. 13 Percentage removal of cresol (750 mg/L) in the presence of Cd(II)

Table 1 IC50 values of different heavy metals on biodegradation of cresol

Metal	Concentration of cresol (mg/L)	IC50 (mg/L)
Chromium(VI)	250	22
	500	21
	750	20
Lead(II)	250	No inhibition was found in the case of Lead (II)
	500	
	750	
Cadmium(II)	250	33
	500	31
	750	32

3.6 Characterization and Identification of Predominant Bacteria from the Mixed Culture

Twenty-two pure bacteria have been isolated from the mixed culture studied here out of which two have been selected for further characterization and identification, based on colony characteristics. Gram staining, few biochemical tests were performed whose results are listed in Table 2. The two isolates named as isolate A and isolate B were identified using 16SrRNA method as *Stenotrophomonas pavanii* and *Bacillus cereus*, respectively.

Table 2 Biochemical characterization and identification results

Name of the tests	Isolate A	Isolate B
Catalase test	+	+
Citrate test	+	+
TSI test	–	+
Carbohydrate utilization tests		
(i) Fructose	+	+
(ii) Lactose	+	–
(iii) Galactose	+	+
(iv) Maltose	+	+
(v) Ribose	+	+
(vi) Dextrose	+	+
(vii) Raffinose	+	+
(viii) Mannitol	+	+
(ix) Starch	+	+
(x) Arabinose	+	+
(xi) Sucrose	+	–
(xii) Mannose	+	+
(xiii) CMC	–	–
Identification results		
	Stenotrophomonas pavanii	*Bacillus cereus*

4 Conclusion

It is evident from the above results that the mixed bacterial culture possesses the capability of biodegradation of cresol in presence of three different heavy metals – Cr(VI), Pb(II), and Cd(II). The biodegradation of cresol was due to acclimatization of the culture using cresol as sole carbon and energy source. But tolerance to several metals is a unique property of this consortium. The defensive strategies used by bacteria to ameliorate the toxic effects of lead comprise biosorption, efflux, production of metal chelators like siderophores and metallothioneins and synthesis of exopolysaccharides, extracellular sequestration, and intracellular bioaccumulation. Although it is quite evident that high concentration of heavy metals inhibited the rate of biodegradation and growth except Pb(II), this consortium of bacteria is capable of treatment of high concentration of phenolic wastewater even in the sites which are co-contaminated with different heavy metal waste. So the versatility of this mixed consortium can be exploited for real-life phenolic wastewater treatment and remediation of heavy metal.

References

1. D. Duraiswami, J. Sekar, S. Liu, A.D. Aruukumar, P.V. Ramalingam, Kinetics of phenol biodegradation by heavy metal tolerant rhizobacteria *Glutamicibacter nicotianae* MSSRFPD35 from distillery effluent contaminated soils. Front. Microbiol. **11**, 1573 (2020)
2. APHA, *Standard Methods for the Examination of Water and Wastewater* (American Public Health Association, Washington, DC, 2017)
3. J. Bai, J.-P. Wen, H.-M. Li, Y. Jiang, Kinetic modeling of growth and biodegradation of phenol and m-cresol using *Alcaligenes faecalis*. Process Biochem. **42**, 510–517 (2007)
4. B.E. Igiri, S.I.R. Okoduwa, G.O. Idoko, E.P. Akabuogu, A.O. Adeyi, L.K. Ejiogu, Toxicity and bioremediation of heavy metals contaminated ecosystem from tannery wastewater: A review. J. Toxicol. **2018**, 2568038 (2018)
5. B. Pal, P. Sarkar, P. Pal, Isolation and characterization of phenol utilizing bacteria from industrial effluent-contaminated soil and kinetic evaluation of their biodegradation potential. J. Environ. Sci. Health A Tox. Hazard. Subst. Environ. Eng. **49**, 67–77 (2014)
6. A. Haddadi, M. Shavandi, Biodegradation of phenol in hypersaline conditions by Halomonas sp. strain PH2-2 isolated from saline soil. Int. Biodeterior. Biodegradation **85**, 29–34 (2013)
7. P. Thavamani, M. Megharaj, R. Naidu, Bioremediation of high molecular weight polyaromatic hydrocarbons co-contaminated with metals in liquid and soil slurries by metal tolerant PAHs degrading bacterial consortium. Biodegradation **23**, 823–835 (2012)
8. K.K. Wong, B. Quilty, A. Hamzah, S. Surif, Phenol biodegradation and metal removal by a mixed bacterial consortium. Biorem. J. **19**, 104–112 (2015)
9. J. Yan, W. Jianping, L. Hongmei, Y. Suliang, H. Zongding, The biodegradation of phenol at high initial concentration by the yeast *Candida tropicalis*. Biochem. Eng. J. **24**, 243–247 (2005)
10. Z. Zhai, H. Wang, S. Yan, J. Yao, Biodegradation of phenol at high concentration by a novel bacterium: *Gulosibacter sp*. YZ4. J. Chem. Technol. Biotechnol. **87**, 105–111 (2012)

Part III
Monitoring of Industrial Emission and Control

Development of a Simplistic Model for the Prediction of Reactive Air Pollutants in the Atmosphere

Tanmoy Bir, Saptarshi Kundu, and Debabrata Mazumder

Abstract Air quality assessment using a mathematical model is essential for planning of pollution abatement. Application of the Gaussian plume model is widely used for prediction of inert pollutants; however, it is hardly applied for reactive pollutants such as NO_X and SO_2. In this paper, the Gaussian plume dispersion model is applied to solve the dispersion equation by FDM (finite difference method) using MATLAB simulation software. The rate coefficient as well as the order of reaction is also considered reasonably. Three case studies concerning two reactive primary pollutants NO_X and SO_2 are chosen for validation of the proposed solution method. Thus, the model is run for SO_2 and NO_X with their variable mass emission rates along with other relevant meteorological data. The mass emission rate for SO_2 was 1.0 g/s, whereas NO_X was emitted with a rate of 1.37 and 147.55 g/s for two different cases. The graphical representation demonstrates the variation between the predicted and reference concentration with very little difference establishing the applicability of the solution procedure.

Keywords Air pollution · Concentration prediction · Gaussian plume model · Simplistic model · Reactive pollutant · SO_2 and NO_x

Abbreviations

FDM	Finite difference method
MATLAB	Matrix Laboratory
ppbv	Parts per billion in volume
ppm	Parts per million
RPM	Reactive plume model

T. Bir (✉) · S. Kundu · D. Mazumder
Department of Civil Engineering, Indian Institute of Engineering and Science Technology, Howrah, West Bengal, India
e-mail: guest3.civil@faculty.iiests.ac.in; debabrata@civil.iiests.ac.in

D. Mazumder (ed.), *Sustainable Advanced Technologies for Industrial Pollution Control*, Springer Proceedings in Earth and Environmental Sciences,
https://doi.org/10.1007/978-3-031-37596-5_15

1 Introduction

Large-scale point-source emissions of primary air pollutants are linked to a set of problems including physical settlement, such as dust, aerosol, adsorption/absorption of SO_2 and NO_x, and photochemical reactions. Primary air pollutants such as SO_2, NO_x, CO, and black carbon (BC) are chemically transformed by photochemical reactions in the atmosphere, resulting in secondary air pollutants. Ozone, peroxyacetyl nitrates (PANs), HCHO, sulfuric acid (H_2SO_4), and nitric acid (HNO_3) are examples of secondary air pollutants that may be even more dangerous to human health and agricultural productivity than primary air pollutants [1, 2]. In particular, large-scale point sources (such as power plants, steel manufacturing, and petrochemical factories) are responsible for a disproportionate share of SO_2 and NO_x emissions in all countries, for example, in South Korea and the United States, where aforesaid gases contribute 64% and 16%, respectively [3].

In 2005, the World Health Organization estimated that air pollution in major cities in Southeast Asia and China was among the worst in the world, directly responsible for the deaths of approximately 500,000 people each year [4]. The Gaussian plume model is applicable for prediction of concentration of inert pollutants such as PM_{10} and $PM_{2.5}$, but not rational for SO_2 and NO_X, which are two major reactive primary pollutants. Therefore, a detailed description of the atmospheric photochemical conversion of primary to secondary air pollutants inside the plumes emitted from large-scale point sources is of paramount importance. Only a few models, including the reactive plume model (RPM), have attempted to simulate the spread of reactive pollutants emitted by an industrial stack. Standard regulatory models are used to estimate atmospheric pollutant concentrations due to emissions from point sources such as industrial stacks. One such model is the RPM version IV [5]. Moreover, photochemical modeling, reactive plume modeling, and integrated Gaussian plume modeling are all reported in the literature, but each has a different algorithm and a paradigm shift in fundamental concept. As a result, the basic numerical solution technique is used in this study, considering a rate constant and second order of reaction. Due to a lack of sufficient experimental data to validate the solution procedure, secondary data from existing literature based on the same concept but following a different procedure is used.

In this study, a reactive air pollutant model with the three-dimensional diffusion equation using Fick's law and finite difference method (FDM) has been developed. The reaction rate constant and order of reaction have been incorporated into the model to consider the impact of reaction. MATLAB software package has been used to simulate the FDM solution for forecasting the concentration of SO_2 and NO_X in all cases.

2 Materials and Methods

2.1 Development of Model

The basic differential equation used in this study is based on the fundamental Fick's diffusion law, which can be represented as

$$\frac{\partial \rho_A}{\partial t} + \nabla . \rho_A . \overrightarrow{q_A} = r_A \tag{1}$$

where:

ρ_A = mass concentration of Pollutant A (g/m^3)
$\overrightarrow{q_A}$ = absolute velocity of Pollutant A relative to stationary coordinate axes (m/s)
r_A = rate of production of Pollutant A by chemical reaction (g/m^3/s).

As the dispersion of air pollutants is principally along the downwind direction, that is, along the x direction, the same along the other two coordinates y and z is neglected. The conceptual diagram of the Gaussian plume model is shown in Fig. 1.

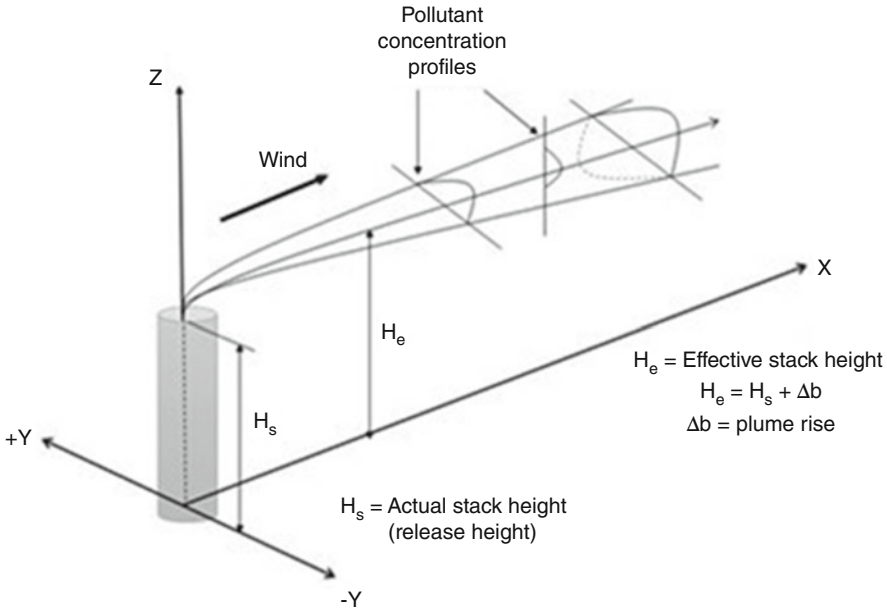

Fig. 1 Schematic diagram of the Gaussian plume model

The final differential equation considering the decay of mass of pollutants can be written as

$$u\frac{\partial(\rho A)}{\partial x} = \frac{\partial}{\partial y}\left(K_{yy}.\frac{\partial(\rho A)}{\partial y}\right) + \frac{\partial}{\partial z}\left(K_{zz}.\frac{\partial(\rho A)}{\partial z}\right) + (-kC^n). \tag{2}$$

The solution of the differential equation involves the following boundary conditions:

I. $(\rho A) <X, Y, Z> \rightarrow 0, X, Y, Z \rightarrow \infty$
II. $(\rho A) <X, Y, Z> \rightarrow \infty, X, Y, Z \rightarrow 0$
III. $K_{zz} < \frac{\partial \rho A}{\partial z} = 0$ for for $Z = 0, X, Y > 0$.
IV. $\iint_{-\infty}^{\infty} \rho A \; U \; dy \; dz = Q \nabla X > 0$

where Q is the source strength or emission rate from a point source as g/s.

Using the finite difference method (in MATLAB) to solve the above equation, a numerical form of Eq. (2) can be expressed as follows.

$$\begin{aligned} &\frac{u}{2h}\left(U_{i+1,j,k} - U_{i-1,j,k}\right) - \frac{K_{YY}}{L^2}\left(U_{i,j+1,k} - 2U_{i,j,k} + U_{i,j-1,k}\right) \\ &- \frac{K_{ZZ}}{P^2}\left(U_{i,j,k+1}2U_{i,j,k} + U_{i,j,k-1}\right) + \lambda\left(U_{i,j,k}\right)^n = 0 \end{aligned} \tag{3}$$

where h is the mesh interval in the X direction, L is the interval in the Y direction, p is the interval in the Z direction, λ is the rate constant, and n is the reaction order.

2.2 Solutions of the Model

In order to solve the model, the finite difference method (FDM) program has been developed in MATLAB for obtaining the results regarding the predicted concentration of SO_2 and NO_X. To validate the developed model, secondary data from literature are used in the aforesaid method of software. The relevant input parameters are mean wind velocity (u in m/s), source emission rate (Q in g/s), stability coefficient (K_{zz}, K_{yy}), stack height including plume rise [6] ($H + \Delta h$ in m), and stability class (D).

The following assumptions are made during the solution of the model keeping parity with the basic Gaussian dispersion model:

1. Continuous emission from the point source.
2. Absence of mechanical turbulence, that is, turbulence developed due to undulation, physical obstacle, etc.
3. The plume is conning in nature, that is, in a neutral condition, the plume travel fairly a long distance.
4. The conservation of mass is followed.

Table 1 Reaction rate constant for the atmospheric reaction of NO_X [8]

Salient reaction	Rate constant	Order
$NO + O_3 \rightarrow NO_X + O_2$	27 ppm^{-1} min^{-1}	First
$NO_2 ++ h\nu \rightarrow NO + O$	0.36 min^{-1}	Second
$O_2 + O + M \rightarrow O_3 + M$	$2.0 \times 10^{(-5)}$ ppm^{-2} min^{-1}	Third

5. This model is primarily applicable to reactive pollutants, but it can be improvised to inert pollutants also.
6. The reaction follows second-order kinetics both in the case of NO_X and SO_2 [7, 8].

The space around the stack is divided into discrete points along the X, Y, and Z axis. The simulation of prediction of concentration of reactive pollutants such as SO_2 and NO_X is performed by solving the numerical form of differential equation as mentioned in Eq. (3) by running the program in MATLAB, and the corresponding concentrations of the pollutants under consideration were determined on each nodal point. In the case of the reaction rate coefficient, it is dependent on the order of reaction. Schofield [9] proposed an empirical formula for the rate coefficient for the reaction of reactive pollutants in the atmosphere as $k = A_{of}\exp(-E_0/RT)$ which is applicable for bimolecular reaction, where A_{of} is frequency factor, E is activation energy (kJ/mol), R is the universal gas constant, and T is the absolute ambient temperature in Kelvin. However, using this expression in the differential form involves more complexity in the solution of this equation. For simplicity, a general rate coefficient is adopted for atmospheric reaction for NO_X as suggested by Kitabayashi and Yokoyama [8] and given in Table 1.

The presence of light causes NO_X to react in a second-order process, leading to the use of the value of k as 0.36 min^{-1}. In the presence of water vapor in the atmosphere, SO_2 goes through a process called wet deposition, which is also a second-order reaction. An atmospheric reaction involving SO_2 proceeds according to the following formula: $SO_2 + \dot{O}H + (O_2 + H_2O) \longrightarrow H_2SO_4 + H\dot{O}_2$.

A rate constant of 0.069 h^{-1} is proposed by Luria et al. [7], which is consistent with a second-order reaction.

Since no experimental data were available, the above values were used in the numerical technique utilizing the finite difference method for validation purposes. The flowchart of the solution of the differential equation using MATLAB is depicted in Fig. 2.

3 Results and Discussion

In order to perform validation, three data sets from the available literature, viz., (a) IPDM (integrated plume dispersion model with chemical reaction) [10] for NO_X, using input data such as emission rate (1.37 g/s), tower diameter (5 m), and inside

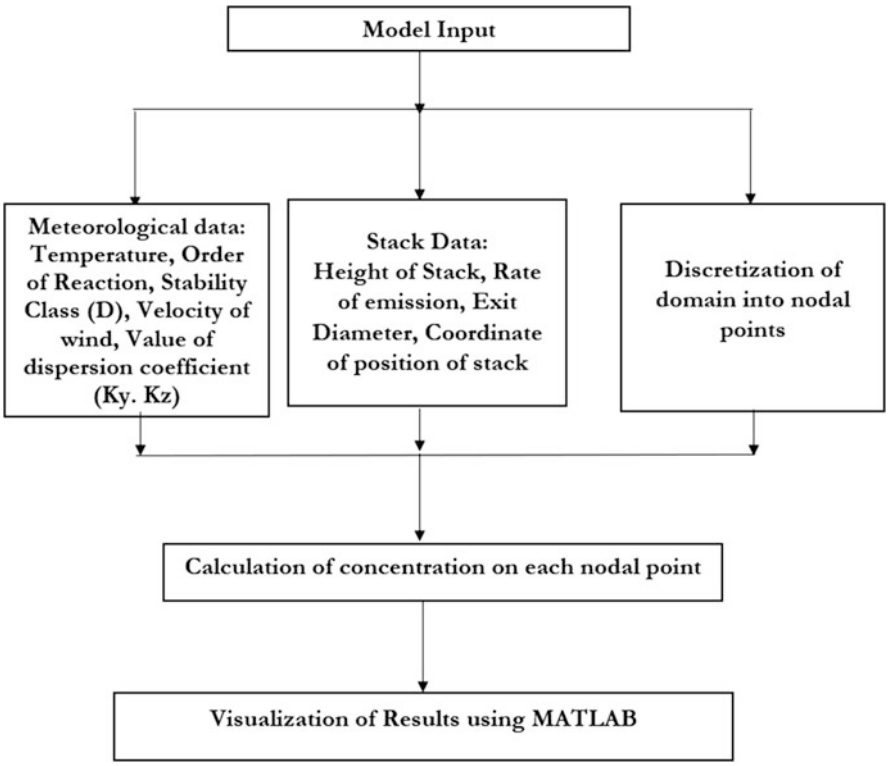

Fig. 2 Flowchart of the solution of the differential equation using MATLAB

temperature (15 °C) under the stability class D, that is, neutral class; (b) AEROMOD model [11] for SO_2 by taking the input data emission rate 1 g/s and tower height (13 m), inside temperature (403 K) under the stability class D, that is, neutral class; and (c) RPM (reactive plume model) [12] for NO_X with the same field data, that is, the emission rate of NOX as 147.55 g/s and mean wind velocity within the range of 6–9 m/s were considered. The generated GLC (ground level concentration) profiles of reactive pollutants are presented in Fig. 3 for NO_X and Figs. 4 and 5 for SO_2 and NO_X, respectively. The GLC profiles as obtained from respective literature are also superimposed on Fig. 3 as well as Figs. 4 and 5 to make a comparison of data.

In case of validation with the literature related to RPM (reactive plume modeling) by Kim et al. [12], the concentration profile is obtained in a crosswind direction, that is, in the *X*–*Y* plane.

The GLC profiles of NO_X and SO_2 as shown in Figs. 3 and 4, respectively, exhibit almost similar nature with regard to the field observations. Hence, the GLC data for both NO_X and SO_2 available from the present solution method satisfactorily corroborate with those reported for various downwind distances in respective literature. In the case of Fig. 5, there is a marginal variation between the results obtained using the

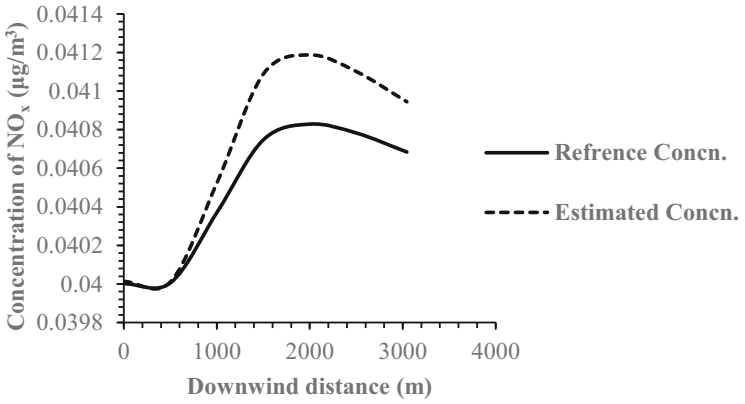

Fig. 3 GLC profiles for NO_X using the finite difference method and from Kitabayashi et al. [10]

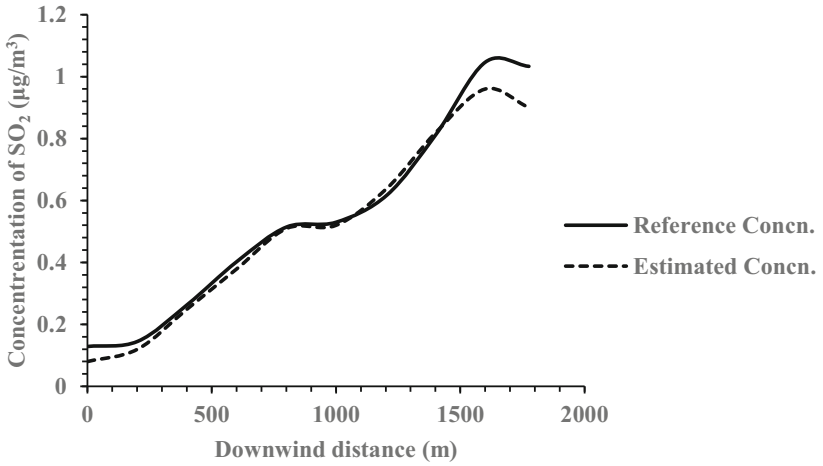

Fig. 4 GLC profiles for SO_2 using the finite difference method and from Yadav et al. [11]

described method and reference method, that is, RPM [12] which also corroborates the validity of the present method.

In order to check the accuracy of GLC data for NO_X, a bar diagram has been plotted for selected downwind distances as shown in Fig. 6. Similarly, another bar diagram has also been plotted for selected downwind distances as shown in Fig. 7 to check the accuracy of GLC data for SO_2. Figure 8 also shows the comparison between the estimated concentration of NO_X obtained by the present numerical solution and the concentration obtained using RPM (reactive plume model) by Kim et al. (2017) for the selected crosswind distance.

Figures 6, 7, and 8 reveal that there is no significant deviation between the reference and estimated concentration of both NO_X and SO_2. In the case of NO_X, the amount of deviation increased up to a downwind distance of 2000 m. There is

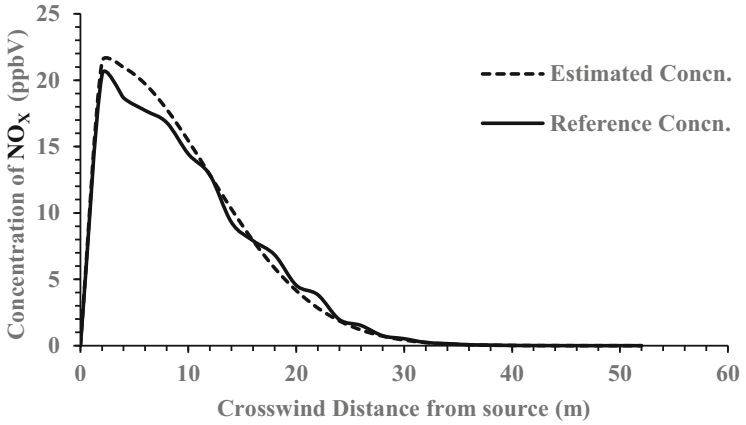

Fig. 5 Concentration profile of NO_X using the finite difference method and from Kim et al. [12]

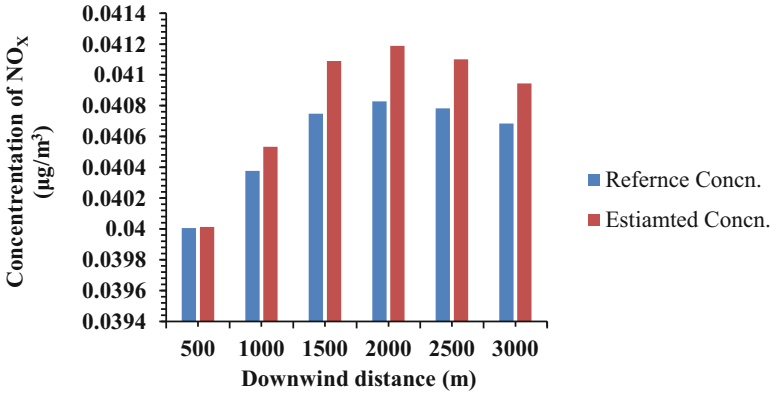

Fig. 6 Comparison of GLC data for NO_X using the present method and from Kitabayashi et al. [10]

little difference between the reference and estimated concentration except under a downwind distance of 1600 m for SO_2. From Fig. 8, it can be inferred that as long as the crosswind distance increases, the concentration of NO_X decreased rapidly due to the effect of chemical reaction. The perspective of the maximum centerline concentration, expressed in terms of ppbv (parts per billion in volume), shows little difference between the plot, obtained using the present method and reported by Kim et al. [12].

In order to develop a correlation between the NO_X and SO_2 concentration predicted by the present method and that stated in the reference method, all the relevant concentration data have been plotted as scatter diagrams as shown in Figs. 9, 10, and 11. In each case, the predicted concentration of NO_X and SO_2 are plotted with respect to their corresponding reference concentration, which resulted in linear relation with a strong correlation ($R^2 > 0.98$). The correlation equation as

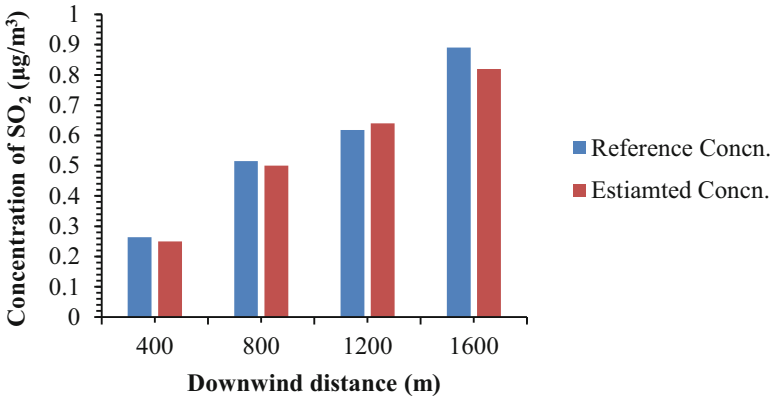

Fig. 7 Comparison of GLC data for SO_2 using the present method and from Yadav et al. [11]

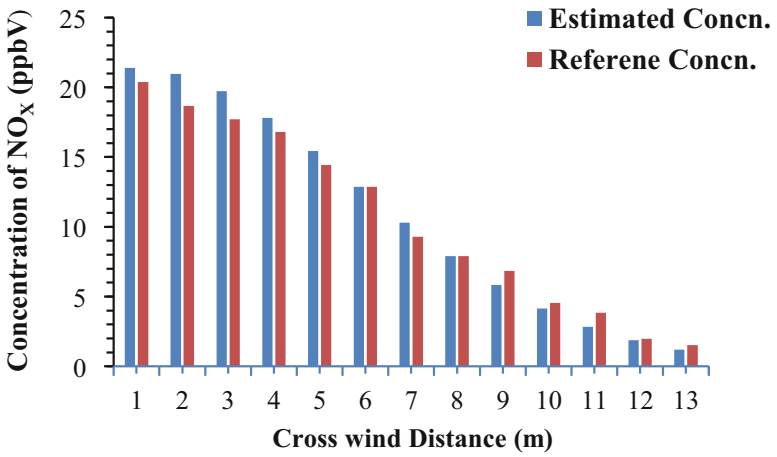

Fig. 8 Comparison of GLC data for NO_X using the present method and from Kim et al. [12]

highlighted in each plot can be considered as a tool to predict the concentration of NO_X and SO_2 for a reference concentration at any downwind distance within the working range.

The strong correlation between the predicted and reference concentration also satisfactorily validates the proposed solution method. The extent of such correlation can also be explored for other downwind and crosswind distances beyond the range under this study.

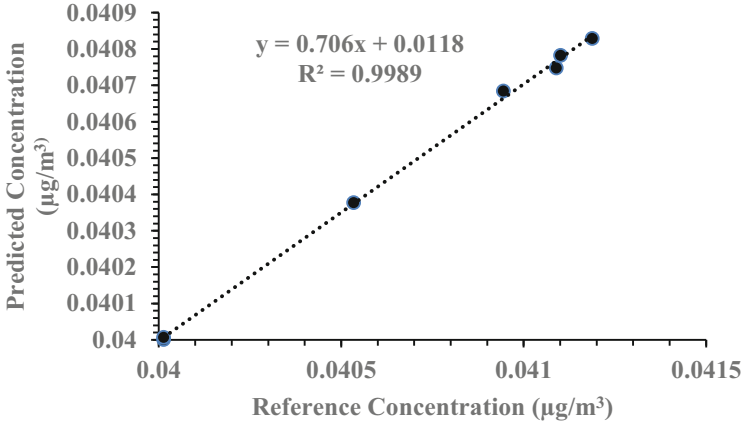

Fig. 9 Correlation between the predicted and actual concentration of NO_X from Kitabayashi et al. [10]

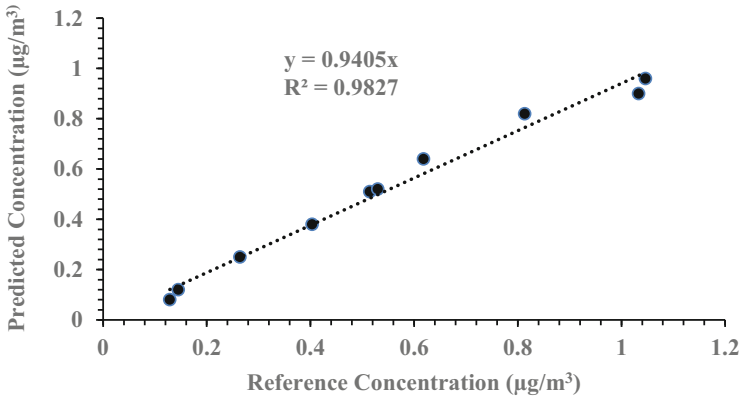

Fig. 10 Correlation between the predicted and actual concentration of SO_2 from Yadav et al. [11]

4 Conclusion

In this study, a comprehensive simplistic approach is used to predict major reactive pollutants emitting from industrial stacks, such as SO_2 and NO_X, using the fundamental concept of three-dimensional partial differential equation. The solution of the fundamental partial differential equation is made using the numerical technique in MATLAB software. Though several modeling software such as ADMS, CALPUFF, AERMOD, and others are available, the prediction procedure using fundamental concepts through mathematical operations is used because it includes several fundamental understandings regarding the development of the Gaussian plume model. The proposed method is a simple technique involving the finite difference method to predict the concentration of a reactive pollutant. Both the rate and order of reaction

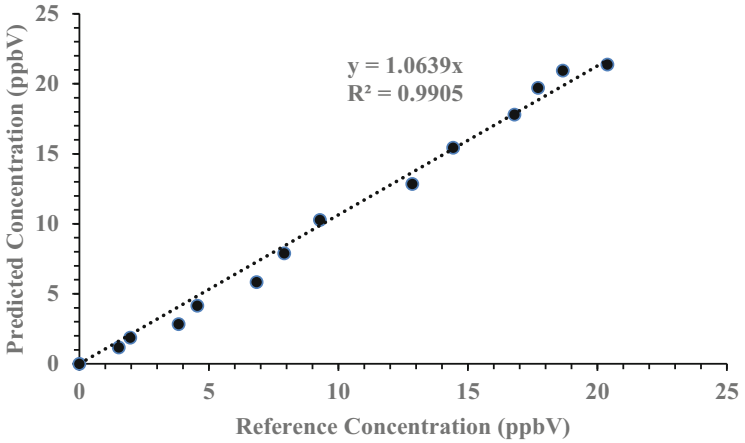

Fig. 11 Correlation between the predicted and actual concentration of NO_X from Kim et al. [12]

could be considered in this method making it rational and effective. The limitations of the Gaussian plume model for predicting the reactive pollutants are also overcome. The major advantage of the proposed method is that any rate and order of reaction can be considered while predicting the concentration of a pollutant. The method has been satisfactorily validated with two existing methods in the case of two classical reactive pollutants, namely, NO_X and SO_2, justifying its applicability to other reactive pollutants also. The strong correlation coefficient value (0.98–0.99) has proved the accuracy of the proposed solution method. Apart from MATLAB software, other simplistic mathematical tools can also be explored to solve the proposed model explicitly.

Acknowledgment This research work is supported under the Research Fellowship Programme of the Ministry of Education, Government of India.

References

1. J. Burney, V. Ramanathan, Recent climate and air pollution impacts on Indian agriculture. Proc. Natl. Acad. Sci. **111**(46), 16319–16324 (2014). https://doi.org/10.1073/pnas.1317275111
2. L.T. Molina, M.J. Molina, *Air Quality in the Mexico Megacity: An Integrated Assessment*, vol 2 (Springer Science & Business Media, 2002)
3. C. Van Atten, A. Saha, L. Reynolds, *Benchmarking Air Emissions of the 100 Largest Power Producers in the United States* (M.J. Bradley & Associates, LLC, 2012)
4. WHO, *WHO Air Quality Guidelines for Particulate Matter, Ozone, Nitrogen Dioxide and Sulfur Dioxide: Global Update 2005. Summary of Risk Assessment* (World Health Organization, Geneva, 2006) http://www.who.int/phe/air/aqg2006execsum.pdf. Accessed 25 Nov 2006
5. E.R. Morris, E.C. Chang, S.B. Shepard, M.P. Ligocki, *User's Guide to Version IV of the Reactive Plume Model (RPM-IV)*. (SYSAPP-92/037) (Systems Applications International, San Rafael, 1992)

6. G.A. Briggs, *Plume Rise, US Atomic Energy Commission. NTIS TID-25075* (NTIS, Springfield, 1969)
7. M. Luria, R.E. Imhoff, R.J. Valente, W.J. Parkhurst, R.L. Tanner, Rates of conversion of sulfur dioxide to sulfate in a scrubbed power plant plume. J. Air Waste Manage. Assoc. **51**(10), 1408–1413 (2001). https://doi.org/10.1080/10473289.2001.10464368
8. K. Kitabayashi, O. Yokoyama, *The Speed of Chemical Reaction of Nitrogen Oxides in the Atmosphere* (Sangyo Kogai, 1977)
9. K. Schofield, An evaluation of kinetic rate data for reactions of neutrals of atmospheric interest. Planet. Space Sci. **15**(4), 643–664 (1967)
10. K. Kitabayashi, S. Konishi, A. Katatani, A NOx plume dispersion model with chemical reaction in polluted environment. JSME Int. J. Ser. B Fluids Therm. Eng. **49**(1), 42–47 (2006). https://doi.org/10.1299/jsmeb.49.42
11. P. Yadav, R.K. Gaurav, B. Jahnavi, G.D. Ram, Prediction of PM, SO2 and NOX – GLC'S from point source emissions using air modeling. Int. J. Sci. Eng. Res. **4**(5), 5–9 (2013)
12. Y.H. Kim, H.S. Kim, C.H. Song, Development of a reactive plume model for the consideration of power-plant plume photochemistry and its applications. Environ. Sci. Technol. **51**(3), 1477–1487 (2017). https://doi.org/10.1021/acs.est.6b03919

Controlling Air and Metal Pollution in Industrial Area Singrauli, India: Role of Plants

Mala Kumari and Tanushree Bhattacharya

Abstract Plants play a pivotal role in purifying the atmosphere by absorbing particulate matter, heavy metals, and toxic substances and have been observed as a natural technique for mitigating air pollution. This study was conducted in the industrial area of Singrauli, Madhya Pradesh. This study aims to assess the air pollution tolerance index (APTI), dust-capturing capacity (DCC), and heavy metals concentration in plant species and the soil of the industrial area. Results showed that tree species such as *Azadirachta indica*, *Mangifera indica*, *and Ailanthus excelsa* had the highest APTI score and were considered the most tolerant species toward air pollution. Species such as *Calotropis gigantea*, *Anogeissus latifolia*, and *Tectona grandis* have low APTI values and are considered bioindicator species of air pollution. The investigation results suggested that tree species *Ficus bengalensis*, *Butea monosperma*, *Alstonia scholaris*, and *Anogeissus latifolia* show higher values in dust-capturing capacity. The study area is also contaminated with heavy metals such as Cu, Mn, Ni, and Zn. Species such as *Ailanthus excelsa*, *Anogeissus latifolia*, and *Alstonia scholaris* are suitable metal accumulator plant species and accumulate metals such as Mn, Al, Zn, Cr, Fe, Mg, Ni, and Cu. Suitable species can be suggested for green belt development in the industrial area.

Keywords Industrial area · Trees · Ascorbic acid · Chlorophyll content · Relative water content · pH · Air pollution tolerance index · Dust-capturing capacity · Heavy metals · Bioaccumulation factor

Abbreviations

AA	Ascorbic acid content
APTI	Air pollution tolerance index

M. Kumari · T. Bhattacharya (✉)
Department of Civil and Environmental Engineering, BIT Mesra, Ranchi, Jharkhand, India
e-mail: tbhattacharya@bitmesra.ac.in

D. Mazumder (ed.), *Sustainable Advanced Technologies for Industrial Pollution Control*, Springer Proceedings in Earth and Environmental Sciences,
https://doi.org/10.1007/978-3-031-37596-5_16

BAF	Bioaccumulation factor
CSE	Centre for Science and Environment
DCC	Dust-capturing capacity
FESEM	Field emission scanning electron microscopy
LpH	Leaf extract pH
RWC	Relative water content
TChl	Total chlorophyll content
TPP	Thermal power plants

1 Introduction

Air and heavy metals pollution nowadays is considered a well-known threat to developing countries' coal mine, industrial, and built-up or urban areas. Significant pollution sources are coal mining, industrialization, and urbanization [1]. The various sources of toxic heavy metals in the dust and soil of the coal mine environment are the air that contains coal dust, the discharge and dispersion of coal mine wastes, and transport activities [2]. Dust or particulate matter is examined as the most common and fastest-growing kind of environmental air pollutant and is the potential to cause a serious problem [3]. Trees are most efficient at absorbing and trapping numerous particles and play a fundamental role as an absorber or percolate of pollutants. The dust-capturing capacity of plants turns to several factors such as plant height, the density of leaves, size of leaves, canopy structure, age of leaves, leaf inclination, and external characteristics such as cuticle hair, and, meteorological condition [4]. The Centre for Science and Environment (CSE), India, states that coal-fired thermal power plants (TPP) are accountable for 50% of SO_2, NO_X emission, 60% of *PM* emission, and more than 80% of mercury emissions including all industries [5]. Chaudhary and Rathore (2019) gave a realistic information about how the dust deposition is influenced by industrialization, traffic behavior, urban development, and climatic condition and in addition, how the native vegetation act against air pollution and help to mitigate it [6]. Similar study is also performed by Mukhopadhyay et al. (2013) at Dhanbad, India, at Jharia coal mine region to control air pollution, and also this technique used to reclaim the coal mine area [7].

Singrauli is a significant coalfield in India and has a thermal power plant, and together this is becoming a threat to the local area. Additionally, many specialists have investigated the adverse effect of air pollution on plants all over the globe. Plant leaves act as an environmental sink, providing a wide surface area for impingement, soaking up, and accumulating air pollutants [8]. Comparatively, green belts adequately mitigate air pollution by trapping particulate matter and capturing gaseous pollutants. The present study focuses on plant species' role in controlling air pollution and metal phytoremediation. The main objective of this study was (i) to find the species which scored high in the air pollution tolerance index; (ii) investigate the species which can accumulate higher dust on the surface of the leaves by calculating (DCC); (iii) estimate the heavy metals present in the soil; (iv) find the bioaccumulation factor between leaves and soil; and (v) by accumulating all parameters, examine air pollution susceptible

plants for developing effective green belts in the coal mine, urbanized, and industrial areas to enhance the soil and air quality.

2 Materials and Methods

2.1 Study Area

Singrauli coalfield is situated between latitudes 23°47′ & 24°12′ N and longitude 81°40′ & 82°52′ E. The coalfields are about 102 km in length from west to east and 45 km wide from north to south, covering a total area of 2202 sq. km. The study area is highly polluted with coal mines and thermal power plants at the site. BIT Mesra, Ranchi, is chosen for the reference site because it is undisturbed by traffic and industrial pollution. It also has a large area surrounded by forest and cultivated land. Figure 1 shows the sampling points.

2.2 Sampling

Fresh and matured leaves of different species and soil samples from the industrial area of Singrauli and BIT Mesra (reference site) were collected in January 2022 because of the calm atmospheric condition. Leaves are plucked gently without disturbing the dust collected in the surface layer; secure the sample in a self-sealing zipper pouch; and instantly keep the sample in the icebox. A total of 27 tree and shrub species are chosen for sampling, commonly available in the study area. Approximately five replicates of each sample were collected so that sufficient quantities were there for further analysis. For soil, the sample is collected with the help of a stainless auger, and it is also collected in a zip lock pouch [9]. Soil samples were taken near the respective plants. A total ten soil samples were collected.

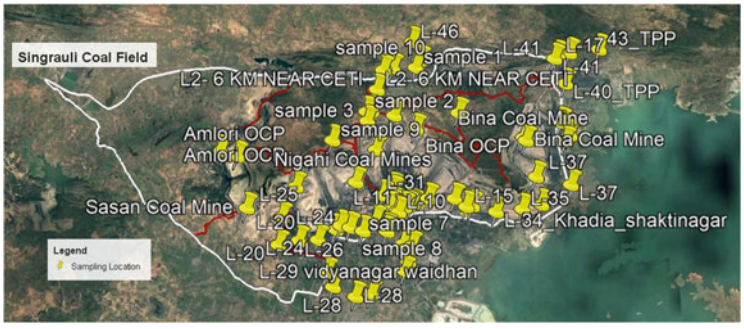

Fig. 1 Sampling location

2.3 Experimental Study

2.3.1 Biochemical Parameter of APTI

The air pollution tolerance index is subjected to basically four biochemical parameters of leaves, namely, total chlorophyll content (TChl), relative water content (RWC), ascorbic acid content (AA), and leaf extract pH (LpH). Ascorbic acid can be calculated by applying the standard method suggested by [10], by extracting 1 g of crushed leaf sample with 4% oxalic acid, and titrating it by taking 5 ml of supernatant sample and adding 10 ml of 4% oxalic acid against 2,6 dichlorophenol indophenol reagent. Ascorbic acid can be calculated by using the equation below:

$$\text{AA (mg/g)} = \frac{(0.5 \times V_2 \times 30)}{(V_1 \times 5 \times \text{weight of sample})} \tag{1}$$

where V_1 is the volume of dye consumed against working solution of standard; V_2 = volume of dye consumed against sample.

The RWC of the plant sample is calculated by using the standard method. The fresh weight (FW) of the leaf were taken; then soak the leaf in distilled water for 8 h and wipe the excess water with the help of tissue paper; then the turgid weight (TW) of the sample was taken; then place the sample at 70 °C for 8 h in the hot air oven; then note the dry weight (DW) of the leaf sample. RWC can be determined by using the following equation given by [11]:

$$\text{RWC (\%)} = \frac{(\text{FW} - \text{DW})}{(\text{TW} - \text{DW})} \times 100 \tag{2}$$

For leaf extract, pH 1 g of leaf is crushed with deionized water and makes up the final volume of up to 10 ml; then take the final pH reading with the help of a digital pH meter.

The TChl content of the sample was analyzed with the help of the standard method here; take 1 g of leaf sample, extract the sample with 80% acetone, and then make up the sample volume up to 30 ml with the help of 80% acetone. Centrifuge the sample at 300 rpm; then take the absorbance of the sample at 645 and 663 nm [12]. Calculate the chlorophyll content of the sample using the formula:

$$\text{Tchl (mg/g)} = \frac{(20.2 \times A_{645} + 8.02 \times A_{663}) + V}{1000 + W(\text{g})} \tag{3}$$

where A_{645} is the absorbance of leaf sample at 645 nm, A_{663} is the absorbance of leaf sample at 663 nm, V is the total volume of extract (ml), and W is the weight of the sample extracted (g).

Table 1 Categorization of APTI values

APTI range	Performance
≤14	Sensitive
15–19	Intermediate
20–24	Moderately tolerant
≥24	Tolerant

Finally, APTI will be calculated by using the formula [8, 13, 14]:

$$\text{APTI} = \frac{\text{AA} \times (\text{Tchl} + \text{pH}) + \text{RWC}}{10} \tag{4}$$

APTI is a reliable way of determining how susceptible various plants are to exposure to different polluted environments. The APTI index can be used to assess a plants capability to combat air pollution. The species which score higher APTI value is proven to be the tolerant species for air pollution, and the species which achieve lower APTI value is proven to be the sensitive species toward air pollution (Table 1).

2.3.2 Dust-Capturing Capacity (DCC)

The surface area of the plant's leaf was calculated using the CM × CM graph sheet to analyze the DCC of the plant species. Then leaves were washed with the help of a soft brush and distilled water. Then collect the washed distilled water in a beaker, and then filter the sample using pre-weighted filter paper [15]. Finally, calculate the DCC using the formula:

$$\text{DCC} = \frac{(\text{Final weight} - \text{initial weight of filter paper})}{\text{Surface area of leaf}}\ \text{mg/cm}^2 \tag{5}$$

2.3.3 Field Emission Scanning Electron Microscopy (FESEM)

The adaxial surface layer of leaf morphology images was detected at different magnification levels by FESEM. For this, the sample was prepared before analysis. The unwashed leaf was dried at 50 °C in hot air for 3 h. Then the leaf were cut 1-cm^2-sized strip. Then the sample was placed in the aluminum stub. A gold conductive layer was applied to the sample in a sputter coater. Finally, the sample was analyzed under FESEM.

2.3.4 Heavy Metal Analysis of Leaf and Soil Sample

Heavy metals in soil: 0.2 g sample was digested with Aqua regia. Make up the sample volume to 50 ml with 1% HNO_3.

Heavy metals in plants: 0.2 g samples were digested with H_2O_2 and HCl. Make up the sample volume to 50 ml with 1% HNO_3. The analysis of metals was done by ICP-OES [16, 17]. The metal standardization was done using multielement Certified Reference Material (CRM) (Perkin Elmer-multielement standard) before the sample analysis.

2.3.5 Bioaccumulation Factor (BAF)

The bioaccumulation factor (BAF) is applied to examine the accumulation capacity of plants for metals from the soil. The bioaccumulation factor can be calculated using the formula [18]:

$$\text{BAF} = \frac{\text{Concentration of metals in plant}}{\text{Concentration of metals in soil}} \text{ mg/kg} \quad (6)$$

2.4 Quality Control

All the analysis was carried out in triplicates, and the average data has been reported. Analytical grade reagents and standards were used for the chemical analysis.

2.5 Statistical Analysis

Correlation and heat map analysis were done between the metals available in soil and plants using Origin Pro 9.0.

3 Results and Discussion

3.1 Biochemical Parameter of APTI

Biochemical parameter estimation of variations in metabolites could be useful in the examination of the tolerant species. All the biochemical parameters have their proper role in the plant species. Chlorophyll plays a vital role in the process of photosynthesis in plants. Chlorophyll acts as an indicator of environmental quality. A high pH

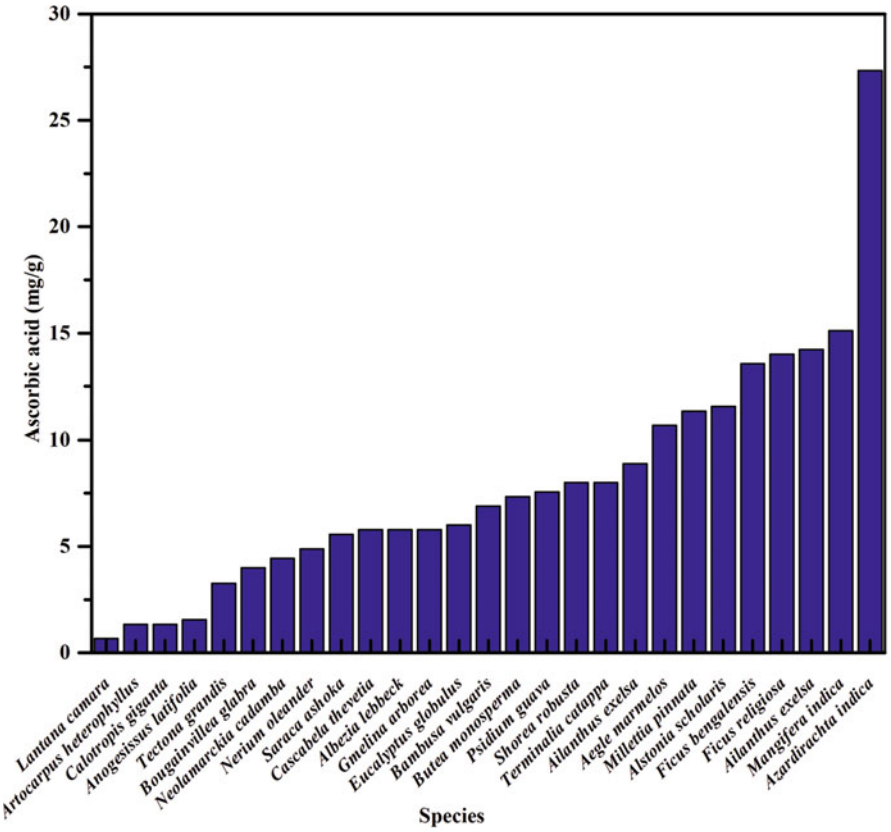

Fig. 2 Ascorbic acid content in leaf sample

value increases the hexo-sugar transformation efficiency to ascorbic acid. The higher value of relative water content in leaves can help in stress conditions to maintain their physiological balance [9].

The range air quality of the sampling site shows NO_2 (3.33–121.66), SO_2 (0.773–179.25), PM_{10} (7.71–253.18), and $PM_{2.5}$ (2.16–71.25μg/m^3). Due to the presence of open-cast mines and thermal power plants, the area is polluted with dust pollution.

From the result, it is found that in industrial areas, the AA content was found higher in the species *Azadirachta indica* dust pollution followed by *Mangifera indica*, *Ailanthus excelsa*, *Ficus religiosa*, *Ficus bengalensis*, *Alstonia scholaris*, and *Millettia pinnata*. This means these plants have a higher tendency to tolerate pollution. The value of ascorbic acid increases with ambient air pollution [5]. Species that found lower ascorbic acid are *Lantana camara* followed by *Artocarpus heterophyllus*, *Calotropis gigantea*, *Anogeissus latifolia*, and *Tectona grandis*. Similar findings were reported by [19] in Punjab, India, where the prime source of

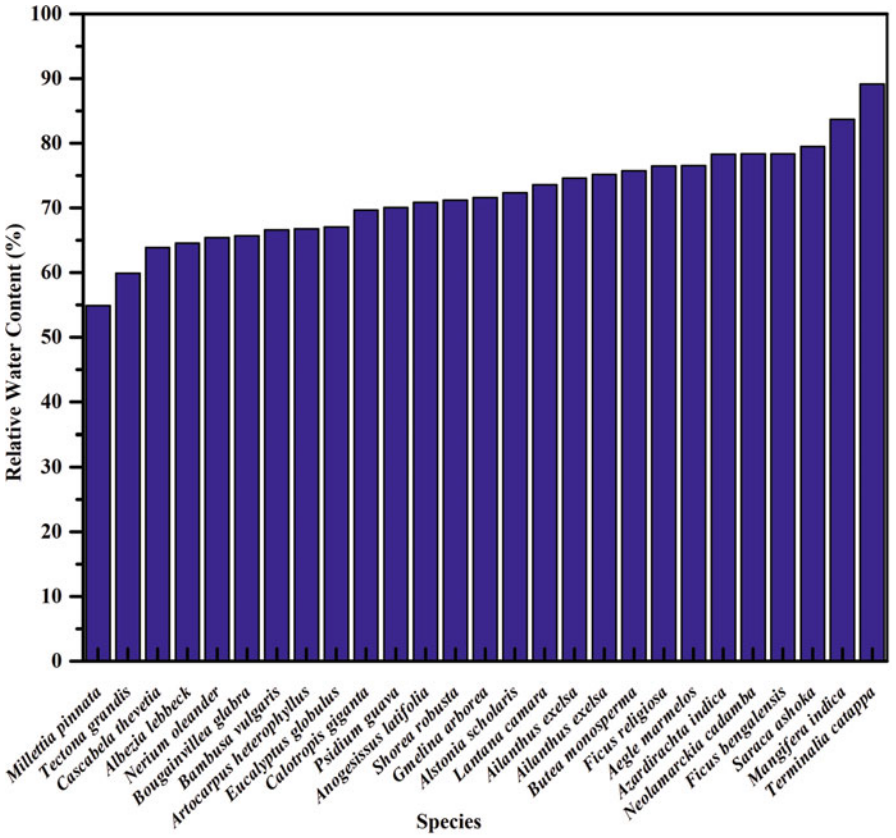

Fig. 3 Relative water content in leaf sample

pollution are urbanization and road traffic. Figures 2 and 3 show the AA value of plant samples in the industrial area.

The RWC was higher in the species of *Terminalia catappa* followed by *Mangifera indica*, *Saraca asoca*, *Ficus bengalensis*, *Neolamarckia cadamba*, *Azadirachta indica*; the lowest values were observed in the species such as *Millettia pinnata* followed by *Tectona grandis*, *Cascabela thevetia*, and *Albizia lebbeck*. A similar kind of study was reported by [20] in Mizoram, India, where also road traffic was the main reason for pollution. The species with higher RWC value can survive stressful conditions and possess an excellent capacity to balance the drought conditions [21]. Figure 3 shows the RWC of the plant sample in the industrial area.

The industrial site's pH range is 4.97–8.65. The findings show a higher pH value in the *Lantana camara* followed by *Psidium guajava*, *Terminalia catappa*, *Aegle marmelos*, *Ficus religiosa*, and *Ailanthus excelsa*. The species with the lowest pH values are *Albizia lebbeck* followed by *Anogeissus latifolia*, *Neolamarckia cadamba*, *Nerium oleander*, and *Eucalyptus globulus*. Figure 4 shows that

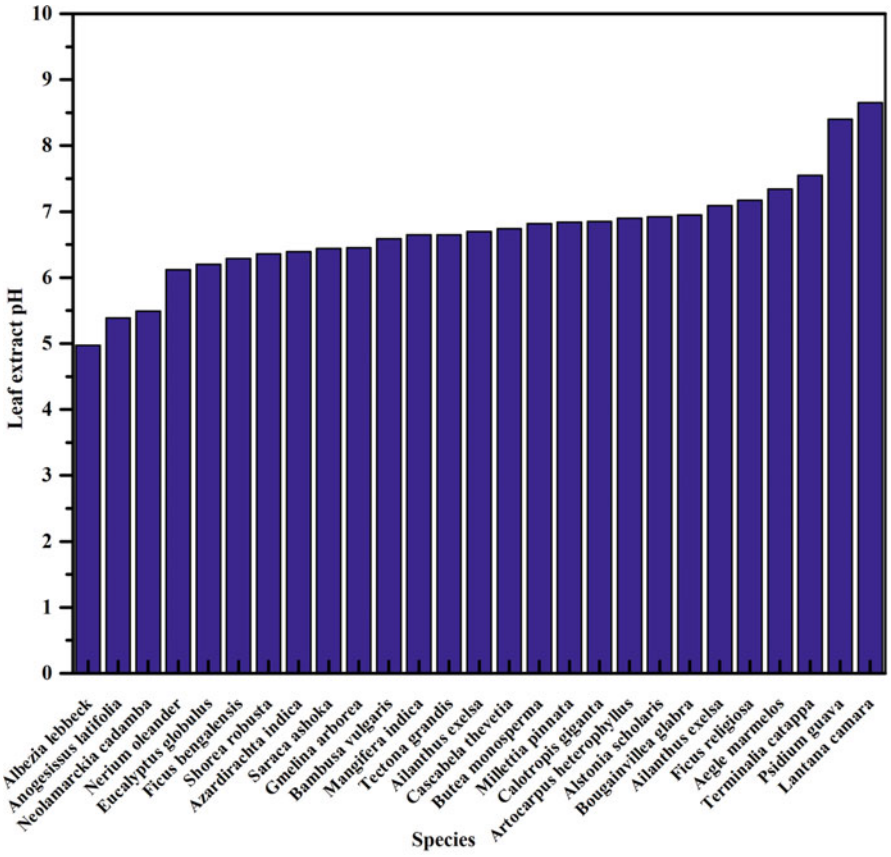

Fig. 4 Leaf extract pH in plant sample

maximum plants have a pH value below 7 which means that the environment is polluted with SO_X and NO_X [22].

The increasing chlorophyll content in plant samples is favorable and augments tolerance to polluted environments. Chlorophyll content in plant species was deteriorated by temperature, gaseous pollutants, particulate matter, and drought conditions [23]. Figure 5 shows the chlorophyll content of plant samples in an industrial area. In the current study, the more excellent value of chlorophyll was observed in the species of *Artocarpus heterophyllus* followed by *Aegle marmelos*, *Ficus religiosa*, *Gmelina arborea*, *Bambusa vulgaris*, and *Bougainvillea glabra.* The lowest total chlorophyll content species are *Ficus bengalensis*, *Ailanthus excelsa*, *Lantara camara*, and *Butea monosperma*. A very similar finding was reported by [24] in Punjab, India.

All four biochemical variables were applied for the calculation of the APTI value. APTI determines the tolerance ability of particular tree species toward air pollution. The value ranges between 7.91 and 28.32. Figure 6 shows the APTI value of plant

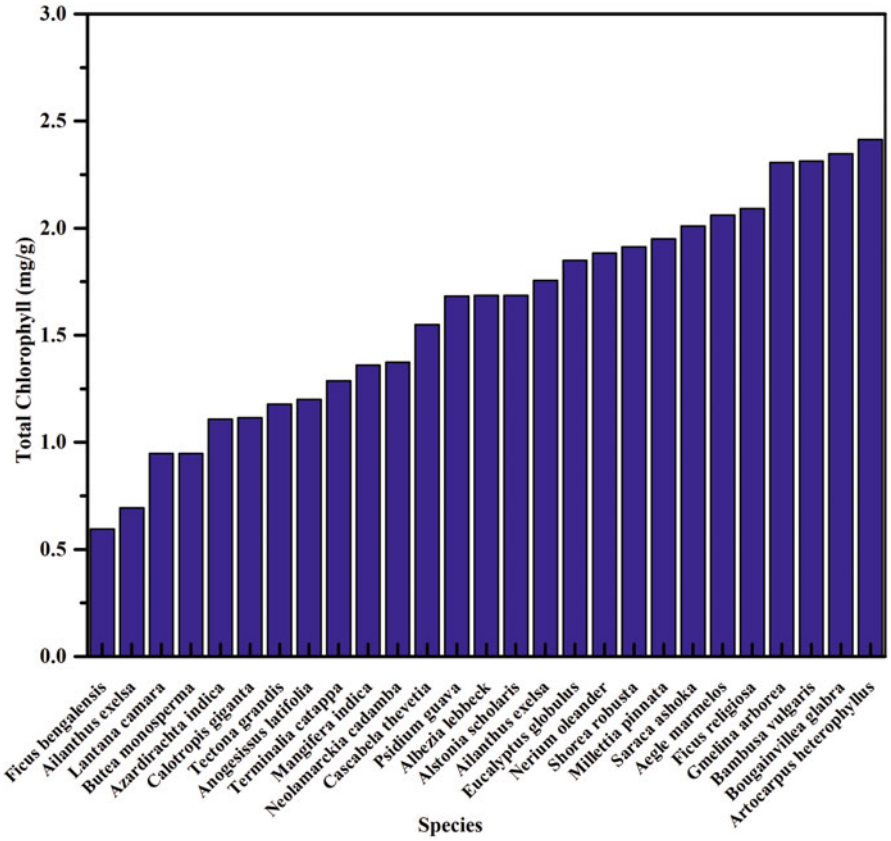

Fig. 5 Total chlorophyll content in plant sample

samples in the industrial area. *Azadirachta indica* is the most tolerant species of all. *Ficus religiosa* and *Mangifera indica* is a moderately tolerant species. *Aegle marmelos*, *Ailanthus excelsa*, *Ficus bengalensis*, *Terminalia catappa*, and *Millettia pinnata* were the intermediate susceptible species. The plant species which score APTI value below 15 are the most sensitive species, such as *Artocarpus heterophyllus*, *Lantara camara*, *Calotropis gigantea*, *Anogeissus latifolia*, and *Tectona grandis*. A similar kind of trend was reported by many studies [19, 20], and [24–26]. Comparatively, the control site (BIT, Mesra) scored the APTI value lower than the industrial site because of the lower pollution in the control site [11]. Figure 7 shows the APTI value of the industrial site and control site.

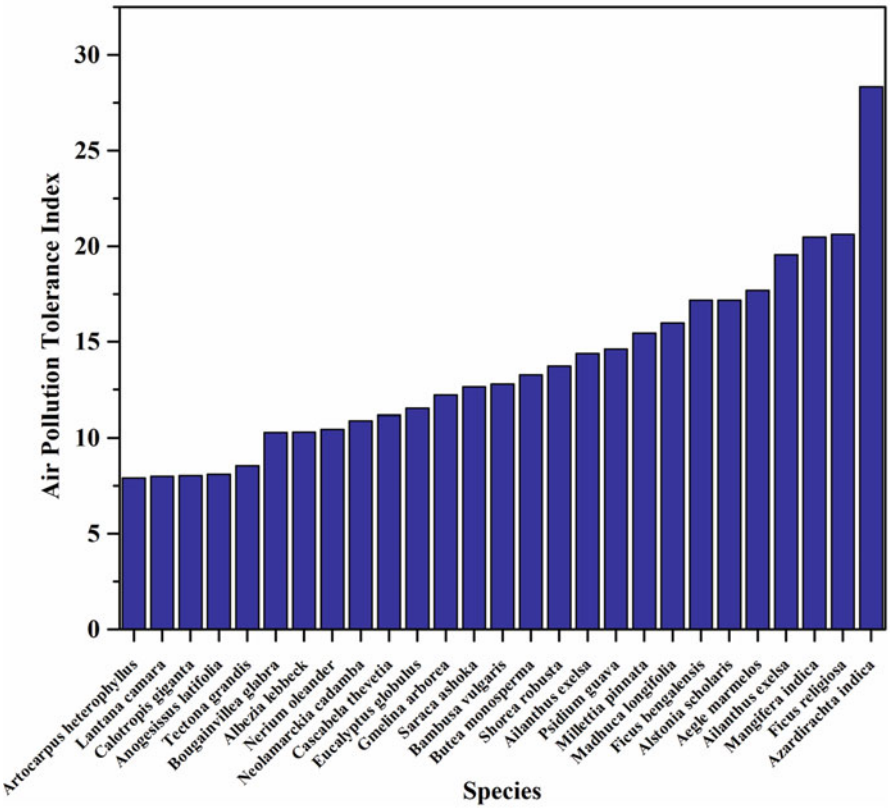

Fig. 6 APTI Score of plant sample in an industrial site

3.2 Dust-Capturing Capacity

The results of the investigation suggested that species *Ficus bengalensis* (3.171), *Butea monosperma* (3.038), *Alstonia scholaris* (2.55), and *Anogeissus latifolia* (2.885) demonstrate the highest dust-capturing capacities. Dust was grasped from the environment and held on the leaf depending on various morphological characteristics such as texture, lamina shape and size, the orientation of the leaf, presence/absence of hairs, and length of the petiole [27]. Figure 8 shows that species such as *Gmelina arborea*, *Eucalyptus globulus*, and *Dalbergia sissoo* have the low dust-capturing capacity, which might be because of the absence of cuticle hair on the surface layer of the leaf, and the inclination of the leaf not supporting in holding the dust [25]. Also the species with a smooth texture and lack of glandular trichomes can accumulate less dust on its surface. Similar values are scored by [28, 29]. Figure 9a, b depicts how the leaf accumulates dust on the surface layer. Figure 9a, b shows how the dust accumulates on the leaves surface.

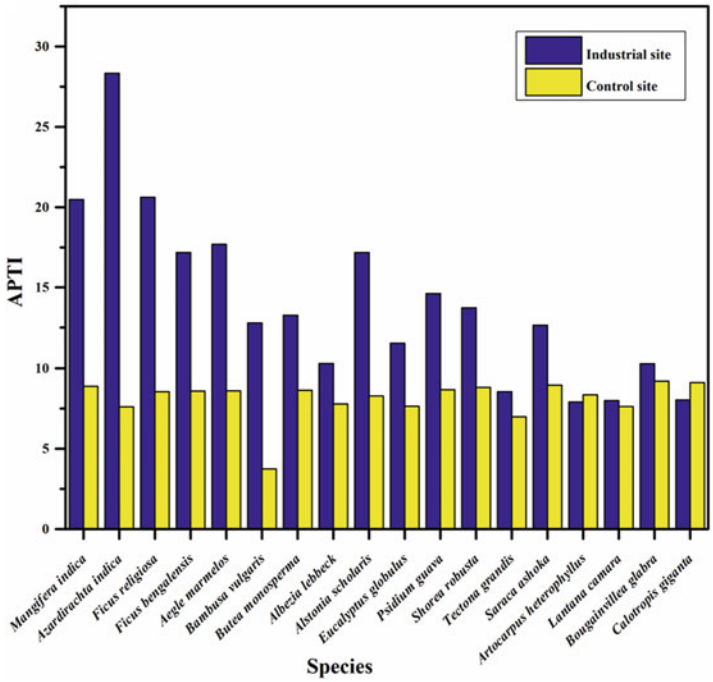

Fig. 7 APTI value of plants in industrial site (Singrauli) and control site (BIT Mesra)

3.3 Estimation of Metals in Soil and Plants

Heavy metals such as Ni (46.25), Cd (1.25), Zn (106.667), and Cu (39.5) surpass the acceptance range according to the WHO (1996) guidelines in soil [30] (Table 2). Heavy metals such as Zn, Cd, Cu, Cr, and Ni in the plant sample also exceeded the permissible limit in almost all species. Heavy metals are very harmful to plant health, but those species that accumulate metals and still exist in the atmosphere are considered the most resilient species [31]. Figure 10 shows the bioaccumulation factor graph. The species such as *Ailanthus excelsa*, *Alstonia scholaris*, and *Shorea robusta* are suitable metal accumulator plant species and accumulate metals such as Zn, Cr, Cu, Fe, Mn, Ni, Mg, and Al. Species such as *Terminalia catappa* ($R^2 = 0.95$), *Anogeissus latifolia* ($R^2 = 0.93$), *Mangifera indica* ($R^2 = 0.91$), *Ailanthus excelsa* ($R^2 = 0.87$), and *Alstonia scholaris* ($R^2 = 0.86$) show significant correlation with the heavy metals in soil. Figure 11 demonstrates the heat map of the correlation between the metals present in the soil and leaf.

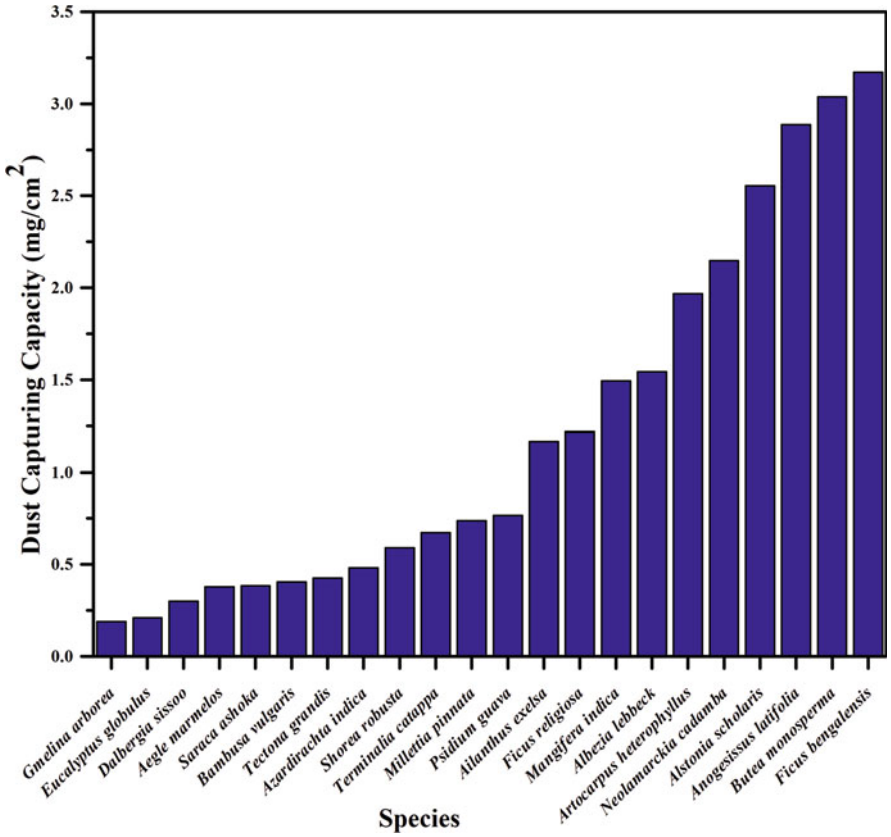

Fig. 8 Dust-capturing capacity of plant sample in industrial area

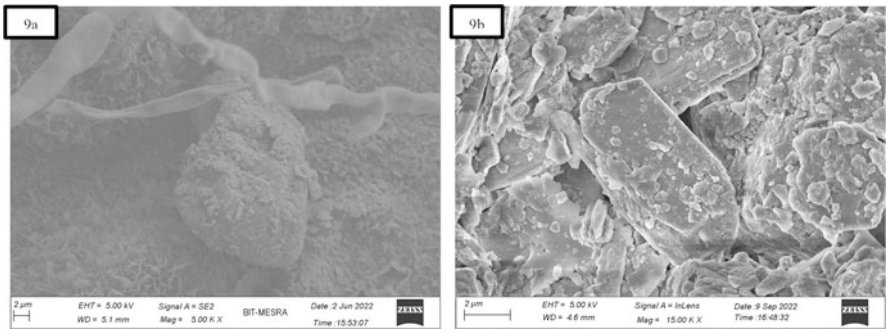

Fig. 9 FESEM images showing dust accumulation on the adaxial surface of leaves. (**a**) *Ficus bengalensis* showing large particles on the surface and glandular trichomes and (**b**) *Butea monosperma* showing the flaky particle present with the large size particles

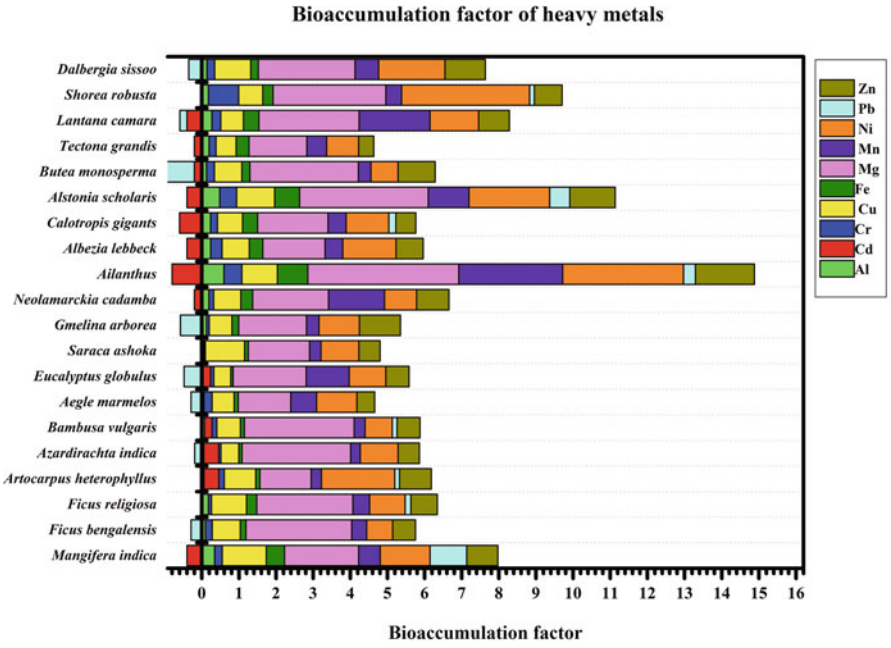

Fig. 10 Bioaccumulation factor plot for heavy metals in plant

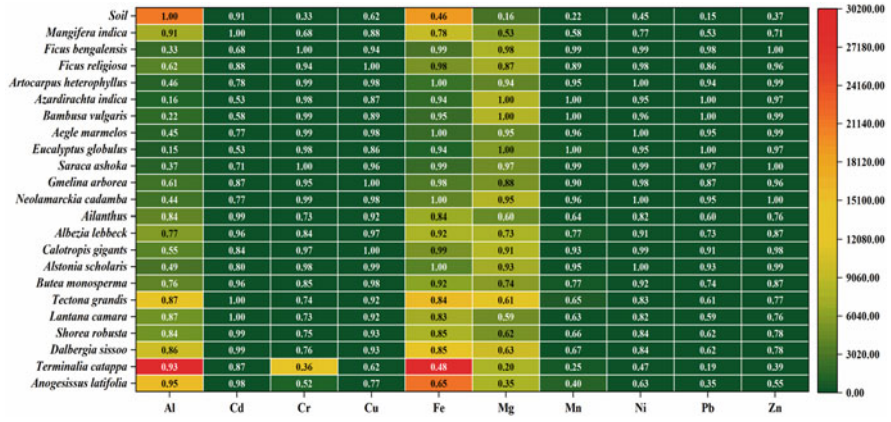

Fig. 11 Heat map shows the correlation between the metal concentration of soil and plant species

Table 2 Metal concentration found in soil sample

Metals	Average metal contamination	Permissible limit according to WHO
Cu	39.5	36
Mg	2843.083	NA
Mn	273.1667	200
Ni	46.25	35
Pb	7.833333	NA
Zn	106.6667	50
Cr	77.41667	100
Co	12.16667	NA
Cd	0.416667	NA
Al	21,090	NA
Fe	19,188.33	55,000

4 Conclusion

This study has recognized and identified various tree species growing commonly in the Singrauli mine area and control site BIT. An overview of the complete result acquire from this study reveals that different individual species respond distinguishable and dissimilar to air pollution. As this study reveals, particular plant species behave distinctively to air pollution. Using metal concentration, DCC, and APTI indicator species, suitable plants should be selected based on their vulnerability to pollution load. The present study shows excellent *Azadirachta indica*, *Mangifera indica*, *Ailanthus excelsa*, *Ficus bengalensis*, *Ficus religiosa*, and *Alstonia scholaris* results in APTI. Plants such as *Ficus bengalensis*, *Butea monosperma*, *Alstonia scholaris*, and *Anogeissus latifolia* are suggested as good species for dust pollution and can be good to plant in industrial and mine areas. Plant species such as *Tectona grandis*, *Calotropis gigantea*, and *Artocarpus heterophyllus* are examples of sensitive plant species that can be used as bioindicators and have lower APTI values. Heavy metals uptake by plants using phytoremediation technology seems to be a prosperous way to remediate the heavy-metal-contaminated environment. The present study found that species such as *Ailanthus excelsa*, *Alstonia scholaris*, and *Shorea robusta* are good bioaccumulator of heavy metals in the environment and can be used to control heavy metals pollution in the environment. Significantly, the susceptible plant species can be appointed into a green belt design of Singrauli coalfield to effectively aid in everlasting air pollution control.

Acknowledgments I am thankful to Birla Institute of Technology, Mesra, Ranchi, for furnishing the institute research fellowship (Ref. No. GO/SS/Ph.D/IRF/2021-22/0997).

References

1. N. Tripathi, R.S. Singh, C.P. Nathanail, Mine spoil acts as a sink of carbon dioxide in Indian dry tropical environment. Sci. Total Environ. **468–469**, 1162–1171 (2014). https://doi.org/10.1016/j.scitotenv.2013.09.024
2. D. Raj, A. Chowdhury, S.K. Maiti, Ecological risk assessment of mercury and other heavy metals in soils of coal mining area: A case study from the eastern part of a Jharia coal field, India. Hum. Ecol. Risk. Assess. **23**(4), 767–787 (2017). https://doi.org/10.1080/10807039.2016.1278519
3. W. Zhang et al., Comparison of the suitability of plant species for greenbelt construction based on particulate matter capture capacity, air pollution tolerance index, and antioxidant system. Environ. Pollut. **263**, 114615 (2020). https://doi.org/10.1016/j.envpol.2020.114615
4. F. Shao et al., Study on different particulate matter retention capacities of the leaf surfaces of eight common garden plants in Hangzhou, China. Sci. Total Environ. **652**, 939–951 (2019). https://doi.org/10.1016/j.scitotenv.2018.10.182
5. S. Mondal, G. Singh, Air pollution tolerance, anticipated performance, and metal accumulation capacity of common plant species for green belt development. Environ. Sci. Pollut. Res. **29**(17), 25507–25518 (2022). https://doi.org/10.1007/s11356-021-17716-8
6. I.J. Chaudhary, D. Rathore, Dust pollution: Its removal and effect on foliage physiology of urban trees. Sustain. Cities Soc. **51**, 101696 (2019). https://doi.org/10.1016/j.scs.2019.101696
7. S. Mukhopadhyay, S.K. Maiti, R.E. Masto, Use of Reclaimed Mine Soil Index (RMSI) for screening of tree species for reclamation of coal mine degraded land. Ecol. Eng. **57**, 133–142 (2013). https://doi.org/10.1016/j.ecoleng.2013.04.017
8. A. Balasubramanian, C.N.H. Prasath, K. Gobalakrishnan, S. Radhakrishnan, Air pollution tolerance index (APTI) assessment in tree species of Coimbatore urban city, Tamil Nadu, India. Int. J. Environ. Clim. Chang. **8**, 27–38 (2018). https://doi.org/10.9734/ijecc/2018/v8i127106
9. M. Krishnaveni, R. Chandrasekar, L. Amsavalli, P. Madhiyan, S. Durairaj, Air pollution tolerance index of plants at Perumalmalai hills, Salem, Tamil Nadu, India. Int. J. Pharm. Sci. Rev. Res. **20**(1), 234–239 (2013)
10. T. Keller, H. Schwager, Air pollution and ascorbic acid. Eur. J. For. Pathol. **7**(6), 338–350 (1977). https://doi.org/10.1111/j.1439-0329.1977.tb00603.x
11. A. Nadgórska-Socha, M. Kandziora-Ciupa, M. Trzęsicki, G. Barczyk, Air pollution tolerance index and heavy metal bioaccumulation in selected plant species from urban biotopes. Chemosphere **183**, 471–482 (2017). https://doi.org/10.1016/j.chemosphere.2017.05.128
12. S. Jain, T. Bhattacharya, S. Chakraborty, *Advances in Waste Management* (Springer, Singapore, 2019)
13. P. Kamble et al., Impact of transport sector emissions on biochemical characteristics of plants and mitigation strategy in Pune, India. Environ. Chall. **4**, 100081 (2021). https://doi.org/10.1016/j.envc.2021.100081
14. S.K. Bharti, A. Trivedi, N. Kumar, Air pollution tolerance index of plants growing near an industrial site. Urban Clim. **24**, 820–829 (2018). https://doi.org/10.1016/j.uclim.2017.10.007
15. Manisha, E. Suresh Pandian, A.K. Pal, Dust arresting capacity and its impact on physiological parameter of the plants, in *Strategic Technologies of Complex Environmental Issues – A Sustainable Approach*, (Excellent Publishing House, New Delhi, 2014), pp. 111–115
16. W. Xiao, G. Lin, X. He, Z. Yang, L. Wang, Interactions among heavy metal bioaccessibility, soil properties and microbial community in phyto-remediated soils nearby an abandoned realgar mine. *Chemosphere* **286**(P1), 131638 (2022). https://doi.org/10.1016/j.chemosphere.2021.131638
17. N. Zheng et al., Health risk assessment of heavy metals in street dust around a zinc smelting plant in China based on bioavailability and bioaccessibility. Ecotoxicol. Environ. Saf. **197**, 110617 (2020). https://doi.org/10.1016/j.ecoenv.2020.110617

18. W. D. C. Office of the Science Advisor, *Framework for Metal Risk Assessment* (U.-S. Environmental Protection Agency (EPA), Washington, DC, 2007)
19. R. Yadav, P. Pandey, Assessment of air pollution tolerance index (APTI) and anticipated performance index (API) of roadside plants for the development of greenbelt in urban area of Bathinda city, Punjab, India. Bull. Environ. Contam. Toxicol. **105**(6), 906–914 (2020). https://doi.org/10.1007/s00128-020-03027-0
20. P.K. Rai, L.L.S. Panda, Dust capturing potential and air pollution tolerance index (APTI) of some road side tree vegetation in Aizawl, Mizoram, India: An Indo-Burma hot spot region. Air Qual. Atmos. Health **7**(1), 93–101 (2014). https://doi.org/10.1007/s11869-013-0217-8
21. V.É. Molnár, E. Simon, B. Tóthmérész, S. Ninsawat, S. Szabó, Air pollution induced vegetation stress – The Air Pollution Tolerance Index as a quick tool for city health evaluation. Ecol. Indic. **113**, 106234 (2020). https://doi.org/10.1016/j.ecolind.2020.106234
22. S.K. Maiti, C. Shee, M.K. Ghose, Selection of plant species for the reclamation of mine-degraded land in the Indian context. L. Contam. Reclam. **15**(1), 55–65 (2007). https://doi.org/10.2462/09670513.690
23. S. Banerjee, D. Palit, A. Banerjee, Variation of tree biochemical and physiological characters under different air pollution stresses. Environ. Sci. Pollut. Res. **28**(14), 17960–17980 (2021). https://doi.org/10.1007/s11356-020-11674-3
24. S.K. Prajapati, B.D. Tripathi, Anticipated performance index of some tree species considered for green belt development in and around an urban area: A case study of Varanasi city, India. J. Environ. Manag. **88**(4), 1343–1349 (2008). https://doi.org/10.1016/j.jenvman.2007.07.002
25. S. Shrestha, B. Baral, N.B. Dhital, H.H. Yang, Assessing air pollution tolerance of plant species in vegetation traffic barriers in Kathmandu Valley, Nepal. Sustain. Environ. Res. **31**(1), 1–9 (2021). https://doi.org/10.1186/s42834-020-00076-2
26. C. Sahu, S. Basti, S.K. Sahu, Air pollution tolerance index (APTI) and expected performance index (EPI) of trees in Sambalpur town of India. SN Appl. Sci. **2**(8), 1–14 (2020). https://doi.org/10.1007/s42452-020-3120-6
27. S. Singh, B. Pandey, L.B. Roy, S. Shekhar, R.K. Singh, Tree responses to foliar dust deposition and gradient of air pollution around opencast coal mines of Jharia coalfield, India: Gas exchange, antioxidative potential and tolerance level. Environ. Sci. Pollut. Res. **28**(7), 8637–8651 (2021). https://doi.org/10.1007/s11356-020-11088-1
28. S.S. Ram et al., Plant canopies: Bio-monitor and trap for re-suspended dust particulates contaminated with heavy metals. Mitig. Adapt. Strateg. Glob. Chang. **19**(5), 499–508 (2014). https://doi.org/10.1007/s11027-012-9445-8
29. A. Roy, T. Bhattacharya, M. Kumari, Air pollution tolerance, metal accumulation and dust capturing capacity of common tropical trees in commercial and industrial sites. Sci. Total Environ. **722**, 137622 (2020). https://doi.org/10.1016/j.scitotenv.2020.137622
30. F.O. Ohiagu, K.C. Lele, P.C. Chikezie, A.W. Verla, C.E. Enyoh, Bioaccumulation and health risk assessment of heavy metals in Musa paradisiaca, Zea mays, Cucumeropsis mannii and Manihot esculenta cultivated in Onne, Rivers state, Nigeria. Environ. Anal. Health Toxicol. **35**(2), 1–9 (2020). https://doi.org/10.5620/eaht.e2020011
31. I. Skrynetska, R. Ciepał, M. Kandziora-Ciupa, G. Barczyk, A. Nadgórska-Socha, Ecophysiological responses to environmental pollution of selected plant species in an industrial urban area. Int. J. Environ. Res. **12**(2), 255–267 (2018). https://doi.org/10.1007/s41742-018-0088-9

Part IV
Industrial Solid Waste Management

Enhancing the Dewatering Ability of Sludge by Locally Available Biomass

Gaurao Chopade and C. P. Devatha

Abstract In this study, the effect of modified coconut shell biochar is analyzed for its efficacy achievable in sludge dewatering properties. Initially the coconut shell biochar is modified at different molar concentrations of $FeCl_3$, i.e., 1, 2, and up to 5 mol/L, and it is analyzed with different dosages at 0.1, 0.2, and up to 0.4 (g/g of dry solids (DS)) for the improvement in capillary suction time (CST) (s), moisture content reduction (%), filterability (min), and settleability (SV_{30}%) of the sludge. It is found that there is significant decrease in each of these parameters. The optimization study is carried out to optimize the process of sludge conditioning, considering independent regression parameters as dosage (g/g of DS), molarity (M), mixing time (min), and response taken as moisture content (%), the optimum values for the dosage, molarity, mixing time is found to be 0.4 (g/g of DS), 2.5 M and 24.72 min, respectively, with optimized moisture content value of 78% was achieved. Hence, the modified coconut shell biochar can be used as a potential candidate to increase the dewatering ability of the sludge.

Keywords Biomass · Biochar · Conditioning · Dewatering · RSM · Optimization · Sludge · Vicinal water · Sewage

1 Introduction

At any wastewater treatment plant, sludge management plays an important role, and it costs a huge investment. Industrial and sewage effluents in the form of a semisolid slurry (sludge consisting of 99% of water and 1% of solids approximately depending on the source of effluent coming out from) are necessary to be managed before releasing them into the natural river streams, or else they will cause a nuisance to the environment [1]. One way for sludge management is conditioning and dewatering

G. Chopade · C. P. Devatha (✉)
Department of Civil Engineering, National Institute of Technology Karnataka, Surathkal, Karnataka, India
e-mail: devathafce@nitk.edu.in

D. Mazumder (ed.), *Sustainable Advanced Technologies for Industrial Pollution Control*, Springer Proceedings in Earth and Environmental Sciences,
https://doi.org/10.1007/978-3-031-37596-5_17

which in the initial stages of development in sludge management methodologies use to be done by implementing the chemical coagulants such as alum or chlorides of aluminum (e.g., $AlCl_3$), along with cationic polyelectrolyte. The disadvantage of this process is that they play the role of chemical conditioners, but do not improve the physical properties namely porosity, permeability, and compressibility [2]. To improve the physical properties, an experimental investigation was carried out on various biochars made from sugarcane bagasse, walnut shell, and rice straw and revealed the improvement in the dewatering ability of the sludge [3–5].

The aim of this work focuses on sludge conditioning and dewatering by modified coconut shell biochar (MCSB-$FeCl_3$) which is abundantly available across the coastal parts of the state of Karnataka, India. Here, in the current study, sludge conditioning and dewatering are performed by adopting the mentioned biochar. Further, its characterization was carried out to check the change in microstructures. It is carried out in three phases. In phase I, preparation of modified coconut shell was performed at different molarities. Phase II includes experimental estimation of dewatering parameters (CST, moisture content, filterability, and settleability), to obtain the range of values to be adopted for the input parameters involved in the optimization study. In Phase III, optimization study was studied, where input parameters include dosage, molarity, and mixing time and the output parameter taken into consideration was moisture content.

2 Materials and Methods

2.1 Materials

The sludge sample for the current study was taken from the sewage treatment plant of NITK, Surathkal, Karnataka, India. Chemicals used for modification purposes are ferric chloride ($FeCl_3$) and HCl made from Loba Chemie Pvt. Ltd., India, and Sbl Ltd. The raw coconut shell was collected from the local areas of Karnataka.

2.2 Methodology

2.2.1 Preparation of MCSB-$FeCl_3$

The preparation of modified coconut shell biochar involves grinding dried coconut shells to make them into a fine powder sieved from the 210 µm sieve. The obtained powder of coconut shells was used for making of biochar at 600 °C for 2 h, which is sieved from the then biochar is soaked in 2 mol/L HCl for about 24 h thereafter on filtering and drying in a hot air oven it is sonicated for 2 h in sonication bath with different molarities of $FeCl_3$ and again filtered and dried and used for further analysis [6] (Fig. 1).

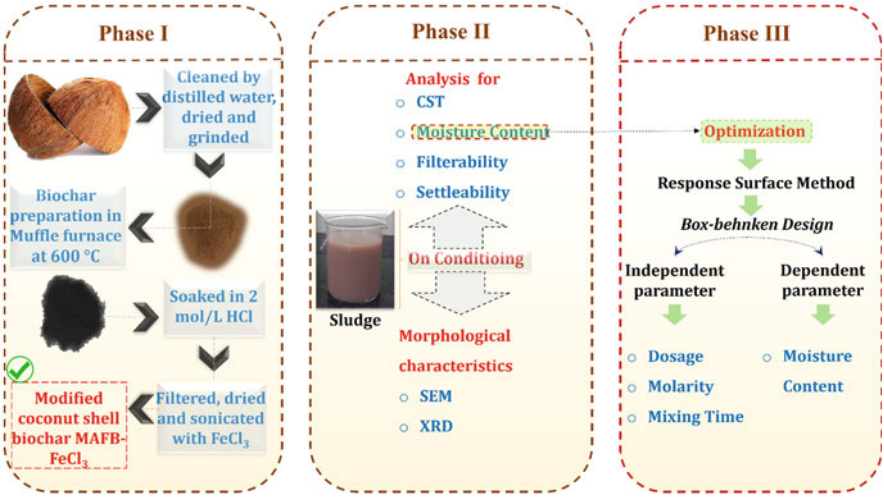

Fig. 1 Representation of methodology adopted for enhancing the sludge dewatering ability

2.2.2 Analytical Methods

Capillary Suction Time (CST)

CST is referred to as the rate of water release from a sludge, and it is a significant parameter in the dewatering aspect. The CST test is performed using the setup which consists of Whatman filter paper #17, a glass tube with both ends opened, and a timer. The conditioned sludge is filled into the tube from the top up to 5 cm from the bottom of the tube and placed on filter paper. The time wetting the filter paper from a 1.5 to 3 cm radius marked on the paper is taken as CST time [7].

Moisture Content (MC)

The MC of sludge solids (sludge cake) obtained was calculated using the Buchner funnel apparatus. The conditioned sludge was poured on top of the Buchner funnel apparatus consisting of filter paper. The wet retained sludge cake on the top of filter paper has to be weighed, and after that the sample of sludge cake dried in the oven for about 24 h at 105 °C, and the dried mass of sludge cake has to be weighed again, and the difference between the dried and wet mass of sludge cake gives the moisture content percentage [8].

Filterability

It is the time taken by the water to drain out from the sludge when poured into the vacuum filtration apparatus. The vacuum filtration setup consists of a filter paper, funnel, and vacuum pump [9].

Settleability

The settleability of sludge is measured as the volume occupied by sludge, when it is allowed to settle for 30 min in the measuring cylinder, and it is expressed as sludge volume (SV_{30}%). The test was performed using the 100 mL measuring cylinders, and the sludge was poured into the cylinder after 30 min of settling, and volume occupied by sludge is noted [10].

3 Results and Discussion

Initial sewage sludge characteristics are shown in Table 1, the pH of 7.4 shows the sludge is slightly in alkaline condition, and also there is approximately 19,769 mg/L of total solids present in the sewage sludge before conditioning.

3.1 Morphological Characteristics

In Fig. 2, morphological characteristics of sludge and biochar are presented. The raw sludge (Fig. 2a) has a denseness within the sludge cake, which acts like a barrier to the flow of water during the mechanical dewatering of the sludge. In contrast, on conditioning the sludge with MCSB-$FeCl_3$ (Fig. 2b), due to the agglomeration of the sludge flocs, more porous microstructures can be seen with slight voided structures. The porous and voids within the conditioned sludge allow the trapped water to pass with ease during the dewatering process; hence, this points toward the improvement

Table 1 Raw sludge characteristics

Parameters	Units	Values
pH	–	7.4
Temperature	°C	27
Total solids	mg/L	19,769
Capillary suction time	s	92
Moisture content	%	97
Filtration time	min	30
Electrical conductivity	ms/cm	3.25
Turbidity	NTU	4

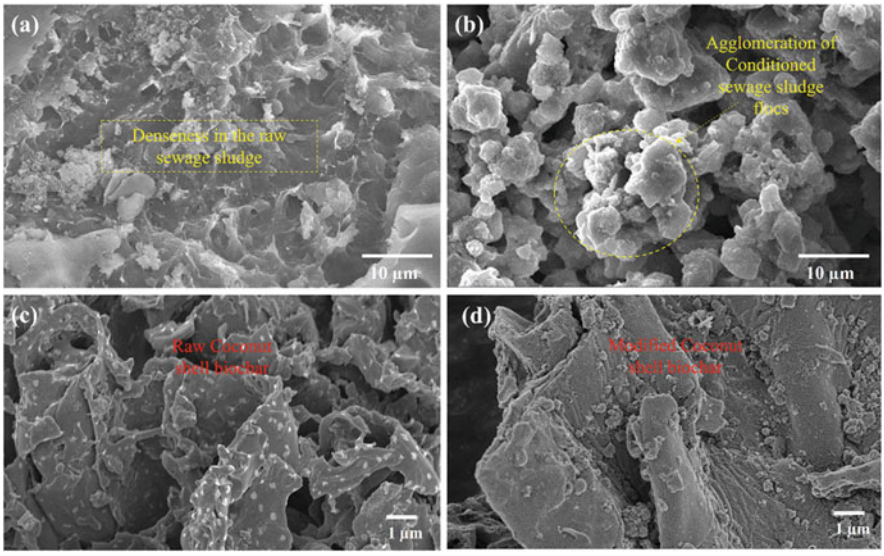

Fig. 2 Morphological characteristics. (**a**) Raw sludge. (**b**) Conditioned sludge. (**c**) Raw coconut biochar. (**d**) MCSB-$FeCl_3$

in the sludge dewatering ability. Figure 2c, d shows the recorded microstructures of the raw coconut shell biochar and MCSB-$FeCl_3$ where porous morphology can be seen. The X-ray diffraction (XRD) of MCSB-$FeCl_3$ is shown in Fig. 3. The XRD graphs represent the compounds present in the material; here peak at 30° indicates the presence of $FeCl_3$ in modified biochar.

3.2 The Effects of MCSB-$FeCl_3$ on the CST, Moisture Content, Filterability, and Settleability

The dewatering properties of sewage sludge were examined in Fig. 4a–d after conditioning with MCSB-$FeCl_3$ at various molarities (1, 2, 3, 4, and 5 mol/L) and dosages (g/g of DS). The study evaluated the effects on CST (s), moisture content (%), filterability, and settleability through experimental analysis. As a control sample, raw sewage sludge values were used without conditioning. Initially, sludge conditioning was performed at a dosage of 0.1 (g/g of DS) and gradually increased by 0.1 (g/g of DS) up to 0.4 (g/g of DS).

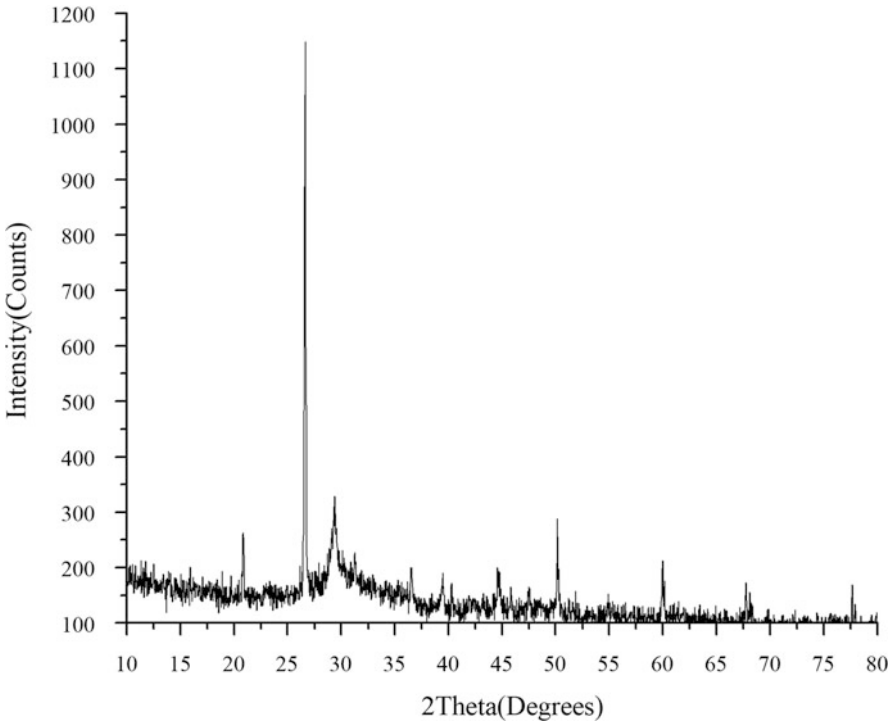

Fig. 3 XRD of MCSB-$FeCl_3$

3.2.1 Effects on CST and Moisture Content

In the range of 0.2–0.4 (g/g of DS) with molarities of MCSB-$FeCl_3$ as 1, 2, and 3 mol/L there was a considerable decrease in CST values of conditioned sludge. The study revealed that the lowest decrease in CST occurred when the sewage sludge was conditioned with MCSB-$FeCl_3$ at 3 mol/L and a dosage of 0.4 (g/g of DS), with a reduction of 60.87%. For dosages of 0.4, no significant decrease in CST values was observed for 4 and 5 mol/L compared to those achieved at lower molarities for the same dosage of MCSB-$FeCl_3$. The reduction in CST values is favorable as it indicates improvement in dewatering efficiency. The possible mechanism can be the structural modifications and release of trapped water inside the sludge flocs. The structural changes were achieved due to the addition of coconut shell biochar which acts as a skeleton builder and provides more porosity to the conditioned sludge (Fig. 2b). Also, $FeCl_3$ helps to release the trapped water from the sludge flocs [11].

The gradual decrease in the moisture content of sludge cake was observed in the range of 0.1, 0.2, and up to 0.4 (g/g of DS) with molarities of MCSB-$FeCl_3$ as 1, 2, and 3 mol/L. The minimum reduction in moisture content (%) was achieved at 3 mol/L with a dosage of 0.4 to 77%. The raw sludge cake has a moisture content of 97%; reduction in the moisture content of sludge cake at a dosage of 0.4 was not

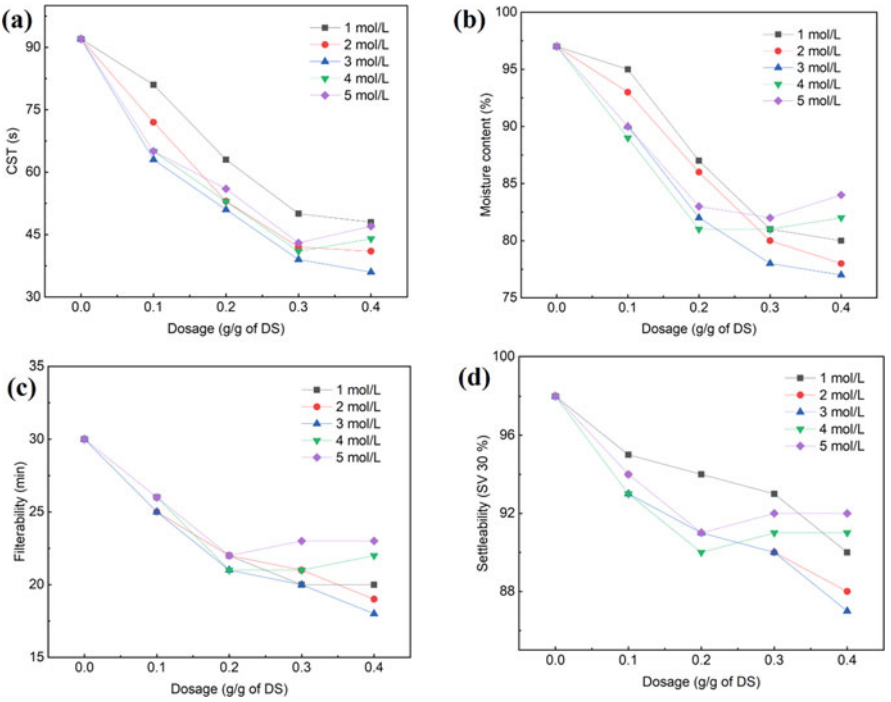

Fig. 4 (**a**) Capillary suction time versus dosage. (**b**) Moisture content versus dosage. (**c**) Filterability versus dosage. (**d**) Settleability versus dosage

significant on a further decrease in moisture content values for 4 and 5 mol/L of MCSB-$FeCl_3$. The decrease in moisture content indicates the improvement in the dewatering ability as now water can be released out easily compared to raw sludge on conditioning. This reduction in moisture content is in accordance with the previous works investigated for sludge conditioning using various biomass as mentioned in earlier sections. The mechanism behind this can be due to more availability of pores and voids after conditioning; also the addition of skeletal material as MCSB-$FeCl_3$ is responsible for the formation of a bridge-like structure by sludge particles which helps to pass the water with ease compared to earlier denseness in the raw sludge [12].

3.2.2 Effects on Filterability and Settleability

The filterability of water from the sludge with respect to dosage (g/g of DS) is shown in Fig. 4c, where the reduction in time taken by water to drain out when poured into the vacuum filtration apparatus is noted which shows the improvement in the sludge dewatering ability. The minimum time noted for the dosage ranging from 0.1, 0.2, and up to 0.4 (g/g of DS) is 18 min, whereas for the raw sludge sample, it is 30 min.

The time for filtration of 18 min is observed at a dosage of 0.4 (g/g of DS) with a molarity of 3 mol/L. There was no considerable decrease in filterability value which was noted for 4 and 5 mol/L at the same dosage of 0.4 (g/g of DS) compared to other molarities. The decrease in time to filter out the water was observed, as upon conditioning, most of the trapped water gets released and flows out as free water from the sludge resulting into the ease in, filtering out the same. Also the cationic and anionic interaction within the sludge solids and inorganic salt ($FeCl_3$) which is used in this work is responsible for making the trapped water to be released effortlessly [13].

In Fig. 4d, on increasing the dosage from 0.1, 0.2, and up to 0.4 (g/g of DS) with molarities of MCSB-$FeCl_3$ as 1, 2, and 3 mol/L, the least possible reduction in settleability (SV_{30}%) from 98% to 87% were recorded when conditioned with MCSB-$FeCl_3$ at a dosage of 0.4 (g/g of DS) when modified with the molarity of 3 mol/L. The conditioners in the form of modified biochars when added to the sludge neutralize the charges on suspended colloids and form the sludge flocs of considerable mass which then settle down when allowed to settle [14].

3.3 Optimization of the Filterability and Moisture Content

The experimental design for this study utilized the response surface methodology (RSM) and included 17 runs of experimentation. To develop the model equation for moisture content, the Box-Behnken design (BBD) was selected, and an analysis of variance (ANOVA) was performed [15]. The output considered for the optimization was moisture content, and the input parameters are MCSB-$FeCl_3$ dosage (g/g of DS), molarity (M), and mixing time (min). The parameters were chosen on the basis of the preliminary observations which directly impact sludge dewatering ability. From the analysis presented in Sect. 3.2, the dosage (% of DS) is taken as 0.2–0.4; molarity is considered as 1, 2, and 3 mol/L; and mixing time is taken as 20, 25, and 30 min as it is inferred from the previously investigated work as desirable mixing times [2] (Table 2).

The optimized values obtained for the moisture content of conditioned sludge are 78% at dosage = 0.4 (g/g of DS), molarity = 2.5 mol/L, and mixing time = 24.72 min. The analysis of variance (ANOVA) (Table 3) shows that the obtained models for given responses are significant, and lack of fit is not significant. The coded equation for moisture content has been presented, where A = dosage (g/g of DS), B = molarity (M), and C = mixing time (min).

The coded equation is as follows:

$$\text{Moisture content}\ (\%) = 80.31 - 4.44 \times A - 0.3112 \times B - 0.1188 \times C - 0.2725 \times AB + 0.7775 \times AC + 0.1350 \times BC + 2.20 \times A^2 + 1.39 \times B^2 + 1.16 \times C^2$$

Table 2 Design of experiment with actual and predicted values of filterability and moisture content

Standard run	*A*: Dosage (%)	*B*: Molarity (M)	*C*: Mixing time (min)	Actual moisture content (%)	Predicted moisture content (%)
1	0.2	1	25	88.47	83.43
2	0.4	1	25	79.8	87.22
3	0.2	3	25	88.55	79.89
4	0.4	3	25	78.79	88.38
5	0.2	2	20	88.91	82.54
6	0.4	2	20	78.8	82.57
7	0.2	2	30	87	80.31
8	0.4	2	30	80	78.88
9	0.3	1	20	83.45	80.31
10	0.3	3	20	82.4	82.92
11	0.3	1	30	83.06	80.31
12	0.3	3	30	82.55	80.31
13	0.3	2	25	80.55	80.31
14	0.3	2	25	81.1	78.58
15	0.3	2	25	80	88.31
16	0.3	2	25	80.01	89.02
17	0.3	2	25	79.9	80.04

Table 3 ANOVA analysis for the equation obtained for moisture content

Source	Sum of squares	Degrees of freedom	Mean square	*F*-value	*p*-Value	Significant/ insignificant
Model	199.40	9	22.16	116.53	<0.0001	*Significant*
A: Dosage	157.89	1	157.89	830.42	<0.0001	
B: Molarity	0.7750	1	0.7750	4.08	0.0833	
C: Mixing time	0.1128	1	0.1128	0.5933	0.4663	
AB	0.2970	1	0.2970	1.56	0.2515	
AC	2.42	1	2.42	12.72	0.0091	
BC	0.0729	1	0.0729	0.3834	0.5554	
A^2	20.41	1	20.41	107.33	<0.0001	
B^2	8.12	1	8.12	42.73	0.0003	
C^2	5.70	1	5.70	30	0.0009	
Residual	1.33	7	0.1901			
Lack of fit	0.2950	3	0.0983	0.3797	0.7738	*Not significant*
Pure error	1.04	4	0.2590			
Cor total	200.74	16				

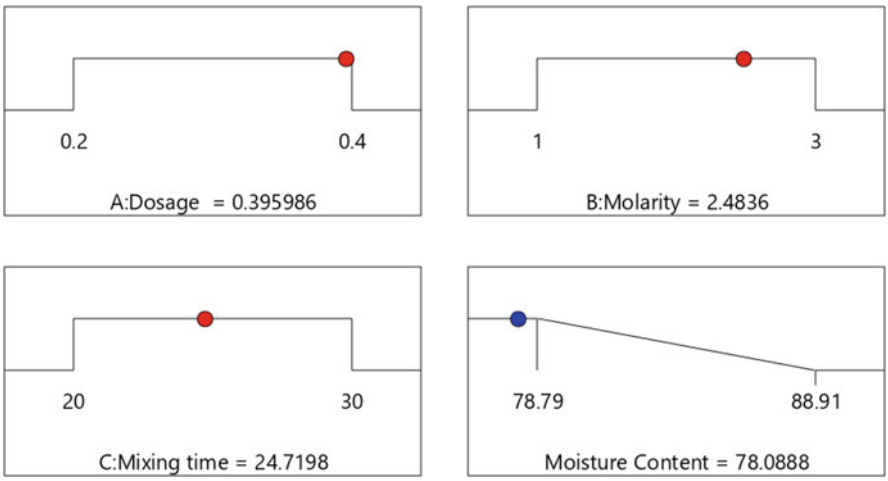

Fig. 5 Optimum values of dosage, molarity, filterability, and moisture content

The use of coded factors in the model equations allows for the interpretation of response predictions based on the levels of each factor. The default coding assigns a value of +1 to high levels and −1 to low levels. This coded equation facilitates the identification of the factors' relative impact by examining the factor coefficients (Fig. 5).

Table 3 displays the ANOVA analysis results for the moisture content equation obtained in this study. The predicted R^2 value was determined to be 0.97, which is very close to the adjusted R^2 value of 0.98, and the difference between the predicted and adjusted R^2 values was less than 2. This indicates that the predicted model is favorable. The achieved ratio of 31.22 for adequate precision indicates a strong signal. The model F-value of 116.53 indicates that the model is significant. In order for the model to fit, the lack of fit should not be significant. The lack of fit F-value of 0.38 for the obtained model suggests that it is not significant in relation to the pure error.

In Fig. 6 the contour plots and 3D plots of two-way interaction terms (AB, BC, AC) have been presented where variations with different combinations of terms which are coded as A, B, and C can be inferred. These graphs have been generated on the basis of the model equation formed for moisture content (%). It can be concluded that the curvatures generated in all 3D graphs have a considerable reduction in moisture content (%).

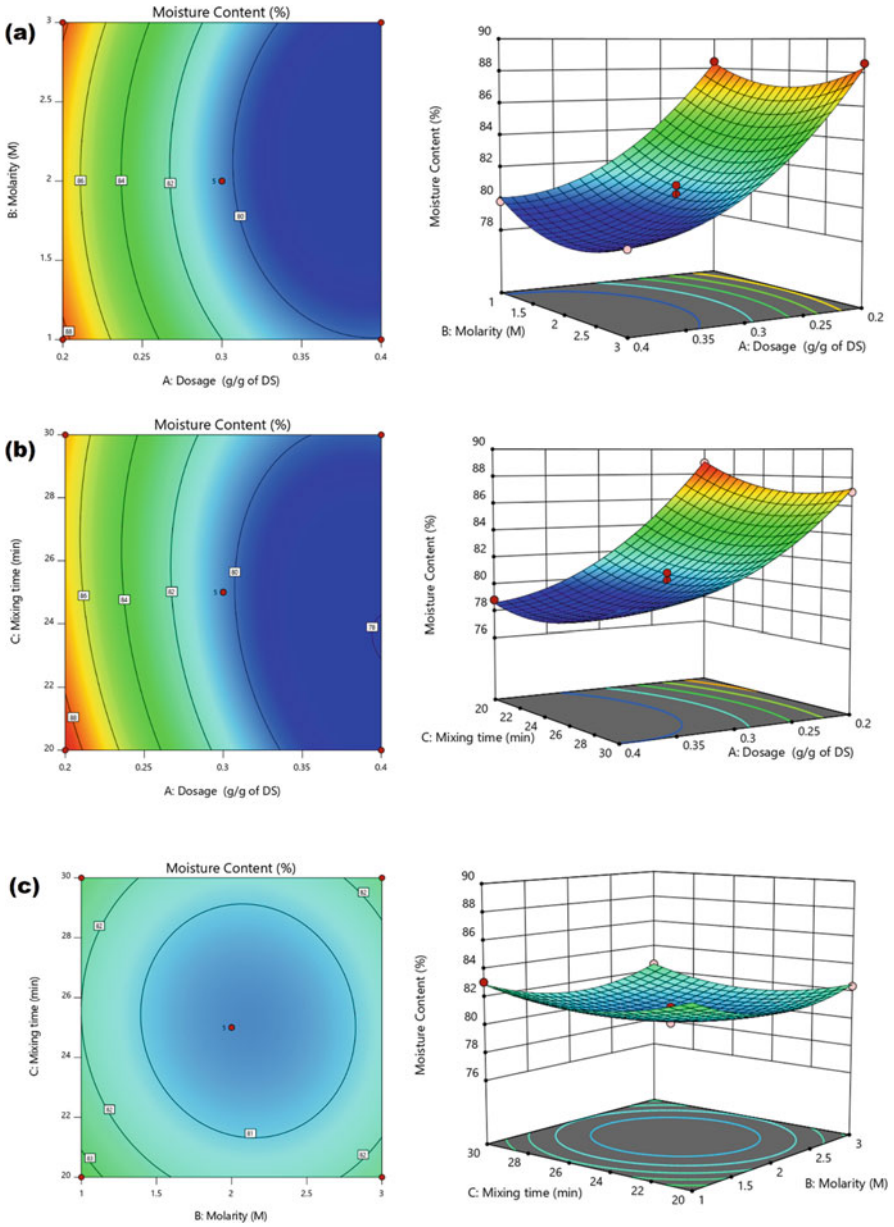

Fig. 6 Contour plots and two-way interaction terms of the coded equation for moisture content

4 Conclusion

This study utilized modified coconut shell biochar and analyzed its improvement in the sludge dewatering properties by analyzing the parameters such as CST (s), moisture content (%), filterability (min), and settleability (SV_{30}%), and optimized value moisture content was obtained as 78% at desirable dosage, molarity, and mixing time. Hence, modified coconut shell biochar proved to be a good conditioner and economical for conditioning and dewatering purpose.

Acknowledgments The authors would like to extend their appreciation to the Department of Chemical, Department of Materials & Metallurgy, and the Centre for Research facility for providing essential laboratory facilities to support this study.

References

1. W.A. Boran, D. Xiaohu, C. Xiaoli, Critical review on dewatering of sewage sludge: influential mechanism, conditioning technologies and implications to sludge reutilizations. Water Res. **180**, 115912 (2020)
2. M. Hamidreza, B.G. Gagik, Using thermal-acidic-modified kaolin as a physical-chemical conditioner for waste activated sludge dewatering. Chem. Eng. J. **412**(2021), 128664 (2021)
3. J. Nematallah, H. Yalda, T. Afshin, A. Mehdi, G. Gholamreza, Evaluation of bagasse pith as a skeleton builder for improvement of sludge dewatering. Environ. Eng. Manag. J. **15**(4), 725–732 (2016)
4. M. Wójcik, Investigation of filtration properties and microbiological characteristics of sewage sludge after physical conditioning with the use of groundwalnut shells. Powder Technol. **361**, 491–498 (2020)
5. G. Junyuan, J. Shilin, P. Yujie, Rice straw biochar modified by aluminum chloride enhances the dewatering of the sludge from municipal sewage treatment plant. Sci. Total Environ. **654**, 338–344 (2019)
6. H.R. Rashmi, C.P. Devatha, Dewatering performance of sludge using coconut shell biocharmodified with ferric chloride. Int. J. Environ. Sci. Technol. **19**, 6033–6044 (2021)
7. M. Scholz, Review of recent trends in capillary suction time (CST) dewaterability testing research. Ind. Eng. Chem. Res. **2005**(44), 8157–8163 (2005)
8. P.A. Vesilind, B. Ormeci, A modified capillary suction time apparatus for measuring the filterability of super-flocculated sludges. Water Sci. Technol. **42**, 135 (2000)
9. P. Aarne Vesilind, The role of water in sludge dewatering. Water Environ. Res. **66**(1), 4–11 (1994)
10. E. Torfs, I. Nopens, M. Winkler, P. Vanrolleghem, S. Balemans, I. Smets, *Settling Tests* (IWA, 2016)
11. C.H. Leem, J.C. Lium, Enhanced sludge dewatering by dual polyelectrolytes conditioning. Water Res. **34**(18), 4430–4436 (2000)
12. Q. Ying, B. Khagendra, I. Thapa, F.A. Andrew, Application of filtration aids for improving sludge dewatering properties – a review. Chem. Eng. J. **171**(2011), 373–384 (2011)
13. A.R. Alkmima, P. Costaa, M. Amarala, L. Netab, B. Riccia, S. Oliveiraa, J. Santiago, The application of filterability as a parameter to evaluate the biological sludge quality in an MBR treating refinery effluent. Desalin. Water Treat. **53**, 1440 (2014)
14. Y.W. Ling, X. Li, K. Luo, Y.H. Song, R.G. Liu, Settleability and dewaterability of sewage sludge with modified diatomite. Environ. Sci. Pollut. Res. **29**, 72159–72168 (2021)
15. D. Rashmi, T. Padmavathi, Statistical optimization of pigment production by Monascus sanguineus under stress condition. Prep. Biochem. Biotechnol. **44**(1), 68–79 (2013)

Production of Xylose from Water Hyacinth Biomass (WHB) (Lignocellulosic Waste) for Xylitol Production: Waste to Wealth

Rohan Jadhav and Apurba Dey

Abstract Water hyacinth is an invasive aquatic weed that is believed to be damaging to both humans and the environment. However, its lignocellulosic biomass, or WHB, can be used as a source for the fermentation of xylitol, resulting in the creation of a value-added product from waste. At the industrial level, it is produced commercially by chemically hydrogenating the five-carbon sugar D-xylose in the presence of a catalyst at high temperature and pressure, and the process is arduous, costly, and energy intensive. Chemical-based pre-treatment of water hyacinth biomass (WHB) is an important step in which lignocellulosic biomass is hydrolyzed with different chemicals to release fermentable sugars. In this study, various methods have been applied to obtain xylose from WHB. The WHB was prepared and treated with three alkalis, three acids, an oxidative agent, and, among them, an alkaline-based pre-treatment method (KOH) was found to be optimum, and concentration was found to be 8.0597 mg/ml. The treated samples were filtered using cheese/muslin cloth, and pH was neutralized and analyzed using a spectrophotometer. A steam explosion at 121 °C, 15 psi, for 15–20 min was found to be favorable for the conversion of WHB to xylose which can subsequently be converted to xylitol.

Keywords Fermentation · Value-added product · Pre-treatment · Lignocellulosic waste · Waste management · Water hyacinth · WHB · Hydrolysis · Xylose · Spectrophotometer · Xylitol

Abbreviations

°C	Degree Celsius
Cal/g	Calorie/gram
FE-SEM	Field emission scanning electron microscopy
FTIR	Fourier transform infrared spectroscopy
g/g	Gram/Gram

R. Jadhav · A. Dey (✉)
Department of Biotechnology, National Institute of Technology, Durgapur, West Bengal, India
e-mail: rhj.18bt1103@phd.nitdgp.ac.in; apurba.dey@bt.nitdgp.ac.in

D. Mazumder (ed.), *Sustainable Advanced Technologies for Industrial Pollution Control*, Springer Proceedings in Earth and Environmental Sciences,
https://doi.org/10.1007/978-3-031-37596-5_18

IAS	Invasive aquatic species
mg/ml	Milligrams per milliliter
ml	Milliliter
nm	Nanometer
psi	Pounds per square inch
rpm	Revolutions per minute
UV-Vis	Ultraviolet–visible
V/V	Volume/Volume
W/V	Weight/Volume
WHB	Water hyacinth biomass
XRD	X-Ray diffraction

1 Introduction

Water hyacinth, an invasive aquatic species (IAS), generally harmful to humans and the environment, can be considered as a solid waste having no positive contribution to the environment [1, 6]. The biomass of water hyacinth has applications in the bioconversion of lignocellulosic components to industrially important products such as xylitol [7]. It has a 12% market share of all polyols and is expected to rise three times in the coming years, making it a crucial product for the industry. It can be utilized as a platform chemical as well as an artificial sweetener. It has more than 50 countries' approval for use as food, and this, along with growing commercial and scientific interest, has generated significant demand for this product on the international market [2]. It is produced industrially by chemically hydrogenating the five-carbon sugar D-xylose in the presence of a catalyst at high temperatures and pressures. This chemical procedure requires a lot of effort, money, and energy. The purifying procedures required for the process are very expensive. The hemicellulosic fraction, which makes up a sizeable portion of lignocellulosic materials, is made up of side-group-heavy uronic acids, pentoses (xylose and arabinose), and hexoses (glucose, mannose, and galactose). The main carbohydrate found in hemicellulose found is xylose, which can be fermented to produce xylitol and ethanol [12]. Moreover, a later step that would involve either acidic or enzymatic hydrolysis is avoided when a bioproduct is obtained from an intermediate pre-treatment step (alkaline or acid). To make fermentable sugars more available to the enzymes that break down the carbohydrate polymers into fermentable sugars, lignocellulosic biomass must undergo pre-treatment. The intention is to compromise the lignin's protective barrier and damage cellulose's crystalline structure and disrupts hemicellulose. Pre-treatment has been viewed as one of the most expensive processing steps in lignocellulosic biomass-to-fermentable sugars conversion [13] (Fig. 1).

Many characteristics define an efficient pre-treatment. It prevents the need for biomass particle size reduction, protects the pentose (hemicellulose) fractions, restricts the production of breakdown products that hinder the growth of fermentative microorganisms, decreases energy requirements, and lowers cost [13]. At an

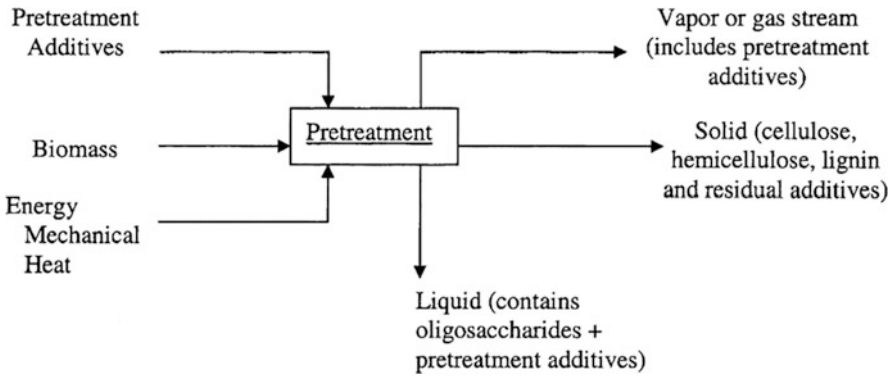

Fig. 1 Schematic of the pre-treatment process [13]

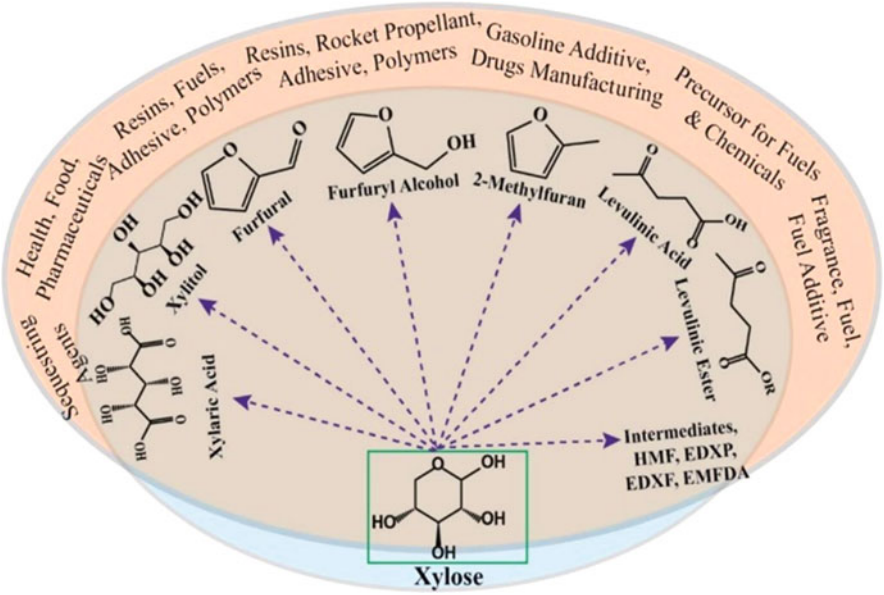

Fig. 2 Value-added products from xylose [22]

industrial level, xylose is catalytically hydrogenated at pressures and temperatures between 80 and 140 °C and 50 atm to produce xylitol. In this procedure, catalysts such as nickel (Ni) and ruthenium (Ru) are utilized [7]. The main disadvantage of this method is upstream processing because the substrate (xylose) needs to be in pure form, which necessitates detoxification and impurity removal along with other sugars, the price to produce which goes up due to this xylose purification method [7] (Figs. 2 and 3).

It has several current and future uses, including those of a sweetener, emulsifier, humectant, stabilizer, thickening, and building block (xylaric acid, propylene glycol,

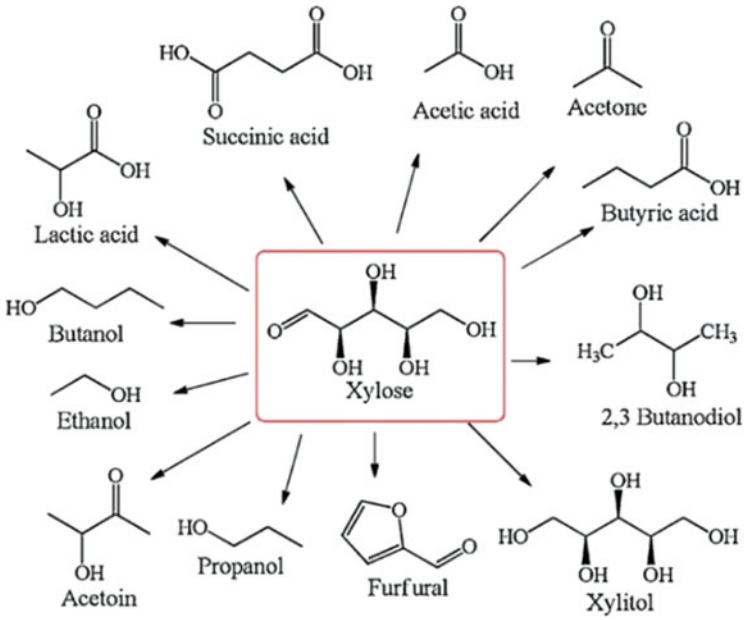

Fig. 3 Chemicals that can be obtained from xylose [14]

ethylene glycol, and glycerol) [15]. Its demand is expected to grow for sugar-free and low-calorie food products. In addition to being one of the top 12 worldwide bioproducts, it has a wide range of applications in the food, nutraceuticals, beverage, and pharmaceutical industries [15, 17]. At the moment, more than 35 countries have approved its use in foods, medications, and oral care products, primarily in chewing gum, toothpaste, syrups, and sweets preparations. The market value of this sugar substitute was 921 million USD by 2020, and according to the International Market Analysis Research Consulting Group (IMARC), that value is expected to increase to 1.37 billion USD in 5 years [16, 17].

As a sugar substitute, it is mostly used in food goods to prevent microbial contamination. It also serves as a sweetener and a preservative. As a result, it is chosen above other sweeteners when making baby food. Another benefit is that the high endothermic heat of the solution (34.8 cal/g), which absorbs heat from the environment and has a cooling effect, produces a cold aftertaste [15]. Xylitol's biological potential has recently attracted study attention [14, 15, 17]. As a result, it is an important product for the pharmaceutical sector since it lowers plaque levels, xerostomia, gingival inflammation, and nasopharyngeal pneumonia. It also reduces the microbial load by multiple mechanisms including anti-adhesive, oxidative stress, low permeability, and futile metabolism [15].

The objective of this study is to obtain a suitable method for hydrolysis of WHB, to release fermentable sugar (xylose), which is a key material for xylitol production and an industrially important pentose sugar.

2 Materials and Methods

2.1 Substrate

Water hyacinth was collected manually from the water pond affected by this weed. The sample was procured from a location *23.452002, 87.446756* (*23°27′07.2″N 87° 26′48.3″E*) in Panagarh, West Bengal, India. The leaves were separated from stem and root and washed with tap water (five times) and distilled water (two times), to remove dirt and other biological contamination followed by ethanol (50–70%, once). Leaves were air-dried and then were kept in a hot air oven at 55 °C for 48 h. The sample was dried and ground for size reduction and then sieved to obtain a sample size of around 250–355 μm. Water hyacinth biomass (WHB) was stored for analysis and experimented in a clean and sterilized glass container. The composition of raw water hyacinth is shown in Table 1.

2.2 Chemicals

For alkali hydrolysis three pre-treatment agents were selected, namely, sodium hydroxide (NaOH), potassium hydroxide (KOH), and calcium hydroxide $Ca(OH)_2$ which were purchased from HiMedia. Hydrogen peroxide ($H_2O_{2)}$ was purchased from Merck, as well as hydrochloric acid (HCl), sulfuric acid (H_2SO_4), and nitric acid (HNO_3) for acid hydrolysis. Distilled water from MilliQ water system was taken for preparing the reaction mixture.

2.3 Materials

A cheesecloth was selected as a filtration medium and was cut into sizes of $1′ \times 1′$, along with a funnel to make a filtration setup, Borosil Make measuring cylinder, Tarsons centrifuge tube (50 ml) (radiation sterilized) for centrifugation, pH meter/pH strips for measuring the changes in the pH of filtrate during neutralization of sample, and cuvette for spectrophotometric analysis.

Table 1 Lignocellulosic composition of WHB

Water hyacinth sample	Parameter	Content (% dry weight of biomass)
Leaves	Cellulose	28.6
	Hemicellulose	*26.86*
	Lignin	12.5

2.4 Glassware

Clean and autoclaved Erlenmeyer flask (250 ml) (conical flask) and Borosil Make were taken for pre-treatment reaction, a glass beaker to collect filtrate after pH neutralization, and autoclaved test tubes for spectrophotometric analysis for sugar estimation.

2.5 Equipment

A UV-Vis spectrophotometer was used for the analysis of fermentable sugars released during pre-treatment of WHB. All chemicals and WHB samples were weighed using a digital weighing balance for accurate measurements. Autoclave was used for pre-treatment as a medium for the steam-explosion method, a pH meter for measuring changes during and after pH neutralization, a hot air oven for sample preparation and drying of pre-treated pellet, and a magnetic stirrer with a hot plate for dissolving alkali and to prepare boiling water bath for sugar analysis.

2.6 Screening for Pre-treatment Method

2.6.1 Alkali Pre-treatment

WHB (substrate) was loaded at 4% (W/V) and pre-treated in an autoclave with 2% (W/V) concentrations of sodium hydroxide, potassium hydroxide, and calcium hydroxide as hydrolysis agents for a 20-min reaction period at 121 °C and 15 psi pressure [4, 5, 8]. The hydrolyzed samples were centrifuged after cooling, and they were then filtered through a muslin or cheesecloth. After collecting the supernatant and washing the pellet containing the hydrolyzed WHB several times in distilled water to bring the pH level back to normal, the residue was dried in a hot air oven at 55 °C on an aluminum foil cup for further analysis [4, 5].

2.6.2 Acid Pre-treatment

WHB (substrate) was loaded at 4% (W/V) and processed in an autoclave with 2% (W/V) concentrations of hydrochloric acid, sulfuric acid, and nitric acid as a hydrolysis agent for 20 min at 121 °C and 15 psi pressure [4, 8, 12]. The hydrolyzed samples were centrifuged after cooling, and they were then filtered through a muslin or cheesecloth. In order to neutralize the pH of the pellet containing the hydrolyzed WHB, the supernatant was collected. The pellet was then washed multiple times in

distilled water, and the residue was then dried in a hot air oven at 55 °C on an aluminum foil cup for further analysis [4, 5].

2.6.3 Hydrogen Peroxide Treatment

WHB (substrate) was loaded at 4% (W/V) and processed in an autoclave for 20 min at 121 °C and 15 psi pressure using hydrogen peroxide produced at 2% (V/V) concentration [4, 8]. The hydrolyzed samples were centrifuged after cooling, and they were then filtered through a muslin or cheesecloth. After collecting the supernatant and washing the pellet containing the hydrolyzed WHB several times in distilled water to bring the pH level back to 7, the residue was dried in a hot air oven at 55 °C on an aluminum foil cup for further analysis.

2.7 Analytical Methods

Cellulose, hemicellulose, and lignin content were determined by the method of Goering and Van Soest (1970) [9, 10], and the estimation of total ribose sugar was done by orcinol method (Bial's method) with extra pure grade xylose as standard [11].

3 Results and Discussion

3.1 Sample Preparation

The acquired water hyacinth sample was cleaned to remove any contamination that might interact or interfere with the experimental or analytical processes (Fig. 4). It was found that high temperature can cause WHB to become a char or to give high

Fig. 4 Pond infested by water hyacinth, cleaned and washed sample, dried leaf sample, and acquired WHB (left to right)

color intensity when it was added to the hydrolysis reaction mixture. It was found that 55–60 °C temperature for 48 h was adequate for drying.

3.2 Pre-treatment of WHB

The substrate was added to an Erlenmeyer flask (250 ml), and a respective pre-treatment agent was added for hydrolysis (Fig. 5). Autoclave provides an environment like the steam-explosion method which subsequently helps in the hydrolysis of complex lignocellulosic biomass like WHB. After pre-treatment, the samples were centrifuged at 7500 rpm for 15–20 min at 4 °C. The hydrolyzed WHB was neutralized using distilled water till the pH is 7. The supernatant was tested for released xylose by orcinol method using a UV-Vis spectrophotometer, and the pellet (hydrolyzed WHB) was dried at 55–60 °C and stored in a dry and clean place which can be used later to analyze the structural changes through FE-SEM [4] and analysis through FTIR as well as XRD.

3.3 Composition of WHB

Xylose primarily comes from the hemicellulose part of the lignocellulose biomass; the yield of the fermentable sugars depends on the pre-treatment method. The hemicellulose content per dry weight of biomass can give us the amount of total sugar released after hydrolysis, and the yield can be calculated (Table 2).

The hemicellulose content was found to be in the adequate range by comparing it to the previously recorded data. It is also noted that lignin and cellulose composition is 12.5% and 28.6% of dry weight, respectively [21].

Fig. 5 Pre-treatment method (2% hydrogen peroxide for reference) filtered and neutralized WHB

Table 2 Comparative analysis of hemicellulose

Sample	Hemicellulose content (% dry weight biomass)	Reference
Water hyacinth biomass	7.4–23.7	[18]
	23	[19]
	45.12	[3]
	27.5–55	[8]
	25.6	[20]
	26.86	*Present study*

Table 3 Effect of different pre-treatment methods

Chemial used	Conc used (%)	Total xylose conc. (mg/ml)
NaOH	2	5.0827
KOH	*2*	*8.0597*
$Ca(OH)_2$	2	2.8075
H_2O_2	2	2.2597
H_2SO_4	2	4.6830
HNO_3	2	7.4638
HCl	2	4.7815
Autohydrolysis	2	2.1791

3.4 Determination of Xylose in Hydrolyzed Sample

The samples were analyzed at 620 nm with orcinol reagent as a blank. The samples were 100 times diluted for analysis, and the data was collected. Table 3 summarizes the result of different pre-treatment methods, and it was found that KOH was giving better results as compared to other chemical agents.

A high acid concentration led to the loss of polysaccharides, while a diluted acid pre-treatment simply changed the lignin carbohydrate bond on the substrate. Lignin is eliminated by alkali pre-treatment without affecting other constituents [8].

3.5 Effect of KOH on WHB Hydrolysis

Potassium hydroxide was prepared in the concentration range of 1–10% (W/V), and 4% (W/V) WHB was added to carry out the hydrolysis. The reaction mixture was kept in the autoclave for 20 min at 121 °C and 15 psi (Fig. 6).

It was found that the 3% (W/V) KOH when used for hydrolysis produced 8.0597 mg/ml xylose, which subsequently can be used for fermentative production of industrially important products such as xylitol. The yield of xylose can be calculated, and it was found to be 0.2014 g/g of WHB. Alkali pre-treatment breaks the connections between lignin and hemicellulose carbohydrates, reduces lignin in the biomass, increases surface area, and allows water molecules to penetrate interior

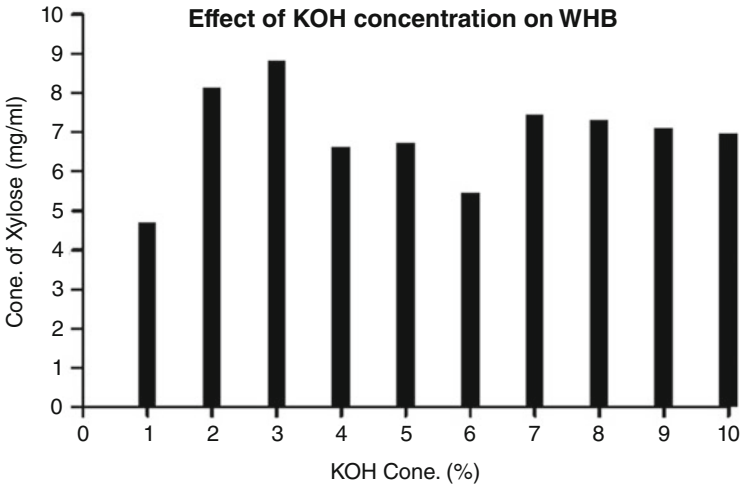

Fig. 6 Effect of KOH on WHB for xylose

layers. For the purpose of eliminating lignin from lignocellulosic biomass, alkali pre-treatment is thought to be an effective pre-treatment technique [8].

4 Conclusions

The composition of lignocellulosic biomass plays an important role in deciding the outcome of the pre-treatment methods. Xylose is the main component of hemicellulose, and its content can affect the fermentation process. It was found that hemicellulose consists of 26.86% dry weight of WHB biomass. Hydrolysis of WHB using various acids and alkalis was studied, and it was found that nitric acid and potassium hydroxide act as better pre-treatment agents when compared to other methods applied. From various methods applied for hydrolysis, KOH treatment showed prominent results giving 8.0597 mg/ml xylose, giving the yield of 0.2014 g/g of WHB. Steam explosion treatment was found to be favorable for this study. The presence of high temperature and pressure for the pre-treatment shows that it helps in the reaction as indicated by the results of autohydrolysis. The suggested method can be used as an effective pre-treatment for WHB.

Acknowledgments This research work was done under the supervision of Dr. Apurba Dey, HAG Professor, Department of Biotechnology, and support received from NIT Durgapur. This research work is supported under the Research Fellowship Programme of the Ministry of Human Resource Development, Government of India.

References

1. A.H. Degaga, Water hyacinth (Eichhornia crassipes) biology and its impacts on ecosystem, biodiversity, economy and human well-being. J. Life Sci. Biomed. **8**(6), 94–100 (2018)
2. S.R. Ravella, J. Gallagher, S. Fish, Chapter 13: Overview on commercial production of xylitol, economic analysis and market trends, in *D-Xylitol*, (Springer-Verlag, Berlin Heidelberg, 2012). https://doi.org/10.1007/978-3-642-31887-0_13
3. K. Shankar et al., Co-production of xylitol and ethanol by the fermentation of the lignocellulosic hydrolysates of banana and water hyacinth leaves by individual yeast strains. Ind. Crops Prod. **155**(6088–6099), 112809 (2019)
4. S. Rezania et al., Changes in composition and structure of water hyacinth based on various pre-treatment methods. Bioresources **14**(3), 6088–6099 (2020)
5. H.R. Madian et al., Bioethanol production from water hyacinth hydrolysate by Candida tropicalis Y-26. Arab. J. Sci. Eng. **44**, 33–41 (2019)
6. S.R. Biswas et al., Do invasive plants threaten the Sundarbans mangrove forest of Bangladesh? For. Ecol. Manag. **245**, 1–9 (2007)
7. S.S. Dalli et al., Development and evaluation of poplar hemicellulose pre-hydrolysate upstream processes for the enhanced fermentative production of xylitol. Biomass Bioenergy **105**, 402–410 (2017)
8. A. Singh, N.R. Bishnoi, Comparative study of various pretreatment techniques for ethanol production from water hyacinth. Ind. Crop. Prod. **44**, 283–289 (2013)
9. X. Jin et al., Determination of hemicellulose, cellulose and lignin content using visible and near infrared spectroscopy in Miscanthus sinensis. Bioresour. Technol. **241**, 603–609 (2017)
10. H.K. Goering, P.J. Van Soest, *Forage Fiber Analyses*, Agriculture Handbook No. 379 (U.S.D. A. Agricultural Research Service, 1970)
11. P.J. Pham et al., A spectrophotometric method for quantitative determination of xylose in fermentation medium. Biomass Bioenergy **32**, 2814–2821 (2011)
12. F.D. Xavier et al., Evaluation of the simultaneous production of xylitol and ethanol from sisal fiber. Biomolecules **8**, 2 (2018)
13. N. Mosier et al., Features of promising technologies for pretreatment of lignocellulosic biomass. Bioresour. Technol. **96**, 673–686 (2005)
14. Y.D. Arcaño et al., Xylitol: A review on the progress and challenges of its production by chemical route. Catal. Today **344**, 2–14 (2020)
15. V. Ahuja et al., Biological and pharmacological potential of xylitol: a molecular insight of unique metabolism. Foods **9**, 1592 (2020)
16. D. Umai, R. Kayalvizhi, V. Kumar, S. Jacob, Xylitol: bioproduction and applications-A review. Front. Sustain. **3**, 826190 (2022). https://doi.org/10.3389/frsus.2022.82619
17. M.E. Vallejos, M.C. Area, Chapter 12: Xylitol as bioproduct from the agro and forest biorefinery, in *Food Bioconversion*, (Elsevier, 2017), pp. 411–432
18. A. Ganguly et al., Studies on the production of xylose from water hyacinth. Adv. Chem. Sci. **2**(1), 1–7 (2013)
19. E.A. Omondi et al., Characterization of water hyacinth (E. crassipes) from Lake Victoria and ruminal slaughterhouse waste as co-substrates in biogas production. SN Appl. Sci. **1**, 848 (2019)
20. S. Tanpichai et al., Water hyacinth: a sustainable lignin-poor cellulose source for the production of cellulose nanofibers. ACS Sustain. Chem. Eng. **7**, 18884–18893 (2019)
21. S. Rezania et al., Review on pretreatment methods and ethanol production from cellulosic water hyacinth. Bioresources **12**(1), 2108–2124 (2017)
22. V. Narisetty et al., Valorization of xylose to renewable fuels and chemicals, an essential step in augmenting the commercial viability of lignocellulosic biorefineries. Sustain. Energy Fuels **6**, 29 (2022)

A Simplistic Mathematical Model for Two-Stage Anaerobic Digestion of Plastic Wastes

Penaganti Praveen and Debabrata Mazumder

Abstract The environmental impact of plastic pollution has been alarmingly envisaged in recent years throughout the globe. Enzymatic hydrolysis of plastic waste is a feasible solution that facilitates biodegradation process. The mathematical modelling of the biodegradation of plastics is a critical task, which has not been addressed so far in a rational way. Application of biodegradation kinetics is difficult due to several important variables in the process. Moreover, as the polymer materials (solid substrates) are highly hydrophobic, mass transfer limits the rate of degradation. This chapter presents a mathematical model using Haldane's kinetics for the biodegradation of plastic wastes, which are mainly polymer materials. The model has been developed consecutively for a two-stage anaerobic stabilization, i.e., hydrolysis stage followed by acidogenesis-cum-methanogenesis. Total organic carbon (TOC) has been used as a substrate parameter. The purpose of this model is to predict the performance of the biodegradation process in respect of time. The proposed model has been validated with the experimental data derived from two-stage anaerobic digestion of polyvinyl chloride (PVC) under mesophilic environment.

Keywords Plastic biodegradation · Anaerobic digestion · Two-stage system · Mathematical modelling · Haldane's kinetics · TOC

Abbreviations

HDPE	high-density polyethylene
LDPE	low-density polyethylene
MLSS	mixed liquor suspended solids
MLVSS	mixed liquor volatile suspended solids
PET	polyethylene terephthalate

P. Praveen (✉) · D. Mazumder
Department of Civil Engineering, Indian Institute of Engineering and Science Technology (IIEST), Shibpur, Howrah, West Bengal, India
e-mail: debabrata@civil.iiests.ac.in

D. Mazumder (ed.), *Sustainable Advanced Technologies for Industrial Pollution Control*, Springer Proceedings in Earth and Environmental Sciences,
https://doi.org/10.1007/978-3-031-37596-5_19

PLA	polylactic acid
PP	polypropylene
PS	polystyrene
PVC	polyvinyl chloride
SBR	sequencing batch reactor
TOC	total organic carbon

1 Introduction

Strong polymers with extremely high molecular weights can be produced synthetically or naturally. Although humans knew and utilized numerous natural polymers, like cellulose, starch, and proteins for ages, the production and usage of synthetic polymers are relatively recent [1]. Presently, synthetic petroleum-derived polymers such as polyethylene terephthalate (PET), high-density polyethylene (HDPE), polyvinyl chloride (PVC), low-density polyethylene (LDPE), polypropylene (PP), and polystyrene (PS) [2] are used as plastics. These materials have several beneficial properties, such as lower density compared to other solid materials, a high strength/weight ratio, good resilience to mechanical stress, resistance to corrosion, and chemical breakdown. But they do have a lot of drawbacks and flaws compared to other materials [3]. They also contribute to non-biodegradable garbage and environmental damage [4]. Physical, chemical, and biological techniques have all been attempted and put forth for this purpose. However, in view of economics and the environment, biological techniques are favored. Stabilization of plastic waste has been proposed under the categories of photo-oxidation, thermal degradation, chemical degradation, and biodegradation [5]. The high predominance of Carbon-Carbon bonds, particularly for polypropylene (PP), polyethylene (PE), polystyrene (PS), and polyvinyl chloride (PVC), makes it difficult for plastics to biodegrade, whereas polyethylene terephthalate (PET) has hydrolysable ester links [6].

The application of enzymatic biodegradation of plastics has gained attention recently as an eco-friendly tool for the conversion of plastics into stable end products. In order to predict the performance of biodegradation process, mathematical models are quite needful, which correlates all the relevant variable parameters. Johnson [7] investigated the need for supplemental nutrients for the enhancement of an efficient Polyhydroxyalkanoates (PHA) producing mixed culture with different levels of carbon and nitrogen limitation on polymer biodegradation using a sequencing batch reactor (SBR). Leejarkpai [8] proposed a kinetic model taking into account the growth phase, stationary phase, and lag phase for composting PE, PLA (polylactic acid), starch, and cellulose that explained the carbon mineralization of diverse organic materials. It was considered that solid carbon that could hydrolyze quickly, moderately, and slowly made up the initial step of external deterioration. A kinetic model for the biodegradation of PET utilizing *Streptomyces* species was established by Farzi et al. [9], and it showed that Michaelis–Menten activation or

inhibition model could more accurately predict experimental results. In a summary of the most recent research on the degradation rates of PET, PVC, PP, PS, LDPE, and HDPE of basic plastics under various environmental conditions using the Arrhenius equation, Chamas et al. [10] have made a general description of the degradation rates (by mass loss) of plastics in the environment. One of the most specified ways is to assume that the process has a first-order or n-order kinetic model. The majority of the researches focused on the mathematical models developed by using microbial cultures, which break down the polymer materials (mostly bioplastics) when they are dumped in landfills or composting facilities or pyrolysis.

With the above background, a mechanistic mathematical model for plastic biodegradation via anaerobic digestion is demonstrated in this chapter using Haldane kinetics [11]. Anaerobic digestion is considered to occur in two stages – hydrolysis and acidogenesis-cum-methanogenesis. When the polymer materials in the solid form enter into the hydrolysis reactor, enzymatic degradation will be initiated under mesophilic/thermophilic condition. The enzymatic hydrolysis involving the breakdown of polymer materials into monomers leads to production of soluble organic carbon. The soluble carbon produced in the biodegradation process is measured in the form of total organic carbon (TOC), which is widely accepted as a monitoring parameter for the biodegradation process.

Thereafter, the hydrolyzed product in form of liquid is transferred to acidogenesis-cum-methanogenesis reactor, which results in the reduction of TOC concentration to end products like methane and carbon dioxide as well as digester effluent. This chapter highlighted the development of a simplistic mathematical model for plastic materials hardly biodegradable in nature in a two-stage anaerobic digester considering TOC and MLVSS (mixed liquor volatile suspended solids) concentration as the process variable. The mathematical model is capable of predicting the TOC level in the reactor system implying the outcome of hydrolysis and acidogenesis-cum-methanogenesis. The model is developed consecutively for hydrolysis reactor followed by the acidogenesis-cum-methanogenesis reactor employing Haldane's kinetics. It is also validated with the two sets of experimental data derived from batch study in each reactor, which are in a good agreement with the data predicted from the model.

2 Materials and Methods

2.1 Development of Mathematical Model

Anaerobic co-digestion of polymer materials involves two stages: hydrolysis and acidogenesis-cum-methanogenesis. The polymer materials after loaded into the hydrolysis reactor are not directly utilized by the microbial cells across their cell walls because they are hydrophobic. Microorganisms can produce energy from these polymers by secreting extracellular enzymes. These enzymes depolymerize polymers outside of bacterial cells and produce soluble organic carbon. Enzymes are

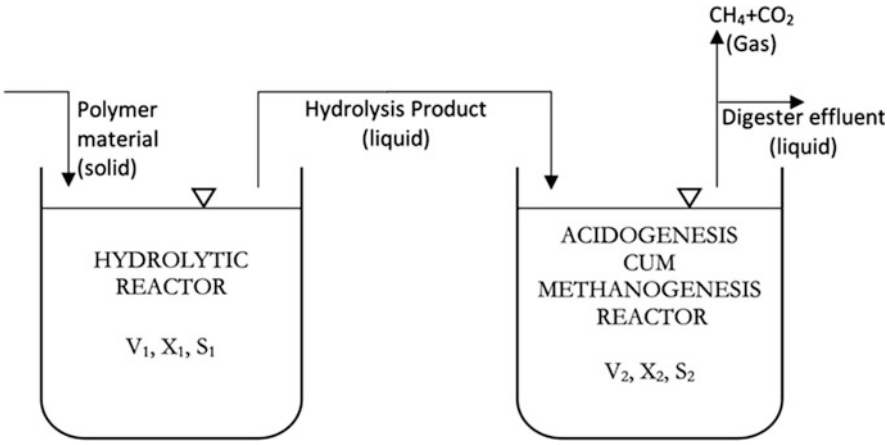

Fig. 1 Conceptual diagram of two-stage anaerobic digestion of polymer materials

involved in the biodegradation of polymers both in intracellular and in extracellular modes. The two processes involved in the biological degradation of polymers are depolymerization and mineralization [12]. Exoenzymes, or extracellular enzymes, degrade larger polymers and create small molecules that are water soluble. These compounds can pass through semi-permeable bacterial membranes and be used as an energy source. Depolymerization refers to the process of breaking down large polymers, whereas mineralization refers to the process of producing inorganic substances such as H_2O, CH_4, and CO_2 [13].

Based on the above theory, mathematical modeling for biodegradation process is done to determine the extent of biodegradation process. The proposed mathematical model assumes enzymatic hydrolysis of polymer material, resulting in soluble organic products, which can be quantified in terms of total organic carbon (TOC). Upon loading of hydrolytic effluent into the acidogenic-cum-methanogenic reactor, the TOC will be available to the anaerobic biomass as substrates. It is further assumed that there is uniform contact between the active biomass and TOC in all the reactors. The conceptual diagram of two-stage anaerobic digestion of polymer materials is shown in Fig. 1.

1. For hydrolytic reactor, substrate mass balance can be written as follows;

$$V_1 \frac{dS_1}{dt} = \frac{k_1 S_1 X_1}{K_{S1} + S_1 + \frac{S_1{}^2}{K_{i1}}} V_1 \left[k_1 = \frac{\mu_{mH}}{Y_H} \right]$$

Or,

$$\frac{dS_1}{dt} = \frac{K_1 S_1 X_1}{K_{S1} + S_1 + \frac{{S_1}^2}{K_{i1}}}$$

The expression $\frac{dS_1}{dt}$ represents the rate of substrate utilization, i.e., $\frac{S_{1f} - S_{1i}}{T_1}$, which denotes the rate of difference of final substrate concentration and initial substrate concentration for a particular batch period T_1.

Where, S_{1f} = final TOC concentration of a particular batch period T_1 in hydrolytic reactor.

S_{1i}= initial TOC concentration of a particular batch period T_1 in hydrolytic reactor.

Therefore,

$$\frac{S_{1f} - S_{1i}}{T_1} = \frac{K_1 S_1 X_1}{K_{S1} + S_1 + \frac{{S_1}^2}{K_{i1}}}$$

Or,

$$\frac{S_{1f} - S_{1i}}{X_1 T_1} = \frac{K_1 S_1}{K_{S1} + S_1 + \frac{{S_1}^2}{K_{i1}}}$$

At $S_{1i} = 0$ *at* $t = 0$ and

$$S_{1f} = S_1 \text{ at } t = T_1$$

Hence,

$$\frac{S_1}{X_1 T_1} = \frac{k_1 S_1}{K_{S1} + S_1 + \frac{{S_1}^2}{K_{i1}}}$$

Or,

$$K_{S1} + S_1 + \frac{{S_1}^2}{K_{i1}} = k_1 X_1 T_1 \tag{1}$$

Where, V_1 = volume of hydrolytic reactor (L)

S_1= TOC concentrationin hydrolytic reactor at any time t (mg/L)
X_1= hydrolytic biomass concentration (mg/L)
k_1= maximum specific growth rate of hydrolytic biomass (day^{-1})
K_{S1}= half velocity constant of hydrolytic reaction (TOC, mg/L)
K_{i1}= inhibition constant for hydrolytic reaction as per Haldane kinetics (mg/L)
T_1 = batch period in hydrolytic reactor (day)

2. In case of acidogenesis-cum-methanogenesis reactor, substrate mass balance can be written as follows:

$$V_2 \frac{dS_2}{dt} = -\frac{k_2 S_2 X_2}{K_{S2} + S_2 + \frac{S_2{}^2}{K_{i2}}} V_2 \left[k_2 = \frac{\mu_{mAM}}{Y_{AM}} \right]$$

As the substrate concentration decreases in acidogenesis-cum-methanogenesis stage, negative sign is considered.

Therefore,

$$\frac{dS_2}{dt} = -\frac{k_2 S_2 X_2}{K_{S2} + S_2 + \frac{S_2{}^2}{K_{i2}}}$$

The expression $\frac{dS_2}{dt}$ represents the rate of substrate utilization as $\frac{S_{2f} - S_{2i}}{T_2}$, which denotes the rate of difference of final substrate concentration and initial substrate concentration for a particular batch period T_2.

Where, S_{2f} = final TOC concentration of a particular batch period T_2 in anaerobic reactor.

S_{2i}= initial TOC concentration of a particular batch period T_2 in anaerobic reactor.

Therefore,

$$\frac{S_{2f} - S_{2i}}{T_2} = \frac{K_2 S_2 X_2}{K_{S2} + S_2 + \frac{S_2{}^2}{K_{i2}}}$$

Or,

$$\frac{S_{2f} - S_{2i}}{X_2 T_2} = \frac{k_2 S_2}{K_{S2} + S_2 + \frac{S_2{}^2}{K_{i2}}}$$

At, $S_{2i} = \frac{S_1 v}{V_2}$ at $t = 0$ and

$$S_{2f} = S_2 \; at \; t = T_2$$

As the hydrolysis product is transferred to the acidogenic-cum-methanogenic reactor, the initial TOC concentration for acidogenic-cum-methanogenic reactor should be considered with volume proportion of two reactors.

Hence,

$$\frac{\frac{S_1 v}{V_2} - S_2}{X_2 T_2} = \frac{k_2 S_2}{K_{S2} + S_2 + \frac{S_2{}^2}{K_{i2}}}$$

Or,

$$\left(K_{S2} + S_2 + \frac{S_2{}^2}{K_{i2}}\right)\left[\frac{S_0 - S_2}{S_2}\right] = k_2 X_2 T_2 \tag{2}$$

Where, V_2 = volume of anaerobic reactor (L)

X_2= total biomass concentration in anaerobic digester (mg/L)
S_2= TOC concentration in the acidogenic-cum-methanogenic reactor at any time t (mg/L)
k_2= maximum specific growth rate of anaerobic biomass (day^{-1})
K_{S2}= half velocity constant of anaerobic reaction (TOC, mg/L)
K_{i2}= inhibition constant for anaerobic reaction as per Haldane kinetics (mg/L)
T_2 = batch period in acidogenic-cum-methanogenic reactor (day)
v = volume of hydrolytic liquid transferred to the acidogenic-cum-methanogenic reactor
$S_0 = \frac{S_1 v}{V_2}$ = initial TOC concentration in the acidogenic-cum-methanogenic reactor (mg/L)

In case of anaerobic digester, for a known values of S_1, v, and V_2, the S_2 can be calculated provided the values of X_2, T_2 as well as k_2, K_{S2}, and K_{i2} are pre-determined for the same specific polymer material.

2.2 Method of Solution of the Proposed Model

The model Eq. (1) can be solved to predict effluent TOC concentration (S_1) in the hydrolytic reactor, provided the values of X_1, T_1 as well as k_1, $K_{S1,}$ and K_{i1} are pre-determined for any specific polymer material. In order to determine k_1, K_{S1}, and K_{i1}, hydrolytic biomass growth curve needs to be developed for both non-inhibition and inhibition zones as shown in Fig. 2.

K_{S1} = Half velocity constant for hydrolyzing reactor (substrate concentration at μ= $\frac{\mu_{mH}}{2}$),
μ_{mH}= maximum specific growth rate for hydrolytic reactor
$S_{\mu_{mH}}$ = minimum substrate concentration of hydrolytic reactor, where inhibition starts
A → non-inhibition zone, B → Inhibition zone

The value of K_{i1} can be determined from the following Eq. (3) using Haldane's Equation in inhibition zone [14].

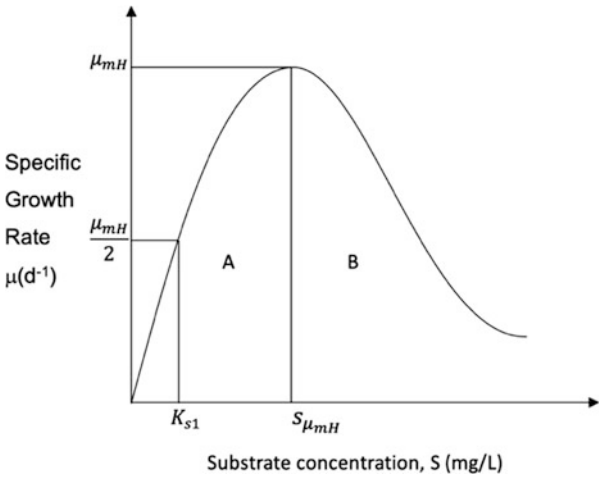

Fig. 2 Biomass growth rate curve for hydrolytic reactor

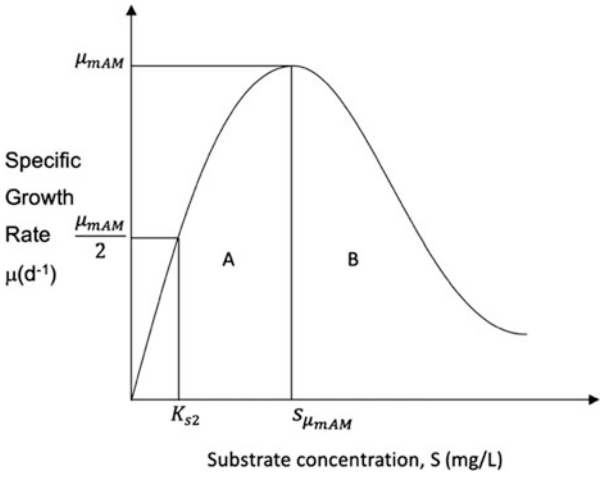

Fig. 3 Biomass growth rate curve for acidogenic-cum-methanogenic reactor

$$K_{i1} = \frac{{S_{\mu_{mH}}}^2}{K_{s1}} \tag{3}$$

From Eq. (3), the Haldane inhibition constant for hydrolyzing reactor (K_{i1}) can be obtained by substituting the K_{s1} value. The Eq. (1) can be used to plot $\left(K_{S1} + S_1 + \frac{{S_1}^2}{K_{i1}}\right)$ values with respect to X_1T_1, the slope of which yields k_1 value.

Similarly, in case of acidogenic-cum-methanogenic reactor, anaerobic biomass growth curve requires to be developed for both non-inhibition and inhibition zones as shown in Fig. 3 for determination of K_{S2} and K_{i2}.

K_{S2} = half velocity constant for acidogenic-cum-methanogenic reactor (substrate concentration at $\mu = \frac{\mu_{mH}}{2}$)

μ_{mA}= maximum specific growth rate for acidogenic-cum-methanogenic reactor
$S_{\mu_{mH}}$ = minimum substrate concentration of acidogenic-cum-methanogenic reactor, where inhibition starts
A → non-inhibition zone, B → Inhibition zone

The value of K_{i2} can be determined from the following Eq. (4) using Haldane's Equation in inhibition zone [14].

$$K_{i2} = \frac{S_{\mu_{mA}}{}^2}{K_{s2}} \tag{4}$$

From Eq. (4), the Haldane inhibition constant for acidogenic-cum-methanogenic reactor (K_{i2}) can be obtained by substituting the K_{s2} value. Eq. (2) can be used to plot the values of $\left(K_{S2} + S_2 + \frac{S_2{}^2}{K_{i2}}\right)\left[\frac{S_0 - S_2}{S_2}\right]$ with respect to X_2T_2, the slope of which yields k_2 value.

2.3 Experimental Validation of the Proposed Model

A reactor system was arranged accordingly as shown in Fig. 1 with two small 500 ml volume capacity containers. The first container acted as hydrolytic reactor filled with the hydrolytic sludge along with 10 gram of plastics beads. The second container acted as acidogenic-cum-methanogenic reactor filled with the anaerobic biomass and fed with the effluent of hydrolytic reactor. When the plastic beads were subjected to enzymatic hydrolysis and soluble carbon was produced in the hydrolytic reactor, the TOC concentration increased. Since the hydrolyzed fraction was transferred to acidogenic-cum-methanogenic reactor, here the TOC concentration decreased due to conversion of organic carbon. The entire setup was maintained under mesophilic environment. The pH was maintained in the range of 7.5–7.8 for effective performance. To monitor the reactors performance, parameters like pH, MLSS, MLVSS, and TOC were measured at certain time intervals as mentioned in Tables 1 and 2.

Table 1 Outcome of performance study in hydrolytic reactor

Day	pH	TOC (mg/L)	MLSS (mg/L)	MLVSS (mg/L)
0	7.65	35.2	2165	1318
2	7.54	74.5	2172	1326
4	7.45	122.6	2182	1336
7	7.42	172.5	2196	1354
9	7.50	234.0	2206	1366
12	7.65	275.4	2230	1382
15	7.60	306.0	2242	1398
18	7.62	320	2252	1410
21	7.64	330	2264	1418

Table 2 Outcome of performance study in acidogenic-cum-methanogenic reactor

Day	pH	TOC (mg/L)	MLSS (mg/L)	MLVSS (mg/L)
0	7.60	325	2242	1407
2	7.58	265.3	2258	1414
5	7.50	228.5	2283	1428
7	7.52	212.4	2292	1440
10	7.56	180.6	2304	1458
13	7.52	125.4	2320	1476
16	7.64	64.3	2344	1490
19	7.60	34.5	2358	1500
22	7.62	29	2368	1506

Table 3 Outcomes of validation of TOC concentration from the proposed model

Process parameters	Predicted value of TOC mg/L	Experimental value of TOC mg/L
Hydrolytic reactor		
$T_1 = 6$ days $X_1 = 1360$ mg/L	152.2	145.5
$T_1 = 8$ days $X_1 = 1370$ mg/L	194.3	192.3
Acidogenic-cum-*methanogenic reactor*		
$T_2 = 6$ days $X_2 = 1434$ mg/L	215.8	211.5
$T_2 = 18$ days $X_2 = 1502$ m/L	37.7	38.2

The developed model was validated based on the experimental data which was monitored on some random time interval periods. Apart from the experimental results mentioned in the Tables 1 and 2, the parameters on some random days were also monitored to validate the proposed model as shown in Table 3. In case of hydrolytic reactor, additional sampling was done on 6th and 8th days, whereas in case of acidogenic-cum-methanogenic reactor, the same was accomplished on 6th and 18th days. The experimental data were validated with that predicted from the proposed model. The outcomes of validation are comparatively presented with experimental results as shown in Table 3.

3 Results and Discussion

The proposed model is developed using Haldane kinetics to predict the TOC concentration for a time period (T) with known total biomass concentration (X). In order to determine the TOC concentration, firstly the kinetic coefficients should be pre-determined for hydrolytic reactor and acidogenic-cum-methanogenic reactor.

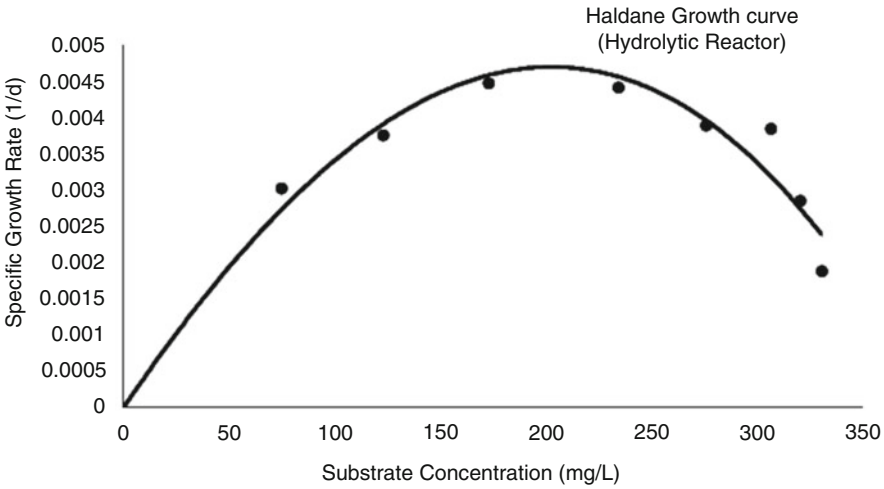

Fig. 4 Biomass growth curve for hydrolytic reactor

The experimental data set of Tables 1 and 2 are used for evaluation of kinetic coefficients as follows. In case of hydrolytic reactor, firstly the biomass growth curve is plotted using substrate concentration (TOC) on X-axis and specific growth rate (μ) on Y-axis as shown in Fig. 4. The μ value is calculated from the total biomass concentration (X_1) and corresponding time interval (T).

From Fig. 4, it is observed that $\mu_{mH} = 0.0047\ \mathrm{d}^{-1}$ and corresponding TOC concentration $S_{\mu_{mH}} = 200$ mg/L. Hence, the half velocity constant for hydrolytic reactor is the TOC concentration corresponding to $\frac{\mu_{mH}}{2} = 0.00235$, i.e., $K_{S1} = 61$ mg. Therefore, K_{i1} is calculated from Eq. (3) as, $K_{i1} = 655.73$ mg/L. Finally, to determine the k_1 value, a graph of $K_{S1} + S_1 + \frac{{S_1}^2}{K_{i1}}$ Vs. X_1T_1 is plotted as shown in Fig. 5, representing linear co-relation. The k_1 value is estimated as $k_1 = 0.0227\ \mathrm{d}^{-1}$ from slope of the best-fit line. Now, the TOC concentration for any time period T_1 can be estimated using Eq. (1).

Similarly, in case of acidogenesis-cum-methanogenesis reactor, the biomass growth curve is plotted using substrate concentration (TOC) on X-axis and specific growth rate (μ) on Y-axis as shown in Fig. 6. The μ value is evaluated from the total biomass concentration (X_2) and corresponding time interval (T). Whereas the substrate concentration values on X-axis should be considered from the experimental data, each substrate concentration is deducted from the initial substrate concentration, i.e., $\left(\frac{S_1\, v}{V_2} - S_2\right)$.

From Fig. 6, it is observed that $\mu_{mAM} = 0.0044\ \mathrm{d}^{-1}$ and corresponding TOC concentration $S_{\mu_{mH}} = 150$ mg/L. Hence, the half velocity constant for acidogenesis-cum-methanogenesis reactor is the TOC concentration corresponding to $\frac{\mu_{mAM}}{2} = 0.0022$, i.e., $K_{S2} = 42$ mg/L. Therefore, K_{i2} is calculated from Eq. (4) as $K_{i2} = 535.42$ mg/L. Finally, to determine the k_2 value, a graph of

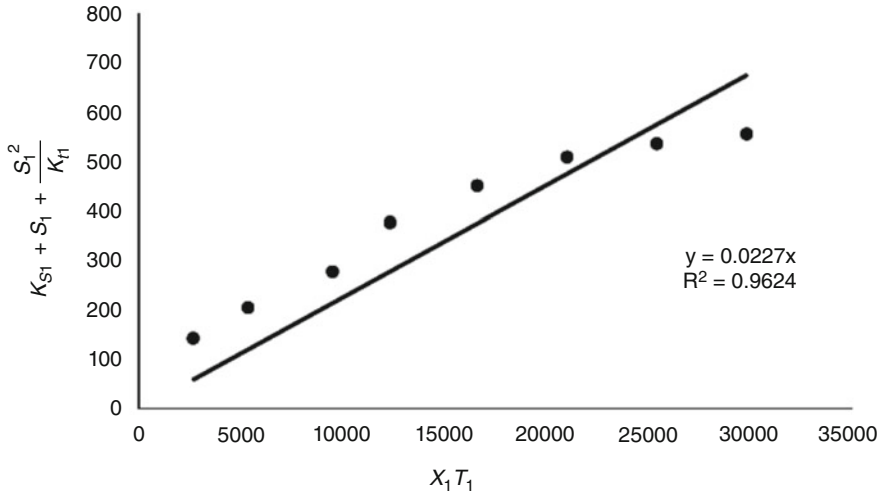

Fig. 5 Linear plot for determination of k_1

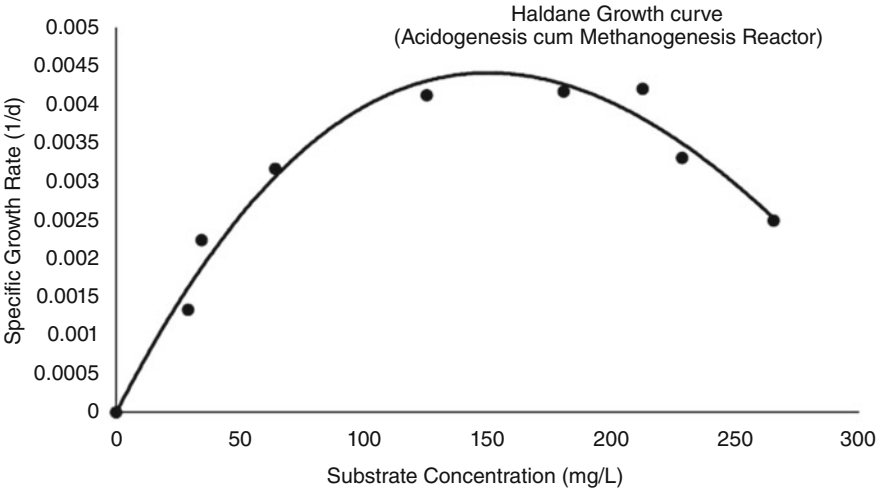

Fig. 6 Biomass growth curve for acidogenic-cum-methanogenic reactor

$\frac{\left(\frac{S_1 v}{V_2} - S_2\right)\left(K_{S2} + S_2 + \frac{S_2^2}{K_{I2}}\right)}{S_2}$ vs. X_2T_2 is plotted as shown in Fig. 7, representing linear co-relation. The k_2 value is evaluated as $k_2 = 0.0208\text{d}^{-1}$from slope of the best-fit line. Now, the TOC concentration for any time period T_2 can be estimated using Eq. (2).

Now, on the basis of kinetic coefficients evaluated, the TOC concentration for any time period (T_1 and T_2) and biomass concentration (X_1 and X_2) can be estimated using Eqs. (1) and (2) for hydrolytic and acidogenesis-cum-methanogenesis reactor,

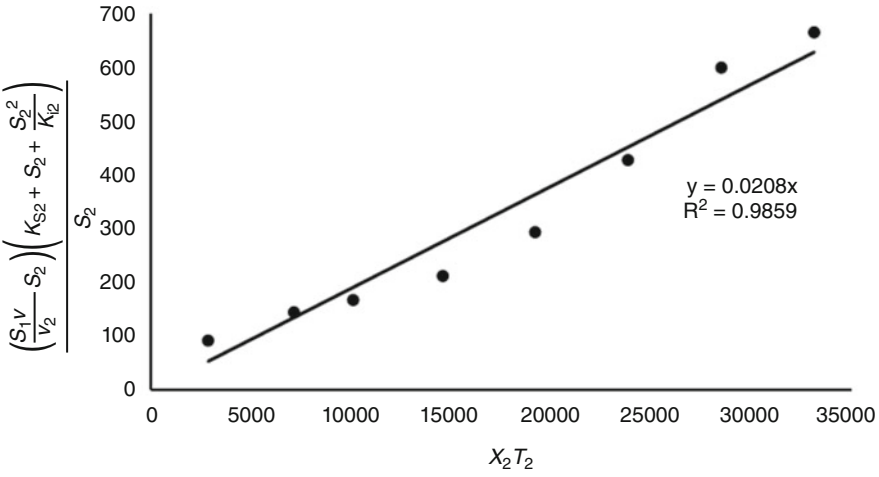

Fig. 7 Linear plot for determination of k_2

respectively. Accordingly, two effluent samples each from the hydrolytic and acidogenic-cum-methanogenic reactor were tested under two different batch periods as well as biomass concentration as depicted in Table 3. The experimental values of TOC concentration for each case were compared with those predicted from Eqs. (1) and (2) in the same to understand the accuracy of the proposed model. It has been observed that there is very small deviation between the experimental and predicted values in both the cases.

4 Conclusion

The biodegradation of synthetic plastics has become a serious concern among the major environmental issues, because of its very slow rate of biodegradation. Biological process, especially anaerobic digestion, is found to be a viable technique considering the huge amount of organic carbon entrapped in polymer materials, which can come out gradually as hydrolytic product. Since, hydrolysis is the first step of anaerobic digestion, there is always a scope of enzymatic reaction to expedite the process of dissolution of organic carbon. Development of mathematical model is quite needful for understanding the biodegradation processes and also for predicting the residual concentration of organic carbon in terms of TOC. The proposed mathematical model separately analyzed the two-stage anaerobic digestion system in a sequential manner considering the process variables like TOC, biomass concentration, and batch period. All the relevant process constants are possible to be determined from specific growth curve of the respective biomass. Using Haldane's kinetics in the proposed model reasonably considered the effect of inhibition during biodegradation of polymer materials. The model has also been validated

satisfactorily with the experimental data available from both hydrolytic and acidogenic-cum-methanogenic reactor. Thus, the model is rational to fulfill the purpose of predicting the biodegradation of plastics via two-stage anaerobic digestion and to apply for process design of a continuous system of same configuration.

References

1. S. Koltzenburg, M. Maskos, O. Nuyken, Introduction and basic concepts, in *Polymer Chemistry*, (Springer, 2017), pp. 1–16
2. C. Zhou, W. Fang, W. Xu, A. Cao, R. Wang, Characteristics and the recovery potential of plastic wastes obtained from landfill mining. J. Clean. Prod. **80**, 80–86 (2014)
3. S.S. Schwartz, S.H. Goodman, Structure and characteristics of polymers, in *Plastics Materials and Processes*, (Van Nostrand Reinhold Co, Toronto, 1982), pp. 130–136
4. J.A. Brydson, *Plastics Materials* (Butterworth-Heinemann, 1999)
5. A.L. Andrady, Degradation of plastics in the environment, in *Plastics and Environmental Sustainability*, (Wiley, Hoboken, 2015), pp. 145–184
6. C. Chen, L. Dai, L. Ma, R.T. Guo, Enzymatic degradation of plant biomass and synthetic polymers. Nat. Rev. Chem. **4**, 114–126 (2020)
7. K. Johnson, R. Kleerebezem, M.C. van Loosdrecht, Influence of the C/N ratio on the performance of polyhydroxy butyrate (PHB) producing sequencing batch reactors at short SRTs. Water Res. **44**, 2141–2152 (2010)
8. T. Leejarkpai, U. Suwanmanee, Y. Rudeekit, T. Mungcharoen, Biodegradable kinetics of plastics under controlled composting conditions. Waste Manag. **31**, 1153–1161 (2011)
9. A. Farzi, A. Dehnadand, A.F. Fotouhi, Biodegradation of polyethylene terephthalate waste using Streptomyces species and kinetic modeling of the process. Biocatal. Agric. Biotechnol. **17**, 25–31 (2019)
10. A. Chamas, H. Moon, J. Zheng, Y. Qiu, T. Tabassum, J.H. Jang, M. Abu-Omar, S.L. Scott, S. Suh, Degradation rates of plastics in the environment. ACS Sustain. Chem. Eng. **8**, 3494–3511 (2020)
11. J.B.S. Haldane, *Enzymes*, vol 84 (MIT Press, Cambridge, MA, 1965)
12. A. Elahi, D.A. Bukhari, S. Shamim, A. Rehman, Plastics degradation by microbes: A sustainable approach. J. King Saud Univ. Sci. **33**(6), 101538 (2021)
13. J.D. Gu, Microbiological deterioration and degradation of synthetic polymeric materials: Recent research advances. Int. Biodeterior. Biodegradation **52**(2), 69–91 (2003)
14. P. Praveen, D. Mazumder, A new approach for determining inhibition constant in the Haldane kinetics using differentiation method. Water Sci. Technol. (2022) (Accepted)

Part V
Handling and Disposal of Hazardous Waste

Modeling of Migration of Cr (VI) Contaminant Through Clay Liner Using HYDRUS-3D

Chandrima Bhadra, Avishek Adhikary, Supriya Pal, and Kalyan Adhikari

Abstract The migration of heavy metals and other contaminants through soil strata can lead to variable geo-environmental questions resulting in soil and groundwater contamination, which may affect the nearby land and water ecosystem. Comparative batch adsorption tests were conducted for both raw and amended clay soil. With AI, it was found that the latter shows an effective removal, i.e., above 90%. The physical and numerical modeling studies on solute transport were conducted to assess the hexavalent chromium attenuation potency of the locally obtainable amended clay soil mixed with neem (*Azadiracta indica* (AI)), which is used as primary liner for waste containment structures. The physical modeling performed in the laboratory in the horizontal migration tank study tends to show a similar approach with a graph plotted with the HYDRUS-3D data. Langmuir and Freundlich isotherms based on the batch experiments were plotted, with the Langmuir model fitting the best (RMSE = 1.38, R^2 = 0.99). Breakthrough curves predicted by the HYDRUS-3D numerical model exhibited that the liner is getting saturated after approximately 38 years.

Keywords Amended clay liner · Cr (VI) contaminant · HYDRUS-3D modeling · Isotherm · Landfill · Natural adsorbents · *Azadirachta indica* · Tannery waste water · Adsorption · Lithospheric pollution · Ground water pollution

C. Bhadra (✉)
Department of Civil Engineering, Heritage Institute of Technology, Kolkata, West Bengal, India
e-mail: chandrima.bhadra@heritageit.edu

A. Adhikary · S. Pal · K. Adhikari
Department of Civil Engineering, National Institute of Technology (NIT), Durgapur, West Bengal, India
e-mail: kalyan.adhikari@ees.nitdgp.ac.in

D. Mazumder (ed.), *Sustainable Advanced Technologies for Industrial Pollution Control*, Springer Proceedings in Earth and Environmental Sciences,
https://doi.org/10.1007/978-3-031-37596-5_20

Abbreviations

AAS	Atomic absorption spectroscopy
AI	*Azadiracta indica*
Al	Aluminum
As	Arsenic
b	Constant related to the free energy of adsorption and a measure of the affinity of binding sites (L/mg)
BOD	Biochemical oxygen demand
BTCs	Breakthrough curves
CCME	Canadian Council of Ministers of the Environment
Cd	Cadmium
Cl-	Chlorine
COD	Chemical oxygen demand
Cr (VI)	Hexavalent chromium
Cr	Chromium
Cu	Copper
Fe	Iron
Hg	Mercury
k_f	Adsorbent capacity (mg/Kg)
MDD	Maximum dry density
n	Adsorbent intensity (L/mg)
Ni	Nickel
NO^{3-}	Nitrate
Pb	Lead
PI	Plasticity index
Q_{max}	Maximum sorption capacity at monolayer
R^2	Regression co-efficient
RMSE	Root mean square
SO^{4-}	Sulfate
SW	Solid waste
TDS	Total dissolved solids
Zn	Zinc

1 Introduction

In former times, it was considered that the surroundings, i.e., land, air, water, and other natural resources, have boundless profusion. Still, today, the living society has shown their negligence to a greater or lesser degree in using those natural resources [2, 12]. The difficulties related to polluted surroundings are rapidly increasing in developing nations worldwide. The hazards caused by hexavalent chromium due to the leaching of hazardous wastes from tannery industries are studied [10]. Chromium

is the major pollutant in the leather industry's effluent and other toxic heavy metals [13, 21] .

The primary objective of this study is to assess the soil quality parameters of the non-engineered chromium-laden waste disposal site and to assess the groundwater quality of the nearby areas of the small-scale leather industries and thereby ascertain the extent of the threat to the hydrogeology in close proximities of the disposal sites [1]. This study also shows the adsorptive efficacy of naturally available fine-grained clay soil blended with *Azadirachta indica* seed shell dust as natural adsorbents to use the same as liner material in waste containment structures for the attenuation of aqueous hexavalent chromium. Also, it gives a brief overview of the migratory behavior of Cr (VI) contaminants through the amended liner using the HYDRUS-3D numerical model to evaluate the optimum design thickness of the liner.

In this study, adsorptive attenuation capacity against Cr (VI) movements with AI-amended clay soil, which was not carried out previously in detail by other investigators. Research on modeling the fate of Cr (VI) through saturated soil media is minimal. Though the literature indicated the availability of numerical models for solute transport in field soils, little work has been reported under Indian soil conditions for contaminants' fate, particularly with chromium compound contaminants. After a thorough literature review, it was found that Cr (VI) migration from a waste disposal site to the underground water using a three-dimensional software model like the HYDRUS-3D software package has not yet been studied using fixed bed adsorption experimental data.

2 Materials and Methods

2.1 Material

2.1.1 Study Area 1

A landfill located in the city of Durgapur, West Bengal, India, which was operative for 10–12 years and presently abandoned due to closure for the past 3 years, was selected as the study area. The boundaries of the study area are defined through a coordinate system using a hand-held GPS instrument, as shown in Fig. 1. The landfill area was subdivided into several grids, and subsurface soil samples were collected from the middle points of each grid.

2.1.2 Study Area 2

The second study area is situated in a small-scale leather industrial zone near the Tangra region in the South Eastern part of Kolkata, West Bengal, India. Various small-scale leather industries have been found adjacent to that area for over 50 years, as shown in Fig. 2. Almost all the leather industries dispose of their tannery effluent

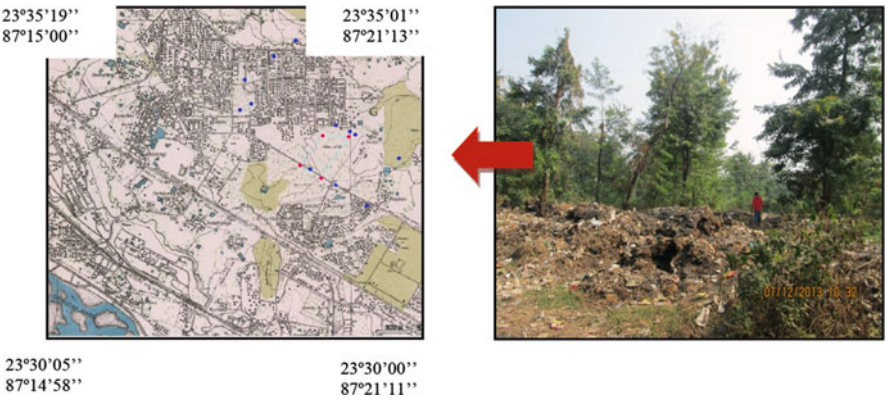

Fig. 1 Study area, West Bengal map, topo sheet no. 73 M/6

Fig. 2 Tangra region of Kolkata, West Bengal, India

directly to the nearby surface water bodies or on the land without pre-treatment. People near these waste disposal points use surface water for household purposes. Moreover, most houses have tube wells to withdraw groundwater for drinking and cooking purposes. The study area lies between 22° 33′ 18″ to 22° 32′ 59″ North latitudes 88° 22′ 47″ to 88° 22′ 59″ East longitudes.

Both the study areas were selected based on the primary pollutant of this study, i.e., hexavalent chromium. From the local survey of study area 1, it was found that Durgapur is a place that is densely packed with industries like thermal power plants, batteries, and coal industries, and the landfill which is selected for collecting the samples is non-engineered. Study area 2 is densely packed with leather industries, a primary chromium source [13].

2.1.3 *Azadiracta indica* (AI)

Azadirachta indica (AI), known as neem or Indian Lilac, belongs to the Meliaceae family and is generally seen in the subcontinent. In this study, AI is used as an

additive in powdered form. Several studies have shown that leaves and bark dust of AI act as good biosorbent of various heavy metals. Studies have indicated that AI leaf powder shows a high adsorptive capacity for hexavalent chromium.

2.1.4 Adsorption Isotherm

The convergence of the solute on the strong surface includes adsorption from aqueous solutions. The adsorption isotherm is the connection between the measure of solute adsorbed per unit weight of the adsorbent and the balance fixation in the mass arrangement at a consistent temperature [4].

2.1.5 Isotherm Model

The isotherm study is beneficial to define the adsorbent's sorption capacity in the aqueous medium. The Linear, Freundlich, and Langmuir models were studied for fitting with kinetic equilibrium experimental results by various researchers earlier.

2.2 Methods

2.2.1 Preparation of Natural Adsorbent

The natural adsorbent was prepared by crushing the seed shells of *Azadiracta indica* (AI). After grinding, these materials are oven dried at 105 °C (approximately) for 24 h. It was mixed with the naturally available clay soil in various percentages by weight of the soil. AI is mixed with soil (10%, 15%, and 20%) by the weight of the soil taken [8].

2.2.2 Physical and Numerical Modeling

A numerical modeling study of the migratory behavior of hexavalent chromium through soil media was carried out with the help of finite element-based HYDRUS-3D solute transport software. Physical modeling of hexavalent chromium migration was conducted by horizontal rectangular tank study. The tank's dimension was (length = 30 cm, breadth = 20 cm, and height = 40 cm, and the material used was a perspex sheet. Three identical perforated cylindrical column with an internal diameter of 3 cm each were placed in the tank at a specified center-to-center distance. The first column is used as an injection well and the other two as observation wells. The whole tank was completely saturated, and then the effluents were collected at specified intervals from the outlet pipes connected at the bottom of the observation wells [20].

The physicochemical characteristics of AI-blended clay soil were considered as input parameters in the solute transport numerical modeling. Water flow and standard single porosity solute transport modules are the boundary conditions considered while conducting the numerical modeling by HYDRUS-3D.The mesh size was kept fine to obtain accurate results.

2.2.3 Methodology for Heavy Metals Estimation

For extracting the heavy metals from the soil samples, wet digestion Kjeldahl method was used, and the experiment was performed in triplicate for each sample. The heavy metals were determined using AAS fitted to a digital readout system. Stock solution for chromium was prepared, and from the stock solution, standards ranging from 0 to 5 ppm were prepared for the study [9].

2.2.4 Langmuir Isotherm Model

The adsorption energy is assumed to be constant and independent of surface coverage according to Langmuir's model from 1918. A monolayer of the adsorbate covering the surface results in maximal adsorption, which happens on a finite number of identical sites. The Langmuir equation is expressed as follows:

$$q_e = \frac{Q_{\max}.b.c_e}{1 + b.c_e}$$

Where $Q_{\max}$ = maximum sorption capacity at monolayer (mg/kg); b = constant related to the free energy of adsorption and a measure of the affinity of binding sites (L/mg).

2.2.5 Freundlich Isotherm Model

The assumption behind the Freundlich model (1926) is that adsorption takes place on a heterogeneous surface. The isotherm equation is expressed as follows:

$$q_e = k_f.c_e^{1/n}$$

Where k_f = adsorbent capacity (mg/Kg) and n = adsorbent intensity (L/mg), respectively.

2.2.6 Zero-Point Charge Test for Clay Soil

This test was performed to definethe zero-point charge of the soil. 0.1 M $NaNO_3$ was first prepared. For each 100 mL of 0.1 M $NaNO_3$ solution taken, 1 g of the soil

sample was added, and the pH was set accordingly using HCl and NaOH solutions. The pH range was maintained between 2 and 12. The solutions were kept in a BOD shaker for 48 h, at a temperature of 27 ± 1 °C and a rotational speed of 150 rpm. After 48 h, the samples were filtered and pH was measured again. The point of zero charge pH was obtained by locating the pH of the intersecting point by plotting a graph of the initial pH vs. final pH measured [7].

3 Result and Discussion

Statistical analysis for background pollutants, including heavy metals concentrations in all the soil samples collected from the solid wastes (SW) dump site at Durgapur, is presented in Table 1, which indicates a wide range of variation of the contaminant concentrations. However, the mean value of Cr concentration (10.16 mg/kg) in soil exceeded the permissible limit as depicted in the CCME [9] standards. The high concentration of Cr in the soil in the study area was due to continued disposal of solid waste from many industries, viz. tannery, steel plant, metal processing, chemical, and lubricant, situated in Durgapur city.

The above results show that a very high amount of hexavalent Chromium is present in the soils of the surrounding areas and inside the landfill. The primary cause of vertical and lateral dispersion of the leachate into the surrounding subsurface environment can be the landfill soil's high permeability value (10^{-4} cm/s).

Table 2 presents the descriptive statistical analysis for groundwater samples collected from and the surrounding areas of the tannery industry, which indicate a wide variation of pH (2.35–8.69), TDS (32.1–210), COD (400–2100), BOD (0.9–25.2), and hexavalent chromium (0.04–2.60 mg/l) in the studied water (WHO, Guidelines for drinking-water quality, 1963) (All the test are performed according to APHA).

In this study, an effort was made to employ naturally occurring clay soil as the major liner material in the landfill structure to stop contaminants from the waste disposal site from migrating below the surface [6]. The physicochemical characteristics of the clay soil to be employed as a liner material are listed in Table 3.

Clay soil was used as an adsorbent in laboratory-scale batch adsorption investigations (Fig. 3), which used a synthetically generated Cr (VI) solution as the test

Table 1 Statistical analysis of soil parameters (mg/kg) collected from Municipal Solid Waste site

	As	Cd	Pb	Fe	Hg	Cr	Cu	Al	Ni
Mean	0.74	0.38	4.63	8010	0.14	10.16	5.80	7336	5.02
SD	0.23	0.09	2.37	2747	0.06	2.91	3.25	3603	1.69
Max	1.05	0.48	8.65	11,413	0.24	12.50	10.93	13,333	7.90
Min	0.48	0.23	2.33	4733	0.09	6.43	2.18	4657	3.80
Threshold	12	1.4	70	–	6.6	1.4	63	–	50

Table 2 Water samples quality parameters from the nearby areas of small-scale tannery industry in mg/l

	pH	COD	BOD	TDS (NTU)	Cl^{-}	NO^{3-}	Cd	Cr^{+6}	Pb^{2+}	Fe	Zn^{2+}	SO^{4-}
Mean	6.67	1298	6.2	102.01	296.6	9.441	0.004	4.40	0.03	0.935	2.556	38.64
SD	2.16	596.50	2.34	56.33	202.53	7.492	1.81E-18	0.009	1.81E-18	0.079	0.0089	33.195
Max	8.69	2100	25.2	210	801.3	19.26	0.005	2.6	0.05	1.8	4.8	98.71
Min	2.35	400	0.9	32.1	107.7	0.796	0.001	0.04	0.003	0.05	0.115	2.24
Permissible limit (IS 10500:2012)	6.5–8.5	250	NIL	500–2000	250–1000	45	0.003	0.05	0.01	0.3	5–15	200–400

Table 3 Properties of the clay soil for liner material

Properties	Test results
Permeability (cm/sec) [15]	6.5×10^{-7}
pH	7.80
Specific gravity	2.56
Maximum dry density (MDD)	15.6 kN/m^3
Grain size distribution	Clay – 57%, silt – 31%, sand – 12%
Optimum moisture content	24.6%
Plasticity index (PI)	14.6
Liquid limit (%)	47
Plastic limit(%)	19.33
Cr^{6+} (mg/l)	NIL

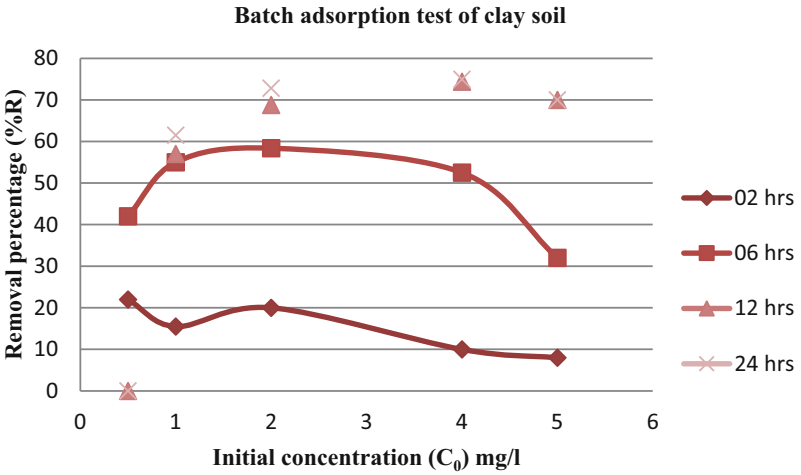

Fig. 3 Batch adsorption study using hexavalent chromium as adsorbate and naturally available clay soil as adsorbent

contaminant. The study reveals that a lower removal efficacy (74%) of Cr (VI) was achieved by clay soil, as shown in Fig. 3.

In this study, *Azadiracta indica* seed shells are blended with clay soil to increase adsorption efficacy. Hence the pH_{ZPC} of amended soil was observed as 6.75. As depicted in Fig. 4, the pH of the solution throughout is kept constant at 6.5. The clay soil is blended with AI seed shells in varying proportions of 10%, 15%, and 20% to increase the soil adsorptive capacity, which was only 70% when raw soil was directly used for adsorption. The proportions were fixed by reviewing the literature and performing the batch adsorption test. Hence, no such prominent adsorptive capacity was observed when less than 10% of AI-amended soil was used, and 20% of amended soil showed more than 90% removal of hexavalent chromium.

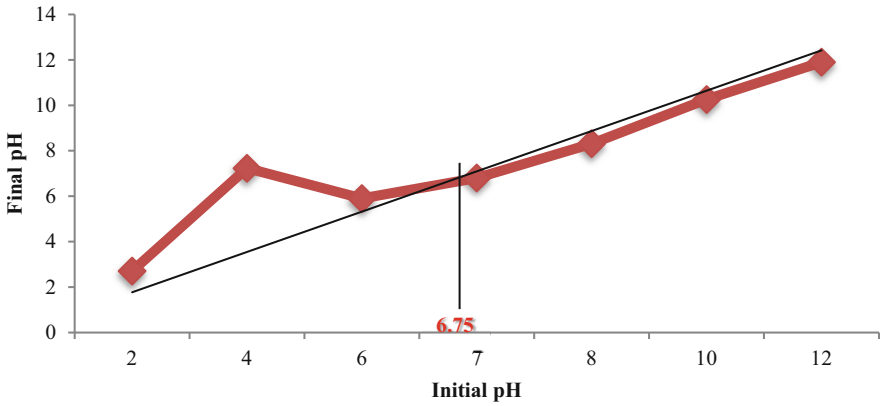

Fig. 4 pH_{ZPC} test of the amended clay soil

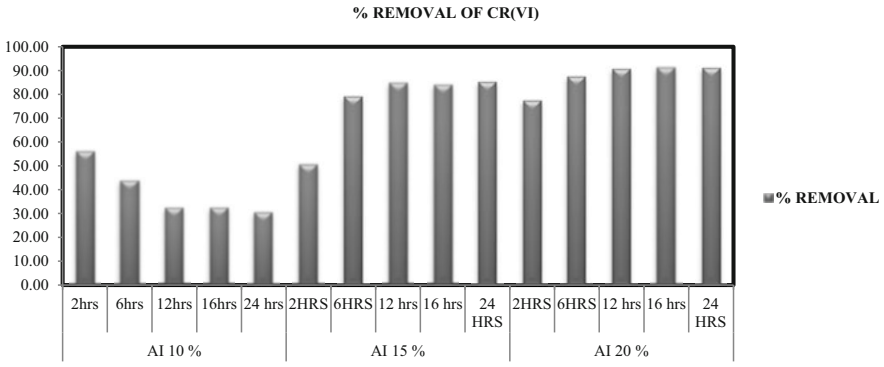

Fig. 5 Batch adsorption of AI blended with clay soil as adsorbent and hexavalent chromium solution as adsorbate

Figure 5 shows that the percentage of adsorbent dosage in aqueous medium increases as the contact time varies. It is evident from the graph that maximum removal was observed when the test was conducted for 12 h of contact time. The removal percentage was above 90% when amended with 20% (by weight) AI. It was evident from Fig. 5 that the rate of removal percentage of hexavalent chromium increased up to 44% during the first two hours when blended with *Azadiracta indica* 10% by weight of soil. Also, the removal percentage gradually decreased to 30% with the increasing contact time of up to 24 h. These trends don't show up when blended with *Azadiracta indica* 15% and 20% by weight of clay soil. The presence of more functional groups and surface area due to an increasing percentage of adsorbent is directly proportional to Cr (VI) sorption, resulting in higher removal of Cr (VI). Conversely, the specific surface area gets reduced at lower adsorbent dosage, resulting in lower contaminant adsorption due to faster saturation of the sorbent surface with contaminants.

3.1 Adsorption Isotherms

The Langmuir isotherm model fits best ($R^2 = 0.98$) compared to the Freundlich isotherm ($R^2 = 0.92$) model in the hexavalent chromium adsorption study with amended clay soil as adsorbent. Amended soil showed higher efficacy in adsorbing hexavalent chromium ($Q_{max} = 64.89$ mg/g), as depicted in Figs. 6 and 7. Amended clay soil can be considered as a potential primary liner material hence it is having low hydraulic conductivity, high adsorption capacity, and good chemical compatibility of the AI [10] (Table 4).

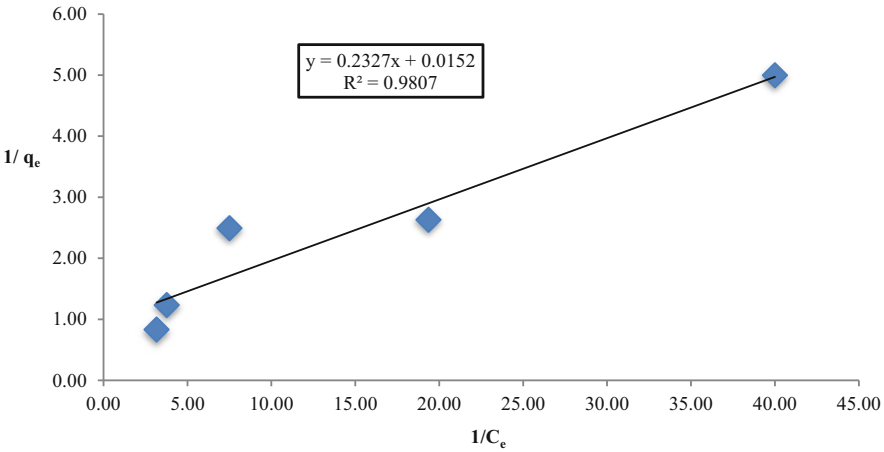

Fig. 6 Adsorption Langmuir isotherm model (AI-amended clay soil)

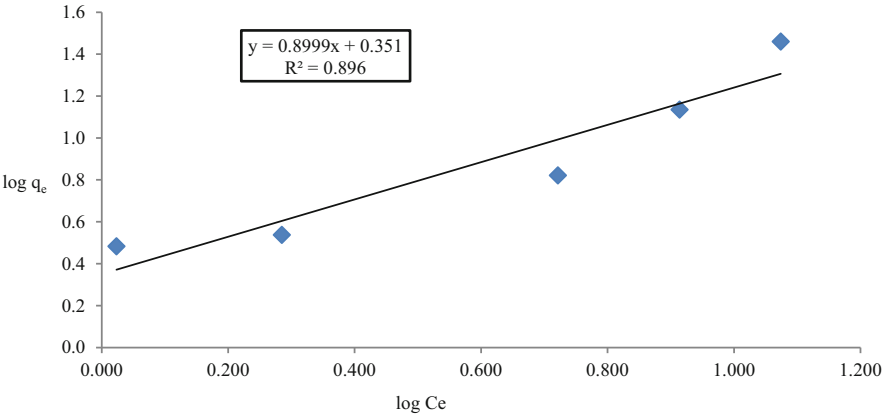

Fig. 7 Freundlich model for adsorption of hexavalent chromium by AI-amended clay soil

Table 4 Comparative study of Cr (VI) adsorption capacities of different adsorbents along with AI

Absorbent	Adsorption capacity (mg/kg)
Coconut tree sawdust	3.60
Beech sawdust	16.10
Treated sawdust of Indian rosewood	10.00
Hevea brasiliensis sawdust-activated carbon	44.05
Treated sawdust of sal tree	9.55
Mango sawdust	37.73
Moringa olifera dust	33.44
Neem seed dust	**65.789**

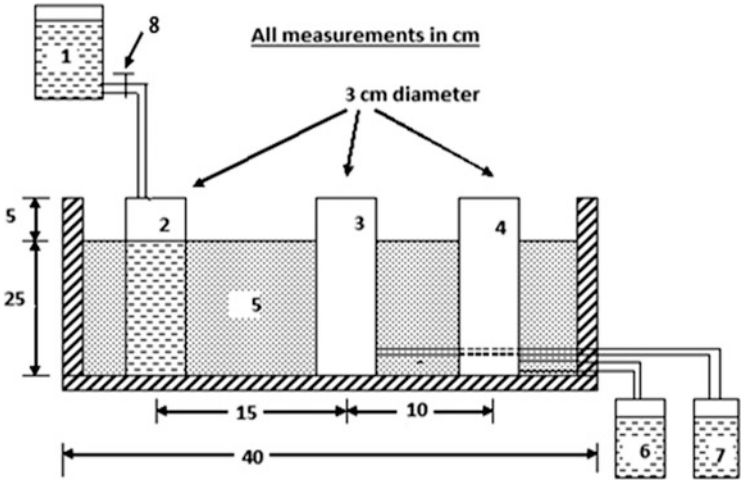

Fig. 8 Horizontal tank used for the hexavalent chromium migration test
1. Hexavalent chromium solution; 2. Injection well for the synthetic solution; 3. First observation well; 4. Second observation well; 5. Filled with amended clay soil; 6. Leachate collected from second observation well; 7. Leachate collected from first observation well; 8. Controlling valve [19]

3.2 Modeling of Hexavalent Chromium Migration Through AI-Amended Clay Soil

A laboratory-scale tank setup made of a perspex glass was used for a physical modeling study to assess the three-dimensional migratory behavior of hexavalent chromium through the amended clay soil strata [20]. The measurements of the horizontal tank were 30, 15, and 40 cm (height, breadth, length, respectively), and it was compacted with AI-blended clay soil up to a height of 25 cm (Figs. 8 and 9). The soil sample inside the tank was first completely saturated by flooding at the top with distilled water for 7 days. After that, synthetic Cr (VI) solutions with an input hexavalent chromium concentration of 5 mg/l were injected into the first well, and effluent concentrations were measured at a predetermined time interval from two observation columns, as shown in Figs. 8 and 9.

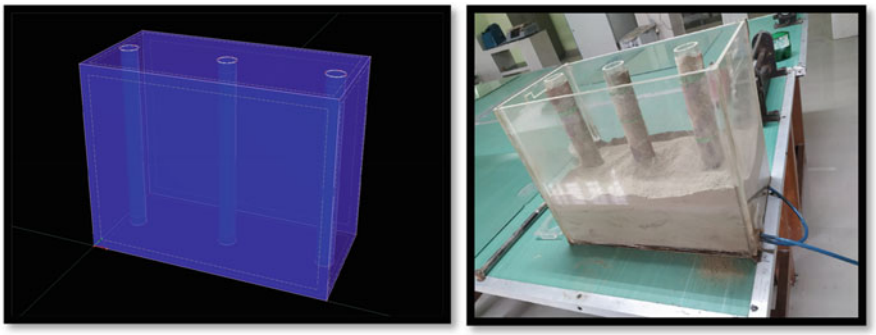

Fig. 9 Experimental setup (horizontal tank) in HYDRUS-3D and laboratory setup

Using the HYDRUS-3D software program, numerical modeling of Cr6+ movement through the soil was carried out. The HYDRUS-3D model used the nonlinear isotherm coefficients as input parameters to calculate the Cr6+ breakthrough curves (BTCs), using a 0.5 soil tortuosity value.

The experimental and HYDRUS-3D predicted breakthrough curves for observation points 1 and 2 are shown in Fig. 10a, b. It is observed from the Figs. 10 and 12 that almost 50% of experimental breakthrough was reached within the experimental time (Fig. 11).

The HYDRUS-3D predicted BTCs closely resembled up to 50% of the experimental BTCs. However, the numerical model–predicted BTCs reached exhaustion after 400 and 1000 days for observation points 1 and 2, respectively (Figs. 10 and 12). To use the same bottom liner material in the waste containment structure, the HYDRUS-3D model was further expanded to estimate the migration of the contaminant in the amended clay soil, which is 1 m thick. According to Fig. 11 breakthrough curve, which was anticipated by the HYDRUS-3D model, the liner bed exhaustion occurs after 40 years. This study's outcome indicates that the AI-amended clay soil has a high potential to restrict the subsurface spreading of contaminants emanating from chromium laden wastes disposed to open land or water bodies.

4 Conclusions

This study shows a higher level of hexavalent chromium pollution in the nearby areas of the subsurface soil at the solid waste disposal site. The soil quality analysis revealed that the amount of chromium concentration (12.6 mg/kg) in the soil surpassed the prescribed limit (1.4 mg/kg) as depicted in the CCME [9] guidelines. The surface and groundwater near the small-scale leather industries at Kolkata, West Bengal, India, were also highly contaminated with Cr (VI) pollutants [17]. Hence, immediate preventive measures are needed to restrict the contaminant migration

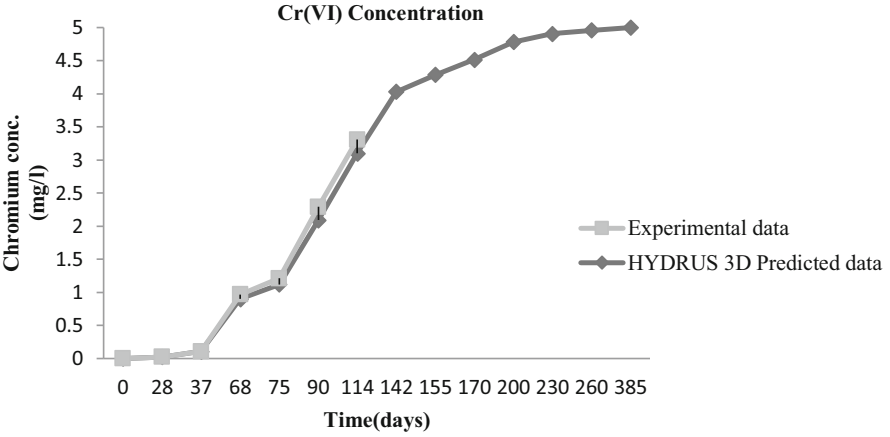

(a) 1ST OBSERVATION WELL OF TANK TEST

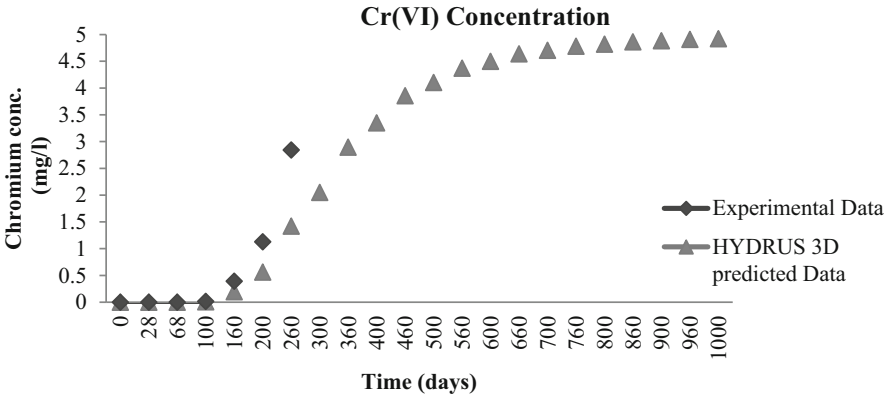

(b) 2ND OBSERVATION WELL OF

Fig. 10 BTC drawn from lab experimental data and modeling predicted data. (**a**) FIRST observation well of test tank. (**b**) Second observation well of tank test

resulting in soil and groundwater pollution. Keeping this in mind, the study assessed the efficiency of *Azadirachta indica*–blended clay soil in a predefined ratio as a liner in the waste containment structures. It was observed that AI-blended clay soil provides efficient chemical compatibility and good chromium uptake capacity, thereby conforming to its use as a liner material.

Future testing with real-life Cr (VI) aqueous solutions is to be carried out further to examine the efficacy of the AI-amended clay soil as adsorbent at the bottom of the landfill or any waste containment structure for mitigating the leachate flow to the nearby soil and groundwater. Field-scale studies are to be conducted for verification of the physical as well as numerical modeling of Cr (VI) transport in soil media.

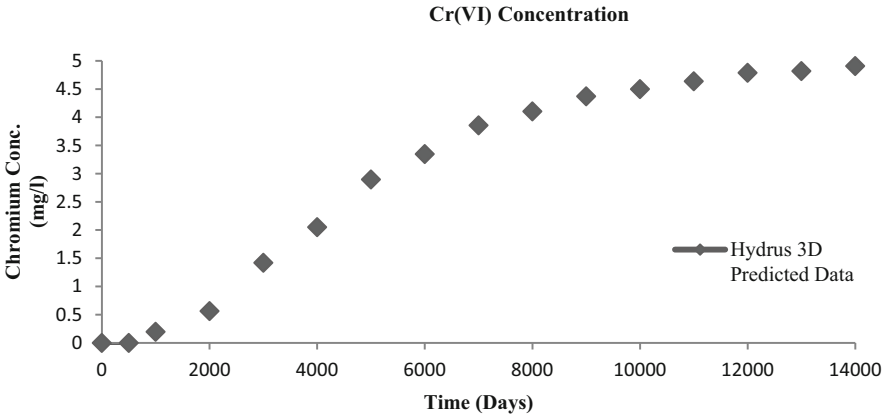

Fig. 11 Hydrus-3D predicted breakthrough graph for 1 m thick amended clay liner

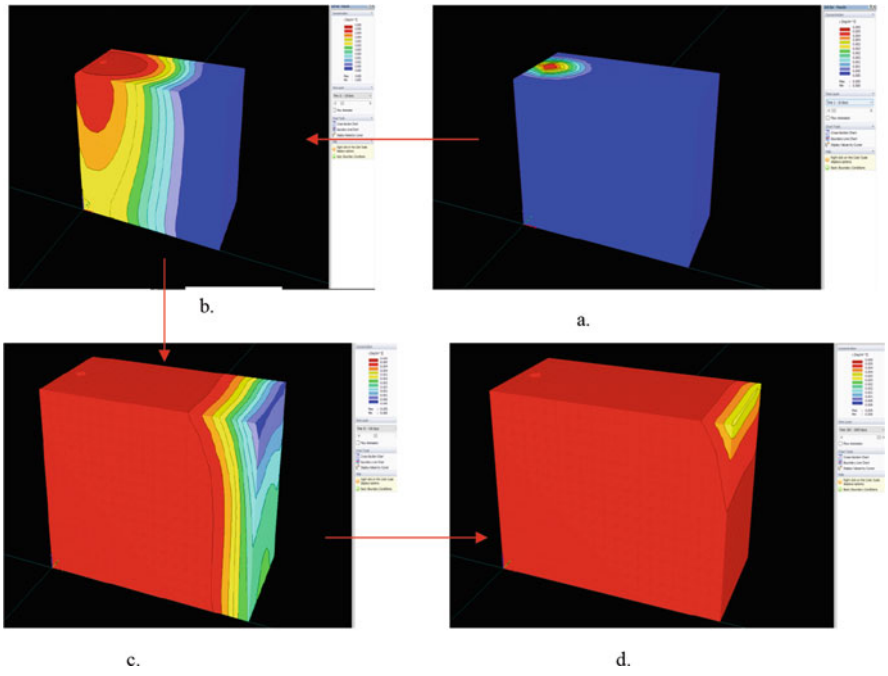

Fig. 12 Solute transport through clay soil media: (**a**) 0–10 days, (**b**) 11–110 days, (**c**) 41–410 days, (**d**) 100–1000 days

Acknowledgment The authors express their wholehearted gratitude to the Department of Civil Engineering and Department of Earth & Environmental Studies, NIT Durgapur, and Civil Engineering Department of Heritage Institute of Technology, Kolkata, West Bengal, India, for providing all necessary supports and assistance to carry out this research. The authors also wish to convey their sincere thanks to the Director, NIT, Durgapur, West Bengal, India, for his constant encouragement throughout the study.

References

1. J.C. Akan, E.A. Moses, V.O. Ogugbuaja, Assessment of tannery industrial effluent from Kano metropolis, Nigeria Asian Network for Scientific Information. J. Appl. Sci. **7**(19), 2788–2793 (2007)
2. J.C. Akan, F.I. Abdulrahman, G.A. Dimari, V.O. Ogugbuaja, Physicochemical determination of pollutants in wastewater and vegetable samples along the Jakara wastewater channel in Kano metropolis, Kano State, Nigeria. Eur. J. Sci. Res. **23**(1), 122–133 (2008)
3. APHA-AWWA-WPCF, *Standard Methods for the Examination of Water and Wastewater*, 20th edn. (American Public Health Association, Washington, DC/New York, 2005)
4. V.O. Arief, K. Trilestari, J. Sunarso, N. Indraswati, S. Ismadji, Recent progress on biosorption of heavy metals from liquids using low cost biosorbents: Characterization, biosorption parameters and mechanism studies. Clean Soil Air Water **36**, 937–962 (2008)
5. J.A. Barry, B.W. Karney, Z. Members, C.J. Cormier, A. Lat, Artesian landfill liner system: Optimization and numerical analysis. J. Water Resour. Plan. Manag. **124**, 345–356 (1998)
6. C. Bhadra, S. Pal, K. Adhikari, Use of compacted clay liner for the attenuation of landfill leachate migration from a MSW site in Durgapur, West Bengal. J. Indian Chem. Soc. **95**, 235–242 (2018)
7. C. Bhadra, S. Pal, K. Adhikari, Efficacy evaluation of chromium(VI) adsorption on clay soil blended with Azadiracta indica (Neem) and Moringa oleifera (Drum stick) seed shell. J. Indian Chem. Soc. **96**, 1–5 (2019)
8. CCME (Canadian Council of Ministers of the Environment), Interim Canadian environmental quality criteria for contaminated sites, CCME, Winnipeg, 1991
9. R. Chakraborty, M. Chakraborty, A. Mitra, Infrared irradiation aided fabrication of Mn impregnated-natural bone adsorbent: Efficacy evaluation in aqueous Cr (VI) removal. J. Water Process Eng. **6**, 32–41 (2015)
10. M. Chowdhury, M.G. Mostafa, T.K. Biswas, A.K. Saha, Treatment of leather industrial effluents by filtration and coagulation processes. Water Resour. Ind. **3**, 11–22 (2013)
11. K. Cooman, M. Gajardo, J. Nieto, C. Bornhardt, G. Vidal, Tannery waste water characterization and toxicity effects on Daphnia Spp. Environ. Toxicol. **18**, 45–51 (2003)
12. Council of leather export (CLE), Sponsored by Ministry of Commerce & Industry, Government of India
13. R. Ganesh, R.A. Ramanujam, Biological waste management of leather tannery effluents in India: Current options and further research needs. Int. J. Environ. Monit. **3**, 232–237 (2009)
14. IS 10500, *Drinking Water – Specification* (Bureau of Indian Standards, New Delhi, 2012)
15. IS 2720: Part III: Sec 2: 1980, Test for soils: Determination of Specific Gravity of fine-grained soil
16. IS2720: Part 17: 1986, Methods of test for soils: Laboratory determination of permeability
17. S.R. Khan, M.A. Khwaja, S. Khan, G.H. Kazmi, Environmental impacts and mitigation costs of cloth and leather exports from Pakistan. Environ. Dev. Econ. **6**, 383–403 (2001)
18. S. Pal, S.N. Mukherjee, S. Ghosh, Optimizing phenol sorption in peat by response surface method. J. Environ. Geotech. **1**(3), 142–151 (2013)
19. S. Pal, S.N. Mukherjee, S. Ghosh, Application of HYDRUS 1D model for assessment of phenol–soil adsorption dynamics. Environ. Sci. Pollut. Res. **21**(7), 5249–5261 (2014)
20. P. Scholl, D. Leitner, G. Kammerer, W. Loiskandl, H.-P. Kaul, G. Bodner, Root induced changes of effective 1D hydraulic properties in a soil column. Plant Soil **381**, 193–213 (2014)
21. United States Environmental Protection Agency 2002
22. WHO, *Guidelines for Drinking-Water Quality* (World Health Organization, Geneva, 1963)

Electrokinetic Remediation of Total Chromium from Contaminated Soil

Pravin Lal and Supriya Pal

Abstract Exploitation of nature by various human-made activities to serve humanity has led to environmental pollution. Soil decontamination is an important aspect of environmental remediation. Electrokinetic (EK) remediation is an efficient, economical, and less time-consuming process for soil decontamination. It is a non-invasive method, meaning that it does not require excavation or excavation-related disturbance of the contaminated soil. This can reduce the risk of further contaminants spreading and minimize potential environmental harm. This electrokinetic study results indicate that the removal efficiencies of total chromium (Cr) from the soil are considerably influenced by the type of purging solutions as anolyte and catholyte, applied voltage and current, and pH of the soil. Lab-scale electrokinetic experiment was conducted on the Cr-contaminated soil. 0.1 M Citric acid solution was used as anolyte and catholyte. There was a fixed voltage gradient of 1 V/cm applied through graphite rods as anode and cathode. The experiment was run for 200 h. The total chromium (Cr) removal efficiency from soil was 76%. However, electrode configurations and electrolyte conditioning significantly achieve higher heavy metals removal efficiency from contaminated land.

Keywords Chromium · Electrokinetic · In situ · Heavy metal · Remediation · Soil contamination · pH · Citric acid · Cost · Energy consumption · Efficiency

P. Lal (✉)
Department of Earth and Environmental Studies, National Institute of Technology Durgapur, Durgapur, West Bengal, India
e-mail: pl.21p10087@mtech.nitdgp.ac.in

S. Pal
Department of Civil Engineering, National Institute of Technology Durgapur, Durgapur, West Bengal, India
e-mail: supriya.pal@ce.nitdgp.ac.in

D. Mazumder (ed.), *Sustainable Advanced Technologies for Industrial Pollution Control*, Springer Proceedings in Earth and Environmental Sciences,
https://doi.org/10.1007/978-3-031-37596-5_21

Abbreviations

BIS	Bureau of Indian Standards
Cr	Chromium
DC	Direct Current
EK	Electrokinetic
IS	Indian Standard
USEPA	United States Environmental Protection Agency
WHO	World Health Organization

1 Introduction

Electrokinetic remediation is appropriate for in situ remediation of soils with low permeability and/or heterogeneity, which are contaminated with heavy metals, organic contaminants, or both [1–3]. This technique includes applying low-density direct current to the polluted site. Placing electrodes in the contaminated area and running a low-density direct current through them create an electric field that makes the contaminant particles mobile in the soil media. Many other techniques of soil decontamination, such as bioremediation and phytoremediation, are deployed, but their slow rate of reaction, sensitivity to ground susceptibility, and their applications limited to shallow depths make them less efficient than electrokinetic remediation.

Low-level direct current modifies the soil mass and physicochemical and hydrological characteristics, which leads to coupled mechanisms that facilitate species transport [4]. Electromigration and electro-osmosis are important mechanisms in electrokinetic soil processing for eliminating contaminants. The transfer of polar molecules and ions in an electric field is electromigration, and it begins when electrolysis of water dissociates into hydrogen ions in the anode compartment and the acid front migrates across the soil cell where contaminants are desorbed from the soil surface. An ionic liquid flows due to electro-osmosis, which is induced by electric potential when an electric field is applied in relation to a charged surface [5].

Vauquelin discovered chromium as a component of lead ore in 1797. It was immediately noticed in a wide range of industrial uses, including chromates, chromium plating, pigments, leather tanning, refractory materials, and the mordanting of textiles. Compounds of chromium are variably used in the chemical industry as corrosion inhibitors, wood preservatives, fungicides, heliogravure products, and other things [6]. The effluent from such industries contaminates the nearby soil. Dermatitis, skin, and mucous membrane ulcers, allergic asthma reactions, the nasal septum perforation, gastroenteritis, hepatocellular deficiency, bronchial carcinomas, and renal anuric oligo insufficiency are the negative impacts on human health [6]. Therefore, it is necessary to decontaminate soil from chromium.

2 Materials and Methods

2.1 Materials

The sample of soil was collected from a soil quarry in Nadia district, West Bengal, India. The potable source of contamination is handloom and dye Industries in the concerned area. For the purpose of preserving the soil moisture content, soil samples were collected in a container and then sealed. The physical parameters of the soil sample were subsequently assessed after it had been oven-dried for 24 h. According to guidelines of the Bureau of Indian Standards, the physiochemical characteristics of the soil were assessed (BIS: 2720). Three numbers of tests were performed for the determination of each parameter, and average values were considered to produce better reproducibility and repeatability of the tests (Table 1).

2.2 Electrokinetic Experiment

The electrokinetic reactor that carries out the total Cr removal from soil was mainly made of Perspex glass that is open at the top. The box is 49.5 cm long, 20.4 cm wide, and 15.3 cm high. The experiment cell consists of 8 slots for placing the Perspex glass, which is about 10 mm thick, as shown in Fig. 1. By placing two Perspex glasses at two slots, it divides the whole cell into three compartments—anode, cathode, and the middle compartment of the specimen of soil. At the cathode and anode, respective solutions of catholyte and anolyte are placed. The two walls of the electrokinetic cell that divide the three compartments are perforated with numerous holes that range in diameter from 4 to 5 mm. They contribute to the initiation of electro-migration and electro-osmosis. At the beginning of the experiment, filter paper according to the size of the Perspex glass is placed along it. Two electrodes are

Table 1 Physiochemical properties of the studied soil

Parameters	Unit	Standards	Values
Color	–	–	Blackish gray
Bulk density (γ_b)	kN/m^3	IS 2720-29 (1975)	14.7
Maximum dry density (γ_{dmax})	kN/m^3	IS 2720-7 (1983)	15.26
Optimum moisture content (OMC)	%		23.45
Specific gravity (G)	–	IS 2720-3(1) (1980)	2.65
Liquid limit (LL)	%	IS 2720-5 (1985)	25
Plastic limit (PL)	%	IS 2720-5 (1985)	18
Cohesion (c)	kN/m^2	IS 2720-11 (1993)	11.768
Soil pH	–	IS 2720-26 (1987)	6.8
Fine sand	%	IS 2720-4 (1985)	2.53
Silt	%		93.57
Clay	%		3.9

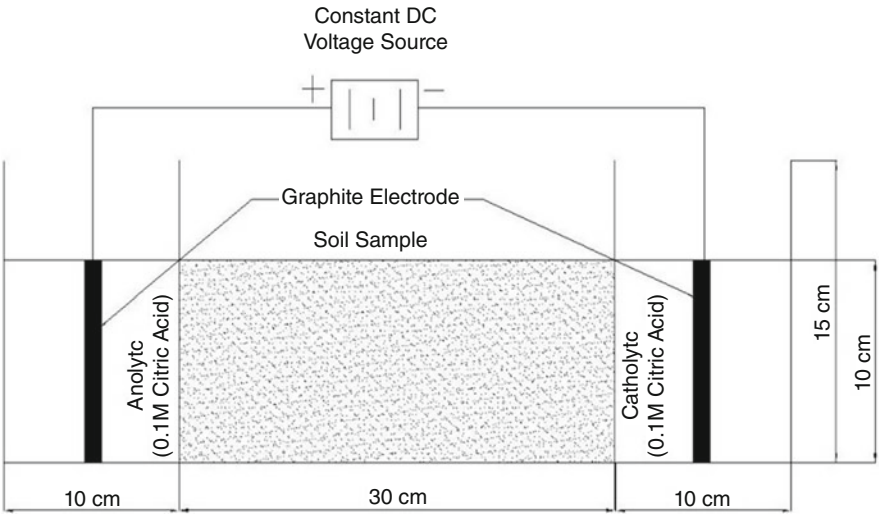

Fig. 1 Experimental electrokinetic setup

placed at the extreme edge of the soil specimen. The electrodes are made of inert graphite, which are 5–6 cm thick. The entire circuit was completed under a constant electric potential.

The electrode arrangement is essential to the entire procedure since it affects installation costs, process efficiency, and operation times. One-dimensional (1-D) and two-dimensional (2-D) electrode combinations are frequently used in electrokinetic remediation. Although a 2D arrangement places the cathode or anode at the center and the other electrode at the apex of a polygon, a 1D configuration places the anode parallel to the cathode. The electrically active region is determined by the electrode configuration: When it comes to electrical conductivity, a 2D design frequently has a larger electrical effective area than a 1D configuration [7].

A method for improving the effectiveness of electrokinetic remediation is electrolyte conditioning. To hasten the desorption and movement of metals in an electric field, electrolyte conditioning solutions that are acidic or basic are used. The catholyte's ability to desorb and move heavy metal ions in an electric field is improved by pretreatment and treatment with an acidic solution [8].

The anode and cathode chambers were filled with the electrolytic solution. As anolyte and catholyte, 0.1 M citric acid solution was employed. Soil sieved through a 600 μm sieve was filled in the middle compartment, as shown in Fig. 1. The soil was then saturated for 24 h by flooding with double distilled water at the top. After the completion of saturation, the experiment was started by maintaining a constant voltage difference of 30 V between the cathode and anode, and the current passing through the circuit was also measured throughout the period of the test at different intervals of time. The constant DC voltage was maintained throughout the experiment using HTC DC-3005 (Made in India) instrument. The pH of the electrolyte was continuously monitored. As the pH of the anolyte and catholyte deviated from the

range of pH 2–6, then the solutions were changed to freshly prepared 0.1 M citric acid solution with pH 2.4.

The completion time of the experiment was indicated by the sharp fall of current density in the DC voltage source equipment. The soil sample was then divided into three slices, viz., anode sample, middle sample, and cathode sample. The samples were further divided into the top layer, middle layer, and bottom layer. The extraction of total Cr was done using acid digestion abiding by the USEPA 3050B. An atomic absorption spectrophotometer (PerkinElmer AAnalystTM 800) was used to measure the concentrations of total Cr in the extracts. The background soil concentration of total chromium was found to be 3220 μg/kg. Chromium levels in industrial effluent must be lowered to 0.5 mg/L before being discharged into the environment (USEPA) and 0.1 mg/L in agriculture soils (WHO). The maximum permitted contamination of Cr (VI) in drinking water, according to Indian standard (IS 10500), is 50 μg/L.

2.3 *Variation of Current Density and Energy Consumption in Electrokinetic Treatment*

The magnitude of current that passes through the area of cross-section of the soil is termed as current density [9]. The higher level of current generates more acid and which in turn increases the overall concentration of ions in the system. This mechanism helps in the mobilization of ions and thereby accelerates the electromigration process. Figure 2 shows the variation in current density and the energy consumption with time. The energy consumption is measured from the following equation:

$$E_c = \frac{V}{1000\,AL}\int_0^t I\,dt$$

where E_c is the energy consumed per unit volume of soil (kWh/m^3), I is the current flowing through the soil specimen (Amp), V is the applied electric potential in Volt, L is the length of the specimen (m), and t is the elapsed time in hours, A is the area of cross-section of the soil specimen (m^2).

The viability of the application of the in situ EK technique mainly depends on the energy consumption in treating the soil mass. Figure 2 shows that the energy consumed per unit volume of the soil mass after 200 h of treatment was comparatively low (78.25 kWh). This estimation clearly shows that the electro-kinetic remediation of total Cr using 0.1 M citric acid purging solution is a rapid and cost-effective in situ ground improvement technique.

Cost Calculation for Energy Consumption
Estimated Cost of ELECTRICITY per unit (kWh) commercial = Rs. 9 INR
(As per the government of West Bengal)

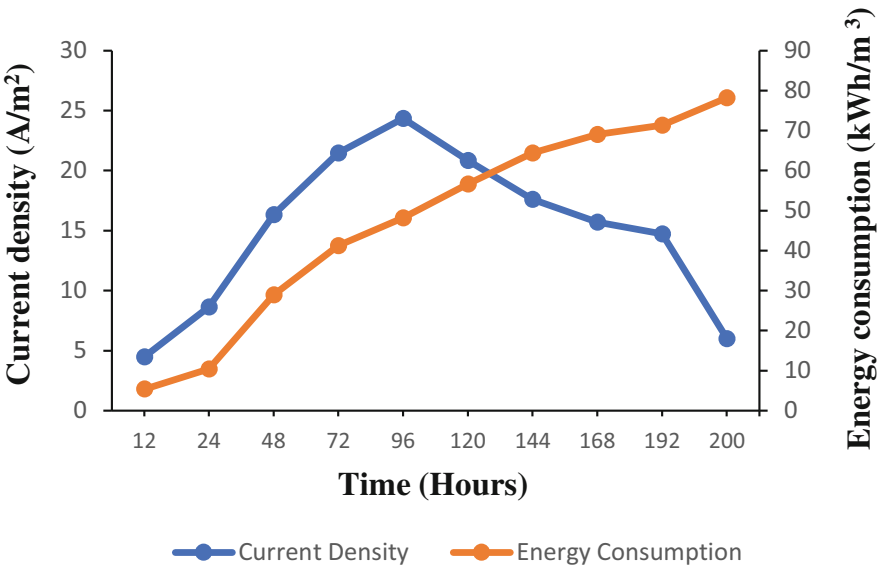

Fig. 2 Plots of current density and energy consumption during electrokinetic treatment

Total units used in experiment = 79 kWh (approx.)
Total cost of energy consumption = 79 × 9 = Rs. 711 INR

2.4 Distribution of pH of Soil

Pulverized soil sample was taken and mixed with water in the ratio 1:2.5 (soil: water) and then the slurry was put into vials and centrifuged at 6000 rpm for a stipulated time of 15 min. The supernatant was filtered, collected in a beaker, and measured by a pH meter. The natural pH of the contaminated soil was found to be pH 6.8. After electrokinetic treatment of contaminated soil sample, it was observed that the soil pH adjacent to the anode (pH = 1.8) and cathode (pH = 7.2) was acidic and alkaline, respectively. The pH distributions throughout the soil specimen are exhibited in Fig. 3.

During the electrolysis process in both the electrolytes, hydroxyl (OH^-) and hydrogen (H^+) ions are released due to reduction and oxidation at the cathode and anode, respectively. As a result, the soil near the cathode and anode, respectively, became alkaline and acidic. The released H^+ ions close to the anode compartment migrate toward the cathode compartment, mainly governed by electro-migration and the electro-osmotic flow of pore fluid [9]. The electrolytic reactions are shown below:

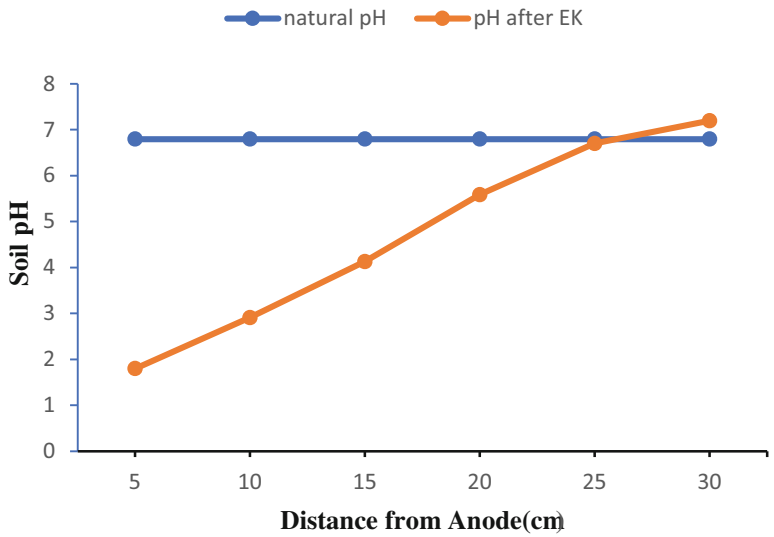

Fig. 3 Plot of distributions of soil pH after EK treatment

$$\text{Anode} : 2H_2O - 4e^- \rightarrow O_2 \uparrow + 4H^+$$

$$\text{Cathode} : 2H_2O + 4e^- \rightarrow H_2 \uparrow + 2OH^-$$

3 Results and Discussion

In contaminated soil, the total Cr concentration was 3220 µg/kg soil initially. The Cr concentration close to the anode and cathode was 733 µg/kg and 801 µg/kg, respectively, after the experiment was run for 200 h at 30 V. The total Cr in the mid-section of the soil sample was 755 µg/kg. Figure 4 shows the different concentrations of total chromium in the contaminated soil sample after EK treatment. Within a range of pH 2–6, electrokinetic remediation of polluted soil was studied. Acidic environments facilitate the removal of heavy metals [10]. The outcomes demonstrate a steady reduction in pH in the anode compartment and an increase in pH in the cathode compartment, which together resulted in an increase in electroosmotic flow. A change in pH within a soil specimen does not have a significant impact on the voltage gradient [11]. This method can also be deployed for the remediation of other metal contaminants as Cd, Cu, Zn, and Pb using citric acid. Various other studies have been made using different electrolytes along with different voltage gradients to remove other metal contaminants [12, 13]. Electrokinetic remediation's viability in the field is dependent on several variables, such as the kind and degree of

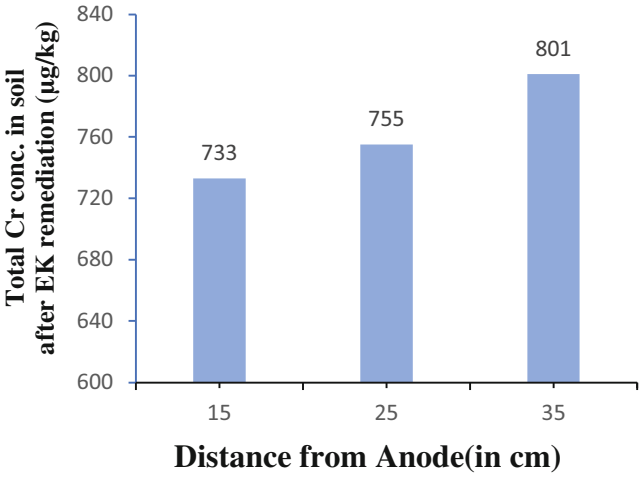

Fig. 4 Concentrations of total chromium in contaminated soil after EK treatment

Table 2 Chromium removal efficiency in EK setup

Type of soil	Target contaminant	Purging solution	Duration of Experiment	Removal efficiency (%)
Clayey-silt	Total chromium (Cr)	0.1 M citric acid	200 h	76%

contamination, the physical characteristics of the site, and the availability of resources. Installation of electrodes and the deployment of an electric field are necessary for electrokinetic remediation, which can be challenging in places with extremely porous soils or high groundwater flow rates. Electrokinetic remediation might not work if the contaminants are not soluble or do not have a charge. Despite various challenges, electrokinetic remediation has been successfully applied in several field applications, such as the remediation of mine tailings, silt in rivers and lakes, and soil and groundwater at hazardous waste sites [14]. The field applicability of this method ultimately rests on a careful evaluation of the site's conditions, the characteristics of the contaminants, and the resources available, as well as careful planning and execution of the restoration process (Table 2).

4 Conclusion

In this study, it was found that citric acid as an electrolyte helps to enhance the electrokinetic process for the removal of total chromium from contaminated soil. The transportation and dissolution of complex metals out of the soil specimen are much more successful with citric acid. The energy consumption of the in situ

experiment shows the cost-effectiveness and efficacy of the system. Electrokinetic remediation process can be enhanced by utilizing appropriate electrolytes, and voltage gradient, furthermore combining with a cost-effective suitable electrode to increase the efficiency and can be considered as a promising technique for in situ land decontamination. There is a scope for future development of this study. Further experiments can be done by carrying out EK treatment with mixed metal contaminants spiked soil mass and the effect on the removal efficacy. This method can also be coupled with bioremediation and phyto-remediation for the removal of contaminants.

Acknowledgment The National Institute of Technology (NIT) Durgapur in West Bengal, India, in conjunction with its departments of Civil engineering and Earth and Environmental studies, gave the authors the assistance and support they required to accomplish their work. The authors also acknowledge Professor Anupam Basu, Director of NIT Durgapur, West Bengal, India, for his continuous support throughout the endeavor.

References

1. K. Reddy, Iodide-enhanced Electrokinetic remediation of mercury contaminated soils. J. Environ. Eng. **129**, 1137–1148 (2004)
2. P.V. Sivapullaiah, Electroosmotic flow behavior of metal contaminated expansive soil. J. Hazard. Mater. **143**, 682–689 (2007)
3. S.-O. Kim, Evaluation of electrokinetic removal of heavy metals from tailing soils. J. Environ. Eng. **128**, 705–715 (2004)
4. S.-O. Kim, S.-H. Moon, K.-W. Kim, Removal of heavy metals from soils using enhanced electrokinetic soil processing. Water Air Soil Pollut. **125**, 259–272 (2001)
5. Y.B. Acar, R.J. Gale, A.N. Alshawavkeh, Electrokinetic remediation: Basics and technology status. J. Hazard. Mater. **40**, 117–137 (1995)
6. F. Baruthio, Toxic effects of chromium and its compounds. Biol. Trace Elem. Res. **32**(1–3), 145–153 (1992)
7. H. Xu, L. Cang, Y. Song, J. Yang, Influence of electrode configuration on eletrokinetic-enhanced persulfate oxidation remediation of PAH-contaminated soil. Environ. Sci. Pollut. Res. **27**(35), 44355–44367 (2020)
8. B.-G. Ryu, G.-Y. Park, J.-W. Yang, K. Baek, Electrolyte conditioning for electrokinetic remediation of As, Cu, and Pb-contaminated soil. Sep. Purif. Technol. **79**(2), 170–176 (2011). ISSN 1383-5866
9. H. Moayedi, R. Nazir, K.A. Kassim, B.K. Huat, Measurement of the electrokinetic properties of peats treated with chemical solutions. Measurement **49**, 289–295 (2014). ISSN 0263-2241
10. L.M. Ottosen, H.K. Hansen, P.E. Jensen, Electrokinetic removal of heavy metals, in *Electrochemical Remediation Technologies for Polluted Soils, Sediments and Groundwater*, (2009), pp. 95–126
11. A. Arti, R.P. Tiwari, R.P. Singh, Effect of pH of anolyte in electrokinetic remediation of cadmium contaminated soil. Int. J. Eng. Res. Technol. **1**, 10 (2012)
12. C. Cameselle, S. Gouveia, A. Cabo, Enhanced electrokinetic remediation for the removal of heavy metals from contaminated soils. Appl. Sci. **11**, 1799 (2021)

13. N. Xie, Z. Chen, H. Wang, C. You, Activated carbon coupled with citric acid in enhancing the remediation of Pb-Contaminated soil by electrokinetic method. Appl. Sci. **308**, 127433 (2021)
14. J.M. Purkis, P.E. Warwick, J. Graham, S.D. Hemming, A.B. Cundy, Towards the application of electrokinetic remediation for nuclear site decommissioning. J. Hazard. Mater. **413**(125274), 125274 (2021), ISSN 0304-3894)

Low-Cost Recovery of Cadmium from Wastewater by Soil Bacteria

Mahindra Kothuri and C. P. Devatha

Abstract Cadmium is a toxic heavy metal with significant health and environmental concerns. It accumulates in soil and water, contaminates the food chain, and causes severe health problems, including kidney damage, anemia, and cancer. Industries involving the production of pigments, batteries, and alloys discharge wastewater containing high levels of cadmium. Hence, wastewater can serve as a valuable and viable source of cadmium, reducing the need for costly and environmentally damaging mining and refining activities. This study aims to recover cadmium from wastewater using bioprecipitation. Ureolytic bacteria from rhizospheric soil were used to separate cadmium from synthetic wastewater of different strengths. The recovery efficiency of the bioprecipitation method was more than 95%, according to the atomic absorption spectroscopy (AAS) analysis. X-ray diffraction (XRD), scanning electron microscopy (SEM), and energy dispersive X-ray spectroscopy (EDS) studies were conducted to identify the residue. In conclusion, bioprecipitation method has been found to be an effective and sustainable approach to recover cadmium from wastewater, making it a promising solution to economic and environmental challenges. This method is efficient, cost-effective, and easy to operate, making it suitable for in-field applications.

Keywords Bioprecipitation · Rhizosphere · Urea hydrolysis · Otavite

Abbreviations

AAS	Atomic absorption spectroscopy
EDS	Energy dispersive X-ray spectroscopy
SEM	Scanning electron microscopy
XRD	X-ray diffraction

M. Kothuri (✉) · C. P. Devatha
Department of Civil Engineering, National Institute of Technology Karnataka, Surathkal, Mangaluru, Karnataka, India
e-mail: mahindrakothuri.187cv006@nitk.edu.in; devathafce@nitk.edu.in

D. Mazumder (ed.), *Sustainable Advanced Technologies for Industrial Pollution Control*, Springer Proceedings in Earth and Environmental Sciences,
https://doi.org/10.1007/978-3-031-37596-5_22

1 Introduction

Cadmium (Cd) is a mobile carcinogenic trace element in the environment. Its bioavailability leads to health-related issues due to bioaccumulation and biomagnification [1, 2]. Anthropogenic activities such as electroplating, waste incineration smelting, and battery manufacturing generate high cadmium wastewater [3, 4]. Cost-effective and low-cost approaches for recovering essential metals from secondary sources have been devised to address economic and environmental restrictions. Adsorption, membrane filtration, electrochemical treatment, coagulation, and flocculation are the conventional methods of cadmium recovery from wastewater. However, these are slow recovery processes and expensive procedures in terms of initial capital and maintenance costs [5]. This chapter presents bioprecipitation as an instant solution for cadmium recovery from wastewater.

Bioprecipitation uses microorganisms such as bacteria to produce biominerals by providing suitable substrates and environmental conditions. It is possible through several mechanisms, and urea hydrolysis is the most efficient pathway [6]. The urease enzyme governs the rate of urea hydrolysis. It is secreted by several bacteria abundant in the rhizospheric soil zone [7]. The rhizospheric zone is the thin soil surrounding the root systems of plants and is highly influenced by root secretions. Soil bacterial species like *Bacillus pasteurii, Bacillus sphaericus,* and *Bacillus cereus* are instrumental in bioprecipitation [8].

Urea provides an alkaline environment suitable for bioprecipitation. When it gets dissolved in water, it produces carbonate ions. They are divalent anions and readily react with the available cations in their environment. Since cadmium ions in the wastewater are free cations, they react with the carbonate ions to form cadmium carbonate. It is a stable form of cadmium and is deposited on the negatively charged extracellular polymeric substance on the bacterial surface [9] (Fig. 1). Hence, the bacterial surface provides the nucleation site for the reaction between cadmium and carbonates [10].

$$\mathrm{CO(NH_2)_2} + 2\mathrm{H_2O} + \text{Bacterial cell.}\ \mathrm{Cd^{2+}} \xrightarrow{\text{Urease}} \text{Bacterial cell.}\ \mathrm{CdCO_3} + 2\mathrm{NH_4^+} \quad (1)$$

There are various methods for removing cadmium from wastewater, including chemical precipitation, ion exchange, coagulation with flocculation, electrodialysis,

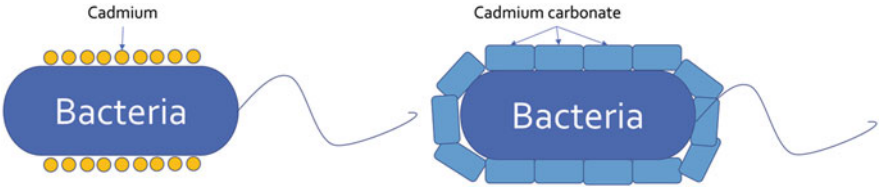

Fig. 1 Schematic of bioprecipitation by soil bacteria

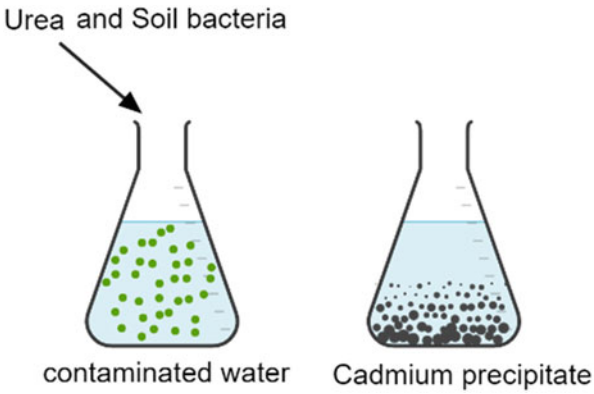

Fig. 2 Schematic of cadmium precipitation through urea hydrolysis by soil bacteria

photocatalysis, membrane separation, and the use of nano-adsorbents and hydrogels. They offer benefits such as economic feasibility and ease of operation. However, they have the drawbacks of high operational cost, energy consumption, and sludge production [11]. This study attempts to overcome the disadvantages of existing technologies.

The objective of this study is to estimate the cadmium recovery efficiency through the bioprecipitation technique from wastewater. Figure 2 is a pictorial representation of cadmium recovery in wastewater through bioprecipitation. The precipitates formed in this process were analyzed for composition using X-ray diffraction, and the surface morphology was observed using FESEM.

2 Materials and Methods

The work methodology of this study is presented in Fig. 3. Synthetic wastewater was prepared by spiking cadmium concentration in water, containing soil bacteria with an optical density of 0.85. Cadmium chloride salt was blended such that the cadmium concentration in the water was about1000ppm, 500 ppm, 200 ppm, 100 ppm, 50 ppm, and 10 ppm in different batches. Aliquots from each reactor were analyzed using an atomic absorption spectrometer (SYS-816) to determine the actual cadmium concentration. Urea was added to the reactors at 15 g/l, mixed at 30 rpm on a rotary shaker for 2 min, and left undisturbed. After about 10 min, the solid residues settled down, and clear water was observed as the supernatant, unlike the color water with high cadmium content. Supernatant samples from each reactor were filtered using a 0.45 µm filter to avoid tiny particles. The filtrates were analyzed for the cadmium concentration. The sediments retained over the filter were oven-dried for 30 min at 60 °C. SEM analysis was conducted to visualize the microstructure and surface morphology of the deposition. EDS analysis determines the elemental composition, and XRD analysis of the sediment determines the mineralogical composition.

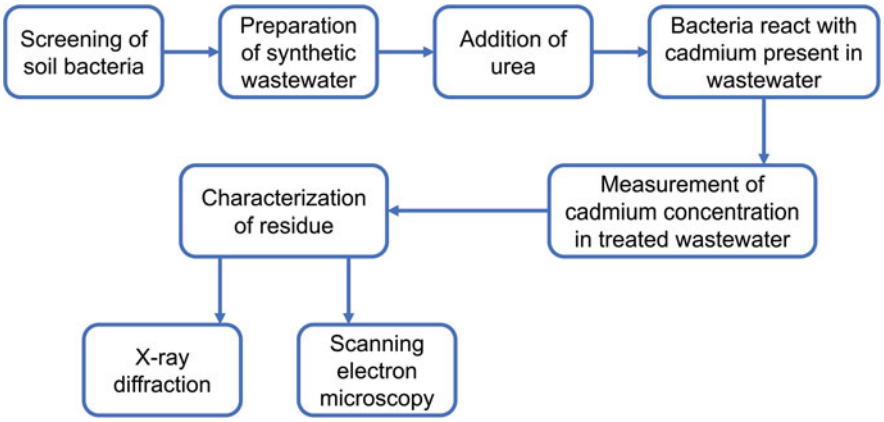

Fig. 3 Working methodology

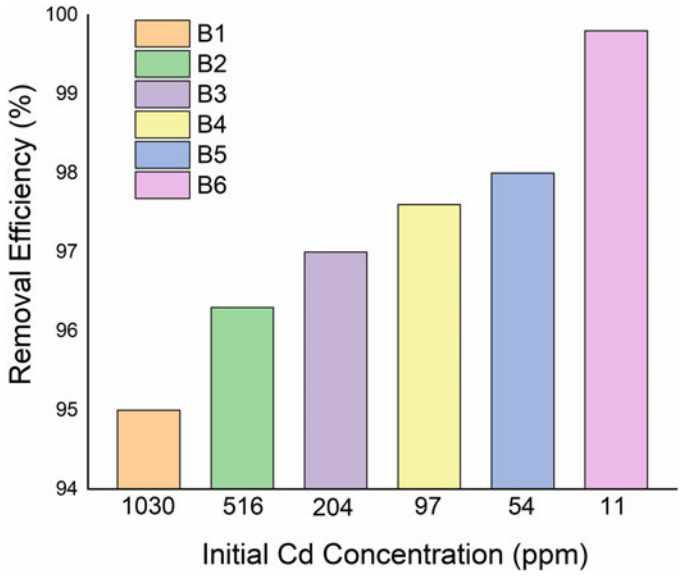

Fig. 4 Removal efficiency of bioprecipitation with different initial cadmium concentrations

3 Results and Discussion

Process Efficiency As shown in Eq. 2, the removal efficiencies were evaluated with different initial cadmium concentrations. As seen in Fig. 4, the cadmium concentration was 1030 ppm in the B1 reactor. Due to the addition of urea, it reduced to 51 ppm. Hence, the recovery efficiency is approximately 95%. Cadmium concentration in the B2 reactor was 516 ppm before and 19 ppm after the treatment. The

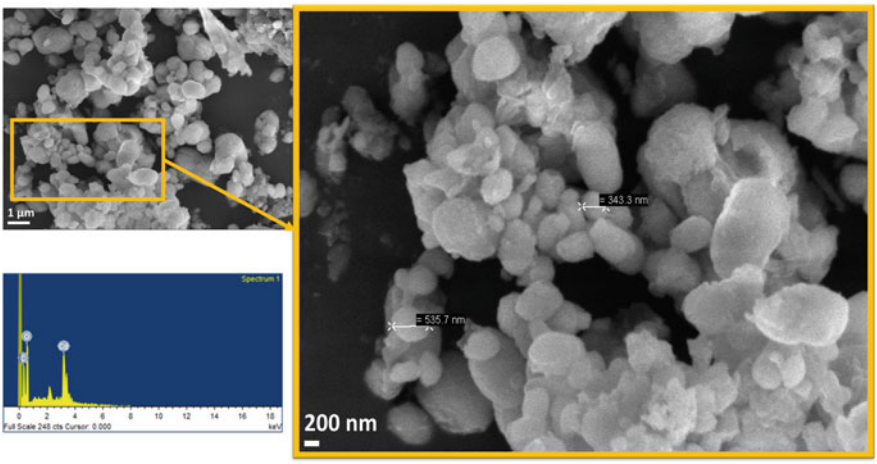

Fig. 5 Morphology of bioprecipitate

removal efficiency was found to be 96.3%. When the wastewater contained 204 ppm of cadmium in the sample from the B3 reactor, urea addition brought down the cadmium concentration to 6 ppm with an efficiency of 97%. Cadmium concentrations in B4 and B5 reactors were 97 ppm and 54 ppm before the treatment and 2 ppm and 1 ppm after. The initial concentration of cadmium was 11 ppm in the B6 reactor. However, cadmium was not detected in the B6 reactor after the treatment. It is observed that the bioprecipitation technique is more effective when the initial concentration of the cadmium is less. However, it is reasonably efficient with an initial concentration of about 1000 ppm.

$$\text{Removal Efficiency } \% = \frac{(C_1 - C_2)}{C_1} \times 100 \tag{2}$$

Where,

C_1 = Initial cadmium concentration in wastewater before adding urea.
C_2 = Cadmium concentration in water after bioprecipitation.

Comparing treatment efficiency with the concentration of cadmium before treatment indicates that the initial concentration of cadmium is a critical factor in determining removal efficiency. It is observed that the efficiency of the treatment was more when the initial concentration of cadmium in wastewater was relatively less due to the resistance of the bacteria against cadmium at toxic levels.

Scanning Electron Microscopy The surface morphology of the precipitate was captured by scanning electron microscope equipped with Energy Dispersive X-Ray (ZEISS EVO18). Samples were sputter-coated with a thin layer of gold before the analysis. The surface morphology of the residue is shown in Fig. 5. SEM-EDS observations of residues from the batch study showed nanometer-scale

Table 1 Composition of precipitate

Element	Weight %	Atomic %
C	9.89	23.26
O	34.92	61.69
Cl	2.16	1.72
Cd	53.04	13.34

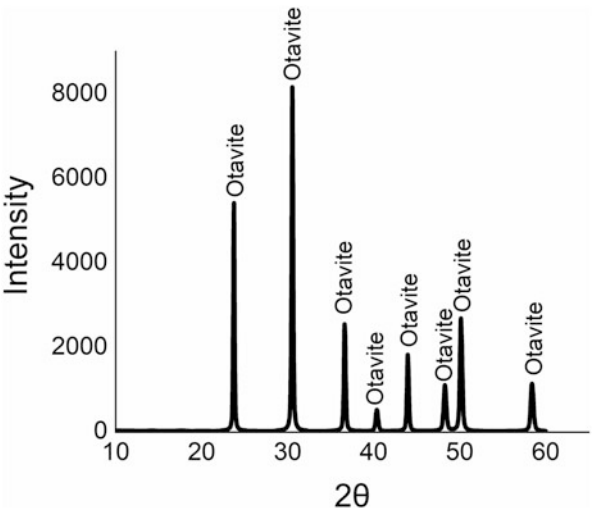

Fig. 6 Diffraction pattern of bioprecipitate

particles and rhombohedral structure. This observation is good with previous studies on cadmium carbonate [12, 13]. The elemental composition found by the EDS analysis acknowledged that 53% of the sediment was cadmium (Table 1).

X-Ray Diffraction X-ray diffraction analysis was conducted on the sediment to identify the mineral composition. The sediment was tested on a diffractometer (EMPYREAN PAN analytical) in the range of diffraction angle between 10°and 60° with Cu-Kα 1.54. The characteristic spectrum of the sediment was processed using the X'pert Highscore software. It contained peaks of high intensity at 23.74°, 30.32°, 36.61°, 40.43°, 43.94°, 50.15°, 58.37° (Fig. 6). The peak positions were compared with those from the International Centre for Diffraction Data (ICDD) database. Consequently, the sediment was identified as otavite. Several studies have reported similar peak positions representing the presence of otavite [12–16].

Since cadmium carbonate is an insoluble material in water, it settles quickly due to its self-weight and is easily separated from wastewater [4, 17]. Bacteria have the propensity to produce urease enzyme continuously [18]. Therefore, this process is also suitable for continuous-flow reactors. Rhizospheric soil is readily available everywhere, and urea is the only chemical required. This method easily removes the cadmium, and the treated wastewater can be used for other purposes, such as cooling towers and gardening. Thus, bioprecipitation is a simple and cost-effective technology. This study determined the efficiency of bioprecipitation for cadmium

removal for different concentrations of cadmium in synthetic wastewater. The results indicated that the bioprecipitation mechanism is practical and suitable for treating wastewater with diverse cadmium concentrations reflecting the actual industrial conditions of daily, monthly, and seasonal variations in cadmium concentration in wastewater.

4 Conclusion

This study aims to develop an efficient and low-cost method for cadmium recovery from industrial wastewater. It was achieved using bacteria from rhizospheric soil. Precipitation by urea hydrolysis mechanism effectively treated the wastewater with cadmium concentrations as high as 1000 ppm with a removal efficiency of 95%. Maximum efficiency was observed with the B7 reactor with an initial cadmium concentration of 11 ppm. The XRD, SEM, and EDS analyses characterize the developed sediment as otavite. Overall, bioprecipitation using soil bacteria is a high-efficient and economical method for cadmium recovery.

Acknowledgment This research work was supported by the research fellowship program of the Ministry of Education, Government of India. The authors thank the Department of Metallurgy and Materials Engineering, NITK and Central Instrumentation Facility, Manipal Academy of Higher Education, for providing the research facilities.

References

1. Q.U. Zaman et al., Silicon fertilization: A step towards cadmium-free fragrant rice. Plan. Theory **10**(11), 1–12 (2021). https://doi.org/10.3390/plants10112440
2. A. Kubier, R.T. Wilkin, T. Pichler, Cadmium in soils and groundwater: A review. Appl. Geochem. **108**, 1–42 (2019). https://doi.org/10.1016/j.apgeochem.2019.104388
3. M. Mahajan et al., A comprehensive study on aquatic chemistry, health risk and remediation techniques of cadmium in groundwater. Sci. Total Environ. **818**, 151784 (2022). https://doi.org/10.1016/j.scitotenv.2021.151784
4. I. Suhani, S. Sahab, V. Srivastava, R.P. Singh, Impact of cadmium pollution on food safety and human health. Curr. Opin. Toxicol. **27**, 1–7 (2021). https://doi.org/10.1016/j.cotox.2021.04.004
5. A.A. Azmi, J. Jai, N.A. Zamanhuri, A. Yahya, Precious metals recovery from electroplating wastewater: A review. IOP Conf. Ser. Mater. Sci. Eng. **358**, 1 (2018). https://doi.org/10.1088/1757-899X/358/1/012024
6. B. Krajewska, Urease-aided calcium carbonate mineralization for engineering applications: A review. J. Adv. Res. **13**, 59–67 (2018). https://doi.org/10.1016/j.jare.2017.10.009
7. N. Ling, T. Wang, Y. Kuzyakov, *Microbiome of the Rhizosphere: from Structure to Functions* (Reseach Square, 2021), pp. 1–15
8. A.U. Charpe, M.V. Latkar, Effect of biocementation using soil bacteria to augment the mechanical properties of cementitious materials. Mater. Today Proc. **21**, 1218–1222 (2020). https://doi.org/10.1016/j.matpr.2020.01.072

9. N.J. Nkoh, Z.D. Liu, J. Yan, S.J. Cai, Z.N. Hong, R.K. Xu, The role of extracellular polymeric substances in bacterial adhesion onto variable charge soils. Arch. Agron. Soil Sci. **66**(13), 1780–1793 (2020). https://doi.org/10.1080/03650340.2019.1696016
10. A. Zamani, B.M. Montoya, Undrained cyclic response of silty sands improved by microbial induced calcium carbonate precipitation. Soil Dyn. Earthq. Eng. **120**, 436–448 (2019). https://doi.org/10.1016/j.soildyn.2019.01.010
11. R. Shrestha et al., Technological trends in heavy metals removal from industrial wastewater: A review. J. Environ. Chem. Eng. **9**(4), 105688 (2021). https://doi.org/10.1016/j.jece.2021.105688
12. C. Ma et al., Dissolution and solubility of the calcite–Otavite solid solutions [(Ca1−x Cdx) CO3] at 2° C. Fortschr. Mineral. **12**(6), 1–18 (2022). https://doi.org/10.3390/min12060756
13. R.P. Lefojane et al., CdO/CdCO3 nanocomposite physical properties and cytotoxicity against selected breast cancer cell lines. Sci. Rep. **11**(1), 1–11 (2021). https://doi.org/10.1038/s41598-020-78720-5
14. J.A. Heredia-Cancino, K.J. Mendoza-Peña, H.J. Higuera-Valenzuela, M. A. Soto B, R. Ochoa-Landín, S.J. Castillo, Synthesis optimization of cadmium carbonate films as potential precursor to produce CdSe, CdTe, and CdO films. Coatings **12, 11**, 1691 (2022). https://doi.org/10.3390/coatings12111691
15. Y. Yan, F. Qi, L. Zhang, P. Zhang, Q. Li, Enhanced cd adsorption by red mud modified bean-worm skin biochars in weakly alkali environment. Sep. Purif. Technol. **297**, 121533 (2022). https://doi.org/10.1016/j.seppur.2022.121533
16. L. Habte, N. Shiferaw, M.D. Khan, T. Thriveni, J.W. Ahn, Sorption of Cd2+ and Pb2+ on aragonite synthesized from eggshell. Sustainability (Switzerland) **12**, 3 (2020). https://doi.org/10.3390/su12031174
17. K.M. Patel, C.P. Devatha, Investigation on leaching behaviour of toxic metals from biomedical ash and its controlling mechanism. Environ. Sci. Pollut. Res. **26**(6), 6191–6198 (2019). https://doi.org/10.1007/s11356-018-3953-3
18. W. Li, Y. Zhang, V. Achal, Mechanisms of cadmium retention on enzyme-induced carbonate precipitation (EICP) of Ca/Mg: Nucleation, chemisorption, and co-precipitation. J. Environ. Chem. Eng. **10**(3), 107507 (2022). https://doi.org/10.1016/j.jece.2022.107507

Part VI
Case Studies on Industrial Pollution Control

Tannery Waste Management in India: A Case Study

Indrasis Das, S. V. Srinivasan, Abhinandan Kumar, A. K. Vidyarthi, and Raj Kishore Singh

Abstract Tannery or leather industries are one of the oldest industrial sectors in India as well as in the world where rawhide is processed to chrome- or veg-tanned wet-blue/white or finished leather for manufacturing different leather products. These industries create considerable numbers of employment opportunities for downtrodden people in India and other developing countries. However, huge quantity of wastewater (28–40 kl/ton of skin) and different categories of solid wastes (300–600 kg/ton of hide) are generated during the processing of leather. Waste management practices in leather industries vary based on the manufacturing processes (such as complete or partial processing of hide or skin and vegetable or chrome tanning) which generate diverse effluent characteristics, including 2–3 kl/ton of chrome-bearing effluent for chrome tanning. About 400 tanneries and 21 centralized effluent treatment plants for tannery clusters are visited by us in the last few years out of about 1600 tanneries in India, and water and solid waste management practices adopted by those tanneries are accessed in a detailed manner. Here in this case study, our objective is to highlight the tannery waste management practices that are adopted in the different locations in India based on our visit and assessment.

I. Das (✉) · S. V. Srinivasan
Environmental Engineering Department, CSIR-Central Leather Research Institute, Adyar, Chennai, Tamil Nadu, India

Academy of Scientific and Industrial Research (AcSIR), Ghaziabad, Uttar Pradesh, India
e-mail: indrasis@clri.res.in; svsrinivasan@clri.res.in

A. Kumar
CSIR-Central Leather Research Institute Regional Centre, Kanpur, Uttar Pradesh, India
e-mail: abhinandan@clri.res.in

A. K. Vidyarthi · R. K. Singh
Central Pollution Control Board, New Delhi, India
e-mail: vidyarthi.cpcb@nic.in

D. Mazumder (ed.), *Sustainable Advanced Technologies for Industrial Pollution Control*, Springer Proceedings in Earth and Environmental Sciences,
https://doi.org/10.1007/978-3-031-37596-5_23

Keywords Cleaner technologies · Chrome recovery · Leather industry · Leather processing · Multiple effect evaporator · Solid waste management · Tannery clusters in India · Tannery waste management · Wastewater treatment · Zero liquid discharge

Abbreviations

ATFD	Agitated thin-film dryer
BCS	Basic chromium sulphate
BOD	Biochemical oxygen demand
CCRU	Common chrome recovery unit
CETP	Common effluent treatment plant
COD	Chemical oxygen demand
CRU	Chrome recovery unit
CSIR	Council of Scientific and Industrial Research
DAF	Dissolved air floatation
ETP	Effluent treatment plant
HRT	Hydraulic retention time
kl	Kiloliter
MEE	Multiple effect evaporation
MLD	Million liter per day
RO	Reverse osmosis
SS	Suspended solids
TDS	Total dissolved solids
TSS	Total suspended solids
UASB	Up-flow anaerobic sludge blanket
ZLD	Zero liquid discharge

1 Introduction

The tannery sector and leather product industries are important industrial sectors in India and a considerable amount of revenue is earned by exporting finished leather and leather goods to other countries. According to the data, India accounts for 13% of global leather production [1]. In addition, this sector provides employment for about 4.5 million people among whom more than 30% are women [2].

Rawhide/skin is a by-product/waste generated from the meat industry or slaughterhouses, and it is processed by tannery industries and converted into useful valuable end products. For the processing of rawhide to finished leather, different steps are involved which majorly include operations such as soaking, liming, fleshing, deliming, pickling, tanning, dying, fat-liquoring, re-tanning, finishing, and dry operations [3]. In soaking and liming, the discharged effluent has high salinity and organic content [4]. The pH of the effluent is also higher for the liming

effluent [4]. The effluent discharged during deliming, pickling, and tanning are acidic with high organic content [5]. During the chrome tanning process, basic chromium sulphate (BCS) is used as chrome-tanning agent which consists of Cr^{+3} and because of this high total chromium concentration is observed in chrome-tanning effluent. After the post-tanning operations such as dying, fat-liquoring and re-tanning, the effluent is colored and consists of refractory compounds, because of the usage of dyes, fat liquors, synthetic tanning agents, etc. If re-tanning is performed by chrome tanning, the traces of chromium (Cr^{+3}) is also observed in this effluent.

Leather processing is a batch operation and simultaneous discharge of all waste streams together is not observed. Processing of rawhides to tanned hides (wet blue – chrome tanned hides; and wet white – vegetable tanned hides) requires 3–5 days depending upon the raw material and equipment used. The post-tanning operation takes about 24 h of processing. Tanned hides are stable non-putrescible product and can be stored for longer duration [6]. In general, tanned hides are stored for a minimum of 2 days or more up to few months based on the market orders and requirements before initiating post-tanning operations and manufacturing the finished leather goods. Significant fluctuations in the day-to-day quantity and quality of effluent generation are observed. A considerable variation in the day-to-day quantity of effluent poses major challenge for meeting the consistent effluent quality at the outlet. Leather processing also involves the generation of solid wastes along with different waste streams which includes dry salts, fleshing waste, chrome-bearing wastes, treatment plant chemical, and bio sludge [7, 8]. Previously case studies were performed on biological tannery effluent treatment [9] and localized case studies of Kanpur region [10]. However, an overall aspect of tannery waste management including solid and liquid waste in Indian perspective was not conducted. Considering the scenario, a detailed analysis by highlighting the tannery waste management practices in Indian tanneries is a novel work.

The main goal of this investigation is to summarize the information collected during visit of tanneries and tannery clusters and highlight the present practices of tannery wastewater treatment and solid waste management in India and the recent introduction/implementation of advanced and cleaner technologies in the tannery waste minimization or treatment sector based on our physical assessment.

2 Data Collection

The leather tannery industries are small- and medium-scale industries mostly situated in clusters. In India, the major tannery clusters are situated in Kanpur (Jajmau, Unnao, and Banthar), Tamil Nadu (Ranipet, Ambur, Vaniyambadi, Dindigul, Chennai and Erode), Kolkata (Bantala), and Jalandhar (Fig. 1). Small leather industry clusters are also situated in Jammu & Kashmir, Hyderabad, and Rajasthan. Stand-alone tanneries are located in Bihar (Muzaffarpur), Haryana, the outskirts of Kanpur, and the Delhi region. Stand-alone tanneries are only about 5–10% of the total number of tanneries present in India. In the last few years, about 400 tanneries and

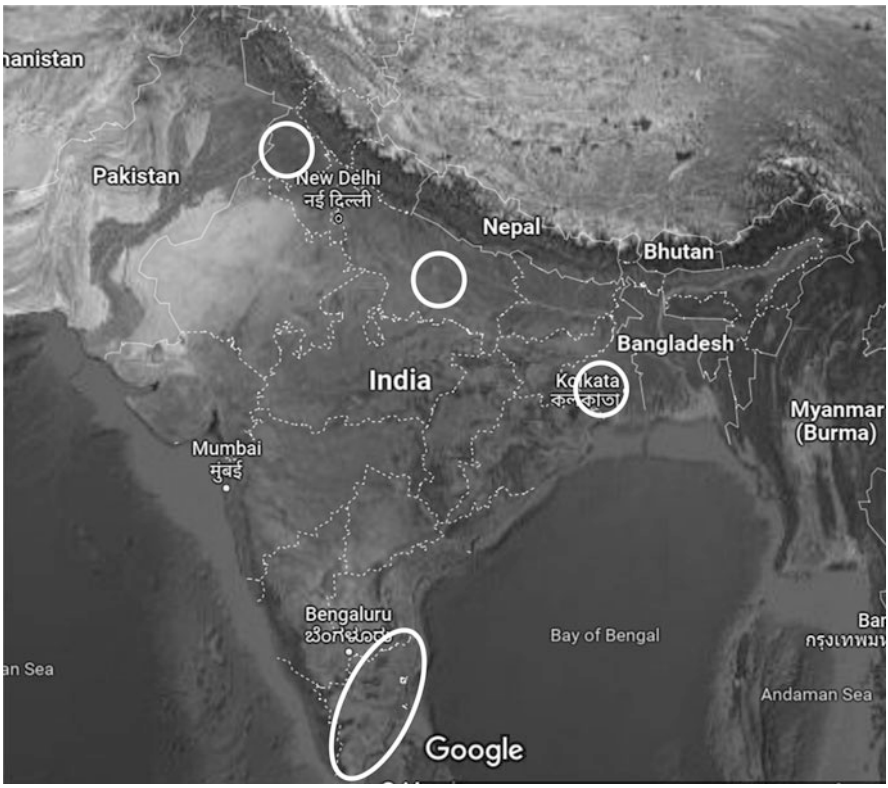

Fig. 1 Major tannery clusters in India. (Source: Google Map)

21 common effluent treatment plants (CETPs) of tannery clusters are physically visited and accessed, the waste management practices of those tanneries are summarized, and possible use of cleaner technology options and future roadmaps are briefed in this case study.

3 Data Assessment

In India, more than 90% of the tanneries are located in the clusters and 21 CETPs are constructed for managing the effluent generated from these clusters. The tanneries situated in the clusters are connected to the CETP by conveyance pipeline or open channel. Remaining stand-alone tanneries have their individual effluent treatment plants (ETPs) for the treatment and safe disposal of wastewater generated from these tanneries. In the last decade, CETPs in the Tamil Nadu and few ETPs are upgraded to zero liquid discharge (ZLD) units because of the limited scope of effluent discharge and strict local regulatory restrictions. Upgradation and modification of

effluent treatment plants are continuously going on in different tannery clusters to efficiently manage the tannery effluents quantitatively and qualitatively. New tannery clusters and expansion of the existing clusters are also proposed in the Kanpur and Kolkata region for increasing the production capacity of the finished leather and leather goods. The proposed and adopted treatment scheme is majorly based on the wastewater characteristics, freshwater availability in the locality, scope of effluent discharge and dilution, regulatory norms, and land availability.

In a typical tannery, sequential batch processing of hides/skins to finished leather is mostly performed in drums and paddles and in very few cases in pits. This is a two-stage process where the first stage involved the processing of rawhide to chrome- or vegetable-tanned leather and second stage involves post-tanning operations. During each batch operations, different categories and types of solid and liquid wastes are generated as highlighted in the Table 1. The dry operations such as splitting, trimming, buffing do not generate measurable quantity of effluent, and therefore the water discharge from these operations were not quantified in Table 1. However, processing of rawhide/skin to finished leather processing is not executed by all the tanneries, and many individual tannery or tanneries in clusters only have the consent for processing partial operations such as rawhide or skin to tanned/semi-finished leather or the processing of tanned/semi-finished leather to finished leather. The complete or partial processing of hides/skins is sometimes dependent upon the raw material availability or market orders or local restrictions which effects the overall effluent characteristics. For example, in Kanpur region, industries are restricted to operate during religious festivals or bathing rituals in Ganga. Restrictions are also imposed by CETP operators. The quantity of effluent generations in tanneries are also vary based on the executed partial operations of the tanneries. The execution of partial processing of hides discharges different quality of effluent which is different from the typical tannery effluent characteristics. The quantity of effluent discharge is also significantly affected by the tannery operations performed at a specific day. Precise measures are required to adequately operate the treatment units in this challenging scenario.

In the tanneries present in the tannery clusters, only the pretreatment unit is installed within tannery premises (Fig. 2), and the remaining primary, secondary, and tertiary treatments are carried out in a centralized CETP [11]. A typical pretreatment unit is consisting of a simple collection tank having 12–24 h storage capacity followed by a pre-settler with 1.0–2.0 h hydraulic retention time (HRT) or chemical dosing and primary settling tank with 2.5–4.0 h HRT based on the effluent quality requirements at the point of discharge as per regulatory norms. In some units, dissolved air floatation (DAF) is also available to reduce suspended solids (SS) concentration. Provision of settled solids/sludge removal from the settling tank and dewatering in the sludge drying beds or filter press are also observed in these tanneries. These pretreatment units are used for the preliminary treatment of the composite effluent of the tanneries other than chrome liquor. Specific arrangements for the segregation of chrome (Cr^{+3}) liquor and recovery of chromium in individual or common chrome recovery unit (CRU or CCRU respectively) are mandatory in India as per the regulatory norms. In the tanneries having their own

Table 1 Wastewater and solid waste generated from different tannery processes

Process	Water discharge (kl/ton)	Wastewater characteristics values in g/l	Solid waste	Solid waste quantity (kg/ton)
Desalting	–	–	Dry salt	30–100
Soaking	5–8	BOD (2–3), COD (3–6), SS (3–5), salts (20–45), and organic N (0.1–0.3)	–	–
Unhairing and liming	6–9	BOD (5–10), COD (8–12), SS (5–10), TDS (7–15), sulphides (1–4), and organic N (0.5–1.5)	Hair, lime-containing sludge and organics	10–20
Lime fleshing	~0	–	Alkaline fat containing organic	150–350
Raw trimming	–	–	Lime split waste and trimmings	40–100
Deliming, bating, and degreasing	6–8	BOD (1–2), COD (2–4), TDS (3–7), ammonia N (0.5–1.5)	–	–
Pickling, tanning (Cr/Veg)	2–3	BOD (1–2), COD (2–5), TDS (80–100), chromium (1–3)/vegetable tans, and syntans (20–30)	–	–
Chrome splitting, shaving	–	–	Chrome-bearing waste	100–300
Re-tanning, dyeing, fat-liquoring	7–8	BOD (1–3), COD (3–5), TDS (4–7), chrome (0.2–0.5), vegetable tans (2–5)	–	–
Buffing, trimming	–	–	Chrome-bearing waste	20–40
Finishing	1–2	Liquid residues of finishing solutions (organic compounds, pigments). Water required for washing BOD (0.2–0.5), COD (1–2)	Solid residues of finishing solutions	5–10

Note: *BOD* biochemical oxygen demand, *COD* chemical oxygen demand, *SS* suspended solids, *DS* dissolved solids, *N* nitrogen

CRU, the supernatant after recovery of chromium is further treated in the treatment facility established within the tannery and treated effluent is conveyed to the CETP. However, specifically in the tannery cluster of Jajmau, Kanpur, tanneries and residential areas are situated together. In the CETP of Jajmau, 36 MLD (million liter per day) up-flow anaerobic sludge blanket (UASB) reactor-based secondary treatment unit has been implemented to treat 9 MLD of tannery wastewater and 27 MLD of domestic sewage. As primary treatment is not available in this CETP,

Fig. 2 Pretreatment units of the tanneries connected to CETP

individual tanneries connected with this CETP have to carry out primary treatment before discharging their effluent into the CETP drain.

Tanneries present in the cluster have to meet pH, total suspended solids (TSS), and Cr(total) as per the regulatory norms set by the state pollution control boards and any other parameter set based on the design of the CETP inlet characteristics. As an example, a tannery present in Jajmau or surrounding tannery clusters where pH adjustments and coagulant addition are performed, the Cr (total) concentration is restricted to 10 mg/l by local regulatory body, that is, State Pollution Control Board. The primary treated effluent of the tanneries of Jajmau are conveyed to the CETP where tannery effluent mixed with and diluted by domestic sewage in a 1:3 ratio and treated by anaerobic UASB reactor and the treated effluent is discharged for irrigation [9].

In total, 21 CETPs are existing for the tannery clusters in India. Extended aeration-based activated sludge process is available as a secondary treatment option in the majority of the CETPs in India. However, UASB based or UASB followed by extended aeration process is also used in some tannery clusters (Table 2). Before secondary treatment, primary treatment options such as manual or mechanical screens, equalization tank, chemical dosing with flash mixer and flocculator, and primary clarifier are common in most of the CETPs. Sulphide removal by aeration with/without using catalyst is also adopted before secondary biological treatment processes in few CETPs. Tertiary treatment units, such as nitrification, denitrification, ammonia removal, sand, activated carbon and dual media filters, and ultrafiltration are also implemented in different CETPs. The treated effluent discharge

Table 2 CETPs for tannery clusters in India

Name of the CETP	Capacity in MLD	Major units
Jalandhar, Punjab	5.0	Primary and extended aeration
Lassipora, Jammu & Kashmir	0.6	Primary and extended aeration
Jajmau, Uttar Pradesh	9 (tannery) +27 (Sewage)	Primary and UASB
Unnao, Uttar Pradesh	2.15	Primary and extended aeration
Banthar, Uttar Pradesh	4.5	Primary and extended aeration
Kolkata, West Bengal	20 (another 20 MLD proposed)	Primary and extended aeration
Kunoor, Telangana	0.6	Primary, UASB, and extended aeration
Pallavaram, Chennai, Tamil Nadu	3.0	Primary, extended aeration, and 30% recycle by RO and remaining dilution with treated sewage
Madhavaram, Chennai, Tamil Nadu	1.0	Primary, extended aeration and dilution with treated sewage
Ranipet, Tamil Nadu	4.5	Primary, extended aeration, nitrification denitrification, and ZLD by RO and MEE
SIDCO Phase-I, Ranipet, Tamil Nadu	2.5	Primary, extended aeration, and ZLD by RO and MEE
SIDCO Phase-II, Ranipet, Chennai	1.56	Primary, extended aeration, and ZLD by RO and MEE
Perundurai, Tamil Nadu	2.0	Primary, UASB, extended aeration, ZLD by RO and MEE
Ambur (Thuthipet), Tamil Nadu	2.2	Primary, extended aeration, and ZLD by RO and MEE
Ambur (Maligthope), Tamil Nadu	1.1	Primary, extended aeration, and ZLD by RO and MEE
Vaniyambadi, Tamil Nadu	3.3	Primary, extended aeration, MBR, and ZLD by RO and MEE
Melvisharam, Tamil Nadu	3.4.	Primary, extended aeration, and ZLD by RO and MEE
Dindigul, Tamil Nadu	2.5	Primary, UASB, extended aeration, ZLD by RO and MEE
Perunambut, Tamil Nadu	0.9	Primary, extended aeration, ZLD by RO and MEE
Trichy, Tamil Nadu	0.2	Primary, extended aeration, ZLD by RO and MEE
Jaipur, Rajasthan	0.2	Primary and extended aeration

quality parameters assigned for disposal of CETP effluents are pH of 6–9, BOD of 30 mg/l, COD of 250 mg/l, total suspended solids or TSS of 100 mg/l, fixed dissolved solids (FDS) of 2100 mg/l, sulphides of 2 m/l, total chromium of 2 mg/l, oil and grease of 10 mg/l, and chlorides of 1000 mg/l. For land and sea discharge,

BOD is relaxed till 100 mg/l and for sea discharge the FDS is not specified. The environmental norms are very stringent in Tamil Nadu because of the very limited freshwater source and non-availability of the suitable effluent discharge points. Therefore, most of the CETPs in Tamil Nadu are upgraded or under upgradation to the ZLD by using two or three stage reverse osmosis (RO) filtration followed by the multiple effect evaporation (MEE) and agitated thin-film dryer (ATFD) to evaporate the concentrated reject from RO system, store salt residues, and reuse the RO permeate and MEE condensate water in leather processing. Although the advanced technology options are mandatory due to strict regulatory guidelines, the cost of treatment by using the advanced technology options increases the treatment cost of effluent almost 10 times (500–800 Indian rupees per kl).

In the individual stand-alone tanneries, individual ETPs are established to handle the effluent generated to meet the prescribed discharge norms set by the state pollution control boards. In general, these are large leather processing units as compared to the tanneries situated in the clusters. In most of these units, aerobic biological treatment process such as activated sludge process or extended aeration-based secondary treatment is used. Prior to the biological treatment, primary treatment units such as manual/mechanical screen, equalization tank, chemical dosing, and primary clarifier are common. In few stand-alone tanneries, the soak liquor is also segregated and reusable salts are recovered. In this aspect, a pilot investigation has been conducted and suggested to have preliminary coagulation, flocculation, and biological treatment followed by direct evaporation or RO followed by evaporation of the RO reject [12]. Chrome liquor is segregated and treated in individual CRU installed within the tannery premises of the isolated tanneries. Treated water of the ETP is discharged on land or into the nearby water bodies after meeting the regulatory standards of pollution control board authority. The limit of TDS is flexible till 3100 mg/l for higher initial TDS (above 1100 mg/l) of the freshwater source. In stand-alone tanneries, proper operation of the existing primary, secondary, and tertiary treatments could meet the above discharge norms except TDS. In order to meet the discharge norms of TDS, the option available for stand-alone tanneries is to upgrade ETP to ZLD system by employing sand, carbon filter, multigrade filters, membrane pretreatment systems, and RO filtration followed by reject management system. In most of the stand-alone tanneries, ZLD-based ETP has been implemented for recovery and reuse of water. Cleaner technology options are also suggested to reduce TDS in the effluent.

Specific technology is used for the recovery of basic chromium sulphate from chrome liquor. At present, the chrome recovery is performed in individual CRU in tanneries as well as centralized CRUs. A typical setup of a CRU is presented in Fig. 3. This is a precipitation-based technology where chrome liquor from chrome-tanning drums is stored into chrome liquor collection or storage tank. The chrome liquor from the collection tank is pumped to the chrome recovery tank where MgO solution is added for increasing the pH and precipitation of chrome. The $Cr(OH)_3$ slurry precipitated at the bottom is transferred to the redissolving tank and sulfuric acid is added to adjust the pH for redissolving the chromium. The supernatant from the chrome recovery tank is further treated in ETPs or CETPs. The recovered chrome

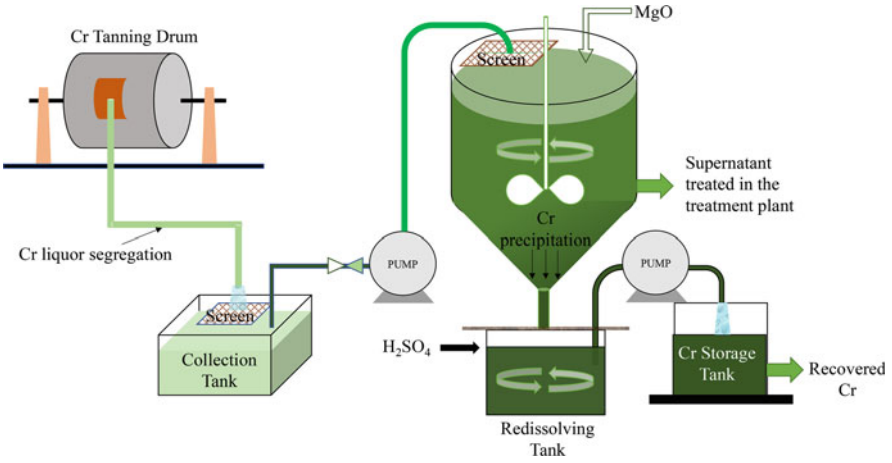

Fig. 3 Chrome recovery unit

liquor is further pumped from the redissolving tank and stored in recovered chrome storage tank for reusing in chrome tanning. The chrome recovery efficiency in this technology is very high (about 98%), and this is a suitable and easy way to successfully segregate and reuse chromium in the leather process repeatedly. However, recently waterless chrome-tanning technology is successfully established and around 100 units got this technology and trained to process hides using this technology. In this process, pickling operation is avoided and no wastewater is discharged from the tanning operation.

Solid waste management is also a major concern for the tanneries, about 75% of the rawhide or skin is rejected as solid waste, and only 15–25% is converted to finished leather product. The major contributors for these wastes are fleshings, chrome shaving splitting and buffing dusts, skin trimmings, hair, and these solid wastes generated during beam house, tanning, and finishing operations. Other than the portion of the solid wastes that are generated directly from the hides during leather processing, a portion of solid waste is generated from the effluent treatment units as treatment plant sludge. Salts are also generated during initial desalting operation of the hides. Specific regulatory guidelines are imposed for handling or management of these solid wastes, and industries need to adhere those directions.

The sludge generated from the pretreatment, primary treatment, or centralized or individual effluent treatment plants are managed by sludge drying beds and mechanical sludge dewatering units such as filter press, belt press, and decanter. The tannery sludge is considered as a hazardous waste and continuous tracking of the waste and disposal in the secured hazardous landfill is mandatory. However, recently, alternative sludge management option such as coprocessing of tannery sludge in the cement industry is also being promoted in Tamil Nadu to promote circular economy. Few initiatives such as manufacturing of bricks or tiles using tannery sludge are also

attempted in small scale, and mostly non-chrome-tanning industries are preferred in this regard. However, regulatory approvals are necessary before commercialization.

Dry salt as solid waste is generated majorly from two sources in the tannery. Initially, salted hides are transported from slaughterhouse to the tanneries and before processing of hides, manual or mechanical desalting of hides is mandatory to reduce the salinity in the tannery effluents. During this desalting operation, dry salt of 30–60 kg/ton hide is generated. These salts are collected and transported to the slaughterhouses or hide storage areas for reuse. In stand-alone tanneries and CETP with ZLD plants after recovery of water, the reject of RO plant is evaporated in MEE-ATFD setup and dry salt residue is obtained. This salt residue is majorly a mixture of sodium chloride and sulphate, and without segregating, reuse of these two salts is not possible. The storage and disposal of these salts were also a serious concern. Recently, salt separation based on washery technology and adiabatic chilling-based technology are developed (by CSIR – Central Salt and Marine Chemicals Research Institute) for recovery of sodium chloride and sulphate separately for potential reuse. The installation of these salt purification units are proposed in the CETPs of Tamil Nadu region.

During leather processing, rawhides are trimmed and fleshing are removed. The solid wastes generated from raw trimmings are reused in dog chew preparation and fleshing are reused for glue or tallow preparation. Technological options such as composing and biomeathanasation of the excess unused fleshing and trimmings are also available for the industries. After chrome tanning, buffing, trimming, and shaving unit operations are performed which generates chrome-bearing solid wastes. These wastes are reused in leather board manufacturing purposes. Several leather board manufacturing units were observed during this investigation in Kanpur region. Alternative technological options for reuse of chrome-bearing wastes are reuse as construction material component in roads and biomethanisation of residue after chrome separation from chrome-bearing waste.

Different cleaner technology options are also proposed to reduce the waste generation at the source. Salinity in leather industrial effluent is a serious challenge to manage it sustainably and economically. To resolve this issue, manual or mechanical desalting is mandatory now and processing of fresh or green hides are available. Infrastructure development for proper coordination between leather industry and slaughterhouses for processing of green hides and development of centralized chilling infrastructure for hide storage is also need of the hour. Reduction of water wastage by installation of valves and water meters in drums are also initiated in different tanneries. Solenoid valves on fleshing machines are also installed to control water wastage during fleshing operation of the rawhide. Enzyme-based unhairing is also proposed as alternative cleaner technology to reduce sulphide levels in the tannery effluent. Recently, utilization of solar radiation is also being explored for evaporation and concentrating RO reject or pre-heating of RO reject to reduce the energy consumption during dry salt recovery using MEE. Field scale plants are also coming up in the CETP of the tannery clusters to reduce energy consumption during tannery wastewater management.

4 Conclusion

Tanneries are considered as highly polluting industries; however, ZLD-based treatment systems have been established to ensure that there is no effluent release outside the tannery, and recovered water is reused in the process reducing the water footprint in the leather processing. In order to achieve circular economy and zero waste discharge in tannery sector, efforts are taken to purify recovered salts from ZLD system for reuse in industrial application and reuse of hazardous tannery sludge in cement industries for co-processing. Technological improvements and proper awareness of the industry personals are needed for successful implementation as well as to reduce the capital and operation and maintenance cost of this zero-waste concept in tanneries.

Acknowledgments This work is funded by Central Pollution Control Board, New Delhi, and Department for Promotion of Industry and Internal Trade, Ministry of Commerce and Industry, Government of India. CSIR-CLRI Communication No. 1807.

References

1. Council for Leather Exports 2021 Tannery Sector
2. Council of Scientific and Industrial Research 2021 Leather for employment
3. J. Kanagaraj, T. Senthilvelan, R.C. Panda, S. Kavitha, Eco-friendly waste management strategies for greener environment towards sustainable development in leather industry: A comprehensive review. J. Clean. Prod. **89**, 1–17 (2015)
4. M. Chowdhury, M.G. Mostafa, T.K. Biswas, A. Mandal, A.K. Saha, Characterization of the effluents from leather processing industries. Environ. Process **2**, 173–187 (2015)
5. K. Khan, E. Jhahan, Reuse of pickling and chrome tanning liquor and treatment of tannery effluent. Sci. Lett. **5**, 186–194 (2017)
6. R. Ricky, S. Shanthakumar, G.P. Ganapathy, F. Chiampo, Zero liquid discharge system for the tannery industry—An overview of sustainable approaches. Recycling **7**, 31 (2022)
7. N. Fathima, R. Rao, B.U. Nair, Tannery solid waste to treat toxic liquid wastes: A new holistic paradigm. Environ. Eng. Sci. **29**, 363–372 (2012)
8. J. Kanagaraj, K.C. Velappan, N.K. Chandra Babu, S. Sadulla, Solid wastes generation in the leather industry and its utilization for cleaner environment – A review. J. Sci. Ind. Res. **65**, 541–548 (2006)
9. V. Tare, S. Gupta, P. Bose, Case studies on biological treatment of tannery effluents in India. J. Air Waste Manag. Assoc. **53**, 976–982 (2003)
10. P.S. Akhand, P.D. Rao, Assessment of tannery effluent: A case study of Kanpur in India. Eur. Chem. Bull. **2**, 461–464 (2013)
11. R.A. Thomas, Peer review on sewage treatment of tannery industries. Int. Res. J. Eng. Technol. **5**, 3511–3517 (2018)
12. S. P. Gautam, Recovery of better quality reusable salt from soak liquor of tanneries in solar evaporation pans. Central Pollution Control Board, India. (2009)

Removal of Natural Organics and Selected Antibiotics Using PAC and Al Electrodes: A Study of the Jumar River

Garima Chaturvedi, R. Naresh Kumar, and Kirti Avishek

Abstract Modern age has witnessed excessive use of pharmaceuticals at its peak. The presence of such contaminants poses a significant role in human health. This study focuses on removing acetaminophen, tetracycline, natural organic matter (NOM), and turbidity by coagulation and electrocoagulation (multiple electrodes). For this study, oly-aluminum chloride (PAC) as a coagulating agent and cationic polymer as a flocculant were selected. With coagulation, optimum dose for PAC turns out to be .06 ml, and flocculant (Cationic polymer) dose is 1.5 ml for 1 L. For electrocoagulation, the aluminum electrode has shown excellent performance for NOM and antibiotic removal with 1 cm inter-electrode distance, 12 V current, and 25 minutes reaction time. The highest reduction of acetaminophen can be seen at 2 mg/L with 95% removal efficiency and 80% tetracycline removal efficiency at 10 mg/L dosage (highest) by electrocoagulation process. In the case of coagulation, the removal of acetaminophen, NOM, and turbidity seems highest at 2 mg/L, which is 52%, 78.5%, and 88%, respectively. For tetracycline, 84% drug removal was achieved at 4 mg/L, turbidity 56% at 2 mg/L, and NOM 42% at 4 mg/L.

Keywords Poly-aluminum chloride (PAC) · Cationic polymer · Electrocoagulation · Natural Organic Matter (NOM) · Acetaminophen · Tetracycline · Coagulation · Jar test · Aluminum electrode · MP-S type

1 Introduction

For quite a few years, pharmaceuticals have been gaining popularity. The modern age has witnessed excessive use of pharmaceuticals and personal care products at its peak. Such trends burden the landfill excessively as the wastes generated from such products are persistent. This number is supposed to increase as the population rises,

G. Chaturvedi (✉) · R. N. Kumar · K. Avishek
Department of Civil and Environmental Engineering, Birla Institute of Technology, Ranchi, Jharkhand, India
e-mail: phdcee10052.20@bitmesra.ac.in; rnaresh@bitmesra.ac.in; kavishek@bitmesra.ac.in

D. Mazumder (ed.), *Sustainable Advanced Technologies for Industrial Pollution Control*, Springer Proceedings in Earth and Environmental Sciences,
https://doi.org/10.1007/978-3-031-37596-5_24

with more people affording high living standards in underdeveloped and developing countries. The fundamental nature/chemical structure of such products varies, for example, a simple pill can contain many active pharmaceutical ingredients (APIs), excipients, and additives [1]. Such compounds make their way by directly discharging treated/ untreated wastewater, seepage from landfill sites, sewer lines, and human/animal waste [2, 3]. Different studies proved the presence of tetracycline in the environment, as traditional treatment plants cannot remove them [4]. Studies also suggest that such compounds can enter metabolic pathways producing more toxic metabolites than the original compound [5]. Some antibiotics lay unpropitious effects, such as antibiotic resistance [6]. Also, long-term, low-dose exposures lead to internal dysfunction such as resistance to antibiotics and disjunction of the endocrine system [7]. With constant research, different technologies evolved for their degradation. Some studies [8, 9] have suggested conventional technologies (RO, nanofiltration, microfiltration, ultra-filtration) for water purification, while other studies [10, 11] highlight unconventional technologies for purification such as sedimentation, ozonation, Fenton /UV Fenton, adsorption, chemical settling, ion exchange, and biological degradation.

Electrocoagulation technology uses a pair or more than a pair of sacrificial electrodes (anode) for contaminant removal. When an electrical charge is provided, the pollutant separates pollutants in sludge/ flocs, and the purified water can be harvested [12]. This study focuses on removing antibiotics acetaminophen, tetracycline, and natural organic matter from the Jumar River. The basic idea behind this study is to identify the best suitable method for drug and NOM removal. Two ways were put to the test to finalize the best process for contaminant removal. Previously studies were performed for the same, where two Al electrodes and 1 h reaction time were enough for maximum acetaminophen removal. In another study, equilibrium was reached at 15 min of reaction time [13, 14]. As for this study, the comparative removal of the aluminum-based compound was tested to find the most efficient technique for pollutant removal. Four Al electrodes were used to study the metal's abundance and reliability. Most studies have suggested that aluminum electrodes enhance the pollutant removal capability more than Iron electrodes.

2 Material and Methods

For the study, raw water from the Jumar River, from BIT Mesra campus, was taken for analysis. Among ferric chloride, alum, and PAC, only PAC has produced satisfactory results in terms of turbidity and NOM removal efficiency incorporated with cationic polymer. A jar test was performed to optimize the coagulant and flocculent dosage. First, coagulant dose was optimized for which PAC coagulant has opted as mentioned in some literature [15]. Different coagulant quantities were used, such as 0.1, 0.2, 0.3, 0.4, 0.5, and 0.6 ml of coagulant (diluted 1% with original). Rapid mixing took 1 min (120 rpm), followed by gradual mixing of 15 min (60 rpm). The resting period was 30 min. Visible micro flocs were visibly

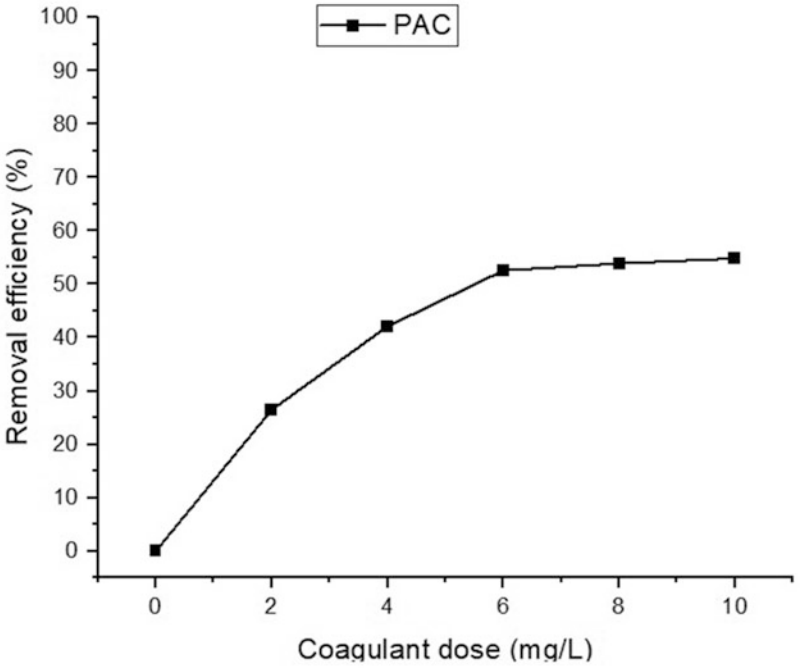

Fig. 1 PAC optimization

settled at the bottom of the container; the height measurement for each container was followed by a physical parameter study (pH, conductivity, turbidity, UV absorbance). Later flocculant (cationic poly electrolyte) dose was optimized using the earlier methods. For cationic polymer, the optimized dose was 1.5 ml. Different physiochemical parameters such as pH, turbidity, and UV absorbance were tested immediately after each run. Optimized pH for PAC was seven. NOM removal efficiency of PAC was recorded 52.6%.at .06mg/L dose of PAC (Fig. 1).

Al electrodes with size 50*70 mm were used with 1 mm thickness. MP-S (monopolar serial) type electrode arrangement was followed as it is more economical than other arrangements [16]. At the beginning of every cycle, the electrodes were scraped using coarse sandpaper and washed with 1 N HCl solution, followed by oven drying for a few minutes. Finally, with a 1 cm inter-electrode distance, the batch mode of the experiment was followed with a 1 L working volume. No additional electrolytes for pH adjustment were added as the experiment was performed on the natural pH of the river, which is 7 ± .5. Two different types of antibiotics acetaminophen and tetracycline were used from Sigma Aldrich. For the electrocoagulation, samples were deliberately spiked with the known concentration of the antibiotic. A triplicate cycle was run for 180 min. Samples were taken after every 10 min of each run and immediately analyzed for pH, conductivity, and UV absorbance to observe possible change. All experiments were conducted at room temperature. Among available electrode arrangements, monopolar and bipolar

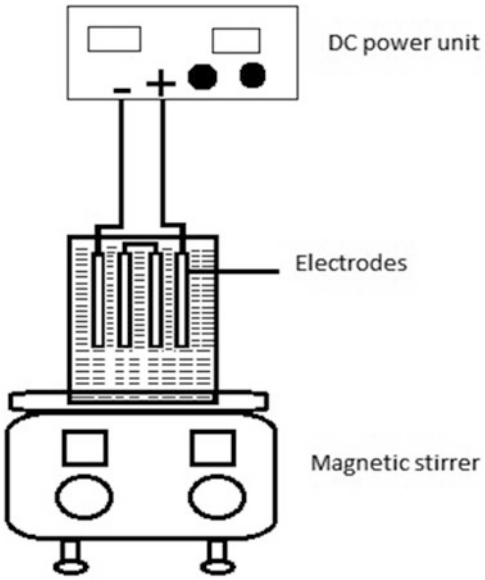

Fig. 2 EC setup in the batch mode setting

electrodes were considered for the investigation. From these two, the bipolar electrodes have shown remarkable results in contaminants removal from water [17] (Fig. 2).

3 Result and Discussion

3.1 River Water Characterization

Physiochemical parameters of the Jumar River were analyzed. Essential parameters such as pH, electrical conductivity (EC), turbidity, alkalinity, total hardness, chemical oxygen demand (COD), sulphate, phosphate, and nitrate were analyzed as per the methods mentioned in [18] (Table 1).

3.2 Acetaminophen, NOM, and Turbidity Removal Using PAC

The antibiotics removal was studied at different doses, which are 2, 4, 6, 8, and 10 mg/L [19]. In another study [13], degradation of acetaminophen at different concentrations (1, 2, 5, 10, and 20 mg/L) was performed using two aluminum electrodes and 60 minutes reaction time. The removal of acetaminophen, NOM, and turbidity seems highest at 2 mg/L, with 52%, 78.5%, and 88% removal

Table. 1 Physiochemical analysis of Jumar River

Parameters	Jumar River	Standard (BIS)	Method
pH	7.2 ± .5	6.5–8.5	4500-H electrometric method Instrument – digital pH meter (Orion Star A111)
Electrical conductivity (μs/cm)	0.39 ± .03	–	2510 laboratory method digital conductivity meter (Orion Star A212)
Turbidity (NTU)	52 ± 8	1	2130 Nephelometric method Digital turbidity meter (Oakton T100)
Total hardness as $CaCO_3$ (mg/L)	196	200	2340 EDTA titrimetric method
TDS (mg/L)	320	500	2540 Total dissolved solids dried at 180 °C
Alkalinity (mg/L)	158	200	2320 Titrimetric method
Chemical oxygen demand (mg/L)	255	–	5220 Open reflux method
Sulphate (mg/L)	27.314	200	4500 Turbidimetric method
Phosphate (mg/L)	0.522	0.1	4500 Stannous chloride method
Nitrate (mg/L)	20.18	45	4500 Ultraviolet spectrophotometric screening method

efficiency, respectively. The UV absorbance result shows a gradual decrease in drug and NOM presence after coagulation. The lowest removal can be seen at 10 mg/L for acetaminophen 42%, NOM 61%, and turbidity 88% (Fig. 3).

3.3 Tetracycline, NOM, and Turbidity Removal Using PAC

The tetracycline dose was kept at 10, 20, 30, 40, and 50 mg/L. One study presented tetracycline concentration in water from 0.5 to 10 mg/L [20], while another suggested 30 mg/L [21] after the coagulation process, tetracycline removal efficiency by PAC was highest at 84% at 4 mg/L. In contrast, for turbidity (2 mg/L) and NOM (4 mg/L), it was 56% and 42%, respectively (Fig. 4).

3.4 Electrocoagulation Process Affecting Parameter Optimization

3.4.1 Effect on Time

The reaction time has an essential impact on the electrode's removal efficiency, as it increases with the evolvement of the reaction (Fig. 5).

The removal of pollutant increases to a certain point and becomes constant, and the rate of change of a reaction is stable. A different form of metal hydroxide gets

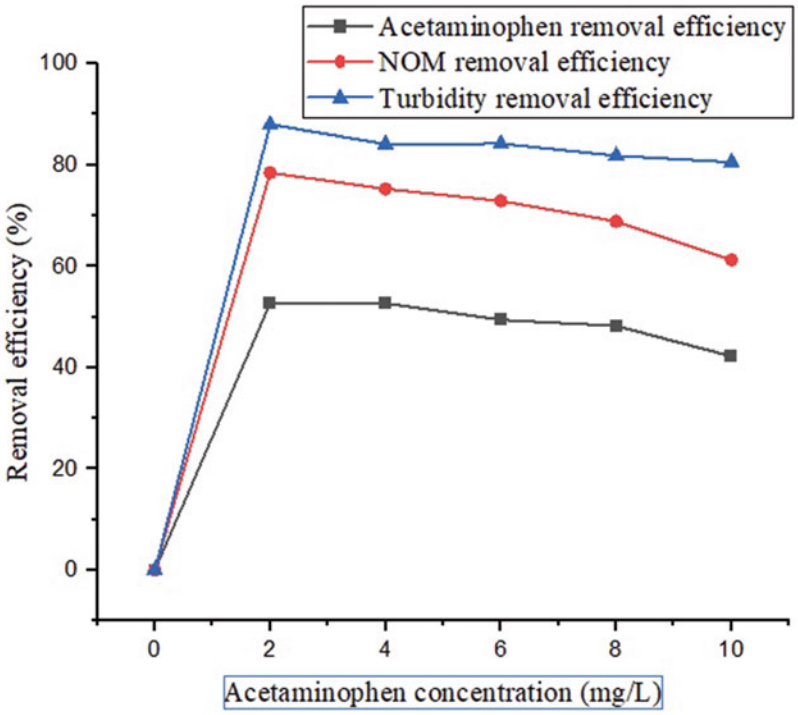

Fig. 3 Acetaminophen, NOM, and turbidity removal using PAC

from as the oxidation-reduction begins to occur. After the supreme EC process time, the removal efficiency becomes constant as sufficient coagulant species have been formed [22]. In 25 min, 90% of NOM was removed.

3.4.2 Current and Voltage

The current and voltage play an essential role in EC treatment efficiency. Different methods and procedures are applied as per the need. The author concluded that the potential and current density distribution could not distribute uniformly during the study. Also, the electric field density was supreme in the conventional EC system at the corner/edge of the electrode. The study aimed to identify the effective reaction mechanisms or processes involved. The authors [23] concluded that with different electrode setups, the performance of EC was enhanced at uniform current density and potential.

Furthermore, the kinetics of anode dismissal can be enhanced without changing the applied current density. Using references from such studies, we optimized parameters such as current at different voltages, that is, 6, 9, 12, and 15. Here the best-optimized voltage was 12 volts (Fig. 6).

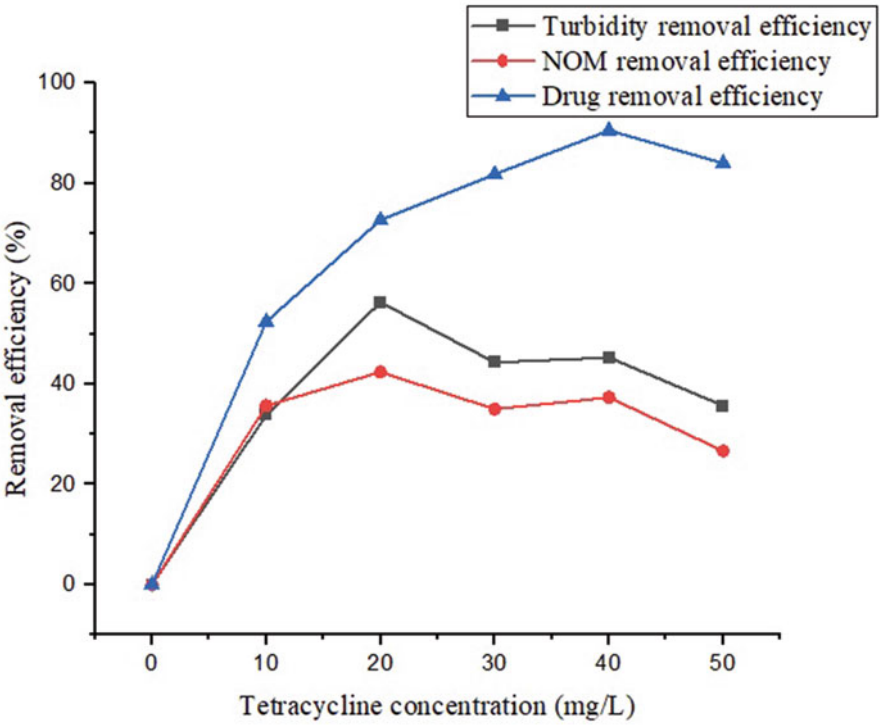

Fig. 4 Tetracycline, turbidity, and NOM removal using PAC

3.5 Acetaminophen Removal by Electrocoagulation

As can be seen in the graph, the highest withdrawal of acetaminophen by the electrocoagulation process is 87% after 10 min of the process run. Turbidity was removed 95% after 10 min of the cycle at a 2 mg/L dosage. Although the removal efficiency decreases in higher concentrations, the overall change is not enormous. A possible justification is that the formation of hydroxyl species of aluminum results in higher coagulant generation which can remove the pollutant [24, 25] (Fig. 7).

3.6 Tetracycline Removal by Electrocoagulation

At the lower dosage, tetracycline removal was highest at 80%, while maximum turbidity was removed at 87% for acetaminophen and 83% for tetracycline. The pale-yellow pigment in tetracycline was removed majorly after process completion, which could not be achieved by the coagulant process. The pH plays a significant part in the removal of antibiotics. As the EC process occurs, the reactor's pH

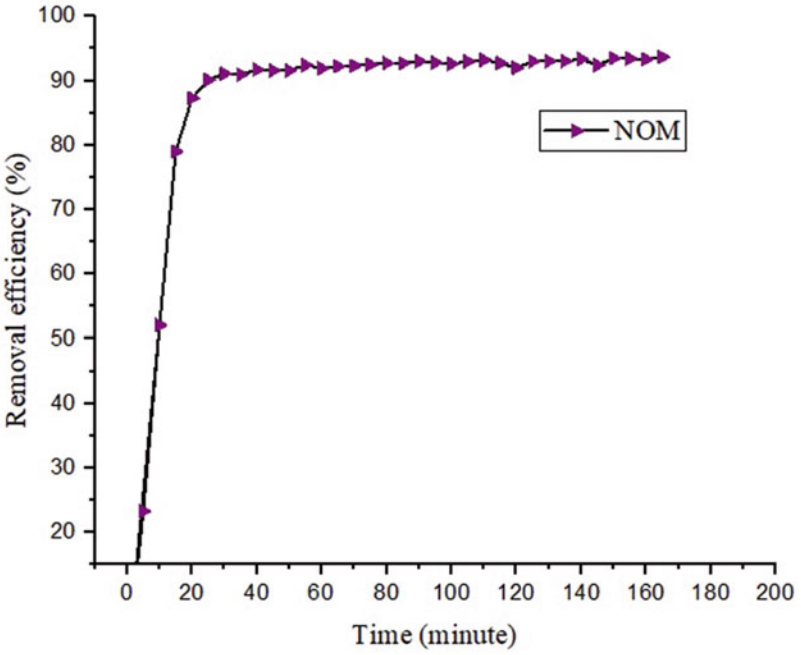

Fig. 5 NOM removal efficiency of electrocoagulation with time

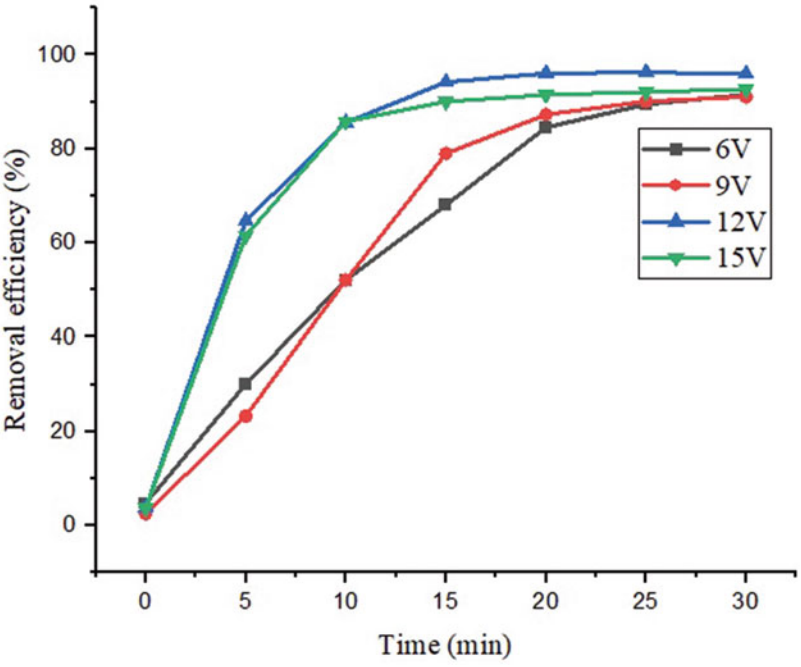

Fig. 6 EC operation at different voltage

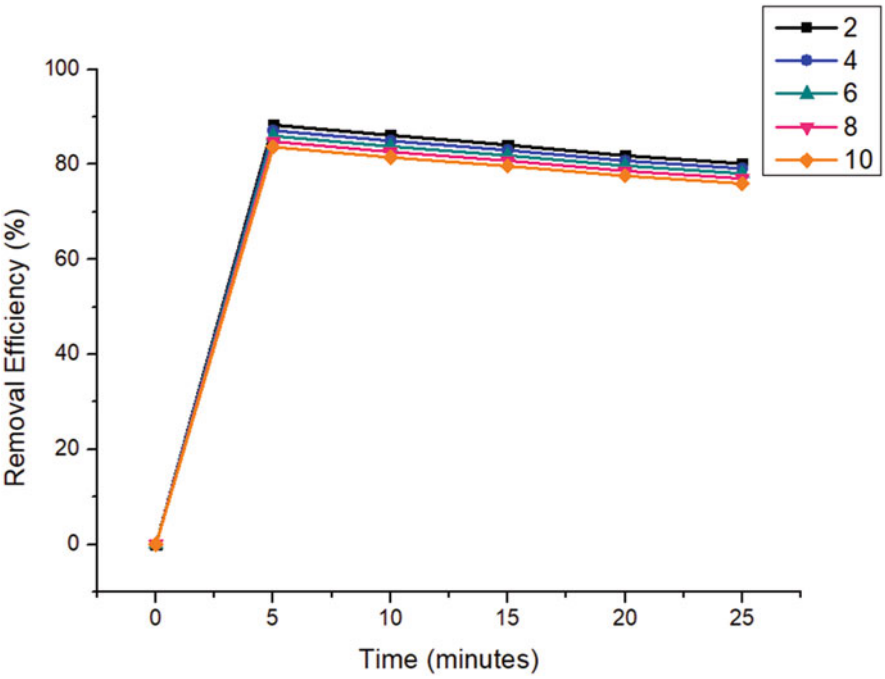

Fig. 7 Acetaminophen removal

increase, helping increase hydrogen gas production. A quick rise in pH was noted, possibly because of the generation of hydroxyl ions and the liberation of hydrogen gas [26]. When the pH was between 4 and 10, the $Al^{3+}$and OH ions generated by the electrode reacted to form various monomeric species such as Al $(OH)_2{}^{+}$ and Al $(OH)_2{}^{2+}$, and polymeric species such as $Al_6(OH)_{15}{}^{3+}$, $Al_7(OH)_7{}^{4+}$, $Al_{13}(OH)_{34}{}^{5+}$ which are finally converted into insoluble amorphous $Al(OH)_{3(S)}$ through complex polymerization/precipitation kinetics [27] (Figs. 8 and 9).

3.7 Cost Analysis

The cost analysis for the coagulation process includes the cost of chemicals (PAC, cationic polymer) and energy charge. The cost estimation formula is given below [28].

$$\text{Total cost (TC)} = (0.03)\ \text{cost of chemicals} + (0.149)\ \text{energy cost}$$
$$E_c = P_c f^* t^* c$$

Here, P_C is power used by the instrument, F is load factor (in full mode, so $b = 1$), T is instrument usage time (16 min), and, C is electricity cost (5.75 per unit in Mesra,

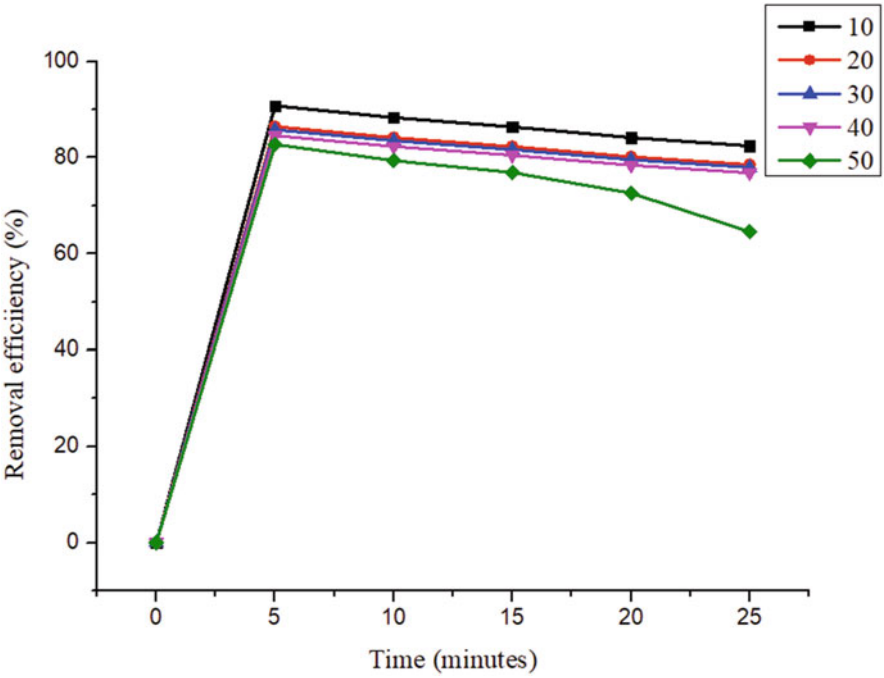

Fig. 8 Tetracycline and turbidity removal

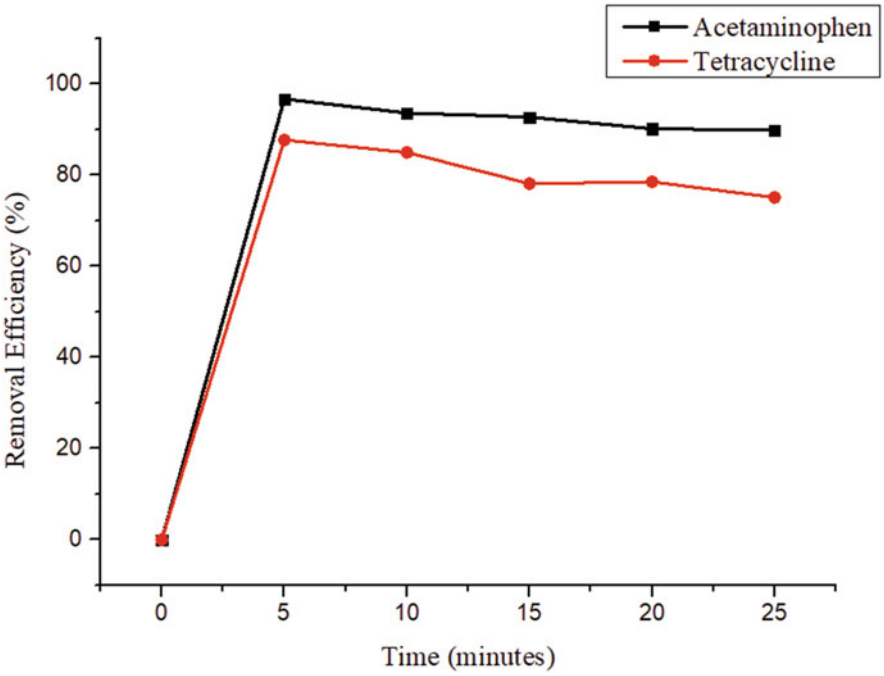

Fig. 9 Turbidity removal

Table 2 Cost of material used

Coagulant (PAC) /kg	Flocculant (cationic polymer)/kg	Electrode (per kg)	Energy (per unit)	HCL/5 L
25	10	280	5.75	1454

Jharkhand, as it comes under rural domestic consumer on 30/3/2023). Treating 1000 L of water will cost 179 ₹ or US $2.18.

The cost for electrocoagulation process can be estimated by overall cost of energy, electrode, and chemicals cost. For chemicals, only HCl was used for electrode preparation. The cost for the entire process will be 32,449.96 ₹ or US $394.72 for 1000 L of water. Here C_{energy} is 30,000 kWh/m^3 $C_{\text{electrode}}$ is 27.9623 kg Al electrode/m^3 and $C_{\text{chemicals}}$ is 2422 kg/m^3. The cost estimated from following formula [29]

$$OC = \text{Cenergy} + \text{Celectrode} + \text{Chemicals}$$

$$C_{\text{energy}} = \frac{U * I * t_{EC}}{v}$$

$$C_{\text{electrode}} = \frac{M_w I * t_{EC}}{zFv}$$

U is cell voltage (V), I is the current (A), t_{EC} is the electrocoagulation operating time (min), and v is the volume (m^3) of water; M_w is the molecular mass of aluminum (26.981 g/mol), z is the number of electrons transferred ($z = 3$); and F is Faraday's constant (96,487 C/mol). 8.33 ml 12 N HCl gets utilized for preparing 1 N 100 ml HCL solution. The current market price of 8.33 ml HCL is 2.422 ₹. HCL was used for rinsing and preparation of electrodes. The pricing of all the materials is mentioned in the table belowed (Table 2).

3.8 Removal Efficiency

In the case of drug degradation, several parameters play an essential role as the reaction continues. The pH of the solution proceeds, which leads to more hydroxyl ion generation and more floc formation and hence increased removal of the target pollutant. Although the pH stabilizes after a certain point and does not exceed, the hydrogen gas produced during metallic dissolution helps lift the formulated flocs to the surface.

The drug degradation was studied by calculating the removal efficiency of pollutants by coagulation and electrocoagulation using the following formula

$$\text{Removal efficiency } \% = \frac{Ct - Ci}{Ci} * 100$$

Here Ci is initial concentration, and Ct final concentration.

3.9 Reaction Kinetics and Drug Degradation Study

The reaction kinetics was determined based on the value of the correlation coefficient (r^2) and equation. The first-order reaction follows a linear curve, while the actual values form a straight angle in concentration vs. time, initial concentration, and the r^2 value for the second order is .964, and for the first order, it is .986. For the pseudo-second-order kinetics, the rate is directly proportional to the concentration of the reactant to the second power. Integrate rate law expression depicts the relationship linking concentration and time for a given reactant [30]. Equations (1) and (2) were used for calculating reaction kinetics [31].

$$In\frac{C}{C_0} = -k_1 t \tag{1}$$

$$\frac{1}{C} = \frac{1}{C_0} + k_2 t \tag{2}$$

Here C and C_0 are the concentration and initial concentration of the reactant (antibiotics, NOM), t is time, and k is the rate constant (Fig. 10).

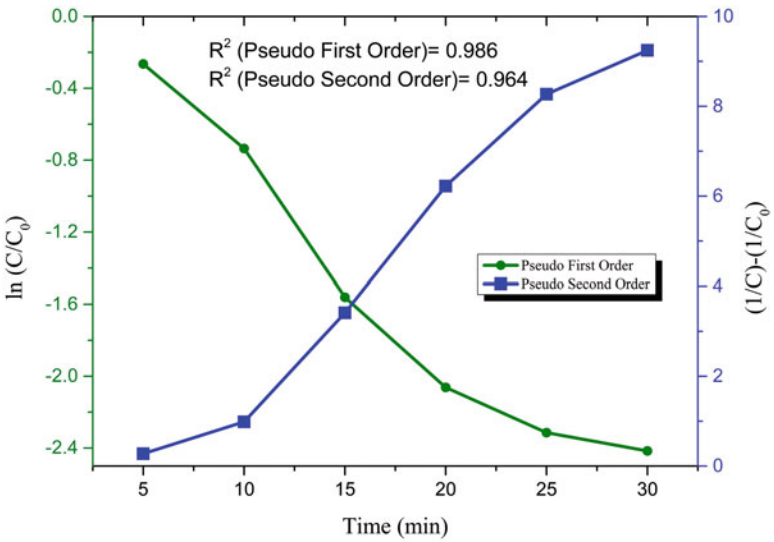

Fig. 10 Reaction kinetics study

4 Conclusion

The electrocoagulation process is very efficient in antibiotic and NOM removal. The process gives satisfactory results with minimum time and minimum use of the chemical. No additional electrolyte was used for pH adjustment as the process worked fine within the natural pH range of the river. The novelty of the approach lies behind the use of multiple electrode systems and MP-S type configuration. The EC process follows pseudo-second-order kinetics, and the different optimized parameters affect the kinetics. As for the coagulation process, the number of chemicals used and the formation of disinfectant by-products in a later stage is a matter of concern. The method described in this study is promising and can be opted for wastewater plants or other large-scale treatment plants.

Acknowledgment The scholar expresses gratitude to the institute for providing the necessary instruments with a lab facility and the institute fellowship.

References

1. K. Kümmerer, Pharmaceuticals in the environment. Annu. Rev. Environ. Resour. **35**, 57–75 (2010)
2. Y. Yang, Y.S. Ok, K.-H. Kim, E.E. Kwon, Y.F. Tsang, Occurrences and removal of pharmaceuticals and personal care products (PPCPs) in drinking water and water/sewage treatment plants: A review. Sci. Total Environ. **596**, 303–320 (2017)
3. J. Rivera-Utrilla, M. Sánchez-Polo, M.Á. Ferro-García, G. Prados-Joya, R. Ocampo-Pérez, Pharmaceuticals as emerging contaminants and their removal from water. A review. Chemosphere **93**(7), 1268–1287 (2013)
4. F. Saadati, N. Keramati, M.M. Ghazi, Influence of parameters on the photocatalytic degradation of tetracycline in wastewater: A review. Crit. Rev. Environ. Sci. Technol. **46**(8), 757–782 (2016)
5. A. Gogoi, P. Mazumder, V.K. Tyagi, G.G.T. Chaminda, A.K. An, M. Kumar, Occurrence and fate of emerging contaminants in water environment: A review. Groundw. Sustain. Dev. **6**, 169–180 (2018)
6. J. Chen, G.-G. Ying, W.-J. Deng, Antibiotic residues in food: Extraction, analysis, and human health concerns. J. Agric. Food Chem. **67**(27), 7569–7586 (2019)
7. K. Fent, A.A. Weston, D. Caminada, Ecotoxicology of human pharmaceuticals. Aquat. Toxicol. **76**(2), 122–159 (2006)
8. T.A. Ternes et al., Removal of pharmaceuticals during drinking water treatment. Environ. Sci. Technol. **36**(17), 3855–3863 (2002)
9. M. Gholami, R. Mirzaei, R.R. Kalantary, A. Sabzali, F. Gatei, Performance evaluation of reverse osmosis technology for selected antibiotics removal from synthetic pharmaceutical wastewater. Iran. J. Environ. Health Sci. Eng. **9**(1), 1–10 (2012)
10. J. Zhao et al., Ferrate-enhanced electrocoagulation / ultrafiltration system on municipal secondary effluent treatment : Identify synergistic contribution of coagulant and oxidation. Sep. Purif. Technol. **298**, 121587 (2022). https://doi.org/10.1016/j.seppur.2022.121587
11. X. Liu et al., Insight into electro-Fenton and photo-Fenton for the degradation of antibiotics: Mechanism study and research gaps. Chem. Eng. J. **347**, 379–397 (2018)

12. M.Y.A. Mollah et al., Treatment of orange II azo-dye by electrocoagulation (EC) technique in a continuous flow cell using sacrificial iron electrodes. J. Hazard. Mater. **109**(1–3), 165–171 (2004). https://doi.org/10.1016/j.jhazmat.2004.03.011
13. S. Kumari, R.N. Kumar, River water treatment using electrocoagulation for removal of acetaminophen and natural organic matter. Chemosphere **273**, 128571 (2021)
14. Y.A. Ouaissa, M. Chabani, A. Amrane, A. Bensmaili, Removal of tetracycline by electrocoagulation: Kinetic and isotherm modeling through adsorption. J. Environ. Chem. Eng. **2**(1), 177–184 (2014)
15. A. Shirafkan, S.M. Nowee, N. Ramezanian, M.M. Etemadi, Hybrid coagulation/ozonation treatment of pharmaceutical wastewater using ferric chloride, polyaluminum chloride and ozone. Int. J. Environ. Sci. Technol. **13**(6), 1443–1452 (2016)
16. M. Bayramoglu, M. Eyvaz, M. Kobya, Treatment of the textile wastewater by electrocoagulation: Economical evaluation. Chem. Eng. J. **128**(2–3), 155–161 (2007)
17. A.K. Golder, A.N. Samanta, S. Ray, Removal of Cr3+ by electrocoagulation with multiple electrodes: Bipolar and monopolar configurations. J. Hazard. Mater. **141**(3), 653–661 (2007)
18. A. Apha, *WEF (2005) Standard Methods for the Examination of Water and Wastewater* (American Public Health Association, American Water Works Association, Water Environment Federation, Washington, DC, 2007)
19. P. Verlicchi, M. Al Aukidy, E. Zambello, Occurrence of pharmaceutical compounds in urban wastewater: Removal, mass load and environmental risk after a secondary treatment—A review. Sci. Total Environ. **429**, 123–155 (2012)
20. F. Wei et al., Removal of tetracycline hydrochloride from wastewater by Zr/Fe-MOFs/GO composites. RSC Adv. **11**(17), 9977–9984 (2021)
21. K. Panplado, M. Subsadsana, S. Srijaranai, S. Sansuk, Rapid removal and efficient recovery of tetracycline antibiotics in aqueous solution using layered double hydroxide components in an in situ-adsorption process. Crystals **9**(7), 342 (2019)
22. B.M. Sharma et al., Health and ecological risk assessment of emerging contaminants (pharmaceuticals, personal care products, and artificial sweeteners) in surface and groundwater (drinking water) in the Ganges River basin, India. Sci. Total Environ. **646**, 1459–1467 (2019)
23. A. Vázquez, I. Rodríguez, I. Lázaro, Primary potential and current density distribution analysis: A first approach for designing electrocoagulation reactors. Chem. Eng. J. **179**, 253–261 (2012)
24. R. Keyikoglu, O.T. Can, A. Aygun, A. Tek, Comparison of the effects of various supporting electrolytes on the treatment of a dye solution by electrocoagulation process. Colloid Interface Sci. Commun. **33**, 100210 (2019)
25. K.D. Cruz, J.T.J. Francisco, K.J.M. Mellendrez, J.M.F. Pineda, Electrocoagulation treatment of swine slaughterhouse wastewater: Effect of electrode material, in *E3S Web of Conferences*, vol. 117, (2019), p. 20
26. C.E. Barrera-Díaz, B.A. Frontana-Uribe, M. Rodríguez-Peña, J.C. Gomez-Palma, B. Bilyeu, Integrated advanced oxidation process, ozonation-electrodegradation treatments, for nonylphenol removal in batch and continuous reactor. Catal. Today **305**, 108–116 (2018)
27. B. Merzouk, B. Gourich, A. Sekki, K. Madani, C. Vial, M. Barkaoui, Studies on the decolorization of textile dye wastewater by continuous electrocoagulation process. Chem. Eng. J. **149**(1–3), 207–214 (2009)
28. C.A. Igwegbe, J.O. Ighalo, O.D. Onukwuli, I.A. Obiora-Okafo, I. Anastopoulos, Coagulation-flocculation of aquaculture wastewater using green coagulant from Garcinia kola seeds: Parametric studies, kinetic modelling and cost analysis. Sustainability **13**(16), 9177 (2021)
29. M. Kobya, E. Demirbas, N.U. Parlak, S. Yigit, Treatment of cadmium and nickel electroplating rinse water by electrocoagulation. Environ. Technol. **31**(13), 1471–1481 (2010)
30. A.I. Adeogun, P.B. Bhagawati, C.B. Shivayogimath, Pollutants removals and energy consumption in electrochemical cell for pulping processes wastewater treatment: Artificial neural network, response surface methodology and kinetic studies. J. Environ. Manag. **281**, 111897 (2021). https://doi.org/10.1016/j.jenvman.2020.111897
31. A.K. Jha, S. Chakraborty, Photocatalytic degradation of tetracycline and ciprofloxacin antibiotic residues in aqueous phase by biosynthesized nZVI using Sal (Shorea robusta) leaf extract. AQUA Water Infrastruct. Ecosyst. Soc. **72**(3), 230–245 (2023)

Quantification of Floating Plastics Using UAV Images and Identification of Microplastics in Ukkadam Tank, Coimbatore, Tamil Nadu

Karunya Baburaj, J. Brema, and Jims John Wesley

Abstract Plastics are becoming a serious threat to environment and it is a global concern now. Economic development and urbanization are the two factors that lead to water pollution. Wetlands and lakes, particularly those located near urban centers, are subjected to severe threat due to the plastic wastes. Ukkadam Lake is one of the major lakes in Coimbatore, also known as Periyakulam, is facing this issue due to the inflow of domestic sewage. In this study, an attempt has been made to assess the quantity of floating plastics and microplastics that enters the Ukkadam Lake using remote sensing techniques and microscopic studies. The assessment is carried out for the year 2021 using unmanned aerial vehicle (UAV) images and water sampling in the lake. The extent of floating macroplastics has been carried out using spectral signatures and classification techniques. The identification of microplastics was carried out by an experimental method by way of collecting water samples in the lake. The extent of availability of macroplastics and identification of microplastics were produced as results in this research.

Keywords Classification techniques · Image classification · Support vector machine classification · Random tree classification · Maximum likelihood classification · Feature extraction · Microplastics · Macroplastics · Spectral signatures · UAV images · Areal extent

K. Baburaj · J. Brema (✉)
Civil Engineering Department, Karunya Institute of Technology and Sciences, Coimbatore, Tamil Nadu, India

J. J. Wesley
Aerospace Engineering Department, Karunya Institute of Technology and Sciences, Coimbatore, Tamil Nadu, India
e-mail: jims_john@karunya.edu

D. Mazumder (ed.), *Sustainable Advanced Technologies for Industrial Pollution Control*, Springer Proceedings in Earth and Environmental Sciences,
https://doi.org/10.1007/978-3-031-37596-5_25

Abbreviations

KOH Potassium hydroxide
MLH Maximum likelihood classification
RT Random tree classifier
UAV Unmanned aerial vehicle
VHR Very-high-resolution

1 Introduction

The plastic waste in the aquatic ecosystems is one the most obvious indicator of the pervasive and growing problem of plastic pollution. Aquatic life, ecosystems, and human health are all threatened by plastic wastes. It has become obvious that plastic pollution can turn into an environmental threat as more and more plastic garbage are being dumped in the lakes and water bodies. This environmental issue in aquatic ecosystems has a severe effect on the flora and fauna and aquatic species in the ecosystem. Plastics are made to last, so when they are improperly disposed of, they stay in the environment for a very long period. The term "microplastics" refers to a broad category of polymer-based particles (<5 mm) that have come to represent human waste and environmental contamination [1]. Microplastics, either primary or secondary, are released into the environment. The majority of primary microplastics that are released into the environment as microbeads come from textiles and personal care items. The manner in which weathering of plastic trash causes macroplastics to fragment, secondary microplastics are created. Our ecology is being silently destroyed by microplastics, which impact both aquatic and terrestrial creatures. By reducing their desire to eat, obstructing digestive tracts, and changing the eating behavior, it lowers growth and reproductive output of creatures and some animals have even starved to death as a consequence of this pollution. In terrestrial or continental systems, plastics are created, utilized, and discarded, where they interact with the biota [2]. Plastics are the most common, durable, and reasonably priced synthetic materials used in industry that are reported to continuously produce general municipal solid waste [3]. During their use, all major plastic waste can eventually break down into micro- or nanosized particles, such as fibers released from clothing or textiles, rubber pieces released by car tires from abrasion, plastic mulching, and paint flakes [4]. Urbanization has been identified as a significant contributor to plastics pollution in lakes and rivers, which includes pollution from industrial and land run-offs. Although the consequences of microplastics on human health and aquatic ecosystems are not yet fully understood, reports of their prevalence and detrimental impacts on fresh water biota are growing [5].Given its ease of use and great efficiency, for classifying remotely sensed images, pixel-based image processing has long been a popular method [6]. However, very-high-resolution (VHR) remote sensing images from aircraft, satellites, and unmanned aerial vehicles

(UAVs) have become increasingly popular in recent years for classification [7]. There are numerous image classification methods, each with their own benefits and drawbacks. Finding the ideal hyperplane is the goal of the recently developed non-parametric supervised statistical machine learning method known as the support vector machine (SVMs) [8]. It discretely divides the multispectral feature data into predetermined clusters that are consistent with training datasets. The discipline of remote sensing has found extensive use for maximum likelihood classification, a remarkable classification technique based on multivariate normal distribution theory [9]. The increase in the development of unmanned aerial vehicles (UAVs) now provides a quick and inexpensive method to obtain high quality images of wetlands, which serve as the basis for the subsequent image processing procedure to identify plastic regions. The suggested method makes use of UAV data to extract plastic portions using algorithms quickly and efficiently for image processing and analysis [10]. A supervised classifier, the Random Tree algorithm, creates several different groups. It uses the principle to generate a set of random data in order to build a decision tree [11]. The number of training data, which differs for various satellite picture formats, is a key factor in classification accuracy. The best amount of training samples chosen could improve classification accuracy overall [12]. Coimbatore is blessed with abundant water resources, which have long been a source of drinking water, irrigation, aquaculture, and leisure activities. Increase in urbanization and growth in industries and economy also influence the aquatic ecosystems. Periyakulam Tank, the study area, is one of Coimbatore's major lakes and a popular tourist destination. Hotels and restaurants have encroached toward the lakeside to enjoy the lake's beautiful appeal, which has increased the lake's pollution. The objective of this study is to identify floating macro plastics using UAV image and microplastics in the tank and to assess it.

2 Materials and Methods

2.1 Study Area

The study area identified for the study is Ukkadam Tank situated in Coimbatore district of Tamil Nadu as shown in Fig. 1.The geographic location of tank is 10°58′ 54″ N and 76°57′ 17″ E. The average depth is 5.82 m and the area of the tank is of 1.295 km^2. As shown in Fig. 2, the tank is fed by channels from Noyyal River which is one of the tributaries to river Cauvery. The overflow from Selvachinthamani Tank which is located north to the Ukkadam Tank is also led into it. Due to increase in urbanization, many agricultural lands are changed to residential and industrial areas due to urbanization. Sewage from the urbanized and industrial area leads to increased problems. These sewage effluents highly affect the wetland and have been polluting the environment day by day. The tank has five sewage inlets and the floating macroplastics are identified in one of the open sewage inlets using unmanned aerial vehicle image (UAV). Considering this, the water samples were

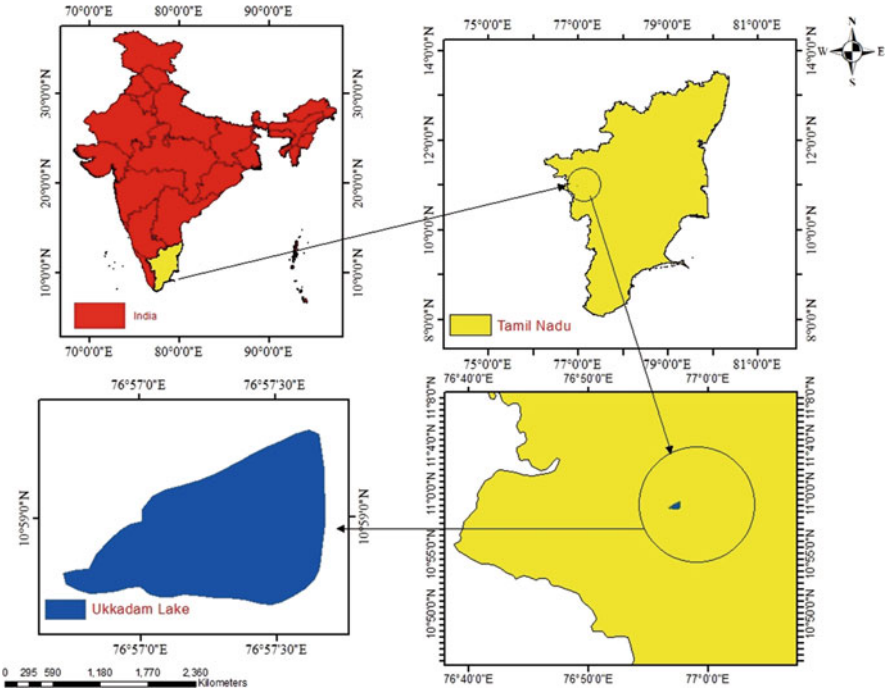

Fig. 1 Ukkadam Tank, Coimbatore

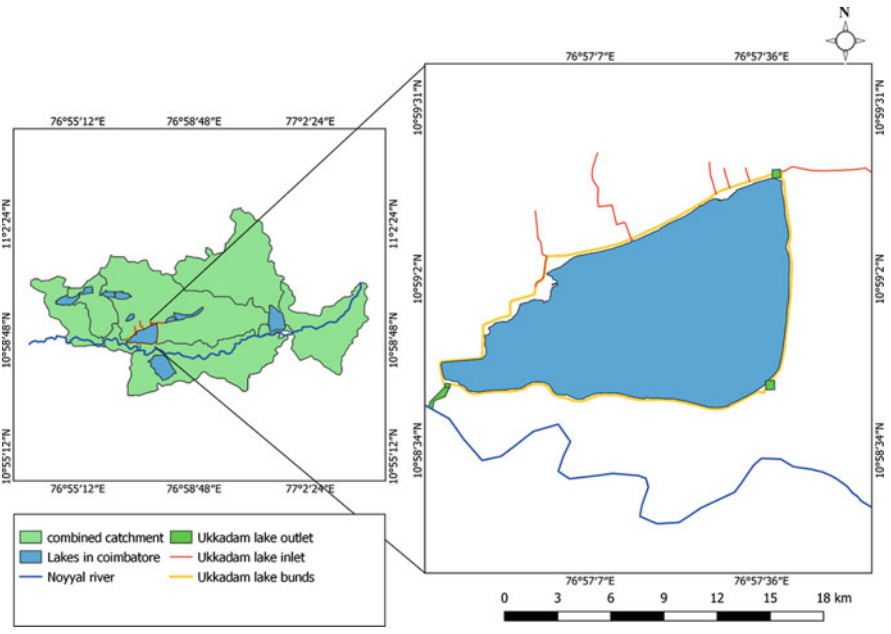

Fig. 2 Combined catchments of lakes

collected in the periphery of the tank for identification of microplastics. The presence of markets, textile industries, and restaurants in the vicinity of the tank produces huge wastes and threatens the lake by way of discharging the sewage into it.

2.2 *Unmanned Aerial Vehicle Image*

An unmanned aerial vehicle image was used for to obtain the image of the Ukkadam Lake. The image acquisition was carried out with a DJI Mavic 2 Pro Quadcopter fitted with FC220 RGB camera. In order to get high-resolution image, the flight height of the drone was fixed at 300 feet. Since the flight height was less and there was no huge influence of the atmospheric factors, the atmospheric correction has not been done to the image.

As shown in Fig. 3, the UAV images were acquired in the location where there were open sewage inlets into the tank. The extracted portion of the image gives the feature classes for the study. The UAV image has three bands: red, green, and blue where each pixel of the image has digital values for all these bands and the reflectance of the classes varies.

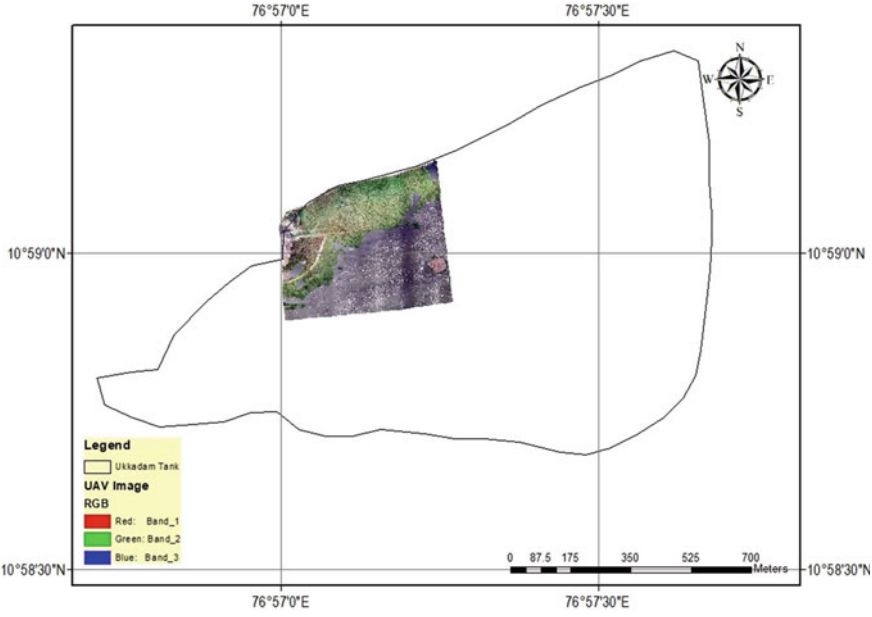

Fig. 3 UAV image of the study location

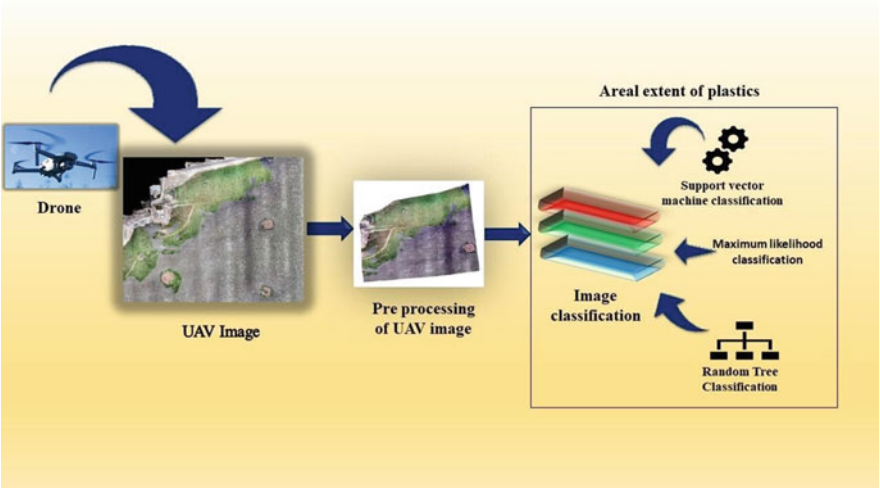

Fig. 4 Methodology

2.3 Image Classification

Image classification is the process of identifying the group of pixels belonging to a particular category from other category of pixels in an image. The classification of an image is also a task to obtain the information classes. In this study, the QGIS software is used for image classification. Figure 4 shows the methodology followed for this study.

2.4 Supervised Classification

Supervised classification is the classification method in remote sensing in which the classification can be applied to all the images which contains red, green, blue bands. The open sewage water inlet to the tank was identified, and the UAV images were acquired to identify the floating macroplastics using remote sensing techniques. The supervised image classification has been carried out by giving the training samples by drawing polygons for different feature classes. The classification techniques such as maximum likelihood, support vector classification, random tree classification were applied to the image. In each of the techniques, the macroplastics were extracted and the difference in results was observed. The supervised classification is different from the other classifications such as unsupervised classification and object-based classification. In this classification, the training samples are given in the UAV image corresponding to the floating plastics, land, vegetation, and water body.

2.4.1 Maximum Likelihood Classification

Maximum likelihood classification (MLH) is one of the mostly used supervised classification techniques. Classification has been carried out in the study area by giving training samples using polygons; these polygons are the training inputs and it is merged for one feature class. The known class distribution of a particular statistic is determined using the MLC procedure [13]. Maximum likelihood classification is a common, pixel-based supervised strategy that also categorizes unknown pixels based on the multivariate probability density functions of the given classes [14].

2.4.2 Support Vector Machine Classifier

In this type of classifier, deep learning algorithms are used for supervised classification of images. The input raster and the input training samples are given to the classifier. The final output from the support vector machine (SVM) classifier shows the classified input features in the image. The final output from the SVM classifier shows the classified input features in the image. With the use of SVM, which is based on an analytical learning process, it is possible to identify where decision borders should be placed in order to achieve the best possible class separation, and the SVM chooses the linear decision boundary that minimizes the error when faced with a two-class pattern overlapping and identification issue where the classes can be linearly separated and where the decision boundary that is chosen will be the one that leaves the maximum margin between the two classes since range is described as the sum of the distance from the closest points in the two classes to the higher dimensional space [15]. The decision boundary that minimizes misclassification obtained during the training phase is referred to as "*optimal separation hyperplane*" [16].

2.4.3 Random Tree Classifier

Another technique used for image classification is random tree (RT) classifier. Multiple decision trees are formed for the selected training inputs and the subset features, and the classifier chooses the subsets randomly for the classification of the image. The image was classified according to the decision trees formed in the classifier. Random trees may be produced quickly, and combining several such random trees typically results in models that are realistic. In the subject of machine learning, there has been a lot of recent study on random trees [17].

2.5 Feature Extraction

The macroplastics are extracted based on the pixels, the corresponding pixels of this class have been demarcated using the three classification techniques for a real extent analysis. Pixels have different values in each classification techniques. The

macroplastics are extracted by eliminating all other feature classes. A formal approach for feature extraction explains the relevant shape information included in a pattern, making the task of classifying the pattern easier. The primary goals of feature extraction are to locate the most relevant details within the initial data and to express it within a reduced dimensional space [18].

2.6 Identification of Microplastics

The water samples were collected from the periphery of the tank for the identification of microplastics. The samples are collected with some solid particles and it is carried out for the laboratory analysis. To keep the sediments and soil particles, the water samples were sieved separately using 0.3 and 5.0 mm screen. Before it is dried, identified, and subjected to further examination, the coarse material is separated from the liquid using a process known as wet sieving. Using this technique, samples can be made ready by being cleaned of debris, having clumps broken up, or having static charges neutralized. For each sample, the solid components were washed with distilled water and then used for additional laboratory testing. Digestion is the next step in which the organic matter is separated from the microplastics. For this process, stirring hot plate, aluminum foil, glasses, beaker, potassium hydroxide (KOH), wash bottle, spoons, and gloves were used. Before starting the procedure, the materials used for testing were rinsed. Potassium hydroxide is a very corrosive substance and one needs to wear glass and gloves for testing purposes. The samples were transferred to the beaker and KOH (10%) was added, with this a magnetic stirrer was also placed inside the beaker for uniform stirring. The beaker was placed on the hot plate of temperature of 60–70 °C with the rotational speed of 5–10 rpm for 24 h. The sample was sieved using distilled water and for separating the solid particles. The solid samples were kept in the hot air oven in the range of temperature of 50–70 °C for drying.

2.7 Visual Observation

Binocular microscopes are frequently employed as an identification tool for minute plastic particles. Using an objective lens, they can enhance images of submillimeter-sized microplastics in the samples [19, 20]. Microplastic sorting and optical detection with the naked eye are the simplest techniques for identifying different varieties of plastic debris with a size greater than a few millimeters. The chemical characteristics of microplastics cannot be determined by using a binocular microscope to study them.

3 Results and Discussion

3.1 Areal Extent of Macroplastics

The area of the floating macroplastics was estimated based on the extraction carried out using the classification techniques. The area was calculated in square meters for the macroplastics alone, the area corresponding to the three classifications varied, and they were analyzed. The area of macroplastics corresponding to the maximum likelihood classification was 4.4783 m^2, in case of support vector classifier it was 2.2778 m^2, and in case of random tree classifier it was 0.9366 m^2. It was observed that the pixels corresponding to the feature class and overlapping of feature class was observed in random tree classification and maximum likelihood classification. Figures 5, 6, and 7 show the classified images corresponding to the three techniques. Figures 8, 9, and 10 show the presence of macroplastics in the water body corresponding to the three techniques (Fig. 11).

From Fig. 12 and Table 1, it can be inferred that in the areal extent of macroplastics, the MLH classifier shows more area than the other two classification methods. The overlapping of feature classification was not occurring in the support vector machine classification and the area of macroplastics obtained from the SVM classification technique was more accurate than the other two techniques.

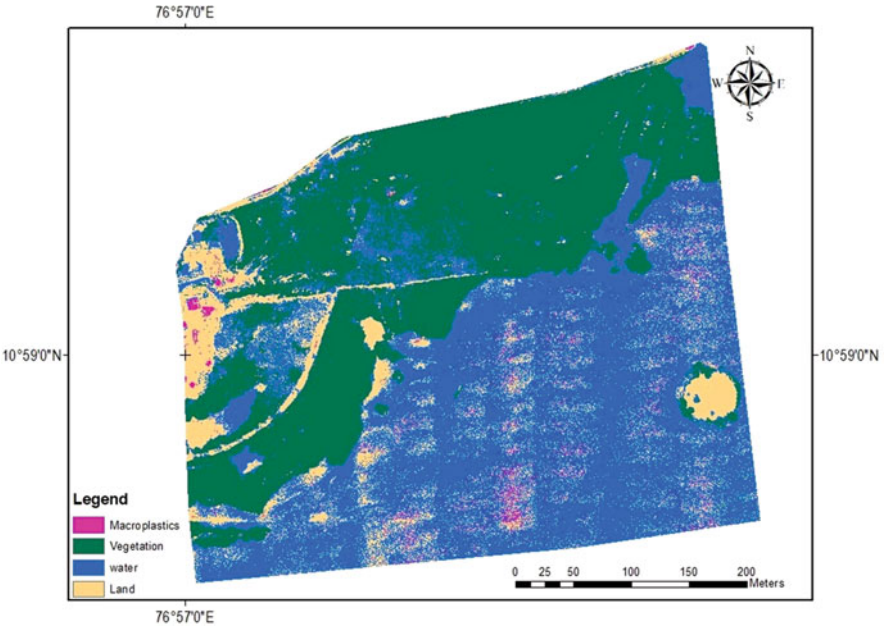

Fig. 5 Classified image using maximum likelihood classification

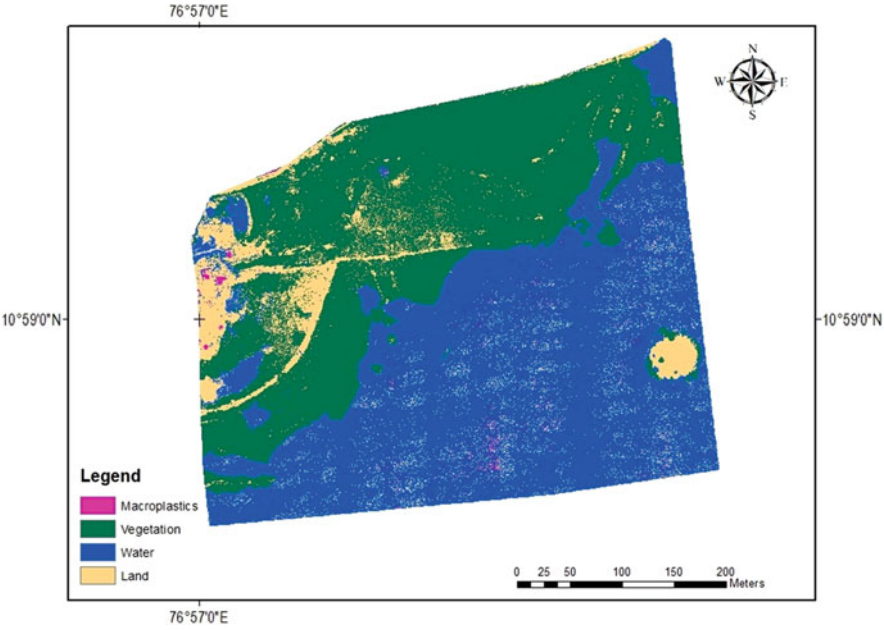

Fig. 6 Classified image using support vector machine classification

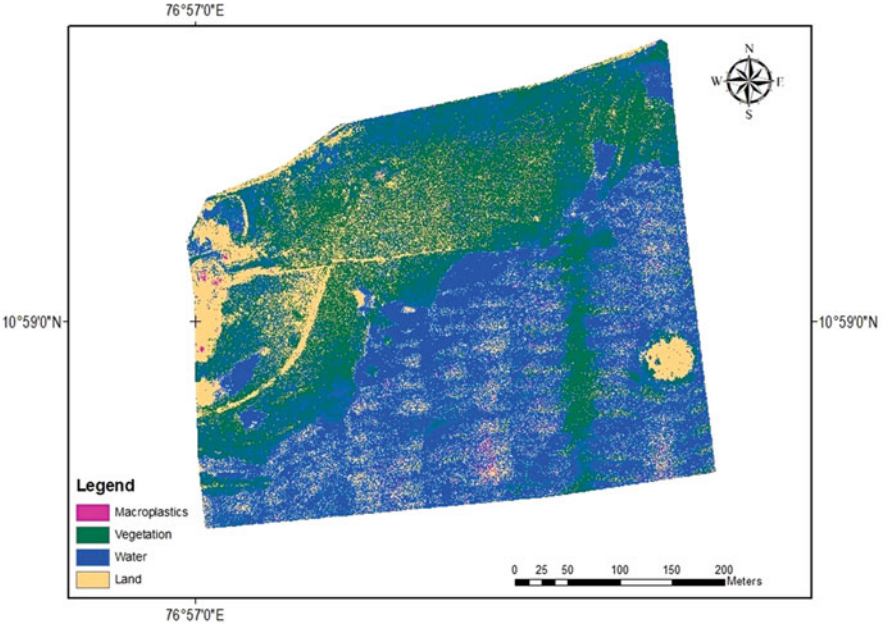

Fig. 7 Classified image using random tree classification

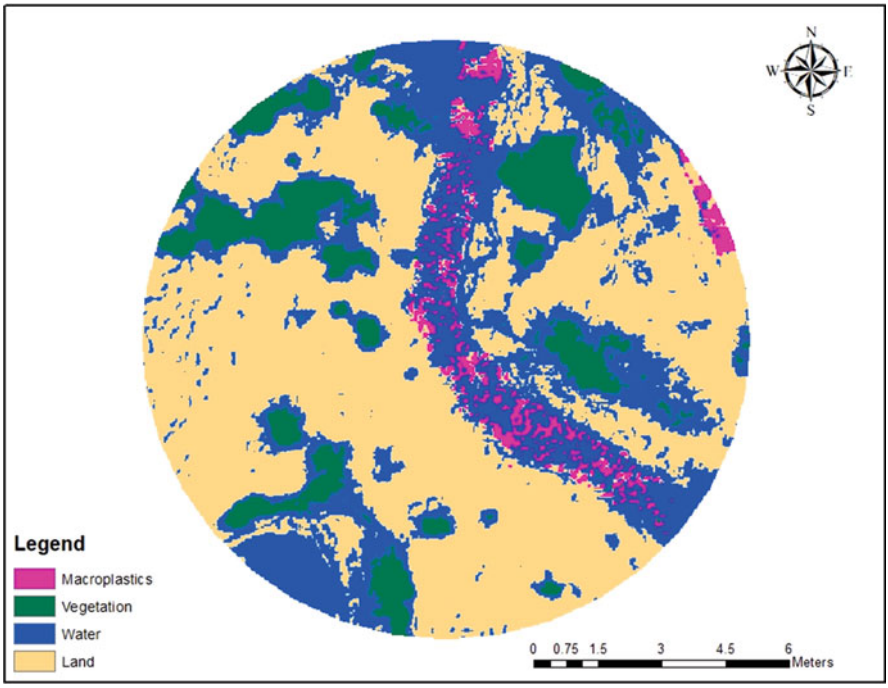

Fig. 8 Extracted image of macroplastics using maximum likelihood classification technique

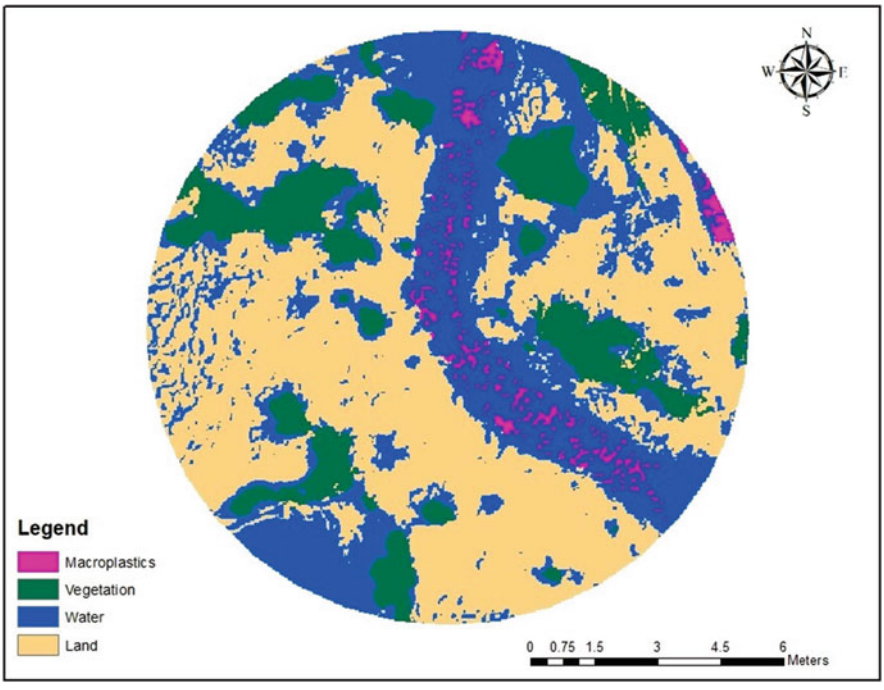

Fig. 9 Extracted image of macroplastics using support vector machine classification technique

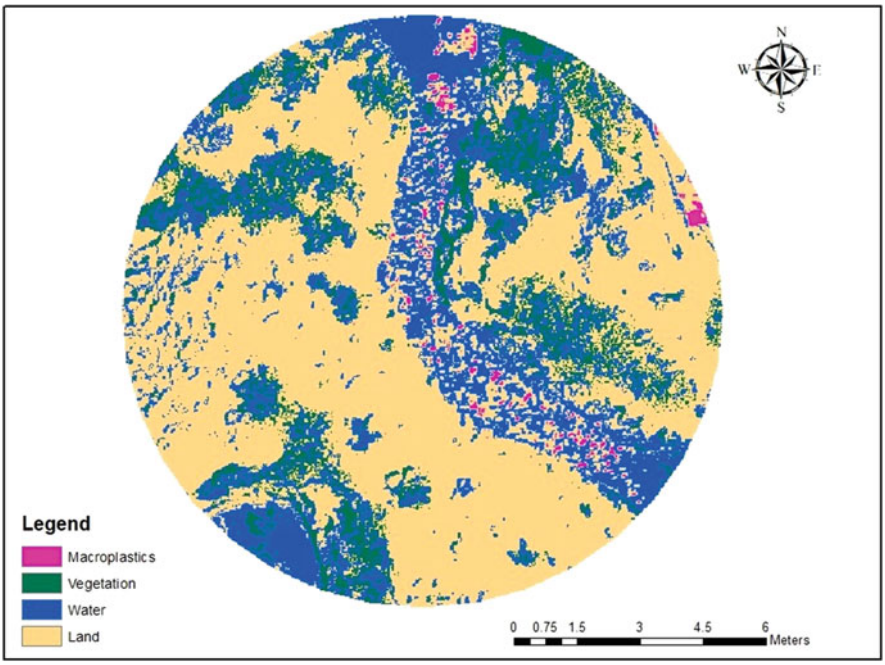

Fig. 10 Extracted image of macroplastics using random tree classifier technique

3.2 Microscopic Observation

In order to verify the presence of microplastics in the water body, samples were collected in different places in the peripheral region of the tank. From the water samples, dry samples were extracted based on the methodology explained earlier. The dry samples were further observed through the binocular microscope. From the images, it could be observed that the fiber and flake shapes were identified as shown in Fig. 13. As the particles were lesser than 5 mm in size, it confirmed the presence of microplastics.

4 Conclusion

In this study, the estimation of the area of the floating macroplastics was carried out using three classification techniques using QGIS software. The difference in results among the three classification techniques was observed. The overlapping of feature

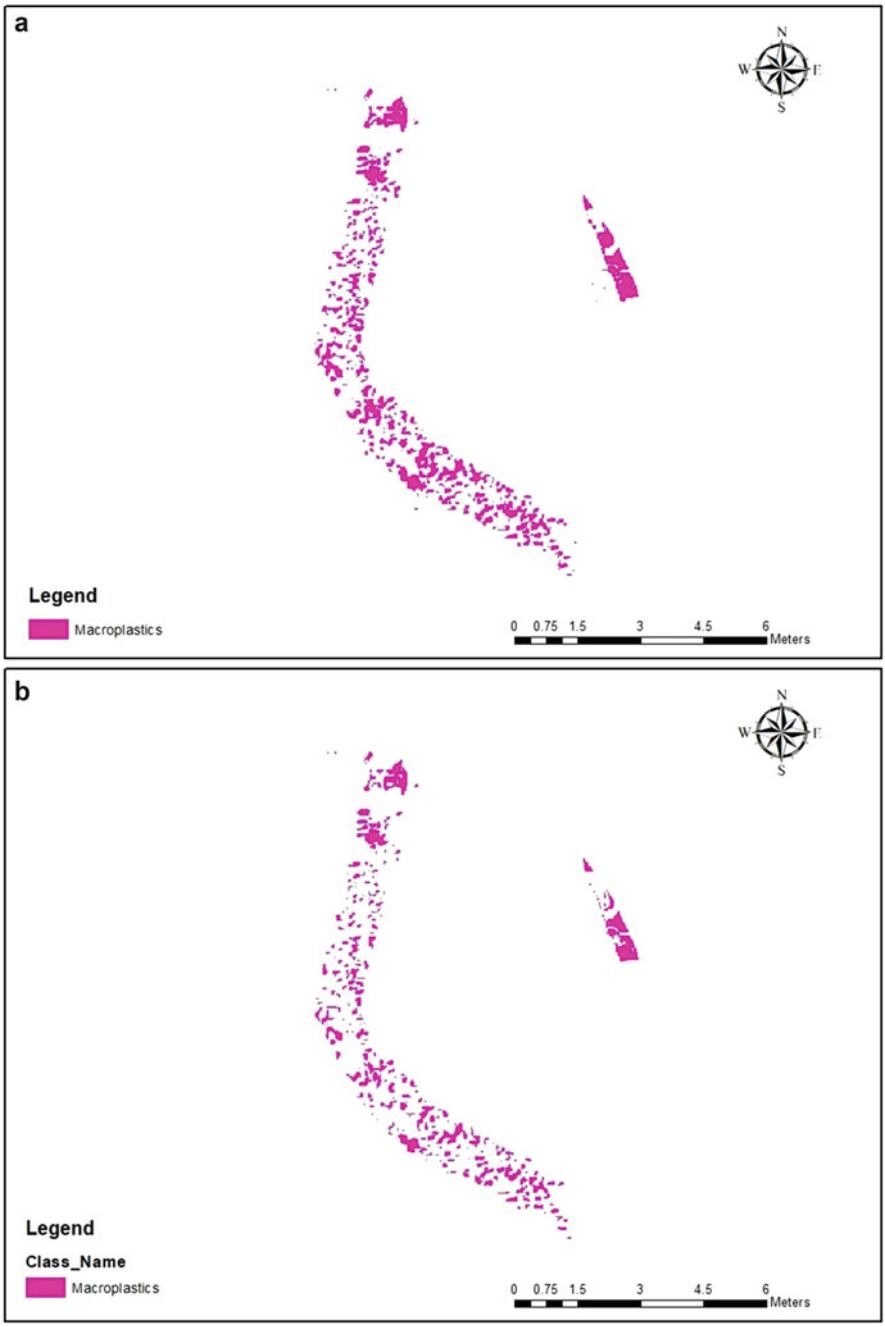

Fig. 11 (**a**–**c**) Extracted features of the plastic objects in the water body

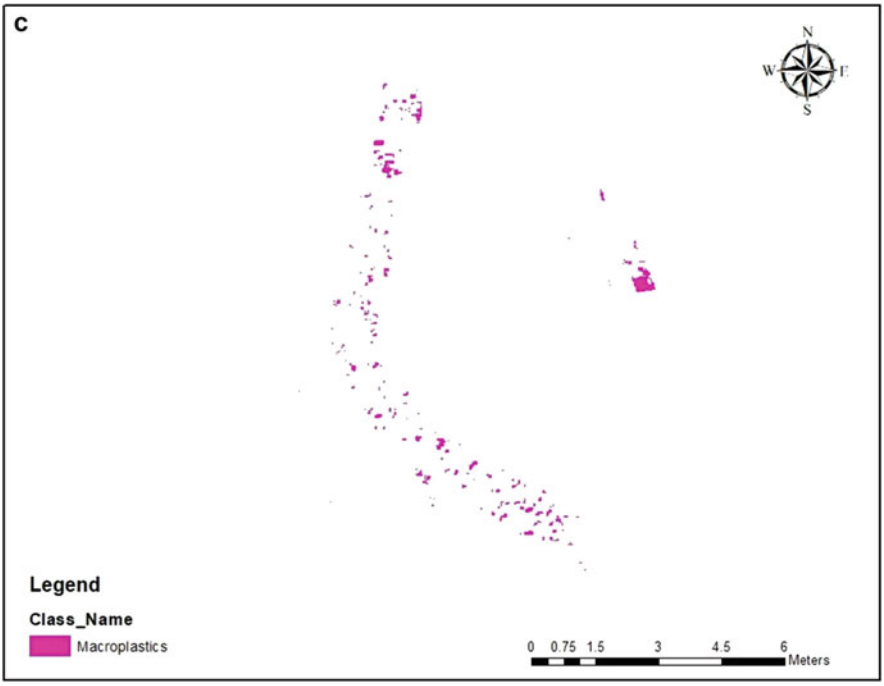

Fig. 11 (continued)

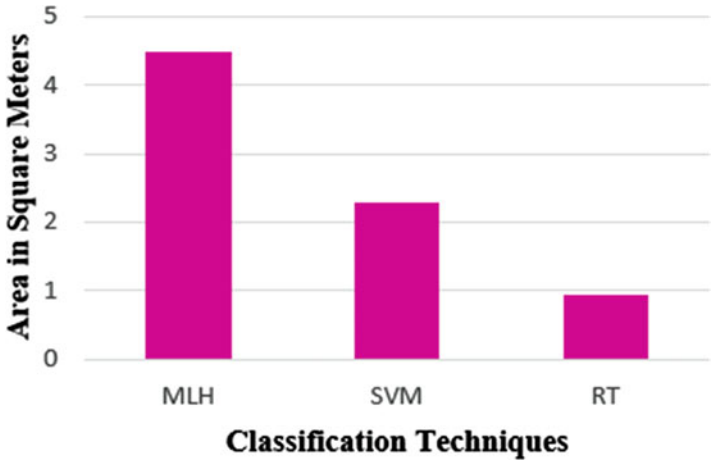

Fig. 12 Area of macroplastics

Table 1 Area of macroplastics

Classification techniques	Area	Unit
MLH	4.4783	Sq. m.
SVM	2.2778	Sq. m.
RT	0.9336	Sq. m.

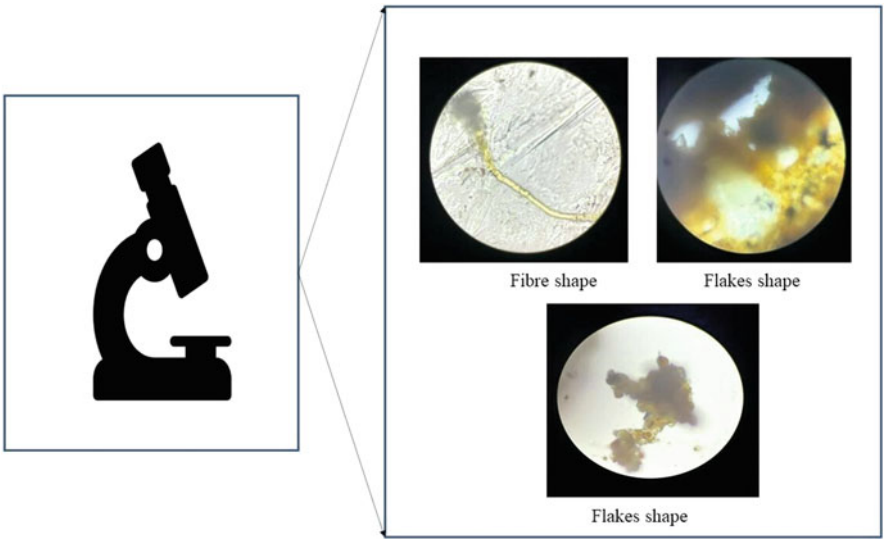

Fig. 13 Images of microscopic observation

class was observed in a random tree and maximum likelihood classification. The areal extent of macroplastics is more accurate in support vector machine classification. The presence of microplastics was also confirmed. This study demonstrated the risk of water body pollution brought on by plastics due to urbanization. Plastic pollution can degrade drinking water quality and potentially harm the lake's ecosystem and environment, as well as the surrounding areas. It is important to raise awareness among the public in order to lower the risk of plastic pollution in water bodies, especially in urban areas. Additionally, enforcing the law strictly against the factories that are in charge of causing water pollution will lessen the likelihood of water contamination.

References

1. T.S. Galloway, M. Cole, C. Lewis, Interactions of microplastic debris throughout the marine ecosystem. Nat. Ecol. Evol. **1**(5), 1–8 (2017)
2. R.C. Thompson, S.H. Swan, C.J. Moore, F.S. Vom Saal, Our plastic age. Philos. Trans. R. Soc. B Biol. Sci. **364**(1526), 1973–1976 (2009)
3. S.H. Gebre, M.G. Sendeku, M. Bahri, Recent trends in the pyrolysis of non-degradable waste plastics. Chem. Open **10**(12), 1202–1226 (2021)
4. A.A. Horton, A. Walton, D.J. Spurgeon, E. Lahive, C. Svendsen, Microplastics in freshwater and terrestrial environments: Evaluating the current understanding to identify the knowledge gaps and future research priorities. Sci. Total Environ. **586**, 127–141 (2017)
5. G. Malafaia, T. Marinho, A. da Luz, P. da Costa, M.A. Araújo, I. Ahmed, T. Rocha-Santos, D. Barceló, Novel methodology for identification and quantification of microplastics in biological samples. Environ. Pollut. **292**, 118466 (2022)
6. T. Blaschke, Object based image analysis for remote sensing. ISPRS J. Photogramm. Remote Sens. **65**(1), 2–16 (2010)
7. X. Zhang, G. Chen, W. Wang, Q. Wang, F. Dai, Object-based land-cover supervised classification for very-high-resolution UAV images using stacked denoising autoencoders. IEEE J. Select. Top. Appl. Earth Observations Remote Sens. **10**(7), 3373–3385 (2017)
8. C. Cortes, V. Vapnik, Support-vector networks. Mach. Learn. **20**, 273–297 (1995)
9. Abkar, Ali Akbar. "Likelihood-Base Segmentation and Classification of Remotely Sensed Images: A Bayesian Optimization Approach for Combining RS and GIS." Int J Appl Earth Obs Geoinf. **2**(2), 104–119 (2000)
10. Y. Yuan, H. Xiangyun, Random forest and objected-based classification for forest pest extraction from UAV aerial imagery. Int. Arch. Photogramm. Remote Sens. Spatial Inf. Sci. **41**, 1093 (2016)
11. S. Kalmegh, Analysis of Weka data mining algorithm REPTree, simple cart and random tree for classification of Indian news. Int. J. of Innov. Sci. Eng. Technol. **2**(2), 438–446 (2015)
12. G.M. Foody, A. Mathur, C. Sanchez-Hernandez, D.S. Boyd, Training set size requirements for the classification of a specific class. Remote Sens. Environ. **104**(1), 1–14 (2006)
13. A.J. Scott, M.J. Symons, Clustering methods based on likelihood ratio criteria. Biometrics **27**, 387–397 (1971)
14. J.Y. Lee, T.A. Warner, Image classification with a region-based approach in high spatial resolution imagery, in *The International Archives of the Photogrammetry, Remote Sensing and Spatial Information Sciences, Istanbul, Turkey*, (2004), pp. 181–187
15. V. Vapnik, *The Nature of Statistical Learning Theory* (Springer Science & Business Media, 1999)
16. G. Zhu, D.G. Blumberg, Classification using ASTER data and SVM algorithms; the case study of beer Sheva, Israel. Remote Sens. Environ. **80**(2), 233–240 (2002)
17. S. Gupta, S. Abraham, V. Sugumaran, M. Amarnath, Fault diagnostics of a gearbox via acoustic signal using wavelet features, J48 decision tree and random tree classifier. Indian J. Sci. Technol. **9**, 1–8 (2016)
18. G. Kumar, P.K. Bhatia, A detailed review of feature extraction in image processing systems, in *2014 Fourth International Conference on Advanced Computing & Communication Technologies*, (IEEE, 2014), pp. 5–12
19. J.-P.-W. Desforges, M. Galbraith, N. Dangerfield, P.S. Ross, Widespread distribution of microplastics in subsurface seawater in the NE Pacific Ocean. Mar. Pollut. Bull. **79**, 94–99 (2014). https://doi.org/10.1016/j.marpolbul.2013.12.035
20. M. Eriksen, L.C.M. Lebreton, H.S. Carson, M. Thiel, C.J. Moore, J.C. Borerro, F. Galgani, P.G. Ryan, J. Reisser, Plastic pollution in the world's oceans: More than 5 trillion plastic pieces weighing over 250,000 tons afloat at sea. PLoS One **9**, e111913 (2014). https://doi.org/10.1371/journal.pone.0111913

Study of Wastewater Treatment in Hindustan Coca-Cola Plant at Khurda

Sushree Sasmita and Bharath Kumar Dudam

Abstract We investigate the performance evaluation of wastewater effluent of beverage plant of Hindustan Coca-Cola Pvt. Ltd., which is situated in Khurda Industrial Estate, Khurda, Odisha, during the operational period of the plant in September 2012. The effluent samples were collected before and after the treatment for each treatment unit of the plant. Different environmental parameters were analyzed including pH, turbidity, chlorinity, total suspended solids (TSS), total dissolved solids (TDS), phenolphthalein alkalinity, total alkalinity, calcium hardness, total hardness, sulphate, chloride content, and soluble and heavy metal ions for input purification unit. Among the analyzed parameters, dissolved oxygen (DO), biochemical oxygen demand (BOD), and chemical oxygen demand (COD) were also included to check the performance of the unit operations. Most of our findings were within the permissible limits as suggested by central pollution control board (CPCB) 2019. In particular, the pH in the outlet of wastewater is found to be 7.37, D.O. to be 7.8 mg/l, total suspended solids to be 130 mg/l, COD to be 27.27 mg/l, and BOD to be 22 mg/l, respectively. However, the plant follows the concept of reuse and recycle technology as it utilizes the wastewater for further treatment.

Keywords Biochemical oxygen demand (BOD) · Chemical oxygen demand (COD) · Mixed liquor suspended solids (MLSS) · Sludge volume index (SVI)

Abbreviations

ACF	Activated carbon filter
BOD	Biochemical oxygen demand

S. Sasmita
School of Civil Engineering-KIIT-DU, Bhubaneswar, India

B. K. Dudam (✉)
Department of Civil Engineering, Chaitanya Bharathi Institute of Technology (Autonomous), Gandipet, Hyderabad, Telangana, India

D. Mazumder (ed.), *Sustainable Advanced Technologies for Industrial Pollution Control*, Springer Proceedings in Earth and Environmental Sciences,
https://doi.org/10.1007/978-3-031-37596-5_26

CaH	Calcium hardness
COD	Chemical oxygen demand
CPCB	Central Pollution Control Board
DO	Dissolved oxygen
MLSS	Mixed liquor suspended solids
NTU	Nephelometric turbidity unit
PSF	Pressurized sand filter
SCC	Solid contact clarifier
SVI	Sludge volume index
TDS	Total dissolved solid
TH	Total hardness
TSS	Total suspended solid
VFA	Volatile fatty acids

1 Introduction

Water is an essential element for all known forms of life. Water pollution takes place when harmful substances including chemicals and microorganisms contaminate different water bodies that degrading water quality and render it toxic to humans or the environment. The increase in production is associated with higher industrial wastewater production [1]. The release of toxic pollutants is hazardous to human health and aquatic life and a major contribution for environmental pollution [2]. These pollutants contain organic and inorganic substances described by the biochemical oxygen demand (BOD) and chemical oxygen demand (COD) [3]. Wastewater generated from the soft drinks industry is likely to be treated as it constitutes mostly of biodegradable organic substances [4]. The major components in soft drinks include primarily water, carbon dioxide, caffeine, sweeteners, acids, and aromatic substances present in small amounts [5] which are present in appreciable amount in wastewater [6–8]. In this study, more emphasis was given on the wastewater treatment in Coca-Cola plant in Khurda district in Odisha [9, 10]. This plant apparently aimed at wastewater treatment with the concept of recycle and reuse concept, where the treated water will be utilized in the input water purification unit. Soft drink wastewater consists of wasted soft drinks and syrup; water from the washing of bottles and cans, which contains detergents and caustics; and finally lubricants used in the machinery. Thus, in turn, the significant associated wastewater pollutants will include total suspended solids (TSS), biochemical oxygen demand (BOD), chemical oxygen demand (COD), and nitrates. Most of the organic matter presence in the wastewater effluent could be removed through biological treatment units or operations particularly for the removal of the soft drink wastewater effluent. High-strength wastewater normally has low flow and can be treated using the anaerobic process, whereas the low-strength wastewater together with the effluent from the anaerobic treatment can be treated by an aerobic process. Our study

emphasizes performance evaluation of Coca-Cola plant through analyzing different pollution parameters. This plant is based in Khurda district of Odisha, which exists in the vicinity of within around 33 km from Bhubaneswar and is situated near the NH-5.

2 Materials and Methods

2.1 Study Site

Study site of this work is situated in Khurda Industrial estate, few kilometers away from the national highway-5 (NH-5).

The location is well communicated by roads and employees reach the location by company bus and own vehicles. The industry is around 33 km from Bhubaneswar and is well located amidst natural beauty in Khurda (refer to Figs. 1 and 2).

2.2 Methodology

To maintain the CPCB standards, most of the industries are required to be monitored or assessed it's efficacy to treat their effluents. We have carried out wastewater parameter (e.g., dissolved oxygen (DO), biochemical oxygen demand (BOD), chemical oxygen demand (COD), pH, volatile fatty acids (VFA), and alkalinity) testing to assess the performance of the plant. Treatment plant consists of input water purification unit (that treats the raw effluent prior to release into the production unit). Wastewater comes out of the production unit undergoes several treatment unit operations including reverse osmosis. Effluent from this unit process will be reused and recycled according to the level of usage.

2.3 Input to Water Purification

Raw water undergoes filtration by pressurized sand filter (PSF) unit made-up of combined three beds (quartz, sand, and gravel) to remove the larger size particles from the raw water. Further the water go through solid contact clarifier (SCC) unit operator in which the solution of $FeSO_4$, slurry of lime, and chlorine gas is added through various inlets, in order to form the sludge. The effluent coming out of the SCC is allowed to pass through activated carbon filter to remove chlorine and monitor color, odor, and taste. It is followed by dealkalizer to reduce the alkali content. Then it is allowed to pass through the degaser unit which is provided with blower through which air free from carbon dioxide is blown into the unit in order to remove dissolved CO_2. The effluent from degaser unit is thoroughly mixed in

Fig. 1 Schematic of Hindustan Coca-Cola Beverages Pvt. Ltd. at Khurda, Odisha

blending tank. In order to change the turbidity and texture, the above treated water was passed through ultrafiltration unit which consists of 14 barrels and having filter of pore size 0.3 microns. The above treated water was stored in the product water tank of capacity 200 kl. Stainless steel-activated carbon filter is connected to the unit after ultrafiltration for the purpose of dechlorination. The SS-activated carbon filter unit consists of three chambers in order to remove chlorine and monitor color, odor, and taste. Water thus treated was passed through lead/lag activated filter to remove

Fig. 2 Depiction of the bottling section in Coca-Cola plant

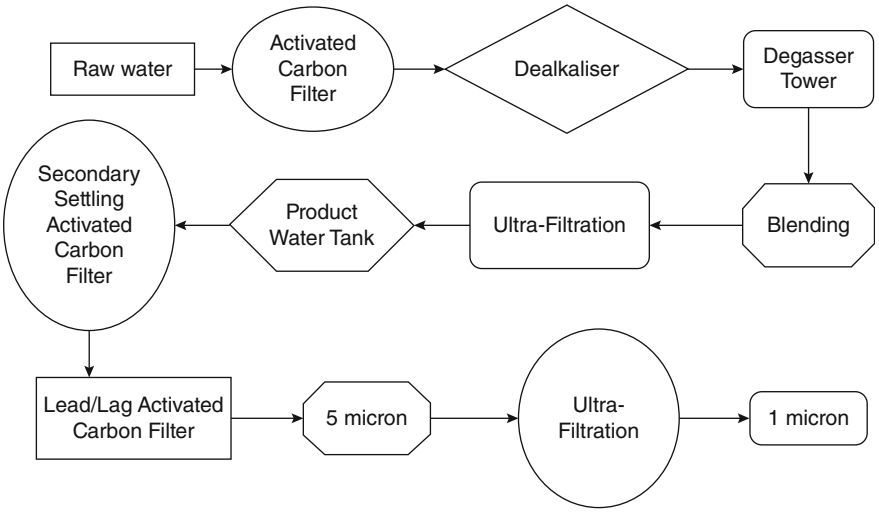

Fig. 3 Reactors involved in the process of input water purification unit

pesticides if present in the source. The treated water was then passed through a unit called 5 micron to reduce total dissolved solids above 5 micron size present in the treated water. Water was passed through three different units such as ultraviolet treatment is done in order to kill the virus and bacteria if present. It is followed by 3 micron unit and this would reduce the total dissolved solids above 3 micron size. It is followed by reverse osmosis which reduces the TDS. One micron unit is provided next in order to remove TDS of size above 1 micron. The treatment of raw water through different units is shown in the flowchart in Figs. 3 and 4. The results of analysis of various parameters are given in Table 1.

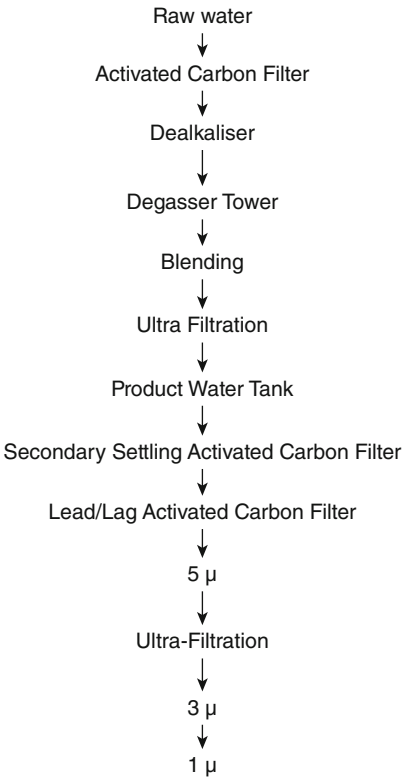

Fig. 4 Flowchart of the process of input water purification unit

Table 1 Input purification unit

	Raw water	ACF inlet	ACF outlet	5 µ outlet	RO	Softener outlet
pH	7.26	7.76	7	7.09	7.0	–
Turbidity/NTU	1.94	–	0.22	0.2	–	–
TDS/ppm	92	–	32.7	6.18	3.12	–
m-Alkalinity/ppm	57	–	44	40	–	–
p-Alkalinity/ppm	0	–	–	–	–	–
TH/ppm	75	–	59	53	–	5
CaH/ppm	58	–	–	–	–	–
Fe/mg/l	0.04	–	–	–	–	–
Cl^{-}/ppm	4	2	0	–	–	0
SO_4^{2-}/ppm	110	–	–	36	–	–
Chloride/ppm	87	–	–	–	–	–

2.4 Wastewater Treatment

The effluent being discharged from various sections of the plant is brought to the effluent treatment plant as shown in Figs. 5 and 6. The wastewater mainly consists of cold drinks and its residues, broken glasses during filling of bottles, plastic bottles, last running, wastewater containing washing from water treatment plant, wastewater containing additions of fruit pulps and its residues, wastewater from all plant sections, and spent solution from the filtration section. Wastewater may contain additions such as sugar syrups, pulps residues, alkaline cleaning water, and warm dirty wastewater and in particular waste caustic from the bottle washer containing insoluble substances such as shredded papers from labels and slurries. Other substances such as soluble substances comprising of adhesives, caustic, metal salts and belt lubricants, traces of oil, and residual cold drinks from returned bottles are present.

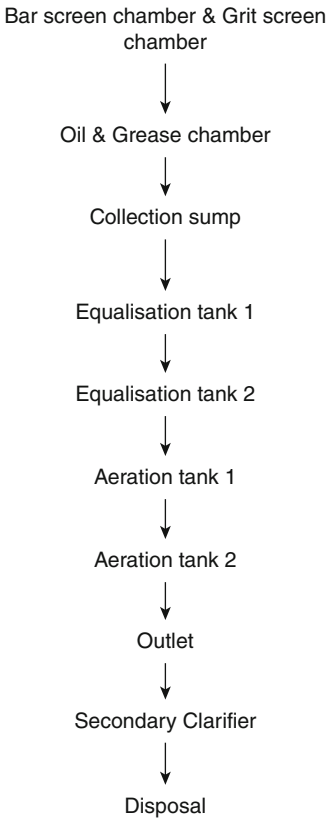

Fig. 5 Steps followed in the process of wastewater treatment

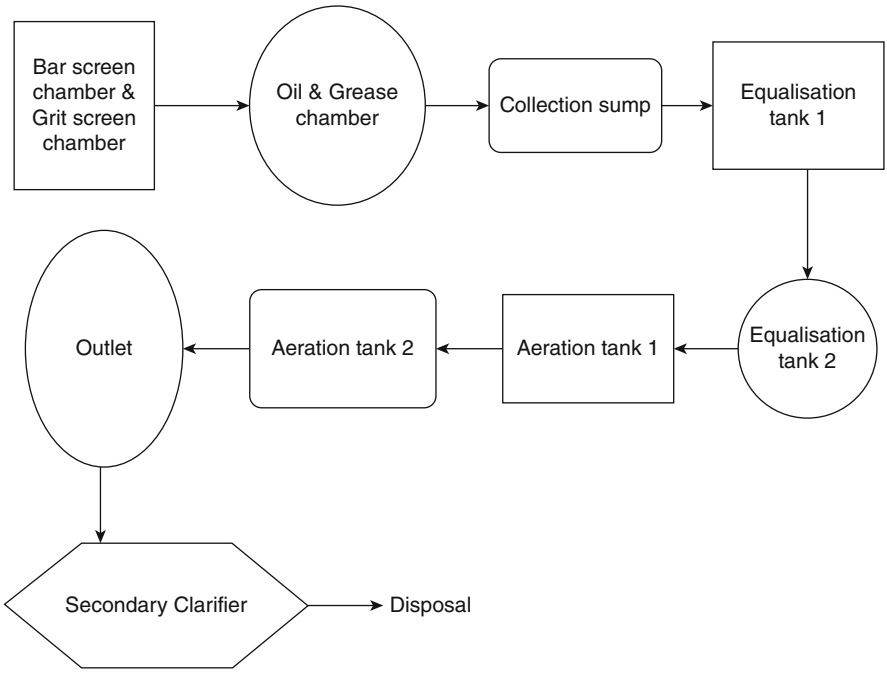

Fig. 6 Flowchart of the process of waste-water treatment

3 Results and Discussion

The raw water treated in the input purification unit for using in the process of production of the drink had been undergone several treatment unit operations including the activation carbon filter (ACF) and 5 micron filter outlet and reverse osmosis and water softener.

Table 1 shows that the pH value increases from 7.26 in raw water to 7.76 in ACF inlet. The increase in pH value may be due to the addition of lime and chlorine in solid contact clarifier. But the value becomes 7 due to complete neutralization. Since the turbidity arises because of the presence of suspended solid particles, the effluent passing through ACF, 5 micron, and ultrafiltration and finally by reverse osmosis unit possesses no turbidity. The turbidity data presented in Table 1 are in good agreement with the assumption. The TDS decreases from 92 ppm in raw water to 3.12 in reverse osmosis as the effluent is subjected to ACF which acts as a measure of different units and their efficacies, 5 micron, and reverse osmosis units. Similarly, total hardness was reduced just after the softening to less than 10% of the initial inlet raw water hardness after undergoing through the mentioned unit processes. It was observed that water softening unit has reduced phenomenal reduction in total hardness from 53 to 5 ppm. As the *P*-values were zero, there were no normal hydroxide or carbonate, and all the alkalinity was bicarbonate. A range of 80–120 ppm is considered optimum for alkalinity of the water. Therefore, it was

Table 2 Wastewater (effluent)

	Equivalization tank 1	Equivalization tank 2	Aeration tank 1	Aeration tank 2	Secondary clarifier
pH	6.69	7.36	7.79	8.24	7.37
DO	7.1	–	–	–	7.8
TSS (mg/l)	–	–	–	–	130
MLSS (ppm)	–	–	2600	3100	–
COD (mg/l)	1530	2430	38.28	43.96	27.27
BOD (mg/l)	645	–	–	–	22

found that the amount of m-alkalinity was running below the lower limit of optimum range. Since hardness arises because of the presence of dissolved salts of bicarbonates, carbonates, chlorides and sulphate of calcium, magnesium and iron, and manganese, a perusal of Table 1 shows that total hardness found in raw water is 75 ppm and decreases to 5 ppm after softener treatment. It was followed by the secondary clarifier in which the parameters analyzed were pH, dissolved oxygen, and chemical oxygen demand.

Table 2 shows that the pH values of wastewater coming out of different outlets are found to be 6.69, 7.36, 7.79, 8.24, and 7.37 for equivalization tanks 1 and 2, aeration tanks 1 and 2, and further for secondary clarifier. This indicate an increased trend of pH as a result of excess levels of dissolved salts of alkali and alkaline earth metals, whereas in the case of secondary clarifier, the pH value decreases to 7.37, owing to the removal of marginal levels of dissolved alkali metals. Similar trends were also seen in the case of dissolved oxygen levels and chemical oxygen demand and biochemical oxygen demand, which were found to be within the permissible limits after undergoing the secondary clarification process (refer Figs. 7, 8, 9, 10, 11, 12, 13, and 14).

Importantly, efficacy of treatment units of the plant was tested through analyzing the presence of traces of heavy metals in raw water samples before and after the treatment as well as for the samples of effluents collected from secondary clarifier (Table 3). Heavy metal analysis exhibits the complete removal iron, nickel, and cadmium from the raw water after the treatment from the prior concentration of 0.09, 0.03, and 0.001 ppm, respectively. Similarly, sodium, potassium, and zinc followed by lead in raw water have decreased to about 10–20% of its initial concentration before the treatment. Further removal was witnessed in raw water after secondary clarification process, which indicates marginal or acceptable levels of heavy metals including sodium, potassium, manganese, lead, and zinc. Interestingly, concentration levels of manganese of raw water after treatment exhibited high compared to the initial levels, which is likely due to the soluble manganese presence in the ingredients of materials. As it was observed in Figs. 15, 16, and 17, the lead followed by the zinc shows reduction after the treatment, but this phenomenon was not considerable which may be due the interaction of raw water with the lead-made pipes and zinc-based containers used in the plant.

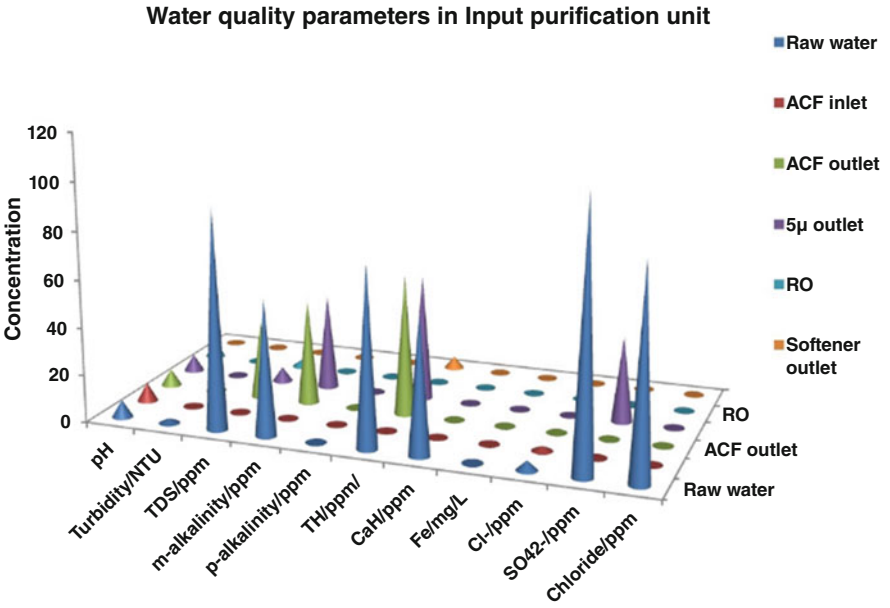

Fig. 7 Variation of water quality parameters in input water purification unit

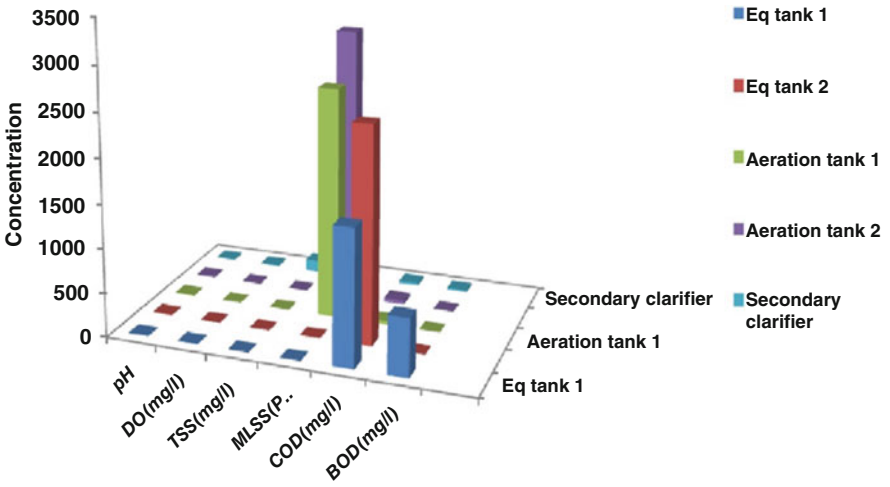

Fig. 8 Variations of water quality parameters in wastewater units

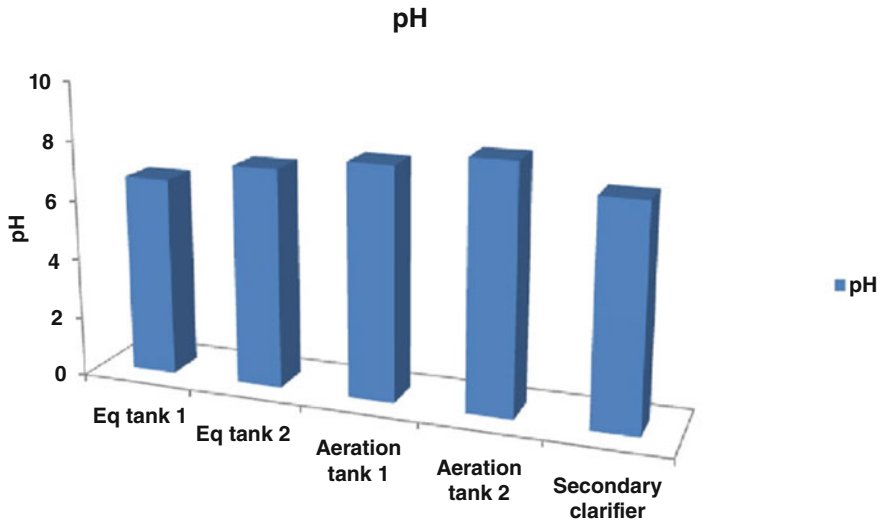

Fig. 9 Variation of pH in various sections in wastewater

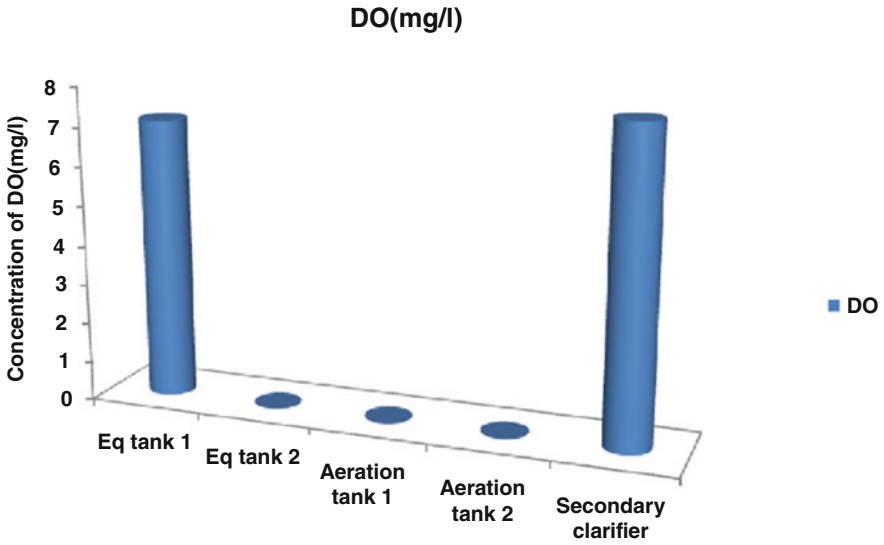

Fig. 10 Variation of DO in various sections in wastewater

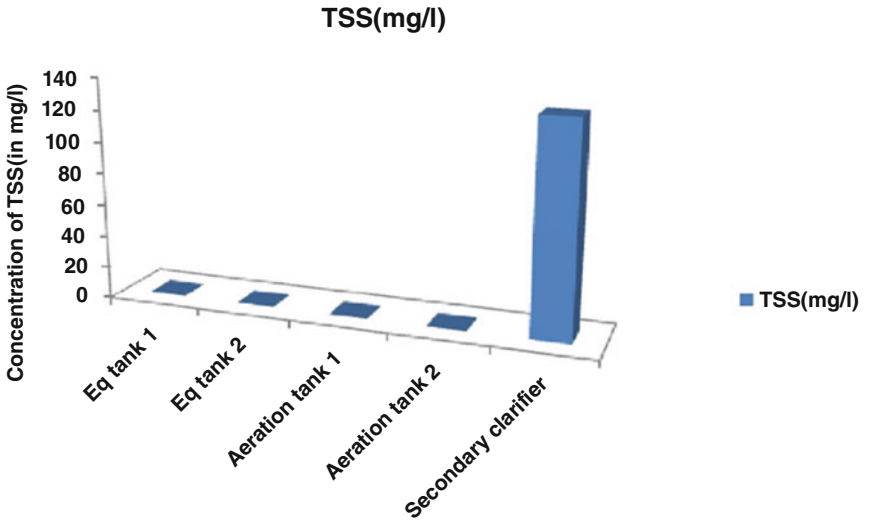

Fig. 11 Variation of TSS in various sections in wastewater

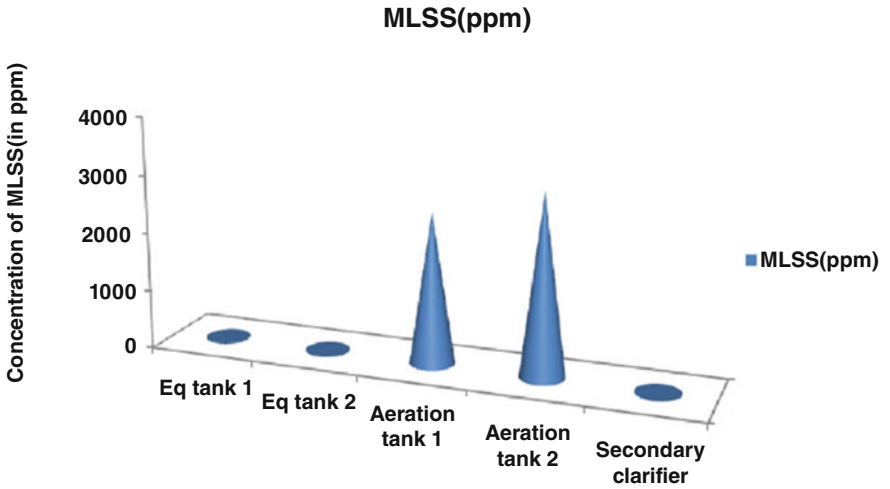

Fig. 12 Variation in MLSS in various sections in wastewater

4 Conclusion

We summarize our study that exhibits the efficacy of a Khurda-based Industrial estate of Coca-Cola beverage plant for the removal of raw water impurities and wastewater effluent pollution levels through secondary clarifier. Few salient features have been observed in the results:

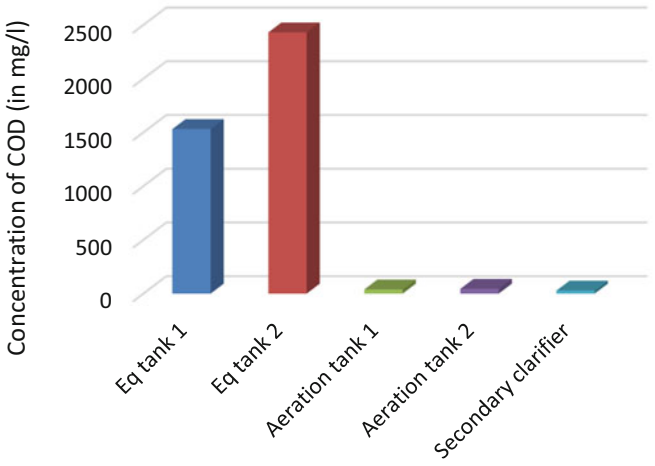

Fig. 13 Variation in COD in various sections in wastewater

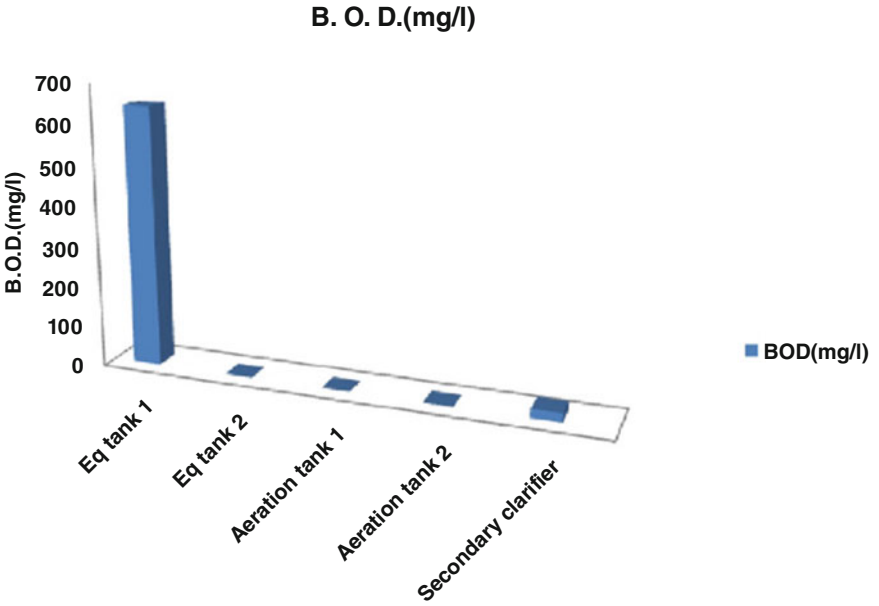

Fig. 14 Variation of BOD in various sections in wastewater

- We observed almost all the analyzed water quality parameters exhibited decremental trend from raw state of existence to the treated effluent. Particularly, total hardness was reduced to 5 ppm after softening process from its initial level of 75 ppm that amounts to have more than 90% of reduction.

Table 3 Heavy metal analysis

	Cu ppm	Fe ppm	Ni ppm	Na ppm	K ppm	Mn ppm	Pb ppm	Cd ppm	Zn ppm
Raw water	0	0.09	0.03	255	25	0.002	0.103	0.001	0.068
Outlet	0	0	0	35	5	0.005	0.071	0	0.013
Secondary clarifier	0	0	0	24	6	0.001	0.08	0	0.06

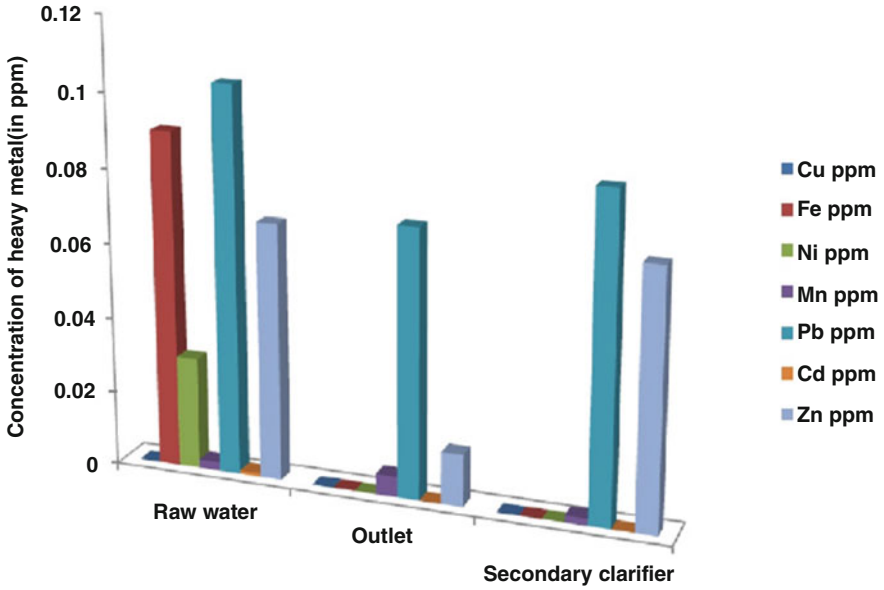

Fig. 15 Variation of heavy metal in various sections of wastewater

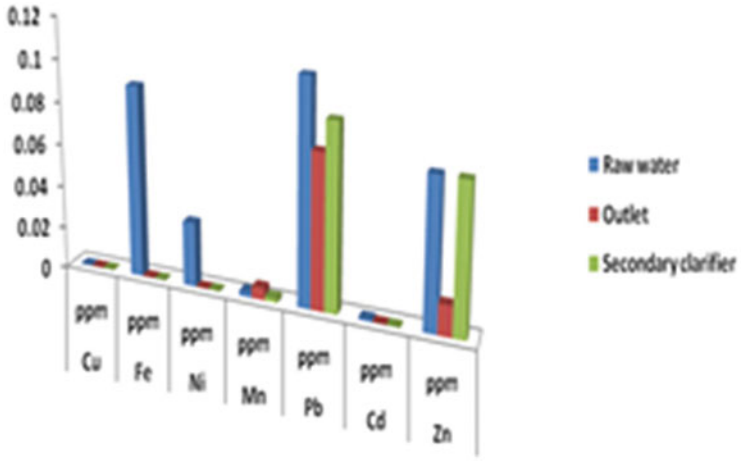

Fig. 16 Heavy metal variation in various sections of wastewater (metal-wise)

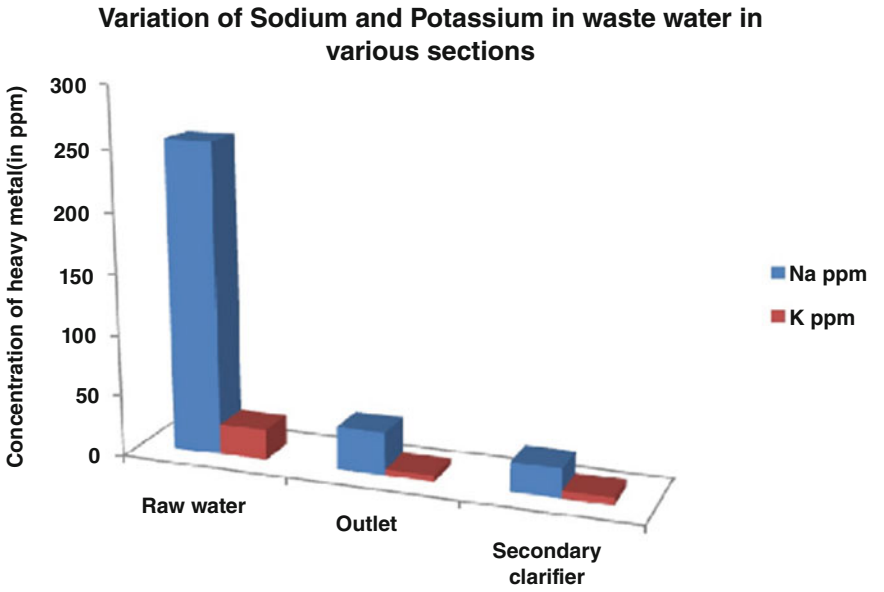

Fig. 17 Variation of sodium and potassium in various sections of wastewater

- Phenomenal increase of dissolved oxygen levels brought BOD and COD levels to the marginal levels after the effluent undergone secondary clarification.
- Except the zinc almost all the metals analyzed have showed a considerable reduction those were within the permissible limits of CPCB guidelines.
- However, it was found in the treatment of raw water and wastewater effluent of the plant that this industrial unit shows safer levels of effluent wastewater parameters prior to release into the atmosphere, which can be concluded as almost all the values were within the permissible limits of Indian standard specifications for the water and wastewater.

Acknowledgments The authors are extremely thankful to Hindustan Coca-Cola Pvt. Ltd. at Khurda, Odisha, for supporting and allowing for carrying out the study in their plant.

References

1. N.K. Chaurasia, R.K. Tiwari, Analysis of heavy metal pollution in effluents of sugar and beverage industry. J. Pharm. Res. **5**(1), 704–706 (2012)
2. A. Emmanuel, J.T.E. Liberty, Effluents characteristics of some selected food processing industries in Enugu and Anambra states of Nigeria. J. Environ. Earth Sci. **3**(9), 46–53 (2012)
3. J. Chen, S. Seng, Y. Hong, *Wastewater Treatment*, vol 7 (AG-Metal Zenica, Taylor & Francis Group, LLC, 2006), pp. 255–269

4. T. Imoobe, P. Okoye, Assessment of the impact of effluent from a soft drink processing factory on the physio-chemical parameters of Eruvbi stream Benin City, Nigeria. J. Pure Appl. Sci. **4**(1), 126–134 (2011)
5. J.P. Chen, S.S. Seng, Y.-T. Hung, Soft drink waste treatment, in *Waste Treatment in the Food Processing Industry*, (Taylor & Francis Group, LLC, 2006)
6. A.K. Sarda, M.P. Sharma, S. Kumar, Performance evaluation of brewery waste water treatment plant. Int. J. Educ. Psychol. Res. **2**(3), 105 (2013)
7. M.F. Chong, D.G. Hassell, C.L. Law, C.J. Yi, A review on anaerobic–aerobic treatment of industrial and municipal waste water. Chem. Eng. J. **155**, 1–18 (2009)
8. V. Breggie, B. Michael, The feasibility of applying material flow cost accounting as an integrative approach to brewery waste-reduction decisions. J. Bus. Manag. **6**(35), 9783–9789 (2012)
9. Y.S. Afriye, *A Study of Industrial Waste Management in Kumasi (Case Study)* (Kumasi Breweries Limited, The Coca-Cola Bottling Company of Ghana, 2009)
10. I. Bodík, J. Derco, J. Gasparikova, S. Kapusta, K. Kratochvíl, Evaluation of anaerobic-aerobic wastewater treatment plant operations. Pol. J. Environ. Stud. **14**(1), 29–34 (2004)

Part VII
Innovative Technologies in Industrial Waste Management

In Vitro Performance Analysis of Ti- and Zn-Doped Hydroxyapatite Made from Waste Eggshells

Dalia Acharjee, Sujan Krishna Samanta, Piyali Basak, Sukumar Roy, and Samit Kumar Nandi

Abstract Million tons of eggshell waste are generated every day anywhere starting from a household kitchen to different food-processing industries. This waste is a big source of calcium (Ca). In this study, zinc- (3%) and titanium (3%)-doped hydroxyapatite (HAP) has been synthesized from two different sources; one is from eggshell waste, and another is from laboratory reagents. All developed HAP powders were compacted in a cylindrical mold (dia. 12 mm) at high pressure by a hydraulic machine. Physical properties such as density, porosity, and hardness were evaluated. Crystal phase analysis and the presence of functional groups were determined through XRD and FTIR. SEM images of apatite layer formation in simulated body fluid of different quantity on top of the pellets were observed. All the materials were hemocompatible and nontoxic, confirmed through hemolysis study and MTT assay. The comparative analysis showed that eggshell-derived HAP and its doped materials produced more apatite than laboratory-grade calcium hydroxide material.

Keywords Eggshell waste · FTIR · Hemolysis · Hydroxyapatite · MTT · XRD · Bioceramic · Apatite · Porosity · Hardness · SEM

Abbreviations

ASTM	American Society for Testing and Materials
EDAX	Energy dispersive X-ray analysis
FTIR	Fourier transform infrared

D. Acharjee (✉) · P. Basak
School of Bio-Science and Engineering Jadavpur University, Kolkata, India

S. K. Samanta · S. Roy
Department of Biomedical Engineering, Netaji Subhash Engineering College, Technocity, Garia, Kolkata, India
e-mail: sujank.samanta@nsec.ac.in

S. K. Nandi
Department of Veterinary Surgery and Radiology, WBUAFS, Kolkata, India

D. Mazumder (ed.), *Sustainable Advanced Technologies for Industrial Pollution Control*, Springer Proceedings in Earth and Environmental Sciences,
https://doi.org/10.1007/978-3-031-37596-5_27

GPa	GigaPascal
HAP	Hydroxyapatite
MTT	(3-(4,5-Dimethylthiazol-2-yl)-2,5-diphenyltetrazolium bromide)
PMBC	Peripheral blood mononuclear cell
SBF	Stimulated body fluid
SEM	Scanning electron microscopy
XRD	X-ray diffraction

1 Introduction

Requirement of bone grafting surgeries because of various bone-related defects and accidents has reached to a very high number. Autografting and allografting are commonly used bone grafting technologies. But these processes have some limitation such as donor site morbidity [1], material shortage, and disease transmission risk. These limitation triggers the researchers to develop synthetically prepared bioceramic materials such as hydroxyapatite which is the main mineral inorganic component of bone. Hydroxyapatite, the natural constituent of the bone, gives the structural integrity and osseointegration in mammals. In laboratory, it is prepared through various processes by taking different chemical reagents [2–4]. Different natural sources are also studied by many [5, 6] researchers for its extraction. Different literatures show that hydroxyapatite can be prepared from egg shell [7, 8] as it contains huge amount of calcium carbonate [9] and a number of trace metals such as magnesium, sodium, copper, potassium, iron, and zinc [10]. Eggshell waste causes a lot of environmental problems. This waste can be recycled and converted to a bone graft material for the benefits of society. As a bioceramic compound, hydroxyapatite is a good choice in bone regeneration and tissue engineering field. But to enhance the mechanical properties and biological effectiveness, some trace elements are added as a dopant [11, 12]. The objective of this study is to prepare a low-cost hydroxyapatite and its dopants (Ti, Zn) from waste products (eggshell) and make a comparative assessment of these products with laboratory-grade hydroxyapatite to conclude the efficacy of different developed products in vitro model.

2 Methodology

2.1 Preparation of Synthetic and Biosourced Hydroxyapatite and Doped Varieties

The collected eggshells were boiled in water and washed many times to make it completely clean and dried in drier at 50 °C for 3–4 h. After drying, it was crushed to make fine powders. The powders were calcined in a furnace at 950 °C for 2 h. A specified quantity of calcined eggshell powders was added slowly (about 30 min) in a beaker containing warmed (80 °C) distilled water. Then orthophosphoric acid

(0.6 M) was added slowly with constant stirring using magnetic stirrer. The mixture was kept overnight to settle down the precipitate. The precipitate was dried in a hot oven at 80 °C. The dried precipitate was calcined at 800 °C in a muffle furnace. For synthesizing laboratory-grade HAP (referred as pure HAP), a wet chemical method was followed by reacting orthophosphoric acid (H_3PO_4) with calcium hydroxide ($Ca(OH)_2$) in a stirred media at a temperature of 75–80 °C with pH of 11–12. In order to synthesize 3% Zn- and Ti-doped varieties, a calculated amount zinc oxide and titanium dioxide powder were mixed with the calcined eggshell powder, and the rest of the process is the same.

2.2 Compaction of Powder and Porosity Measurement

In order to form the fine-grain powder from lump aggregated calcined sample, it was ball milled for about 2 h. The fine-grain powder samples were pressed (2 ton for 2 min) in a mold (12 mm dia.) by a hydraulic press machine (PEECO Hydraulic Pvt. Ltd., Kolkata, India) to get disc-shaped samples of about 5 ± 0.05 mm thickness. Green density was calculated by measuring mass-to-volume ratio. The pellets were sintered in furnace at 900 °C with a soaking time 2 h and heating rate 3° per min in air atmosphere. Universal porosity measurement technique was used to measure the porosity.

2.3 XRD and FTIR Analysis

To analyze the phase composition, lattice parameter XRD (X-ray diffraction) test was done by an X-ray diffractometer (model: BRUKER, D8Advane, Japan). The lattice parameter is calculated by the following unit cell (HCP) plane spacing relationship [13].

$$\frac{1}{d^2} = \frac{4}{3}\left(\frac{h^2 + hk + l^2}{a^2}\right) + \frac{l^2}{c^2}$$

where d is the distance between the adjacent place and h, k, and l are Miller indices. Unit cell volume has been calculated by using the formula $V = 0.866\, a^2 c$ [14]. Crystallite size is calculated by full width half maxima method, followed by Scherrer's equation, $D = 0.9\ \lambda/\beta\cos\theta$ [14]. D is the size of the crystal, λ the wavelength of X-ray, β the broadening of diffraction line at half of its maximum intensity in radians, and θ the diffraction angle. FTIR study was done by using KBr pellets in mid infrared (4000–500 cm^{-1}) region (Perkin-Elmer, model no.:1615, USA).

2.4 Hardness Study

Hardness of implant material plays a vital role in bone tissue development. The prepared materials must be hard enough to withhold the stress that may be felt due to movement of body parts. In this study hardness was measured by Vickers hardness machine (model: VM50, Fuel Instruments & Engineers, India). The sample pellets were intended with diamond indenter forming a square bases having the angles 136 ° C between the opposite faces. One to one hundred kgf load was applied for 10–15 s. After the removal of the load, the sloping surface area created on the sample. The indentation peak was measured, and by dividing the load force in kgf to square millimeter area, Vickers hardness value was calculated.

2.5 SEM Analysis

A thin layer of gold coating (electrically conducting material) was deposited on the surface of the sample via low-vacuum sputter coating technique. In this work, surface morphology, microstructure of the dense samples, and the effect of addition of dopants at high temperature were studied using scanning electron microscope (JEOLSEM, model no.: JSM, 5200, Tokyo, Japan).

2.6 Bioresorption Study (Stimulated Body Fluid Study)

In this study, simulated body fluid (SBF) was prepared in laboratory by maintaining all the compositions level and conditions [15]. The sintered pellets were immersed in SBF solution, and the solution was changed in 3 alternate days during the 1-month study. The surface texture of the pellets was examined through scanning electron microscope after a 1-month timepoint.

2.7 Bactericidal Study

Bactericidal study was done to observe whether the developed compositions were having antibacterial action and in turn can cause living cell destruction in our body. A diluted solution of nutrient agar media was taken in conical flask and autoclaved at 121 °C for 20 min. The media was cooled at 40–45 °C and inoculated with culture of *Staphylococcus aureus*. After thoroughly mixing the culture with media, it was poured into petri dishes. Porcelain bit was dripped into the sample solution (powdered compositions in water) and placed in the petri dishes. Two different bits were

soaked in two different samples concentrations (2 mg/10 ml and 1 mg/10 ml). The petri dishes were incubated at 35 °C for 24 h.

2.8 Hemolysis Study and MTT Assay

In vitro hemocompatibility study was carried out using human blood. The methodology was followed as described by the ASTM specification [16]. A 3.8% sodium citrate was used as an anticoagulant material. The % hemolysis was calculated by performing the experiment in triplicate. MTT assay was done using peripheral blood Mononuclear cells (PBMC) (NCCS, Pune, India). The PBMCs were seeded in 24-well plate at a density of 5×10^4 cells/cm^2. The cells were treated with prepared pure HAP, eggshell HAP, and their doped variants. After incubating for 24 h, MTT was mixed and shaken for 15 min and again incubated for 4 h. The cells in the solution were killed and crystals were formed. Dimethyl sulfoxide was added and crystals were dissolved in it leaving a purple-colored solution. The intensity of the color were dependent on the amount of crystals. The optical density of the color solution was measured at 545 nm against a blank. The test was done in duplicate and mean data was recorded.

3 Results and Discussion

3.1 Physical Properties

The observed physical properties are presented in Table 1. Apparent porosity value signifies the presence of pores which is of substantial amount in different samples.

In Ti-doped eggshell HAP percentage of porosity is more than other samples. The Zn-doped samples also revealed a higher porosity. The greater amount of porosity in these samples may be due to the different crystal lattice formed compared to conventional lattice structure of HAP. This may be due to the inclusion of Ti or Zn which may cause attenuation of the whole matrix [17, 18]. The prepared material was hard enough to withstand the body weight, or stress may develop due to movement of body parts during healing period. On comparison to laboratory-grade HAP, eggshell HAP has better hardness value. This may be due to the presence of

Table 1 Physical properties data

Sample	Hardness (GPa)	Sintered density (g/cc)	Apparent porosity (%)
Pure HAP	3.61 ± 0.41	2.89	19.48 ± 1.01
Egg shell HAP	3.73 ± 0.19	2.76	21.24 ± 1.31
Egg shell HAP + 3% Zn	3.89 ± 0.21	2.94	23.35 ± 1.18
Egg shell HAP + 3% Ti	3.97 ± 0.31	2.98	24.37 ± 1.41

different trace elements such as Ca, P, Mg, Fe, K, Mn, B, Zn, Co, Cr, and Pb [19], which can produce a hard matrix compared to the laboratory-grade HAP, as the latter is lacking with above elements except Ca and P.

3.2 XRD and Lattice Parameter Analysis

X-ray diffraction peak (Fig. 1) of the sintering powder samples were corresponding to various planes such as (0 0 2), (2 11), (2 0 2), (3 0 0), (2 1 2), and (2 2 2) that signify the development of HAP compound which is matched with the reference card no 09-0432 available for standard hydroxyapatite in crystallography. The most prominent peak is present at 2θ angle of ~32.02°. Almost the same kind of curve has been developed by all, although in Ti- and Zn-doped variants, the peaks are slightly shifted.

The lattice parameter values are presented in Table 2. In doped variants the lattice parameters suffered minor changes. The causes behind it is calcium ion substitution by Zn and Ti ion. The atomic radius of these ions are smaller than calcium ion. The doped samples are showing small axis. The percent crystallinity of pure HAP and eggshell HAP are 87.81% and 89.81%, respectively. The crystallinity is decreased in doped variants as their crystal structure is slightly distorted due to the substitution. From XRD analysis it has been observed that hydroxyapatite prepared from eggshell

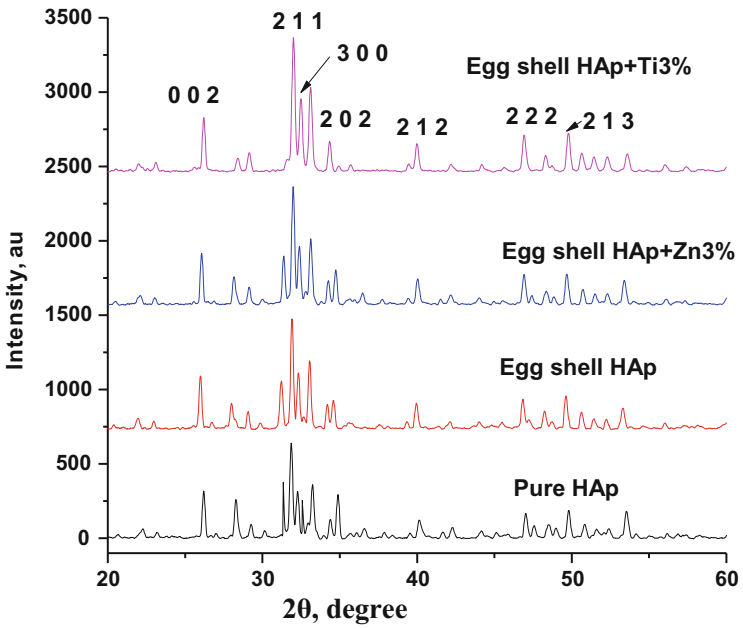

Fig. 1 XRD of pure- and eggshell-derived HAP and dopants

Table 2 Lattice parameters data

Sample	*a*-Axis	*c*-Axis	% Crystallinity
Pure HAP	9.433 ± 0.097	6.541 ± 0.12	87.81 ± 2.82
Eggshell HAP	9.566 ± 0.11	6.687 ± 0.17	89.81 ± 5.06
Eggshell HAP + 3% Zn	9.421 ± 0.51	6.437 ± 0.43	83.58 ± 1.18
Eggshell HAP + 3% Ti	9.22 ± 0.23	6.71 ± 0.37	85.46 ± 3.82

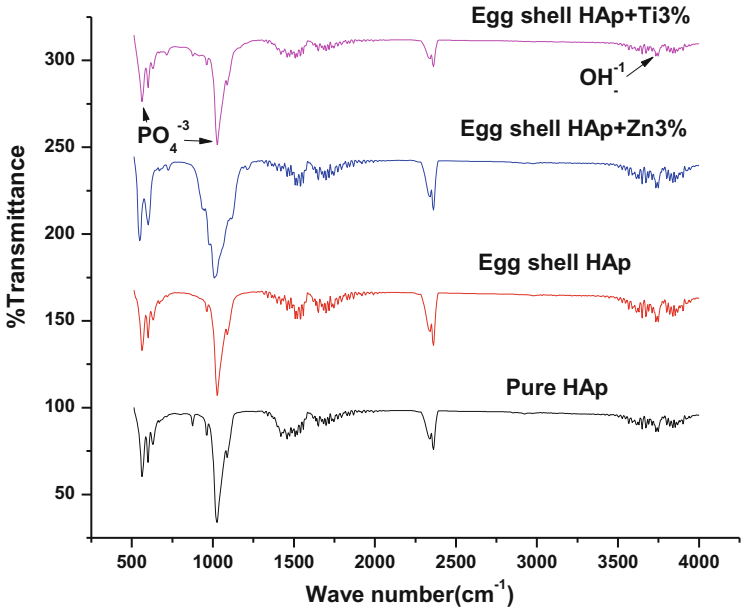

Fig. 2 FTIR curve of pure- and eggshell-derived HAP with their dopants

source has better crystallinity value compared to the laboratory-grade-prepared HAP.

3.3 Functional Group and SEM Analysis

The FTIR curves shows (Fig. 2) the peak at 567; 1006 signifies the presence of phosphate group. Stretching band at 3746 in FTIR graph is due to the presence of hydroxyl group. No peak is shifted due to the doping effect. The SEM images of sintered pellet samples come with the presence of spherical grains with sufficient porosity. HAP particles morphology is having an irregular form (Fig. 3).

The pellet pictures revealed a substantial nearness between crystals which will help to maintain the structural skeleton if these materials are taken for the preparation of scaffold. The crystal is having narrow size distribution, although separation of the

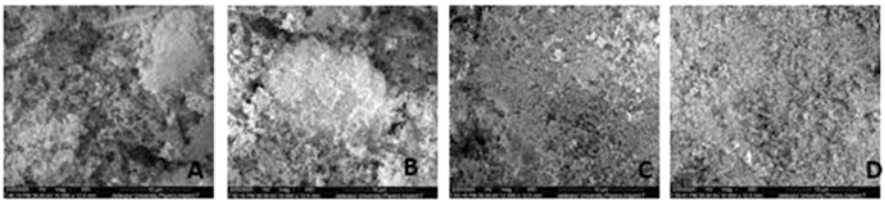

Fig. 3 SEM images of (**a**) pure HAP, (**b**) eggshell HAP, (**c**) Ti-egg HAP, and (**d**) Zn-egg HAP

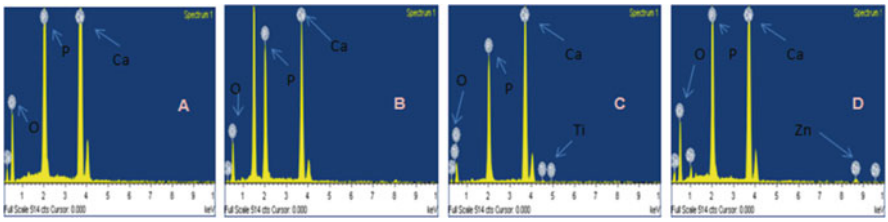

Fig. 4 EDAX spectra of different samples: (**a**) pure HAP, (**b**) eggshell HAP, (**c**) Ti-doped eggshell HAP, and (**d**) Zn-doped eggshell HAP

individual crystals from the whole is very much tough as the whole pellet matrix consisted of small and large particles that form clusters. These observations are quite conforming to the findings of other researchers [20, 21].

3.4 EDAX Study

The EDAX of the developed samples are shown in the Fig. 4. The elemental substitution is clear as the peaks have corresponding dopant ions. The composition analysis showed the other elements such as Ca, and oxygen is also in the peak which also conforms to the elemental makeup of hydroxyapatite.

The Ca:P ratio for all compositions are found to be 1.567 ± 0.21 which are quite similar with stoichiometric Ca:P ratio of the HAP (1.68) [22].

3.5 In Vitro Biofluid Study

The sample pellets were immersed into the SBF solution, the solution was altered in every 3 days interval, and the surface texture was observed under the scanning electron microscopy. At day 9–10, a white thread-like structure was seen on the pellet surface, this became a patch-like layer after 3–4 days, and it was the apatite layer as confirmed by previous researchers [23]. This confirms that the samples exhibited a favorable reaction with the SBF solution. Onset of white apatite layer

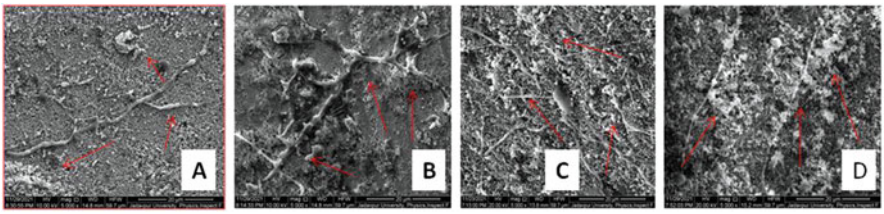

Fig. 5 SEM images of apatite layer: (**a**) pure HAP, (**b**) eggshell HAP, (**c**) Ti-egg HAP, and (**d**) Zn-egg HAP

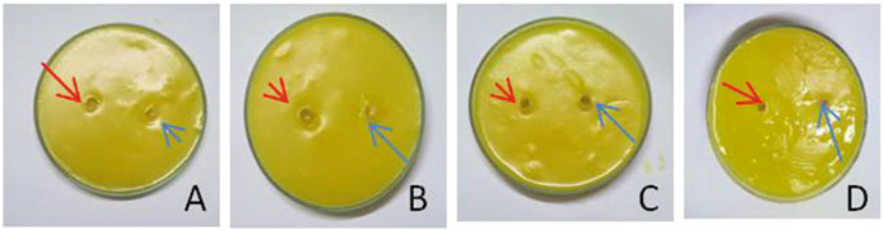

Fig. 6 Petri dishes as seen after a day. (**a**) Pure HAP, (**b**) eggshell HAP, and (**c**) eggshell

was increased to a little more extent as the time passed. This observation conclude that the developed compositions may produce a favorable interaction with the bone tissue as we observed no vigorous reaction in a 1-month study. The Ti-doped egg HAP samples produced the maximum amount of apatite layer, while the other all samples also have developed a lesser amount apatite. The formed apatite layer as seen through SEM revealed the following images (Fig. 5).

3.6 Bactericidal Study and MTT Assay

It has been noted that the prepared samples have no zone of inhibition. The red and blue arrows indicate the presence of samples in porcelain bit having concentration of 2 mg/ml and 1 mg/ml, respectively (Fig. 6).

HAP + 3%Ti, (d) Eggshell HAP + 3%Zn

So, all the prepared compositions have no bactericidal activity at these levels of concentration. The MTT assay result showed more than 80% cell viability for all samples. This result has been shown as bar diagram in following Fig. 7.

For eggshell HAP sample, the percentage cell viability is little bit more. Both these study results for all samples are an indicative of the samples biocompatibility.

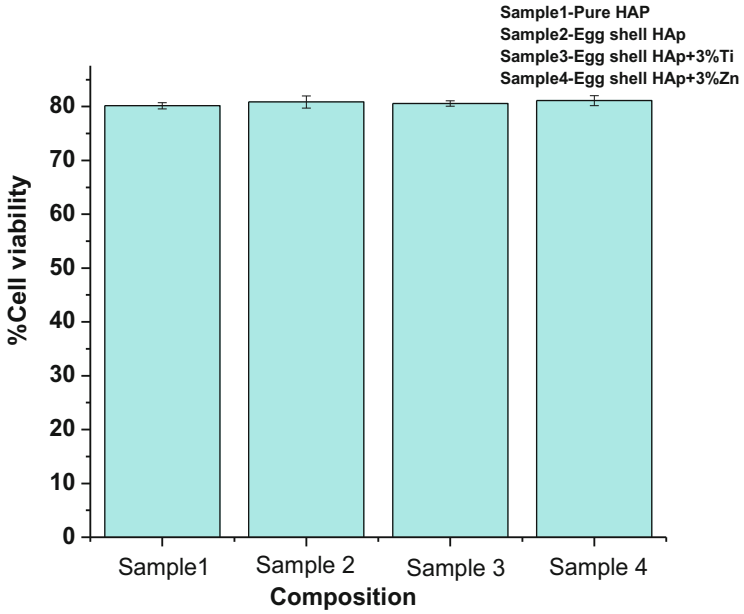

Fig. 7 Cell viability of different samples

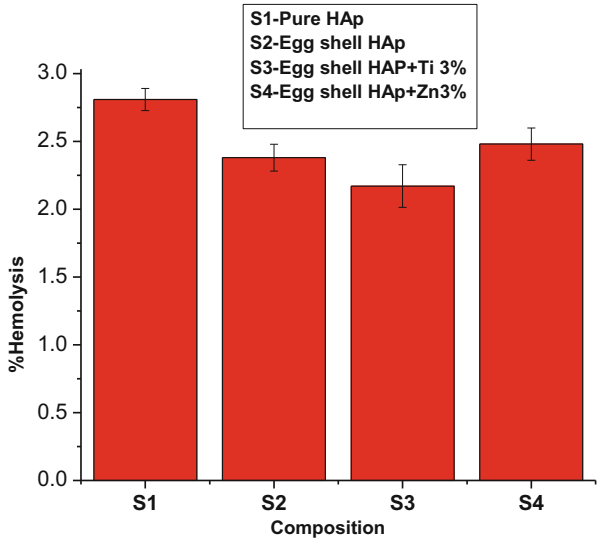

Fig. 8 Bar diagram represents percentage of hemolysis

3.7 Hemolysis Study

All the samples taken for the study produced a very small quantity of hemolysis (Fig. 8) which falls well below (<5%) the standard hemolysis indicator as mentioned

under the guidelines of ASTM F756-00 (2000). The non-hemolytic nature of all the samples are quite advisable for their application in the in vivo part of our body.

The eggshell-derived HAP showed the lowest amount of hemolysis in comparison to the other samples and proved to be the highest biocompatible and non-hemolytic material.

4 Conclusion

Eggshell waste has been successfully converted to hydroxyapatite (HAP). The development of eggshell-derived HAP, Ti-egg HAP, and Zn-egg HAP are confirmed through phase composition, lattice parameters, and functional elemental identification through XRD, FTIR, and EDAX. SEM images showed the presence of pores in all samples that may be essential for bony in growth. Apatite layer formation in SBF is an indicator of osseointegrative properties of the samples. The Ti-substituted eggshell HAP gave the maximum positive effectiveness and interactions with human body fluid. The derived eggshell HAP and its dopants are superior to laboratory-grade HAP. These low-cost biosourced HAPs can be used as bioactive bone graft material.

Acknowledgments The authors wish to acknowledge the Department of Biomedical Engineering, Netaji Subhash Engineering College, Kolkata, India, for extending all kind of help to perform this research study.

References

1. S.K. Nandi, B. Kundu, S.K. Ghosh, D.K. De, D. Basu, Efficacy of nano-hydroxyapatite prepared by an aqueous solution combustion technique in healing bone defects of goat. J. Vet. Sci. **9**(2), 183–191 (2008). https://doi.org/10.4142/jvs.2008.9.2.183
2. H.L. Kim et al., Preparation and characterization of nano-sized hydroxyapatite/alginate/chitosan composite scaffolds for bone tissue engineering. Mater. Sci. Eng. C **54**, 20–25 (2015). https://doi.org/10.1016/j.msec.2015.04.033
3. P. Bhattacharjee, H. Begam, A. Chanda, S.K. Nandi, Animal trial on zinc doped hydroxyapatite: A case study. J. Asian Ceram. Soc. **2**(1), 44–51 (2014). https://doi.org/10.1016/j.jascer.2014.01.005
4. A. Szcześ, L. Hołysz, E. Chibowski, Synthesis of hydroxyapatite for biomedical applications. Adv. Colloid Interf. Sci. **249**, 321–330 (2017). https://doi.org/10.1016/j.cis.2017.04.007
5. A. Pal et al., Mechanochemical synthesis of nanocrystalline hydroxyapatite from Mercenaria clam shells and phosphoric acid. Biomed. Phys. Eng. Express **3**(1), 015010 (2017). https://doi.org/10.1088/2057-1976/aa54f5
6. R. Mustaffa, M.R. Mohd Yusof, Y. Abdullah, A novelty of synthetic hydroxyapatite from cockle shell and characterization. Adv. Mater. Res. **1087**, 429–433 (2015). https://doi.org/10.4028/www.scientific.net/amr.1087.429
7. E.M. Rivera et al., Synthesis of hydroxyapatite from eggshells. Mater. Lett. **41**(3), 128–134 (1999). https://doi.org/10.1016/S0167-577X(99)00118-4

8. K. Prabakaran, A. Balamurugan, S. Rajeswari, Development of calcium phosphate based apatite from hen's eggshell. Bull. Mater. Sci. **28**(2), 115–119 (2005). https://doi.org/10.1007/BF02704229
9. S.C. McClelland, P. Cassey, G. Maurer, M.E. Hauber, S.J. Portugal, How much calcium to shell out? Eggshell calcium carbonate content is greater in birds with thinner shells, larger clutches and longer lifespans. J. R. Soc. Interface **18**(182), 20210502 (2021). https://doi.org/10.1098/rsif.2021.0502
10. S. Ray, A.K. Barman, Chicken eggshell powder as dietary calcium source in chocolate cakes. Pharma Innov. J. **6**(9), 01–04 (2017)
11. C.M. Mardziah et al., Effect of zinc ions on the structural characteristics of hydroxyapatite bioceramics. Ceram. Int. **46**(9), 13945–13952 (2020). https://doi.org/10.1016/j.ceramint.2020.02.192
12. V. Uskoković, Ion-doped hydroxyapatite: An impasse or the road to follow? Ceram. Int. **46**(8), 11443–11465 (2020). https://doi.org/10.1016/j.ceramint.2020.02.001
13. J.H. Kim, S.H. Kim, H.K. Kim, T. Akaike, S.C. Kim, Synthesis and characterization of hydroxyapatite crystals: A review study on the analytical methods. J. Biomed. Mater. Res. **62**(4), 600–612 (2002). https://doi.org/10.1002/jbm.10280
14. B.D. Cullity, *Elements of Diffraction Quasi-Optics*, 2nd edn. (Addison-Wesley Publishing Company Inc, London-Amstrerdam-Don Mills, ON-Sydney, 1977)
15. T. Kokubo, H. Kushitani, S. Sakka, T. Kitsugi, T. Yamamuro, Solutions able to reproduce in vivo surface-structure changes in bioactive glass-ceramic A-W3. J. Biomed. Mater. Res. **24**(6), 721–734 (1990). https://doi.org/10.1002/jbm.820240607
16. ASTM F 756-00, Standard practice for assessment of hemolytic properties of materials. Am. Soc. Test. Mater., 5 (2000). https://doi.org/10.1520/F0756-13
17. A. Ressler, A. Žužić, Ionic substituted hydroxyapatite for bone regeneration applications: A review. Open Ceram. **6**, 100122 (2021)
18. Anushika, P. Sharma, A. Trivedi, H. Begam, Synthesis and characterization of pure and titania doped hydroxyapatite. Mater. Today Proc. **16**, 302–307 (2019)
19. F.A. Al-Obaidi, Identification of inorganic elements in egg shell of some wild birds in Baghdad. Iraqi J. Vet. Med. **36**(0E), 153–157 (2012). https://doi.org/10.30539/iraqijvm.v36i0e.408
20. H.N. Yu, H.C. Hsu, S.C. Wu, C.W. Hsu, S.K. Hsu, W.F. Ho, Characterization of nano-scale hydroxyapatite coating synthesized from eggshells through hydrothermal reaction on commercially pure titanium. Coatings **10**(2), 1–11 (2020). https://doi.org/10.3390/coatings10020112
21. A.A. Hamidi, M.N. Salimi, A.H.M. Yusoff, Synthesis and characterization of eggshell-derived hydroxyapatite via mechanochemical method: A comparative study. AIP Conf. Proc. **1835**, 020045 (2017). https://doi.org/10.1063/1.4981867
22. H. Wang, J.K. Lee, A. Moursi, J.J. Lannutti, Ca/P ratio effects on the degradation of hydroxyapatite in vitro. J. Biomed. Mater. Res. A **67**(2), 599–608 (2003). https://doi.org/10.1002/jbm.a.10538
23. S.K. Samanta, A. Chanda, S.K. Nandi, Physical and mechanical characterization of crystalline pure β-Tri calcium phosphate & its dopants as bone substitutes. IOP Conf. Ser. Mater. Sci. Eng. **577**(1), 012138 (2019). https://doi.org/10.1088/1757-899X/577/1/012138

Production of Non-toxic, Non-polluting Herbal Soaps Using Plant Extracts Having Antimicrobial Activity

Bhaswati Chakraborty, Aishi Bera, Debasmita Banerjee, Subhrojyoti Ghosh, and Ratul Dutta

Abstract The rising concerns of consumers toward the health issue caused by using chemically composed skincare products are driving the consumers to use herbal soaps. For millennia, people have used soap. Therefore, our aim is to produce herbal soap using plant extracts having antimicrobial properties thus reducing the toxic load on the environment. Moreover, the soap is crafted with herbal extracts thus making the soap skin-friendly and suitable for all age groups. The optimization of the composition of soap is done by observing the pH of herbal soap for a few months at the end of which the pH starts decreasing and attains a pH of 7. This study focuses on a new herbal soap composition that incorporates neem leaf and turmeric extract. By doing minimum inhibitory concentration (MIC) testing, lowest optimal concentration of extract was determined from the zone of inhibition. Based on efficacy, pH, consistency, and effects on skin results, the benchmark was set as 3.2 grams of herbal extract in 32 grams of soap bar. Neem showed best antimicrobial properties followed by turmeric. From the results obtained, the antibacterial activity of herbal leaf extract on gram-positive *Lactobacillus* sp. was found to be more effective as compared to gram-negative *Escherichia coli*.

Keywords Bacteria · pH · MIC · Antimicrobial · Plant extracts · Growth kinetics · Saponification · Filtrate · Neem · Turmeric

B. Chakraborty (✉)
Faculty at Department of Biotechnology, Heritage Institute of Technology, Kolkata, India

A. Bera · D. Banerjee · S. Ghosh · R. Dutta
Undergraduate students, Department of Biotechnology, Heritage Institute of Technology, Kolkata, India

D. Mazumder (ed.), *Sustainable Advanced Technologies for Industrial Pollution Control*, Springer Proceedings in Earth and Environmental Sciences,
https://doi.org/10.1007/978-3-031-37596-5_28

1 Introduction

Soaps are sodium or potassium fatty acid salts that are made by hydrolyzing lipids in a chemical reaction known as saponification. Soaps are surfactants that are often used in the home for laundry, bathing, and other household chores. In industrial contexts, soaps are used as thickeners, components of some lubricants, and catalyst precursors. Soap solubilizes particulates and filth, which can then be removed from the item being cleaned when used for cleaning. Soap kills bacteria by disintegrating their membrane lipid bilayer and denaturing their proteins when used as a surfactant during washing of hands with a small amount of water. It also emulsifies oils so that they can be washed away with running water [1]. Nowadays, the choice of which type of soap to use in the home is based on the promises made by the manufacturer and the packaging of their goods. Regular soaps on the market, such as beauty bars and antibacterial soaps, have been shown to contain dangerous chemical ingredients. Parabens, sulphates, and triclosan are some of the harsh ingredients present in ordinary soaps. These substances have serious side effects. They can cause allergies, affect hormones, and even raise the risk of cancer in some people.

Organic soaps, on the other hand, do not include any of these chemicals. They are made out of natural substances including plant-derived base oils, natural fats, essential oils, water, and natural colors.

Because organic soaps are made with natural components, there are no hazardous wastes to dispose of into the environment. They are better for our environment because they decompose easily after the lather is washed down the drain. Furthermore, the hazardous ingredients included in mass-market soaps are damaging to the marine habitat. Regular soaps include potentially harmful pesticides and poisonous chemicals that can alter aquatic animals' life cycles. Organic soaps are considered more eco-friendly, safe, and biodegradable because none of these are utilized to grow organic items [1, 2].

The rise of the usage of organic soaps in the present times have been a remarkable market holding. The COVID-19 crisis had significantly affected the market. There was a change in consumers' buying behavior. Consumers preferred organic products rather than any product made of harsh chemicals. Thus consumption of organic soaps was increased this is because of the growing concerns regarding the impact of synthetic ingredients such as parabens and sulfates in synthetic soaps which can lead to severe skin reaction and damage the skin as well. The awareness toward a sustainable environment, by reducing the impact of chemicals coupled with the government initiatives to support organic products, is also fueling the market growth. The rising concerns of consumers toward the health hazards caused by using chemically composed skincare products are one of the major reasons that is driving the market. The natural oils also have the potential to penetrate your pores and cleanse your skin from the inside out [2, 3]. Therefore, the aim of this research work is production of non-toxic, non-polluting herbal soaps using plant extracts having antimicrobial activity.

2 Materials and Methods

2.1 Preparation of Non-polluting Soap Base and Optimization of pH

Materials Used
Sodium hydroxide (NaOH), distilled water, coconut oil, thermometer, stirrer.

The Protocol Followed Is as Follows
NaOH was weighed and dissolved in distilled water to make the lye. This resulted in exothermic change which can corrode the glass. So, the lye preparation was done in a plastic cup. The temperature of the lye was checked. The coconut oil was weighed, and the temperature was checked. As the temperature of the coconut oil was lower than that of the lye, the coconut oil was heated to match the temperature of the lye. Once the same temperature had been achieved, the two were mixed at the same temperature (80 °F or 27 °C). The two were blended well with a stirrer and allowed to solidify [1–3].

The soap bases were made accordingly by following a pattern of compositions and accordingly the pH were also being calculated. After the different soap bases were made, the consistencies were checked and they were kept for pH optimization because a standard soap has pH of around 7–8.

The pH optimization was actually a time-consuming process with removal of the extra oil present in the soap base which did not undergo saponification. The soap cubes were also dipped in water for the removal of extra oil from the outer layers. There was a daily pH check done for the bases (Table 1).

Table 1 The weights of distilled water and coconut oil taken are given below for the following samples

Sample no.	Weight of NaOH (gm)	Weight of distilled water (gm)	Weight of coconut oil (gm)
1	10.147	29.19	20.35
2	10.149	29.19	24.325
3	10.149	29.22	38.43
4	5	30	18.2
5a	3	18	10.92
6a	4	24	14.56
6b	3.5	18	10.92
6c	2.9	18	10.92
6d	2.8	16.8	10.192

2.2 Verification of Antimicrobial Properties of Various Herbal Aqueous Extracts

The production of herbal soap deals with the most important factor that is the antimicrobial properties of the extract. The soap itself has the ability to restrict the microbes by destroying them, the herbal extracts added into the soap base enhances the antimicrobial effects of them. This part of this research work aims to evaluate the antimicrobial potential of aqueous extracts of neem (*Azadirachta indica*) and turmeric (*Curcuma*) by MIC plating of gram-positive and gram-negative bacterial cultures, respectively [4–8].

Materials Used
Fresh leaves of neem, dry rhizomes of turmeric, mortar and pestle, distilled water, microbial cultures, petri plates, cork borer.

The Protocol Is as Follows
The nutrient broth is prepared for microbial culture. For gram-positive bacterial culture we have used *Lactobacillus* sp. grown overnight by incubation for 24 h in the nutrient media, by using local yogurt as inoculum. Then the bacteria has been confirmed as gram positive by Gram Staining process. For gram-negative bacteria, we have used *Escherichia coli*, subcultured from other fellow students of our university. The leaves of the neem, bringaraj, and lemon and rhizome of turmeric have been cut into small pieces, washed, and then dried. Then they were finely crushed in the mortar and prestle and mixed with measured and limited volume of water. Then the suspension is centrifuged at 5000 rpm for 10 mins. The supernatant is decanted and then filtered. The process done is simple aqueous extraction.

The extract has been divided mainly into four categories for MIC plating—raw extract, filtrate (the main filtrate of the plant extract has been squeezed off through fine cloth), raw dilution (1:1), and filtrate dilution (1:1).

The nutrient media containing plates were prepared, along with the bacterial culture of different concentrations were spread with a spreader on the plate. Then, 4 wells are created for the insertions of the extracts, water and alcohol has been inserted for control. The plates were incubated overnight and the inhibition zones were observed for all the plants and MIC values were calculated. MIC is the lowest concentration of any substance that can inhibit visible growth of a microorganism in solid media (Fig. 1).

2.3 Kinetics of Bacterial Growth in the Presence of Raw Neem Soap

Six flasks were taken and were numbered 1–6. 45 ml of NB has been added in each of the flasks. In each conical flask from numbers 3–6, 4.5 ml of soap solution in a 10:1 ratio were added and 0.5 ml of raw neem extracts were added to flasks numbered

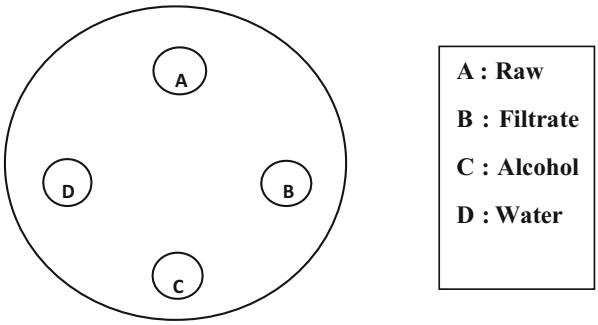

Fig. 1 Schematic representation of minimum inhibitory concentration (MIC) test

5 and 6. To flasks numbered 3 and 5, 5 ml of gram-positive bacterial culture *(Lactobacillus* sp.) were added in each flask. And to flasks numbered 4 and 6, 5 ml of –gram-negative bacterial culture (*E. coli*) has been added. Measurement of optical density for each conical flasks was done with the help of a spectrophotometer every 1.5 hrs. The inhibition kinetic study was done for both neem and turmeric extract and also without the presence of extract and without the presence of soap at every 1.5 hrs interval and a reading was taken after 24 hrs also.

2.4 Kinetics of Bacterial Growth in Presence of Raw Turmeric Soap

For Gram-Positive Bacteria
Absorbance was calculated after every 1.5-time interval with uninterrupted incubation in the floor shaker in between.

For Gram-Negative Bacteria
Absorbance was calculated after every 1.5 h interval with uninterrupted incubation in floor shaker in-between.

2.5 Determination of Efficacy of the Herbal Soap

Efficacy is the ability of an intervention (e.g., a drug or surgery) to produce the desired beneficial effect.

By doing minimum inhibitory concentration (MIC) testing, lowest optimal concentration of extract was determined from the zone of inhibition [4, 7, 8].

The zone of inhibition can be used to measure the susceptibility of the bacteria toward the antimicrobial component.

In case of neem, the zone of inhibition for filtrate extract is the largest, followed by that around raw neem, alcohol. No clear zone of inhibition zone was observed around the well containing distilled water. The same observation was made for both gram-negative and gram-positive bacterial cultures.

3 Results and Discussion

3.1 Preparation of Non-polluting Soap Base and Optimization of pH

As shown in this table, the **5a** sample had attained a pH of 8 in raw soap and pH of 7 in lather which is near the neutral range. The other samples such as **5b, 6a, 6b, 6c**, and 6d had moderate ranges of pH. So, these soap samples were selected for subsequent rounds of observations and the rest were discarded.

The 5a soap sample had attained neutral pH like before. The 6a soap sample was not taken into consideration as the lather was not good. The 6c soap sample was not suitable for soap base preparation as the soap did not solidify well.

The pH of the 5a soap sample was again checked after 4 months and like before, it had a pH of 8 in raw soap and pH of 7 in a lather. After 4 months, the pH of the 5a soap sample was checked which revealed the same measurements.

Thus, the 5a soap sample was the desired soap base with optimum pH and the right amounts of concentrations of the lye and the coconut oil. The optimum pH was attained in about 4 months from the date of manufacture. And it comes out that the pH of soap is 7.

Fig. 2 (**a**) Initial preparation of soap base in Tarsons (**b**) Preparation of soap base cubes

Table 2 Characterization of the soap bases

Sample no.	pH of raw soap	pH of lather	Remarks
5a	8	7	Solid and good lather
5b	10	8	Did not solidify
6a	8	7	Solid and very dry
6b	12	10	Solid but not good lather
6c	8	7	Solid and very dry
6d	9	7	Solid and very dry

3.2 *Verification of Antimicrobial Properties of Various Herbal Aqueous Extracts*

From the observation, we have found that the neem extracts show remarkably better inhibition zones than the turmeric extracts.

The turmeric shows very poor inhibition properties though in reference to various literature reviews, the outcome would have been better.

Fig. 3 (**a**) Inhibition zones for raw neem extract and filtrate extract. (**b**) Inhibition zones for raw neem extract (1:1) and filtrate extract (1:1)

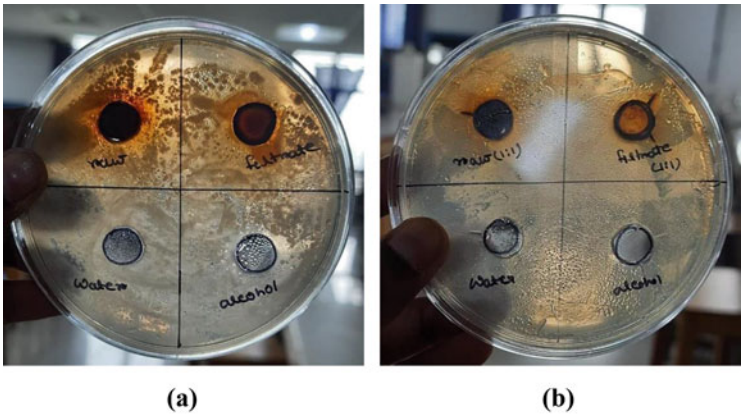

Fig. 4 (**a**) Inhibition zones for raw turmeric extract and filtrate extract. (**b**) Inhibition zones for raw turmeric extract (1:1) and filtrate extract (1:1)

Table 3 Nature of inhibition for neem and turmeric against gram-positive bacterial culture

Plants used	Gram positive			
	Raw (remarks)	Filtrate (remarks)	Raw [1:1] (remarks)	Filtrate [1:1] (remarks)
Neem	Good inhibition zone	Moderate inhibition	Moderate inhibition	Moderate inhibition
Turmeric	Very less inhibition zone	Less inhibition zone	Less inhibition zone	Less inhibition zone

Table 4 Nature of inhibition for neem and turmeric against gram-negative bacterial culture

Plants used	Gram negative			
	Raw (remarks)	Filtrate (remarks)	Raw [1:1] (remarks)	Filtrate [1:1] (remarks)
Neem	Moderate inhibition zone	Very good inhibition zone	Less inhibition zone	Less inhibition zone
Turmeric	Very less inhibition zone	Less inhibition zone	Very less inhibition zone	Very less inhibition zone

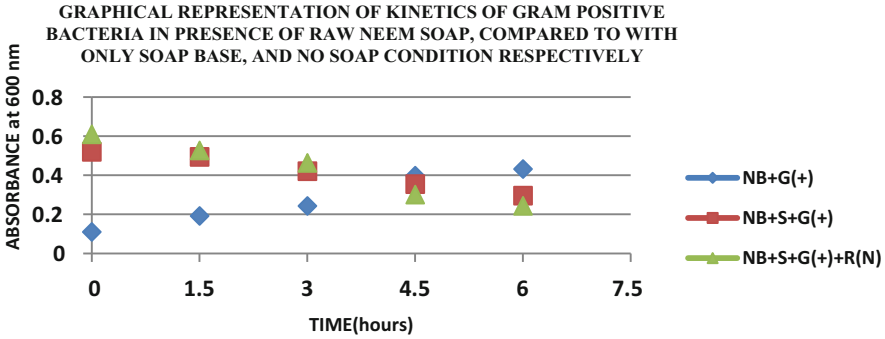

Graph 1 Graphical representation of absorbance at 600 nm for *Lactobacillus* culture in nutrient broth media containing raw neem soap solution at time interval of 1.5 h

3.3 Kinetics of Bacterial Growth in the Presence of Raw Neem Soap

For Gram-Positive Bacteria

It is observed from the graphical representation that with the absence of soap, the growth of gram-positive (G+) bacteria in NB media is gradually increasing with time.

In the presence of soap (S) and gram-positive bacteria in NB media, the growth is decreasing gradually with time which means the presence of soap inhibits the growth of gram-positive bacteria.

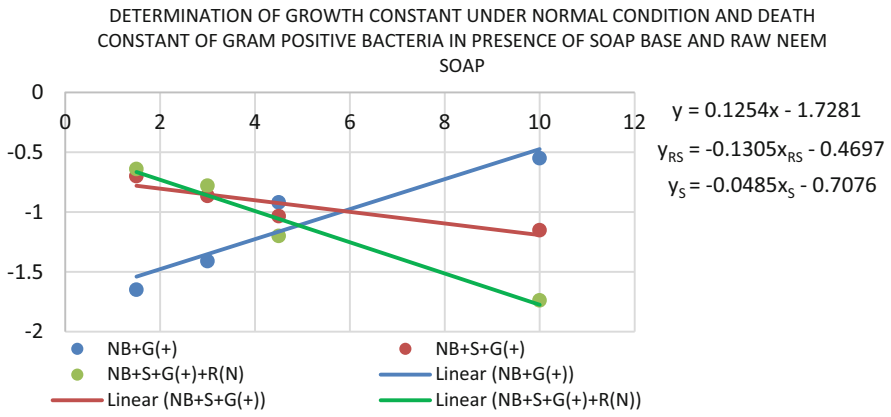

Graph 2 Graphical representation of logarithmic values of *Lactobacillus* culture in nutrient broth media containing raw neem soap solution at time interval of 1.5 h

In the presence of raw neem soap in NB media, the growth of gram-positive bacteria is decreasing gradually further as compared to the presence of only soap base, from which can be concluded that the presence of raw neem extract inhibits the growth of gram-positive bacteria furthermore.

Thus, it can be concluded that both soap base, as well as raw neem soap, has antimicrobial properties over gram-positive bacteria (Graph 2).

From the above graph, the growth of gram-positive (G+) bacteria in NB media gradually increases with time and in the presence of soap (S) and gram-positive (G−) bacteria in NB media, the growth gradually decreases with time. And in the presence of raw neem soap in NB media, the growth of gram-positive bacteria is decreasing gradually further as compared to the presence of only soap base.

From the growth curve equation without soap, the growth constant (μ_{max}) calculated was 0.125 $h^{-1,}$ from the growth curve equation with soap base, the death rate calculated (k_d) was -0.0485 h^{-1}, and that with soap base and raw neem extract was $-$ 0.1305 h^{-1}.

For Gram-Negative Bacteria

Absorbance was calculated after every 1.5 h interval with uninterrupted incubation in a floor shaker in between. The optical density readings are provided in the graphical format below.

It is observed from the graphical representation (Graph 3) that with the absence of soap, the growth of gram-negative (G−) bacteria in NB media is gradually increasing with time. In the presence of soap (S) and gram-positive bacteria in NB media, the growth is decreasing gradually with time which means the presence of soap inhibits the growth of gram-negative bacteria. In the presence of raw neem soap in NB media, the growth of gram-negative bacteria is decreasing gradually further as compared to the presence of only soap base, from which can be concluded that the

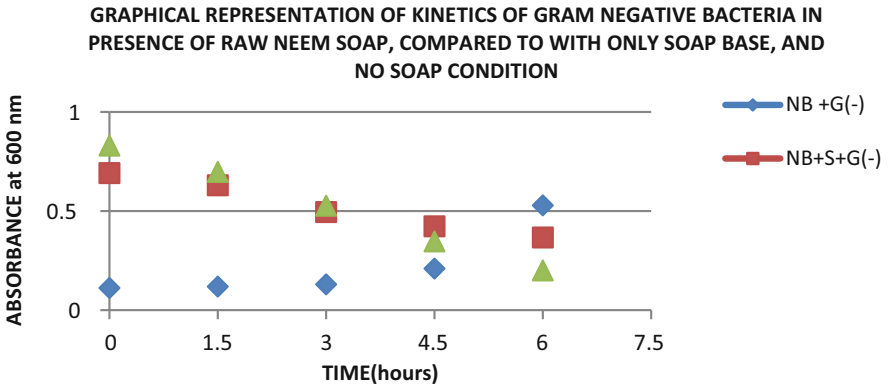

Graph 3 Graphical representation of absorbance at 600 nm for *Escherichia coli* culture in nutrient broth media containing raw neem soap solution at time interval of 1.5 h

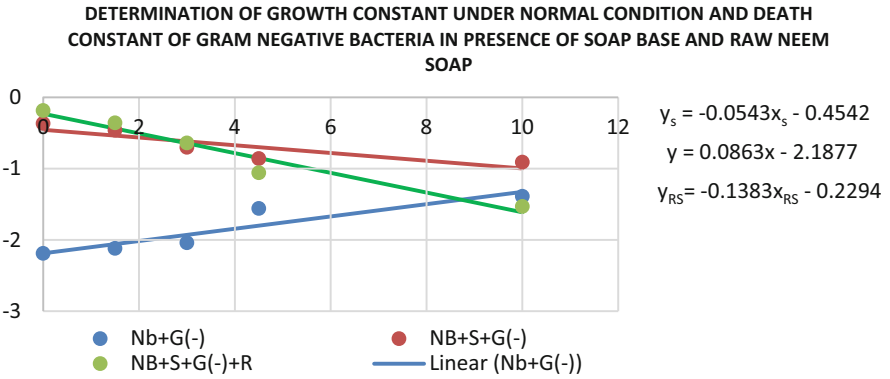

Graph 4 Graphical representation of logarithmic values of *Escherichia coli* culture in nutrient broth media containing raw neem soap solution at time interval of 1.5 h

presence of raw neem extract inhibits the growth of gram-negative bacteria furthermore. Thus, it can be concluded that both soap base and raw neem soap have antimicrobial properties over gram-positive bacteria.

From the above graph (Graph 4), the growth of gram-negative (G−) bacteria in NB media is gradually increases with time and in the presence of soap (S) and gram-negative bacteria in NB media, the growth is decreasing gradually with time. And in the presence of raw neem soap in NB media, the growth of gram-negative bacteria is decreasing gradually further as compared to the presence of only soap base.

From the growth curve equation without soap, the growth constant (μ_{max}) calculated was 0.086 $h^{-1.}$ from the growth curve equation with soap base, the death rate calculated (k_d) was −0.0543 h^{-1}, and that with soap base and raw neem extract was −0.1383 h^{-1}.

3.4 *Kinetics of Bacterial Growth in Presence of Raw Turmeric Soap*

We see from the graphical representation (Graph 5) that with the absence of soap, the growth of gram- positive (G+) bacteria in NB media is gradually increasing with time. In the presence of soap (S) and gram-positive bacteria in NB media, the growth is decreasing gradually with time which means the presence of soap inhibits the growth of gram-positive bacteria. In the presence of raw turmeric soap in NB media, the growth of gram-positive bacteria is decreasing in the same manner as compared to the presence of only soap base as both the slopes of the curves are almost equational. From this observation, it can be concluded that the presence of raw turmeric does not have antimicrobial properties, but it has other valuable properties. Thus, it can be concluded that raw turmeric soap does not have that much of antimicrobial properties over gram-positive bacteria.

From the Graph 6, the growth of gram-positive (G+) bacteria in NB media is gradually increasing with time and in the presence of soap (S) and gram-positive bacteria in NB media, the growth is decreasing gradually with time.

In the presence of raw turmeric soap in NB media, the growth of gram-positive bacteria is decreasing in the same manner as compared to the presence of only soap base, but the slope is somewhat lower than the former. However, turmeric cannot enhance microbial growth. Therefore, it might be due to some instrumental error. Thus, it can be concluded that raw turmeric soap does not have that much of antimicrobial properties over gram-positive bacteria. From the growth curve equation without soap, the growth constant(μmax) calculated was 0.0642 h^{-1}, from the growth curve equation with soap base, the death rate calculated (kd) was −0.025 h^{-1}, and that with soap base and raw turmeric extract was −0.1383 h^{-1}.

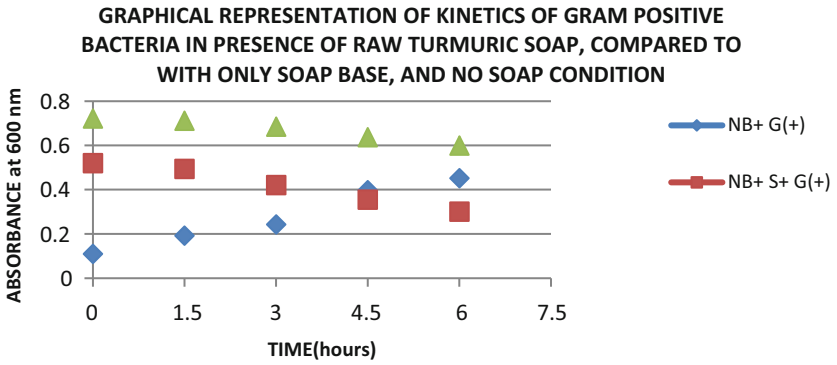

Graph 5 Graphical representation of absorbance at 600 nm for *Lactobacillus* culture in nutrient broth media containing raw turmeric soap solution at time interval of 1.5 h

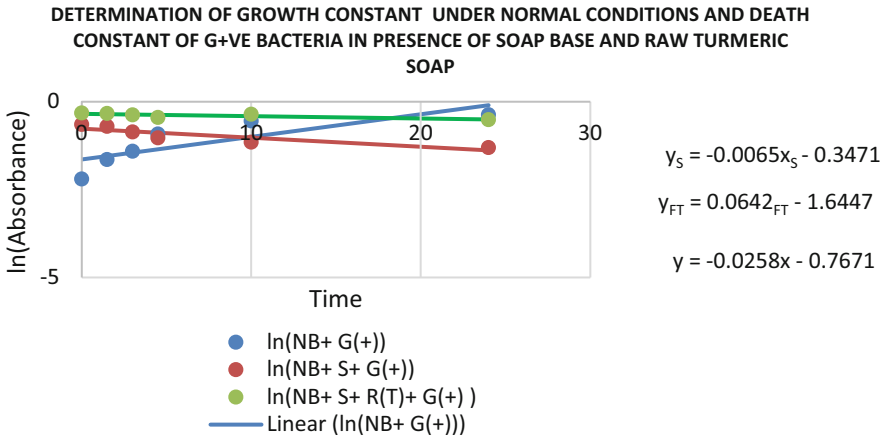

Graph 6 Graphical representation of logarithmic values of *Lactobacillus* culture in nutrient broth media containing raw turmeric soap solution at time interval of 1.5 h

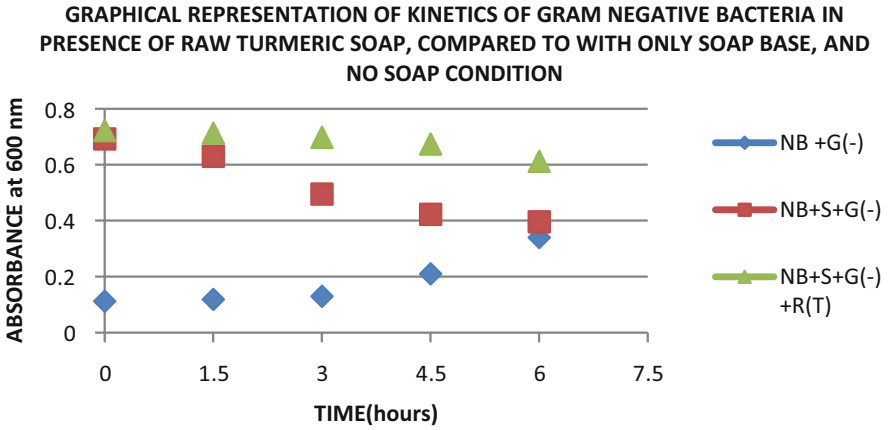

Graph 7 Graphical representation of absorbance at 600 nm for *Escherichia coli* culture in nutrient broth media containing raw turmeric soap solution at time interval of 1.5 h

For Gram-Negative Bacteria

It is observed from the graphical representation (Graph 7) that with the absence of soap, the growth of gram-negative (G−) bacteria in NB media is gradually increasing with time. In the presence of soap (S) and gram-negative bacteria in NB media, the growth is decreasing gradually with time which means the presence of soap inhibits the growth of gram-negative bacteria. In the presence of raw turmeric soap in NB media, the growth of gram-negative bacteria is decreasing in the same manner as compared to the presence of only soap base as both the slopes of the curves are almost equal. From this observation, it can be concluded that the presence of raw turmeric does not have antimicrobial properties, but it has other valuable properties.

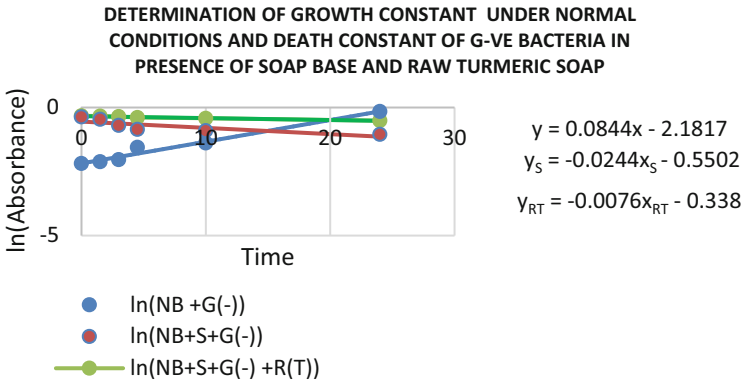

Graph 8 Graphical representation of logarithmic values of *Escherichia coli* culture in nutrient broth media containing raw turmeric soap solution at time interval of 1.5 h

Thus, it can be concluded that raw turmeric soap does not have that much of antimicrobial properties over gram-negative bacteria (Graphs 7 and 8).

From the above graph, the growth of gram-negative (G−) bacteria in NB media is gradually increasing with time and in the presence of soap (S) and gram-negative bacteria in NB media, the growth is decreasing gradually with time.

In the presence of raw turmeric soap in NB media, the growth of gram-negative bacteria is decreasing in the same manner as compared to the presence of only soap base but the slope is somewhat lower than the former. However, turmeric cannot enhance microbial growth. Therefore, it might be due to some instrumental error. Thus, it can be concluded that raw turmeric soap does not have that much of antimicrobial properties over gram-negative bacteria. From the growth curve equation without soap, the growth constant(μ_{max}) calculated is 0.0844 h^{-1} from the growth curve equation with soap base, the death rate calculated (k_d) is 0.0244 h^{-1}, and that with soap base and raw turmeric extract was −0.0076 h^{-1}.

3.5 *Determination of Efficacy of the Herbal Soap*

For neem extract, from MIC data for gram-positive bacteria (*Lactobacillus* sp.) (Table 5),

Efficacy of raw neem extract (MIC) with respect to alcohol for gram-positive bacteria = *Inhibitio n diameter in presence of raw neem extract* for gram-positive bacteria / *Inhibitio n diameter in presence of alcohol* for gram-positive bacteria

$$= \frac{2.06}{1.83} = 1.12.$$

Table 5 Inhibition diameters (in Cm) in gram-positive bacterial culture plate

Inhibition zone diameter for alcohol	Inhibition zone diameter for raw extract	Inhibition zone diameter for filtrate extract
1.80	2.10	2.50
1.90	2.00	2.65
1.80	2.10	2.40
Average = 1.83	*Average = 2.06*	*Average = 2.52*

Table 6 Inhibition diameters (in Cm) in gram-negative bacterial culture plate

Inhibition zone diameter for alcohol	Inhibition zone diameter for raw extract	Inhibition zone diameter for filtrate extract
1.60	1.90	1.90
1.60	1.70	2.10
1.50	2.10	2.00
Average = 1.56	*Average = 1.98*	*Average = 2.00*

Efficacy of filtrate neem extract (MIC) with respect to alcohol for gram-positive bacteria was 1.37. From the above observation, it can be inferred that efficacy of raw neem extract has better antimicrobial properties for gram-positive bacteria than alcohol. Efficacy of filtrate neem extract has better antimicrobial properties for gram-positive bacteria than alcohol.

From Kinetics Data for Gram Positive Bacteria (*Lactobacillus* sp.)
Efficacy of raw neem soap with respect to soap base for gram-positive bacteria

$$= \frac{\text{Death rate for gram postive bacteria in presence of raw neem soap}}{\text{Death rate for gram postive bacteria in presence of soap base}}$$
$$= \frac{0.1305}{0.0485} = 2.69$$

From the above observation, it can be inferred that efficacy of raw neem soap has better antimicrobial properties for gram-positive bacteria than soap base (Table 6).

From MIC Data for Gram-Negative Bacteria (*E. coli*)
Efficacy of raw neem extract (MIC) with respect to soap base for gram-negative bacteria

$$= \frac{\text{Inhibition diameter in presence of raw neem extract for gram-negative bacteria}}{\text{Inhibition diameter in presence of alchol for gram-negative bacteria}}$$
$$= \frac{1.70}{1.56} = 1.089$$

Efficacy of filtrate neem extract (MIC) with respect to alcohol for gram-negative bacteria was 1.28. Efficacy of raw neem extract (MIC) with respect to filtrate neem soap for gram-negative bacteria is 0.85.

From the above observation, it can be inferred that efficacy of raw neem extract has better antimicrobial properties for gram-negative bacteria than alcohol. Efficacy of filtrate neem extract has better antimicrobial properties for gram-negative bacteria than alcohol.

From Kinetics Data for Gram-Negative Bacteria (*E. coli*)
Efficacy of raw neem soap with respect to soap base for gram-negative bacteria

$$= \frac{\text{Death rate for gram negative bacteria in presence of raw neem soap}}{\text{Death rate for gram negative bacteria in presence of soap base}}$$
$$= 2.54$$

From the above observation, it can be inferred that efficacy of raw neem soap has better antimicrobial properties for gram-negative bacteria than soap base.

From the MIC data, we can conclude that, for both the gram-positive and gram-negative bacteria, in case of efficacy of extracts, filtrate neem extract showed better antimicrobial properties compared to raw neem extract, which might be as filtrate dissolved and spread over a greater area compared to raw extract due to presence of higher amount of fluid. However, from kinetics data, raw neem soap showed better results than filtrate neem soap. Thus, it can be concluded that raw neem extract has better antimicrobial properties than filtrate, but could not spread through plate for being more concentrated than filtrate extract.

4 Conclusion

This study focuses on a new herbal soap composition that incorporates neem leaf and turmeric extract. Preliminary phytochemical investigations revealed that the principal phytochemical elements with therapeutic activity are found in the neem leaf and turmeric extract. In a 32 g soap bar, the commercial herbal bath soap of choice contains 3.2 grams of herbal extract. This was used as a benchmark, and the soaps were created with lesser amounts (2.28 g, 1.5 g of extract for 32 g soap). Higher concentrations (16 g, 8 g, 6.4 g, 4 g of herbal extract for 32 g soap) were used to demonstrate efficacy. This research is looking into a novel herbal soap formulation that includes neem leaf and turmeric extract. The main phytochemical components with therapeutic potential are detected in neem leaf and turmeric extract, according to preliminary phytochemical analyses. The commercial herbal bath soap of choice contains 3.2 grams of herbal extract every 32 g soap bar. This served as a guideline, and the soaps were made with lower amounts (2.28 g, 1.5 g of extract for 32 g soap). To demonstrate efficacy, higher concentrations of herbal extract (16 g, 8 g, 6.4 g, 4 g for 32 g soap) were utilized. From the results obtained, the antibacterial activity of aqueous leaf extract on gram-positive *Lactobacillus* sp. was found to be more efficient when compared with gram-negative *Escherichia coli.*. Thus, the formulated soaps have shown good antibacterial activities when compared with the commercial soaps.

Acknowledgment This research work is supported by Department of Biotechnology, Heritage Institute of Technology, Kolkata, India.

References

1. S. Handayani, I.S. Arty, C. Budimarwanti, K. Theresih, E. Yulianti, M. Khairuddean, Preparation and antimicrobial activity analysis of organic soap Bar containing Gnetum gnemon Peel extract. Mol. Ther. **16**(3), 226 (2021). https://doi.org/10.20884/1.jm.2021.16.3.800
2. K. Ruckmani, R. Krishnamoorthy, S. Samuel, H.L.J. Kumari, Formulation of herbal Bath soap from Vitex negundo leaf extract. J. Chem. Pharm. Sci. **2**, 95–99 (2014)
3. Anoop MV, Hasna MP, Jaseena MH, Safna K, Sajna CV and Shamly MK. Anti-Microbial Evaluation of Herbal Soap Containing Neem Oil and Nalpamaradhi Oil. (2015)
4. J. Ridner, Green synthesis and characterisation of natural antiseptic soaps from the oils of underutilised tropical seed. Sustain. Chem. Pharm. **4**, 32–39 (2020). https://doi.org/10.1016/j.scp.2016.07.006
5. A.R. Vaughn, A. Branum, R.K. Sivamani, Effects of turmeric (Curcuma longa) on skin health: A systematic review of the clinical evidence. Phytother. Res. **30**(8), 1243–1264 (2016). https://doi.org/10.1002/ptr.5640
6. N. Wongthongdee, P. Inprakhon, Stability of turmeric constituents in natural soaps. Sci. Asia **39**(5), 477 (2013). https://doi.org/10.2306/scienceasia1513-1874.2013.39.477
7. H. Gopinath, K. Karthikeyan, Turmeric: A condiment, cosmetic and cure. Indian J. Dermatol. Venereol. Leprol. **84**(1), 16 (2018). https://doi.org/10.4103/ijdvl.ijdvl_1143_16
8. O. Atolani, O. Atolani, E.T. Olabiyi, A.A. Issa, H.T. Azeez, E.G. Onoja, S.O. Ibrahim, M.F. Zubair, O.S. Oguntoye, G.A. Olatunji, Chemical characterization, antioxidant, cytotoxicity, anti-toxoplasma gondii and antimicrobial potentials of the *Citrus sinensis* seed oil for sustainable cosmeceutical production. Heliyon **6**(2), e03399 (2020). https://doi.org/10.1016/j.heliyon.2020.e03399

Decolorization of Textile Dye RR 141 Using Electrochemical Process

Budhodeb Biswas and Chanchal Majumder

Abstract The treatment of industrial effluent is currently one of the top most priorities to the research community. One of the main constituents of textile industrial effluent is Reactive Red 141 (RR 141), and it is a major contributor of color to wastewater streams. RR141 is a diazo reactive dye with a vivid red color, a massive molecular structure ($C_{52}H_{26}Cl_2N_{14}Na_8O_{26}S_8$), and reactive group such as sulfonic ($-SO_3Na$). Due to carcinogenic effect and bioaccumulation property, the higher trophic level animals especially human beings are at a stake. Hence, in this study electrochemical process (EP) with two separate chambers (i.e., anodic and cathodic cells) separated by an earthen pot was used to remove RR 141 dye from synthetic dye solution. The effect of pH and time was studied and reported. Our study revealed that at low pH, the color removal is higher, and it was seen that 98.3% of RR 141 color removal can be achieved at a pH and current of 2.16 and 0.5A, respectively, over 60 min of EP operation. Hence, decolorization of RR 141 can be done effectively using two compartment electrochemical cells.

Keywords Decolorization · Earthen pot · Electrochemical process (EP) · Graphite electrode · Reactive Red 141 · Textile dye · Water pollution

Abbreviations

AO	Anodic oxidation
BEF	Bio-Electro Fenton
EAOPs	Electrochemical advanced oxidation processes
EF	Electro Fenton
EP	Electrochemical process
MFC	Microbial fuel cell

B. Biswas (✉) · C. Majumder
Department of Civil Engineering, Indian Institute of Engineering and Science Technology (IIEST), Shibpur, Howrah, West Bengal, India
e-mail: chanchal@civil.iiests.ac.in

D. Mazumder (ed.), *Sustainable Advanced Technologies for Industrial Pollution Control*, Springer Proceedings in Earth and Environmental Sciences,
https://doi.org/10.1007/978-3-031-37596-5_29

PEF Photo-Electro Fenton
RR141 Reactive Red 141
SEF Sono-Electro Fenton

1 Introduction

The textile industry uses a significant amount of water and produces wastewater that contains unconsumed colors and their components. The quantities of organic and inorganic contaminants such as harmful metals, detergents, and dyes have drastically grown in all sorts of water resources as a result of the increased discharge of textile industrial effluent [1, 2]. The major environmental repercussions of the textile sector are air and water pollution. In terms of resource utilization, the textile manufacturing process uses freshwater, energy, and other precious resources [3]. Various synthetic colors such as acid dyes, basic dyes, and reactive dyes are used daily, depending on consumer demand. More than 10,000 commercial colors are predicted to be used by the textile and manufacturing industries worldwide. To meet industrial demand, almost 1.6 million tonnes of dyes are produced each year; roughly 10–15% of this quantity is disposed away as wastewater [4]. The most popular dyes in the textile business are reactive dyes. The majority of reactive dyes have an azo group (-N=N-) in their structural formula. The majority of industries dump wastes including colors, chemicals, and chemical derivatives into water streams. These effluents generate a number of challenges for the ecosystem, including the destruction of the food chain and food web as well as health risks. Colorants come in two different varieties: natural and synthetic dyes. But because certain mordants must be employed with them, even natural colors are rarely low-impact. Mordants are compounds that "fix" color onto the fabric, like chromium [5]. They could be extremely hazardous and could have a significant effect on the effluent quality. Azo dyes are identified by the presence of one or more azo groups. The sulfonic acid group is a substituent that is typically present in azo dyes ($–SO_3H$), for example, ($-SO_3Na$) is present in RR 141 as shown in Fig. 1. Sulfonated and unsulfonated azo dyes are poisonous, carcinogenic, and mutagenic substances and some of their components and biodegraded by-products have a detrimental impact on wastewater [6].

Due to the high solubility of the dyes, which is primarily supported by sulfonic groups, the usual treatment procedures of precipitation and coagulation are inefficient to eliminate these organic contaminants. Due to financial considerations, the biological approach is quite intriguing; yet, when azo dyes (-N=N-) are treated aerobically, the removal effectiveness is quite low. The main disadvantages of the biological treatment include its restrictions due to factors such as pH, salt content, carbon sources, and lengthy treatment durations [7]. Electrochemical advanced oxidation processes (EAOPs) have a lot of potential for dye removal from water-based media. The well-known direct EAOPs, anodic oxidation (AO) is particularly effective at removing colors from aqueous solutions [8]. Electro Fenton (EF), Photo-Electro Fenton (PEF), Sono-Electro Fenton (SEF), peroxi-coagulation, and other

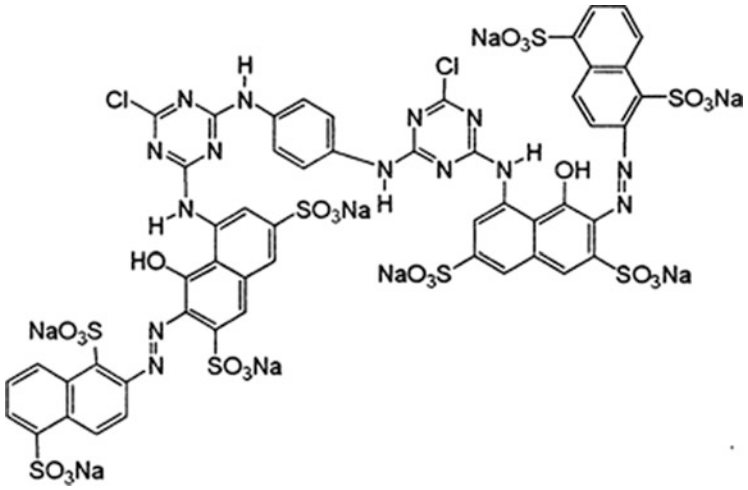

Fig. 1 Chemical structure of RR 141 dye

Fenton process-based EAOPs have all been used successfully to remove dyes [8, 9]. Combined biological process with EAOPs is also a new drift in this field. In Bio-Electro Fenton (BEF), the dye removal takes place by the principle of Microbial Fuel Cell (MFC) due to formation of $OH^{\bullet}$ radicals [10]. However, the BEF process requires more time than the EF process to remove dyes. In electrochemical techniques, notably electrochemical oxidation can be utilized successfully, possibly with high organic removal rates with minimum operating constraints [11]. To accomplish high removal, appropriate electrode material selection and operating conditions are necessary. Furthermore, it is possible to successfully combine various techniques to remove the organic load [12]. In this study, graphite electrodes were used because of chemical inertness, high electrical conductivity, high temperature resistance, and low cost to decolorize RR 141 in a two-compartment electrochemical cell separated by an earthen pot.

2 Materials and Methods

2.1 Experimental Setup

The batch experiments were carried out in a borosilicate beaker of 2000 mL capacity within which one earthen pot was kept to separate the cathode and the anode chamber. The earthen pot has an inner diameter of 80 mm and depth of 115 mm. The graphite electrodes used in cathode and anode were 305 mm long and 10 mm in diameter. The space between the electrodes was 60 mm. The effective electrode area was 17.28 cm^2. The electrodes were connected to a digital DC power supply (scientific 30 V, 5A power supply PSD 3005) to apply desired current for treatment. Reactive Red 141 dye was bought from Modi Dye Chem, Kolkata, West Bengal-

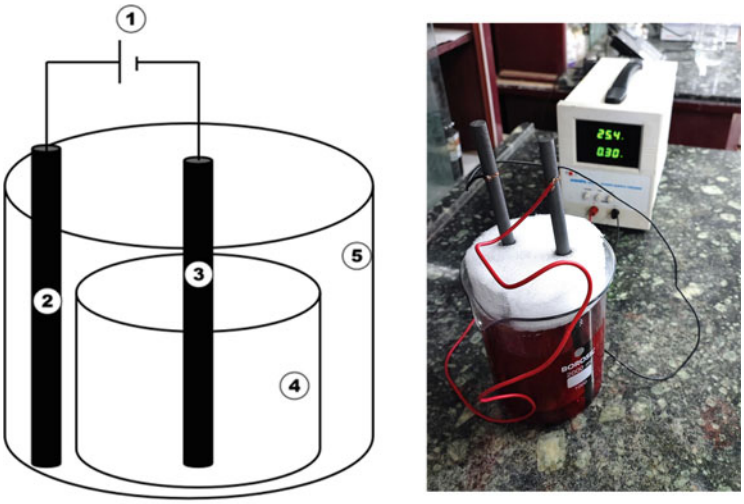

Fig. 2 (**a**) Schematic diagram: 1-DC power supply; 2-Anode (graphite electrode); 3-Cathode (graphite electrode); 4-Cathodic cell (earthen pot); 5-Anodic cell (glass beaker). (**b**) Original experimental setup

700001. The total sample volume for each run was 1400 mL of which 600 mL is in cathodic cell and 800 mL is in anodic cell. A schematic diagram of the experimental setup along with original experimental setup for the EC reactor is shown in Fig. 2.

2.2 Analytical Procedure

Measurement of RR 141 dye was done by Smart UV-Vis Double Beam Spectrophotometer (Systronics, model 2203, India). For the construction of the standard curve, a stock solution containing 200 mg/L of RR 141 was created, and all other working solutions were made from this standard solution by progressive dilution. A scanning of RR 141 of concentration 100 mg/L was done to obtain the maximum absorption peak within the wavelengths (λ) ranging from 500 nm to 550 nm. The maximum absorption peak was obtained at wavelength, $\lambda = 535$ nm and the absorbance value was 1.469. Nine different concentration values ranging from 0 to 80 mg/L were prepared and a standard curve was produced. Linear relation between concentration and absorbance was obtained up to a concentration value of 80 mg/L. The standard curve prepared showed following relation:

$$y = 0.0106x + 0.018 \tag{1}$$

Where, x = concentration of RR141 (mg/L) and y = absorbance. Equation (1) had a good correlation coefficient (r^2) = 0.997. The calibration curve is shown in Fig. 3.

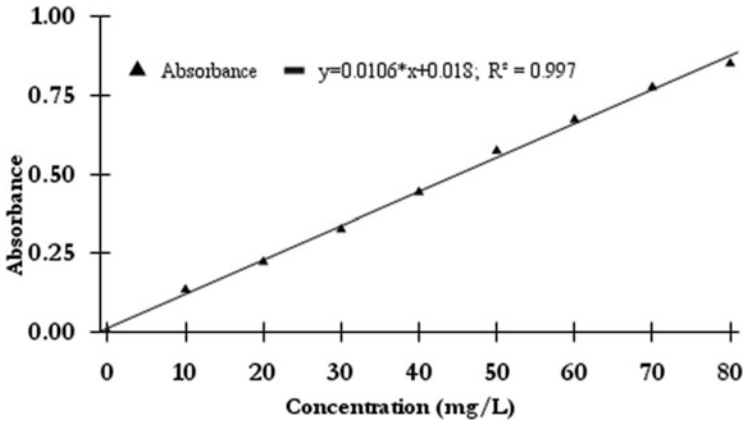

Fig. 3 Calibration curve for Reactive Red 141 dye

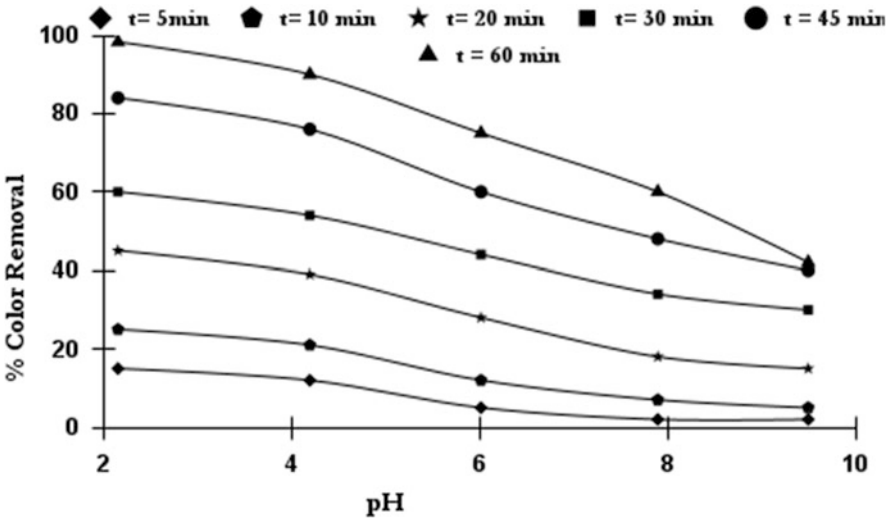

Fig. 4 Influence of pH on percentage color removal at cathodic cell

2.3 Influence of pH

The study on the influence of pH for color elimination from RR 141 was carried out in a borosilicate beaker of 2000 mL capacity having active volume 1400 mL. The pH study was carried out at varying pH ranging from 2 to 10. The required pH was adjusted by adding required amount of 0.1 M NaOH/HCl in the solution. All the studies were carried out for a time interval of 60 min. The applied current was maintained 0.5A. The influence of pH on percent color removal at cathodic and anodic cell was shown in Figs. 4 and 5, respectively.

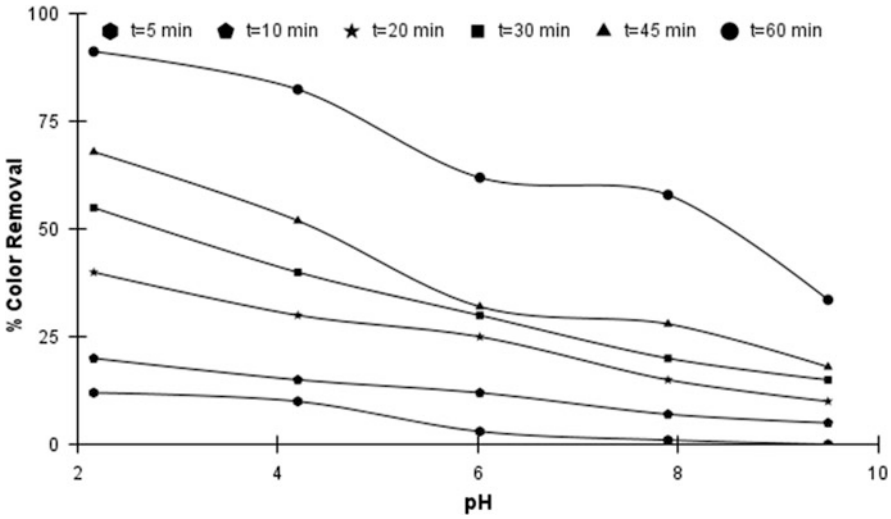

Fig. 5 Influence of pH on percentage color removal at anodic cell

2.4 Influence of Time

The influence of time on color elimination from RR 141 was also carried out in the same experimental condition except the time was varied from 0 to 60 min. The percentage color removal for varying time interval was determined and reported. The influence of time on percent color removal at cathodic and anodic cellwas shown in Figs. 6 and 7, respectively.

3 Results and Discussion

3.1 Influence of pH

The influence of pH on color removal from RR 141 at cathode and anode cell was shown in Figs. 4 and 5, respectively. It was observed from the figures that as the solution pH was increased, the percentage color removal was decreased. On the contrary, the color removal was increased with decreasing pH. Here pH of the solution was lowered by using 0.1 M HCl, which might act as a chlorine precursor during electrochemical process. Hence, at lower pH, generation of nascent chlorine at anode during electrochemical process took place. In the subsequent stage, this chlorine combined with water to form HOCl at lower pH and higher removal was achieved. At lower pH, HOCl generated has an oxidation potential of +1.8 V, which is higher than other chloro-oxidant species. Due to in situ generation of chlorine, the oxidative strength remains high and color removal took place.

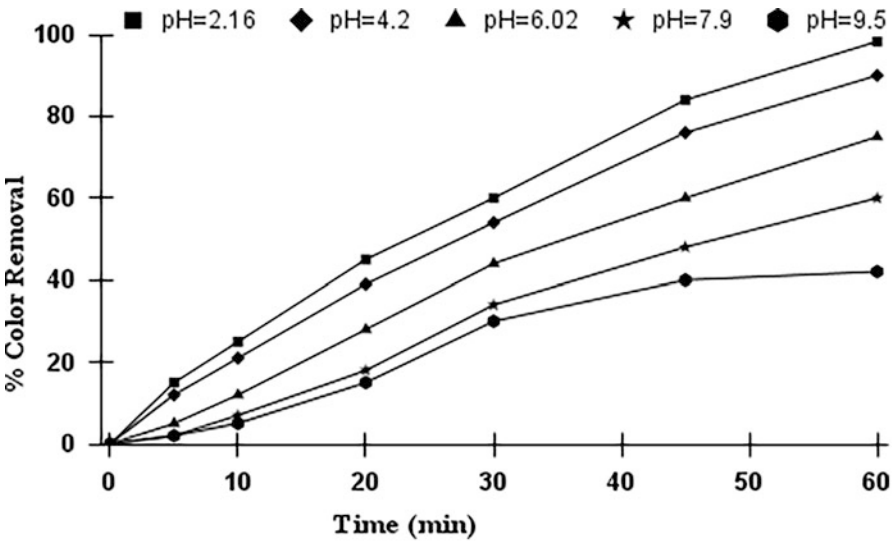

Fig. 6 Influence of operating time on percentage color removal at cathodic cell

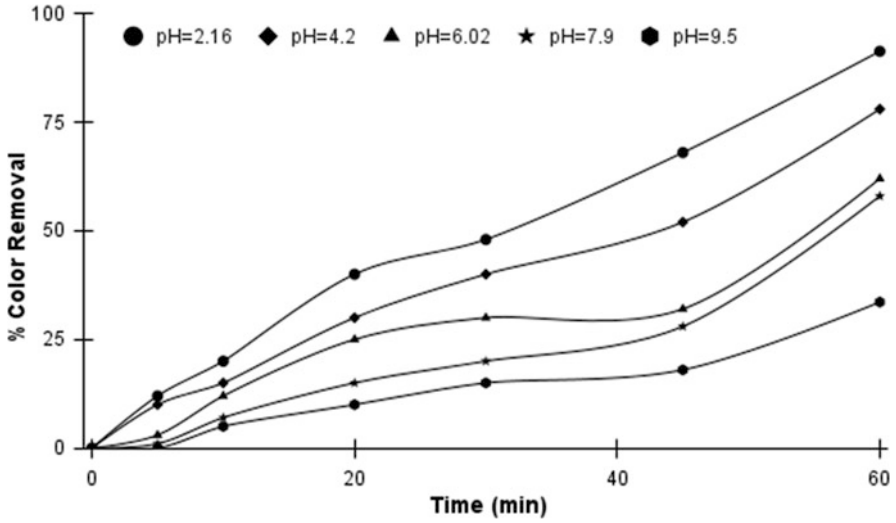

Fig. 7 Influence of operating time on percentage color removal at anodic cell

At basic circumstances (pH > 7.5), the OCl^- species, a feebler oxidant than HOCl, is more likely to develop. Hence, at higher pH level, color removal achieved was not significant. Other chloro-oxidants species (such as ClO^{3-} and ClO^{4-}) with higher oxidation states can also be created in basic conditions (at a higher pH), but they are unable to oxidize dye molecules due to their extremely low oxidation potential (−0.33 V to −0.36 V) [13]. This may be the reason for low removal at

higher pH. Thus, at both anode and cathode the color removal was significantly higher at low pH as compared to higher pH. Comparing Figs. 4 and 5, it was also clear that at lower pH the color removal at cathode was slightly more than that of anode. This may be due to the reason that at cathode, the azo bond (-N=N-) might have broken by reacting with H^+ in solution and reduction on cathode surface by electrons. Reduction by electrons and H^+ ions, the azo bond might have broken down and formed aryl amine such as (Ar-HN-NH-Ar′), where Ar an Ar′ are aryl groups. Similar mechanism was reported by other researchers [14].

3.2 Influence of Time

The influence of time on color elimination from RR 141 at anode and cathode cell was shown in Figs. 6 and 7, respectively. It was clear from the figures that with increasing time of operation, both anode and cathode removed higher amount of color. This may be due to increase in charge density as the time was increased for a constant current of 0.5 A. It was also clear from the figures that at lower pH the color removal at cathode was marginally higher than that of anode corresponding to same time of operation. Solutions, which were at low pH, were showing better results toward color removal than those at higher pH.

4 Conclusion

In this study, UV-Vis Double Beam spectrophotometer was used to monitor the decolorization of RR 141 from synthetic dye solution. From this study, it was clear that at low pH (pH < 4), the color removal of RR 141 dye was higher. The cathodic and anodic removal of color was 98.3% and 91.3%, respectively. The color removal of RR 141 at cathodic and anodic cell can be achieved at a pH and current of 2.16 and 0.5A, respectively, over 60 min of EP operation. The decolorization of RR 141 was dependent on initial pH, applied current, and operating time on the synthetic sample. Similarly, it was also observed that with increasing EP operating time, the percentage color removal increased. The removal at anode perhaps was due to the formation of different chloro-oxidants at different pH [14]. However, in case of cathodic cell, the removal might be due to the formation of H^+ ions at the cathode that helped in electro reduction of the azo linkage to form aryl amines. Hence, decolorization of RR 141 can be done effectively using two compartment electrochemical cells. Further detailed study with different combinations of parameters such as time, applied current, sample volume, dye concentration, and electrode material are required to develop a mathematical model and optimization of the process parameters.

Acknowledgment This research project is funded by the Ministry of Human Resource Development, Government of India, under the Research Fellowship Program.

References

1. S. Al Arni, S. Ghareba, C. Solisio, M.S. Alves Palma, A. Converti, Methods of reactive red 141 dye decolorization, treatment, and removal from industrial wastewaters: A critical review. Environ. Eng. Sci. **38**(7), 577–591 (2021)
2. H. Hafdi, M. Joudi, J. Mouldar, B. Hatimi, H. Nasrellah, M.A. El Mhammedi, M. Bakasse, Design of a new low cost natural phosphate doped by nickel oxide nanoparticles for capacitive adsorption of reactive red 141 azo dye. Environ. Res. **184**, 109322 (2020)
3. S. Bathrinath, R.K. Bhalaji, S. Saravanasankar, Risk analysis in textile industries using AHP-TOPSIS. Mater. Today Proc. **45**, 1257–1263 (2021)
4. J.M. Bidu, B. Van der Bruggen, M.J. Rwiza, K.N. Njau, Current status of textile wastewater management practices and effluent characteristics in Tanzania. Water Sci. Technol. **83**(10), 2363–2376 (2021)
5. S. Saxena, A.S.M. Raja, Natural dyes: Sources, chemistry, application and sustainability issues, in *Roadmap to Sustainable Textiles and Clothing*, (Springer, Singapore, 2014), pp. 37–80
6. A. Telke, D. Kalyani, J. Jadhav, S. Govindwar, Kinetics and mechanism of reactive red 141 degradation by a bacterial isolate rhizobium radiobacter MTCC 8161. Acta Chim. Slov. **55**(2), 320–329 (2008)
7. A. Pandey, P. Singh, L. Iyengar, Bacterial decolorization and degradation of azo dyes. Int. Biodeterior. Biodegradation **59**(2), 73–84 (2007)
8. A.M. Faouzi, B. Nasr, G. Abdellatif, Electrochemical degradation of anthraquinone dye Alizarin Red S by anodic oxidation on boron-doped diamond. Dyes Pigments **73**(1), 86–89 (2007)
9. S. Vasudevan, M.A. Oturan, Electrochemistry: As cause and cure in water pollution—An overview. Environ. Chem. Lett. **12**, 97–108 (2014)
10. H. Olvera-Vargas, T. Cocerva, N. Oturan, , D. Buisson and M.A. Oturan, "Bioelectro-Fenton: A sustainable integrated process for removal of organic pollutants from water: Application to mineralization of metoprolol," J. Hazard. Mater., vol. 319, pp. 13–23, 2016
11. B.Y. Chen, M.M. Zhang, C.T. Chang, Y. Ding, W.M. Chen, C.C. Hsueh, Deciphering azo dye decolorization characteristics by indigenous Proteus hauseri: Chemical structure. J. Taiwan Inst. Chem. Eng. **42**(2), 327–333 (2011)
12. C.I. Pearce, J.R. Lloyd, J.T. Guthrie, The removal of colour from textile wastewater using whole bacterial cells: A review. Dyes Pigments **58**(3), 179–196 (2003)
13. J.M. Aquino, R.C. Rocha-Filho, M.A. Rodrigo, C. Sáez, P. Cañizares, Electrochemical degradation of the Reactive Red 141 dye using a boron-doped diamond anode. Water Air Soil Pollut. **224**(1), 1–10 (2013)
14. K. Rajeshwarand, J.G. Ibanez, *Environmental Electrochemistry: Fundamentals and Applications in Pollution Sensors and Abatement* (Elsevier, 1997)

Index

D. Mazumder (ed.), *Sustainable Advanced Technologies for Industrial Pollution Control*, Springer Proceedings in Earth and Environmental Sciences,
https://doi.org/10.1007/978-3-031-37596-5